



INDIRA GANDHI CENTRE FOR ATOMIC RESEARCH

Golden Jubilee (1971-2021)

ANNUAL REPORT 2020



Government of India
Department of Atomic Energy
Indira Gandhi Centre for Atomic Research
Kalpakkam - 603 102

IGCAR

2020

INDIRA GANDHI CENTRE FOR ATOMIC RESEARCH

ANNUAL REPORT



Government of India
Department of Atomic Energy
Indira Gandhi Centre for
Atomic Research
Kalpakkam 603 102

Editorial Committee**Chairman**

Ms. S. Rajeswari

Members

Dr. John Philip

Dr. T. R. Ravindran

Dr. C. V. S. Brahmananda Rao

Shri A. Suriyanarayanan

Shri M. S. Bhagat

Shri G. Venkat Kishore

Dr. Girija Suresh

Shri M. Rajendra Kumar

Shri S. Kishore

Shri Biswanath Sen

Dr. N. Desigan

Shri Gaddam Pentaiah

Shri K. Varathan

Member-Secretary

Dr. V. S. Srinivasan

CONTENTS

Foreword

Editorial

Articles at a Glance

I. Fast Breeder Test Reactor & Kalpakkam Mini Reactor	1
II. Prototype Fast Breeder Reactor	15
III. R&D for Fast Breeder Reactors	45
IV. Fuel Cycle	93
V. Basic Research	127
VI. Directed Basic Research	145
VII. Infrastructure, Resource Management & Biodiversity	171
VIII. Awards/Publications/Events/Organisation	205

Address for Correspondence

Ms. S. Rajeswari

Chairman, Editorial Committee

Head, Scientific Information Resource Division

Indira Gandhi Centre for Atomic Research

Kalpakkam - 603 102

Phone : +91-44-27480281

Email : raj@igcar.gov.in

e-Copy available at: <http://www.igcar.gov.in>

Published by

Scientific Information Resource Division, SQ&RMG,
Indira Gandhi Centre for Atomic Research, Kalpakkam - 603 102

Golden Jubilee Year of IGCAR



Dr. Vikram Ambalal Sarabhai

(August 12, 1919 - December 30, 1971)

Dr. Vikram Ambalal Sarabhai was a physicist and from a family of industrial entrepreneurs. He was the founding father of India's Space Programme. In 1966, Sarabhai was appointed as the chairman of the Atomic Energy Commission of India. Sarabhai chalked out a '10-year Action Plan for Atomic Energy' to expand nuclear power activities by leveraging indigenous technology and international cooperation to set up nuclear reactors.

He consolidated many atomic energy R&D units during 1966-1969 into new public sector undertakings for sustained progress in the nuclear power program. They are Heavy Water Board for Heavy water production critical to the operation of a nuclear reactor, Electronics Corporation of India, Uranium Corporation of India for extraction of Uranium, Nuclear Fuel Complex for the fabrication of Uranium fuel elements and a Power Projects Engineering Division, for building and operating of advanced power reactors.

On 30th April 1971, Dr. Vikram Sarabhai approved the formation of Reactor Research Centre to pursue R&D in fast reactors by an executive order, which was later renamed as Indira Gandhi Centre for Atomic Research in 1985.

Dr. Sarabhai was awarded the Padma Bhushan (1966) and the Padma Vibhushan (posthumously in 1972).

Foreword



Dear Colleagues,

It is my pleasure to share with you the Annual report of IGCAR for 2020. The achievements of this Centre towards realizing the mission oriented programmes on Fast Reactor and associated closed fuel cycle technologies in the year 2020 are listed in this report.

Towards obtaining regulatory clearance for operating FBTR at its rated power of 40 MWt, neutronic parameters were estimated and the safety of plant was demonstrated under all the anticipated events. In spite of challenges, stagnant sodium in sodium flooding system of FBTR was successfully purified by integrating a purification system. On material front, it was demonstrated that WC can be used as a lower axial shielding material in the fuel sub-assemblies of FBTR to reduce the neutron dose to grid plate for extending its life.

The U-233 fuelled Kalpakkam mini reactor (KAMINI) continued its successful operation for neutron radiography, radiation physics research, calibration and testing of neutron detectors etc. AERB/SARCOP has recently approved the new technical specification limit arrived at by KAMINI and with this limit, KAMINI can continue serving its users with prolonged irradiation requirements.

IGCAR continued its technical support towards design and development of Prototype Fast Breeder Reactor. R&D activities for fast Breeder Reactors focused on performance evaluation of materials, components and systems, development of Non-Destructive inspection

procedures, and studies on protective layer for core catcher to name a few.

The Compact facility for reprocessing of advanced fuels (CORAL) has completed scheduled number of reprocessing campaigns of FBTR spent fuel with very significant reduction in man-rem expenditure. At DFRP, radiation monitoring systems for stack effluent were commissioned and special lighting systems for lead wall shielded hot cells were developed.

Civil construction of nuclear plant buildings for the integrated and self contained Fast Reactor Fuel Cycle Facility (FRFCF) is in the advanced stage of completion. Mega pours involving the cumulative concreting of 4.93 lakhs cu. m and about 7280 cu.m. of heavy density concrete for waste tank form have been completed. Several components are being received and all equipments in analytical certification lab have been installed and commissioned.

Commissioning of injection casting system for fabrication of binary metal alloy fuel slugs, in MCMFCG and study of various chemical processes pertaining to fuel cycle are some of the other notable achievements.

Basic and applied research in IGCAR covers various domains including developing new materials, sensors & processes and studies on physical, chemical and mechanical properties of materials. There are also important contributions on dosimetry and performance evaluation of gamma CT system used to characterize nuclear waste.

As member of the Indian mission program consortium for advanced ultra-super-critical thermal power plants, it is a matter of great pride that DAE units have produced for the first time 10-meter long Alloy 617M boiler tubes starting from melting to final deployment for testing in a specially designed high-temperature loop in an operating power plant. Special welding and nondestructive technologies for the manufacture and inspection of large mono-metallic and bi-metallic forged and cast components have also been developed.

Various resources and infrastructure facilities have been developed to support R&D activities of the centre. This includes, Vi-meet, an indigenous Video Conferencing solution, development of hardware & software modules for various applications and refurbishment and maintenance of plants. In addition, IGCAR subscribed e-resources have been made available on the mobile app for the benefit of the research scholars. Further, we have been successful in meeting the quality of human resources through

Training School, Training Centre and HBNI. There are also interesting articles on biodiversity in this report.

Aligning with the Government's mission of Atma Nirbhar Bharat and the DAE's initiative of setting up of incubation centers to facilitate in-house technology promotion and transfer, Incubation Centre, IGCAR has been remotely inaugurated by Chairman, AEC and Secretary DAE on 30th October 2020, the 111th birth anniversary of Dr. Homi Jehangir Bhabha.

I take this opportunity to appreciate the editorial committee for their earnest and dedicated efforts in bringing out the annual report with the expected quality. As always, we look forward to the feedback from the readers.



(Arun Kumar Bhaduri)
Distinguished Scientist
& Director, IGCAR

Our Primary Mission

To conduct a broad based multidisciplinary programme of scientific research and advanced engineering development, directed towards the establishment of the technology of Sodium Cooled Fast Breeder Reactors (FBR) and associated fuel cycle facilities in the Country. The mission includes the development and applications of new and improved materials, techniques, equipment and systems for FBRs, pursue basic research to achieve breakthroughs in Fast Reactor technology.

Editor's Desk



Dear Reader,

I am pleased to present the Annual Report of IGCAR for the year 2020 as the Editorial Committee Chairman. The Annual Report represents a blend of mission-oriented R&D activities and basic research of the Centre.

This year, the Annual Report has 149 technical articles. The articles have gone through multiple editing stages to ensure accuracy and readability. The articles are grouped into chapters to highlight the activities specific to FBTR & KAMINI, PFBR, R&D for FBRs, Fuel Cycle, Basic Research, Directed Basic Research, Infrastructure, Resource management, Biodiversity, and compilation of events, seminars, awards, etc. I convey my sincere thanks to the Editorial Committee for their dedicated efforts in successfully bringing out the Annual Report.

Chapter-I FBTR & KAMINI has articles on the research reactors of IGCAR. The neutronic and safety analysis were carried out towards the transition from 32 MWt to the full-rated power level of 40 MWt of FBTR. Besides, the chapter includes studies on enriched Boron Carbide, Irradiation studies on shielding materials in FBTR, decay heat measurement, and establishing the safe operating limit for the continued operation of KAMINI.

Chapter-II PFBR is in its advanced stage of commissioning and has an article on the present status. The other articles highlight the R&D contribution of the Centre towards the commissioning of PFBR.

Chapter-III R&D for FBRs has articles on the Centre's efforts towards developing indigenous technology for future nuclear reactor programs.

Chapter-IV Fuel Cycle includes studies related to the design, development, and commissioning of various sub-systems in FRFCF, CORAL, and DFRP.

Chapter-V Basic Research contains articles covering the development of new materials for various applications and novel characterization studies.

Chapter-VI Directed Basic Research refers to the outcome of activities that have immediate applications. This chapter has articles on developing high-temperature alloys and product forms for AUSC applications, creep and fatigue studies on reactor structural materials, research towards environmental and societal applications, and the beneficial/deleterious effect of oxidation on performance of materials.

Chapter-VII Infrastructure, Resource Management, and Biodiversity is a chapter that highlights the efforts & developments to deal with the pandemic situation effectively, public awareness, biodiversity documentation, augmentation and infrastructure management in 2020.

Chapter-VIII details the Publications, the events, awards, meetings, etc., in 2020.

We welcome feedback from readers both concerning the quality of the presentation and the technical content therein. We thank the Group Directors for their support and the enthusiastic authors for providing quality articles in the stipulated time. The committee sincerely thanks Dr. Arun Kumar Bhaduri, Director, IGCAR, for his keen interest and continued guidance. The committee also thanks Dr. B. Venkatraman, Director, SQ&RMG, for the support and suggestions rendered from time to time.

S.Rajeswari
Chairman, Editorial Committee &
Head, Scientific Information Resource Division

Homage to Padma Shri Dr. Sekhar Basu



Padma Shri Dr. Sekhar Basu, former Chairman, Atomic Energy Commission and Secretary to Government of India, Department of Atomic Energy (DAE), from 23 October 2015 to 17 September 2018, passed away on 24-09-2020. He was the Director of Bhabha Atomic Research Centre (BARC), India's premier multi-disciplinary R&D centre from June 19, 2012. He has also worked as the Nuclear Submarine Program's Project Director and later as the Nuclear Recycle Board's Chief Executive in the same institute.

Dr. Sekhar Basu is one of the architects of India's 80 MWt compact Pressurised Water Reactor (PWR), which powers Arihant, the country's nuclear-powered submarine. He had proactively engaged in the design, development, construction, and operation of nuclear recycle plants at Tarapur, Maharashtra and Kalpakkam, Tamil Nadu, involving reprocessing and nuclear waste management. His efforts are credited with bringing perfection in technology, which provided a significant boost to the Indian nuclear power programme.

He had accelerated Nuclear Power deployment in India by getting the approval to construct 10 Pressurized heavy-water reactors (PHWRs) and 2 Pressurized water reactors (PWRs). Under his supervision, DAE has initiated actions for a multi-fold rise in India's uranium exploration and mining.

He initiated, construction/up-gradation of six hospitals for serving about 1.5 Lakh new patients every year. A major thrust has been imparted for the development of indigenous cancer care drugs. He has supervised setting up the first plant in India to be commissioned to treat 100 tons/day sludge and produce manure using a fully automatic process at Ahmedabad, Gujarat. The plant uses radiation technology to cleanse the sludge reliably and affordably and protects health and environment.

Mega science projects involving high energy Superconducting Accelerators, Laser Interferometer Gravitational-wave Observatory (LIGO), International Thermonuclear Experimental Reactor (ITER) have got major boost under the leadership of Dr. Sekhar Basu. He focused on pursuing basic research in science & engineering and other strategic programmes on priority. He has strengthened the public outreach activities for spreading awareness about the technologies fostered by DAE among the general public.

Dr. Sekhar Basu was at Kalpakkam for over 18 years and was passionate about this place. He was instrumental in according the approval for the construction of the Palar Check dam at Vayalur near Kalpakkam, which has improved the water table in the area and helped the farm cultivation increase many folds. He has been awarded Honoris Causa Doctorate degrees by 8 universities and was awarded Padma Shri by the Government of India in 2014.

He was a true visionary, a brilliant technologist & a great nuclear scientist par excellence. His untimely demise is a great loss to the DAE fraternity and nation.

I. Fast Breeder Test Reactor & KAlpakkam MINI reactor

Sl.No	Title
1.01	Transition from 32 MWt to 40 MWt (Full Power) Core for FBTR and Addressing Regulatory Requirements
1.02	Hydraulic validation of Poison Subassembly for FBTR 40 MWt core
1.03	Evaluation of Compression and Flexure Strength of EB ₄ C Specimens for FBTR Poison Rod
1.04	Thermal Property Measurement of 90% Enriched Boron Carbide for FBTR Absorber Rod Application
1.05	Challenges Encountered in Purifying Stagnant Sodium of FBTR Flooding Tanks
1.06	Post-Irradiation Examination of Tungsten Carbide Irradiation Capsule
1.07	Quantitative Measurement of Porosity by Image Analysis of Micrographs of Mixed Carbide and Mixed Oxide Fuels Irradiated in FBTR
1.08	In-house Development of Off-Normal Frequency Logging System for FBTR TG Set
1.09	Evolution of Safe Operating Limit on Reactor Tank Water Activity for Continued Operation of KAMINI Reactor
1.10	Decay heat measurements using Whole Energy Absorption Spectrometer in KAMINI

II. Prototype Fast Breeder Reactor

2.01	PFBR Commissioning Status
2.02	Design & Development of Reactor Core Viewing System (RCVS) for Pre-Commissioning Inspection of PFBR Core
2.03	Experimental verification of the methodology in simulating neutron count rates with 0.1 cps/nv HTFC during initial fuel loading
2.04	Improved Severe Accident Analysis In PFBR Using A Slug-Ejection Model
2.05	Seismic Probabilistic Safety Analysis Study
2.06	Vibration limits for ALIP in Secondary Sodium Main Circuit
2.07	Stability analysis of Secondary Sodium Pump
2.08	Vibration analysis of IHX Down-comer for postulated fluctuating fluid forces
2.09	Technical Support towards Rectification of LRP Bearing
2.10	Design and manufacture of Nickel detectors for SG tube leak detection system
2.11	Simulation of Pressure Transient Under Turbine Trip Event
2.12	Evaluation of Argon and Oxygen Levels in Nitrogen Generated by Pressure Swing Absorption Method
2.13	Studies on flushing efficiency of Kr and Xe gases in sodium using Fission Gas Sparging Module towards the identification of failed fuel sub-assembly
2.14	Estimation of life of Guard Pipe Compartment Bellows in Secondary Sodium Main Circuit
2.15	Numerical Analysis of Dynamic Seals Used in Control and Safety Rod Drive Mechanism
2.16	Performance Evaluation and Endurance Testing of PFBR PSPC Electromagnetic Pump
2.17	Development of Non-destructive Examination Techniques for Qualification of Thin Walled Nickel Tubes for the Hydrogen Sensor Application
2.18	Quality Assurance & Non-destructive Examination for Large Rotating Plug Bearing Balls
2.19	Qualification of Modified Annular Linear Induction Pump by Non-destructive Examination
2.20	Visual Inspection and Quantitative Measurements in Various Components of PFBR using Industrial Videoscope

III. R&D for Fast Breeder Reactors

3.01	Development of Non-Return Valve for sodium
3.02	Performance Evaluation of WLD Layout for Dished End Test Section in LEENA Facility by Creating Sodium Leak
3.03	Plasma Nitriding of P9 Piston Rod of DSR
3.04	Studies on Decomposition Behaviour of Sodium Hydride in Liquid Sodium as a Function of Vacuum Level in the Context of Cold Trap Regeneration
3.05	Improvements in regeneration of sodium Cold trap by altering geometry of wire mesh top cover plate
3.06	Sensitivity Evaluation of 100 NB PM Flowmeters in Sodium Facility for Component Testing
3.07	Finalization of Calibration Scheme for Eddy Current Flow Meter of Primary Sodium Pump
3.08	Evaluation of rotor dynamics coefficients of sodium pumps through CFD analysis
3.09	Numerical Analysis of Hydrostatic Bearing of Large Sodium Pump Using ARMD Software
3.10	Highly Accelerated Life Testing of Switch Over Logic System
3.11	Application of High Contrast Sensitivity Radiology (HCSR) Procedure for Detection of Micro Defects in End Plug Welds of Fuel Pins
3.12	Design and Development of a pressure decay method leak measurement system using MEMS based pressure sensor
3.13	Design and Manufacture of 200 NB Sidewall Permanent Magnet Flowmeter
3.14	Design and thermal hydraulic analysis of secondary sodium based decay heat removal system for FBR 1&2
3.15	Development of High Temperature Ceramic Insulator Coating and Dissimilar Metal Joints for Fabrication of DC Conduction Pump Core
3.16	Development of Ultrasonic Immersion C-Scan Inspection Procedure for Evaluation of De-Bonds in Magnetic Pulse Welded Fuel Pin End Plugs
3.17	Testing of MgO Bricks Towards Development of Sacrificial Layered Core Catcher for SFR
3.18	Submerged Gravel Bed Scrubber for Removal of Sodium Fire Aerosol
3.19	X-Ray Imaging of Simulated Molten Fuel Coolant Interaction Phenomena in Sodium
3.20	Computation and Development Towards Gamma Ray Build-Up Factors for Conventional Shielding Materials
3.21	Study on the effect of Fuel Subassembly Orientation on Gamma Flux
3.22	Long-Term Exposure of $MgAl_2O_4$ and Y_2O_3 Thermal Barrier Coatings in Molten Sodium for FBR Core
3.23	Studies on The Efficacy of Ionic Liquids on Inhibiting Biofilm Formation on Materials Used in Cooling Water Systems
3.24	Parameterization Study To Evaluate Bonding Quality Of Sodium Compatible Ultrasonic Transducer
3.25	Integrated Steady and Transient Pool Thermal Hydraulic Analysis of Primary Sodium Circuit
3.26	Testing of large sized Inconel-625 bellows in high temperature sodium environment
3.27	Computing the Effect of Fission Gases on Thermal Transport in Uranium Dioxide
3.28	Numerical Methodology for the Estimate of Asymptotic Crack Size and Comparison with A16 Master Curve Prediction
3.29	Suppression of Pressure Induced Phase Transformation In Neutron Irradiated Fe_2B
3.30	Effect of Thermal Ageing on Thermal Diffusivity of Ni-Based Hardfacing Alloy Deposit
3.31	Heterogeneous Microstructures and Creep Behavior Across the P91 Steel Weld Joint
3.32	Assessment of Mechanical Properties of Creep exposed Modified 9Cr-1Mo steel using Small Punch Technique
3.33	Air Oxidation of 9Cr-1Mo Steel: Depth Profiling of Oxide Layers Using Glow Discharge Optical Emission Spectrometry
3.34	Threshold displacement and defect formation energies of $Y_4Zr_3O_{12}$ and its implication in radiation stability of Zr and Al-containing ODS alloy
3.35	Atomistic Simulation on Formation of Stacking Fault Tetrahedra due to Irradiation in FCC Metals

IV. Fuel Cycle

4.01	Fast Reactor Fuel Cycle Facility- Current status
4.02	Design, Development & Mockup Of The Hull Tilting System For Chopped Radial Blanket And Fuel Subassembly Pins of PFBR For Fast Reactor Fuel Cycle Facility
4.03	Design and Analysis of Vertical Cask with Electrically Operated Trolley For Transportation Of Hexagonal Wrapper of FSA and RSA from FRP/FRFCF to WMP
4.04	Campaigns for FBTR Spent Fuel Reprocessing at CORAL
4.05	Design and Development of Special LED Lighting System for Lead Wall Shielded Hot Cells in DFRP
4.06	Development and Commissioning of Radiation Monitoring Systems for Stack Effluent in DFRP
4.07	Design & Commissioning of mini Crane and Electrolyser vessel for DOR facility inside Glove box.
4.08	Installation and commissioning of continuous casting system inside glove box for fabrication of metal fuel blanket slug
4.09	Glove Box adaptable Hydrogen Gas Determination for MOX Fuel
4.10	Commissioning of Isopiestic experimental set up for vapour pressure measurements
4.11	Conceptual Design and Development of a Robot for loading the Fuel Pin into a Magazine
4.12	Setting up of a sol-gel facility in walk-in fume hood for the production of ceramic microspheres through internal gelation process
4.13	Design & Structural Analysis of Sub-Assembly & Pin Magazine Handling system with Shielding for Core Sub-Assembly Plant
4.14	Conceptual Design & Structural Analysis of Three Sub-Assembly Transfer Cask (TSTC) Dolly for handling PFBR Sub-Assemblies
4.15	Study of Continuous Cerium (III) Oxalate Precipitation in A Scraped Surface Precipitator
4.16	Process optimization for the catalytic reduction of uranyl nitrate with hydrazine over silica supported Pt catalyst by response surface methodology
4.17	Characterization of insoluble residue found in Centrifugal Extractor's bowl
4.18	Investigation of phase equilibria in LiCl-KCl-SmCl ₃ ternary system
4.19	Ionic Liquid as the Novel and Unique Solvent for the separation of actinides and fission products
4.20	Recovery of Zr from Raffinate Solutions using Tri-n-butyl Phosphate and Tri-iso-amyl phosphate solvents
4.21	Studies on some of the auxiliary processes of Pyrochemical Reprocessing
4.22	Achieving Leak Tightness in 500 m ³ Argon Containment Box of Pyro Process R&D Facility
4.23	Application of lithium-tagged zeolite for spent salt treatment in back-end of pyroprocessing
4.24	Modified diglycolamide solvent systems for the treatment of high-level waste solutions from metallic fuel reprocessing streams
4.25	Study on Attenuation Relationship in Controlled Blasting for Bedrock Excavation of Near Surface Storage & Disposal Facility
4.26	Effective civil construction of waste tank farm roof slab and SS lined pedestals
4.27	QA & NDE Practices During Fabrication of Waste Tank Farm (WTF) Tanks for FRFCF

V. Basic Research

5.01	Synthesis of phase pure AgInO ₂ for gas sensing applications
5.02	Large-scale Induction Melting of Iron Phosphate Glass (IPG) in Alumina Coated Inconel Alloy Vessel
5.03	A Very Low Temperature Crystallization of Amorphous-Ge Thin Film on Glass With High Carrier Mobility
5.04	Structural Insights at Different Length Scales in Alkali-Modified Tellurite Glasses to Tailor Optical Properties
5.05	Ultra Thin Ni Films for Synthesis of Graphene on Diamond Thin Films and Enhanced Electron Field Emission Properties
5.06	Tuning Photoluminescence Emission of Nanocrystalline Diamond Films by N Doping
5.07	Mask-less Single Step Nanofabrication by Focused Ion Beam – Scanning Electron Microscope Dual-Beam Technique
5.08	Atomic Scale Study of Defects in Co ₂ FeAl: A Promising Spintronic Material
5.09	Low Temperature Magneto-Caloric Studies on Rare-Earth Selenide Systems
5.10	Enhancement of Hyperthermia Efficiency in Magnetic Nano-Emulsions at Acidic Ph: Role of Conformational Changes of the Stabilizing Moieties
5.11	Dispersion Module using Time-Varying Source Terms In Online Decision Support SYSTEM ONERS
5.12	EPR, TL and OSL based Retrospective Dosimetry
5.13	The Nature of Phosphoryl Binding in Uranyl Nitrate Complexes

VI. Directed Basic Research

6.01	Development of Alloy 617 ODS for High Temperature Applications
6.02	Development and Demonstration of Manufacturing Process for Mass Production of Long Seamless Tubes of Ni-Based Super Alloy 617M
6.03	Development of Oil-Absorbent Iron Oxide/MnOX Magnetic Nanoparticles and its Applications in Oil Recovery
6.04	Thermal Oxidation of Commercially Pure Titanium (Cp-Ti) for Enhanced Resistance to Corrosion and Biofilm Formation
6.05	Studies on the oxidation behavior of sodium-bonded U-Zr with clad (T91) in the context of aqueous reprocessing of metallic fuel
6.06	Characterization of Low Cycle Fatigue Behaviour of Simulated Microstructures and Actual Weld Joint of P91 Steel
6.07	Creep Deformation and Damage Evolution in 316LN Stainless Steel with Varying Nitrogen Content in the Framework of Continuum Damage Model
6.08	Effect of Temperature on Fatigue Crack Growth (FCG) Threshold (DKTH) of 316LN Stainless
6.09	Effect of Nitrogen on Grain Boundary Character Distribution in AISI Type 316L Stainless Steel
6.10	Effect of Nitrogen on the Intergranular Stress Corrosion Cracking Resistance of 316LN Stainless Steel
6.11	Performance Assessment of Gamma Computed Tomography System As Per The ASTM Standards
6.12	Multi-NDE Techniques for Detection of Inclined Flaws in Small Diameter Ferromagnetic Steel
6.13	Simulation of Gas entrainment phenomena inside FFLM due to interaction of free liquid jet with liquid-gas interface
6.14	Microcantilevers for humidity and temperature sensing applications
6.15	Indigenous instrumentation Development for automated ion implantation and ion beam analysis experiments with nanometric resolution
6.16	An in-house developed auto titrator unit using pulsating sensors for analytical applications
6.17	Thermophysical and thermochemical properties of U-23wt.%Pu-6wt.%Zr alloy fuel: Computational and High Temperature Mass Spectrometric studies
6.18	A Feasibility Study to Measure Magnetocardiogram in Unshielded Environment

VII. Infrastructure, Resource Management & Biodiversity

7.01	Manufacture of Large Size Test Vessels for Sodium Technology Complex Transfer and
7.02	Transfer and Transportation of Sodium from Heavy Water Plant, Baroda
7.03	Design and Development of Advanced Base Station Module with Fault Tolerant Architecture
7.04	Development and Implementation of Indigenous Video Conferencing (VC) Solution - IGCAR Vi-Meet
7.05	Installation, Configuration and Deployment of Audio Video Streaming Facility
7.06	Indigenous Access Control Systems for Security Buildings of DAE Kalpakkam Complex
7.07	Retrofitting and Refurbishment of LV System (Phase-1) to Improve Safety & Reliability
7.08	Unified Portal for Efficient Utilization, Management and Monitoring of High Performance Computing resources
7.09	In-house Development of Customized Application Framework for E-Services (CAFE)
7.10	Development of Secure Webmail Service
7.11	Design & Simulation Centre with High-end Graphics Workstations
7.12	Enhancement and Customization of Online APAR for Deployment at other DAE Units
7.13	Improving Availability of Central Water Chilling Plant by Predictive Maintenance Strategy
7.14	Buildings for State of Art Doppler Weather Radar and Wind Profiler Weather Surveillance Systems
7.15	Microanalytical Methods Aiding the Autopsy of Old Concrete Structures
7.16	Quality Assurance and Non-destructive Examination for FBRs and Fuel Recycle Projects
7.17	Remotely Operable Dry Chemical Powder Dispenser for Sodium Fire Extinguishment
7.18	Industrial and Fire Safety Activities
7.19	Role of Media in Positive Publicity of Nuclear Energy
7.20	Digitally Transformed Research Library
7.21	Implementation of Budget Automation System (DAEBAS) for DAE Units
7.22	Procedure for Formulation of New Capital Projects at IGCAR
7.23	Biodiversity Documentation at the DAE Complex
7.24	FISH - Translocations for Retrospective Biodosimetry
7.25	Relative Biological Effectiveness for alpha particles
7.26	Marine Ecological Studies in and around Kalpakkam Coast and Southwestern Bay of Bengal

VIII. Awards/Publications/Events/Organisation

Awards & Honours

Publications

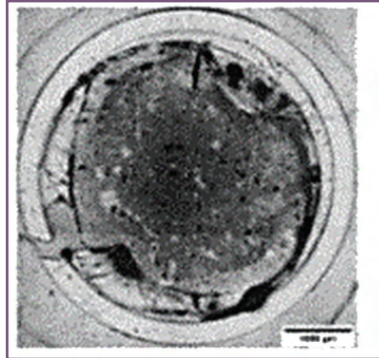
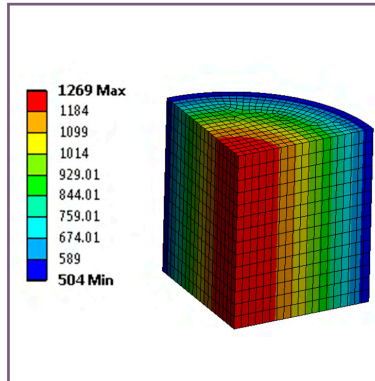
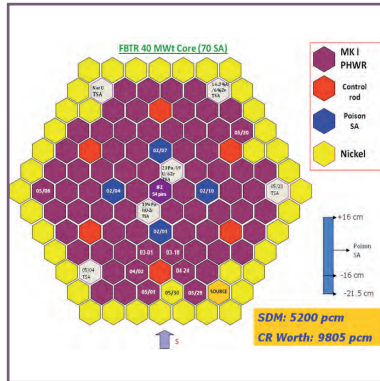
Events

IGC Council

Activities of Various Groups

List of Important Abbreviations

Annual Report Editorial Team



Fast Breeder Test Reactor & Kalpakkam Mini Reactor

CHAPTER I

I.01 Transition from 32 MWt to 40 MWt (Full Power) Core for FBTR and Addressing Regulatory Requirements

FBTR was initially designed as an experimental reactor with rated power of 40 MWt (13.2 MWe) and a core comprising of 65 mixed oxide (MOX 30%PuO₂+70%UO₂, 85% enriched U) fuel subassemblies (FSA) was envisaged. Safety Report for the same was prepared in the year 1983. Due to non-availability of enriched U, the choice of fuel was changed from MOX to mixed carbide (70%PuC+30%UC). A small core with 27 FSA with maximum power of 10.5 MWt was designed. Safety studies were carried out for this core and changes to the chapters reactor physics, shielding, reactor assembly, fuel and special equipment handling and storage and event analysis were carried out in the initial safety report along with minor modifications in other chapters.

Later, power of FBTR was enhanced to 22.5 MWt and then to 32 MWt, with three types of FSAs namely MK-I, MK-II and MOX. This necessitated revisiting the chapters on reactor physics, shielding, core engineering and event analysis after carrying out safety analysis studies.

In order to raise reactor power to its target power of 40 MWt, feasibility studies were carried out and Mark-I core configuration with 70 FSAs, using four boron carbide (B₄C 50% enriched in B-10) poison subassemblies (SA) in second ring was selected (Figure 1). Accordingly, Safety Report for this core was prepared with support from Reactor Design and Technology Group of IGCAR and submitted to AERB in March 2020. The chapters modified in the 22.5 MWt and 32 MWt Safety Reports were revisited.

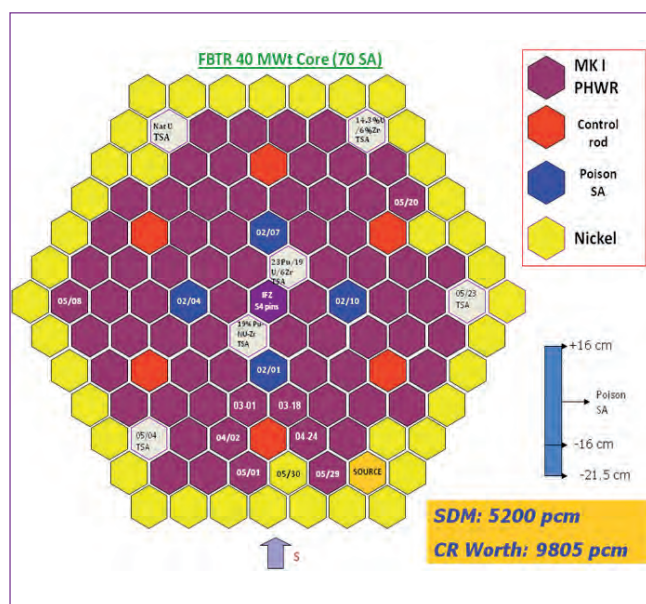


Fig. 1 Core configuration for 40 MWt

Table 1: Core parameters for 40 MWt

No. of fuel subassemblies	70 MK- I (70%PuC+30%UC)
Power (MWt)	41.3(max.) limited to 40 MWt
Number of poison SA (50% enriched in B ¹⁰) in 2 nd ring	4
Number of control rods	6
Prompt neutron life time (s)	1.61x10 ⁻⁷
Effective delayed neutron fraction, (pcm)	270.6
Isothermal temp. coefficient (pcm/°C)	-1.63
Power coefficient (pcm/MWt)	-5.74

Safety analysis report for 40 MWt core configuration

The neutronic parameters were estimated using two dimension diffusion code ALCIALMI, employing the Cadarache (Version 2) (CV2) cross section set. However, transport calculations were performed using Monte Carlo N-Particle (MCNP) code for the exact geometry of the reactor core. Reactivity coefficients were estimated using both ABBN-93 and CV2M cross section libraries.

The estimated neutronic parameters and feedback coefficients are listed in Table 1. Detailed event analysis study was carried out for different postulated events with and without safety actions and safety of the plant was demonstrated under these events. Hypothetical core disruptive accident (HCDA) analysis has been carried out for 40 MWt core and the highest value of mechanical energy release is estimated to be 12 MJ whereas the reactor vessel can take up to 39 MJ (9 kg of tri-nitro-toluene, TNT) of mechanical energy release without failure.

The safety analysis of 40 MWt core with 70 Mark-I type FSAs established that the core neutronic parameters except the temperature coefficient of reactivity are within the present limits as per the stipulations of Technical Specification. Since the event analysis carried out demonstrates the safety of plant under all the anticipated events, it is proposed to revise the technical specification limit on temperature coefficient of reactivity after actual measurement.

I.02 Hydraulic Validation of Poison Subassembly for FBTR 40 MWt Core

For a targeted power of 40 MWt in Fast Breeder Test Reactor (FBTR), it has been decided to use 70 numbers of Mark I sub-assemblies (SA) in the FBTR core. In order to provide the required shutdown margin of core due to additional fuel SAs, it is proposed to load four numbers of identical Poison Sub-Assemblies (PSA) in the second ring of core. These four PSAs contain 50% enriched B₄C. Hydraulic characteristics have to be established for these PSAs before introducing to FBTR core. Hydraulic characterization of PSAs includes the characterization of pressure drop, flow induced self-lifting and cavitation. Pressure drop estimation and cavitation studies in PSA require a geometrically similar 1:1 scale SA model with surface finish similar to actual PSA. Along with above mentioned considerations, apparent weight of the dummy PSA also needs to be simulated for flow induced lifting force assessment. Hence, for the hydraulic characterisation, a dummy PSA with same physical dimensions, without any B₄C material inside and simulating the weight of the actual PSA was used (Figure 1). Hydraulic experiments were carried out using water as simulant.

The experimental measurements of pressure drop were transposed to reactor condition using Reynolds and Euler number similitude. The estimated sodium mass flow rate in PSA for FBTR core pressure drop of 278 kPa is 0.409 kg/s at 428°C. From the experiments it is found that the actual pressure drop in PSA is ~12%

lower than core pressure drop (Figure 2) and this reduction in pressure drop leads to a rise in mass flow rate of sodium through SA by 6.82% than the anticipated value. From studies on flow induced self lifting, it was observed that the lift of PSA happens at a range of pressure drop between 776 – 852 kPa (Figure 3). This random distribution of pressure drop at PSA lift is due to the uncertainties in orientation of gripper spring in sleeve and the resulting uncertainties in locking force by gripper spring. The 776 kPa which is the lower bound value of pressure drop among the total sets of experiment is taken conservatively as the value of pressure drop at which normal PSA lift. In order to establish the margin available for blocked PSA in comparison to normal PSA, experiments were carried out by completely blocking the entry hole of the PSA with a metal plug. For a blocked PSA, it is found that the lift occurs at a pressure drop of 750 kPa. The pressure drop at which PSA lift is 270 % higher than the core pressure drop. Hence, there exists a large margin for PSA to lift in the core. Further, experiments were carried out to investigate the cavitation performance of PSA. Experiments were carried out over a range of cavitation index and the cavitation characteristic in PSA was observed using two numbers of accelerometers connected in the pipe, one at the downstream of SA and another at the upstream of SA. From these experiments, the PSA is found to be free from cavitation even at a flow corresponding to 110% of nominal flow.



Fig. 1 PSA connected to the loop with flanges welded at both ends

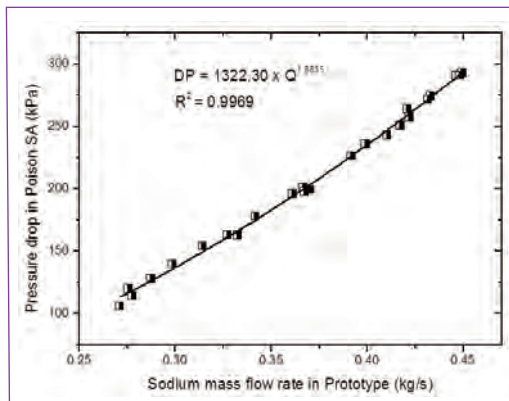


Fig. 2 The pressure drop characteristics in prototype PSA, extrapolated from model studies

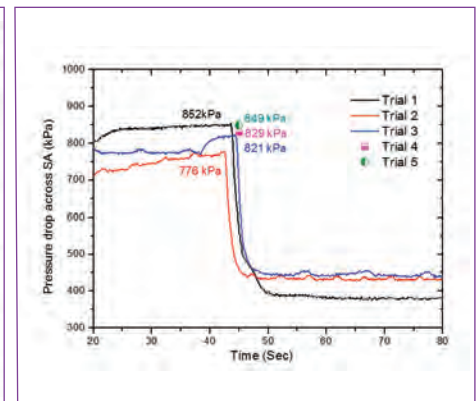


Fig. 3 Pressure drop characteristics in model during hydraulic lift of unblocked PSA

I.03 Evaluation of Compression and Flexure Strength of EB₄C Specimens for FBTR Poison Rod

Enriched Boron Carbide (EB₄C) pellets are proposed to be used in poison rods of FBTR 40 MWt core. B-10 enrichment is 50% in the poison rods. Heavy Water Board (HWB), Manuguru has supplied the poison pellets, which need to be qualified for their compression and flexural strengths. Towards this, compression & flexure strength specimens as per ASTM standards were manufactured at Central Workshop Division (CWD) and the mechanical tests were carried out at Metallurgy & Materials Group (MMG). The strength requirements of poison pellets, preparation of specimens and results of the compression & flexure strength tests are summarized in this report.

Strength requirements

The significant stress on the pellet comes from the thermal gradient due to heat generation. The peak linear heat rating of the Poison SA pellet is 1140 W/cm. The typical temperature distribution and hoop stress distribution are shown in Figures 1 and 2 respectively. As the tensile stresses in the pellet are much higher than the expected tensile strength of B₄C pellet, there will be cracking of the pellet. Due to cracking, stress relaxation takes place. Figure 3 shows the stress pattern along the radius (at mid-section of pellet) with two through cracks (four segments) respectively. At mid-section of the pellet, the peak stress of 787 MPa has reduced to 488 MPa because of cracking. Similarly, axial stress also significantly relaxed due to cracking which is shown in Figure 3. The pellet cracking continues till the peak stresses falls below the fracture strength of the pellet. Further, with helium generation in the pellet,

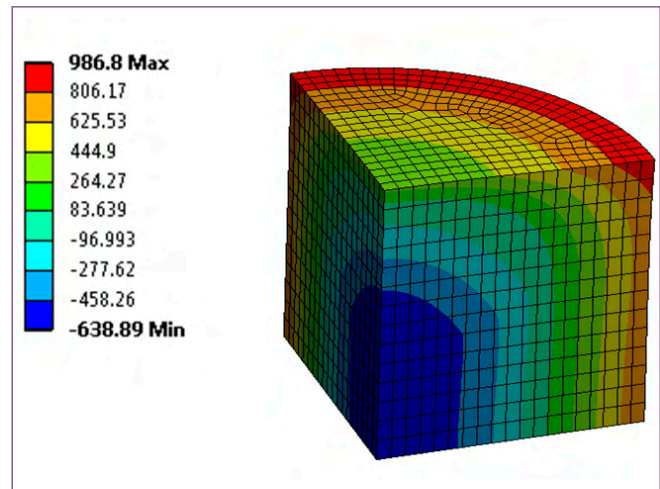


Fig. 2 Maximum principal stress (hoop stress-MPa) for poison pellet with LHR of 1140 W/cm

the matrix is prone to become weaker with irradiation. From the stress analysis, it is concluded that the pellet is subjected to severe thermal stress which fragments the pellet. Fragmentation relieves the stresses. If the pellet tensile strength is very low, the number of fragments will be more. Hence, pellets with very low strength are not acceptable.

It was decided to verify the tensile as well as compression strength tests to evaluate its acceptability. The following mechanical properties are targeted to be met:

- Minimum Tensile strength = 120 MPa
- Minimum Compressive strength = 1080 MPa

For ceramics, the compressive strength is higher than the tensile strength. Tensile strength of ceramics is commonly measured by indirect methods such as four

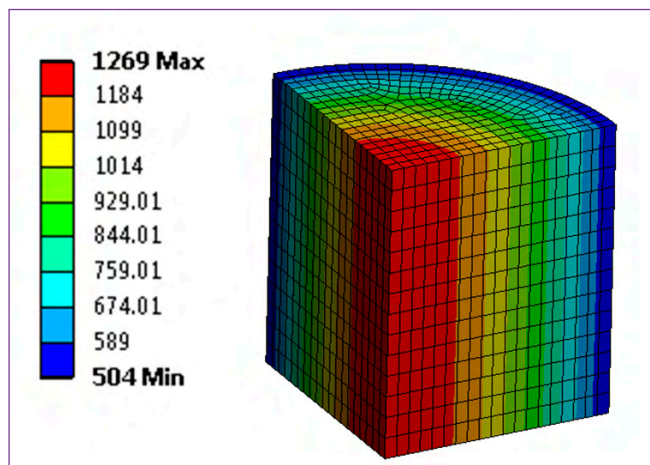


Fig. 1 Temperature distribution (°C) in poison pellet with LHR of 1140 W/cm

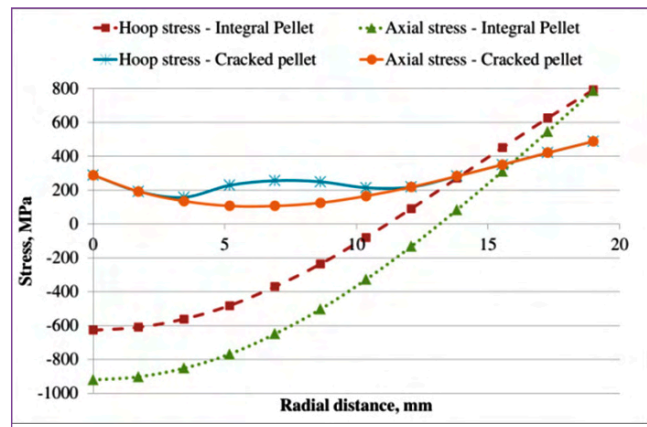


Fig. 3 Thermal stress distribution across the cracked (four segment) poison pellet with LHR of 1140 W/cm at mid-section

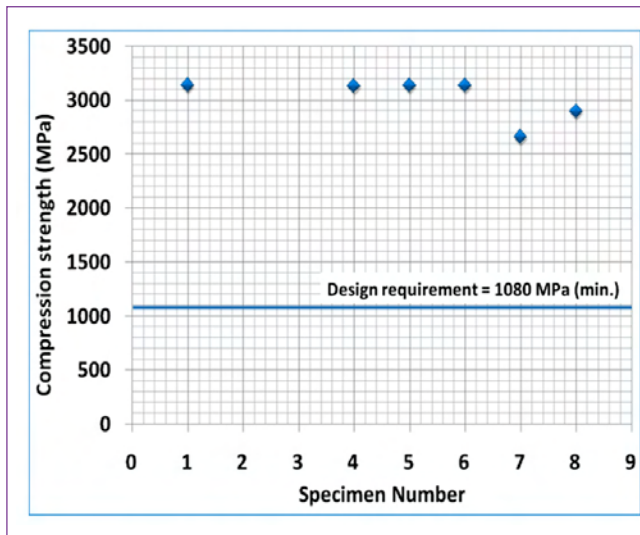


Fig. 4 Compression test results on EB_4C specimens of poison pellet

point or three point flexure test as per ASTM standards. The ratio of flexure to tensile strength for boron carbide varies between 1.27 and 1.33 as per the literature data. Based on the test reports of FBTR imported absorber pellets (90% enriched Boron pellet), 1.25 was considered for the ratio of the flexure strength to the tensile strength to arrive at the flexure strength. Considering the same, the minimum flexure strength required is fixed as 150 MPa.

Specimen preparation and inspection

The dimensions of FBTR poison pellet is 38 mm in diameter and ~ 50 mm in length. The specimens have to be extracted from the FBTR pellet. EB_4C is a ceramic and hard material. Since the specimen dimension is small and in order to minimize the material losses (EB_4C), CNC Wire-cut Electric Discharge Machining (Wire EDM) process was selected for extracting the specimens, where surface finish up to ~ 1 micron could be achieved. Several trials were conducted at CWD, IGCAR in order to optimize machining parameters to make the EB_4C specimens. Based on trials, two special fixtures / job holder designs were conceived which support the specimens during cutting and also helps in achieving the form tolerances. Regarding flexure strength test of specimens, in accordance with the ASTM C1161 guidelines, surface preparation of test specimens can introduce machining micro-cracks which may have a pronounced effect on flexural strength. In order to ensure that the surfaces are free of cracks, all the flexure test specimens were subjected to fluorescent penetrant examination and the specimens had passed the test without any detectable cracks.

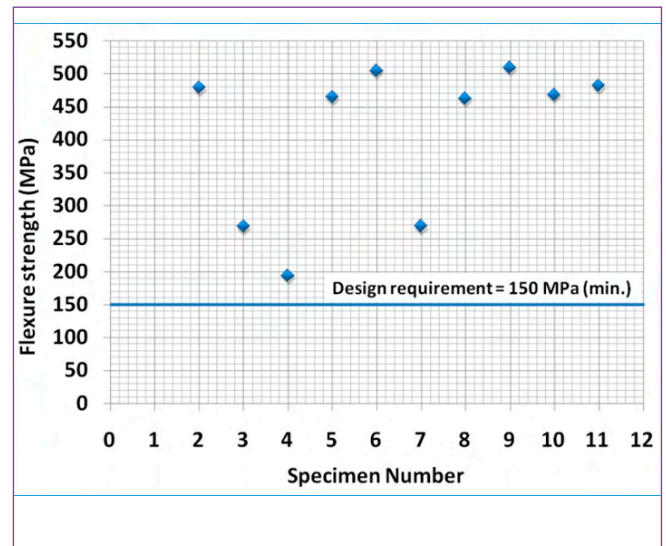


Fig. 5 Flexure test results on EB_4C specimens of poison pellet

Results of compression and flexure tests

The compression and three point flexure strength tests were carried out at MMG. Six specimens were used for compression strength tests and 10 specimens for the flexure strength tests as per ASTM standards. The compression test results are shown in Figure 4. The minimum & mean compressive strength of pellet tested as per ASTM C1424 was found out to be 2660 MPa & 3017 MPa, which are higher than the required compressive strength of 1080 MPa. The flexure strength test results are shown in Figure 5. The minimum & mean flexure strength of pellets tested as per ASTM C1161 was found out to be 192.9 MPa & 409.6 MPa respectively. Both these values are also higher than the targeted value.

Enriched Boron Carbide (EB_4C) pellets are proposed to be used in poison rods of FBTR 40 MWt core, which need to be qualified for mechanical strength requirements. For poison pellet, the compression test was conducted on six specimens and the minimum and mean compressive strengths were found to be 2660 MPa & 3017 MPa respectively, which are much higher than the target requirement of 1080 MPa. Also, the flexure tests were conducted on ten specimens and the minimum and mean flexure strength were found to be 192.9 MPa & 409.6 MPa respectively, which are also well above the target requirement of 150 MPa. Thus, the EB_4C pellets produced by HWB for the poison rod of FBTR 40 MWt core were qualified with respect to the targeted compression & flexure strengths.

I.04 Thermal Property Measurement of 90% Enriched Boron Carbide for FBTR Absorber Rod Application

The Absorber Rod (AR), which primarily controls the reactivity of the core, is a crucial safety component in any fast breeder reactor (FBR). Boron carbide (B_4C) has been the preferred material for AR applications, due to the high neutron absorption cross section of boron atoms, contributed mainly by its B^{10} isotope. It may be mentioned that natural boron contains only 19.8% of B^{10} . Further, in FBRs, the high energy neutrons not only reduce the absorption cross section, but also introduce significant irradiation damage. Presently, 57% and 65% B^{10} enriched B_4C is being proposed for the AR of 500 MWe Prototype Fast Breeder Reactor (PFBR). However, to achieve enhanced neutron absorption and to increase the resident life time of AR, 90% enriched B_4C (90% E- B_4C) is being used for FBTR absorber rod application. In this regard, appropriate qualification of material requires a precise estimation of its thermal conductivity at reactor operating temperature. Towards this cause, the present study has been taken up to obtain estimates of heat capacity, thermal expansion, density, thermal diffusivity and thereby thermal conductivity for the 90% E- B_4C , from room temperature up to 1262 K.

The measurements of heat capacity (C_p), temperature induced dilation $\Delta l(T)$ (i.e. $l_T - l_{298}$) and thermal diffusivity (a) for 90 % E- B_4C specimens were carried out as a function of temperature using differential scanning calorimetry (DSC), push rod dilatometry and laser flash method respectively, following appropriate ASTM standards. The mean coefficient of thermal expansion (CTE) i.e. α_{mean} was estimated from measured $\Delta l(T)$ using the following relation.

Table 1: Thermal properties of 90% E- B_4C at select temperatures

T (K)	C_p (J/kgK)	α_{mean} ($10^{-6}/K$)	a ($10^{-6} m^2/s$)	k (W/mK)
294	981	--	8.87	20.27
374	1352	5.45	5.95	18.69
472	1656	5.49	4.55	17.48
572	1819	5.54	3.85	16.21
675	1909	5.58	3.40	15.02
773	1960	5.63	3.10	14.03
874	2001	5.67	2.79	12.85
975	2039	5.71	2.57	12.04
1074	2077	5.75	2.40	11.44
1174	2120	5.79	2.26	10.97
1262	2162	5.83	2.12	10.45

$$\alpha_{mean} = [(l_T - l_{298}) / l_{298}] / (T - 298)$$

Here l_T and l_{298} stand for the measured lengths at any arbitrary temperature 'T' and at room temperature (298 K) respectively. Further, the measured α_{mean} was used to estimate the bulk density (ρ) of 90% E- B_4C assuming isotropic expansion. From the measured values of C_p , ρ and a , the thermal conductivity (k) was calculated as per the following equation.

$$k = \rho a C_p$$

Measured values of CTE (α_{mean}), isobaric heat capacity (C_p), thermal diffusivity (a) and thermal conductivity (k) of 90% E- B_4C are shown in Figures 1a to 1d respectively. Further values at select temperatures are also given in Table 1.

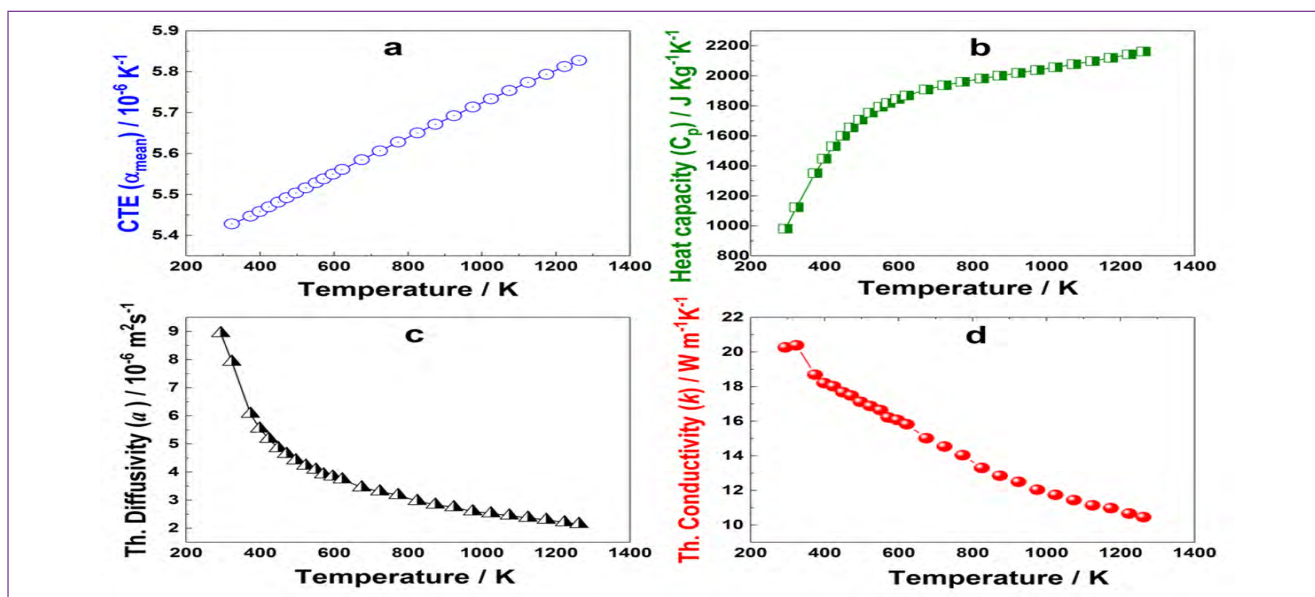


Fig. 1 Variation in measured (a) mean coefficient of thermal expansion (CTE, α_{mean}); (b) heat capacity (C_p); (c) thermal diffusivity (a); and (d) thermal conductivity (k) of 90% E- B_4C with temperature

I.05 Challenges Encountered in Purifying Stagnant Sodium of FBTR Flooding Tanks

Sodium flooding system in FBTR is an engineered safety system to inject sodium into reactor vessel (RV) in case of Loss Of Coolant Accident (LOCA) to keep the fuel subassemblies submerged in sodium. Flooding system consists of auto flooding tank with 1.5 m³ sodium with provision for automatic injection into RV when a set of conditions are satisfied and two manual flooding tanks with 32 m³ sodium in each tank with provision for manual injection into RV when need arises. Sodium in these tanks were only filtered and not purified to nuclear grade when filled in 1990s. Moreover, no provision existed to either purify or measure the purity of sodium. As the sodium in these tanks remained stagnant for about 30 years, it was decided to purify the sodium by incorporating a purification circuit. A skid mounted mobile purification system comprising of an air cooled Cold Trap (CT) and a Plugging Indicator (PI) available with RDTG was identified for integrating with the Flooding System. Being an engineered safety system, this system needs to be available in all states of the reactor. Any intervention in this system for any modification will affect its availability resulting in violation of relevant clauses of FBTR Technical specifications. Hence, a detailed micro scheduling of various activities was done to minimize the non-availability of the system at various stages of integration. With this micro planning and scheduling, regulatory approval could be obtained for violation of Technical Specification for very minimum duration during the integration work.

The first major challenge faced was in shifting and locating the purification circuit of size 2.2 x 1.94 x 2.68 m weighing 980 kg over a platform erected at +10 m elevation over the flooding tanks. As such no opening or handling facility was available in Flooding tank building. Also, the shifting should not affect or damage any of the flooding system pipelines as the system is kept poised. To facilitate the shifting and erection of the purification system, a portion of the wall was removed at the eastern side of the building and temporary lifting and shifting arrangement was erected.

As the ambient temperature in the flooding tank area was very high due to the presence of auto flooding tank and manual flooding tanks with 65.5 m³ molten sodium at 160°C, working continuously in this area posed a major challenge for the working personnel. Despite this, the skid mounted purification system was successfully erected without any disturbance to the Flooding system following all Industrial Safety rules and FBTR protection code.

Integration of the purification system needed identification of the fill/drain nozzles of the flooding tanks as they were dummied after filling in the initial stage. The marking in the drawings were not very clear regarding the proper identification of the nozzles. For identification, there was a need to remove the dummies one by one from the tanks containing molten sodium. Because of the risks involved in intervening sodium systems with large inventory of molten sodium, a Job Hazard Analysis (JHA) was carried out and required fire protection measures and safety measures were taken. Based on the information available in the plant records, blanks from fill and drain nozzles were cut and removed. On checking, both lines were found dipped in sodium. By adopting argon purge method, depth of dipping of the nozzles was measured to identify fill and drain nozzles.

The integration of interconnecting lines of purification system to flooding tank nozzles was also fraught with several welding issues. The welding needed to be carried out in an inert atmosphere with purge gas taken from the flooding system. Since the flooding tank sodium is maintained at 160°C, the argon cover gas above the molten sodium contains sodium vapours which posed problem for getting sound weld joints. With a combination of external purge with fresh argon and lowering the sodium temperature below 150°C, this problem could be overcome and sound welds could be made. Required provisions were made for venting the purification system to the argon space of auto flooding tank.

The integration of purification system with Flooding system was done with reactor in shutdown state and the decay heat was negligible. Other than the challenges in the work execution, the duration allowed by AERB/SARCOP to complete the work was very short. In order to respect the time frame, very detailed micro-planning was done for the work and several contingency measures were in place to restore the flooding system in case of any demand.

After completing the dry checking of logics and interlocks, sequential heating of Flooding Sodium Purification Circuit (FSPC) was done and the circuit was filled. The plugging temperature of sodium in both tanks was measured to be 132°C and 114°C respectively. Purification of sodium was done using FSPC and the Plugging temperature was brought to below 105°C for both the tanks corresponding to oxygen content of less than 1 ppm.

I.06 Post-Irradiation Examination of Tungsten Carbide Irradiation Capsule

The operational life of FBTR is limited by the neutron damage to the grid plate which is a non-replaceable component. To reduce the neutron flux to the grid plate, Boron Carbide (B_4C), Tungsten Carbide (WC) and Ferro-Boron (FeB) were considered as axial shielding by replacing the existing 316 SS rods in the lower portion of the core sub-assemblies. Based on evaluation of shielding effectiveness to reduce the dpa rate to grid plate and the reactivity loss caused by its introduction in the FBTR core, WC was found to be suitable as the lower axial shield material without requiring major modifications in the design of FBTR fuel sub-assembly. Chemical and metallurgical compatibility studies also demonstrated excellent stability of WC with reactor grade sodium at 673K at sustained exposures. To study the irradiation behaviour of tungsten carbide, pellets and discs of WC, fabricated by Spark Plasma Sintering (SPS) process at IGCAR, were irradiated in FBTR along with pellets and discs of Tungsten (W) in a capsule with Type 316L SS clad material to a peak fluence of $1.64 \times 10^{22} n/cm^2$. The irradiation capsule and loading scheme for pellet and disc samples are as shown in Figure 1.

Post irradiation examination involving visual examination, dimensional measurement, pre & post irradiation Neutron radiography (NR), density measurement, microstructural analysis of W/WC clad sections using optical and scanning electron microscopy (SEM) were carried out to study the in-pile behaviour of W/WC. NR analysis indicated that W and WC pellets in all three compartments were intact after irradiation, while the disc samples were crumbled, which is attributed to thermal cycling stresses generated during reactor service. The capsules were

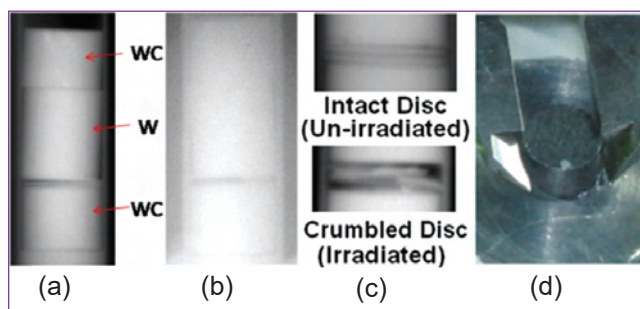


Fig. 2 NR image of (a) un-irradiated, (b) irradiated pellets & discs in compartment #1, (c) intact and crumbled images of discs, (d) photograph of irradiated WC pellet

dismantled using laser and CNC milling inside hot cells and pellets were extracted using a special tool. On visual examination, score marks were observed on both W and WC pellets and edge chipping was observed on WC pellets. Maximum diameter increase measured in WC and W pellets was 0.37% and 0.66% respectively and length increase was 0.64% and 0.13% for WC and W respectively. The overall maximum dimensional change of WC and W was ~0.66% for the pellet of compartment #2 at peak dpa location (dpa~2.9). Figure 2 shows pre & post irradiation NR images of the W/WC pellets & crumbled disc in the compartment #1 and photograph of irradiated WC pellet. The maximum volumetric swelling measured by liquid immersion method for WC and W pellets in compartment #2 was 4.6% and 2.7% respectively. The microstructure of the inner surface of clad material adjacent to WC pellet did not show any evidence of carburisation (Figure 3) indicating that there is no adverse chemical interaction of WC with the clad material due to irradiation.

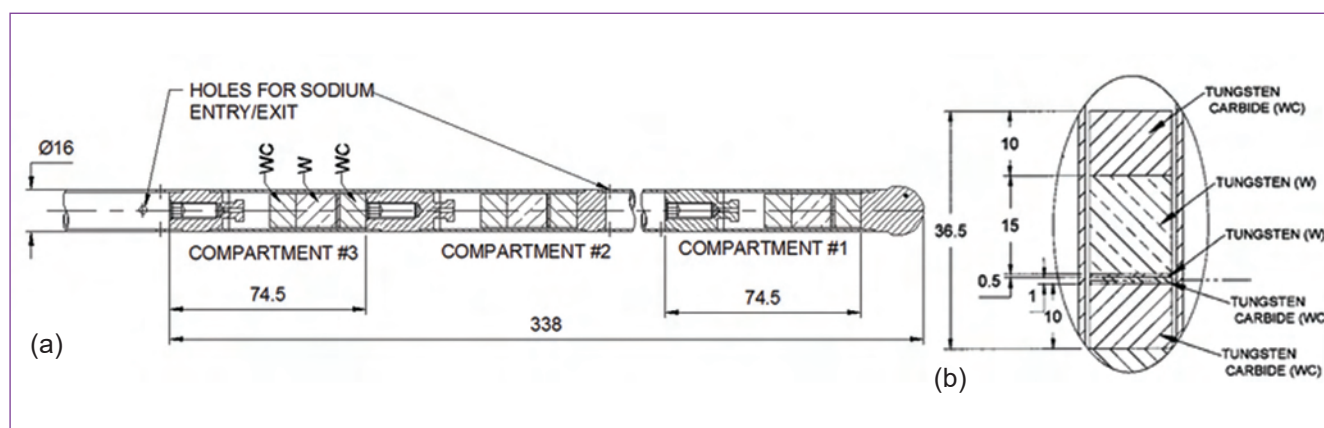


Fig. 1 Schematic of (a) irradiation capsule (b) loading of pellets and disc samples

PIE of W & WC pellets irradiated to a peak fluence of 1.64×10^{22} n/sq.cm has indicated that pellet integrity is maintained with very nominal irradiation induced swelling. No evidence of WC - 316L SS clad chemical interaction or clad carburisation was found. Based on the PIE, it is concluded that WC can be considered for lower axial shielding in the fuel sub-assemblies of FBTR to reduce the neutron dose to the grid plate for extending its life.

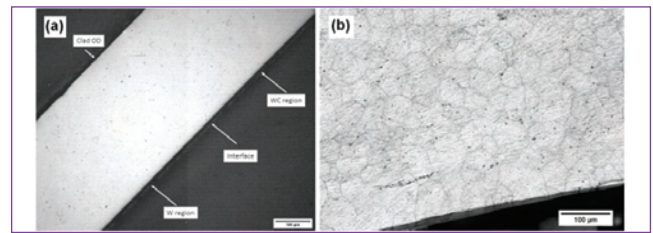


Fig. 3 Microstructure of (a) longitudinal, (b) transverse section of clad adjacent to WC pellet region in compartment #1

1.07 Quantitative Measurement of Porosity by Image Analysis of Micrographs of Mixed Carbide and Mixed Oxide Fuels Irradiated in FBTR

Knowledge of in-pile behavior of fuel and other in-core components through Post Irradiation Examination (PIE) is vital for achieving higher burn-up. During irradiation in reactor, fuel undergoes extensive restructuring. Due to solid-state diffusion and vapour phase transport, grain growth and porosity migration would proceed at a significant rate at high temperature (~ 2900 K) and steep temperature gradient (10^4 K/cm) across the fuel pellet. As a result, different microstructural regions develop in the fuel during irradiation at distinct radial positions according to the temperature profile. Quantification of porosity in these microstructural zones could help in understanding in-core fuel behavior such as fission gas release behavior, swelling of fuel and fuel clad mechanical interaction and facilitate correlating them with various design parameters of fuel like density and thermal conductivity.

In this study, microstructures of mixed carbide (MC) and mixed oxide (MOX) fuels having compositions ($U_{0.3}Pu_{0.7}$)C and ($U_{0.71}Pu_{0.29}$)O₂ respectively after irradiation in Fast Breeder Test Reactor (FBTR) were subjected to porosity measurements by image analysis technique. MC fuel pin examined had undergone a peak burnup of 155 GWd/t and linear heat rating (LHR) of 400 W/cm. In the case of MOX fuel, fuel is enriched with 53.5% ²³³U to attain the LHR of 450 W/cm targeted in Prototype Fast Breeder Reactor and the maximum burnup is 112 GWd/t. For carrying out porosity measurements, transverse and longitudinal sections extracted from the fuel pins were subjected to sequential grinding, polishing and etching inside the hot cell. The samples prepared from MC fuel were examined using a customized metallurgical microscope installed in the hot cell. In the case of MOX fuel pins sections, micrographs obtained from replicas

of polished and etched samples were analysed. The images captured from the optical microscope were converted to 8-bit images for analysis in image analysis software, ImageJ. The brightness and contrast of the image were adjusted for manual thresholding of grey scale intensity. The artifacts in the micrographs were excluded by applying image filters using combination of parameters such as circularity & size and features of interest were identified and quantified.

Post irradiation microstructure of the fuel depends on the irradiation history of the fuel pin, which varies based on the axial and radial position in the core. Fuel undergo mechanical interaction with the clad at higher burn-ups, after the closure of fuel-clad gap. Since restructuring and porosity evolution could be unique for each fuel pin section under study, selection of regions for analysis was based on the features and contrast of different microstructural zones. MOX fuel exhibiting distinct microstructural zones was divided in terms of zones by manually selecting the analysis window. For a particular micrograph, porosity size distribution obtained from the software was normalized with respect to area fraction of the section for comparison between sections. Again in each section, normalized number of pores for a given size range was divided with similar number obtained from most porous section (highest percentage of porosity) to get the relative pore size distribution for easy comparison of porosity distribution among all sections. This is represented in following equations.

$$N_s = \frac{n}{f} \quad \text{and} \quad R_s = \frac{N_s}{N_f}$$

where N_s is the normalized number of pores in the section, R_s is the relative number of pores in the section,

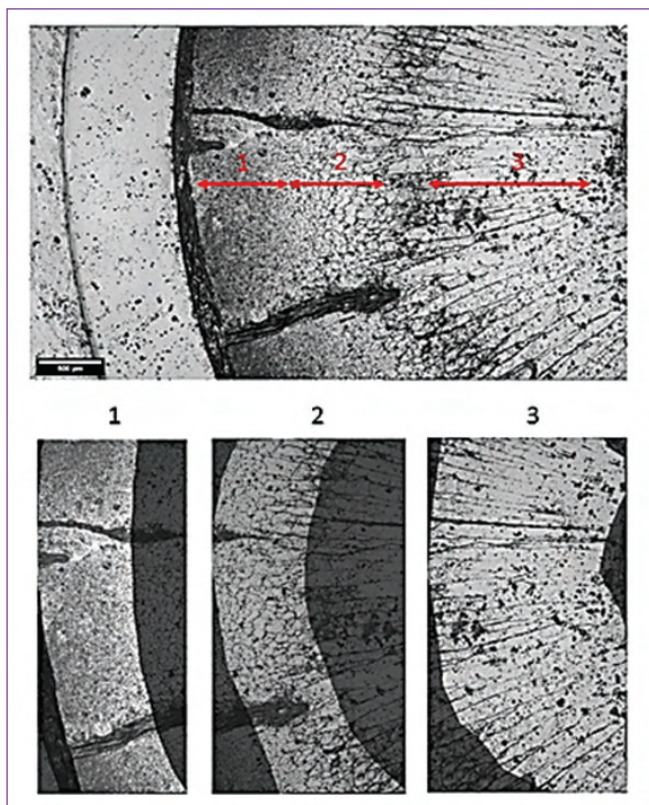


Fig. 1 Selection of regions in MOX fuel

n is the number of pores within a pore size range, f is the area fraction of the section w.r.t full cross section and N_f is the normalized number of pores of highest porosity in the section.

Porosity distribution in MOX fuel

MOX fuel pin cross-sections taken up in this study have undergone LHR of 450 W/cm and 300 W/cm (at axial locations of 60 mm and 210 mm from the bottom of fuel column). Different microstructural zones could be observed across the MOX fuel pin section from the prefabricated central hole to the clad inner surface. The fuel region adjacent to central hole has spherical pores with larger pore size as compared to other zones. This porous region is attributed to the annular pellet design intended for reducing the fuel centre line temperature.

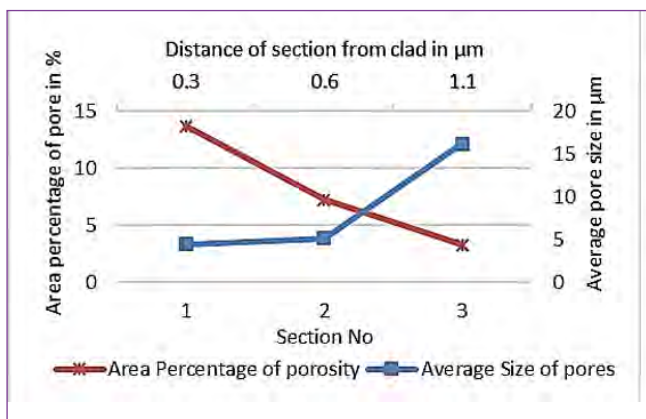


Fig. 2 Porosity area percentage and size distribution in MOX fuel

This zone is followed by the columnar grain zone with very fine lenticular pores. Transition zone with different bands is formed between equiaxed grain zone and the columnar grain zone. The fuel outer periphery has as-fabricated microstructure. For porosity measurements, the irradiated MOX micrograph obtained at 60 mm from the bottom of the fuel column is divided into 3 sections as shown in Figure 1. In section 1, the outer rim of fuel, porosity is measured to be ~13% with average pore size of 4μm, which is comparable to as-fabricated porosity. Section 2 comprises of equiaxed grain with small spherical pores giving lowest porosity fraction and average pore size of around 4 μm with presence of pores in all size ranges. Due to grain growth and relatively higher temperature in this region, porosity fraction is reduced from as-fabricated values. Section 3 is the combination of dense columnar grain and porous region around the central hole, where complete exhaustion of smaller pores is observed. Here, average area percentage of pores is 3%. Pore sizes in section 2 and 3 are relatively higher due to coalescence at higher temperature. Figures 2 and 3 gives the area percentage and size of pores and pore size distribution at three different sections.

Porosity distribution in mixed carbide fuel

Unlike the MOX fuel pin, irradiated MC fuel did not show distinct microstructural zones. However, variation in porosity content could be observed at different radial locations. Selection of regions for porosity analysis is given in Figure 4. The outer rim of the fuel has a porosity exhausted region attributed to combination of stress and temperature. Image analysis indicated that the rim region has area percentage of porosity of 2% as compared to pre-irradiation value of 10%. This region has higher population of small size pores of less than 5 μm as shown in Figure 5. In contrast to this, in section 3

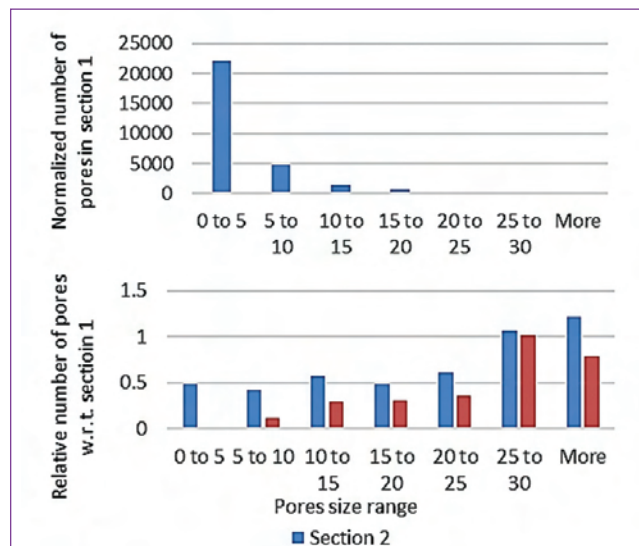


Fig. 3 Porosity size distribution in MOX fuel

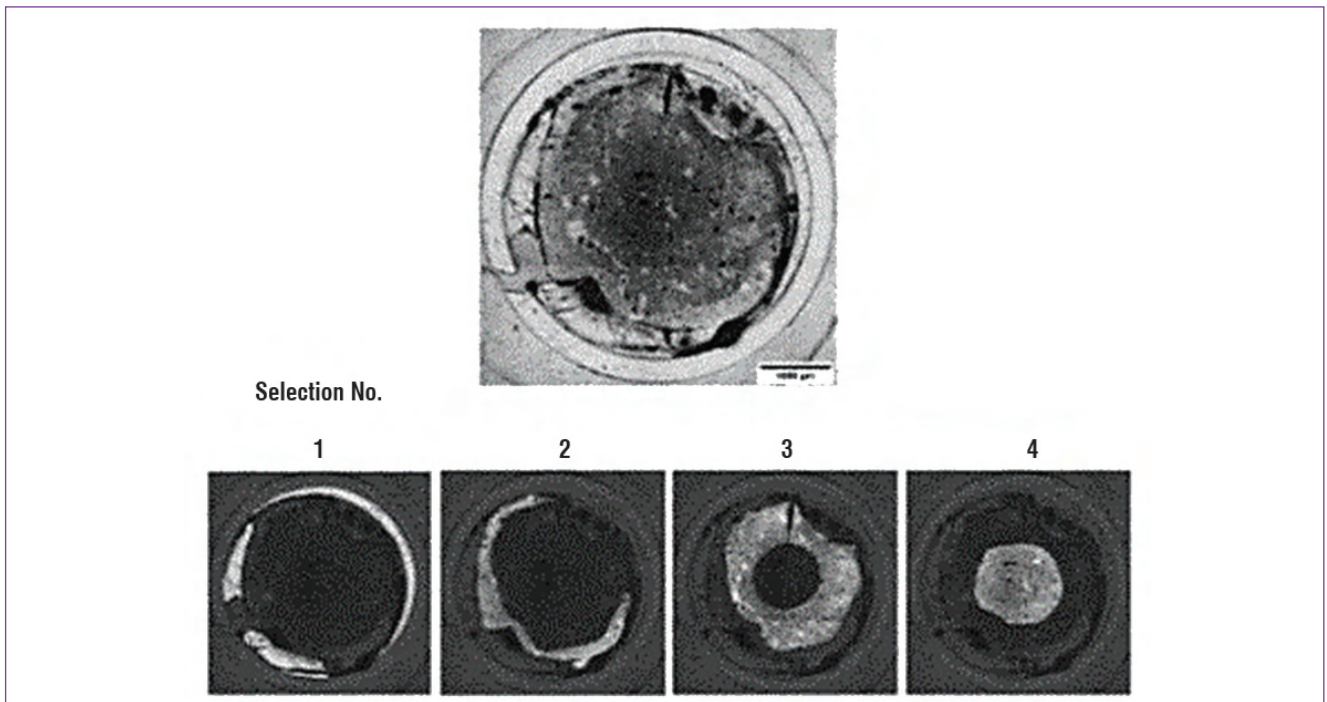


Fig. 4 Selection of regions in carbide fuel

(at the centre of the micrographs) the average area percentage of porosity is 17%. Instead of formation of central hole by pore coalescence in MOX fuels, higher porosity content is evident in carbide fuel. As the fuel swelling progress with burn-up, stress is exerted in the peripheral region of the fuel pellet causing densification. This results in migration of bigger size pore to pellet central region and enrichment of smaller size pores (~5 μm) in pellet peripheral region. The middle zones (Section 2) appears as a transition zone showing porosity profile between the centre and periphery. The average pore size and percentage of porosity is found to be similar to as-fabricated microstructures. Porosity size distribution in these transition zones is almost equal to section 1 with a few bigger size pores of greater than 30 μm. Radial profile of average percentage of porosity

follows an inverted U-shape with central zone being most porous. Porosity variation is spanning between 2% and 16%.

Image analysis is a powerful tool for extracting the characteristic features in a micrograph. Various challenges in the image analysis of irradiated fuel microstructure have been successfully met. The results obtained on the irradiated MOX fuel are found to be in agreement with the reported values in the literature. In irradiated carbide fuel pin sections, valuable data has been obtained on the extent of porosity exhaustion in the outer rim of the fuel due to Fuel-Clad Mechanical Interaction. The data on the porosity evolution for the unique composition of FBTR MC fuel and its irradiation conditions will serve as a crucial input to the designers for fuel pin modeling.

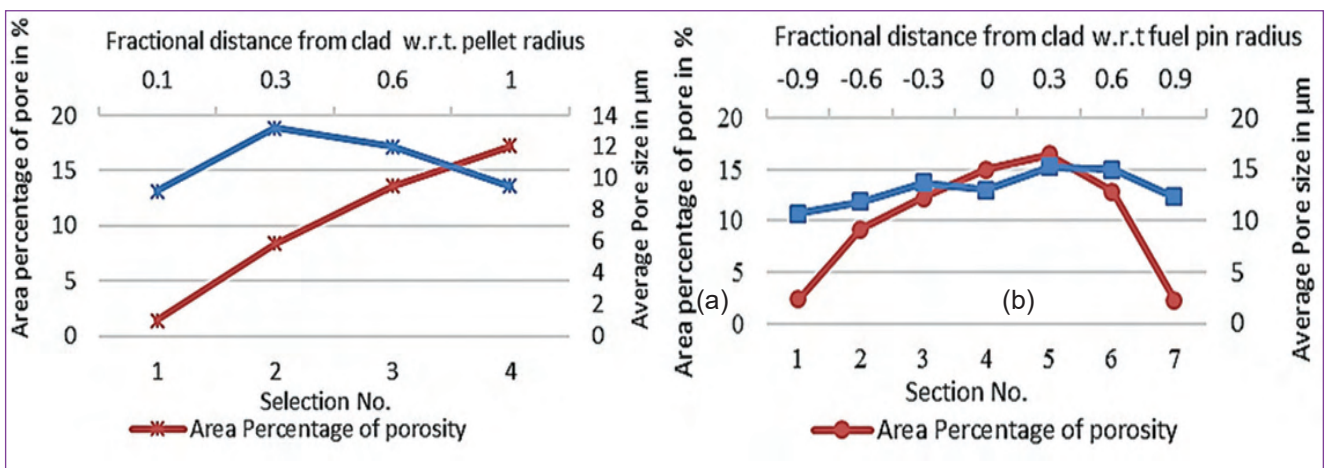


Fig. 5 Porosity area percentage and size distribution (a) in carbide fuel and (b) across the fuel pellet diameter

I.08 In-house Development of Off-Normal Frequency Logging System for FBTR TG Set

The safe operation frequency range of FBTR Turbo-Generator (TG) set is 47.78 Hz to 51.5 Hz. Low frequency operation stresses turbine blade, causes blade resonance, shortens blade life and even makes blade break. Over-frequency will lead to high vibration and stress accompanied by reduction of fatigue life leading to eventual failure. So there is a need to monitor and log the cumulative off-normal frequency operation to decide on turbine internal inspection periodicity. For this purpose, Turbine Off-normal Frequency Logging System (TOFLS) has been developed in-house. The TOFLS is a Smart Touch panel PC based computer system along with a Multi-Function USB DAQ module.

The block diagram of TOFLS system is shown in Figure 1. A frequency signal of 0 to 10 V DC corresponding to 45 to 55 Hz is generated from alternator Potential Transformer and connected to TOFLS. The TOFLS will scan the frequency and Turbine lockout condition at every second. The system initiate logging time of off-normal frequency only when the turbine lockout is RESET and the turbine is rolling. The off-normal frequency settings are mentioned in Figure 2.

Application software is developed using “C” in Ubuntu environment. The GUI software is developed using JAVAFX. Linux Kernel 3.19.0 with Ubuntu 14.04.3 LTS is used in the Smart Touch panel PC System. The

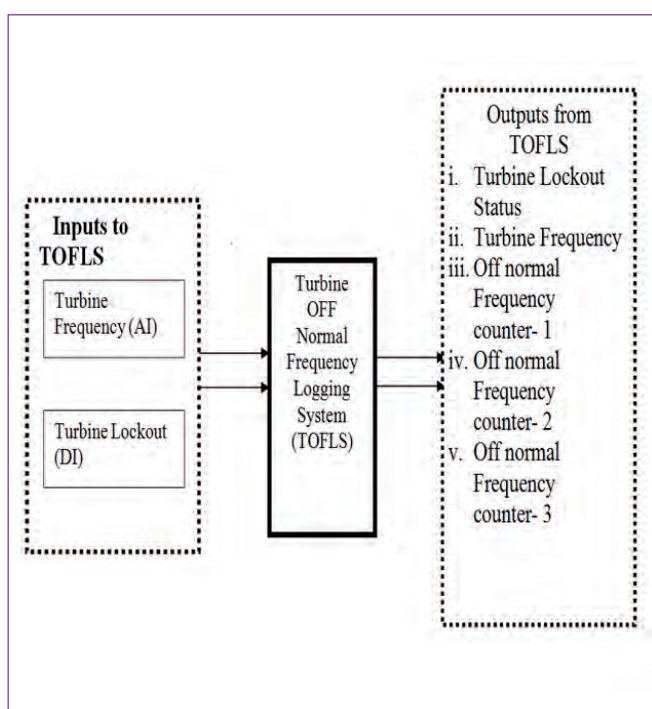


Fig. 1 Block diagram of TOFLS

Turbine off-Normal Frequency Time Logger		
Date and Time	2020-05-20 12:11:10	
Turbine Lockout Status	RESET	
Current Frequency	49.99	Hz
Off-normal Freq counter-1 (47.78 To 48.00 Hz)	0:0:0	Hrs
Off-Normal Freq Counter-2 (51.00 To 51.50 Hz)	0:0:1	Hrs
Off-Normal Freq Counter-3 (51.20 To 51.50 Hz)	0:0:1	Hrs
Under Frequency Alarm (<= 48 Hz)	RESET	
Over Frequency Alarm (>= 51 Hz)	RESET	
49.99 Turbine Frequency 49.99 49.99 Hz		

Fig. 2 Turbine off-normal frequency settings

USB Multi-function DAQ module has both analog and digital input channels. This module is connected to the Smart Touch panel PC through USB and it is self powered. The Turbine frequency signal is connected to the USB DAQ module through a unity gain Isolation amplifier. Turbine lockout signal is extended from relay room to Control Desk CDcr 05 and then connected to the DAQ module kept in PNcr 17. The industrial touch panel system is energized with 230 V UPS supply.

The TOFLS scanning module scans the TG set frequency signal at one second interval and checks the current frequency lies in the Range-I, Range-II or Range-III provided the Turbine lockout is in RESET condition. The current turbine frequency is compared with the ranges of frequency settings. If the frequency lies in Range-I, Range-II or Range-III, then the respective frequency counter will be incremented. The accumulated time for all the three frequency ranges is stored and displayed.

The current frequency of TG set, Turbine Lockout status, off-normal frequency counter for Range –I, II and III are displayed in GUI and updated every 1 second interval. The TOFLS application software writes the scanned input signal status into a Mysql Database at every second and the GUI software reads the scanned information from the Mysql server and displays it in the GUI screen. The Figure 2 shows the GUI display of TOFLS System.

The system has been commissioned successfully and was validated when TG was synchronized during 28th and 29th irradiation campaigns.

I.09 Evolution of Safe Operating Limit on Reactor Tank Water Activity for Continued Operation of KAMINI Reactor

KAMINI is a 30 kW, U-233 fuelled, BeO reflected low power research reactor used for multifaceted applications viz. neutron radiography, neutron activation analysis, radiation physics research, calibration and testing of neutron detectors etc. In this reactor, demineralized light water is used as moderator, coolant, reflector and shield. During operation of the reactor, build up of activity in reactor tank water is being observed due to release of short lived fission product noble gases (FPNGs) produced by fission of fuel materials sticking over the surface and subsurface of fuel clad and activation of corrosion products. Figure 1 shows the buildup of water activity over the years. During initial phase of commissioning in 1998, maximum water activity observed was 42 Bq/ml at 30 kWt power operation due to the presence of short lived FPNGs. The limit was raised to 50 Bq/ml from 20 Bq/ml with the approval of Project Design Safety Committee (PDSC) on par with the limit in APSARA reactor considering the effect of surface contamination on the fuel. In 2008, based on plant requirement, AERB/SARCOP has approved the enhanced limit on water activity to 300 Bq/ml (1 hour delayed activity). Water activity was found to be varying between 100 and 265 Bq/ml till 2012. Since then, the stipulations on limits on radiation field in control room (0.1 mR/h), on top of mixed bed (2 mGy/h) and ensuring no solid fission products in reactor tank water after reactor operation were being complied with.

The B₁ subassembly causing the high water activity at that time was replaced with Pu-Al assembly in 2012 and water activity got reduced to 130 Bq/ml. In September 2018, increase in water activity was observed during reactor operation at 20 kWt. In addition, the increase in water activity limited the operating power level and duration of reactor operation so that the technical specifications limit (300 Bq/ml) is respected. In order to operate the reactor for maximum duration to meet user requirements, further enhancement on limit on water activity was required. In

order to arrive at safe operating limit on water activity, water activity saturation tests were conducted at different power levels as recommended by AERB/SARCOP.

The reactor was operated at different power levels, viz., 30 kWt, 25 kWt and 20 kWt for eight hours. During the above operations, the parameters, online water activity, immediate and 1 hour delayed activity of reactor tank water grab samples and reactor vault air activity were measured. The radiation field in various areas and top of mixed bed was monitored to respect the already stipulated limits.

Though the immediate water activity was getting stabilized after 3 hours of operation at any power level, the 1 hour delayed activity was found getting stabilized after 6 hours of operation irrespective of the power level. The 1 hour delayed activity got saturated around 355 Bq/ml, 437 Bq/ml and 467 Bq/ml respectively at 20 kWt, 25 kWt and 30 kWt. Figure 2 shows the variation of 1 hour delayed water activity with respect to time (hours) observed during operation of reactor at specific power levels. The spectral analysis of air sample indicated the presence of FPNGs. The estimated maximum specific activity at 30 kWt in the exhaust duct gas sample was 12.63 pCi/cc. Radiation survey was conducted in all areas during reactor operation. The radiation levels were found to be within acceptable limits.

The maximum radiation level noticed in control room during reactor operation was 0.04-0.08 mR/h. The maximum contact dose level on mixed bed top region during reactor operation was observed to be 1.6-1.8 mGy/h (limit 2 mGy/h).

Based on the above, AERB/SARCOP has approved the KAMINI technical specification limit on reactor tank water activity as 600 Bq/ml. With this new limit, KAMINI reactor could continue serving its users satisfying the prolonged irradiation requirements.

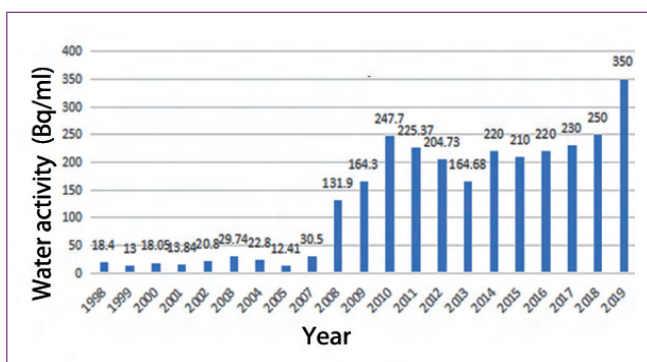


Fig. 1 Water activity from 1998 to 2014

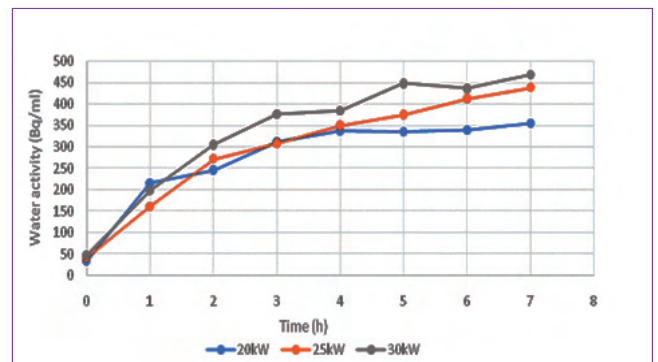


Fig. 2 1-hour delay water activity during reactor operation

I.10 Decay Heat Measurements using Whole Energy Absorption Spectrometer in KAMINI Reactor

The decay power is theoretically estimated using nuclear material evolution codes such as ORIGEN2 and CHANDY. To gain confidence on the prediction, the results need to be validated against experimental/theoretical benchmarks. But no such benchmarks are available at IGCAR for validating the decay heat predictions. Therefore an uncertainty of about 20% is usually taken over the predicted values for practical applications. This uncertainty is considered to accommodate approximations involved in the numerical methods, uncertainty in nuclear data and neutron flux.

With an intention to reduce the uncertainty margin and to validate the decay power predictions, decay heat measurements using Whole Energy Absorption Spectrometer (WEAS) were carried out. WEAS consists of a pair of large bismuth-germanate ($\text{Bi}_4\text{Ge}_3\text{O}_{12}$, BGO) scintillators mounted on a movable assembly for 4π geometry and associated electronics facilitating high efficiency measurement. Figure 1a gives the WEAS set-up assembled near Pneumatic Fast Transfer System (PFTS) of KAMINI Reactor. The system gives three outputs viz. signal from individual detectors and sum from each detector. This system is housed inside acrylic, copper and lead (10 cm thick) shields to reduce background as shown in Figure 1b. WEAS has been successfully commissioned near PFTS of KAMINI reactor. After installation, the functioning of the detectors, electronics and the background radiation were verified.

The detector efficiency for photons is close to 100% below 0.5 MeV, ~90% at 1 MeV and ~80% at 2 MeV and for electron ~100%. The energy scale of the two detectors are calibrated using Cs-137 (662 keV), Co-60 (1173 keV and 1333 keV) and Na-22 (511 keV and 1275 keV) gamma sources and it is also verified by measuring the gamma rays from Ba-133 and Eu-152.

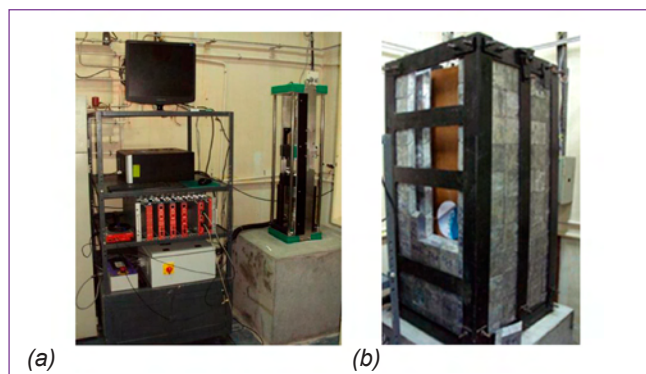


Fig. 1 (a) WEAS set-up and (b) background radiation and optical shielding

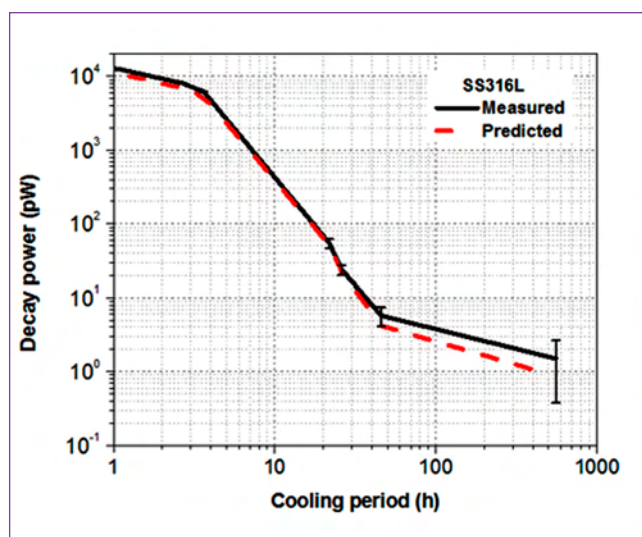
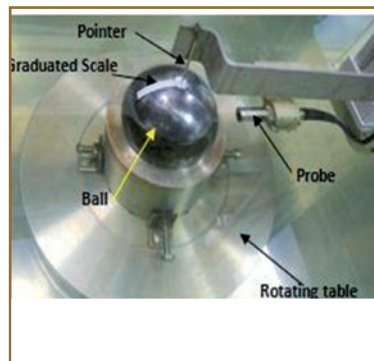
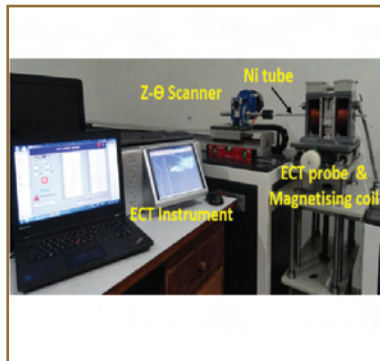
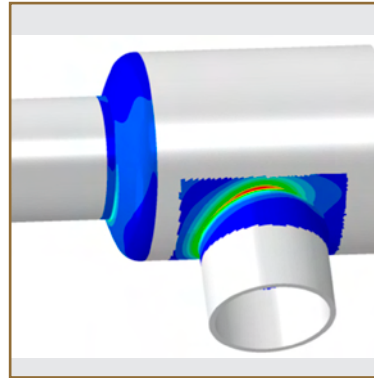
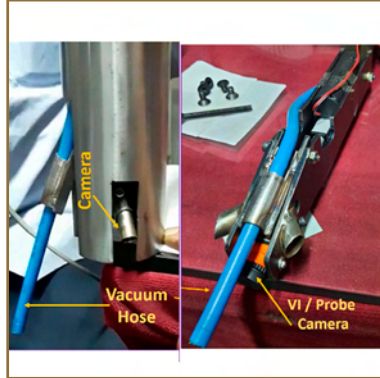


Fig. 2 Comparison of measured and calculated decay powers from SS316L

Decay power from various steels viz. D9, P91, SS316L and SS304L foils irradiated in PFTS location of KAMINI reactor was measured. The reactor power and irradiation period are different for each foil. So the foils are introduced one at a time and irradiations are performed. The irradiated foils are transferred to WEAS set-up for measurements. In general, it takes about 6 to 8 minutes to transfer the irradiated sample from PFTS to WEAS. This delay includes, dose rate measurements, transferring to sample holder, placing the sample holder on the detector surface, closing the lead shielding door, power supply to detector and starting counting. Once the WEAS set-up is ready, data are recorded, until the counting reaches background level.

WEAS gives the energy deposits of both beta and gamma rays simultaneously. The decay power is deduced from the measured sum pulse height spectrum (Sum-PHS) after deducting the background and applying correction factors. The total counts from 10 keV to 5 MeV are considered. By considering the respective powers and irradiation periods of the samples, the decay powers are calculated using the code ORIGEN2 for comparison. Figure 2 gives the estimated and measured decay powers from SS316L sample. It is observed that the calculated to measured (C/E) is generally in the range of 1.05 to 0.9 upto 25 h of decay time. Large deviation observed beyond 25 h of decay time is due to feeble counting statistics. Sample irradiation with higher power and longer irradiation duration is planned to improve the long duration C/E factors.



Prototype Fast Breeder Reactor

CHAPTER II

II.1 PFBR Commissioning Status

Prototype Fast Breeder Reactor (PFBR) at Kalpakkam is a 500 MWe (1250 MWt) liquid sodium cooled, pool type fast reactor using mixed oxide of uranium and plutonium as fuel. The plant is located 500 m south of the existing Madras Atomic Power Station. After completion of construction, manufacture & erection of all the systems / components of PFBR, commissioning of the individual system and the integrated commissioning are in progress. Figure 1 shows the Overall view of PFBR. The major works that have been completed during the year 2020 are as follows:

After successful operation of both the secondary sodium loops, from March 2019 till Oct, 2019, it was shut down for initiating rectification & in-situ modification of the large rotatable plug bearing. Presently, the bearing rectification/modification has been completed, which required innovative & meticulous planning by both designers (from IGCAR) and commissioning teams (from BHAVINI) and also necessitated R&D and technology development efforts for manufacture of large diameter spacer balls through an MSME. Further, the Transfer Arm (which forms a part of the fuelling machinery), which had been suitably modified and re-installed back on pile, was also tested extensively, for confidence building. Further, during the period of secondary sodium loop operation, extensive vibration measurements were carried out on the secondary sodium pumps (SSP), at various speeds of operation, and also on the piping and intermediate heat-exchangers (IHX), in order to closely validate their theoretical designs and performance at high operating temperatures.

Considering that there have been a number of

performance shortfalls and equipment faults during the past four years of commissioning efforts, a graded approach is being undertaken, wherein the commissioning of the various systems & equipment are being taken up, systematically & sequentially, in incremental steps and their performance is checked at each step. A detailed design validation exercise was also undertaken, by expert teams from BARC and also other units of DAE, since all the PFBR systems, structures & equipment (SSE) are first-of-a-kind (FOAK) design, and the graded approach being undertaken for commissioning, were also closely reviewed and approved. Presently, testing & commissioning of the various systems & equipment of both the primary systems and fuel-handling systems, are progressing in parallel and at various stages. The commissioning procedures and associated safety aspects are being closely formulated/reviewed along with the design teams and regulatory teams. Further, various other on-pile testing jobs and minor in-situ reactor-assembly modifications, are in progress, as a pre-requisite to commissioning of the primary system.

Modification of Guard Pipe Nitrogen Circuit pipe lines of Decay Heat Exchanger & Intermediate Heat Exchanger lines for design improvement and preparation for replacement of balls in the bearing of Small Rotatable Plug (SRP) are in progress. Commissioning of fuel handling system is in progress in parallel. After completion of modifications in SRP bearing, pre-heating of reactor assembly will be done towards commencement of sodium filling in Main Vessel. This will be followed by isothermal testing and fuel loading.



Fig. 1 Overall view of PFBR

II.2 Design & Development of Reactor Core Viewing System (RCVS) for Pre-Commissioning Inspection of PFBR Core

During the Pre-commissioning stage of PFBR, it is proposed to view the core internals for visual inspection (VI) of the components of the reactor core and to scan for any foreign debris at the top of Grid Plate. Since, it is difficult to do visual inspection inside reactor assembly in pressurised nitrogen environment, it is imperative to carry out the inspection remotely. Hence, a Reactor Core Viewing System for Room Temperature (RCVS-RT) has been designed and developed in-house. It is intended to be mounted on the Observation Port (OP) on the small rotatable plug of the reactor and by the combination of large rotatable plug (LRP) and small rotatable plug (SRP) motions, remote access to any location of the core is achieved. The RCVS-RT is designed to deploy the camera probe to the core top, which is about 11.5 m below the OP and negotiate through the extracted sub-assembly(SA) slot to reach down to the Grid Plate(GP) top level for inspection for any foreign debris. The base module of the RCVS-RT below the OP enables a global view of the reactor internals and the camera extender, pipes facilitated by a camera and illumination module augments localized views for alignment of the system for insertion into the SA slot for inspection (Figure 1a).

The RCVS-RT system is designed to have a precise radial motion, R (range: 200 mm), rotary motion, Θ (range: 360°) camera vertical motion, Z (range: 100 mm) and azimuth motion to localize the VI probe camera to target position. The major challenge in the design of RCVS-RT is that the automation system must have a reasonably good accuracy with very high ratio of longitudinal to lateral motion. The camera module which has extender pipes, reaches up to the GP top position from the observation port. The camera extender pipes have spherical coupling to maintain verticality and to transmit radial (R), rotary (Θ), vertical (Z) and azimuth motions

to the inspection camera probe. Two pinhole cameras mounted at the end of the tube facilitate a combined radial and axial viewing during deployment of RCVS. A suction hose is terminated at the camera probe end to suck any small debris during the inspection and the other end of the hose is connected to a vacuum pump. The VI probe camera is attached with the suction hose, which is actuated through a linear actuator mechanism. The movement of the linear actuator provides a swing to the hose-camera combination w.r.t. to the RCVS centre-line. This swing (0° to 30°) facilitates the visual inspection by providing the required orientation of camera, once the camera module reaches the grid plate top surface. The VI probe camera is designed to have direct and lateral viewing to view the required target position with LED lighting (Figure 1c). The entire system is specially sealed for all the R, Θ and Z motions to mitigate leaks through the RCVS-RT system during deployment (Figure 1b). The RCVS-RT system has been manufactured and tested on reactor core mock test setup (1:1) with 19 dummy SA maintaining the same reactor core dimensions and GP top distance from the observation port. The virtue of the RCVS system is in the fact that it can be assembled and operated from top shield platform and inspection can be undertaken remotely. Since the RCVS-RT is mounted on the observation port, which is adjacent to the Transfer Arm (TA) assembly, it is quite convenient to use the RCVS-RT system to view and monitor TA operation to evaluate its performance. Hence, under room temperature conditions, the RCVS-RT can also be functionally utilized as a TA viewing and monitoring device for the tasks and activities of TA. The RCVS-RT empowers the plant personnel for conducting the visual inspection within the reactor internals at room temperature. RCVS control panel is shown in Figure 1d. Preparatory activities for deploying RCVS-RT in the reactor are underway.

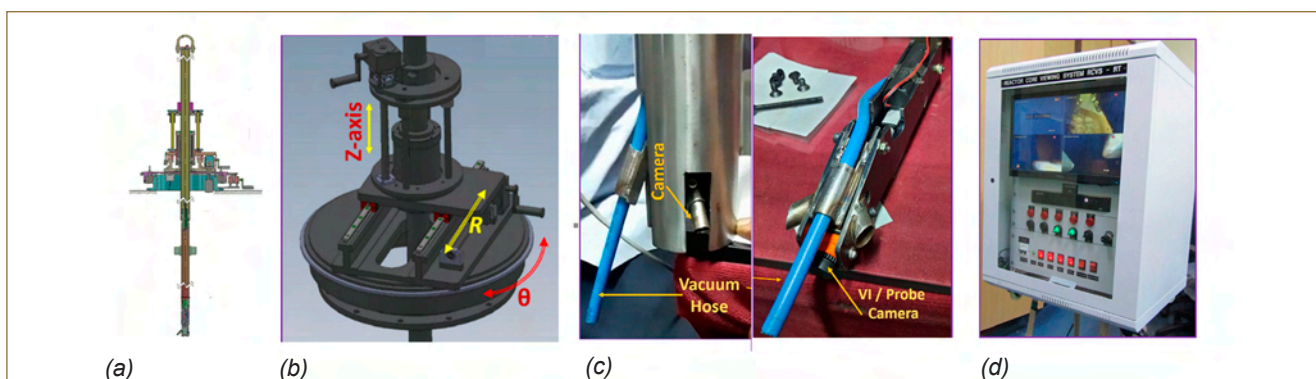


Fig. 1 (a) General assembly of the RCVS mounted over OP, (b) R, θ and Z motion for the RCVS, (c) visual inspection (VI) module and (d) RCVS control panel

II.3 Experimental Verification of the Methodology in Simulating Neutron Count Rates with 0.1 cps/nv HTFC during Initial Fuel Loading

Core monitoring during initial fuel loading and first approach to criticality of PFBR is carried out using three 0.1 cps/nv high temperature fission chambers (HTFCs), which are housed in the Start-up Neutron Detector Handling Mechanism (SNDHM). These detectors inserted in the Instrumented Central Sub-assembly (ICSA) are used to record neutron count rates. The performance of these detectors is very crucial during initial fuel loading and criticality predictions. Hence, an out-of pile experiment is performed to verify the detector response and the simulation methodology of count rates using fission equivalent fluxes in PFBR type spectrum.

Though the lattice pitch in the simulated measurement was much more than that of PFBR core, neutron spectrum is relatively closer to it. Based on simulations, two locations (Location 1 & 2) were identified for this test. In each of these locations, the measurements were carried at various axial positions using a special

mechanism. The test was repeated by covering the detector with a Cd foil which cuts the thermal neutrons and obtain a spectrum more close to the reactor. Theoretical evaluations of neutron spectrum, one group cross-sections and neutron count rates are performed using 3-D Monte Carlo neutron transport methods.

The experimental (E) and computed (C) counts at Locations 1&2 are given in Tables 1 and 2. With a bare detector, agreement is, in general, good at all active fuel regions. But, significant deviations are seen in the simulated counts at axial locations far away from the centre of active fuel due to thermal neutrons (moderation by concrete walls). At all locations of active fuel zone where neutron spectrum resembles to that of PFBR (with Cd covered detector) simulation agrees with the measurement for both locations 1&2. Thus, this experiment verified the simulation methodology of neutron count rates using HTFC detectors during initial fuel loading of PFBR. Further, the experiment establishes the sensitivity of HTFC detectors (0.1 cps/nv) in the fast spectrum environment of PFBR.

Table 1: C/E Values Neutron Count Rates at Location 1

Axial Location	Bare HTFC			Cadmium Foil Covered HTFC		
	C	E	C/E	C	E	C/E
Concrete Roof	4.64	2.80±0.07	1.65	0.95	0.86±0.05	1.10
Upper Axial Blanket (UAB)	4.05	4.11±0.08	0.99	2.70	2.99±0.10	0.90
Interface of Fuel and UAB	4.75	4.53±0.09	1.05	3.37	3.33±0.09	1.01
Center of Fuel Region	4.72	4.94±0.08	0.96	3.25	3.82±0.09	0.85
Lower Axial Blanket (LAB)	4.53	4.56±0.09	0.99	3.18	3.28±0.08	0.97
Plenum	3.75	3.95±0.09	0.95	2.40	2.81±0.07	0.85

Table 2: C/E Values Neutron Count Rates at Location 2

Axial Location	Bare HTFC			Cadmium Foil Covered HTFC		
	C	E	C/E	C	E	C/E
Concrete Roof	5.75	2.24±0.07	2.56	1.01	0.67±0.04	1.51
UAB	15.97	11.63±0.20	1.37	3.31	3.72±0.10	0.89
Interface of Fuel-UAB	18.54	12.84±0.18	1.44	4.22	4.56±0.10	0.92
Fuel Center	19.07	15.13±0.16	1.26	4.96	4.78±0.11	1.04
Interface of Fuel and LAB	18.99	13.71±0.19	1.39	4.04	4.39±0.09	0.92
Plenum	13.00	9.71±0.14	1.34	2.93	3.12±0.09	0.94

II.4 Improved Severe Accident Analysis In PFBR Using A Slug-Ejection Model

In an Unprotected Loss Of Flow (ULOF) driven core disruptive accident, sodium void propagation (in pre-disassembly phase) leads to large reactivity insertion in the reactor core. It is therefore important to characterize the rate of void propagation, which is determined by the pressure build up under two-phase flow. The existing model used for severe accident analysis does not have detailed two-phase flow module and hence leads to a slower void propagation. Here, the void fraction is estimated using Lockhart-Martinelli correlation and the subsequent pressure surge is not considered. To have more realistic simulation, the present model is improved by incorporating two phase pressure drop and slug ejection models.

For the coolant dynamics calculations, two different models are used to account for coolant boiling. Slip flow model is used for the initial stage where the vapour and the liquid moves with their characteristic velocities; the vapour “slips” past the liquid as it has higher velocity. Slug ejection model is used when the void fraction (α)

crosses 0.9. In a voided channel, there is a differential pressure which drives the liquid slug out of the core. The slug motion is studied using a force balance model, which helps to estimate the column of coolant voided in that channel. In this study, single bubble with two liquid slugs are considered. The slugs move apart in either direction with high velocity. Preliminary results on PFBR with slug-ejection model shows that the pre-disassembly phase has shorter duration of 53.3 s as against 78.8 s without slug ejection model. The axial location of coolant void and the two liquid slugs in a representative channel is given in Figure 1a. The movement of these liquid slugs along various channels (i.e. bottom surface of upper slug and top surface of lower slug) after slug ejection is depicted in Figure 1b. This model gives increased volume of core voiding in a shorter time. It is found that the reactivity addition rate at the end of pre-disassembly phase is lower resulting into a lower mechanical energy release. Further improvements in the fast voiding model using multi-slugs are being incorporated in the analysis.

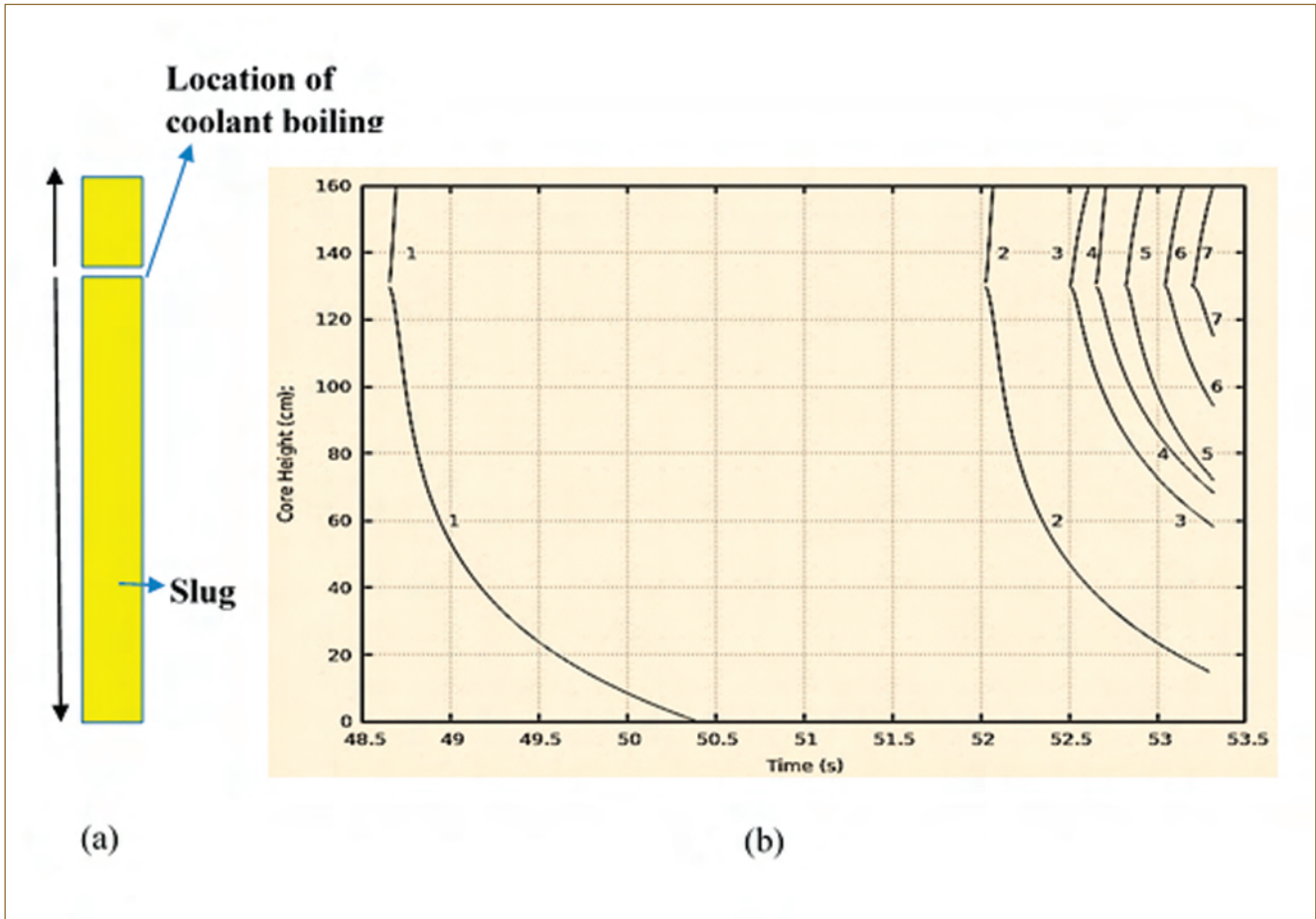


Fig. 1 Movement of slug with time in various channels after slug ejection

II.5 Seismic Probabilistic Safety Analysis Study

Level-1 Seismic Probabilistic Safety Analysis (PSA) for PFBR is about estimating earthquake caused core damage frequency of the plant. The scope of analysis is limited to full power operating state of the reactor and consist of three major parts, viz., assessing the seismic hazard at the ground level at site, assessment of the seismic fragility of various safety systems, structures and components and integration of seismic hazard with fragility information through logic models of plant safety systems. The earthquake catalogue is prepared with earthquake data of more than 200 years within approximately 300km radius surrounding the Kalpakkam site. The completeness of earthquake catalogue is studied with Stepp's method. Due to the poor correlation of historical data with seismic sources, aerial source model is used in this analysis. Four and six aerial sources are considered in this study. The de-aggregation of seismic activity among different sources is carried out using energy based approach and assumption of constant rate of activity. Attenuation relationship developed for east coast region of India is used in this analysis. Logic Tree approach with appropriate weights is followed to combine the hazard curves obtained from different models. The seismic hazard curve obtained from this study is shown in Figure 1.

Seismic fragility of a structure or equipment is defined as the conditional probability of its failure for a given value of the seismic response parameter. Peak Ground Acceleration (PGA) is the seismic response parameter considered. Zion method fragility model is used in this analysis. Since a power plant will have a very large number of components, a smaller but important list of components / structures needs to be identified based on the inputs from previous internal events PSA model and in consultation with appropriate domain experts and plant walk downs.

The next important task is to identify different failure modes of components following a seismic event and collect data for fragility estimation of these components.

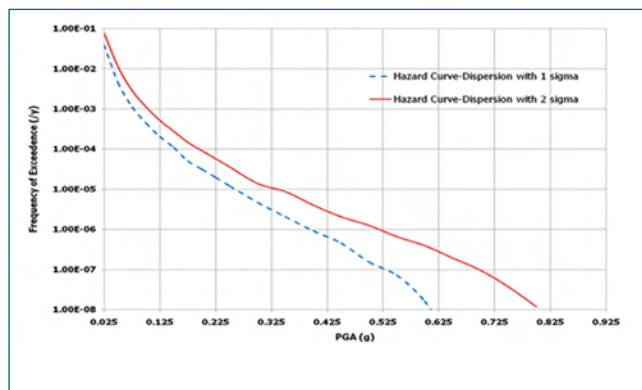


Fig. 1 Seismic hazard curve for Kalpakkam site

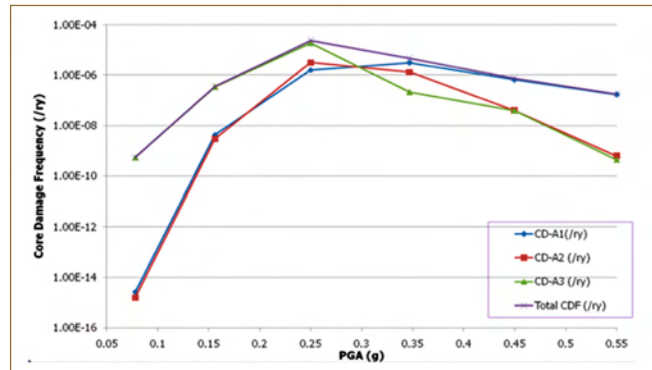


Fig. 2 Core damage frequency as a function of PGA

The data required for fragility estimation are median acceleration capacity and the associated uncertainties. The seismic margins collected from component/structure specific seismic qualification experiments, and seismic analysis are used to derive median acceleration capacity. The safety system fragility is estimated from component fragility using fault trees.

The accident sequence models with seismic event as initiator is developed with the help of event trees. The event tree analysis is carried out with conservative hazard curve of one sigma dispersion instead of the mean hazard curve. Core Damage Frequency (CDF) estimated for different PGA levels and its total are summarized in Table 1.

The estimated total core damage frequency from seismic events is ~3.0E-05 / ry. The variation of Core Damage Frequency as a function of PGA is shown in Figure 2. A sensitivity study using AERB recommended seismic hazard curve is also carried out. This analysis would meet capability category II of ASME standard with respect to level of detail and plant specificity. Future directions for the improvement of this study such as including the secondary effects of seismic events, fragility of civil structures, reactivity changes due to relative motion and its impact on process parameters are also identified.

Table 1: Estimated Core Damage Frequency				
PGA Midpoint (g)	CD-A1 (1/ry)	CD-A2 (1/ry)	CD-A3 (1/ry)	Total Δ CDF (1/ry)
0.078	2.60E-15	1.60E-15	5.50E-10	5.50E-10
0.156	4.30E-09	3.00E-09	3.50E-07	3.57E-07
0.25	1.62E-06	3.24E-06	1.92E-05	2.40E-05
0.347	3.16E-06	1.34E-06	2.17E-07	4.72E-06
0.45	6.72E-07	4.00E-08	4.00E-08	7.52E-07
0.55	1.76E-07	6.30E-10	4.50E-10	1.77E-07
Total CDF				3.0E-05
A1-large & early CD; A2-large & late CD; A3-non-energetic late CD				

II.6 Vibration Limits for Annular Linear Induction Pump in Secondary Sodium Main Circuit

Electromagnetic (EM) pumps are used in secondary sodium loops in PFBR. The vibration measurements carried out on EM pump dished end, suction and discharge locations show the vibration in EM pump contains predominantly high frequencies. There is a possibility of fatigue at critical locations due to internal vibration of EM pump or piping layout. In the absence of qualitative force data, measured accelerations data are used as guiding source for generating forces in EM pump.

In series of dynamic analysis, forces in EM pump at the various location are applied and scaled, such that the measured acceleration can be re-produced. Figure 1 shows the vertical acceleration obtained from FEM analysis and measurements. In the piping region, surface traction is applied in suction and discharge side, with applicable piping frequency to create resonance on both sides, such that bounded velocity response attained due to resonance is 12 mm/sec.

With these generated forces, detailed dynamic analysis of integrated model with EM modeled with solid elements to assess fatigue damage. To capture stress concentration effect at nozzle locations, suction and discharge nozzle regions of EM pump-2 are modelled with solid elements. Figure 2 shows mesh used in analysis at suction and discharge locations. Figure 3 shows the piping layout with one pump partially modelled with solid elements and remaining domain modelled with shell elements.

Stress at suction is nozzle location are extracted at maximum stress location. Figure 4 shows the maximum stress distribution at suction nozzle. The maximum stress range ($\Delta\sigma$) is found to be 84.83 MPa. The stress

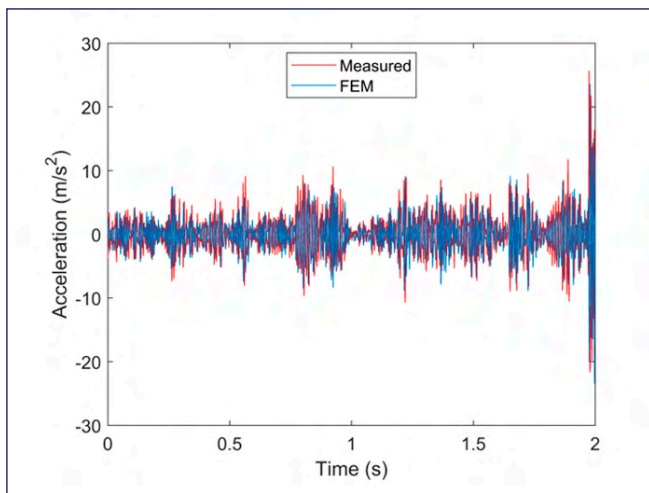


Fig. 1 Comparison of vertical acceleration from measurement and FEM analysis at dished end

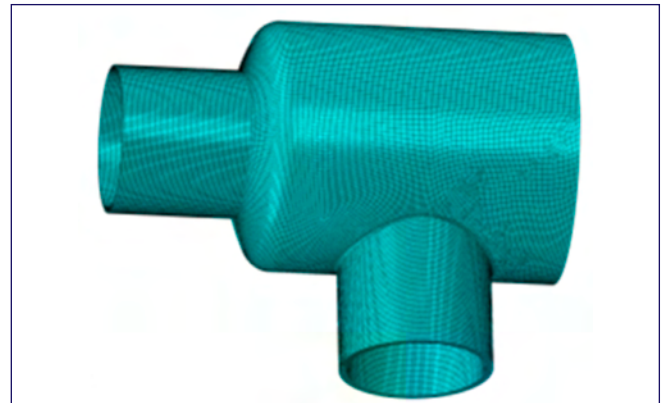


Fig. 2 Mesh details of EM pump region modelled with solid elements

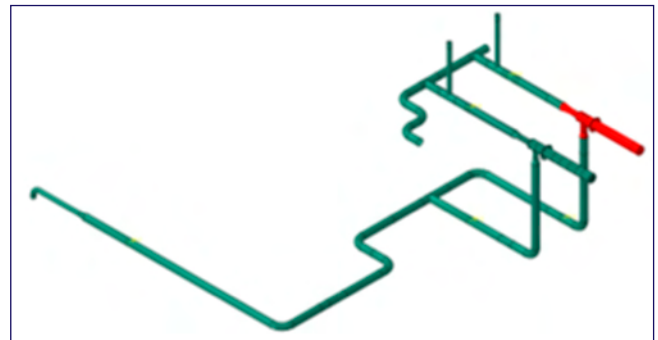


Fig. 3 Integrated piping EM pump layout with pump with solid elements shows in red color

amplitude computed from stress range as per ASME Sec VIII Div 2 is 60.51 MPa, which is less than endurance limit of S-N curve. Based on dynamic analysis, in suction and discharge piping layout, vibration velocity of 12 mm/sec is acceptable. However, frequency of vibration shall be in piping frequency regime (5-20 Hz). The vibration acceleration on EM pump dished end less than 25 m/s² in vertical direction, 15 m/s² in horizontal direction and 15 m/s² in axial direction is acceptable.

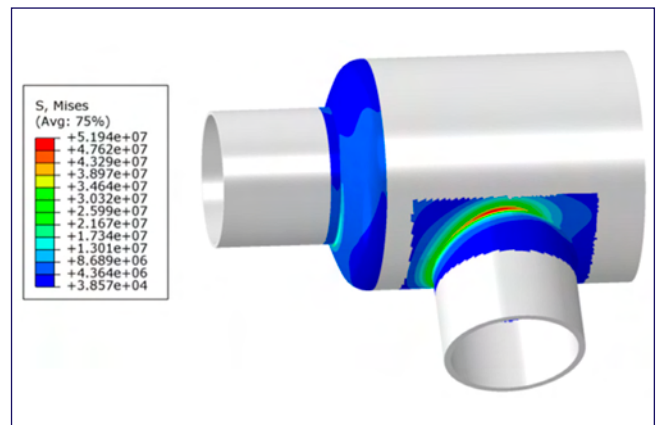


Fig. 4 von Mises stress (pa) distribution in EM pump nozzle location

II.7 Stability Analysis of Secondary Sodium Pump

The Secondary Sodium Pump (SSP), shown in Figure 1, consists of a 5.6 m long hollow vertical drive shaft supported by thrust bearing and radial bearing at the top and hydrostatic bearing at the bottom within a cylindrical casing. The space between shaft and casing is partially filled with liquid sodium. The pump impeller is mounted at the bottom most portion of the shaft. The hydrostatic bearing (HSB) which is guiding the shaft at bottom portion is positioned just above the impeller and is fed by pressurized sodium from the pump discharge. HSB is connected to the discharge casing, which in turn is connected to the outer casing through a slip joint. The spherical header which is part of outer casing is having two discharge nozzles and one suction nozzle. The outer casing as shown in Figure 1 is bolted to the floor at EL 37.5 m. The suction nozzle connecting the suction piping is restrained laterally at the bottom. The pump shaft is coupled to the drive motor shaft by means of a flexible coupling. The pump drive is a variable speed AC induction motor, capable of running at any speed between 15 and 100 % of the nominal speed.

Other than HSB, suction wear ring (SWR) and discharge wear ring (DWR) play key role in ensuring the stability of the pump. The required radial stiffness for HSB and wear rings is provided by the pressure head of sodium, delivered by the pump itself. Thus, the stiffness is a strong function of pump speed as shown in Figure 2.

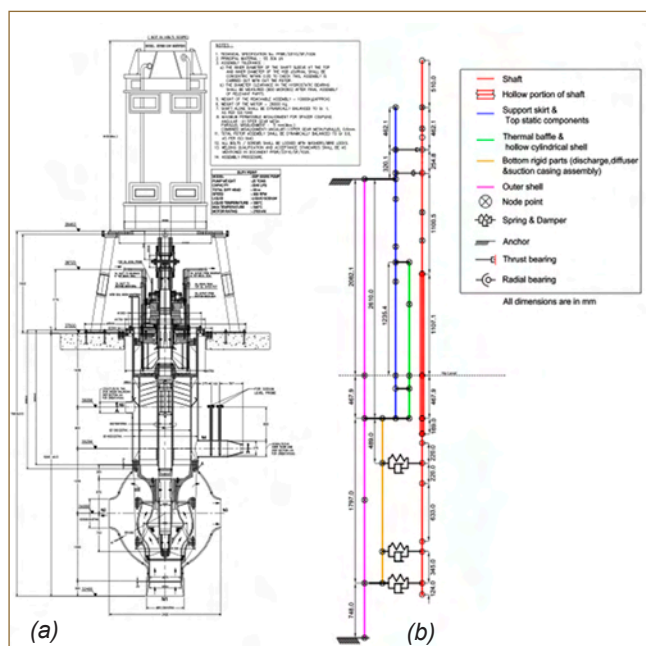


Fig. 1 (a) schematic of SSP pump; (b) finite element model of SSP

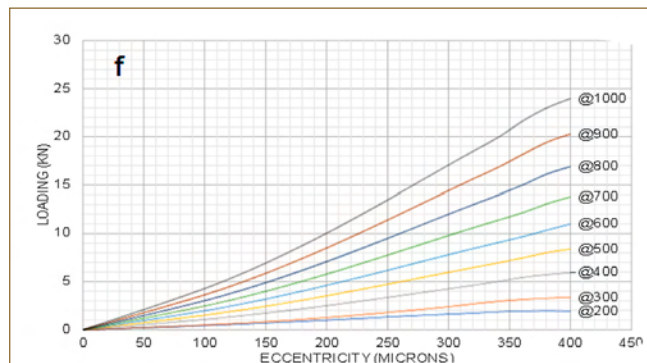


Fig. 2 Load characteristic of HSB for various RPM

The rotor-dynamic parameters of wear rings are strong function of radial clearance and the inlet swirl. The temperature of sodium has a negligible effect on the wear ring parameters. The stiffness, damping, and mass terms of the discharge and suction wear rings for $R\omega/4$ and $R\omega/2$ inlet swirl values and 0.5mm & 1.0 mm radial clearance are calculated where R is the radius of wear ring and ω is rotational speed of the pump.

The stiffness values of HSB are determined by solving a set of strong non-linear fluid mechanics equations along with appropriate boundary conditions. Apart from effect of HSB and wear rings, effect of gyroscopic coupling is also included in finite element formulation which is also a function of pump speed. The effect of sodium is considered as added mass on the shaft by modifying the equivalent density. Other than the mass effect, the damping effect of sodium is accounted by computing the equivalent damping coefficient based on published literature.

An in house code is developed in CAST3M for rotor dynamic analysis. The network analysis of the HSB is solved using the segregated CFD approach where the system of equations is mapped on to a FEM mesh and solved for pressure. The stability analysis is performed by numerically solving dynamic equation for complex eigen values in state space formulation using Implicitly Restarted Arnoldi Method. The root locus plot for the secondary pump is shown in Figure 3. The root locus plot shows that the system is stable with respect to all eigen modes. In Figure 3 up to six modes are shown for 1 mm and 0.5 mm clearance in suction and discharge wearing. The shaft is stable due to the stabilizing effect of damping and cross-coupling stiffness. Therefore, the performance of the Top radial bearing, HSB, the

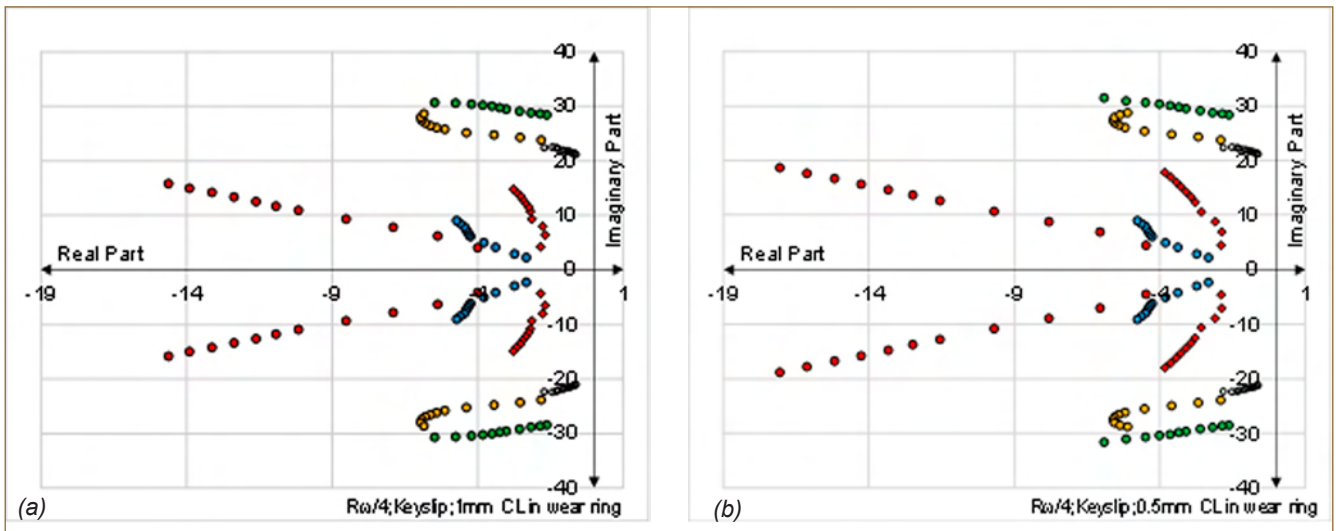


Fig. 3 Root locus plot for secondary sodium pump (a) for 1 mm and (b) for 0.5 mm clearance in suction and discharge wear ring

impeller and the discharge and suction wear rings are very important to understand the system.

Statistical energy analysis is done to evaluate the performance of top radial bearing (TRB), HSB, impeller and the wear rings. The statistical energy analysis is done based on the time domain analysis of the pump. The energy plot shows the potential and the kinetic energy distribution per cycle stored by the system from the external work done by the vibratory force of shaft imbalance. The damping in the system dissipate the energy and reduce the response of the system. This plot will also give an idea of how the bearings and wear rings are effective in controlling the response of the shaft. Figure 4 shows the kinetic energy and the potential energy distribution in the system for imbalance, coupling force and the shaft sleeve eccentricity load case.

The energy dissipation in the system is shown in the

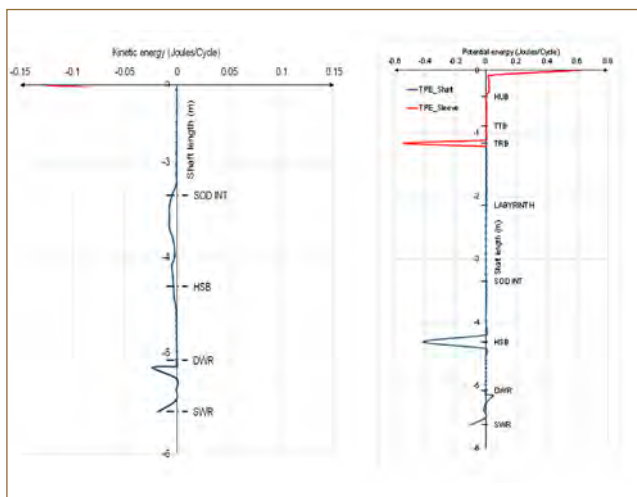


Fig. 4 Kinetic and potential energy of shaft of secondary sodium pump

Figure 5. The total energy dissipated is positive for all pump rpm. Small hump at 700 rpm in the total energy dissipation plot is due to the coupling force exciting the second mode in the shaft. The response due to this is kept under control by the hydrostatic bearing (HSB) at the bottom and the top radial bearing which contributes maximum to energy dissipation. The contribution of discharge and suction wear rings and the impeller (IMP) are comparatively less.

The root locus method shows that the system is stable with respect various modes of pump. While the energy analysis gives a detailed picture of how each component is performing during the operation of the pump. From these two analyses, it can be concluded that the pump is stable within its operating range.

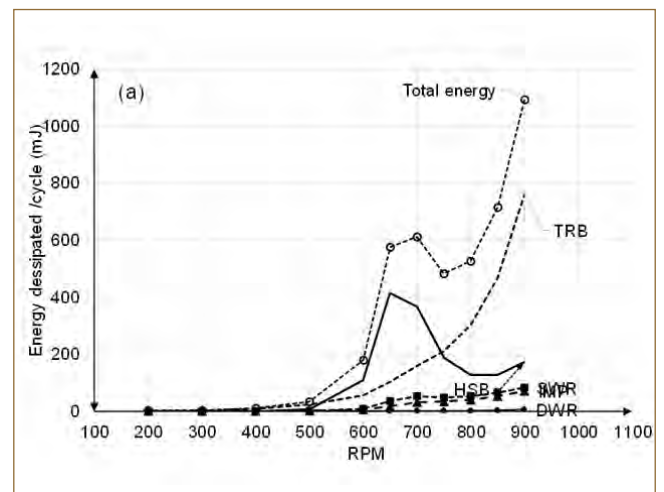


Fig. 5 Energy dissipated by key components of SSP

II.8 Vibration Analysis of IHX Down-comer for Postulated Fluctuating Fluid Forces

To improve the thermal flexibility, Intermediate heat exchanger (IHX) of PFBR has to be modified by removal of first guard pipe compartment weld joint provided near IHX inlet & outlet nozzles. To study the effect of this weld removal on dynamic behavior of the downcomer pipe, free vibration analysis is carried out. The fundamental frequency of inlet sodium pipe line along with down-comer reduces to ~ 1 Hz when the guides (spacer pads) provided for the down comer at two elevations is in open condition. When the guide supports are in closed condition, the natural frequencies of downcomer are above 8Hz.

The present work involves analytical estimation of steady and fluctuating fluid forces on pipe elements and the analysis of dynamic responses of piping along with down-comer due to a postulated fluid flow fluctuation of $\pm 10\%$ of nominal flow and with a frequency of 0.5/1 Hz. From the calculated net reaction forces on the guide support due to thermal-mechanical loads and fluid forces, it is checked whether any external force/support is additionally required or thermo-mechanical force itself

is sufficient for maintaining the guide in closed condition to avoid vibrations of the down-comer.

Pipe line model

Finite element model of secondary sodium main circuit piping from secondary sodium pump (SSP) to IHX along with downcomer has been generated in CEASAR using pipe elements as shown in Figure 1. Apart from piping supports, the down comer has two guide supports inside IHX. Unlike other supports, in these two guide supports, a gap of 1mm is available between guide support plate and the inner shell of IHX. During seismic conditions, these two guide locations will behave like lateral restraints, as the displacement due to seismic motion will be much higher than 1mm gap. But for vibration analysis, the effect of gap has to be considered as the vibration amplitude may be low and continuous and can give rise to noise during operation due to small amplitude hitting. For static analysis, these guides are modelled as gapped restraints with 1mm gap. During transient time history analysis, these guide supports are considered as open in one case and closed in another case.

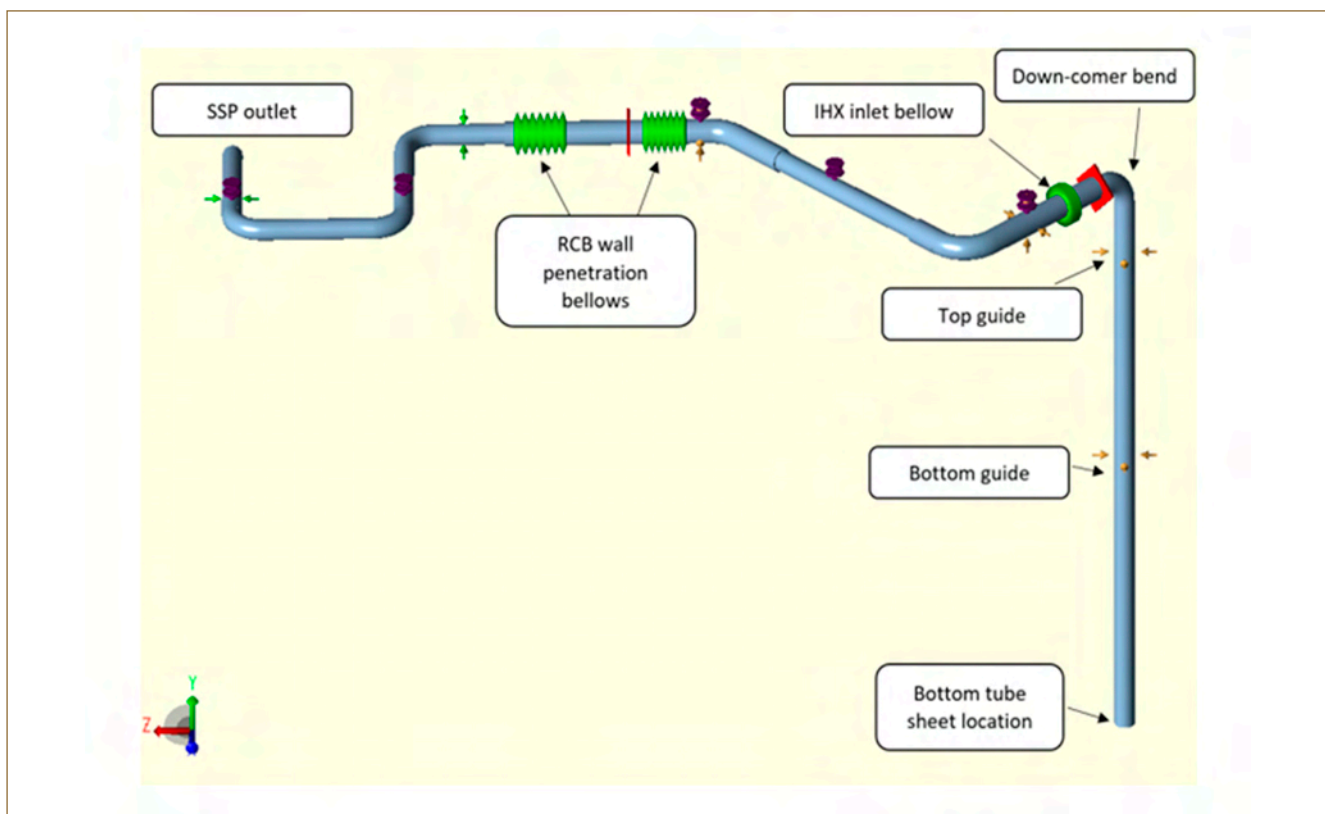


Fig. 1 Pipe line model from SSP to IHX bottom tube sheet

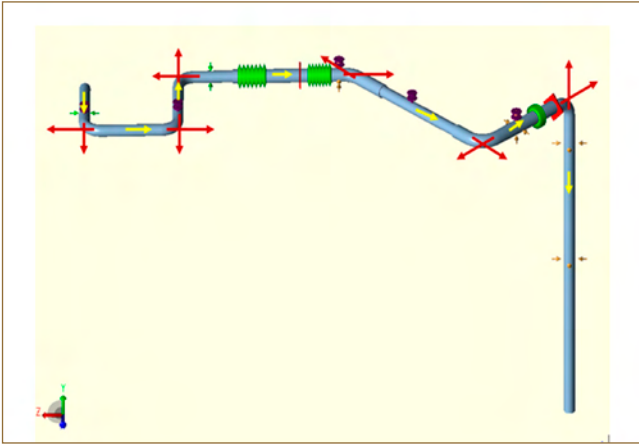


Fig. 2 Fluid forces on sodium pipe line

Fluctuating fluid flow

In order to understand the dynamic behaviour of pipeline, the flow is assumed to be harmonic with mean (2900 kg/s) and amplitude (290 kg/s) with frequency of 0.5 Hz in one case and 1 Hz in another case

Forces on pipeline due to fluctuating fluid flow

Due to fluctuating flow, the flowing fluid is getting accelerated and decelerated along the flow direction. Due to this acceleration and deceleration, apart from static pressure, dynamic pressure is developed at SSP outlet. The amplitude of dynamic pressure is maximum at SSP outlet, linearly reducing over the length of the pipeline and diminishing at the surge tank location. Due to this additional dynamic pressure, the pipe element is experiencing time varying forces along with the static pressure forces. The direction of forces acting on each pipe line segments are shown in Figure 2.

Natural frequencies

Eigen value analysis were carried out to find the natural frequencies of the system for different boundary conditions and findings are given in Table 1. If the guides

Condition	Natural Frequency (Hz)
With gap closed condition before weld removal	9.44 Hz
With gap closed condition after weld removal	8.80 Hz
With gap open condition before weld removal	8.8 Hz
With gap open condition after weld removal	1.03 Hz

are assumed to be in closed condition, the natural frequency of the downcomer plus pipe is still above 8 Hz even after removal of first compartment weld joint. When guides are assumed in open condition, the natural frequency of the down-comer plus pipeline is reduced from 8 Hz to ~1 Hz which is in the range of the flow oscillations frequency considered.

Static analysis for thermo-mechanical and steady fluid flow loads

Static analysis was carried out for the dead weight, pressure load, and thermal load for different reactor operating conditions i.e., transient, normal, isothermal and shutdown conditions. It is found that the gap will be closed in top guide location due to thermal expansion of pipe and the minimum reaction force exerted by pipe on guide location is found to be 7.5 kN during reactor shutdown condition.

Dynamic analysis for fluctuating fluid loads

Later, dynamic response analysis was carried out to find the dynamic responses with different guides open-close conditions for fluctuating fluid forces with 0.5 Hz and 1 Hz oscillations. In order to have negligible vibrations in the down-comer pipe, at least gap in the top guide should be in closed condition in all the operating cases. In order to confirm the gap will be remaining in closed condition, the net reaction forces were computed using algebraic summation for different reactor operating conditions. These reaction forces are vectorised in two orientations of spacer pads respectively global X-Z axis and 30 axes. For both the orientation, the net static forces on top guide location for all the operating conditions are higher than the fluctuating components as given in Table 2.

Hence top guide gap will be always in closed state and vibrations due to flow fluctuations will be negligible.

Cases	Steady		Fluctuating (1 Hz)	
	X	Z	X	Z
Transient	-16.5	-19.7	3.7	0.6
Normal	-21.1	-15.8	3.7	0.6
Isothermal	-24.6	-21.0	2.9	0.5
Shutdown	-8.1	-7.5	0.7	0.1

II.9 Technical Support towards Rectification of LRP Bearing

During rotation trials of LRP & SRP at PFBR under pre-heated condition, light noises coupled with increased torque were noticed. Subsequently, several investigative studies & activities were carried out to understand the cause and arrive at remedial measures. As an outcome of these studies, following three possible reasons for the problem were narrowed down:

- Excessive non-uniform temperature distribution along the circumference of bearing support structure, leading to non-uniform thermal expansion between top & bottom races when the bearing is rotated.
- More than the recommended unevenness of bearing support structure.
- Bearing ball configuration where only load balls are provided without spacer balls.

Coupling & de-coupling arrangement for LRP

To access the bearing for further investigation, the load of LRP needs to be relieved from bearing and the bearing top race along with top & middle ring (TMR) is to be lifted. Towards this, a novel mechanical arrangement was designed and detailed out (Figure 1). The arrangement uses the concept of multiple screw-nut arrangement (86 Nos.) positioned along the inner circumference of TMR. A separate ring plate is provided at the inner edge of TMR to support the screw-nut arrangements and transfer the LRP load to bearing before the same is lowered. The tie

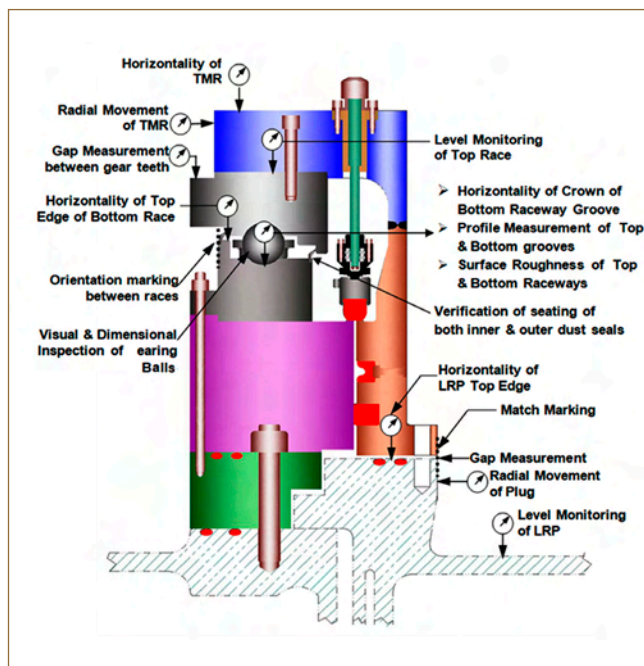


Fig. 2 Identified inspection requirements

rod, which is part of the arrangement is threaded to the M24 holes, one by one by removing the existing M24 screws connecting LRP to TMR.

Further, a detailed procedure was worked out to relieve the load of LRP from bearing using the installed tie-rod arrangement and lift the top race and TMR. The same was qualified in a simulated scaled mock-up.

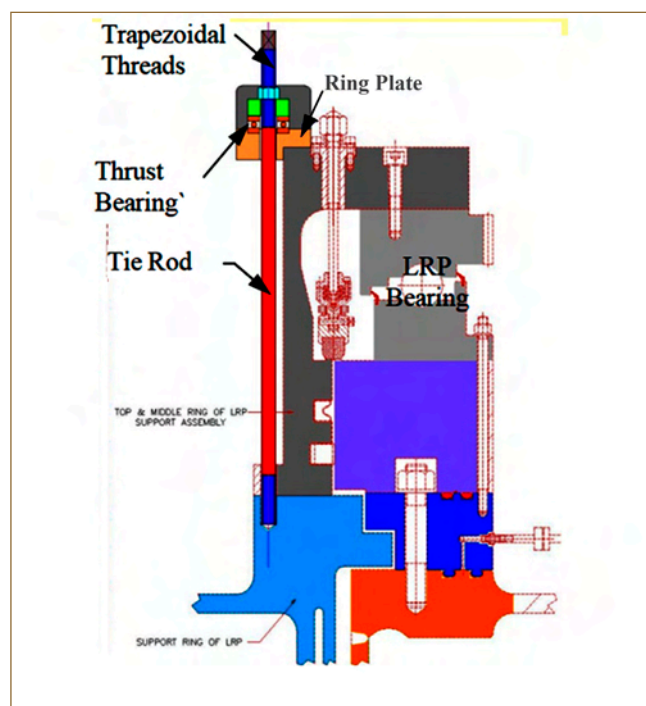


Fig. 1 LRP coupling / de-coupling arrangement

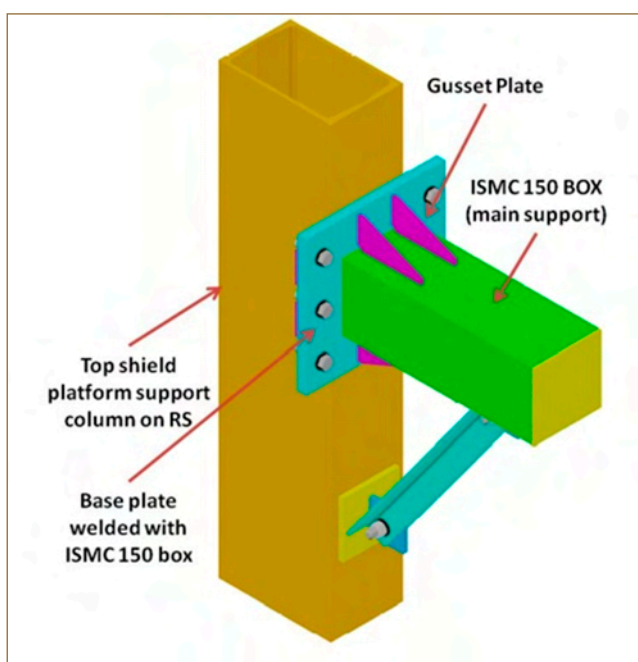


Fig. 3 3D View of Temporary support structure for TMR along with bearing top race

Subsequently, LRP weighing ~400t was lowered to directly over the roof slab.

Inspection requirements during bearing rectification

An inspection scheme was prepared identifying requirements before, during and after de-coupling/ coupling to ensure that both LRP bearing and plug are brought back to their original position. The list of baseline data to be generated prior to de-coupling were also identified. Figure 2 gives the schematic of inspection requirements specified.

Towards handling and supporting the TMR temporarily, the design & analysis of temporary support structure (Figure 3) and lifting spider (Figure 4) were carried out. To facilitate comfortable space for cleaning and inspection of races, the elevation of temporary support structure was finalized suitably.

Analysis for Presence of wear particles

Subsequent to hoisting the TMR along with top race, the grease samples were extracted from the bottom race throughout circumference for analytical ferrography. The samples were tested for the concentration & distribution of wear particles and following salient observations were made:

- Presence of ferrous particles in the grease were varying from 111-238 ppm against the acceptable concentration of 10000 ppm.
- Severe sliding wear particles of up to 128 microns, laminar wear particles of up to 188 microns & fatigue wear particles of up to 142 microns have been seen.
- The concentration of wear particles were slightly higher in the sector from 30° to 240°.

Raceways & balls inspection

After cleaning the grease from the races, visual inspection of the races were carried out. Small indentation marks (Figure 5) were noticed along the rolling track, which are characterized by video stereoscopy.

Study of bearing support undulations

After the unloading of bearing and cleaning of races,

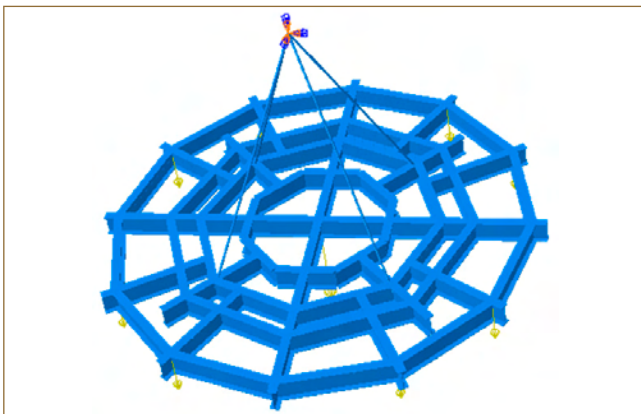


Fig. 4 Lifting spider for TMR & top race



Fig. 5 Visual inspection of races

horizontality measurement of bearing bottom race crown portion, the top surface of flange and top outer edge of bottom race were carried out to find out the undulations in bearing support structure. From the measured readings, slope part and undulation part are separated by fitting a sine curve along the reading as the slope part of the error will be in the form of sinusoidal curve when plotted. The observed maximum undulation is only marginally higher than the recommended undulation.

Sizing & production of spacer balls

Decision was taken to change the bearing ball configuration from only load balls to load+spacer arrangement. Calculations were done to optimize the spacer ball dimension as well as load acting through the spacer ball under various conditions postulated when the ball navigates an undulation. Since the spacer ball rotates in one direction whereas it slides in reverse direction, the load acting on spacer ball is taken as a criteria for sizing the ball and based on the study, ϕ 92 mm is chosen as spacer ball diameter. Subsequently, the spacer balls were produced following the hardening heat treatment procedure established by MMG/IGCAR.

Selection & procurement of lubricant grease

With load+spacer ball configuration, number of load carrying balls are reduced significantly, which results in increased load per ball. Also, it is observed that frequent re-lubrication is not an easy task in the absence of dedicated provision except for re-greasing nipples. Hence, necessity of using a grease, which has got very high load carrying capacity (four ball weld load) and also having large re-greasing interval was identified. Based on literature review and discussions with experts, a proprietary grease from an indigenous supplier was recommended and procured.

The necessary technical support towards inspection / rectification of LRP bearing was extended. Based on the detailed inspection, it is decided to box-up the bearing after changing the bearing ball configuration with load+spacer balls configuration and replacing the grease with a new grease having high load carrying capacity and long life.

II.10 Design and Manufacture of Nickel Detectors for Steam Generator Tube Leak Detection System

Following a tube leak event in PFBR Steam Generator (SG), high pressure water/steam from tube side enters the sodium side (shell side) which results in a violent sodium-water reaction, liberating hydrogen. To detect the tube leak, steam generator tube leak detection (SGTLD) system is provided. Hydrogen in Sodium Detection Circuit (HSDC) is provided in each SG sodium outlet line and one at the common outlet header in the secondary sodium main circuit. HSDC in each individual SG is provided with Electro Chemical Hydrogen Meter (ECHM) which uses the principle of EMF generated between reference and sample electrodes. At the common outlet, in addition to ECHM, Nickel detector with shell side vacuum maintained by Sputter Ion Pump (SIP) is provided to confirm the leak. The schematic arrangement of HSDC with both ECHM and Nickel detector is shown in Figure 1.

In order to improve the reliability of hydrogen detection, additional nickel detector for each SG outlet is now conceived as a diverse detector. The schematic arrangement of the conceived scheme is shown in Figure 2. The Nickel detector consists of four tubes made of 99.9 % pure nickel of diameter 6.6 / 7.2 mm bent to 90° and connected to a 32 NB SS 316LN pipe. The sodium flows

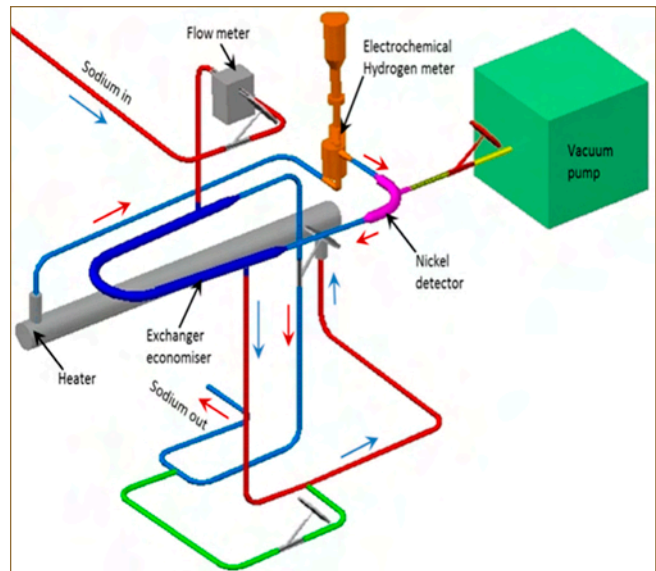


Fig. 2 Scaled 3D layout of hydrogen in sodium detection circuit

through the tubes. The area of nickel tubes wetted by sodium is 184 cm². The cross sectional view of Nickel detector assembly is shown in Figure 3. The shell side of the detector is kept under high vacuum maintained by an ionic pump and the quantity of hydrogen diffusing through

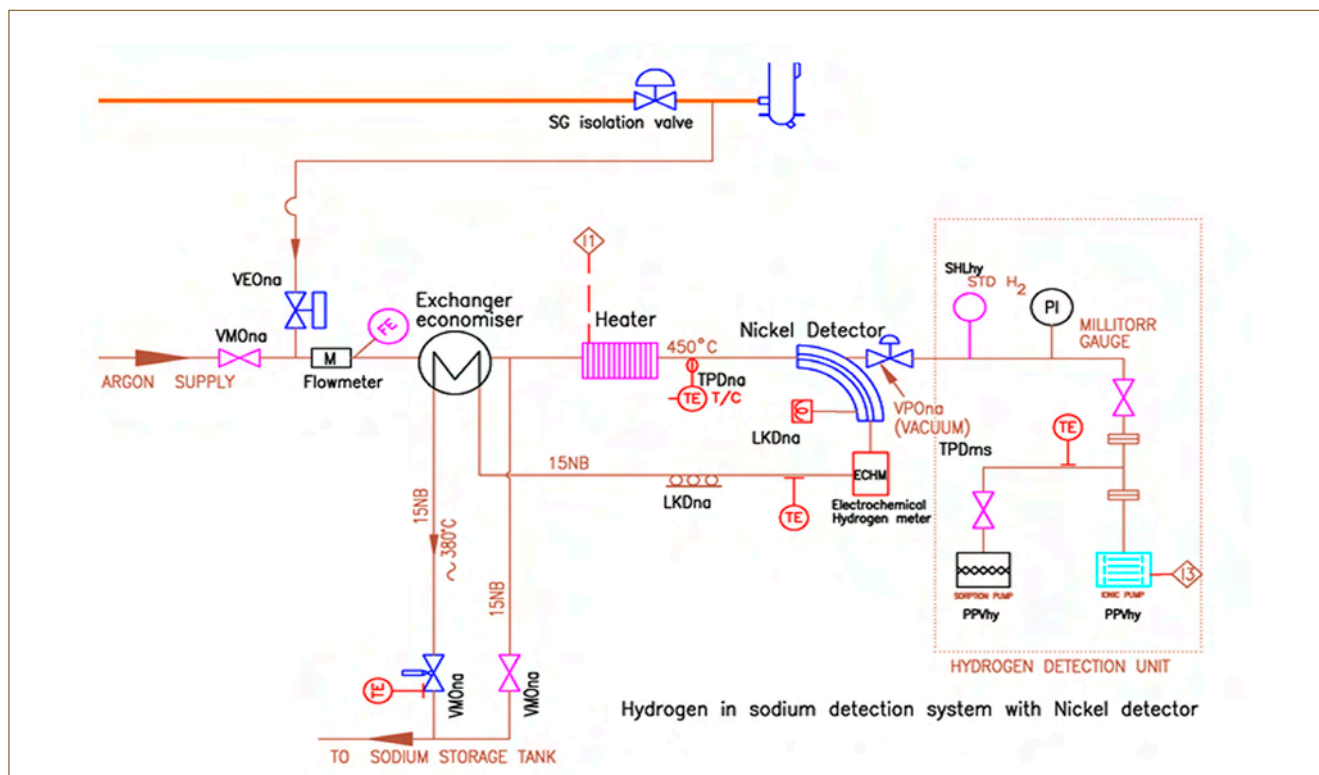


Fig. 1 Schematic arrangement of hydrogen in sodium detection circuit

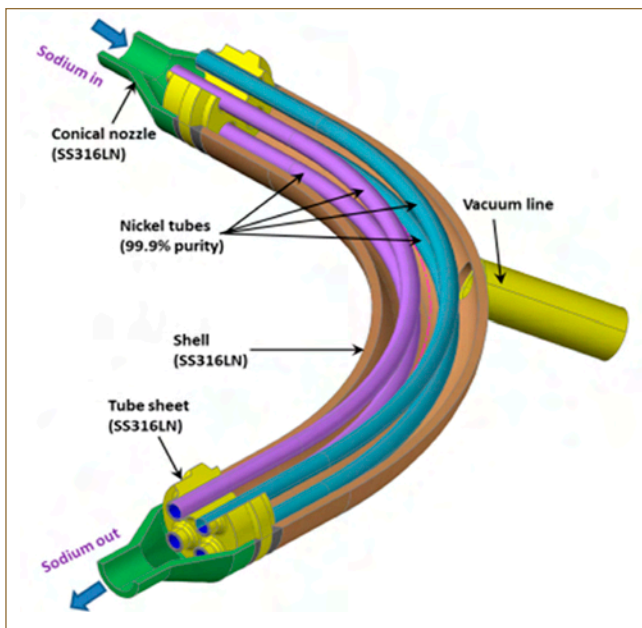


Fig. 3 Cross sectional view of nickel detector assembly

the thin walled nickel tubes is measured based on current consumed by sputter ion pump. The flow rate of sodium through the nickel tubes is maintained at 1 m³/h which is indicated by the flow meter provided in the individual circuit.

The small diameter, thin walled nickel tubes made of high purity nickel, meeting the required quality standards were manufactured by Nuclear Fuel Complex as an import substitute. The nickel detectors were manufactured in-house by Central Workshop Division, IGCAR. Since the nickel detector is a critical component, the manufacturing process includes stringent requirements of visual examination, ultrasonic testing, LPE and helium leak test at various stages. Finally, pneumatic test at 32 bars (g) was carried out to qualify each nickel detector assembly for its structural integrity. The entire SGTLD piping system was re-verified with newly introduced nickel detectors for both static and dynamic loading conditions.

II.11 Simulation of Pressure Transient under Turbine Trip Event

In the Steam Water System (SWS) of PFBR, there are isolation valves provided at the inlet of turbine to isolate the turbine whenever required. Event of spurious closure of these isolation valves (turbine trip event) during full power operation has been studied using FLOWNEX code. This is a category 2 Design Basis Event (DBE) for the plant. Due to the sudden closure of these valves, steam lines will be pressurized due to water hammer effect. Turbine bypass valves (High Pressure and Low Pressure By Pass Valves – HPBPV&LPBPV) get opened based on high pressure developed in the line and part of the steam from the steam generators (SGs) (maximum 60%) will be diverted through this path (Figure 1). The remaining part find a path for its escape through steam relief valves known as Electromatic Relief Valves (ERVs) provided in the circuit. Depending on the extent of pressure transient occurring, Safety Relief Valves (SRVs) may also get opened to relieve the pressurization. Turbine bypass valves, ERVs and SRVs are provided at different locations in the steam line with respect to the turbine isolation valve. The pressure

transient scenario in steam line during turbine trip event depends on various factors, viz., (i) size and layout of steam circuit, (ii) closure / opening times of isolation and relief valves, (iii) opening set points of various valves and (iv) location of various valves in the circuit. Studies were carried out earlier for a reference layout configuration of steam line. Presently, analysis of turbine trip event has been carried out using FLOWNEX code to establish the dynamic pressurization scenario possible in PFBR for the as built conditions in the plant.

The computational domain included the steam lines from SG outlet to turbine inlet, reheater (RH) lines up to RH outlet (since a part of the steam from SGs always flows through RH) and bypass lines up to bypass valve outlet. All pipes are considered rigid in the simulation conservatively to obtain higher values predicted for the transient pressure. Heat losses from the pipes to the ambient is neglected. Default friction factor correlations are used to calculate friction pressure drops (Darcy Weisbach type) in the pipes. Pipe roughness for all pipes is assumed as 50 µm. Valve loss coefficients are

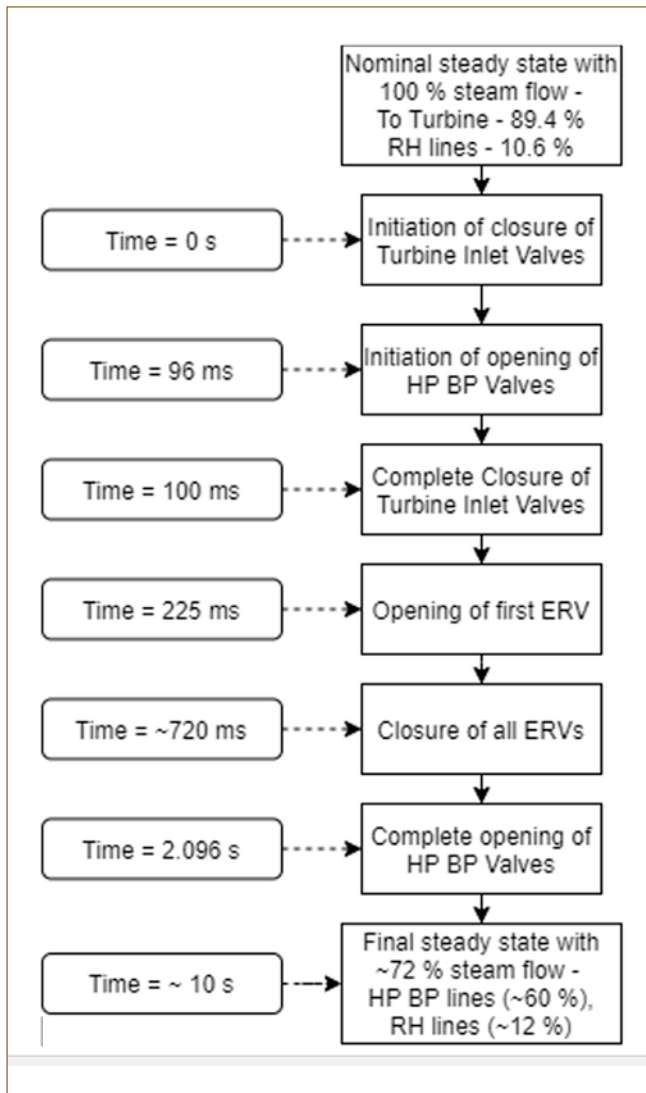


Fig. 1 Sequence of actions during the event (approach 1)

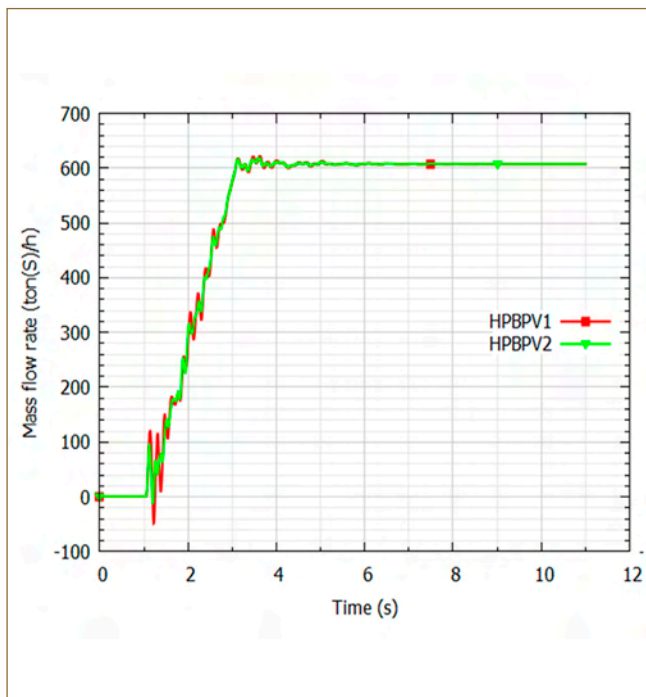


Fig. 2 Evolution of steam flow rates in the HP bypass lines (approach 1)

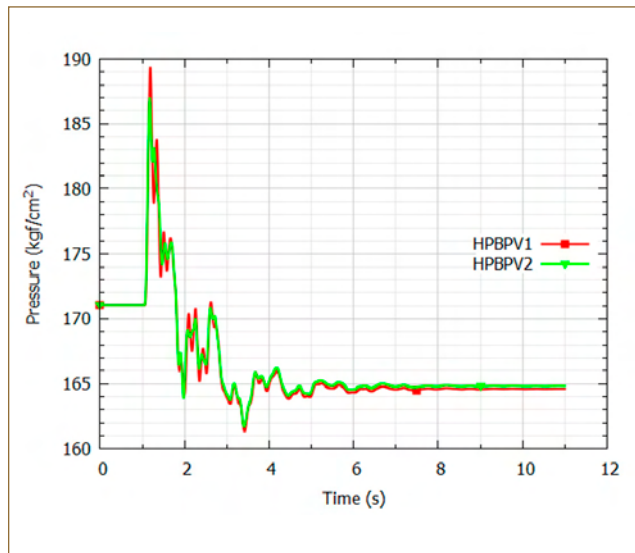


Fig. 3 Evolution of steam pressures (at HPBPV upstream in approach 1)

assumed to be the same in both forward and reverse directions. SRVs and ERVs are assumed to open/close instantaneously without any delay and HP bypass valve is assumed to open linearly in 2 s duration. The isolation valve closure time considered is 100 ms.

Steady state simulation was carried out first to establish initial conditions corresponding to normal full power operation of the plant. Pressures at upstream of various relief valves were all less than their respective set pressures. Then the transient event simulation was carried out using 2 bounding approaches – one by considering SG outlets as constant pressure and constant temperature reservoirs, and the other by considering SG outlet as constant mass source supplying steam continuously at specified quality. Two approaches were followed because of the restricted domain of the system without SG, RH, Boiler feed pump etc. considered for the analysis. Approach 2 is more conservative as it results in more amount of steam addition to the steam lines from the SGs. In both the approaches, HPBPVs get opened and 60 % of the steam from the SG flow through this path (Figure 2). In approach 1, only the ERVs are blown for a short duration and SRVs remain closed. In approach 2, 1st and 2nd set of ERVs are blown and remain open, while the 3rd set ERVs are blown for a short duration and then close. SRVs open for a short duration (1-2 s) and then close. The maximum pressure reached in the steam lines during the transient is ~ 14 % higher than the nominal value in both the approaches (Figure 3) which is within permissible level. In future, it is planned to extend the model domain to full SWS circuit so that event simulation in the whole plant in a coupled manner (SWS + NSSS Nuclear Steam Supply System) becomes possible.

II.12 Evaluation of Argon and Oxygen Levels in Nitrogen Generated by Pressure Swing Absorption Method

Argon is used as the cover gas for PFBR main vessel and nitrogen in the annular space between the main and the safety vessel. Continuous monitoring of argon in nitrogen therefore, provides the information about any breach in the main vessel. Similarly, oxygen level in nitrogen also needs to be monitored to prevent the oxidation of structural materials. The nitrogen gas is generated by the pressure swing absorption (PSA) technique for filling inter annular space between main and safety vessel. This work describes the analysis of nitrogen sample received from nitrogen storage tank of PFBR using online gas chromatography. Online gas chromatography (OLGC) employed for quantitative assessment of argon and oxygen in nitrogen is provided with a molecular sieve of 5 Å size as the stationary phase packed in a column which is maintained at 323 K and a high purity (99.999%) helium flowing at the rate of 40 cc/min through the column serving as the mobile phase. About 1 cc of the sample gas is admitted into the stationary phase using an automatic sampling valve provided in the carrier gas circuit. A stainless steel sampler of volume 2.5 litres filled with UHP nitrogen up to a pressure of 7 bar (absolute) is added with a calculated quantity of argon gas for calibration of OLGC. Prior to nitrogen filling, the vessel is evacuated and then filled with UHP (Ultra High Purity) nitrogen. The process of evacuation and filling is repeated three times to remove any residual oxygen/argon present in the vessel. This vessel is connected to the inlet line of GC and the chromatograms are recorded for different gas mixtures of argon and nitrogen. The stainless steel sampler filled with the sample gas drawn from the nitrogen surge tank of BHAVINI at a pressure of 7 bar (absolute) is then connected to OLGC and the chromatograms are recorded. The experiments are repeated several times for reproducibility. An efficient

oxygen scrubber containing calcium getter maintained at 573 K is connected to the carrier gas circuit of GC to remove oxygen and moisture from UHP nitrogen. The chromatograms are recorded before and after scrubbing oxygen from the sample gas. Five different concentrations of argon in nitrogen were prepared and analyzed. The plot of area under the peak versus the concentration of argon is shown in the calibration graph (Figure 1a). The peak with a retention time of 9.75 min is characteristic of argon. In the same way, calibration of argon in nitrogen containing different quantities of oxygen is also carried out. While the peak with a retention time of 9.75 min corresponds to argon, another one appearing as a shoulder with a retention time of 9.97 min is characteristic of oxygen. Typical elution profile of 200 vpm of argon and 130 vpm of oxygen in nitrogen is shown in Figure 1b. After performing the calibration, nitrogen samples received in batches on different occasions from PFBR were analyzed. Figure 2 shows the elution profile of the gas sample received. The experiment was repeated thrice as marked by three runs to rule out any error during sampling. An intense peak appearing at a retention time of 9.75 min without any shoulder at 9.97 min indicates that argon is present in large quantities and oxygen in trace levels. Based on the area under the peak, the concentration of argon in nitrogen sample is deduced to be 1.33%. Nitrogen samples received on different occasions were also analyzed and the patterns were nearly similar and reproducible. The results show that argon in nitrogen is in percentage levels and its level was found to vary from 0.91% to 1.34%.

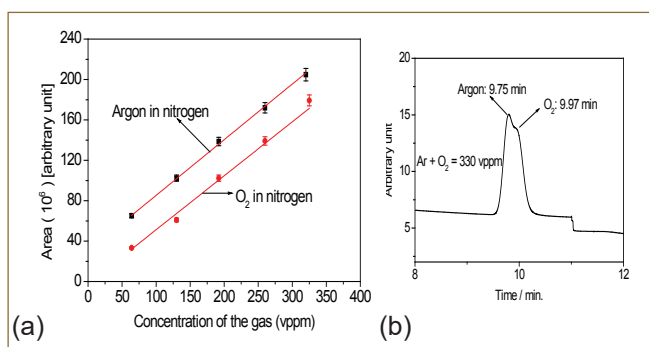


Fig. 1 (a) Calibration of argon and oxygen in nitrogen using standard argon and oxygen and (b) chromatogram representing the elution profile of 200 vpm of argon and 130 vpm of oxygen in nitrogen

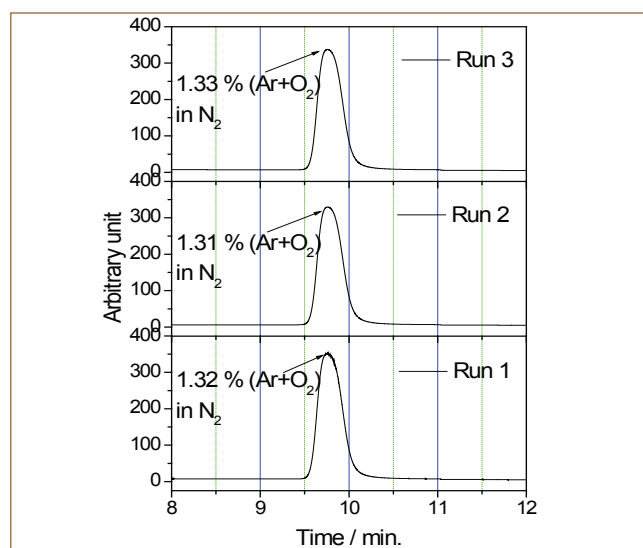


Fig. 2 Chromatogram representing the elution profile of argon and oxygen in nitrogen from nitrogen storage tank of PFBR

II.13 Studies on Flushing Efficiency of Kr and Xe in Sodium using Ar Gas Sparging Module towards the Identification of Failed Fuel Sub-Assembly

During the dry rupture of the fuel pin, the fission gas sparging module (FGSM) that has been designed and developed in-house is used to separate gaseous fission products (Kr and Xe) from liquid sodium sampled by failed fuel location module (FFLM) using Ar purge. FGSM is a segment in FFLM, feasibility of detecting the presence of Kr/Xe in model FGSM under static sodium condition is the inevitable requirement to establish the flushing efficiency of these gaseous fission products towards the identification of failed fuel subassembly. Thus, the flushing efficiency of Kr and Xe gases was studied using gas chromatography (GC). Accessories such as mixing chamber for purging Ar, Xe/Kr introduction line, activated charcoal bed and the series of gas samplers for collection of Xe/Kr were fabricated in-house. The studies of the recovery of Xe/Kr separately in sodium under both static and dynamic purging conditions were carried out by collecting the probe gases along with excess Ar in different gas samplers sequentially. The determination of Xe/Kr in different gas samplers individually was accomplished using GC with thermal conductivity detector.

The experimental set-up consists of a mixing chamber for purging Ar gas in to the FGSM (Figure 1). The mixing chamber was connected with Ar gas inlet on one side and the other side was connected to a predetermined gas line (of 90 mL volume). A pressure gauge (PG1) attached to this gas line was used to monitor the pressure of Xe/Kr/Ar introduced. FGSM was coupled to this gas line with high precision dosing valve. On the other side, FGSM was connected to the activated charcoal bed to trap the Xe/Kr gases along with Ar at Liquid Nitrogen (LN₂) temperature

(77 K). A sodium aerosol trap was installed between FGSM and activated charcoal bed to trap the sodium aerosol generated during the experiments from liquid sodium. The outlet valve of activated charcoal bed was connected to the series of four gas samplers (each with a volume of 180 mL) for the collection of Xe/Kr gases along with Ar. The complete system was evacuated (with the vacuum of 1×10^{-2} mbar) using rotary pump before start of the experiment. Vacuum gauges were installed at two additional locations i. e. (i) PG1, between sodium aerosol trap and activated charcoal bed to measure/monitor the pressure inside the FGSM during experiments and (ii) PG1, between activated charcoal bed and gas samplers to fill the required pressure of Ar (760 torr) in the gas samplers. H₂ gas was used as a carrier and a standard calibration graph plotting peak area of Kr/Xe against volume of gas was obtained and the recovery was calculated based upon the volume of Kr/Xe gases.

FGSM was fabricated out of stainless steel and the module has a 415 mm length cylindrical vessel with a flat bottom and the outer diameter of the cylinder was ~ 100 mm. The top end of the vessel was closed using CF-160 flange. CF-flange has four quarter inch connectors with bonnet valves. The central quarter inch line was dedicated for Ar purge and this central line was attached to Ar header, which in turn was connected to five quarter inch tubes that has a length of ~ 365 mm from Ar header. To enhance the residence time of liquid sodium in the FGSM for the effective removal of Kr/Xe gases using Ar purge, an inner cylinder of 65 mm diameter was welded onto the flat bottom flange with an approximate height of ~ 310 mm from the bottom flange. The quarter inch line

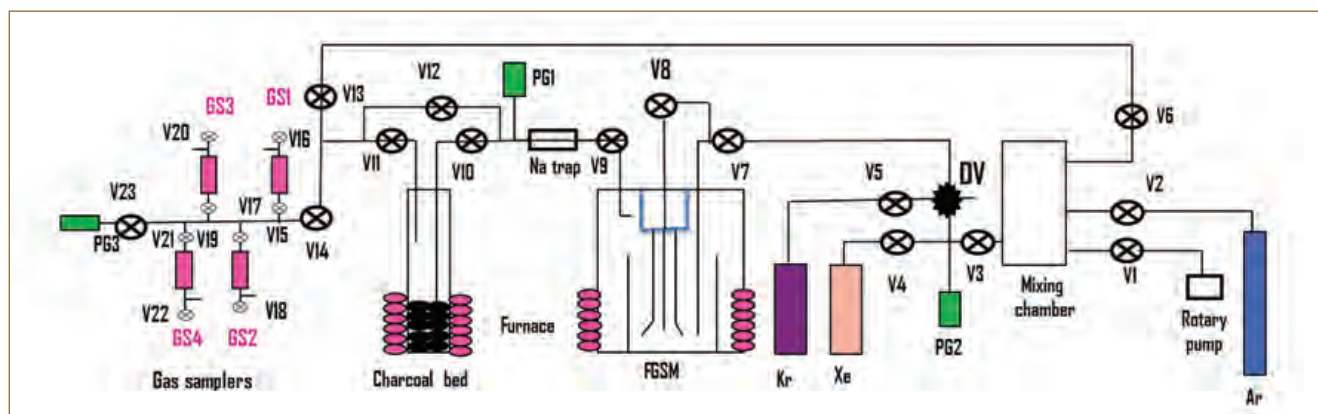


Fig. 1 Complete experimental set-up along with FGSM.(GS1, GS2, GS3 and GS4 → gas samplers ; PG1, PG2 and PG3 → pressure gauges; V1, V2, V3... → bonnet valves; DV → dosing valve)

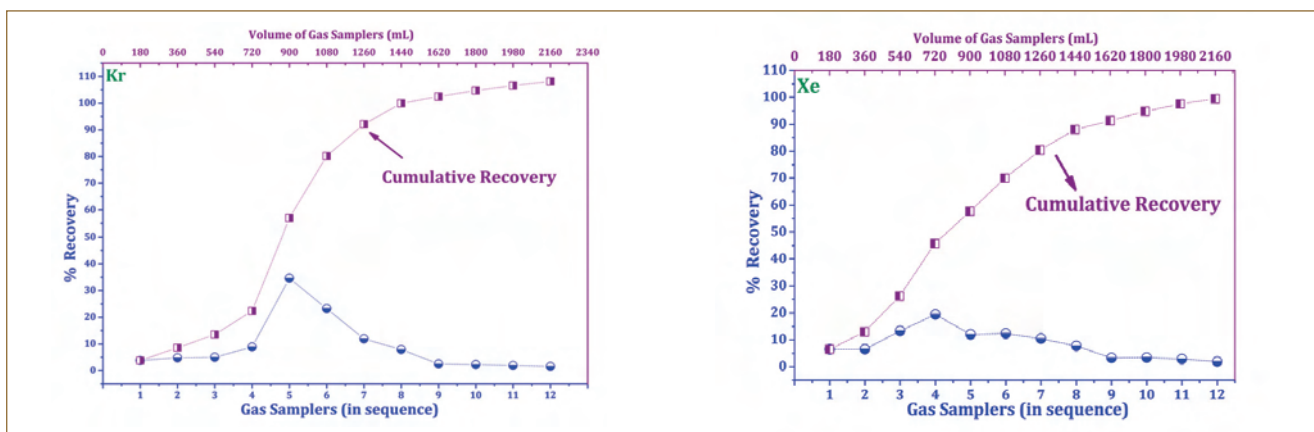


Fig. 2 Recovery (in %; both individual and cumulative) as a function of gas samplers and volume of gas samplers for Kr and Xe gases introduced separately through mass flow controllers. Ar purge was accomplished through mass flow controller via Ar header

meant for introducing Kr/Xe was approximately ~ 400 mm in length that can penetrate deep into liquid sodium was connected to the inner cylinder. FGSM module was filled with ~ 1900 mL of liquid sodium in both inner and outer cylinders (almost to the brim of inner cylinder) and the filling was accomplished. After filling ~1900 mL of sodium, the plenum area (~ 1400 mL) of FGSM was filled with 760 torr of Ar for prevention of oxidation of sodium. Mass flow controllers were installed for all Kr/Xe/Ar gases separately when experiments were conducted in dynamic mode.

FGSM with liquid sodium was subjected to helium leak testing and the leak rate was observed to be better than 10^{-6} mbar lit⁻¹ sec⁻¹. Furthermore, the leak testing was performed on the entire set-up and was ensured that the system is completely leak proof. Sodium in FGSM was heated to 360°C and Xe (450 torr) and Kr (450 torr) gases were sequentially introduced from a pre-calibrated line volume of 90 mL to FGSM against 760 torr of Ar above sodium at 360°C. The resultant Kr/Xe was adsorbed onto charcoal bed maintained at LN₂ temperature. Subsequently, the charcoal bed was heated to 150°C with Ar purge and the gas samplers were filled sequentially, each at an Ar pressure of 760 torr. A representative 1 mL of the sample from each sampler was injected into GC and the peak area corresponding to Kr/Xe was calculated. After the injection of all four samplers, the samplers were evacuated and fresh Ar was purged from mixing chamber to FGSM/activated charcoal bed to push the remaining Kr/Xe (if any) to the gas samplers. As mentioned before, the gas samplers were filled sequentially with 760 torr of Ar. A quantitative recovery in excess of ~ 90 % was achieved for both Kr/Xe employing GC. The recovery obtained with simultaneous introduction of Kr/Xe was similar to the

results of sequential introduction as described before.

Experiments were repeated by varying the charcoal temperatures from 50°C, 100°C and 150°C. As the temperature of charcoal bed was lowered, the resultant rate of release of these dopant gases out of the charcoal bed was also found to fall. As a consequence, the number of gas samplers required to collect Xe turned out to be larger. While with a charcoal temperature of 50°C, within 8 samplers, quantitative recovery of Kr was obtained, almost 36 gas samplers were required to achieve a recovery of ~75% for Xe. The difference in recovery was attributed to the strong affinity of Xe over Kr towards charcoal.

To simulate the actual dynamic conditions, experiments were performed using mass flow controllers to control the flow of Kr, Xe and Ar individually. Experiments were performed for Kr and Xe along with Ar carrier gas separately. Kr/Xe/Ar at a flow rate of ~ 1.5/3.0/25 mL/min respectively was expanded against sodium in FGSM at 360°C at 760 torr of Ar pressure for ~ 30 minutes. During the simultaneous introduction of Kr/Xe and Ar for 30 minutes, the charcoal bed was maintained at LN₂ temperature to facilitate the adsorption of the resultant Kr/Xe along with Ar. Subsequently, the charcoal bed was heated to 150°C and the gas samplers were filled sequentially and were analysed by GC. A quantitative recovery in excess of ~ 90% was accomplished both for Kr and Xe. The percentage recovery (both individual and cumulative recovery) as a function of number of gas samplers and volume of gas samplers for Kr/Xe is illustrated in Figure 2. Overall, the study distinctly demonstrates that the gaseous fission products (Kr/Xe) can be quantitatively separated out of liquid sodium in FGSM which therefore establishes that the interaction of these gases with liquid sodium is negligible.

II.14 Estimation of Life of Guard Pipe Compartment Bellows in Secondary Sodium Main Circuit

Prototype Fast Breeder Reactor (PFBR) comprises two secondary sodium main circuits, one of them is extended to Steam Generator Building (SGB)-1 and the other in SGB-2. Each loop originates from two Intermediate Heat Exchangers (IHX), from IHX to surge tank (ST), ST to steam generators (SG), SG to secondary sodium pump (SSP) and back to IHX. The sodium piping systems within the Reactor Containment Building (RCB) is provided with a guard pipe surrounding the main pipes. These guard pipes are terminated at specified distances with the main pipe and it is known as compartments (Figure 1).

Based on the analysis of in-situ conditions of IHX, recommendations have been proposed to remove the first compartment weld provided close to IHX for both the inlet and outlet piping system to provide the required

thermal flexibility. However, this results in an additional thermal duty to the first compartment bellows in both the inlet and outlet piping system. A detailed 3-D transient thermal analysis of the IHX assembly is performed to estimate the bellow duty by considering all possible transient's influence. Based on these findings, bellow's design check including its life is evaluated.

Life estimation of bellows

the first compartment bellow's duty (axial, lateral and bending) is estimated for the transients viz.: (i) one PSP trip, (ii) off-site power failure, (iii) continuous withdrawal of one control rod, (iv) spurious SCRAM, (v) one SSP trip, (vi) one feedwater pump trip, (vii) feedwater flow reduction in one loop and (viii) total loss of feedwater flow to SG. The contribution of bellow stiffness in the estimation of lateral duty is very significant compared to axial duty. This

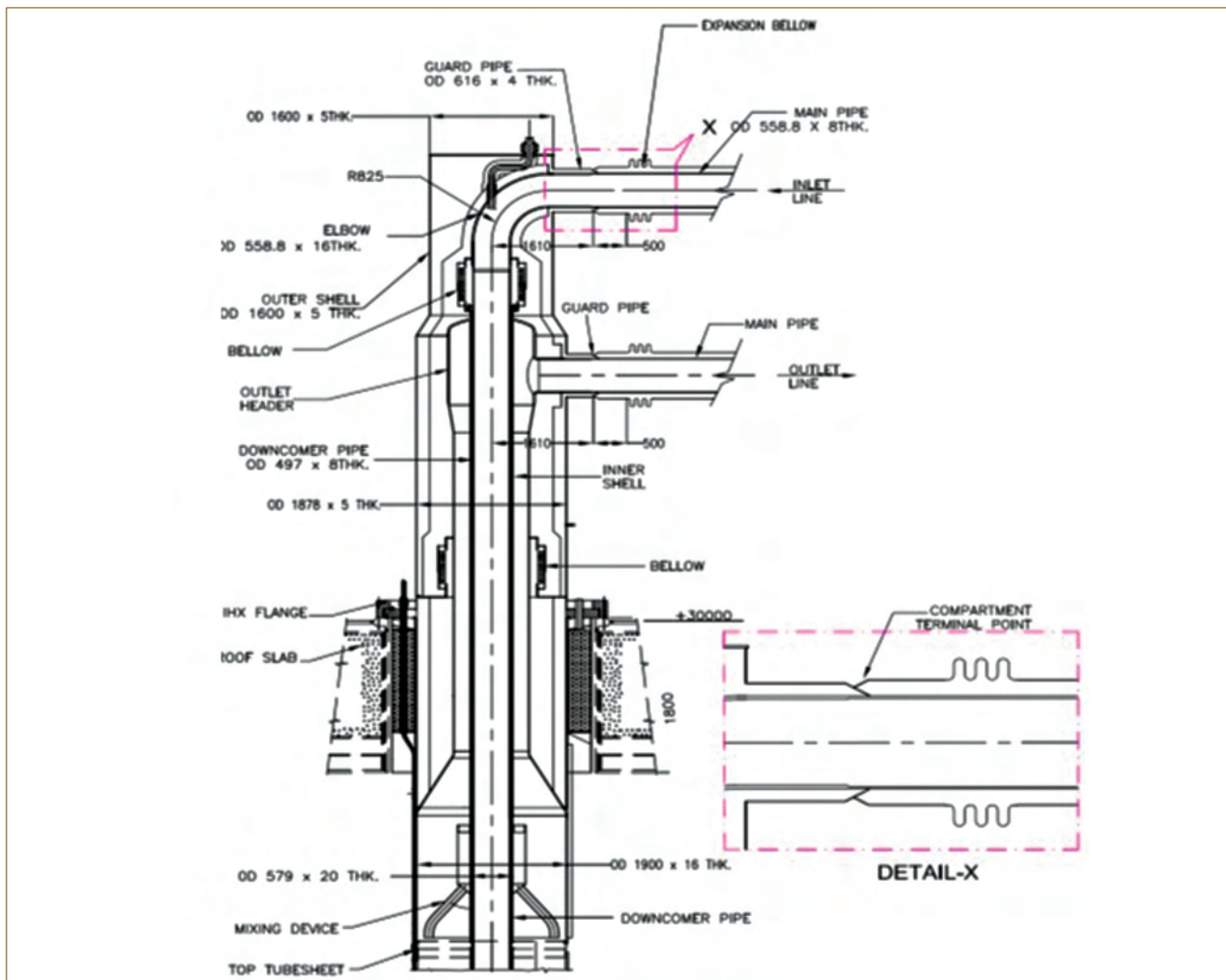


Fig. 1 Intermediate heat exchanger assembly and top portion details with compartment

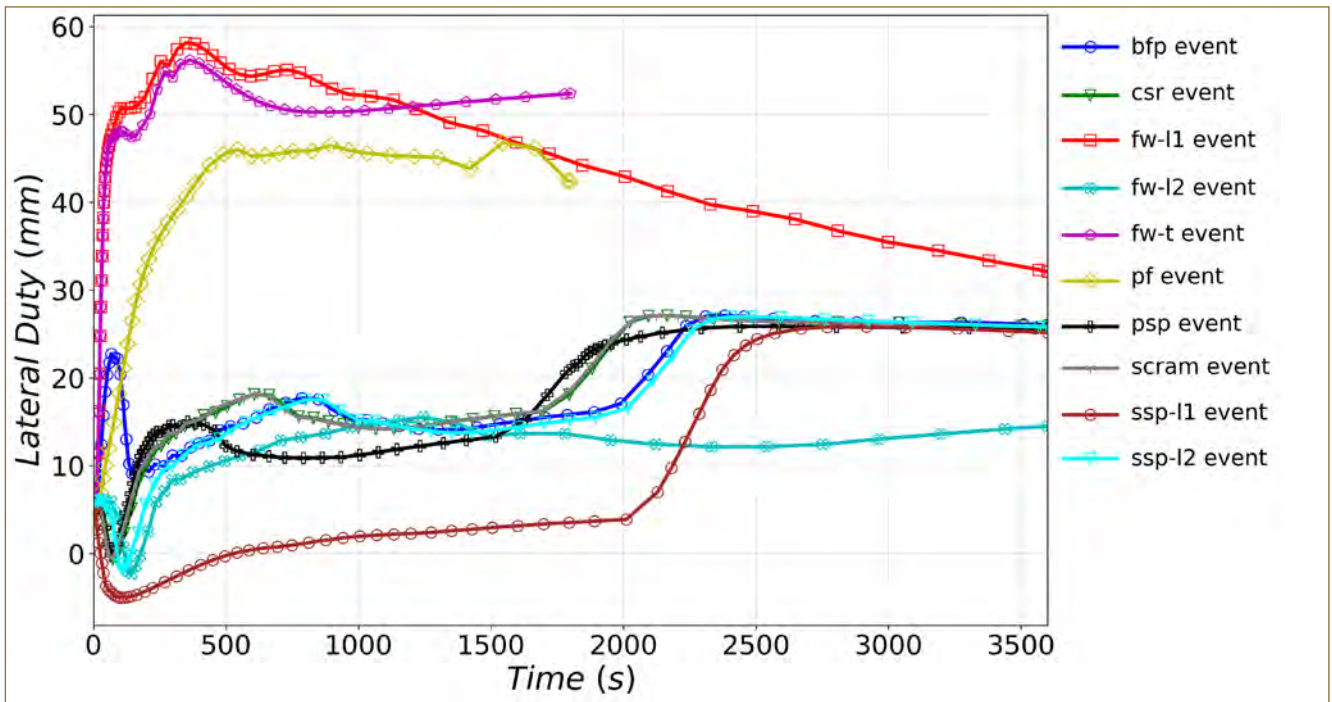


Fig. 2 The lateral duty on inlet line's bellow under the transients (without bellow participation)

can be attributed to the relative magnitudes of pipe and bellow stiffness. The axial stiffness of the pipe is relatively higher than the bellow's axial stiffness. In contrast, the pipe's lateral stiffness is significantly lower than that of the bellow. The estimated lateral duty evolution for inlet line during various transients without considering bellow stiffness is shown in Figure 2 and by including bellow & adjoining pipe is shown in Figure 3.

The stresses induced in the bellows (of both inlet and outlet line) due to the pressure (design pressure ~0.98

bar) & thermal loading are evaluated and compared with allowable stresses as per the Expansion Joints Manufacturer Association (EJMA) and found to be below the allowable limits. The life of inlet and outlet line bellows is estimated for various transients under the loading observed after interconnecting the compartments. The EJMA code is followed to estimate the life and various parameters like total equivalent axial movement, stresses, spring rate, etc. The fatigue curve available in the EJMA code is applicable up to 425°C

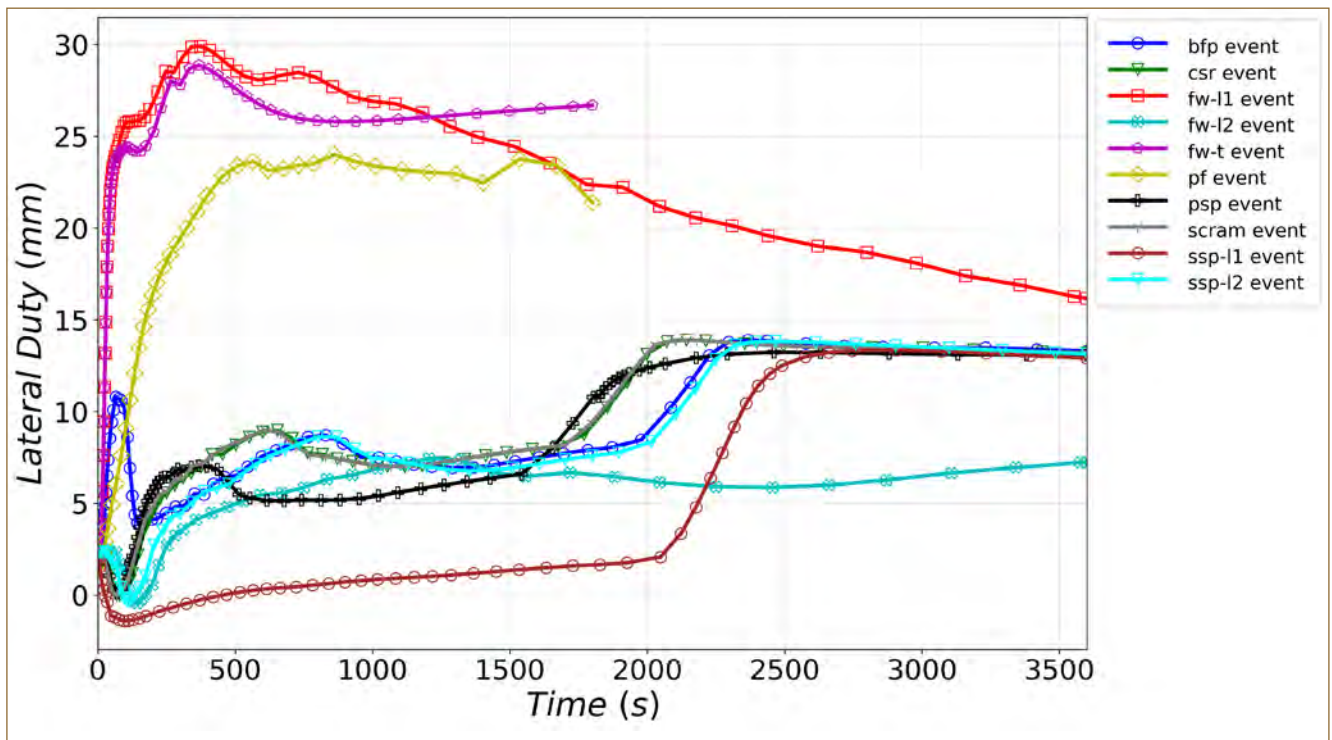


Fig. 3 The lateral duty on inlet line's bellow under the transients (including bellow and adjoining pipe)

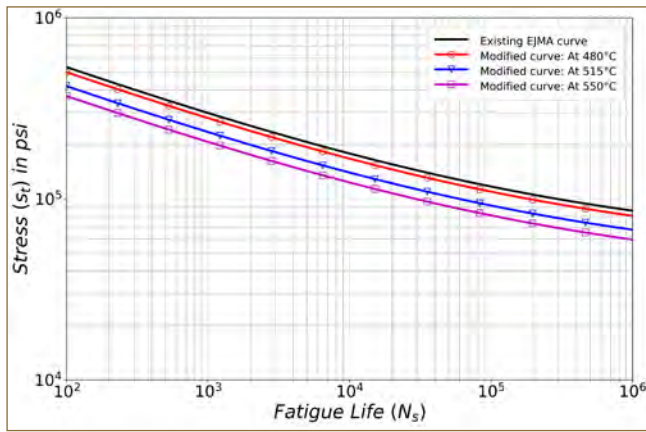


Fig. 4 Modified design fatigue curve for bellow as per the EJMA

only. However, in the EJMA procedure, the use of room temperature elastic modulus results in the overestimation of stiffness and stress values. Subsequently, it may compensate for the influence of higher temperatures on life to some extent. The corresponding cumulative damage for the inlet line bellow is 0.466, and for the outlet line bellow is 0.471.

Modified EJMA fatigue curve for higher temperature

Due to the lack of material data above 425°C, EJMA fatigue curve is modified based on the ASME fatigue curves to predict life. The strain range vs number of cycles for temperature range from 40°C to 705°C is available in ASME for the material SS-316. From this curve, the ratio of strain range at design temperature (DT) to strain range at 425°C is calculated for each set of allowable number of cycles. The ratio of Young’s modulus at DT to Young’s modulus at 425°C has been applied appropriately in the estimation of a correction factor (CF) to transform the strain vs. number of cycles (ASME fatigue curve) to stress vs number of cycles (EJMA fatigue curve). The CF (Eq. 1) mean value over the number of cycles gives the correction factor at the DT for accounting higher temperature effects on the existing EJMA fatigue curve for austenitic stainless steel bellows.

$$(CF)_{on\ stress} = \frac{\sigma_{DT}}{\sigma_{425}} = \frac{E_{DT}}{E_{425}} \cdot \frac{\Delta\epsilon_{DT}}{\Delta\epsilon_{425}} \quad (1)$$

The existing EJMA fatigue curve (unreinforced bellows), along with the modified curves for DT values of 480°C, 515°C, 550°C is shown in Figure 4. This curve facilitate to estimate the life of the bellows at design temperature by accounting for the effect of material degradation due to temperature and retaining the component characteristics of the EJMA based fatigue curve.

For the inlet line, the DT rises beyond 425°C for three events viz. (i) Off-site power failure, (ii) Feedwater flow reduction in one loop and (iii) Total loss of feedwater flow to SG. For these events, the fatigue life is calculated as per the derived curve and it is observed that existing EJMA rules (use of room temperature Young’s modulus with its fatigue curve) are conservative up to 500°C as the allowable cycles increased with the modified fatigue curve. The cumulative damage as per the modified fatigue curve for (i) the inlet line has decreased to 0.39 and (ii) the outlet line increased to 0.62 as compared to the existing EJMA rules.

The comparison of fatigue damage estimation in bellows on inlet/outlet lines as per the PFBR’s initial specifications and the latest loading are summarized in Table I.

It is evident from the results that the inbuilt margin on the bellow design has helped to accommodate the additional thermal duty introduced due to the in situ modifications and the resultant cumulative damages are well below (0.39 & 0.62) the allowable limit of unity.

In summary, the IHX guard pipe interconnected compartments bellow duty & life is estimated concerning the modifications proposed for the in-situ conditions for both the inlet and outlet main piping system. Both the inlet and outlet line bellows are meeting the design requirements for internal pressure capacity and stability as per the EJMA guidelines. The life of the bellow is estimated for interconnected configuration as per the existing EJMA methodology as well as using the modified fatigue curves. The respective life is viz., (i). 0.466 as per current EJMA methodology, and 0.39 as per the modified fatigue curves for the inlet line bellow and (ii) 0.471 as per current EJMA methodology, and 0.62 as per the modified fatigue curves for the outlet line bellow. All these values are less than the allowable limit of unity.

Table 1: Comparison of fatigue damage for the inlet/outlet line bellow

Pipeline of bellow	Initial Specifications of PFBR	Bellow’s Life after Interconnected Compartments as per EJMA	
	Damage for 861 cycles	Existing Procedure	Modified Fatigue Curve
Inlet bellow	0.025	0.466	0.39
Outlet bellow	0.0072	0.471	0.62

II.15 Numerical Analysis of Dynamic Seals used in Control and Safety Rod Drive Mechanism

An in-house designed and developed labyrinth type V-ring seals are used as dynamic seals in Control and safety rod drive mechanism of PFBR. The main design objectives of the seal are to provide leak-tightness and offer low frictional resistance. Detailed stress analysis of the seals is carried out using the finite element method with commercially available software.

The photograph of labyrinth type V-ring seal is shown in Figure 1a and schematic diagram is shown in Figure 1b. Construction features of V-ring seal include the body, the flap and the hinge. The teeth, located on the flap, are pressed against the chrome-plated central tube, producing the necessary sealing force. The five teeth on the flap decrease the leakage further by offering higher resistance to leakage flow. In the present geometry, the outer diameter of the central tube is 110 mm and the inner diameter of the seal is 106 mm, i.e., an interference of 4 mm.

The seal geometry was modelled using 4 noded axi-symmetric elements and material property of silicone rubber for seal material was taken from the literature. The seal was modelled using Marlow hyperelastic

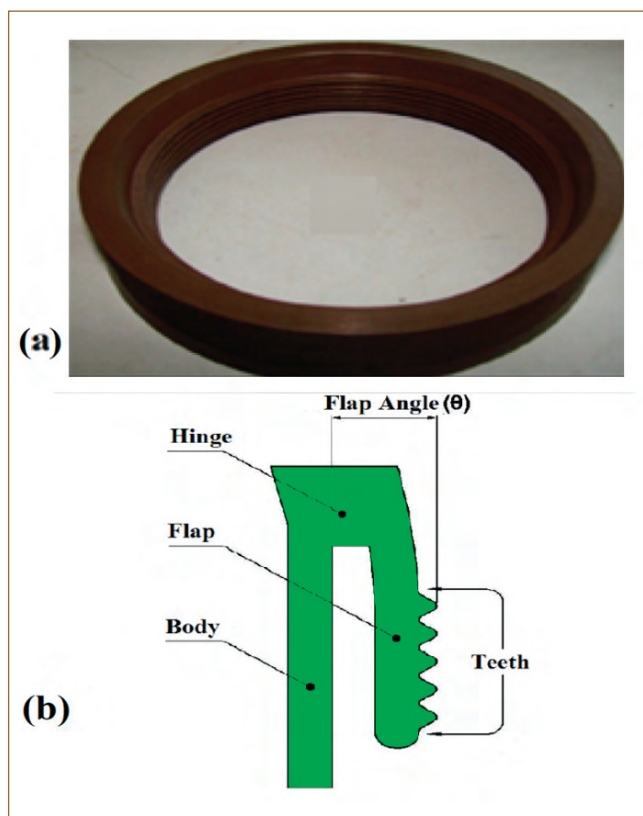


Fig. 1 (a) Photograph of labyrinth type V-ring seal and (b) schematic diagram of V-ring seal

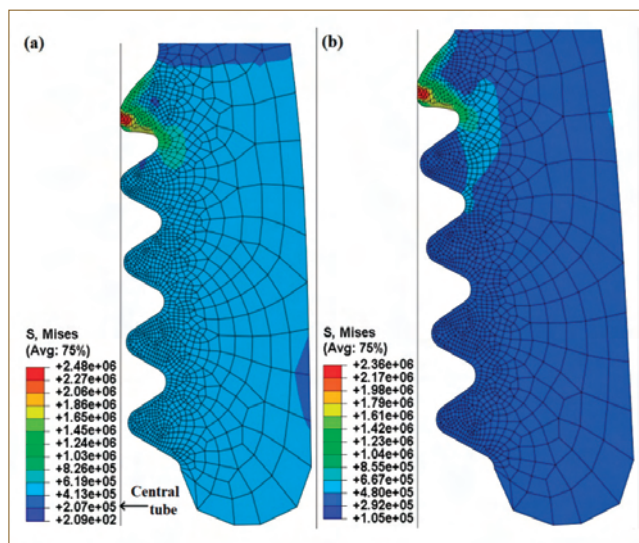


Fig. 2 von Mises stress distribution of labyrinth type V-ring seal: (a) at room temperature and (b) at 110 °C temperature

material model. Surface to surface contact technique was employed to establish contact between central tube (master) & seal (slave) and 0.5 value of friction coefficient was assigned for tangential property using penalty based technique. Global seed size was taken as 0.0016 m while local seed size in the vicinity of teeth was taken as 0.0001 m to get converged results. Validation of the numerical model was performed with the benchmark data obtained from the literature.

Figures 2a and 2b shows the von Mises stress distribution for labyrinth type V-ring seal at room temperature and at 110 °C temperature respectively. Close examination of the results for labyrinth seal reveals that only top tooth among the five teeth is in contact with central tube. The peak stress is located at the top tooth tip. The peak values of von Mises stress is found to be 2.48 MPa at room temperature & 2.36 MPa at 110 °C temperature, which are less than the allowable stress of 5 MPa. The contact pressure is around 3 MPa for both the case, which is very much higher than the differential pressure across the seal (0.01 MPa). At elevated temperature, the flap is bent more outward from the top to bottom of the seal with the lesser gap between the seal and the central tube at hinge region.

Detailed numerical study of in-house designed labyrinth type V-ring seal was carried out. The numerical analysis provided greater insights into the mechanical behaviour of the V-ring seal. Design optimisation studies are under progress.

II.16 Performance Evaluation and Endurance Testing of PFBR PSPC Electromagnetic Pump

Purification of primary sodium in PFBR is done by means of an ex-vessel purification circuit consisting of a cold trap and an electromagnetic (EM) pump. This circuit is called Primary Sodium Purification Circuit (PSPC).

An Annular Linear Induction Pump (ALIP) which is one variant of EM Pump is used in PSPC of PFBR. The designed ALIP has capacity to deliver maximum flow rate of 50 m³/h at a pressure of 4 kg/cm². The ALIP was manufactured earlier and installed in PFBR. A spare PFBR ALIP of same design was available and was installed in Sodium Facility for Component Testing (SFCT) for its performance evaluation. The schematic of ALIP is shown in Figure 1. It is a reflux type of ALIP where the inlet and outlet lines are at the same end. This type of arrangement facilitates winding removal for repair, if required, without cutting of sodium pipeline. The photograph of ALIP installed in SFCT sodium loop is depicted in Figure 2.

Characterisation of annular linear induction pump (ALIP) is important for predicting its behaviour in actual reactor system. The performance of an ALIP is evaluated in terms of various characteristics like the head vs flow characteristics and input power vs flow characteristics. Sodium flow rate was measured using a permanent



Fig. 2 50 m³/h annular linear induction pump installed in SFCT loop

In order to measure the pressure developed by ALIP, cover gas pressure balancing technique is used. In this technique, pressure at pump suction and discharge is measured by means of two sodium pressure pots with argon as cover gas which are at same height. The levels of sodium in the two pressure pots are maintained at same value by adjusting the pressure of argon as per pressure developed by ALIP. Thus the the difference of cover gas pressures in the two pressure pots gives the pressure developed by ALIP. The input power drawn by the pump was measured by means of a power analyzer. Sodium flow rate was measured using a permanent

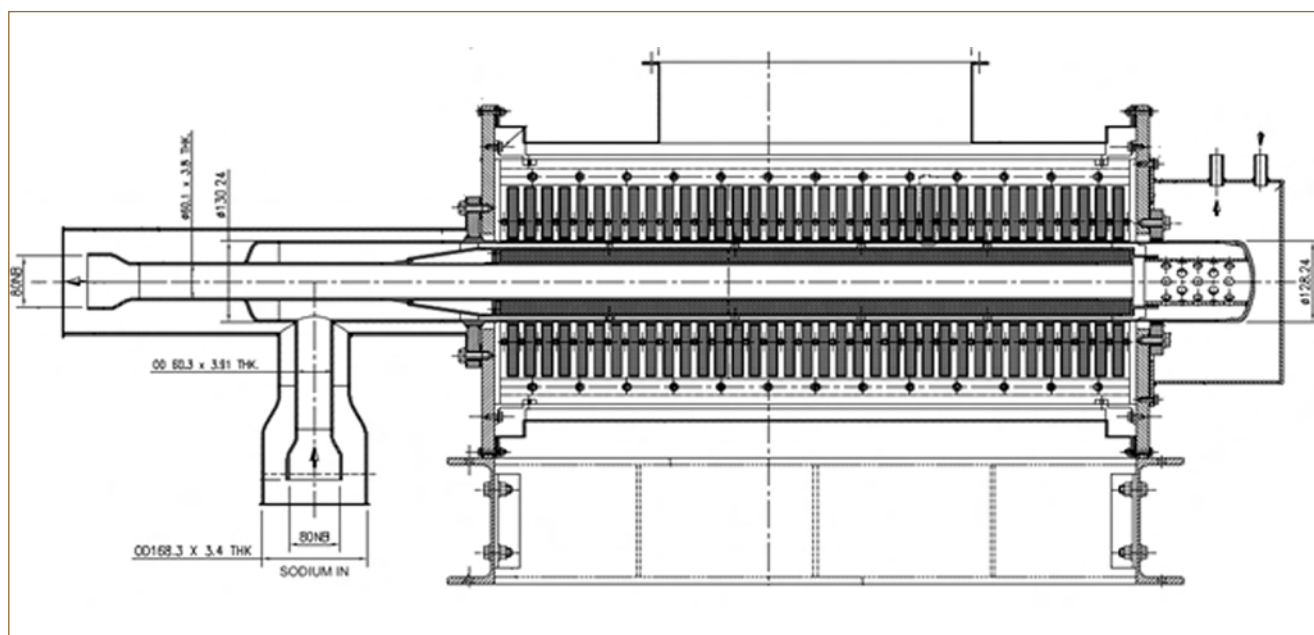


Fig. 1 Schematic of PSPC annular linear induction pump

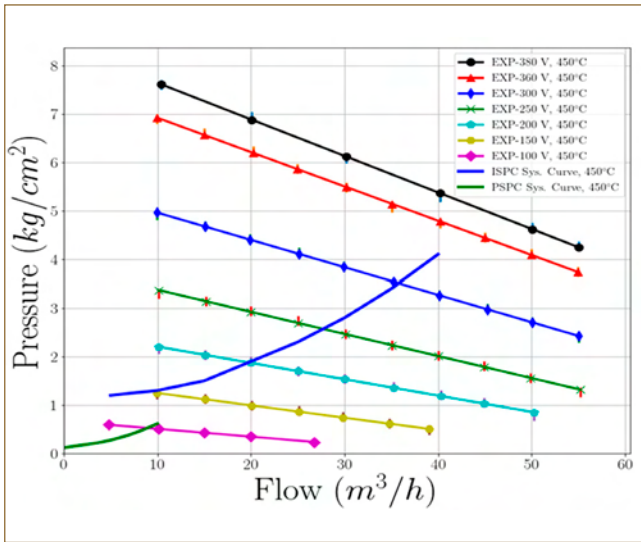


Fig. 3 Experimental head versus flow characteristic of ALIP

magnet electromagnetic flowmeter.

Performance of the pump was evaluated at various terminal voltages, temperatures and flow rates. At a given terminal voltage and temperature, different flow rates were obtained by throttling the valve at pump discharge. At each flow rate, pump parameters like differential pressure, input power were measured. The variation of developed pressure with flow rate (i.e. pressure vs flow characteristics) at sodium temperature of 450°C is shown in Figure 3. For comparison, load characteristics of Initial Sodium Purification Circuit (ISPC) and load characteristics of normal Primary Sodium Purification Circuit (PSPC) both are also plotted

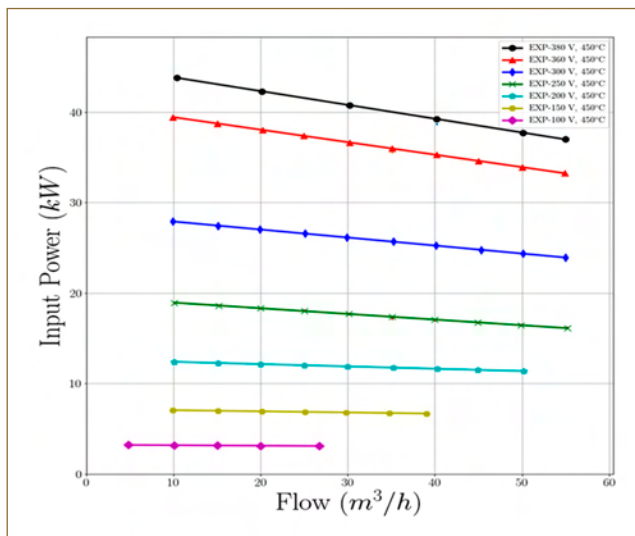


Fig. 4 Input power variation with flow rate

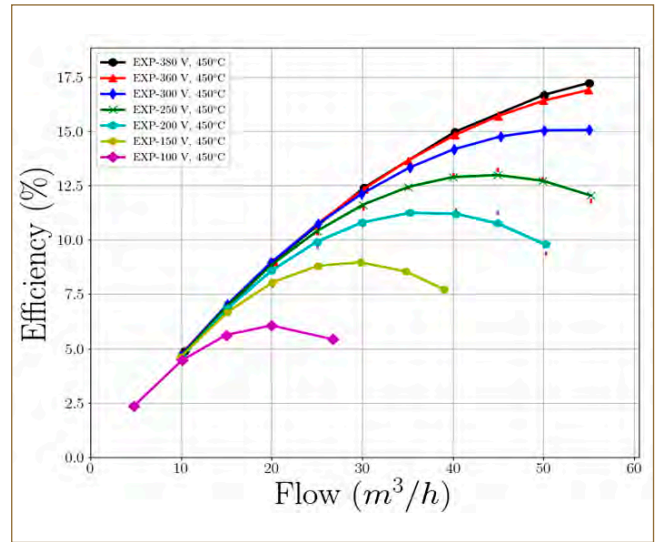


Fig. 5 Variation of efficiency with flow rate

in Figure 3. It is observed from this comparison that the pump would be able to meet the system requirements both during initial sodium purification and during normal sodium purification in PFBR.

The input power variation with flow rate is depicted in Figure 4. The input power decreases linearly with increase in sodium flow rate. As the pump terminal voltage increases, the input power also increases. Efficiency of ALIP is defined as the ratio of output hydraulic power to input electrical power and is plotted in Figure 5. Maximum efficiency obtained at rated condition is 16.5 % which is close to computed efficiency during design stage.

After performance evaluation, long term test was conducted on pump. During this test, ALIP was operated at rated flow of 50 m³/h at rated operating voltage of 360V for 2000 hours. After completion of 2000 hours of operation, pump hydraulic characteristics were obtained once again and no significant variation in characteristics was observed.

This comprehensive experiment of performance evaluation at various voltages and flow rates and their comparison with system characteristics during initial sodium purification and during normal primary sodium purification and long term testing of spare PSPC ALIP has validated the design of ALIP. The experimental test in sodium has established that the designed pump has capability to meet the system requirements in PFBR.

II.17 Development of Non-destructive Examination Techniques for Qualification of Thin Walled Nickel Tubes for the Hydrogen Sensor Application

Nickel tubes of outer diameter 7.2 mm and wall thickness 0.3 mm are used for fabricating sensors that would be used to measure hydrogen in the argon cover gas regions so as to identify any steam leak in sodium in the steam generator of PFBR. These tubes fabricated at Nuclear Fuel Complex (NFC), Hyderabad demand stringent quality as it is required to be free of any axial and transverse defects. Non-destructive qualification of these tubes for axial defects was carried out at NFC using immersion ultrasonic testing (UT). However ultrasonic qualification of the transverse defect was a challenge due to high radius of curvature involving lower wall thickness. In order to meet the stringent quality requirement, guided wave based immersion ultrasonic and saturation eddy current (EC) techniques were developed at NDE Division, IGCAR for qualification of Nickel tubes for transverse defects. The calibration and standardization of NDE parameter (Ultrasonic and Eddy current) were established on calibration tube containing transverse reference defects (ID and OD notches obtained using EDM) having dimension 8 mm x 0.1 mm x 0.1 mm (Length x Width x Depth) as shown in Figure 1a.

In order to detect ID and OD transverse defects with better SNR, immersion ultrasonic guided wave testing was developed. Ultrasonic parameters such as transducer frequency, incident angle and water path were optimized as 5 MHz, 31° and 19 mm, respectively.

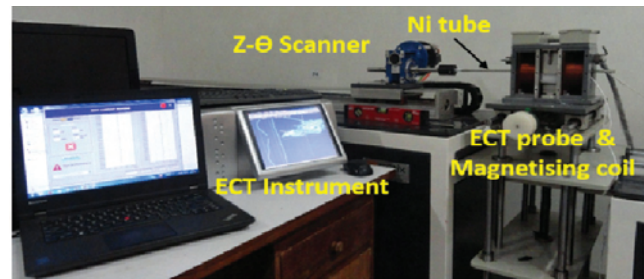


Fig. 2 Photograph of the saturation eddy current test setup

The dispersion curves confirmed that non-dispersive flexural F(1,2) mode with group velocity 2959 m/s is being generated in the tube for the above experimental configuration. This velocity value was found to be in good agreement with that observed experimentally. The ultrasonic C-scan image shown in Figure 1b clearly demonstrates the reliable detection of both ID and OD transverse reference defects. Though ultrasonic C-scan images could reliably detect the defects, the generation of this C-scan based on B-scans obtained along the length of the tube for different circumferential positions was time consuming. In order to overcome this limitation, noncontact EC technique was attempted. Nickel being ferromagnetic in nature, magnetic saturation based EC testing was used to minimize noise due to permeability variations in EC signals. A magnetizing current of 5 A was optimized to minimize noise due to permeability variations. Figure 3 shows the photograph of the test

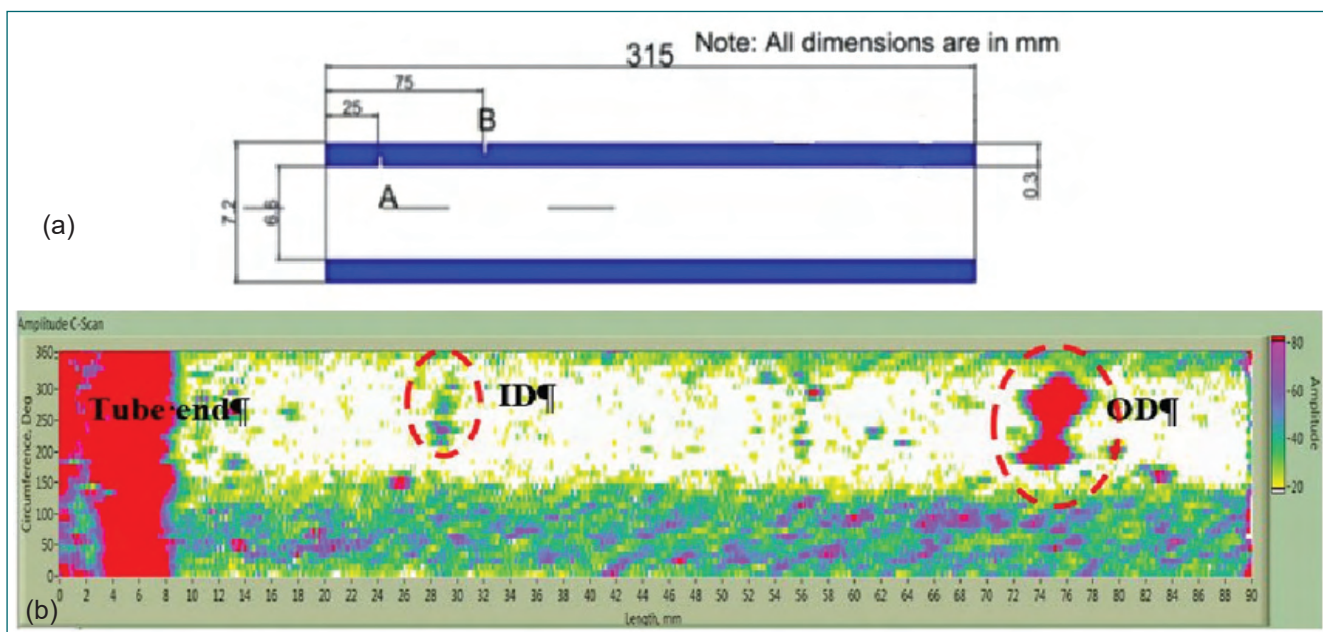


Fig. 1 (a) Schematic of the reference nickel tube with transverse and longitudinal notches (b) ultrasonic C-scan image of ID and OD transverse notches in reference nickel tube

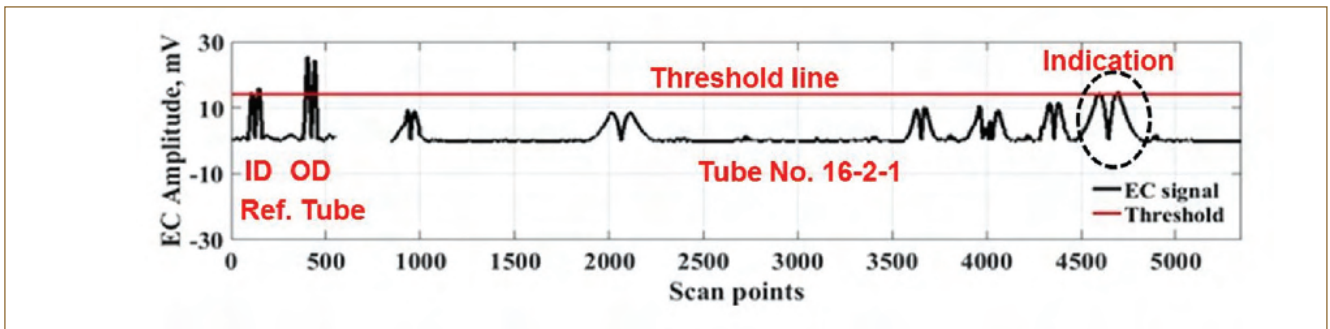


Fig. 3 Eddy current signals of reference nickel tube and tube having indications

setup which consists of magnetizing coil, EC probe, instrument and the ZΘ scanner. The test frequency was optimized as 150 kHz based on skin depth consideration and by maximizing the phase angle separation between the ID and OD reference notches. In each nickel tube of 1 m length, four axial scans at different tube rotations were performed and the average was considered as raw signal to minimize the effect of probe ovality and to ensure repeatability. Further reduction of the permeability noise was achieved by post-processing of the raw EC signals using discrete wave let transform based digital

signal processing methodology. Figure 1d shows the EC signal from the reference tube along with a typical 1 m long nickel tube which showed a rejectable indication. The developed test procedures were successfully applied for qualifying a total of 37 tubes using immersion ultrasonic and 14 tubes using saturation EC testing. While both UT and ECT techniques have resulted in improved quality of the Nickel tubes, the EC technique was found to have higher inspection speed for implementation in shop floor conditions.

II.18 Quality Assurance & Non-destructive Examination for Large Rotating Plug Bearing Balls

In PFBR, combined rotation of Large rotating plug (LRP), small rotatable plug (SRP) and transfer arm (TA) is possible to access all the subassemblies located within the handling diameter. To enable the rotation, SRP & LRP are supported through large diameter bearings known as slewing rings. These bearings are designed for slewing operation and steel balls (92 mm diameter) are used as spacer balls (Figure 1a). High carbon anti-friction bearing steel material conforming to ASTM A295 Grade 52100 is used in the form of forged bars in fully spheroidised annealed condition and is free from defects such as seams, pipes, laminations, excessive inclusion of non-metallic impurities for bearing balls.

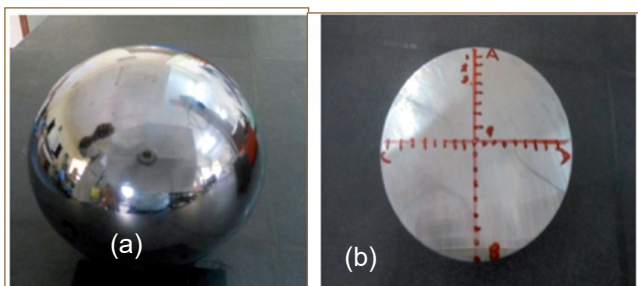


Fig. 1 (a) Steel ball in LRP (92.0 mm dia) and (b) line hardness marking at 5 mm

Entire length of forged bar stock was scanned by ultrasonic examination as per ASTM A 388 for detection of both longitudinal and transverse defects and accepted as per ASME Section VIII Division.

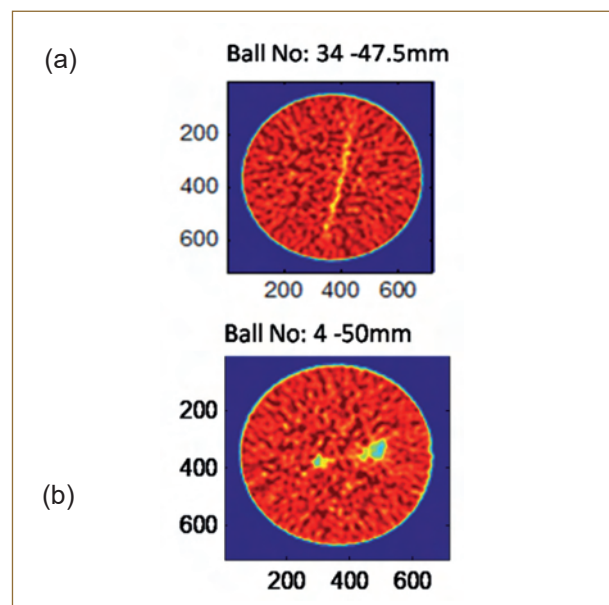


Fig. 2 CT image of ball at (a) 47.5 mm and (b) 50 mm

Important quality requirement of bearing balls are surface and core hardness which shall meet minimum 60 HRC at surface and 50 HRC at core of the ball. A set of 15 balls were examined visually to ensure surface imperfections such as black spots, un-feelable flash lines, pits, etc., Dimensions including its geometric features as per grade 200 of IS 2898 and surface hardness before final machining/ lapping. Among the 15 balls, three of them are randomly selected and sectioned into two hemispheres. Line hardness in HRC on sectioned ball (Figure 1b) was measured using calibrated Digital Rockwell Hardness Tester. Based on the satisfactory test results, the manufacturing process was standardized.

LRP bearing spacer balls (165 numbers) were manufactured in three batches (60, 60 & 45) as per technical specifications. First, second and third batches are split into 4, 4 and 3 lots. Fifteen identified balls were inspected for 100 % visual examination under diffused light of 1000 lux and measurement of diameter and sphericity were carried out using coordinate measuring machine. The measured surface hardness value varies from 63 to 50 HRC (surface to ball center).

Gamma computed tomography of the large diameter bearing ball was carried out using the first generation gamma ray based computed tomographic system.

Gamma source of ¹³⁷Cs (1.329 Ci) and high purity germanium detector were used as source and detector. Gamma-ray CT tomogram image of the ball no-34 indicates the presence of linear feature at height of 35 mm to 67.5 mm and at height of 47.5 mm (Figure 2 a).

Figure 2b shows the reconstructed layer images of ball number 4 where two defects (dumbbell shape) near the centre of the ball is observed between 47.5 mm to 55 mm

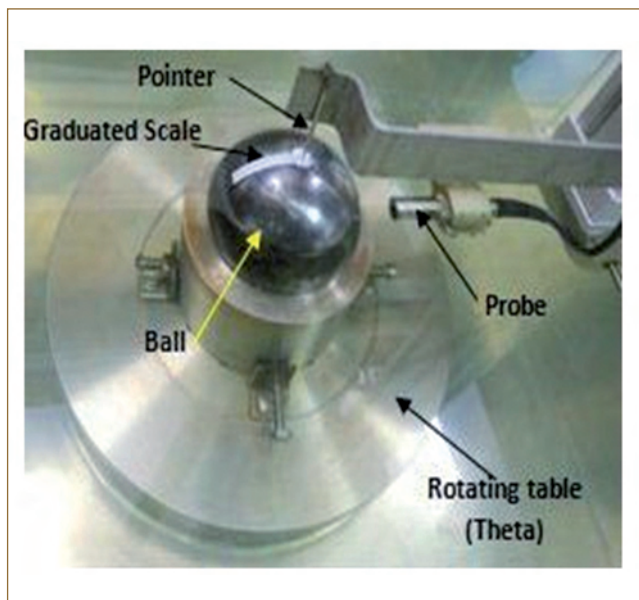


Fig. 3 Steel ball scan set up

height. This defect may be due to the unfilled section of the layer during manufacturing.

The volumetric defects in large diameter spherical bearing steel balls were measured by using immersion ultrasonic testing (UT) technique (Figure 3). The UT of spherical steel balls of diameter 95 mm was conducted by many scanning trials using different frequencies and depth of focus. Steel balls with and without defects have been scanned and compared in order to evaluate the defects. The A, B and C scan data from the immersion scanning have been collected to extract the co-ordinate of the defects. Results show the high reliability of immersion ultrasonic testing for defect detection and volumetric mapping and sizing of defects for spherical steel balls (Figure 4).

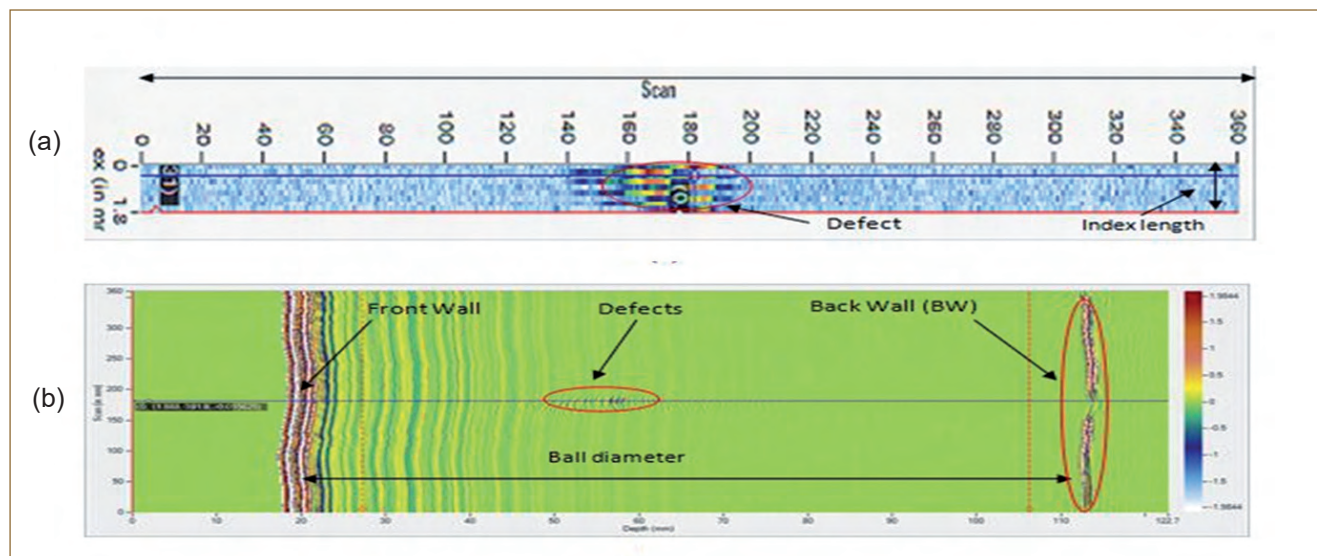


Fig. 4 Images showing defects (a) C-scan and (b) B-scan

II.19 Qualification of Modified Annular Linear Induction Pump by Non-destructive Examination

In PFBR, 170 m³/h Reflux type Annular Linear Induction Pump (ALIP) is used in Fill and Drain circuits for filling sodium and maintaining the required sodium level in Secondary Sodium Main circuit during operation. The pump consists of an outer duct and an inner duct. The inner duct is 1 metre long with 189 mm ID and thickness varies from 2 to 4 mm along the duct. The outer duct is machined out of ASTM-A-312 TP 304LN, 200 NB Sch 120 seamless pipe. Sodium enters through a 4" line and flows in the annular space between the inner and outer duct and comes out through the central 4" line. The pump has been modified by the designer to improve its performance for trouble free operation. The modified design requires hard facing of components to improve resistance to high temperature wear, especially self-welding/ galling of mating surfaces in sodium. In modified design, hard faced spacers & front spacer pads were introduced and the slotted cylinder is replaced with porous cylinder (Figure 1). The failure of hard facing during service will lead to misalignment of sliding components affecting the performance of the pump and rapid wear & damage of components. Hence qualification of hard facing is important before the component is put into service.

Ni-based Colmonoy grade-5 as per AWSR NiCr-B is used for hard facing in modified ALIP. It has hardness value (HRC) of 45 to 50. The plasma transferred arc (PTA) welding process is selected for deposition due to its least dilution of base metal into hard facing metal. Porous shells have 24 numbers of equi-spaced circular holes of diameter 25 mm. The outer diameter of porous shell, front spacer pad (4 numbers) and spacer blocks (4 numbers) have colmonoy-5 hard facing of 1.5 mm thickness (Figure 2a). A stringent quality requirement for hard facing has been enhanced by carrying out surface and volumetric NDE. Immersion ultrasonic testing has been used for qualification of Colmonoy grade-5 hard faced components before final matching. Normal beam and Surface wave ultrasonic testing (UT) technique has been used for



Fig. 1 ALIP of PFBR

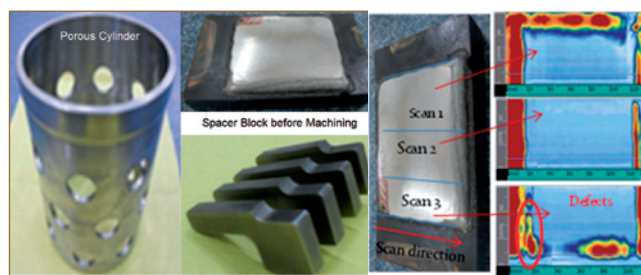


Fig. 2 (a) Porous shell and spacer block; (b) PAUT C-scan image of spacer block

detection of surface and subsurface defects. Reference reflectors, such as \varnothing 3 mm Flat Bottom Holes (FBH) for de-bonding type defects and \varnothing 2 mm SDH for volumetric defects have been used for UT.

Phased array UT (PAUT) is used for de-bonding detection in spacer blocks. For PAUT inspection, the hard facing thickness of 4 mm was taken as a reference block with 3 mm FBH. A 5 MHz, 64 element probe was used with active aperture of 32 elements. In PAUT, size of defect can be evaluated accurately in C-scan image compare to conventional UT while B-scan images give the depth information.

After the final machining, stringent dimensional and geometrical tolerances such as perpendicularity, radius profile, surface finish of 0.5 μ m were measured and found within the permissible range as per approved drawing.

Conventionally, normal beam ultrasonic contact method is widely used for bond quality evaluation of hard facing. Accuracy of contact method is limited due to dead zone/near zone effects of the transducer (for thin coating) and in-consistency of ultrasonic coupling.

To overcome the limitations of conventional UT (single crystal), inspection of hard faced components has been carried out using miniature twin crystal probe. Immersion ultrasonic method was also applied for detection of debonds in hard facing (more reliable than conventional pulse echo contact method).

Advanced UT technique such as PAUT has been applied successfully for scanning and imaging the hard faced coating. It is demonstrated that de-bonded areas can be imaged accurately for evaluation and assessment of the bond quality by PAUT (Figure 2b).

A stringent quality control has been done during fabrication modified ALIP to qualify the hard faced machined components as well as weld joints.

II.20 Visual Inspection and Quantitative Measurements in Various Components of PFBR using Industrial Videoscope

Commissioning of a mega project like PFBR involves lots of inspection challenges. During commissioning, many times it is required to visually examine and ascertain integrity of selected installed critical components located at inaccessible (no direct access) areas. Industrial video scope (IV) has been judiciously deployed in such conditions to obtain vital information remotely. A few important applications of IV such as in Intermediate Heat Exchanger (IHX), Large Rotating Plug (LRP) and Biological Shield Cooling System (BSCS) are reported here. The information obtained helped in taking informed decision for further plan of action. Figure 1a shows the IV used in these inspections.

Intermediate heat exchanger

Abnormal noise was observed during operation of one of the IHXs. One of the possible sources of this noise was suspected to be the hitting of down-comer pipe with the outer pipe of the IHX. A snap shot of the videoscopic examination carried out at the suspected location through N7 nozzle is shown in Figure 1b. Special arrangements were made to cool the IV camera to obtain images of the components. The examination revealed no movement of down-comer pipe towards the outer pipe which helped in ruling out the suspicion, which otherwise is of serious concern.

Large rotating plug back-up seal

A tear was observed in one of the LRP back-up seals. In order to ascertain the condition at adjacent

locations along LRP circumference (from 0° to ±54°, covering 3 m) IV was used. The inspection revealed wide opening of the groove on either side up to 1.5 m. A through opening was also observed in the LRP back-up seal at a location of 50 mm from the start point as shown in Figure 1c. Based on the information provided, replacement of back-up seal was decided.

LRP top and bottom race

Quantitative characterization of the dents formed on the top and bottom bearing races of LRP was sought. Stereoscopic inspection using IV was envisaged for dent quantification. A typical dent mark and its characteristic features are shown in Figure 1d. The maximum size of the dent was found to be 3.04 mm in length with 0.71 mm width and 0.41 mm depth. On the basis of this information, the bearing race is ascertained to be free of any major defects.

Biological shield cooling system

There was a requirement to know the surface condition and identify the location of DM water leak in the BSCS. IV examination revealed corrosion features like pitting and blisters as shown in Figure 1e. The exact location of the leak was identified Figure 1f to be a through thickness hole at a location of 1.4 m from the pipe start. The length and width of the hole are found to be 4.93 mm and 1.19 mm, respectively based on the stereoscopic measurements. This was a vital input for the future plan of action.

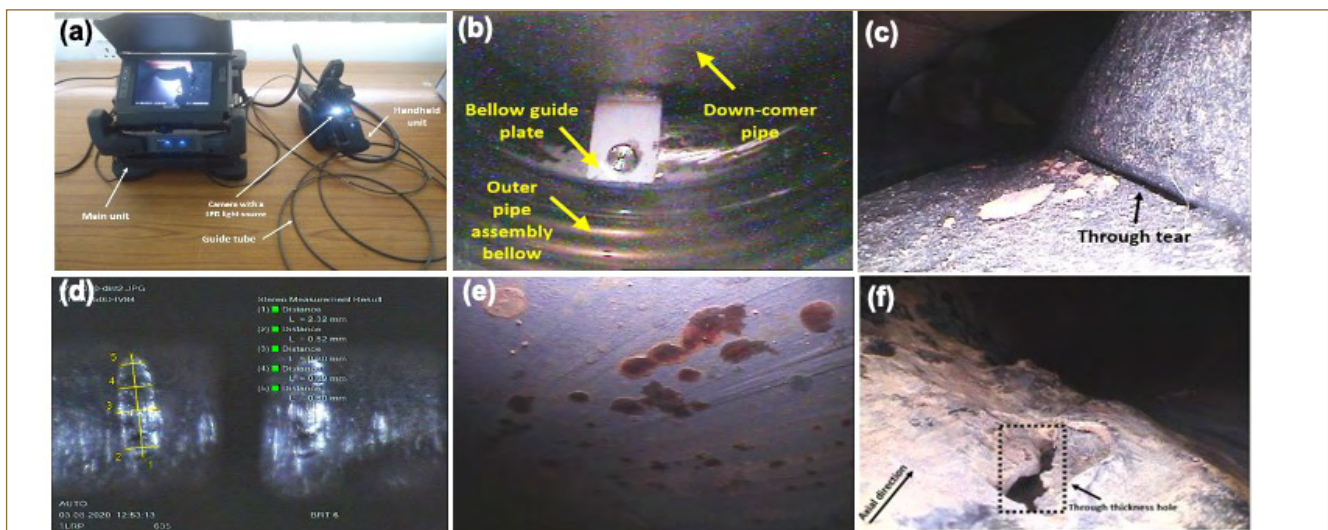
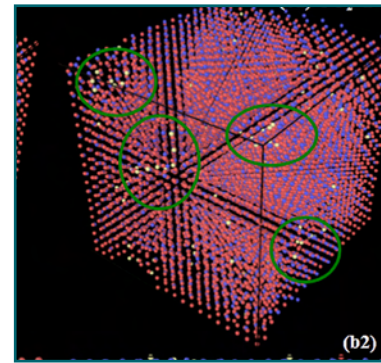
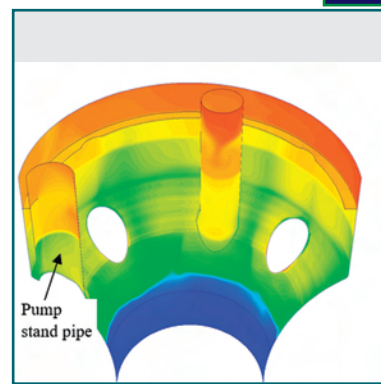
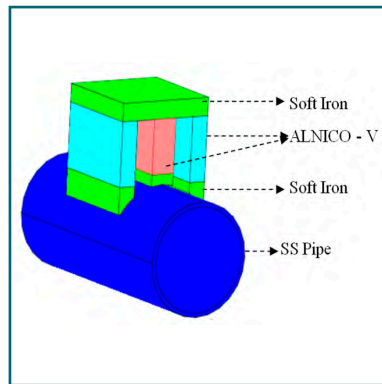


Fig. 1 (a) Industrial videoscope (b) image of IHX components (c) through tear in LRP backup seal (d) characterization of dent in LRP race (e) pitting corrosion in a BSCS pipe and (f) through thickness hole in a BSCS pipe



CHAPTER III

R&D for Fast Breeder Reactors

III.01 Development of Non-Return Valve for Sodium

Lift type Non Return Valves (NRV) are used in sodium circuits of FBRs. A 150 NB size NRV is used in the fill and drain sodium circuit (F&D circuit) of PFBR secondary sodium loops. It is installed in the vertical leg of discharge line of Annular Linear Induction Sodium Pump (ALIP). A new design of NRV for future FBRs which would offer a stable operation for a wide range of sodium flow has been conceived. The NRV is designed to have a disk type plug which would move axially upward when the upstream pressure acts on the disc. This arrangement will allow unidirectional sodium flow when the pressure difference across the valve exceeds the unseating pressure, which is due to the apparent weight of plug and static head of sodium in the downstream side of the NRV. The plug is designed to get lifted up and positioned at top most point by the lift force generated due to the sodium flow past the plug. For chatter free operation, the lift force generated needs to be always higher than the apparent weight of the plug. At the same time, pressure drop imparted by the NRV should not be high but moderate. The valve is designed for a minimum possible volumetric sodium flow rate of 40 m³/h. Besides minimum flow, it was also aimed to constrain the pressure drop within 20 kPa at nominal flow. The NRV is intended for a stable operation at sodium flow rates ranging between 40-170 m³/h.

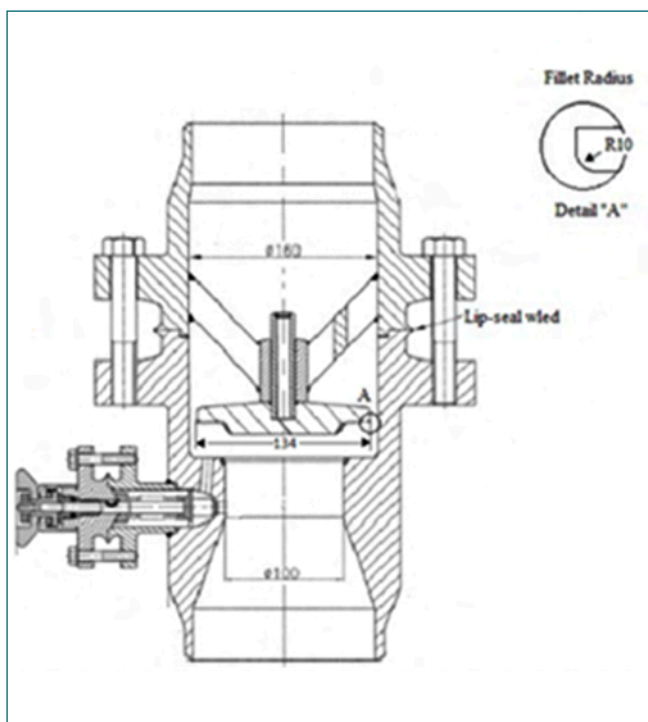


Fig. 1 New design of NRV for hydraulic testing

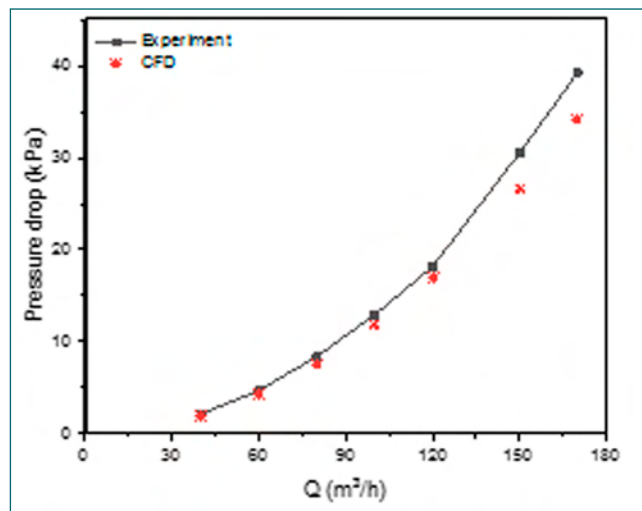


Fig. 2 Characterizes of new design of NRV

The proposed NRV with a disc shaped plug and seat design is found more effective in generating lift force. The schematic of NRV is shown in Figure 1. In the new design, the diameter of plug and seat of the valve are selected such that there is relative increase of 80% in the projected area of plug as soon as plug gets lifted from seat. The reduction in the magnitude of differential pressure acting across plug after lifting is compensated by an increased projected area. After lifting the plug from the seat, differential pressure generated by flow is mainly across the annular gap between valve body and plug. The pressure recovery in the new design is negligible. Due to this valve will have constant pressure loss coefficient with respect to various flow rate in the design range. Hence when the flow is higher than the minimum design flow, the valve plug will stay at top without any chattering.

The shape and final geometrical parameters of plug and valve seat were arrived from numerical studies. The diameter of plug and seat arrived at are 134mm and 100mm respectively. The weight of the plug is 16.7N whereas the lift force generated at minimum design flow is 18.9N at design basis minimum volumetric flow rate. The estimated pressure drop across the valve for the nominal sodium flow of 120 m³/h is 17 kPa. A full scale model of new NRV has been manufactured and tested in water medium for flow range of 40-170 m³/h. The performance of NRV including chatter free operation and seat leakage as intended in design are successfully demonstrated. Experimental characteristics of NRV and prediction by numerical studies are shown in Figure 2.

III.02 Performance Evaluation of WLD Layout for Dished End Test Section in LEENA Facility by Creating Sodium Leak

Wire type leak detectors (WLD) working on conductivity principle are employed in FBR's for detecting sodium leak in the secondary sodium circuits. Detection time of sodium leak detectors depends on many factors such as leak rate, distance between the leak point and the detector, temperature of leaking sodium, electrical contact resistance between the leaked sodium and detector wire, heater layout, the insulation material used, packing density of insulation and ambient conditions. It is planned to arrive an optimized leak detector layout for the dished end of tanks and components so as to enable early detection of sodium leak. Sodium leak experiments were conducted in LEENA facility with dished end test section having leak detector wound in spiral fashion on the dished end with a pitch of 150 and 250 mm.

LEENA facility consists of a sodium storage tank, a test vessel, test sections (TS) and interconnecting pipelines. Dished end test section is of dia 750 mm and provided with a leak simulator with a leak hole of dia 0.75 mm. Test leak detector (TLD) is provided in a spiral fashion and leak simulator is placed in the middle of two adjacent WLD winding. A leak detector labelled as planned leak detector (PLD), is placed near to the leak simulator hole so as to indicate the initiation of the sodium leak. Thermal insulation similar to the dished ends is provided on the outer surface of the TS. For preheating, surface heaters along with thermal insulation are provided on the inner side of the TS.

Test vessel was filled with sodium up to middle level and the sodium temperature was raised to 550°C. Test section and its associated lines were heated to 550°C. Initial sodium level and time was noted when inlet valve was opened. Reduction in test vessel sodium



Fig. 2 TS after sodium leak experiment

level and appearance of planned leak indication was monitored. Immediately after the test leak detector indication appeared, the time and final sodium level was noted. From the above readings, total quantity of leaked sodium, leak rate and detection time was estimated. Then test section inlet valve was closed and facility sodium was drained. Figures 1&2 show the photo of TS before and after the experiment. Table 1 gives the experiment results.

It was found from the sodium leak experiments that leak rate from 580 to 1993 g/h can be detected within 55 minutes with the WLD layout of pitch 150mm and leak rate from 330 to 2109 g/h can be detected within 50 minutes with the WLD layout of pitch 250mm. Maximum sodium leaked out during the leak experiments was 1827 g for 150 mm WLD pitch and 1757 g for 250 mm WLD pitch ie within two kg as per ASME Section XI.



Fig. 1 TS before sodium leak experiment

Table 1: Experiment results				
Exp. No.	Pitch of WLD mm	Qty leaked out g	Leak rate g/h	Detection time Minute
1	150	377	905	25
2	150	679	1404	29
3	150	203	580	21
4	150	1827	1993	55
5	250	1757	2109	50
6	250	684	1283	32
7	250	110	330	20

III.03 Plasma Nitriding of P9 Piston Rod of DSR

P_FBR is equipped with two independent, fast acting and diverse shut down systems namely Control & Safety Rod (CSR) and Diverse Safety Rod (DSR) along with their drive mechanisms CSRDM and DSRDM, respectively. The DSR sub assembly consists of hexagonal sheath, dashpot cylinder, and a geometrical feature to orient and support the sub assembly on grid plate. The dashpot piston rod made up of P9 material (9Cr-1Mo steel) and an armature is attached to the top and bottom of DSR, respectively. The DSR and DSRDM are coupled through armature and electromagnet. During normal operation, DSR is parked above the active core. On receipt of a scram signal, the electromagnet is de-energized and the DSR is released to fall freely under gravity. At the end of free fall travel of the DSR, it is decelerated by a sodium dashpot-piston arrangement. Throughout the travel of the piston inside dashpot, deceleration is achieved by displacing sodium in the dashpot out of it. The piston is expected to slide with a high velocity against the dashpot cylinder at the entry cone portion. In view of this, Plasma Nitriding (PN) of the piston rod has been attempted to enhance the wear resistance of the outer rubbing surface of the piston during continuous operation.

Mock up pistons of 9Cr-1Mo steel were fabricated and stress relieved at 730°C in vacuum. The piston rods and the control test samples were prepared to achieve a fine surface finish. One set of piston rod and control samples were directly plasma nitrided at 500°C for about 24h, while the other set of piston rod and the control samples were plasma nitrided at identical conditions after Cr-plating to a thickness of about 100 µm. Quality inspection reports indicated that the component did not

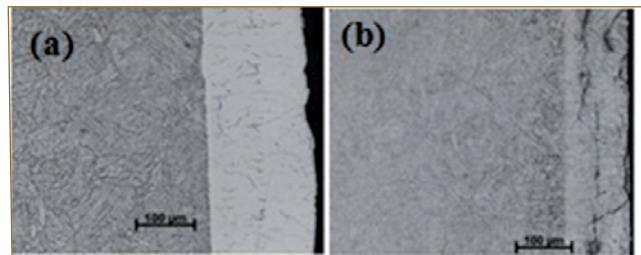


Fig. 2 Optical micrographs of (a) plasma nitrided steel after Cr-plating and (b) direct plasma nitrided steel

undergo any major distortion during plasma nitriding process. Systematic structural and microstructural characterization, including hardness depth profiling measurements were carried out on control samples at every stage of the entire process. XRD analysis was carried out to identify the phases present in the plasma nitrided layer and is shown in Figure 1. Stress relieved 9Cr-1Mo steel shows the presence of ferrite. Cr-plated steel showed peaks corresponding to only bcc Cr, with a slight shift of the peak positions corresponding to that of ferritic steel. The presence of CrN, Cr₂N nitride phases in the nitrided layer is confirmed by XRD. Microstructure of the plasma nitrided steels shown in Figure 2 reveals the presence of distinct nitrided layer of about 100 µm thickness in both conditions. The hardness profile in Figure 3 indicates that the directly nitrided steel possesses a lower hardness of about 300VHN with a case depth of about 80 µm. However, for the Cr plated and nitrided surface, the hardness is found to be in the range of 600-800 VHN with a case depth of about 100 µm. These studies suggest that Cr plating followed by plasma nitriding is both preferable and a viable case hardening technique for components, made of 9Cr Ferritic- Martensitic steels.

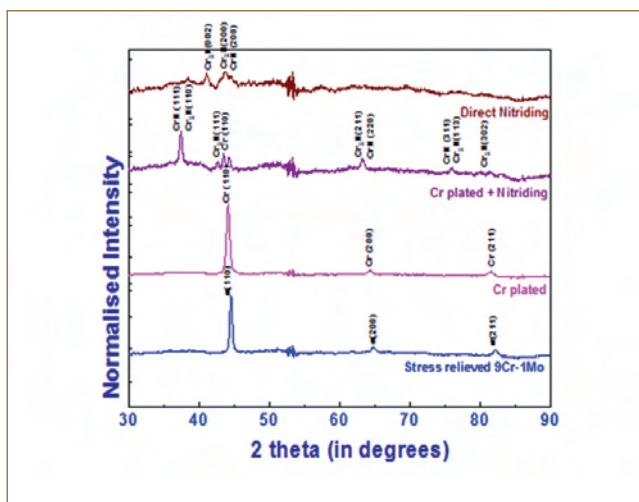


Fig. 1 XRD pattern of 9Cr-1Mo steel in different conditions

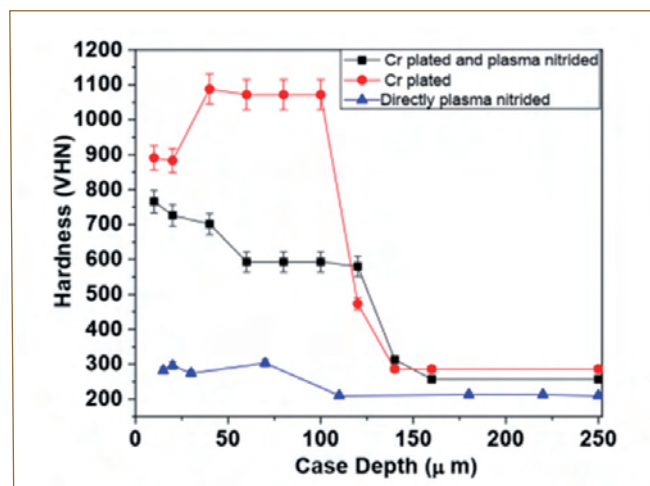
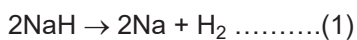


Fig. 3 Micro-hardness depth profile of Cr plated and nitrided steels

III.04 Studies on Decomposition Behaviour of Sodium Hydride in Liquid Sodium as a Function of Vacuum Level in the Context of Cold Trap Regeneration

Cold traps (CT) are employed to remove hydrogen and oxygen impurities in the sodium coolant circuits in PFBR. Secondary Cold trap of PFBR needs to be regenerated in regular interval of five years since it gets saturated by hydrogen impurity as sodium hydride. Regeneration of CT is carried out by thermo vacuum process which releases large quantity of hydrogen as per equation 1. Decomposition rate (DR) of sodium hydride or hydrogen release behaviour depends on temperature of deposited NaH in liquid Na and vacuum level maintained above liquid sodium during CT regeneration. Study of decomposition phenomenon as a function of temperature with varying vacuum level will render better insight of the regeneration process which will facilitate to standardize the parameters for safe regeneration of CT with respect to hydrogen release rate. In this work, NaH decomposition behaviour was studied by measuring the release rate of hydrogen as a function of temperature and pressure.



The photograph of the experimental set-up for NaH decomposition studies is shown in Figure 1. The experimental set-up consists of reaction vessel (RV), UHP (Ultra High Purity) argon supply, diaphragm pump, pirani gauge, tubular furnace and hydrogen sensor. Reaction vessel is a leak tight one end closed cylindrical SS 316 vessel and other end closed with CF 35 blank flange which has provision for gas inlet, outlet tubes and for inserting thermocouple. Known quantity of NaH and liquid sodium are loaded in RV in glove box. The RV with sample was positioned in a furnace. The inlet was connected with UHP argon gas line and outlet was connected to diaphragm pump (DP). The outlet of DP was connected to hydrogen

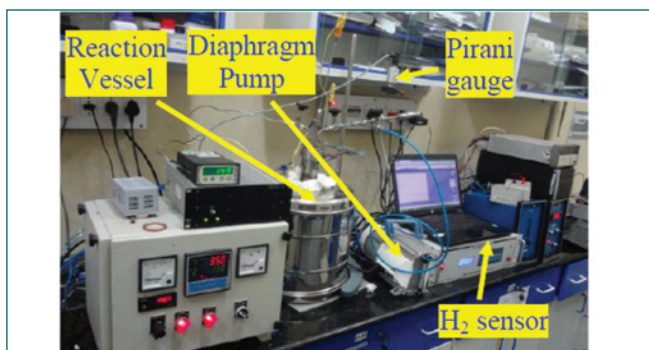


Fig. 1 Photograph of the experimental set-up for NaH decomposition studies as a function of vacuum level

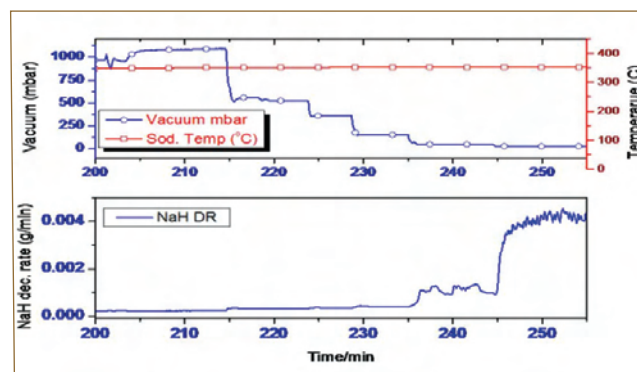


Fig. 2 NaH decomposition profile at 350°C as a function of vacuum

sensor. Prior to decomposition experiments the hydrogen sensor was calibrated in-situ by passing known concentrations of hydrogen through the reaction vessel. The experimental parameters such as argon flow rate, sodium temperature, vacuum level and hydrogen concentration were measured continuously as a function of time and data were logged in the PC. The experiments were conducted at 325, 350, 375 and 400°C and the vacuum level at each temperature was maintained at 1000, 550, 330, 150, 50 and 20 mbar. Figure 2 gives the typical decomposition behaviour of NaH at 350°C as a function of vacuum level from 1000 mbar to 50 mbar. The decomposition profile indicates increase in the decomposition rate as a function of vacuum level and is significant below 150 mbar. DR of NaH as a function of temperature and at various vacuum levels are shown in Figure 3. DR drastically increased beyond 150 and 20 mbar. The generated data on decomposition rate of NaH in the study will facilitate to control CT regeneration process at desired rate of hydrogen release by suitably fixing the temperature and vacuum level.

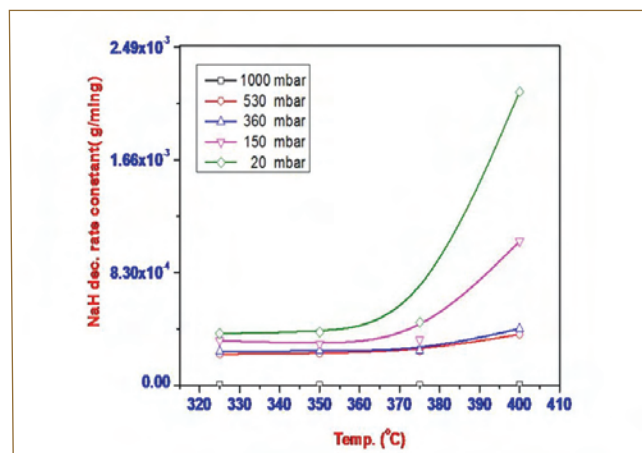


Fig. 3 NaH decomposition rate as a function of temperature at various vacuum levels

III.05 Improvements in Regeneration of Sodium Cold Trap by Altering Geometry of Wire Mesh Top Cover Plate

Cold trap (CT) is the equipment used in sodium systems to maintain the impurity level in sodium within acceptable limits. It make use of the temperature depended solubility of hydrogen and oxygen in sodium. PFBR secondary cold trap is designed for trapping hydrogen predominantly. Sodium hydride will accumulate to its maximum design capacity in the CT in 5 years of reactor operation. Hence, periodically cold trap in PFBR would be regenerated in-situ by Vacuum decomposition technique in which NaH will be dissociated into hydrogen gas and sodium. During regeneration, CT containing sodium would be externally heated to about 400°C in moderate vacuum. NaH accumulated in the bottom wire mesh bundle of CT decomposes into hydrogen gas and sodium. Tiny gas bubbles rise through the sodium column to the cover gas space, which is evacuated by a vacuum pump. Ultimately the hydrogen is disposed through an electro chemical burner. A flat cover plate is provided above the wire mesh of CT to provide sodium flow laterally through the wire mesh. With respect to CT regeneration, experiments in sodium are going on with a scaled down model of secondary CT of PFBR called Model Secondary Cold Trap (MSCT) which simulates PFBR CT geometry as well as the physical and chemical phenomena during the regeneration process.

During the experiments, conducted with the MSCT, the rate of hydrogen release was found to be non-uniform and having multiple peaks. It is deduced from these observations that the sudden increase in the hydrogen release rate to the cover gas space is due to the sudden release of accumulated hydrogen. Hydrogen bubbles emanating from the bottom wire mesh would get collected on the lower surface of top cover plate of wire mesh bundle. It could coalesce together to form a larger bubble and get released when it become sufficiently large to reach the periphery of the plate. Accumulation of the hydrogen inside cold trap and sudden release of the same to the cover gas space make the entire system away from its process equilibrium. A uniform release of

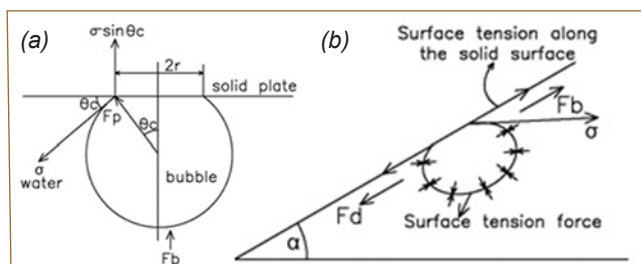


Fig. 1 Force balance on a bubble under a plate:(a) flat surface; (b) inclined surface

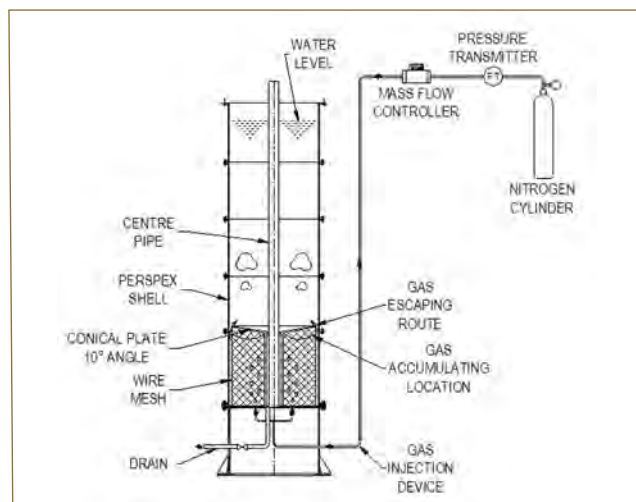


Fig. 2 Schematic drawing of the experimental setup

hydrogen is preferred during regeneration process for the reasons of safety and the effectiveness of hydrogen disposal system.

Both, buoyancy force (F_b) and the upward component of surface tension force (σ) act upwards as shown in Figure 1a, causing the bubble to attach to the surface. Therefore the bubble is unable to detach from a perfectly horizontal plate. The horizontal component of surface tension force opposes the expansion of the bubble, while the force of the internal bubble pressure (F_p) expands the base diameter. The contact angle (θ_c) of the bubble changes as small bubbles accumulates to form large bubble leading to change in shape of the bubble from spherical to elliptical. The accumulation of gas bubbles can be reduced by providing a favorable slope at the wire mesh cover plate. The primary forces that affect a sliding bubble on an inclined surface are the buoyancy force (F_b), surface tension and drag force (F_d) as shown in Figure 1b. The x and y components of the buoyancy force, flattens the bubble and initiates bubble sliding, respectively. The drag force opposes the motion of the bubble while the surface tension force influences to sustain a spherical shape. The escape velocity of bubbles will increase and bubble volume will reduce with increase in angle of inclination (α) of the top cover plate. An angle of inclination of 10° was selected for the study.

To study the above phenomenon, experiments were conducted in water with full scaled Perspex model of the MSCT. Water-Steel system was used in place of Sodium-steel system. Schematic drawing of the experimental setup for characterization of gas bubbling during regeneration process is shown in Figure 2. The

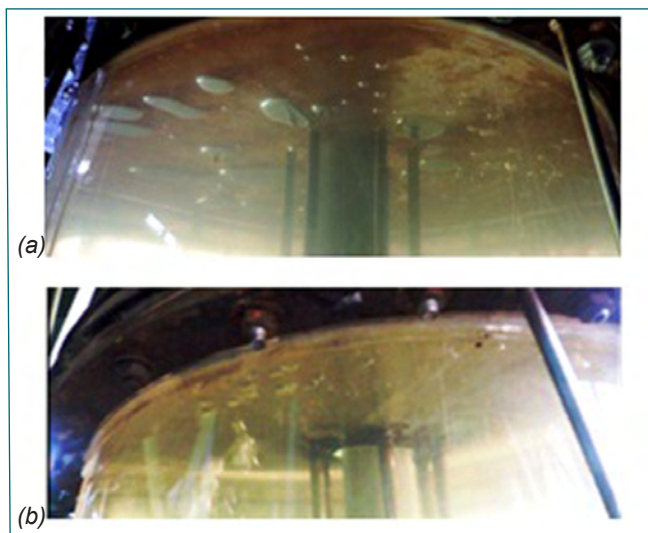


Fig. 3 Visualization of bubble below the top cover plate: (a) flat plate and (b) inverted conical plate

experimental setup consist of a Perspex model of MSCT filled with water, a gas injection device containing four orifices of 0.5 mm diameter to generate gas bubbles, gas delivery, measuring and controlling system. Injection device was connected to a nitrogen gas cylinder via mass flow controller and pressure transmitter. The process of hydrogen evolution from the reaction site is simulated by small diameter nozzles at multiple locations through which nitrogen gas was injected to the experimental system with a preset mass flow rate. Behavior of nitrogen bubble in the experimental system is more or less same as that of hydrogen in cold trap system except for the chemical interaction between gas and liquid and contact characteristics of solid-liquid-gas interfaces. Nitrogen gas was passed through the orifices at a flow rate of 3 lit/min based on average generation rate of hydrogen in MSCT during regeneration. The experiment was performed initially with a flat top wire mesh cover plate without winding wire mesh to visualize the accumulation of bubbles below the top cover plate

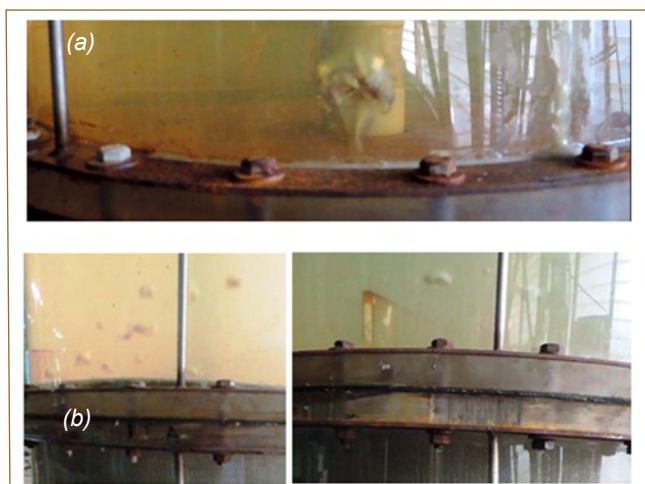


Fig. 4 Comparison of escape of a bubble from the top cover plate with wire mesh: (a) flat plate; (b) inverted conical plate

Top cover plate geometry	Bubble size without wire mesh (mm)	Bubble size with wire mesh (mm)
Flat geometry	33	42
Inverted conical geometry	10	24

of the cold trap. Thereafter, the wire mesh top cover plate was made in the form of an inverted conical plate with an angle of inclination of 10° and the experiment was repeated. The bubble formation, accumulation and travel were recorded in a camera. The visual of gas accumulation below the wire mesh top plate in a cold trap is captured and shown in Figure 3. Gas accumulation below the wire mesh top plate is compared for the two geometries. In case of flat geometry, it was observed that small bubbles generated from orifice were slowly rising to the bottom surface of the top plate and getting accumulated to form larger bubbles. The contact angle of bubble changes as small bubbles accumulates to form large bubble, leading to change in shape of the bubble from spherical to elliptical as shown in Figure 3a. However, in case of inverted conical geometry it was observed that the small bubbles escape continuously from the bottom of wire mesh top plate. In this case the bubble's shape is more close to spherical due to less coalescence as shown in Figure 3b.

The experiment was repeated after winding wire mesh over the center pipe. It was observed that the size of bubble escaping from the top cover plate was increased. Visualization of gas bubble from the top cover plate with wire mesh is shown in Figure 4. The increase in the size of bubbles was attributed to the fact that probability of escape of bubbles will decrease because of the additional surface and the resistance to move between surfaces. Even though the size of bubbles is larger with wire mesh, the bubbles were escaping continuously and the size of escaped bubbles was less compared to flat geometry as shown in Figure 4b. Comparison of size of gas bubbles observed in the experiments is given in Table 1.

The accumulation of gas bubbles would be further higher in Na-SS system because water-steel system is having much better wettability than Na-SS system.

With these experiments it is concluded that, an inclined top cover plate of wire mesh in secondary cold trap will assist an easy scavenging of hydrogen generated during regeneration process to the cov gas space. The effect of change in angle of inclination on bubble size will be established with further studies.

III.06 Sensitivity Evaluation of 100 NB PM Flowmeters in Sodium Facility for Component Testing

Two 100 NB PM Flowmeters installed in the Test Vessel-3 (TV-3) fill line of Sodium Facility for Component Testing (SFCT) is used for the flow measurement during the performance testing of PFBR 50 m³/h ALIP. Since more accurate sodium flow measurement is needed during the performance testing, it is required to evaluate the sensitivity of these flowmeters by draining constant volume of sodium through the flowmeters. During draining of sodium, millivolt output of flowmeters was acquired in every second and stored in the PC. Based on millivolt readings and time obtained from the trial runs, total millivolt seconds was estimated for known sodium volume draining. The total millivolt seconds (mV.s) and the quantity of sodium drained were equated to obtain the millivolt output per m³/h flow.

Sensitivity evaluation setup

SFCT consists of sodium storage tank, three test vessels, purification circuit, EM Pump, heater vessel and interconnecting pipe lines. Flowmeters are installed in the TV-3 fill line of SFCT. The volume of TV-3 between low level and operation high level is 0.86 m³ at room temperature. When the respective drain valve of TV-3 is opened, sodium in TV-3 flows to dump tank by gravity. An instrumentation system was made ready for acquiring millivolt output from each pair of electrode by

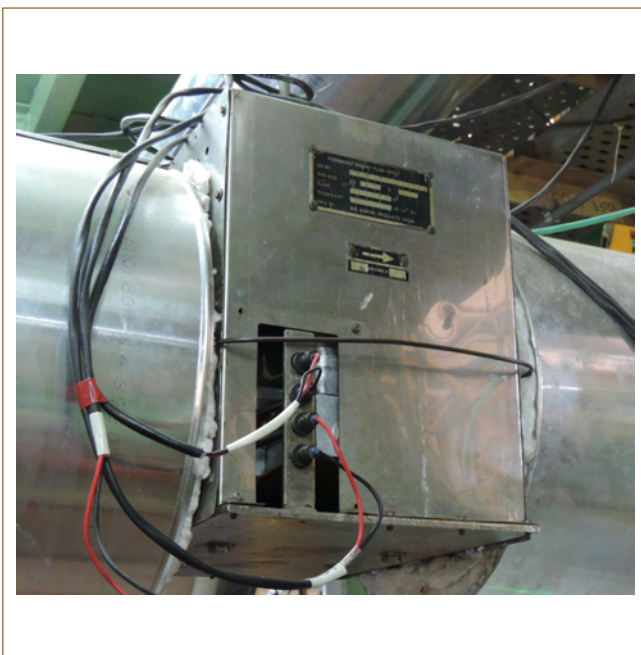


Fig. 1 Photograph of 100 NB PMFM

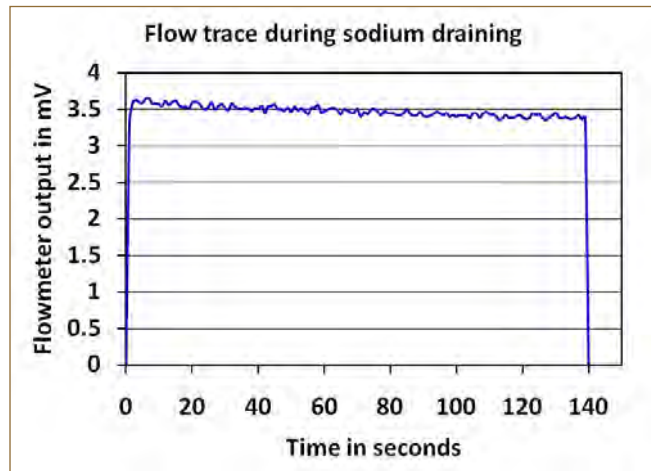


Fig. 2 Flow trace during sodium draining

using a 60 channel, HP make Data Acquisition System and communicated to PC through Bench Link software. While draining sodium, millivolt output of all the electrode pairs of the flowmeters was acquired in each second and stored in the PC. Photograph of flowmeter installed in SFCT is given in Figure 1.

Sensitivity evaluation procedure

TV-3 was filled up to operation high level and sodium temperature was raised to required level. TV-3 sodium was allowed to drain through both the flowmeters by gravity by opening the fill line valves. After draining known quantity of sodium, valves were closed. While draining sodium, millivolt output of flowmeters were acquired in every second by DAS and stored in the PC. From this data, the sensitivity of the flowmeters were estimated. Trial runs were repeated at different sodium temperatures and flow rates. Typical Flow trace during sodium draining is given in Figure 2.

Summary of sensitivity evaluation results

Sensitivity evaluation of 100 NB PM flowmeters was completed with different sodium flows and sodium temperatures. Sensitivities of these flowmeters were evaluated by constant volume method. Accuracy of this sensitivity evaluation is well within $\pm 1.5\%$. Flowmeter output is found to be linear at all sodium temperatures and found that both the electrode pairs of each flowmeter are giving uniform millivolt output. Average sensitivities of flowmeter 1 & 2 based on sensitivity evaluation were found to be 0.151 and 0.1538 mV/m³/h respectively. Sensitivity deviations with respect to flow and temperature are found to be within the acceptable limit.

III.07 Finalization of Calibration Scheme for Eddy Current Flow Meter of Primary Sodium Pump

In PFBR, the eddy current flow meters (ECFM) are used to measure the flow delivered by each pump to monitor the pump performance and to obtain the flow through the core, thereby providing one of the SCRAM signals for the event of primary pipe rupture. The ECFM sensor is designed and developed in-house. All ECFM sensors required for PFBR (8 nos. including 4 nos. as spare) are calibrated in 500 kW loop located in Hall-I, IGCAR.

During the calibration of sensors, the raw signals of the sensor coils were recorded continuously with a PC based data logger. In this testing, null adjustment was carried out digitally at each temperature (250° C to 400° C). With this procedure, sensor accuracy of ± 2% was achieved. Thus, the zero reading of a given sensor is temperature dependent. Hence, it is necessary to make null adjustment automatically based on temperature to achieve the required accuracy at PFBR. But, the ECFM electronics of PFBR does not have the provision for automatic null adjustment at multiple temperatures and a single factor can only be used at all temperatures. Moreover, the zero reading is different for different sensors, even though all the sensors are identical. All these factors together result in reduction in the overall accuracy of the core flow measurement.

A study was carried out to propose and evaluate various means to achieve the required sensor accuracy. The data generated during the calibration of 8 nos. of ECFM probes was used for this study. The various calibration schemes proposed are given in Table-1. Common calibration curve for all sensors simplifies the electronics design. However, it is expected to result in higher error compared to using the individual calibration curve for each sensor. The advantage of null adjustment at 200°C / 250°C is that it can be verified /corrected during isothermal testing as part of reactor commissioning. The operating temperature of the sensor is approximately 400°C during all reactor power operations, and null adjustment at 400°C results in a minimum error at reactor power operation, even though the error could be high at other reactor conditions. In Options 2B and 3B, separate calibration curves for each sensor are used. Further, it is to be noted that only 250°C data is used for generating the calibration curve for Option 2B and the 400°C data is used for generating the calibration curve for Option 3B. Figure 1 shows a typical sensor response for varying flow rates for null adjustment at 400°C. The corresponding calibration curve for option 3B is also shown in the figure.

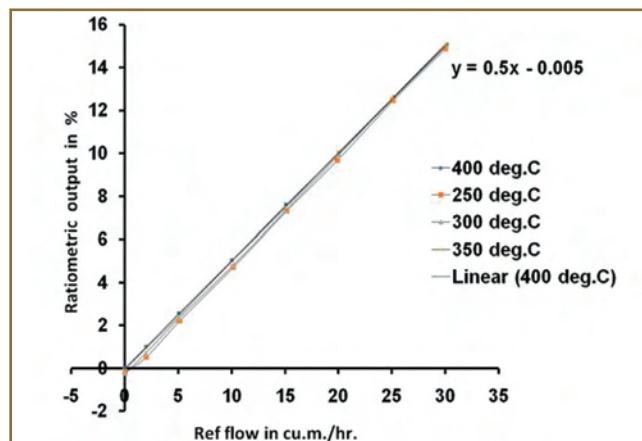


Fig. 1 Sensor response for varying flow rates for null adjustment at 400°C

The measurement errors for each calibration scheme are calculated using the data generated previously, and given in Table -1. It can be seen that option 2B & 3B result in acceptable error at 250°C & 400°C respectively whereas the errors for overall temperature range is more than ± 12% for these schemes. Since the important function of ECFM is to give SCRAM signal for primary pipe rupture event and the sodium temperature in ECFM during such event is 400°C, the option 3B gives least error for scram operation. Hence this option is recommended for PFBR. To reduce the error for pump/core flow measurement at other temperatures, it is recommended to use a temperature dependent calibration curve in the software based display station of the control room.

This study enabled to finalize a suitable calibration scheme for flow sensors of PFBR to meet the safety & process requirements, The necessary data for implementing the scheme in PFBR is also generated.

Table 1: Various options and resulting errors		
Options	Options/schemes proposed	Measurement error
1	Common characteristic curve for all the sensors without any null adjustment	-80 % to + 48%
2A	Null adjustment at 250° C with common calibration curve over the temperature range	-18 % & +7.4%
2B	Null adjustment at 250° C with individual calibration curve	± 12 % (over the full temperature range) ± 1 % (at 250 °C)
3A	Null adjustment at 400° C with common calibration curve	- 8.6% & +12%
3B	Null adjustment at 400° C with individual calibration curve	± 13 % (over the full temperature range) ± 1 % (at 400 °C)

III.08 Evaluation of Rotor Dynamics Coefficients of Sodium Pumps Through CFD Analysis

Seals are widely used in various turbo-machinery for the reduction of the leakage flow through rotor-stator clearances from high pressure regions to low pressure regions. Although the primary function of seals is to control leakage flow, forces generated by the seals have a strong influence on the rotordynamic characteristics of the machine, and hence, play an important role in successful operation of these machineries. In Secondary Sodium Pump (SSP) of PFBR, there are two wear rings (plain seals), called as suction wear ring and discharge wear ring, to reduce the backflow of high pressure sodium from discharge side (Figure 1). Backflow of high pressure sodium through suction wear ring is through the impeller-casing clearance region.

Stiffness and damping coefficients of seals known as the rotordynamics coefficients are essential for carrying out dynamic analysis of machineries. The dynamic analysis establish the stability of rotating parts and hence the comfortable operation of machineries. The rotordynamic coefficients of the suction wear ring and impeller-casing

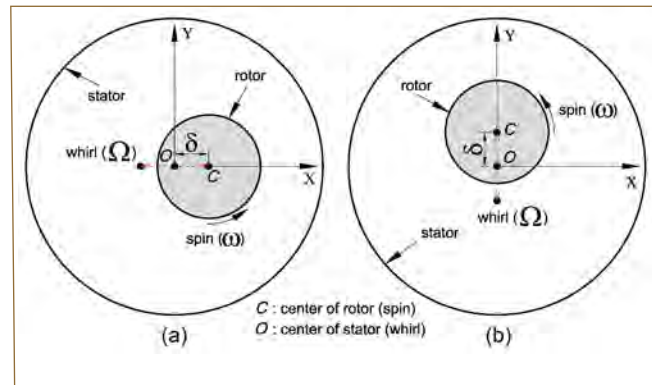


Fig. 2 1D rotor whirling model

region of SSP have been evaluated using CFD technique. In this analysis, the rotor is excited with a known transient perturbation and the time varying response forces on the rotor surface is estimated using general purpose CFD software and from this, the rotordynamic coefficients are estimated. The transient CFD methods require a rotor whirling model to define the equation of rotor whirling motion as the excitation signal. One-dimensional whirling model is shown in Figure 2. It is assumed that the rotor vibrates in a X-direction (Figure 2a) or Y-direction (Figure 2b) normal to the rotation axis along a periodic straight line orbits with maximum amplitude of vibration δ and angular frequency $\Omega (= 2\pi f)$.

Equations of rotor motion for X-direction excitation,

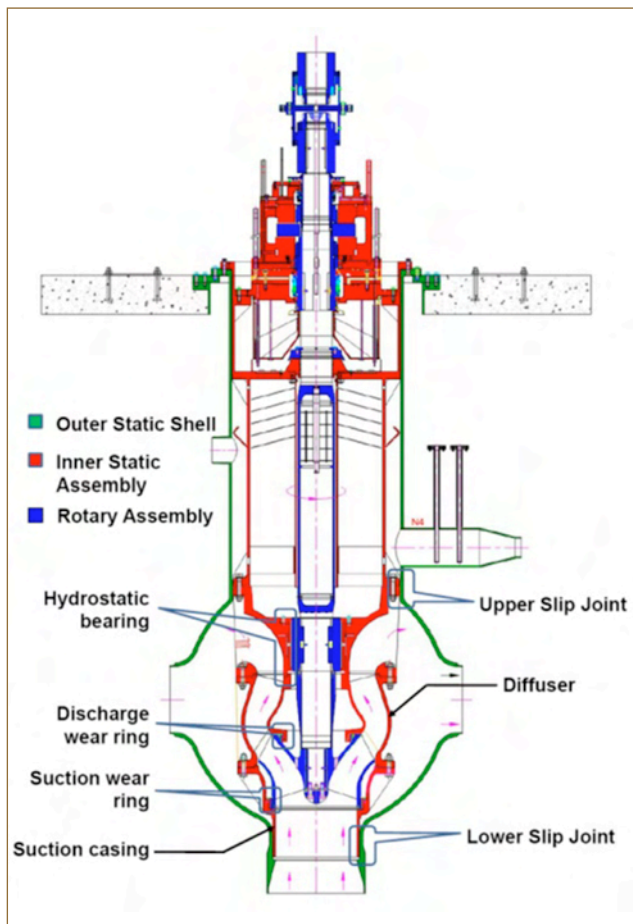


Fig. 1 Schematic of SSP

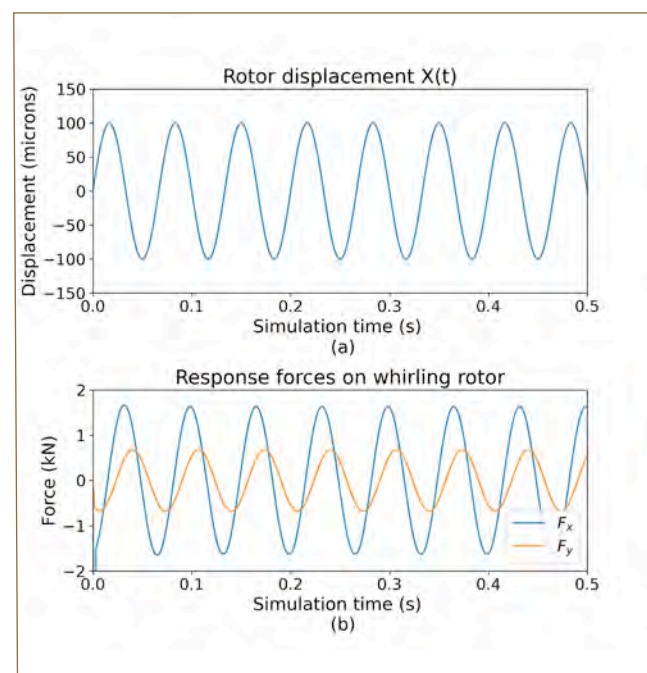


Fig. 3 (a) Displacement of rotor from centre & (b) Response forces on rotor due to whirling at 15 Hz

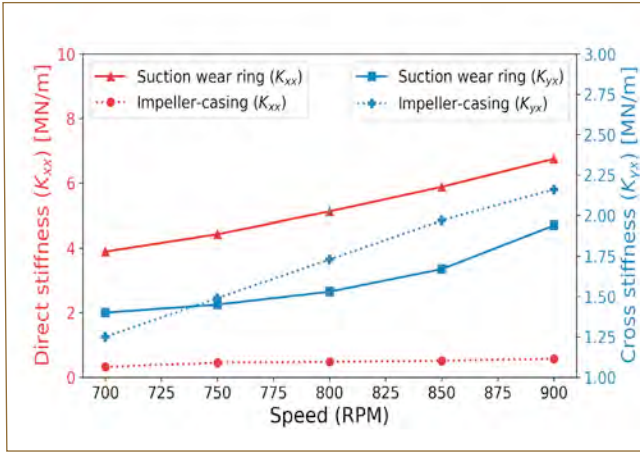


Fig. 4 Stiffness coefficients at various SSP speeds

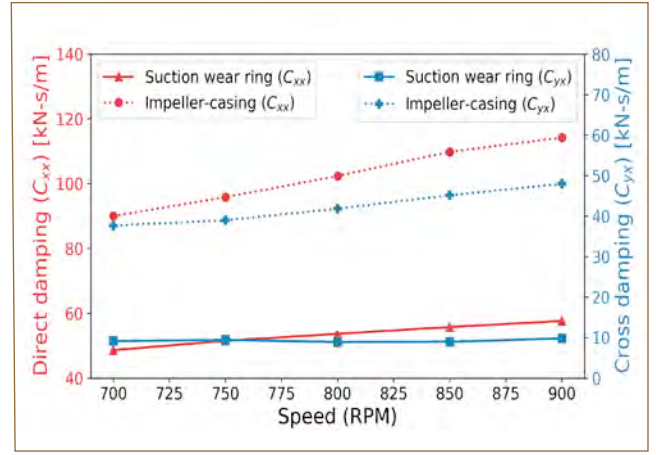


Fig. 5 Damping coefficients at various SSP speeds

Table-1: Comparison of experimental data with CFD results

Parameter	Experimental [Marquette et al.]	Analytical [Childs]	2D CFD [Andres]	Transient CFD [Present]
Direct stiffness (MN/m)	29.5	25.9	22.5	22.7
Cross stiffness (MN/m)	8.5	17.3	11.5	5.7
Direct damping (kN-s/m)	27	42.0	34	35.4

$$X = \delta \sin(\Omega t), Y = 0 \quad (1)$$

Equations of rotor motion for Y-direction excitation,

$$Y = \delta \sin(\Omega t), X = 0 \quad (2)$$

For a small motion of the rotor about a centred position within a seal, the seal response forces can be modelled using the reaction-force/seal-motion as in equation (3). It relates the response forces (F_x, F_y) due to the rotor whirling motion (X, Y), to velocity (\dot{X}, \dot{Y}) and acceleration (\ddot{X}, \ddot{Y}) through direct & cross stiffness coefficients ($K_{xx}, K_{yy}, K_{xy}, K_{yx}$), direct & cross damping coefficients ($C_{xx}, C_{yy}, C_{xy}, C_{yx}$) and added mass coefficients ($M_{xx}, M_{yy}, M_{xy}, M_{yx}$).

$$-\begin{bmatrix} F_x \\ F_y \end{bmatrix} = \begin{bmatrix} K_{xx} & K_{xy} \\ K_{yx} & K_{yy} \end{bmatrix} \begin{bmatrix} X \\ Y \end{bmatrix} + \begin{bmatrix} C_{xx} & C_{xy} \\ C_{yx} & C_{yy} \end{bmatrix} \begin{bmatrix} \dot{X} \\ \dot{Y} \end{bmatrix} + \begin{bmatrix} M_{xx} & M_{xy} \\ M_{yx} & M_{yy} \end{bmatrix} \begin{bmatrix} \ddot{X} \\ \ddot{Y} \end{bmatrix} \quad (3)$$

Response forces on rotor surface due to whirling obtained from CFD analysis (F_x and F_y) are used for evaluating rotordynamic coefficients of seals through equation (3). Dynamic mesh smoothing method is used to update mesh

for placing rotor at prescribed location after each time step as per equations (1, 2).

CFD methodology discussed is validated against the experimental data as well as analytical and numerical data for rotordynamic coefficients published in literature (Table 1). Rotordynamic coefficients of SSP suction wear ring and its impeller-casing are estimated by considering the wear ring clearance of 1 mm for various SSP rotational speeds using methodology as discussed earlier. Figure 3a shows the displacement of whirling rotor from its centre (given as input). Figure 3b shows the response forces generated by liquid sodium (obtained from CFD) on SSP rotor surface due to whirling at 15 Hz frequency (900 rpm).

Figures 4 and 5 shows the variation of stiffness and damping coefficients with increasing SSP speeds respectively. It has been observed that the rotordynamic coefficients increase with increasing speed. Stiffness coefficient increases steeply as compared to damping coefficients with speed. However, added mass coefficients are not significantly affected by speed and are estimated as ~110 kg and ~1010 kg for suction wear ring and impeller-casing respectively.

III.09 Numerical Analysis of Hydrostatic Bearing of Large Sodium Pump Using ARMD Software

Secondary Sodium Pump (SSP) circulates liquid sodium in the secondary loop of the Prototype Fast Breeder Reactor (PFBR). It consists of a rotor assembly, an inner skirt assembly, and a pump tank. Overall length of the rotor assembly is 5.5 m, and it is supported at 3 locations, axially and radially (Figure 1). A Kingsbury tilting pad thrust bearing for axial and a hydrodynamic bearing for radial support is provided near the top, while radial support at the bottom of this long rotor is provided by a Hydro Static Bearing (HSB). A six-pocket HSB is chosen for SSP, and pressurized fluid, fed by the pump's discharge itself, is supplied to each pocket through an orifice. The fluid from the pockets escapes axially through the clearance between the journal and the bush.

To compute the SSP rotor assembly's critical speeds, estimation of HSB stiffness is vital; HSB stiffness depends upon supply & exit pressures, density, viscosity, and eccentricity ratio. As the pump's discharge pressurizes the HSB, its stiffness is dependent on the

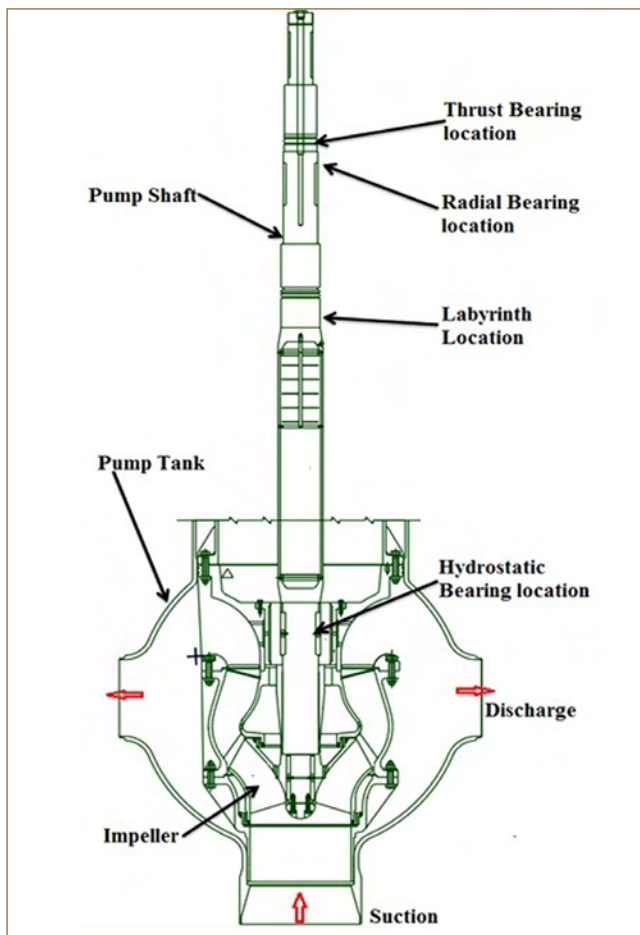


Fig. 1 Rotor shaft of SSP with support locations

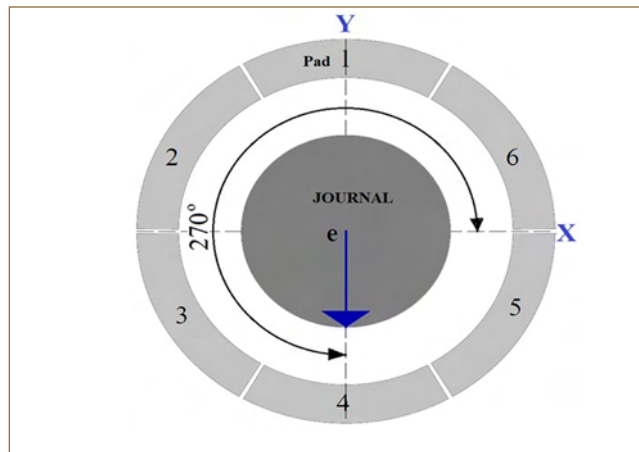


Fig. 2 HSB model with six pockets & journal

pump's operating speed. The top side exit pressure of HSB is governed by cover gas pressure, while the bottom side exit pressure is equal to the pump's discharge pressure. The directional stiffness of HSB, i.e., K_{xx} , K_{yy} , K_{xy} , K_{yx} , also depends on the eccentricity angle, i.e. the angle between the line of action of eccentricity w.r.t HSB bush. Estimation of the stiffness of HSB w.r.t. all the parameters discussed here are carried out using a commercially available software - Advanced Rotating Machinery Dynamics (ARMD). HSB model with 6 pads/pockets & journal with eccentricity along Y-axis (eccentricity angle = 270°) is shown in Figure 2.

Figure 3 shows the K_{yy} vs. eccentricity ratio at different speeds at operating temperature of 355°C and 270° eccentricity angle. Since the journal here is eccentric along Y-axis, clearance along this axis is least and hence, corresponding stiffness i.e., K_{yy} is maximum; pad grid

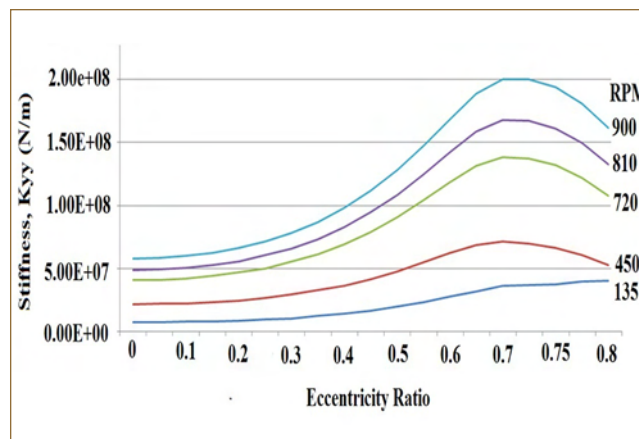


Fig. 3 Stiffness, K_{yy} vs. ecc. ratio at various speeds

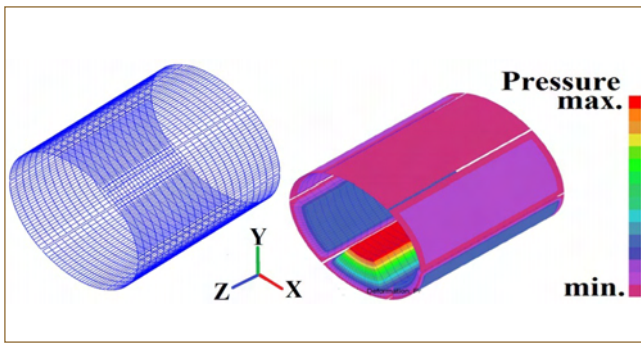


Fig. 4 Grid model & pressure distribution at 270°ecc. angle

model and pressure profile under this orientation is shown in Figure 4. With a change in eccentricity angle, values of directional stiffness changes. Figure 5 shows the change in stiffness as a function of eccentricity angle.

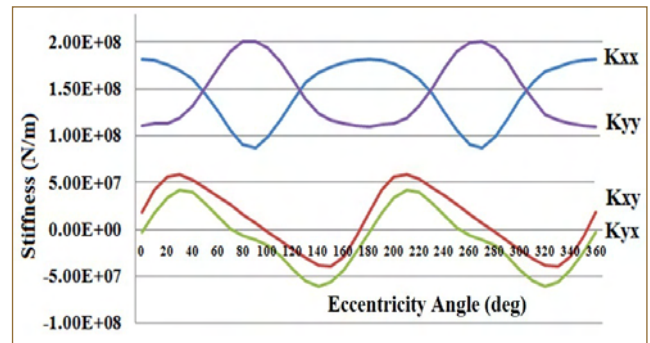


Fig. 5 Stiffness vs. ecc. angle at 900RPM and 0.7 ecc. ratio

At 0°, stiffness Kxx is maximum and as the eccentricity angle changes from 0 to 90°, Kxx decreases while Kyy increases. Periodicity of 180° is obtained in the stiffness values as the bearing is symmetric about X axis.

III.10 Highly Accelerated Life Testing of Switch Over Logic System

Highly Accelerated Life Testing (HALT) and Highly Accelerated Stress Screening (HASS) use much higher stimuli than would exist in the field with the result of forcing failures or revealing design flaws in the device in significantly less time. This allows a product designer to see how their design would hold up “over the years” without having to wait that long. Defects are uncovered in the space of hours and observed with the purpose of making ongoing corrections. Samples of the corrections that can be made are improvements to the assembly process, making mechanical revisions to the design

to remove stress or inherent design flaws or revising components that are not performing according to their advertised potential (Figures 1 to 3).

The specifications for the facility is given below

- HALT/HASS Temperature Range: -100° to 200°C
- HALT/HASS Temperature Change Rate: 70 - 100° per minute

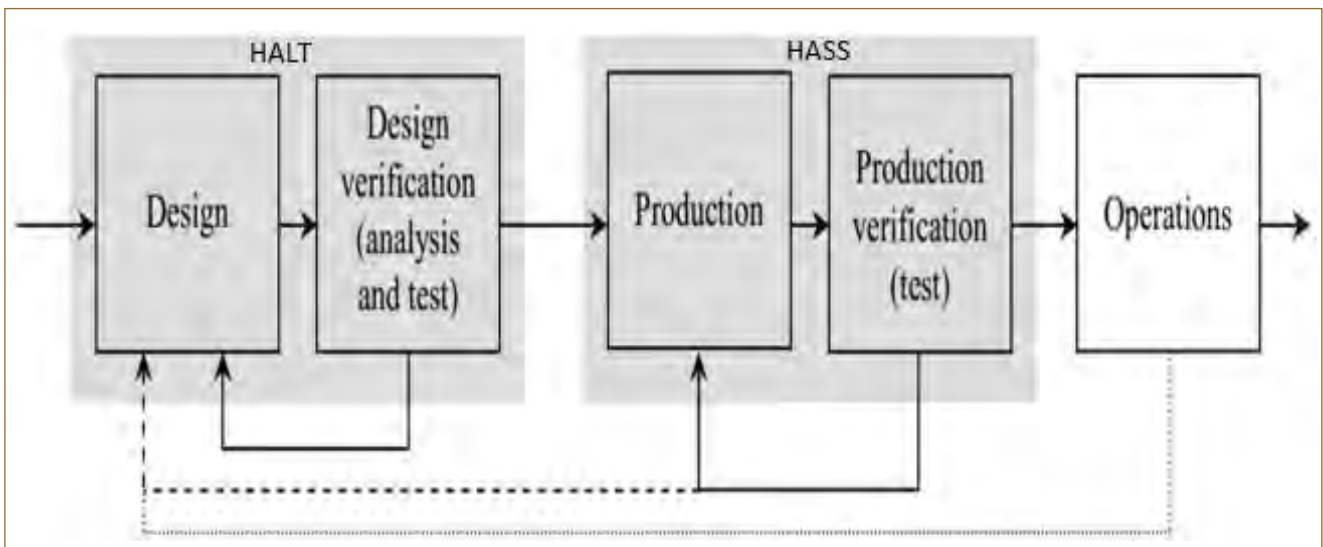


Fig. 1 HALT/HASS cycle

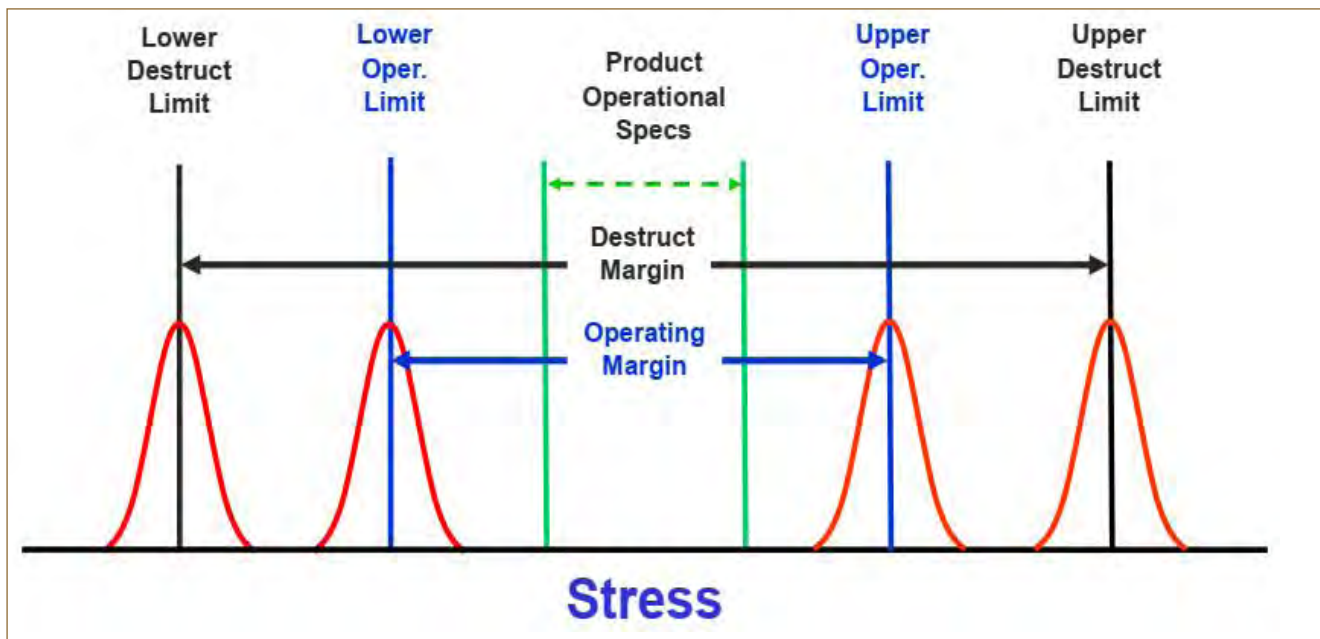


Fig. 2 Establishment of design & destruct margin

- c) HALT/HASS Temperature Stability: $\pm 1^{\circ}\text{C}$ after stabilization
- d) HALT/HASS Vibration Type: Repetitive shock, tri-axial non-coherent. Product experiences 6 degrees of freedom broadband random vibration.
- e) HALT/HASS Table Size: 36"x36"
- f) HALT/HASS Maximum Vibration Power: 70g RMS
- g) HALT/HASS Frequency Ranges: 10 to 5,000 Hz

The installation had both outdoor and indoor components and completed successfully. The high capacity compressor and auxiliary LN2 cylinders are used to generate the random vibration in 6 axis. The LN2 cylinders are used for rapid cooling of the equipment under test.

In Safety Class-2 & Fault-Tolerant Non-Nuclear Safety system architecture of PFBR, two real-time computer systems with Switch Over Logic System (SOLS) is

implemented. The Switch Over Logic System consists of Switch Over Logic Circuit (SOLC) card and OR-ing logic (OLC) cards in a 19", 6U backplane. The SOLC checks the healthiness of both the systems and commands the OR-ing logic to route one of the healthy system's output to the plant as per the logic incorporated in the design of Switch Over Logic System. The SOLS system was configured with one SOLC card and one OLC card. Manual switchover command was provided which will force the SOLS output to switch over to the other healthy system. Failure to switchover was one of the criteria for system failure. Test was conducted at elevated temperatures starting from 45°C to 125°C and an acceleration ranging from 0-40g (Figure 4).

Transient failure was detected at two points i.e., a) 95°C @ 2g and b) 125°C @ 2g. The board was designed to survive temperature up to 55°C . After highly accelerated life testing, it was found to survive high temperature up to 95°C and vibration up to 40g.



Fig. 3 HASS installed facility

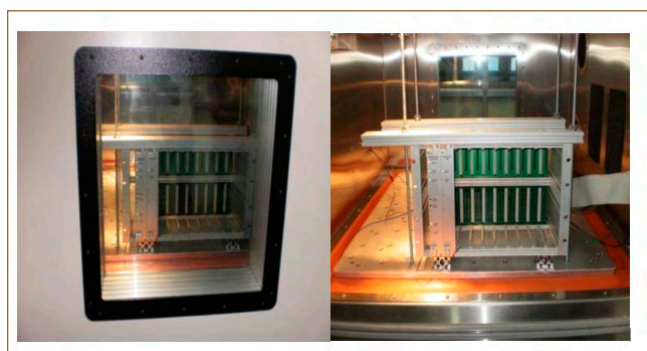


Fig. 4 SOLC under testing

III.11 Application of High Contrast Sensitivity Radiology (HCSR) Procedure for Detection of Micro Defects in End Plug Welds of Fuel Pins

The mixed oxide (MOX) fuel pellets of Prototype Fast Breeder Reactor (PFBR) are encapsulated in thin walled 20% cold worked alloy D9 stainless steel clad tubes which are autogenously Tungsten Inert Gas (TIG) welded to the end plug made of SS 316LN stainless steel. The quality of the end plug welds of the fuel pin is very important since the weld defect can cause fission products release in to the coolant circuit. Using conventional X-ray radiography inspection procedure, 80 μm image quality indicator (IQI) is obtained as the radiographic defect detection sensitivity. The pixel intensity variations arising due to the different noise sources viz., statistical photon noise, thermal noise and structural noise of the X-ray detector (pixels) limit the sensitivity. Therefore, to enhance the defect detection sensitivity of fuel pin end plug welds, a modified digital X-ray inspection methodology using high contrast sensitivity radiology (HCSR) calibration correction procedure is proposed. In the HCSR procedure, the calibration images are acquired with varied exposure conditions on standard SS plate of 7.0 mm thickness. These images are linearly interpolated for getting a uniform pixel response of the X-ray flat panel detector during the evaluation of radiography images of end plug welds.

To optimize the application of HCSR procedure on digital radiography images, end plugs were welded with artificially created defects during welding of dummy fuel pins. These dummy fuel pins with end plugs are inserted in a SS shape correction block of thickness 7 mm. Table 1

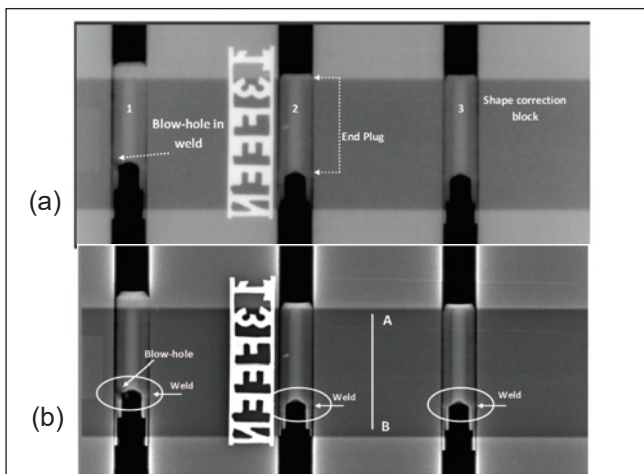


Fig. 1 (a) Raw digital radiography image of the end plug weld (before processing) and (b) enhanced digital radiography image of the end plug weld after applying the HCSR procedure

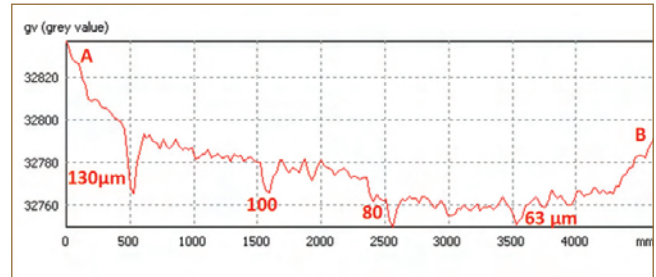


Fig. 2 Gray-level profile plot across the wire IQI in Figure 2

shows the typical X-ray radiographic parameters used for obtaining the images. Figures 1a and 1b show the radiographic images of the end plug welds before and after applying HCSR procedure, respectively. The normalized signal-to-noise ratio (SNR_n) improved from 90 to 305 after application of the HCSR correction procedure in the weld region. Further improvement in SNR_n , to 1800 was achieved by applying a 2D Fast Fourier Transform (FFT) based high pass filter to the HCSR image. Figure 2 shows the gray level profile plot (along line AB in Figure 1b) across 13 FE EN wire IQI penetrameter. Due to the combined effect of HCSR procedure and image processing operations, an IQI sensitivity of 63 μm is demonstrated despite using a 127 μm pixel detector. Among the three welds, in one of the weld, as indicated by an arrow in Figure 1b, a blow-hole defect is observed whereas this defect is not clearly observed in the raw image (Figure 1a). It is demonstrated from this study that with the implementation of HCSR correction procedure, micro defects and tight linear indications in the end plug weld region could be detected with improved sensitivity.

Table 1: X-ray radiographic exposure parameters

Parameters	Calibration plate	End plug welded fuel pin
Specimen thickness	7 mm	7 mm
Voltage applied	180 kV	180 kV
Current	2 mA	2 mA
Exposure time/ Integration of exposure	210 s /50 frames	4.2 s per frame /105 s (25 frames integration)
Source-to-Object Distance	1000 mm	1000 mm
Object-to-Detector Distance	Contact	Contact

III.12 Design and Development of a Pressure Decay Method Leak Measurement System Using MEMS Based Pressure Sensor

To qualify any pressure boundary for its leaktightness, it is required to carry out stringent leak detection and quantification tests. While helium and ion leak detection methods are effective, they are more time consuming and require expensive equipment. Pressure decay measurement can give a good estimate of the leak rates in the closed system. Such methodologies require the application of precise pressure sensing devices in real time. This development is towards making such an autonomous system which can sense and report leak rates in real time. From the ideal gas equation, the volume of gas leaving the system can be easily deduced by knowing the pressure drop. However, for the leak rate measurement at very low levels, the pressure sensing interval has to be increased which leads to extended measurement time. Longer measurement duration will significantly affect the pressure variation due to variation in the atmospheric temperature. Hence, a sensor module complementing the pressure measurement with a temperature sensing shall help in carrying out temperature corrections on the leak rates.

A MEMS based sensor with embedded pressure and temperature measurement has been used in this development. The sensor module with suitable housing secured by an O-ring and with leak tight enclosure is shown in Figure 1. A versatile design has been made for easy replacement of sensor by removing the enclosure cap and re-fixing it again with the O-ring. The smart MEMS based sensor output is measured through an Arduino microcontroller programmed to read I2C protocol data. A LCD display is also added to directly show the pressure, temperature and the leak rate in the system estimated using the ideal gas equation programmed in the microcontroller as shown in Figure 2. In order to enhance further and generalize the system for any application, the Arduino microcontroller



Fig. 2 Micro-controller based DAC unit for sensor module

is programmed to send serial data in RS232 format to the industrial Human Machine Interface (HMI). A custom communication protocol has been designed for proper handshaking between the microcontroller and the HMI. The HMI is programmed for showing real time pressure variation, temperature variation and leak rate plots as shown in Figure 3. The HMI also gives the option to the user to choose the recording time which helps in increasing the sensitivity of the system during very low leak measurements. The developed system has been qualified using standard helium leak test and shows a leak rate of less than 10^{-6} std. cc/sec. The system has been validated by inducing artificial leak to demonstrate characteristic exponential decay curve. This test tank is provisioned with a flange arrangement, so that any system to be measured for leak rates can be properly mounted on this test stand with appropriate adapters. The system is so developed to be generically available for any leak quantification and also qualification of any system. The front end HMI program is done in PLC ladder logic and made completely user friendly. The configuration option also provisioned in the HMI to choose the units, set the sampling time, graph plot options, with/without temperature corrections which makes it a versatile leak detection and leak rate quantification system.

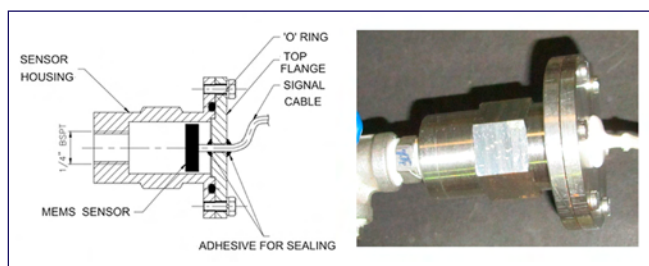


Fig. 1 MEMS pressure sensor (CAD drawing & Photograph)



Fig. 3 Photograph of leak test setup with HMI

III.13 Design and Manufacture of 200 NB Sidewall Permanent Magnet Flowmeter

Permanent magnet flowmeter (PMFM) is used for measuring sodium flow in the sodium circuits. Conventional PMFM is constructed with magnets placed on opposite sides of the pipe. Heavy weight, large space requirement and high manufacturing cost are the main problems with these flowmeters. Instead a smaller PMFM, which can be fixed on one side of the pipeline, called Sidewall PMFM has been conceived. The weight of a 200NB pipe PMFM made with ALNICO-5 is 290 kg. The main objectives of sidewall PMFM development are measurable millivolt output against rated flow, overall weight and size reduction, suitability of operation at 550°C sodium and stability of sensitivity with respect to time, temperature & other demagnetising effects. One sidewall PMFM for 200 NB pipe size was designed and manufactured.

Magnet circuit design and analysis

ALNICO-5 is selected as the magnetic material due to its superior magnetic properties like high remanance, coercive force, high energy product, high curie point, high operating temperature and temperature stability. To establish the flux density distribution in SS piping and predict the sensitivity of the flowmeter, three dimensional modeling in COMSOL multi physics software (COMSOL 3.5a) was carried out (Figure 1). In the model, the magnetic circuit made up of ALNICO-5 and mild steel blocks were used to simulate the magnetic fields in SS pipe. Based on modeling studies average flux density near the central limb was found to be 0.06 Wb/m².

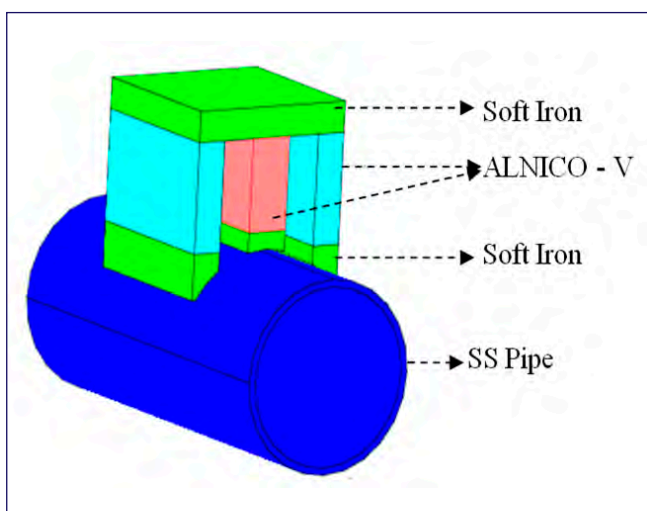


Fig. 1 Three dimensional model of sidewall PMFM

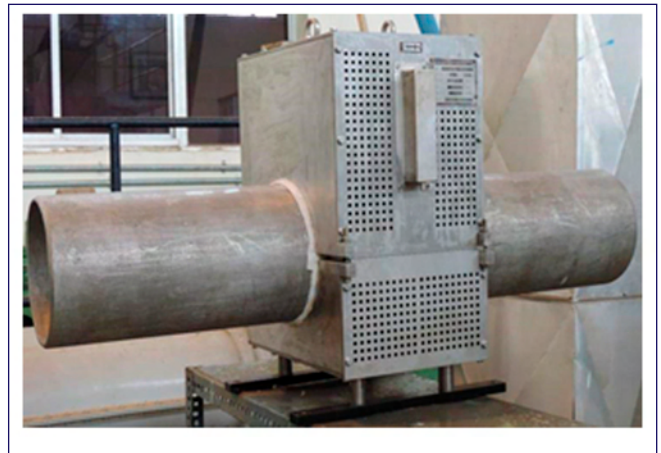


Fig. 2 200 NB PMFM after manufacture

Construction details

Three ALNICO-5 magnet blocks, MS pole faces and MS rectangular block were used for making the magnet assembly. The MS pole faces were fixed to north and south pole sides, on either side of the central magnet block. A MS rectangular block was placed and fixed over the three ALNICO-5 magnet blocks. This provided the path for magnetic flux. Three pairs of electrode wires were welded axially on either side of the central magnet block at an angle of 20 degrees with respect to central line of central magnet block and routed to the terminal connector. Electrodes are of 4mm dia, SS sheathed MgO insulated SS conductor. These electrodes are used to collect the millivolt output generated during sodium flow. The entire assembly was covered with perforated SS cover plates. To get a stable flux density distribution, magnet assembly was subjected to magnetization, stabilization by AC knock down and temperature stabilization by rapid and gradual heating cycles. Figure 2 gives the photograph of 200NB PMFM after manufacture. A 200 NB sidewall PMFM was designed and manufactured. Average flux density value was found to be 0.06 Wb/m². Estimated sensitivity based on model analysis and theoretical studies are found to be 0.01377 and 0.02532 mV/m³/h respectively. Accuracy of the sensitivity estimate is within $\pm 7\%$. Overall weight of the 200 NB sidewall PMFM is found to be 145kg and this weight is 50% lesser than that of conventional ALNICO-5 based 200 NB PMFM.

III.14 Design and Thermal Hydraulic Analysis of Secondary Sodium Based Decay Heat Removal System for FBR 1&2

The design of Fast Breeder Reactors (FBR-1&2) are conceived based on experience from Fast Breeder Test Reactor (FBTR) and Prototype Fast Breeder Reactor (PFBR). PFBR has two diverse paths for removing decay heat namely, Safety Grade Decay Heat Removal System (SGDHRS) and Operation Grade Decay Heat Removal System (OGDHRS).

OGDHRS requires at least one secondary sodium circuit, steam water circuit and off-site power supply for removing decay heat. SGDHRs is operated when OGDHRS is not available. In order to further improve the reliability of decay heat removal system for future FBRs, it is planned to have an additional system operating on secondary sodium system, thus reducing the dependency on SGDHR system. The reliability of this system is higher as compared to OGDHRs due to its independence of offsite power supply and steam water system components. The design of Secondary Sodium based Decay Heat Removal System (SSDHRs) is carried out for FBR-1&2.

SSDHRs is designed for a heat removal capacity of 15MWt/loop. It is provided with an Air Heat Exchanger (AHX) with hot sodium flowing in tube side by forced circulation using Secondary Sodium Pump (SSP) and air flowing over the tubes by forced circulation using blower. The inlet to the AHXs is taken from the Surge Tank (ST)

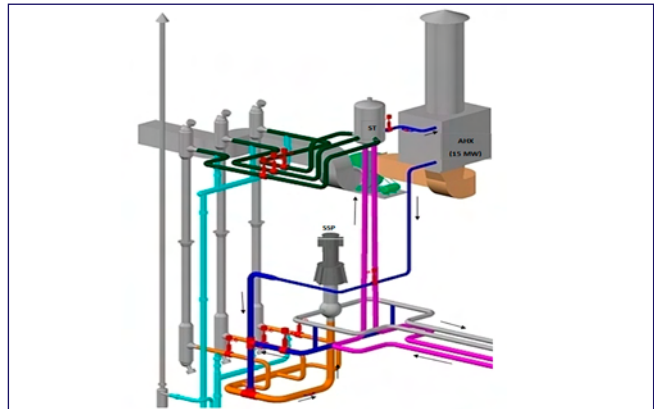


Fig. 2 Three dimensional scaled layout of secondary sodium based decay heat removal system for FBR 1&2

located in hot leg of SSMC. The discharge line of the AHX is joined to the inlet header of SSP. During normal operation of SSDHRs, both primary and secondary sodium pump run at 20% and 26 % of rated flow respectively and all Steam generators are isolated. Out of the 26% secondary flow through SSP, 4% will go to IHX-ST-AHX, and the remaining flow is bypassed through separate bypass path. This bypass provision is designed to improve the head developed by the pump and shift the operating point of pump towards best efficiency point. The schematic arrangement of SSDHR system is shown in Figure 1. The scaled 3D model along with part of secondary sodium main circuit is shown in Figure 2.

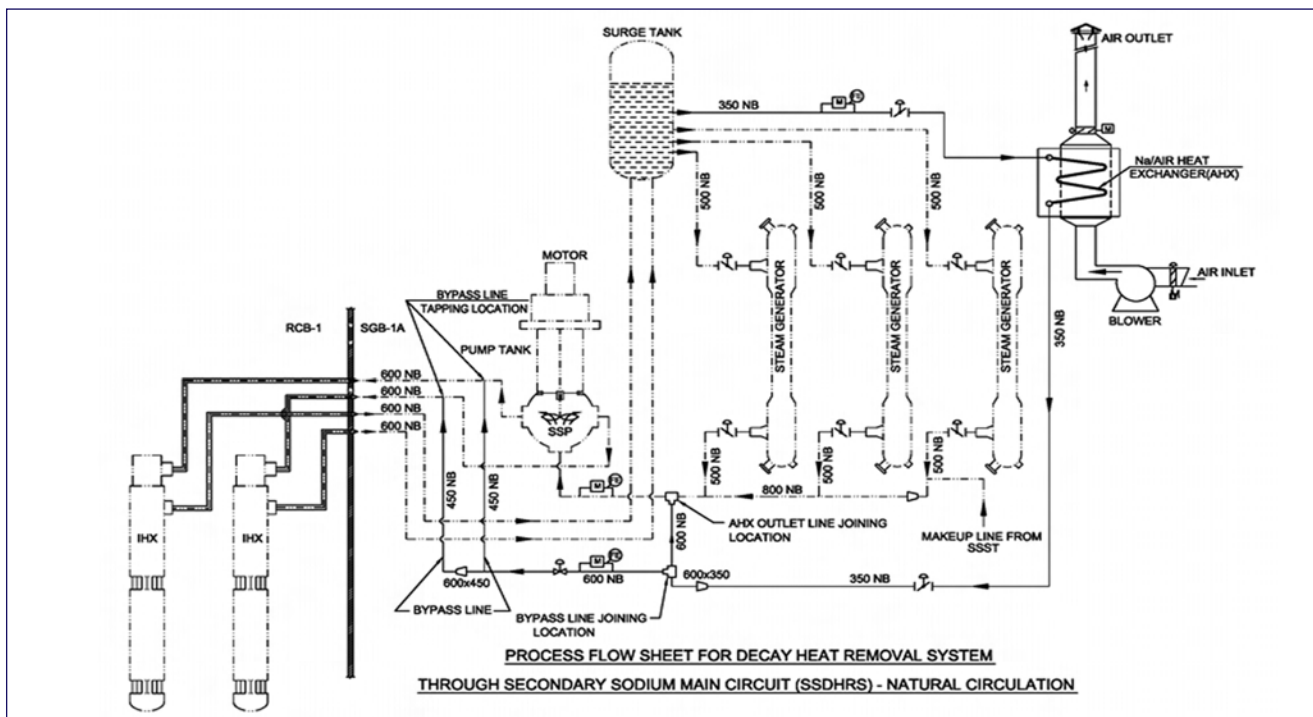


Fig. 1 Process flow sheet for decay heat removal system through secondary sodium main circuit (Natural circulation)

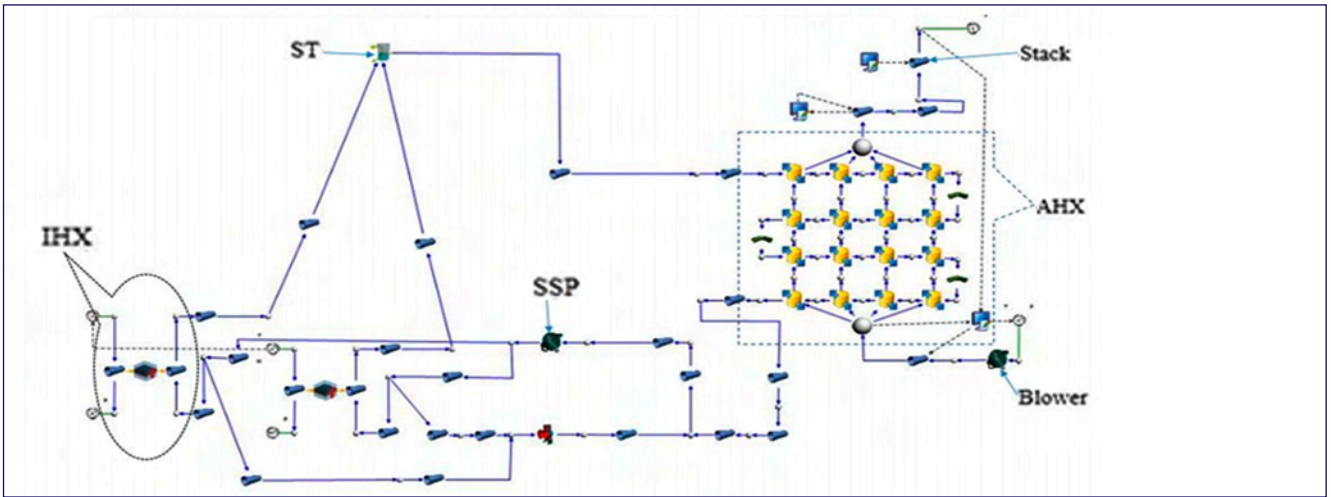


Fig. 3 SSDHRS model developed using Flownex

Heat removal capacity of the system with passive mode of operation (both sodium and airside) is also studied and found to be 60% of that of active mode. System optimization was carried out to arrive at the sizing of various equipment of SSDHRS (Dimensions of AHX, blower capacity, height of stack and circuit design). SSDHRS is envisaged to cater to fuel handling and other maintenance conditions instead of relying on OGDHRS which requires external power supply, recirculation pumps, condenser cooling fans and steam generators to function.

Thermal hydraulic analysis has been carried out to establish the performance of the system under steady state and transient conditions. The SSDHRS has been modeled using the general purpose system dynamics code Flownex and schematic of the model is shown in Figure 3. Various components of the system, viz., IHX, AHX, stack, SSP, blower are modeled using the library components. IHX is modeled as a counter current sodium to sodium heat exchanger using composite heat transfer (CHT) element. AHX is modeled using user defined compound components. Grid independent

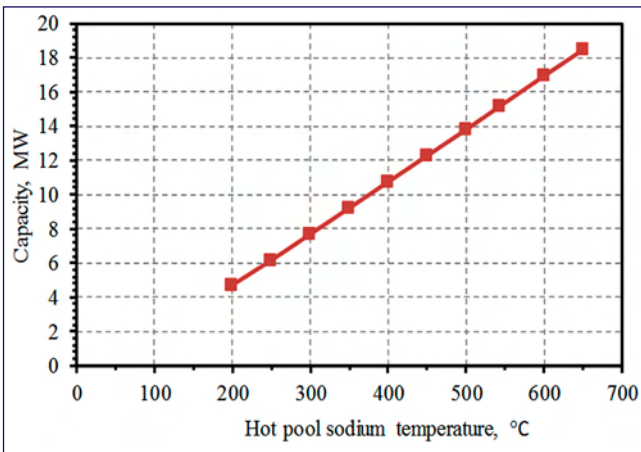


Fig. 4 Heat removal capacity of SSDHR at various hot pool sodium temperature

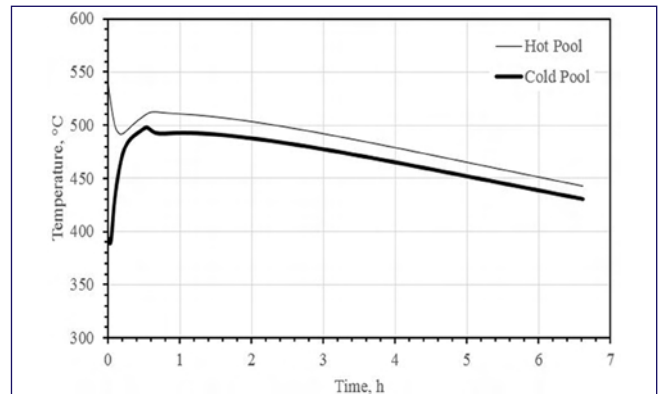


Fig. 5 Evolution of hot pool and cold pool temperature with SSDHRS in operation following off-site power failure

study has been carried out to arrive at suitable number of grids for IHX and AHX. Centrifugal pump based model has been adopted for representing the secondary sodium pump and blower in the sodium and air circuits respectively. Stack and secondary sodium pipes are modeled using pipe elements.

Steady state performance of SSDHRS have been analyzed by varying the temperature of hot pool sodium in the range of 200 °C to 650 °C and the results are shown in Figure 4. The heat removal capacity is estimated as 15.17 MWt at the normal steady state operating hot pool temperature of 544°C. Heat removal capacity increases with increase in hot pool sodium temperature and the variation is found to be nearly linear.

Analysis has also been carried out to study the performance of the system during off-site power failure event in the plant. Evolution of hot pool and cold pool temperatures are shown in Figure 5. It is seen that, hot pool temperature reduces initially, and reaches a minimum value at ~ 10 min, after which it starts rising. Cold pool temperature rises due to loss of heat removal through steam generators before starting to reduce by the operation of SSDHRS. The maximum hot pool and cold pool temperatures reached are 513°C and 498°C respectively, which are well within the design safety limits for the event.

III.15 Development of High Temperature Ceramic Insulator Coating and Dissimilar Metal Joints for Fabrication of DC Conduction Pump Core

Direct current conduction pumps (DCCP) are electromagnetic pumps used for sodium pumping in auxiliary sodium circuit of Fast Breeder Reactors (FBRs). The pump comprises an electromagnet made of low carbon iron (according to ASTM A848), a copper bus bar, an electromagnet coil made of 1% Ag bearing Oxygen Free Electronic Copper (OFEC), and a pump duct made of stainless steel AISI type 316L. Using the bus bar, a current is passed through sodium in the duct, which is positioned in the magnetic field produced by the electromagnet. As per the functional requirements of the DCCP, the Cu bus bar and the stainless steel pump duct are coupled and integrated into a close mating configuration with an electrical insulation ($\sim 10^{12} \Omega$ at RT, $\sim 10^8 \Omega$ at OT) barrier between them. This forms the core of the pump. An electrically insulating ceramic coating (Al_2O_3) by plasma spray on Cu is the most recommended insulating method for high operating temperature ($\sim 600^\circ\text{C}$) and thermal cycling environment. Generally, plasma spraying of monolithic feedstock alumina tends to stabilize non-equilibrium cubic γ -phase due to rapid solidification. On thermal cycling, this metastable γ -phase tends to undergo a series of phase transitions to other stable phases, progressively with time, leading to onset of coating cracking and premature delamination. Ytria (Y_2O_3) is one other candidate ceramic material having high electrical resistance and thermodynamic stability with no phase transformation up to its melting point of 2325°C . However, the use of commercially pure Y_2O_3 coating by plasma spraying as an electrical insulation is scarce, because of economic factors. Mixing of Al_2O_3 with equal weight fraction of Y_2O_3 helps in the retention of cubic γ -phase of Al_2O_3 along with the stable cubic phase of Y_2O_3 , during thermal cycling. This will enhance the thermal fatigue endurance of the composite ceramic coatings. In the present study, a plasma spraying approach using the composite ceramic, Al_2O_3 : Y_2O_3 at 55:45 weight fraction, is followed. To further

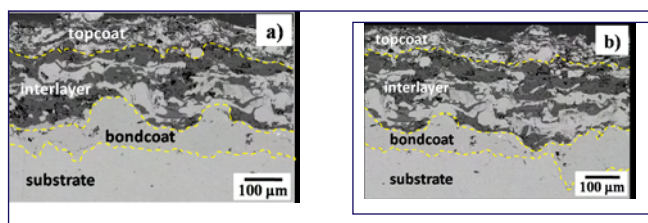


Fig. 1 Coating cross section (a) before and (b) after 1000 thermal cycles

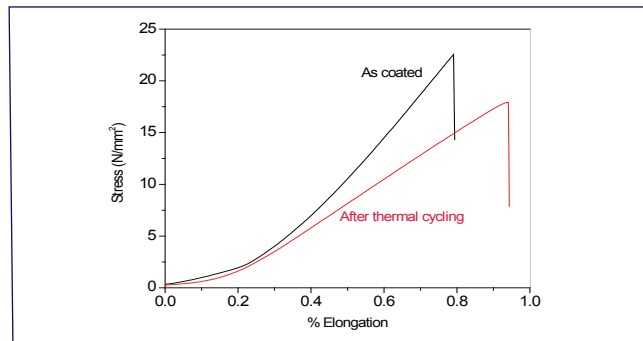


Fig. 2 Tensile adhesion strength

enhance the thermal fatigue life of the composite ceramic coating, an interlayer of 30 wt% NiAl-70 wt% Al_2O_3 cermet coating having intermediate thermal expansion coefficient, α of $\sim 9.6 \times 10^{-6} \text{K}^{-1}$ is attempted. Towards qualification of this novel composite ceramic coatings for DCCP applications, a thermal fatigue life up to 1000 cycles under simulated temperature cycling between 200°C and 600°C is set as the acceptance criterion. Constructional requirements of DCCP necessitates the joining of the insulator coated OFEC bus bar to a sodium-flowing pump duct made of AISI type SS 316LN. As the substrate materials of these two components, to be joined, significantly differ in their thermal properties, the most suitable joining method is reckoned as brazing with appropriate filler. As DCCPs in FBRs are operated at $\sim 600^\circ\text{C}$, the service temperature of the braze-filler also should be above this range. Hence Nickel-based filler which have excellent oxidation resistance, corrosion resistance, and high-temperature service properties up to $\sim 1093^\circ\text{C}$ is one of the options. The commercial nickel based brazing filler (BNi-6) having excellent brazeability and fluidity and quite adequate for joining dissimilar metals is chosen.

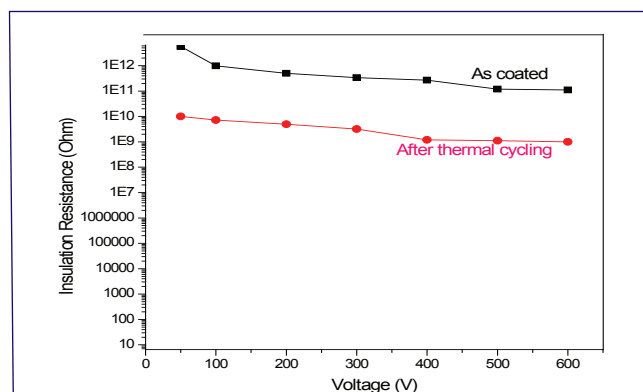


Fig. 3 Coating electrical resistance



Fig. 4 Insulator coating on OFEC bus bar

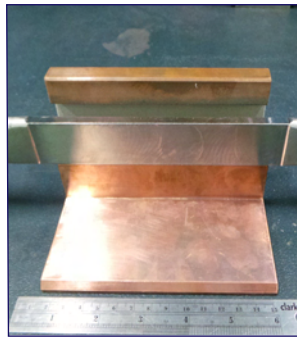


Fig. 5 Fabricated pump core

The first part of the work is to optimize the process parameters for developing a composite ceramic coating with adequate thermal fatigue resistance, mechanical stability and electrical resistance. For the purpose, OFEC samples were subjected to alumina grit blasting using 16 mesh grits to produce an oxide-free active and rough surface measuring 10-13 μm Ra. The bond coat NiCrAlY powder (AMDRY 962, Oerlikon Metco) was deposited on the freshly grit-blasted surface of substrates using a Diamond Jet-MDJ 2650 HVOF gun (Metalizing Equipment Co. Pvt. Ltd.). Subsequently, a cermet interlayer of 30 wt% NiAl-70 wt% Al_2O_3 blend was deposited over the bond coat using air plasma spray (APS) gun (Metalizing Equipment Co. Pvt. Ltd.) to mitigate thermal expansion mismatch stresses between the NiCrAlY bond coat and the Al_2O_3 top coat. Finally, the composite ceramic topcoat was deposited over the cermet interlayer in successive passes using APS process. The process parameters for depositing the cermet interlayer and topcoat using APS, and that for depositing bond coat using HVOF were optimized to have the best adhesion and thermal fatigue endurance. Thermal fatigue tests were carried out in a high-temperature box type muffle furnace with cooling stations on either side, by thermal cycling between 200 and 600 $^\circ\text{C}$ for 1000 cycles. One complete thermal cycle consists of taking the samples to 600 $^\circ\text{C}$, holding at 600 $^\circ\text{C}$ for 10 minutes, and ambient cooling to 200 $^\circ\text{C}$ in 15 minutes. The detailed structural, surface and cross-sectional morphology of the as-coated and thermal fatigue tested specimens were analyzed using optical microscopy, electron microscopy and XRD analysis. The composite ceramic multilayer coating with cermet interlayer showed good endurance up to 1000 thermal cycles. Neither macro-cracks nor delamination nor spallation were seen on the topcoat even at the sample edges/corners, indicating the composite coatings can endure for ~ 40 years of reactor life, which is the prime selection criterion. From the surface appearance, it is also evident that there exists a smoothening phenomenon after thermal exposure, which could be accounted by the densification in the porous ceramic topcoat. The cross-

section of as-coated sample reveals a 110 ± 50 μm thick bond coat, a cermet interlayer of thickness 180 ± 30 μm , and a composite ceramic topcoat of thickness 100 ± 10 μm (Figure 1). Cross-sectional micrograph after 1000 thermal cycles revealed a stable microstructure with neither morphological change nor deleterious cracks nor presence of thermally grown oxides (Figure 1). XRD analysis on post thermal cycles revealed neither phase changes nor the formation of new phases, confirming the phase stability of the ceramic coating under a higher number of thermal cycles and long thermal exposure. Uniaxial tensile pull-off test of as-coated and thermal cycled cylindrical samples (three sets each in number) was carried out to estimate the adhesion/cohesion strength of the coatings following the ASTM C633 standard. Tensile adhesion pull-off strength values for three sets each of as-coated and thermal cycled samples are given in Figure 2. From the adhesion strength values, it is evident that there exists $\sim 20\%$ drop in adhesion strength of the composite ceramic coating after thermal cycling up to 1000 cycles. Only a single type of failure mode, i.e., cohesive failure within the NiAl- Al_2O_3 interlayer, was seen in all the pull-off tests (both as-coated and thermal cycle samples). The drop in adhesion strength is not detrimental to the functional requirement, as the coating does not experience any mechanical loading during its operation in the DC conduction pump. Insulation resistance of the as-coated and thermal fatigue tested flat samples was measured. The resistance values of the multilayer composite ceramic coating in as-coated and thermal cycled conditions, was found to be $\sim 10^{12}$ Ω and 10^{10} Ω respectively and no electrical break down observed up to 600 V DC (Figure 3). The two order drop in the IR value is acceptable as long as the coatings are intact and there is no breakdown leakage and drop in the efficiency of the DC conduction pump. Based on the above results and the optimized process parameters the insulation coating was made on OFEC (Figure 4). To optimize the vacuum brazing of SS 316LN duct with OFEC bus bar, OFEC and SS 316LN pieces were brazed at various conditions and the micro-structure evolution at the braze zone and braze-affected zone, mechanical properties and joint-strength of the lap and butt joints are evaluated. Vacuum brazing conditions were optimized to ensure no oxidation, excellent flow characteristics, good metallurgical bond with complete eutectic morphology, braze joint thickness of 100 ± 20 μm , adequate hardness at the braze zone and braze-affected zone (~ 650 $\text{Hv}_{0.1}$) and tensile strength (44 MPa). Based on the optimized process parameters, SS duct was joined onto the alumina-yttria composite coated OFEC bus bar to make pump core (Figure 5). The system is being tested in auxiliary sodium circuit.

III.16 Development of Ultrasonic Immersion C-Scan Inspection Procedure for Evaluation of De-Bonds in Magnetic Pulse Welded Fuel Pin End Plugs

Currently fuel pin to end plug welding is being carried out using fusion welding process such as GTAW/Laser. Solid state welding process such as Magnetic Pulse Welding (MPW) is being considered at IGCAR over this fusion welding process. The advantages of MPW technique include: (1) hot cracking problem can be avoided for austenitic steels, (2) no requirement for post weld heat treatment in martensitic steels and (3) maintenance of weld integrity by avoiding coarsening and coagulation of Y_2O_3 particles in oxide dispersion strengthened (ODS) ferritic martensitic steel. Non-destructive ultrasonic qualification of the fuel pin end cap welds pose serious challenge due to the smaller dimension of the component and the tapered weld, where the thickness varies continuously across the weld region as shown in Figure 1a. Hence, an immersion ultrasonic inspection technique is developed for the first time at NDED, IGCAR to qualify the MP welded fuel pin end plugs based on the extent of bonding achieved and the same is implemented for inspection of MPW end plugs welds of two plug designs: (i) solid plug and (ii) partially hollow (5mm) plug. In order to overcome the normal beam inspection challenge in the tapered region, the ultrasonic transducer angle with respect to the fuel pin top surface has been optimized at 5° . The ultrasonic inspection is carried out for a scan length of 40 mm along the axis of the fuel

pin and at a step size of 10° around the circumference of the fuel pin.

The experimental setup used for immersion ultrasonic C-Scan inspection is shown in Figure 1b. A computer controlled ultrasonic pulser-receiver and a 25 MHz point focused immersion ultrasonic transducer of 12.5 mm diameter and 35 mm focal length (water-path 6 mm) are used for ultrasonic measurements. Figure 1c shows typical A-scans received from the bonded and un-bonded regions of a MPW. The back wall echo (BWE) corresponding to the end plug observed in Figure 1c clearly indicates good bonding and the multiple back wall echoes (MBWE) corresponding to fuel pin thickness observed in Figure 1d reveals un-bonding. Figure 1e shows a typical B-scan of the fuel pin to end plug weld region where in the extent of bonded region is marked using an ellipse. Based on the ratio of the amplitude in the end plug BWE region to the amplitude in the fuel pin BWE region, C-scan images are generated and are shown in Figure 1f for solid end plug and (Figure 1g) partially hollow end plug. It is observed that the weld region width is ~ 5 mm for solid end plug and ~ 7 mm for partially hollow end plug. The developed C-scan imaging based inspection methodology can be used for assessing the extent of bonding/debonding for reliable qualification of the MP welded fuel pin end caps.

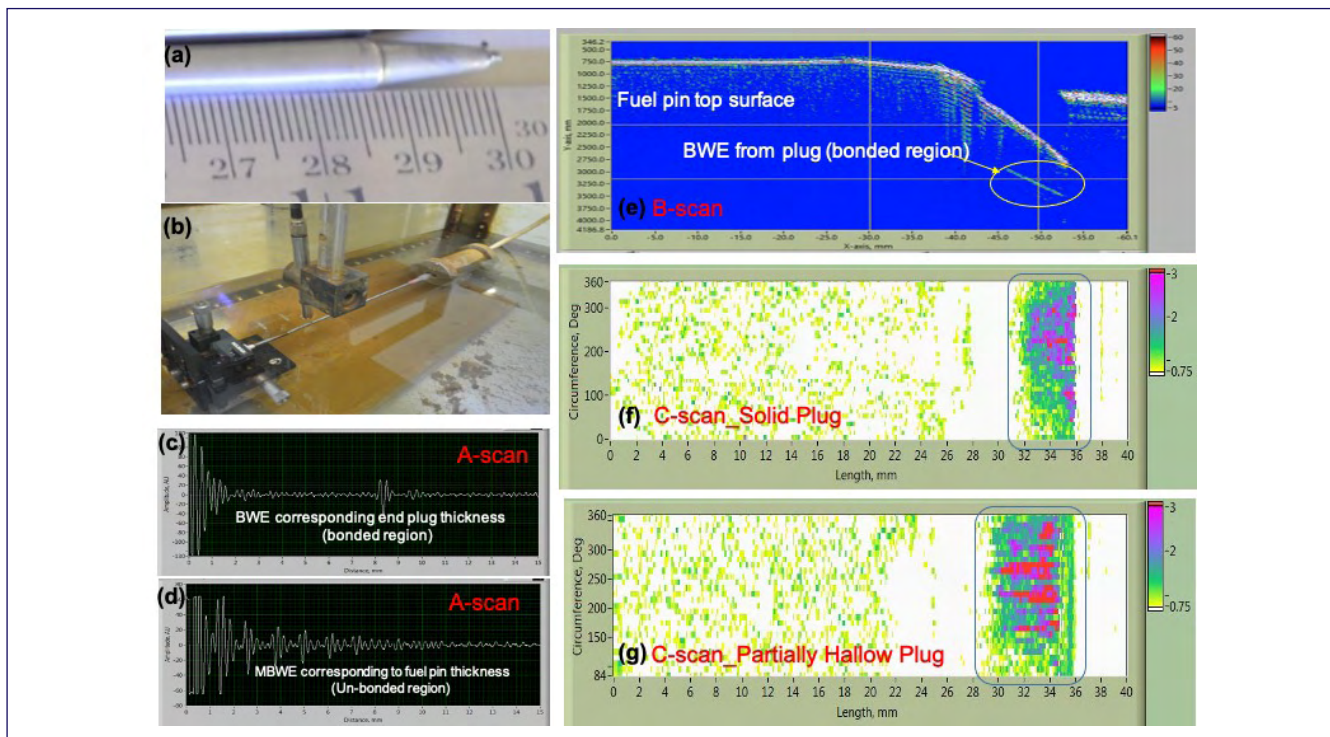


Fig. 1 (a) Magnetic pulse welded fuel pin to end plug specimen showing the ultrasonic inspection region; (b) photograph of the immersion ultrasonic c-scan experimental setup; Typical A-scans from (c) bonded and (d) un-bonded regions; (e) typical B-scan image showing the length of the bonded region; Typical C-scan scan obtained for fuel pin welded with (f) solid end plug and (g) partially hollow end plug

III.17 Testing of MgO Bricks Towards Development of Sacrificial Layered Core Catcher for SFR

Core catcher (CC) is a passive safety device provided below the core, for collection, cooling and long term retention of core debris (corium) in sub-critical geometry, after a hypothetical core melt accident. Whole core relocation over CC would impose higher decay heat resulting in temperature rise beyond design safe limit for the structural material. Feasibility of a refractory layer over CC is being investigated to protect it from high thermal load and probable ablation due to hot corium. Based on preliminary studies, sintered magnesia has been chosen as candidate material and experiments are being carried out to assess its sodium compatibility and thermal stability under melt attack.

Two dedicated experimental setups were designed for carrying out experiments. The set-up designated for melt attack experiments has melt generator and leak tight test vessel connected through a melt transfer port (Figure 1a). Two-colour pyrometers (two numbers) were used for measuring melt stream temperature. The experimental set-up designated for sodium compatibility studies, consists of flanged test vessel kept in tubular furnace with microprocessor-based temperature controller (Figure 1b). Pure sodium obtained from sodium glove box is used for sodium compatibility studies.

High purity magnesia specimen ($75 \times 50 \times 45 \text{ mm}^3$) was exposed to simulated high temperature corium generated by thermite process. Minor surface deterioration was observed at the surface of the specimen upto a depth of about 1 mm (Figure 2a). A thin skin of MgO was observed as fused with melt (Figure 2b). Visual examination revealed no gross damage due to thermal shock and specimen remained structurally intact (Figures 2c and 2d). Due to rapid cooling of melt, maximum recorded



Fig. 1 Experimental setups for (a) melt impingement and (b) sodium compatibility studies



Fig. 2 (a) fresh specimen of MgO (b) melt covered specimen (c) specimen after removal of melt splat and (d) surface of melt splat (e) MgO unexposed (f) sodium exposed

temperatures in the specimens were only 180, 170 and 150 °C at corresponding depths of 15, 30 and 45 mm.

Cubical magnesia specimens ($10 \times 10 \times 10 \text{ mm}$) exposed to sodium at 850 °C in a sealed SS tube for the desired duration of time (240 h) were retrieved from the SS capsules and then subjected to vacuum distillation for removal of sticking sodium on the surface of the specimen. Visual examination revealed that all the specimens remained intact without any deterioration (Figures 2e & 2f). XRD analysis revealed that MgO is chemically inert with sodium (Figure 3).

Sintered magnesia bricks exposed to simulated melt generated in thermite process at $\sim 2500 \text{ }^\circ\text{C}$ revealed that impingement attack is insignificant. The experimental findings from both the qualification tests confirmed satisfactory performance of magnesia refractory under severe thermal shock and also stability in sodium environment. Hence, magnesia can be considered as potential candidate material as protecting layer for core catcher.

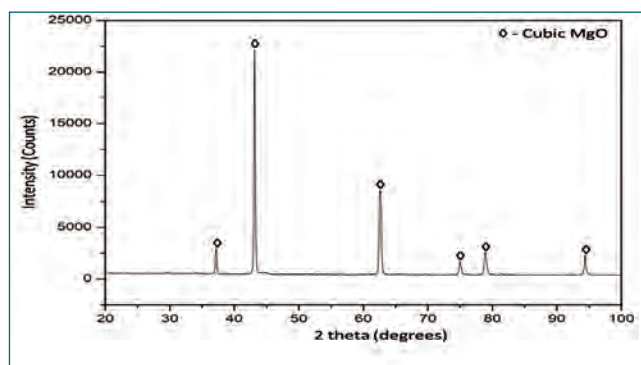


Fig. 3 XRD pattern of sodium exposed MgO

III.18 Submerged Gravel Bed Scrubber for Removal of Sodium Fire Aerosol

Air cleaning systems typically used for sodium fire aerosol control are dry (fiber filters) and wet scrubbers (venturi, packed bed and fibrous scrubber system). The dry filters feature high aerosol removal efficiency but lower mass loading. Wet scrubbers have high aerosol removal efficiency and suitable for high mass loadings. However, an ideal scrubber for containment venting requires features such as passive operation, self cleaning, less space occupation, high reliability after long standby periods, low cost, and minimal electric power requirements.

Submerged gravel bed based scrubber system (SGBS) has been developed for removal of sodium fire aerosol in air. The SGBS consists of an inner SS 304 packing tube that holds the bed material kept inside an outer SS 304 tank (0.78 m x 0.78 m x 0.93 m), filled with water (Figure 1). The packed tube is supported at 0.15 m above the bottom of an SS tank. The bed material is blue metal chips (crushed granite stones) of 6-10 mm size with density of 2500 kg/m³. Air consists of sodium combustion aerosol is forced to enter through the packing tube from bottom of the bed. The bed surface area is 0.068 m². The SGBS is connected to a sodium fire aerosol chamber for evaluating its performance. A blower is used to induce gas flow rate of 2.2 m³/h through SGBS. The bottom outer tank is fitted with a 0.76 m high lid to avoid entrainment of water to the blower.

Preliminary experiments were conducted with burning sodium (100 g) in the chamber. The sodium fire aerosol concentration in the chamber was measured by analysing the aerosol samples collected in filter papers. Experiments were repeated with various quantities of sodium fire i.e. at various inlet aerosol concentrations as a parameter. Aerosol samples collected at the outlet duct immediately preceding the scrubber were analyzed for aerosol mass concentrations.

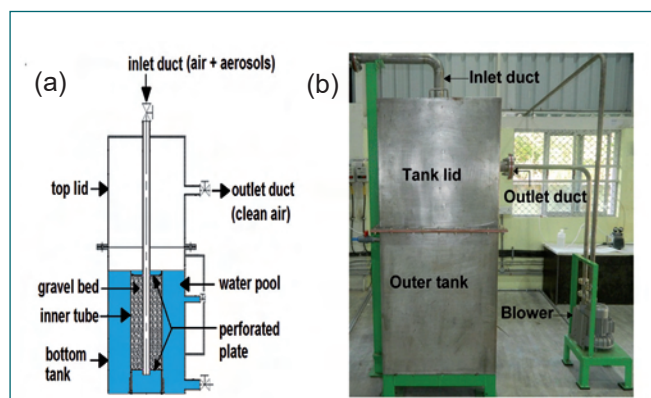


Fig. 1 Schematic and photograph of the Submerged gravel bed scrubber system

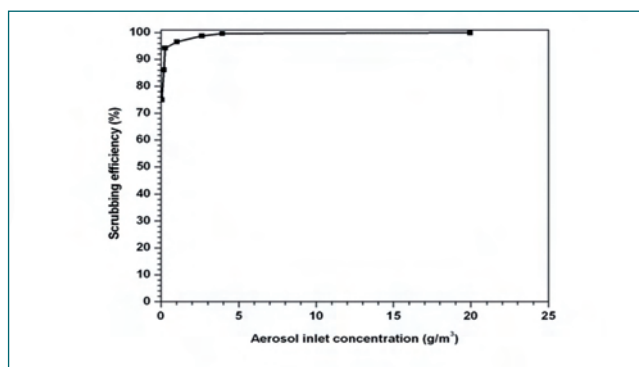


Fig. 2 Variation of efficiency with inlet sodium fire aerosol concentration

The efficiency of the scrubber is determined by using the following equation.

$$\text{Scrubber efficiency} = \frac{\text{Conc. of Na aerosol (inlet)} - \text{Conc. of Na aerosol (outlet)}}{\text{Conc. of Na aerosol (inlet)}} \times 100$$

Figure 2 shows the scrubber efficiency versus the scrubber inlet aerosol concentration. The efficiency is shown to be a function of the aerosol concentration, with lower concentrations resulting in lower efficiencies.

Air with sodium aerosol is cooled as it passes through water in SGBS by evaporative cooling. The gas leaving the SGBS is cooled by about 2-3 °C. Figure 3 shows the inlet and outlet temperatures of air containing sodium fire aerosol and the liquid temperature as a function of time.

The indigenously developed SGBS needs very low gas flow rate (~2 m³/h) and it has potential application in scrubbing sodium fire aerosols with a removal efficiency of 75-99.2 % for inlet aerosol concentrations in the range of 0.04 – 1.0 g/m³. The results confirm passive nature and hence ideality of using SGBS as an effective aerosol scrubber system during accidental scenarios in SFR containments.

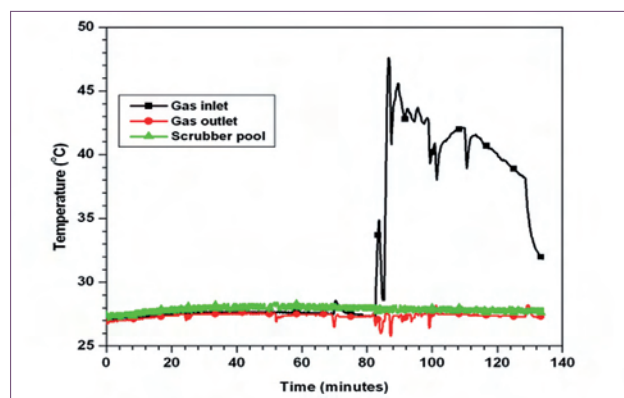


Fig. 3 Cooling of air by SGBS

III.19 X-Ray Imaging of Simulated Molten Fuel Coolant Interaction Phenomena in Sodium

During hypothetical core meltdown accident in Sodium cooled Fast Reactors (SFR), the corium (mixture of molten fuel and structural material) comes in contact with sodium, resulting in Molten Fuel Coolant Interaction (MFCI). Consequences of MFCI are rapid heat transfer from molten fuel to sodium leading to sudden evaporation of liquid sodium. X-ray based imaging system is commissioned and integrated with the test facility to depict MFCI phenomena such as jet breakup length, jet front velocity and fragmented particle size.

An experimental setup consisting of melt generation chamber, sodium interaction vessel with pneumatic isolation valve was designed, fabricated and installed (Figure 1). The photograph of the experimental setup along with dynamic X-Ray imaging unit is shown in Figure 2. Melt generation chamber is designed to generate simulated corium (mixture of iron and alumina) at ~2500 °C using aluminothermy reaction (equation 1).



The melt flow path is internally coated with refractory paste to minimize heat loss and maintain integrity of generator made up of steel. An isolation valve is placed to maintain inert atmosphere (argon) in interaction vessel during preheating. The dynamic X-ray imaging unit consists of 450 kV X-ray source with flat panel detector and associated auxiliary systems. The source is chosen based on steel equivalent thickness of the experimental setup. The X-ray unit is housed in a concrete test chamber with 45 cm wall thickness. Adequate additional steel shielding has been provided

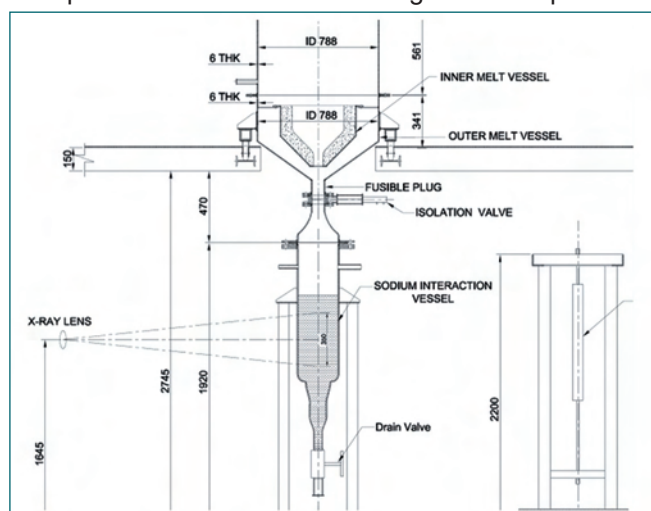


Fig. 1 Schematic of MFCI experimental setup



Fig. 2 MFCI experimental setup with X-ray imaging to reduce exposure outside the building to acceptable level. The digital flat panel detector (DFPD) with 16 inch scintillation screen is used for acquiring images at maximum acquisition rate of 30 fps with 400 μm resolution. The X-ray unit has been calibrated using a steel calibrator immersed in static sodium (Figure 3a).

MFCI experiment was conducted by releasing 2 kg of simulated corium at ~2500 °C into sodium (35 kg) maintained at 400 °C. Dynamic X-ray images obtained during MFCI event were found to have low contrast. Image processing algorithms have been developed to perform background subtraction, image filtering of noise and image segmentation to obtain the desired MFCI parameters. The melt was observed to get fragmented instantaneously upon contacting sodium at entry. Large vapor fraction of sodium is observed at the surface of liquid sodium (Figure 3b). No energetic interaction was noticed. After the run, fragmented debris from sodium was retrieved and analyzed for particle size distribution. The Mass Median Diameter (MMD) of the debris was found to be about 0.35 mm. Further parametric studies are in progress with various energies and intensities of X-rays.

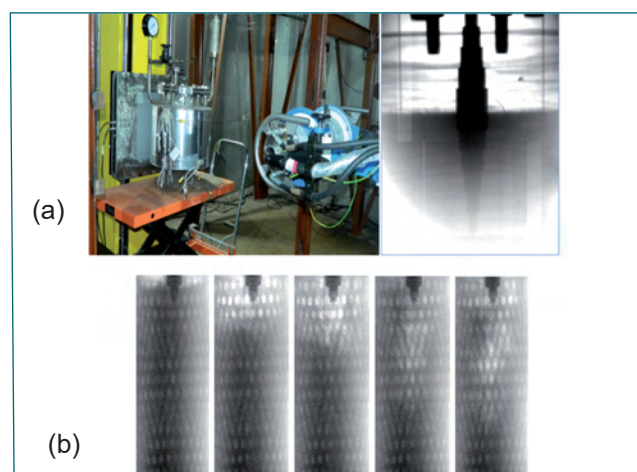


Fig. 3 (a) Calibration setup with phantom and X-ray image and (b) movement of sodium vapour during MFCI

III.20 Computation and Development Towards Gamma Ray Build-Up Factors for Conventional Shielding Materials

Gamma ray buildup factors (BUFs) of conventional shielding materials such as lead (Pb), tungsten (W), iron (Fe), and concrete have been studied for their diverse uses in nuclear facilities. For practical shielding applications, various fitting forms by Taylor, Berger, Capo, and geometric progression (GP) are available for estimating the BUFs. Many studies have investigated BUFs upto a penetration depth of 40 mean free paths (mfps) but limited data are available for thicknesses beyond 40 mfp. Though, penetration depth of 40 mfp is very large, it is necessary to extend BUF for higher penetration depths in cases like possibility of severe nuclear reactor accidents, bulk shielding for active containers, nuclear power plant shielding etc. Hence, in the present work, BUFs are computed up to a penetration depth of 100 mfps using GP fitting form for Pb, W, Fe, and concrete. Various double layered configurations of these materials such as Pb+concrete / Fe+concrete or reverse configurations are found in nuclear facilities (hot cells) as complementary shielding. In transport cask design, shielding configurations of Pb+Fe or W+Fe are highly popular. Transport computations are performed by several investigators to express the double layer BUFs (DBUFs) in the form of simple empirical formulae. DBUFs estimated using the published empirical formulae results in over/under estimation of the scattered dose rate due to the change in source-shield geometry and selection of materials. Hence, Monte Carlo simulation (MCS) is performed to calculate the DBUFs for point isotropic source with double layered slab shielding configurations of W, Pb, Fe and concrete.

BUF values are found to increase with gamma energies. The minimum BUF value observed at a thickness of 100 mfp is 1.0 at 15 keV and maximum at about 70 keV (1.15×10^{34}). Its value decreases between 70 to 150 keV and thereafter, it increases with energies upto 15 MeV (1.70×10^{14}).

The source-shield configuration assumed in MCS is shown in Figure 1. The DBUFs increases with thickness of shield but lies within the bounds of BUFs of the constituent medium. DBUFs obtained for $Z_{low}+Z_{high}$ configurations are always lower than the reverse orientation of the shields. The BUFs computed for Pb is lower compared to DBUFs for Fe+Pb by only 8%. Hence, $Z_{low}+Z_{high}$ configuration (instead of Z_{high} alone) is found to provide equivalent shielding for the materials investigated. For shielding configuration of Pb+concrete, the replacement of Pb with Fe increases the contribution

of scattered gammas by 1.33, whereas, for the shielding configuration of Concrete+Pb, the replacement of Pb with Fe increases the contribution of scattered gammas by a factor of 2.3. Therefore, in the double layered shielding configurations, Z of the shielding material near the detector plays an important role in attenuating the scattered radiation. The scattered radiation generated by the Z_{low} material near the source is effectively absorbed by the Z_{high} material near the receptor. Hence, higher the Z of the material near the receptor more is the attenuation of the scattered gammas.

A modification in correction factors of KF is proposed since the estimated DBUFs using MCS is observed to vary significantly ($\sim 40\%$) compared to the values obtained using existing empirical formulations. The DBUFs obtained from KFM and MCSs for gamma ray energy ranging from 0.5 MeV to 15 MeV are found to vary within $\pm 9\%$.

It is concluded that GP fitting form is suitable for for conventional shielding materials upto a penetration depth of 100 mfp in determining BUFs. The data for shielding computations with W at thicknesses above 40 mfp and gamma energies between 15 keV to 15 MeV are evaluated for the first time. The KFM developed in the present study is observed to provide better estimates of DBUFs as compared to the existing empirical formulations for double layered configurations with W, Pb, Fe, and concrete.

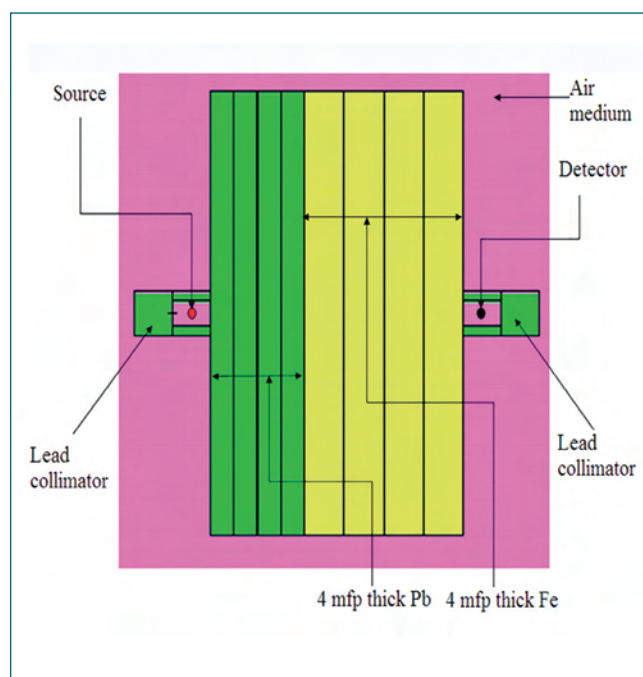


Fig. 1 Double layered computational shield model

III.21 Study on the effect of Fuel Subassembly Orientation on Gamma Flux

There is often requirement to know the radiation field around a fuel subassembly (FSA) for many applications such as subassembly identification, shielding or dose calculation. To a good approximation for hexagonal SA, the field is usually assumed to be symmetric. This would normally be sufficient for shielding applications. For source strength characterization problems like Fissile Zone Identification System (FIZIDS), where it is required to differentiate between the two enrichment zones, the radial profile of radiation becomes important. In this study the gamma transport through the fuel subassembly has been modeled using Monte Carlo simulations. Detailed pin-wise model of the FSA has been made in the first case to determine the gamma field around the FSA. The gamma source term consists of all the discrete decay gammas from fuel isotopes distributed uniformly throughout the fuel pellet regions. The resulting contour plot for the gamma flux field is shown in Figure 1. As per the pin level model, the near field flux at the edges are less than that from the flat faces. But at larger distances, the flux is symmetric. Subsequently LaBr₃(Ce) detector and lead shield as used in the FIZIDS is added to a homogenized FSA model and Monte-Carlo simulations performed. The model and geometric details are shown in Figure 2.

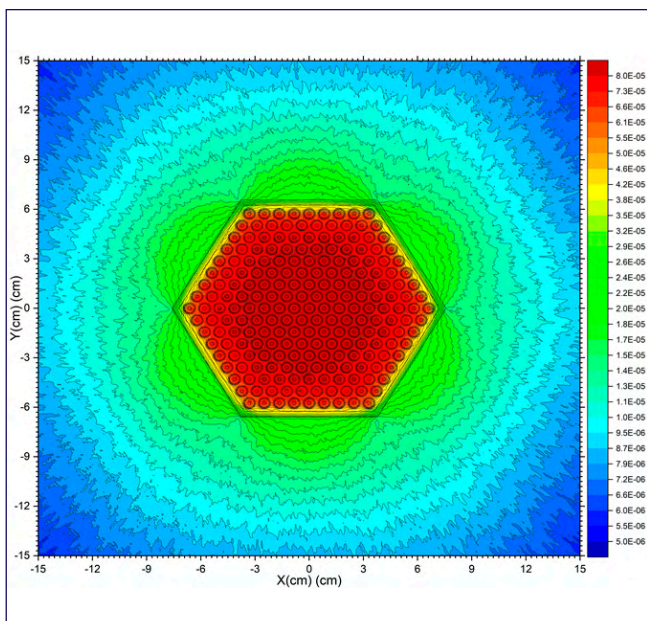


Fig. 1 Gamma flux field around a fuel subassembly (red indicates high and blue indicates low flux)

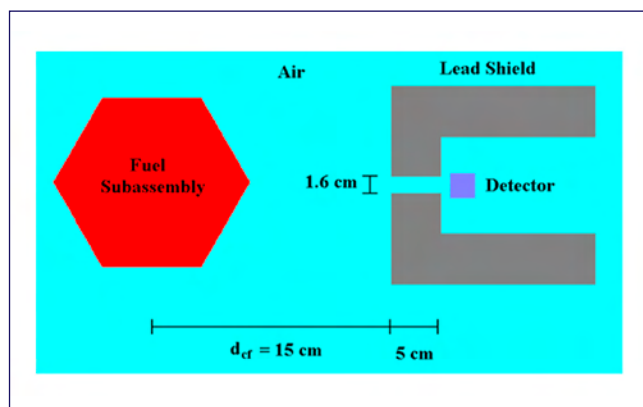


Fig. 2 Model for studying effect of FSA orientation on gamma flux

The detector has been modeled as a cylinder of 1 inch diameter and 1 inch length. The distance between the face of the detector to FSA center is around 22 cm. The effect of orientation of the FSA with respect to detector geometry is depicted in Figure 3. It can be seen that very close to the FSA, the gamma flux for flat face configuration dominates over edge facing configuration. However, as the distance increases (after about 4 – 5 cm from FSA surface), the differences become small. This trend is confirmed by experiments. Further calculations are in progress with pin level FSA model and detector to improve the prediction.

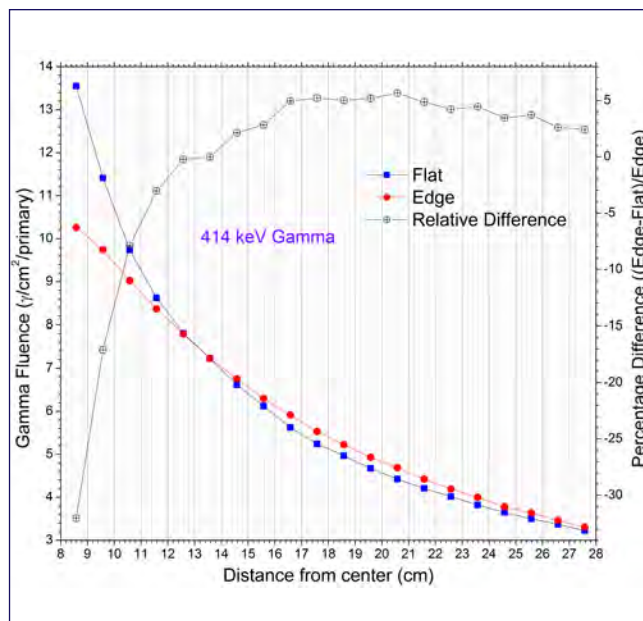


Fig. 3 Variation of gamma flux with distance

III.22 Long-Term Exposure of MgAl₂O₄ and Y₂O₃ Thermal Barrier Coatings in Molten Sodium for FBR Core

Whole core meltdown is an accidental situation that can occur in a sodium-cooled fast reactor, and the result of such a meltdown is a mixture of structural materials and radioactive fuel, called corium. The temperature of corium can be as high as 2400 °C in the initial hours of the meltdown. The molten corium after meltdown comes in contact with comparatively cold liquid sodium to form fragmented debris which moves down to the bottom of the reactor vessel. To avoid the discharge of radioactivity to the surroundings in such a hypothetical situation, main vessel integrity has to be ensured. For this, reactor assembly is equipped with a structure called core catcher, to collect and retain the corium in a subcritical and coolable configuration. Type 316LN SS is the typical material used for the construction of in-vessel core catchers. Provision of a ceramic refractory over the core catcher as a sacrificial thermal barrier layer can restrict the temperature rise within the safe limits. The molten sodium environment inside the fast breeder reactors necessitates long term resistance to liquid sodium-induced failure for the Thermal Barrier Coatings (TBC). Thus, it is essential to study the effect of molten sodium exposure on the properties of TBCs towards qualifying as a sacrificial layer for core catcher applications.

Thermal barrier coatings of magnesium aluminate spinel (MgAl₂O₄) and yttria (Y₂O₃) were investigated for long term compatibility with molten sodium. Thermal barrier ceramic coatings were deposited over 316LN SS samples, with an intermediate NiCrAlY bondcoat, using Atmospheric Plasma Spray technique. The coated samples were exposed to high purity molten sodium at 400°C under an inert argon atmosphere for 500 h and 1000 h. The fixture with samples and exposure setup is shown in Figure 1. Molten sodium exposed samples were subjected to post-cleaning by vacuum distillation, followed by chemical cleaning for effective removal of sodium from the specimens.

The SEM analysis showed neither thickness loss nor

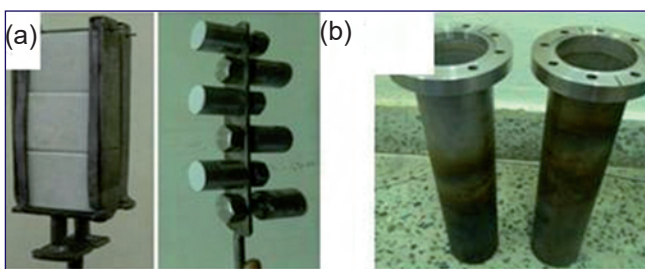


Fig. 1 (a) Fixture and (b) exposure vessel set up

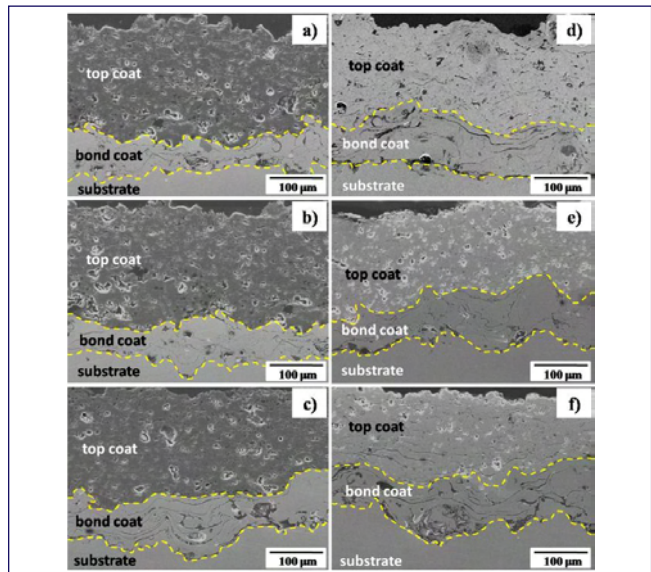


Fig. 2 (a) As-coated, (b) 500 h and (c) 1000 h exposed MgAl₂O₄ coatings and (d) as-coated (e) 500 h and (f) 1000 h exposed Y₂O₃ coatings

dissolution in Magnesium Aluminate Spinel coatings while Yttria coatings revealed a thickness reduction of ~20% and ~30% after 500 h and 1000 h of sodium exposure, respectively (Figure 2). Surface SEM analysis of both ceramic coatings indicated densification after sodium exposure. Defect density reduced in spinel topcoats while; major cracks were developed on Yttria topcoats after 1000 h exposure.

XRD analysis of the coatings after sodium exposure indicated no crystalline phase change (Figure 3). Tensile adhesion test showed ~62% and ~33% drop in the adhesion strength values for magnesium aluminate spinel and yttria coatings respectively, after 1000 h of molten sodium exposure. The deterioration in microstructural and mechanical properties of the plasma sprayed MgAl₂O₄ and Y₂O₃ coatings is attributed to the molten sodium infiltration through the pores and microcracks of the coatings. MgAl₂O₄ as TBC performed satisfactorily in long term exposure to molten sodium environments

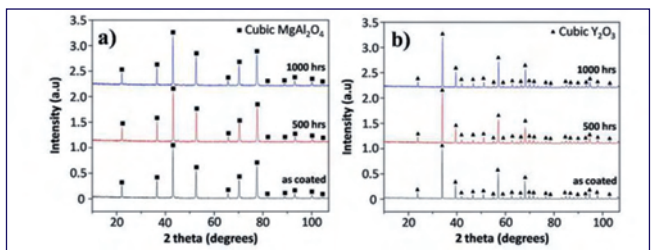


Fig. 3 XRD pattern of a) MgAl₂O₄ and b) Y₂O₃ coatings before and after sodium exposure

III.23 Studies on the Efficacy of Ionic Liquids on Inhibiting Biofilm Formation on Materials used in Cooling Water Systems

Ionic liquids (ILs) are the novel chemicals of low temperature (<100 °C) molten salts, composed of an organic cationic rings (imidazole, pyridinium) and an inorganic anions like tetra fluoroborate, hexafluorophosphate. These cationic structures (imidazolium, pyridinium) resemble the quaternary ammonium compounds (QACs) and the micellization of QACs in aqueous solutions exhibit antimicrobial activity. Recent investigations showed that ILs are ideal candidates for antibacterial applications because of their physico-chemical characteristics such as negligible vapor pressure, high polarity, high thermal and chemical stabilities, ionic conductivities and solubility. In the present study, the efficacies of three different cationic and anionic ionic liquids (ILs) on biofilm formation on Titanium and Carbon steel, materials used in cooling water systems were evaluated.

Three ILs 1-Ethyl 3-methylimidazolium tetrafluoroborate designated (IL-E); 1-Butyl-3-methylimidazolium chloride (IL-I) and N-methyl-N-propylpiperidinium bis(trifluoromethylsulfonyl)imide (IL-M) have been chosen. The efficacy of these ILs were evaluated on planktonic and sessile cells of major biofilm formers in cooling water systems using Gram negative and positive *Pseudomonas* sp. and *Bacillus* sp., respectively and also their effect on inhibiting biofilm formation on material surfaces. Total viable count, luminescence

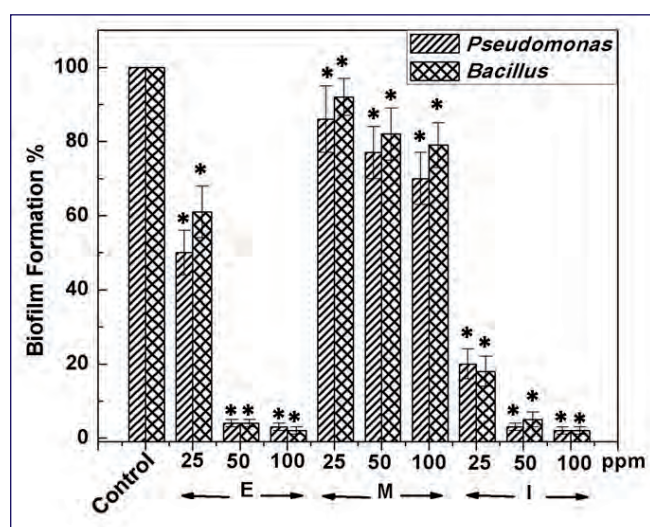


Fig. 1 Eradication of matured biofilms with ILs in absorbance based crystal violet assay. Control refers to bacterial biofilms without any ILs, set as 100%. Results were expressed as the percentage of biofilm formed with respect to the control. The error bars denote the standard deviations. * $p < 0.01$ vs control in the ANOVA test

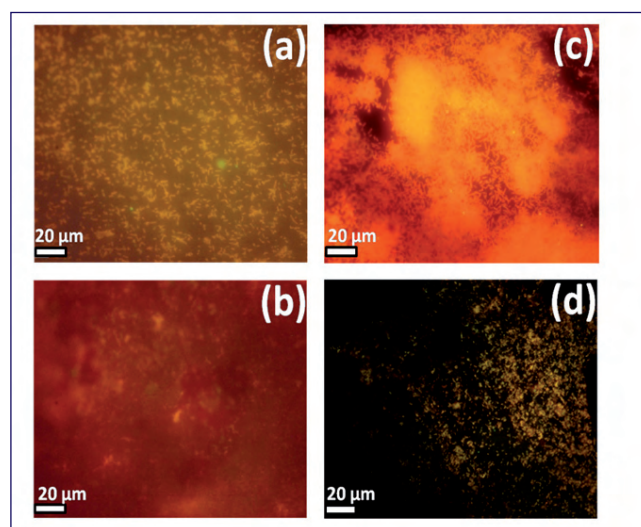


Fig. 2 Epifluorescence micrographs of AO stained CS specimens: Control CS (a); CS silanized with IL-E (b) with *Pseudomonas aeruginosa* and Control CS (c) CS silanized with IL-E (d) with *Bacillus cereus* (b)

and fluorescence based assays results show 25 ppm of IL-M and IL-E provides anti-bacterial activity against planktonic cells of *Pseudomonas* and *Bacillus* culture, respectively. IL-I and IL-E in the concentrations of 50 ppm showed 80-90% inhibition of biofilm formation and 90% eradication of mature biofilms of *Pseudomonas* and *Bacillus* sp. (Figure 1). These results suggest that Imidazolium based ILs are effective in controlling sessile cell formation and eradicating mature biofilm as compared to piperidinium based IL. Further, Anti-adhesive property of ILs on sessile bacterial cells assayed with CS having silane based IL coatings showed four orders of reduction in the bacterial counts confirming a better efficacy of IL-E Figure 2, as compared to IL-M and IL-I. Imidazolium based IL with fluoride anion (IL-E) (imidazolium cation and BF_4 anion) due to the fluoride formation as the results of hydrolysis of the anions in water inhibited the metabolic activities of bacterial cells by blocking Na^+ , K^+ , ATPase present on the cell surface. Thus, IL-E was the best in inhibiting adhesion of these bacterial cells and thereby biofilm formation on material surfaces. This study establishes the feasibility of using ILs in cooling water system for bacterial biofilm control along with other conventional biofouling control methods. Though ILs are having some limitations with respect to their cost and stability in water, the ILs may be applied on material surfaces and used in conjunction with other conventional biofouling control methods to achieve enhanced cleanliness factor in the cooling water systems.

III.24 Parameterization Study to Evaluate Bonding Quality of Sodium Compatible Ultrasonic Transducer

In FBR, Ultrasonic transducer is the key element to carry out under sodium imaging. The bonding between active lead zirconate titanate (PZT) and Nickel (Ni) face plate is carried out by soldering/ diffusion bonding technique. Evaluating the bond quality would help in fabricating high quality transducers. The experiment was carried out in recently procured 6 axis ultrasonic scanner. The scanner consists of control system for six mechanical movement (X, Y, Z, Alpha, Beta & Roller), ultrasonic pulser receiver unit, a computer loaded with software for online acquisition and report generation.

The bonding experiment is carried out by fixing the in-house developed 1 MHz ultrasonic transducer in the tank and moving a focused water immersible transducer of frequency 15 MHz with focal length 50 mm (in water) in Y and Z direction. The test setup is shown in Figure 1. The acquired A scan data is plotted in the offline analysis software to get the C-scan image for obtaining the result. To assess the bonding quality, the following parameters are optimized :

- (i) Gating of A scan data – is done by calculating the transit time and relating it with the thickness of the nickel diaphragm of in house developed transducer. Gate is set for the interface echo obtained at 0.5 microseconds from the first peak as shown in Figure 2. When the bonding is good, the amplitude of the interface echo is less compared to the back wall echo.
- (ii) Focal point – when a test sample is introduced in the path of ultrasonic beam, the geometry of the beam changes. So the water path distance will reduce to 39.4 mm to focus the ultrasonic beam at 2.8 mm below the nickel surface of the transducer.
- (iii) The frequency of the transducer - C scan images of 1

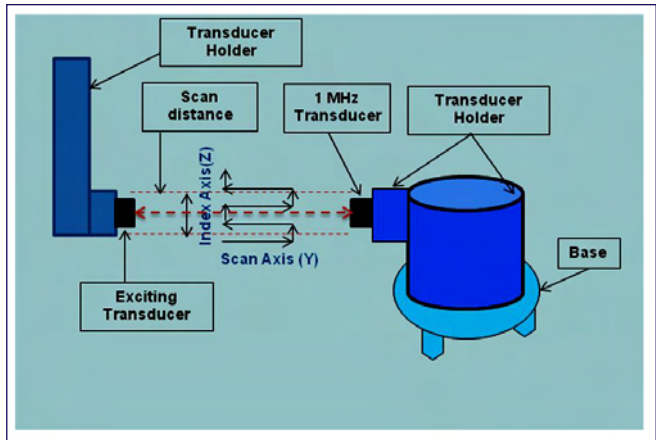


Fig. 1 Experimental test set up

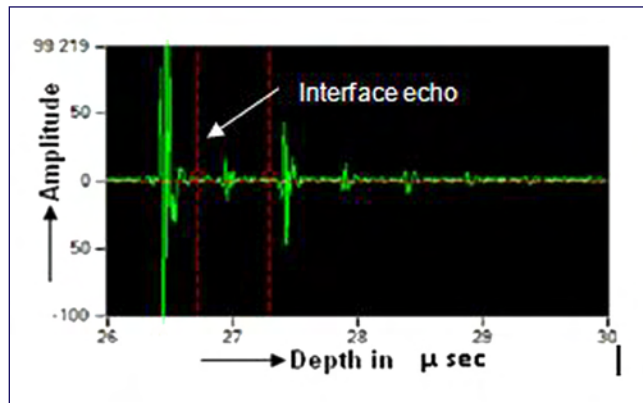


Fig. 2 Gate setting

MHz transducer using 15 and 25 MHz transducer is shown in Figures 3a & 3b. (blue colour indicates good bonding). The frequency of 15 MHz is optimized by keeping the gating and focal distance as constant.

In the present study, the parameters are obtained for evaluating the bonding quality and implemented on ultrasonic transducers of frequency 1 and 2 MHz.

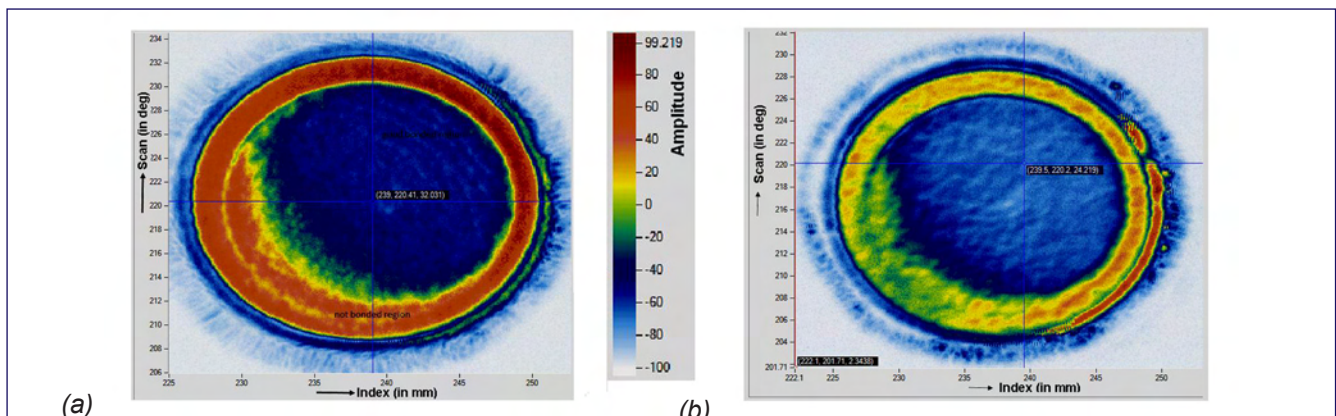


Fig. 3 (a) C scan image – 15 MHz and (b) C scan image – 25 MHz

III.25 Integrated Steady and Transient Pool Thermal Hydraulic Analysis of Primary Sodium Circuit

FBR1&2 is a proposed two loop 600 MWe pool type fast reactor design. At present, studies towards optimisation of design aspects are ongoing. In view of this, a comprehensive CFD model of reactor pool and immersed components is developed for detailed thermal hydraulic studies. Hot and cold pools along with immersed components represent the primary heat transport system. Hot and cold pools are physically separated by Inner Vessel (IV), which completely envelopes the hot pool. Cold pool along with inner vessel is enveloped by Main Vessel (MV). Thus, IV is in contact with both hot and cold pools, having widely different temperatures. Apart from this, the complex flow patterns in hot and cold pools introduce circumferential and axial temperature asymmetry on both IV and MV. The main focus of this work is on resolving temperature distributions of important structural components, viz., IV, MV, Primary piping, standpipes for sodium pumps, spherical headers etc during full power operating

conditions of reactor. Apart from structural temperatures, heat transfer from hot to cold pool through IV is another important quantity estimated from this study. This heat transfer has repercussion on plant efficiency. The combination of complex flow physics necessitates a detailed three dimensional CFD study. Further during reactor transients, both IV and MV along with immersed components are subjected to rapid temperature changes, making thermal loads important for both. Development of 3D-CFD model is a challenging task due to the large dimensions, several immersed solid structures and requirement of modeling components with widely different scales. For example, the diameter at top of IV is about 13.5 m with its thickness being about ~15 mm. Further inclusion of internal structures like spherical headers, Primary piping etc. complicates the task of mesh generation. The model developed for the present study is a 180° sector model to take advantage of inherent geometrical symmetry. The complete CFD model is

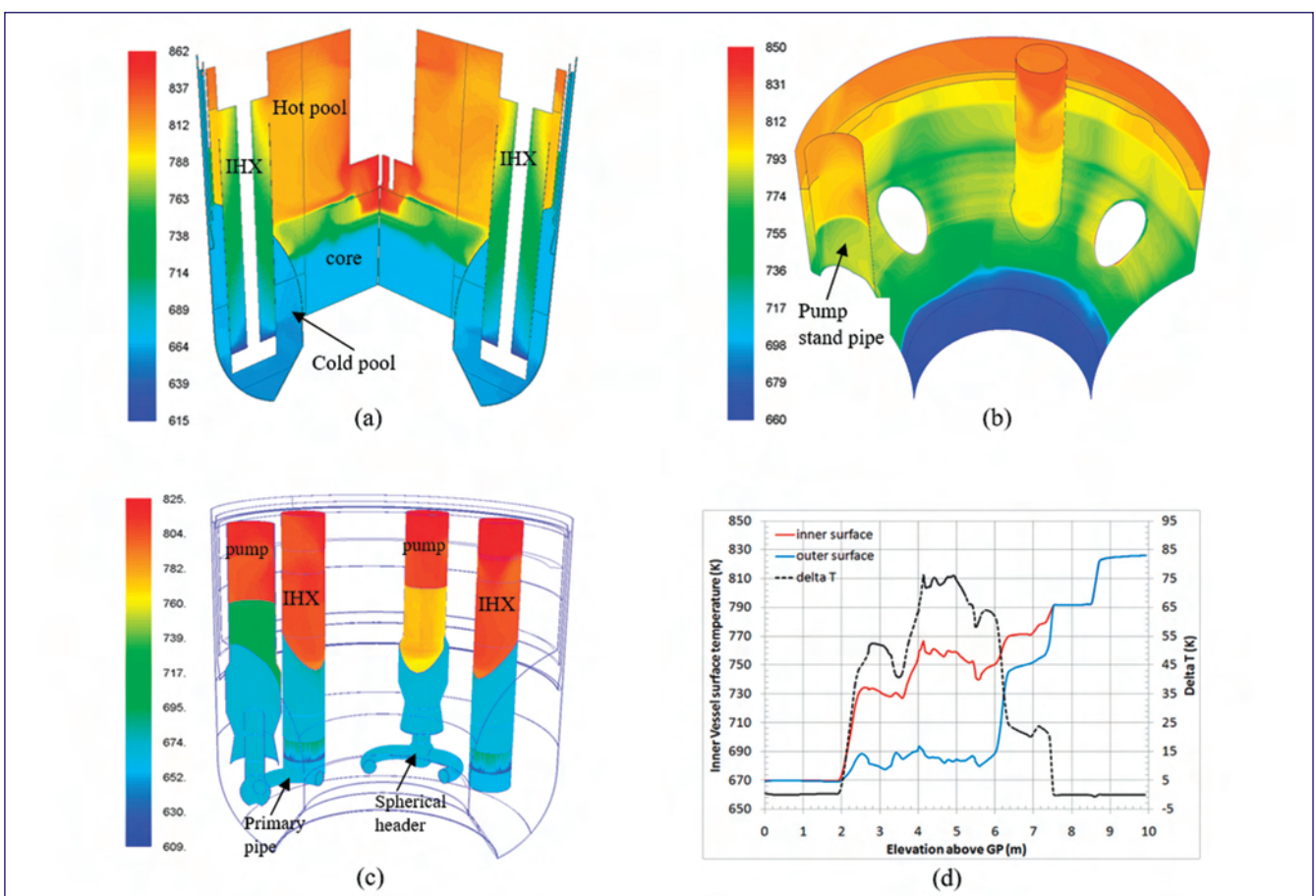


Fig. 1 Results of steady state analysis: Temperature contours (K) in (a) reactor pool (b) inner surface of IV (c) surface temperature of immersed components and (d) axial temperature variation of inner and outer surface of IV at a circumferential position between two pumps

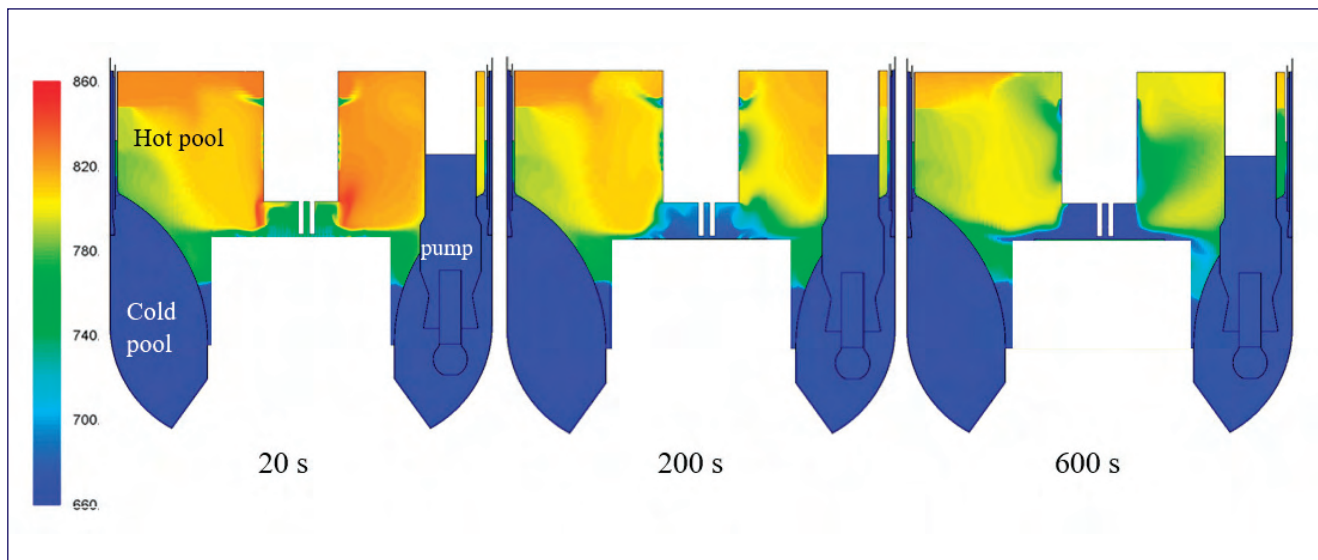


Fig. 2 Temporal evolution of temperature (K) of hot and cold pools following reactor SCRAM

discretised using about 3 million hexahedral cells in combination with judicious use of mesh interfaces.

From the steady state analysis, important results including temperature distribution on inner vessel, main vessel, PSP standpipe, primary pipes etc. have been determined. Important results including overall temperature contours in hot and cold pools, temperature of inner surface of IV, surface temperatures of major immersed components are shown in Figure 1. The axial variation of temperatures of inner and outer surface of IV along with temperature difference across its thickness is also shown in Figure 1. The maximum temperature difference across inner vessel is found to be about 82 K. Heat flow through inner vessel from hot to cold pool is found to be 15.4 MW. This is an important result as these estimates are necessary towards calculation of thermal load on IV. Some of the other important results available from the steady state analysis include (i) cross flow velocity patterns in cold pool, (ii) free surface velocity profile in hot pool (maximum velocity of 0.4 m/s) and (iii) velocity & temperature distributions at inlet and outlet windows of intermediate heat exchangers (IHX).

During reactor transients, both IV and MV along with immersed components are subjected to rapid temperature changes, making thermal loads important for both. Primary coolant, viz., liquid sodium exacerbates the problem of thermal loads on IV and MV and their internals due to its high thermal conductivity. In view

of this, transient temperature evolution of reactor pool components during reactor SCRAM is determined as extension to the steady state calculations. During a transient like SCRAM, control rods are inserted into reactor core to stop fission heat generation. At the same time, primary sodium pumps coast down to 20% speed. Secondary sodium pumps also coast down to 20% speed. The above sequence of events leads to significant temperature changes at core outlet and subsequently at IHX outlet. Sodium entering hot pool, after exit from core top, influences components in hot pool that includes IV. IHX outlet temperatures affect both MV and IV along with other cold pool components. An additional influence arises out of the temperature changes in MV cooling system, affecting upper parts of IV and MV. In the present study, effect of temperature and flow at core top during SCRAM on hot and cold pool components is studied. Since the present study is a transient analysis, with a total duration of about 600 s, computational economy has to be given due importance so that obtaining a solution stays feasible. The run time for the present analysis with a time step of 0.01s is about 4 weeks. Temporal evolution of temperature of hot and cold pools is shown in Figure 2. Evolution of temperatures for all important reactor components is obtained from the same study. These results are useful in the thermo-mechanical analysis of reactor assembly components.

III.26 Testing of Large Sized Inconel-625 Bellows in High Temperature Sodium Environment

Towards possible use of bellows in secondary sodium main circuit particularly at the inlet pipe of secondary sodium pump, indigenous design and development of the large-sized bellows (size 800 NB) has been carried out. Inconel-625 is chosen as the material of construction. Due to its higher mechanical strength, the required thickness and stiffness of the bellows with Inconel-625 is less compared to austenitic stainless steel. Manufacturing of 800NB bellows was carried out (Figure 1). At the supplier's shop, the bellows were subjected to pressure hold test, dimensional inspection and Helium Leak Test (HLT) under vacuum. The leak rate of the bellows was found to be less than 10^{-8} Pa-m³/s. After receipt at IGCAR, the HLT of the bellows was repeated, and the bellows were found to be leak tight. A test setup for carrying out testing of the bellows in air was designed, and the bellows were tested in air at 3 bar pressure, and ± 60 mm axial movement for 500 cycles. The movement of the bellows was applied through a hydraulic drive system with all safety and control features.

Subsequently, the bellows were assembled in Test vessel-2 of Large component test rig (LCTR) for testing in sodium (Figure 2). The conditions during sodium testing of the bellows were (i) Sodium temperature: 530°C, (ii) Cover gas pressure: 100 mbar, (iii) Sodium level: bellows completely immersed in sodium and (iv) Movement of the bellows: ± 60 mm axial, (v) internal pressure : 3 bar



Fig. 1 Bellows as-manufactured



Fig. 2 Bellows as-assembled

inside bellows. The bellows assembly consists of two halves based on manufacturing consideration joined with an intermediate pipe of SS316L (Figure 3). Two closure plates were welded at the top and bottom of the bellows assembly. The top and bottom closure plates of the bellows were connected internally with a pipe so that the axial thrust force developed due to the internal pressure does not act on the bellows and is absorbed by the two end plates. The central pipe of the bellows was welded with four brackets to which the top actuating plate is connected by four tie rods. The bellows were supported from the top flange of TV-2 by four support rods. The actuating plate of the bellows was connected to the hydraulic actuating mechanism through a central rod.

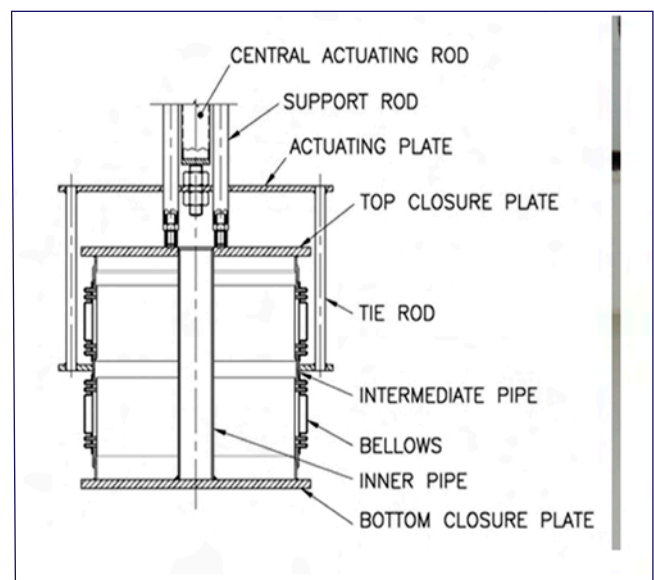


Fig. 3 Test setup details

The central actuating rod passes through the top plate in which two lateral O-rings were provided to prevent the leakage of cover gas argon from TV-2. A ¼" pipe was provided for pressurization of the bellows and monitoring the bellows healthiness by pressure hold testing. The argon supply pipe was routed through the level probe nozzle provided in the TV-2 top flange assembly.

TV-2 was provided with the necessary sodium instrumentation such as heaters, thermocouples and level probes. The pressure inside bellows was monitored continuously using a pressure gauge. A control panel was provided for the actuation of the hydraulic actuator (Figure 4a). The number of cycles of testing carried out in argon at room temperature, argon at 150°C, and in sodium at 530°C are 200, 300, and 2730 respectively. After sodium testing, the bellows were dismantled from the TV-2 (Figure 4b), sodium cleaned and then

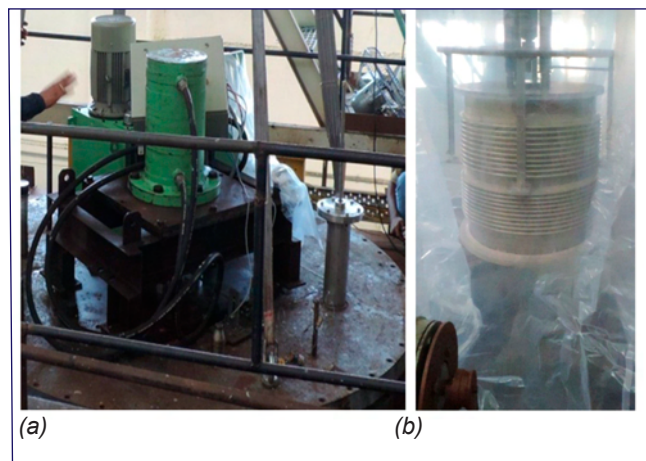


Fig. 4 (a) Hydraulic drive for bellows actuation and (b) handling after testing

subjected to helium leak testing. The leak rate of the bellows was found to be less than 10^{-8} Pa-m³/s.

III.27 Computing the Effect of Fission Gases on Thermal Transport in Uranium Dioxide

Uranium dioxide (UO₂) is the most commonly used fuel material in nuclear industry. Thermal conductivity (TC) of UO₂ is a key aspect in nuclear applications, which determines the rate of thermal energy transport from the fuel to the coolant. Radiation induced fission gases (FGs) degrade the TC of UO₂ and affect the thermal transport. Understanding the consequence of such volatile fission products on thermal transport is crucial for safety reasons. Here, the effect of FGs (Xe and Kr) on the thermal properties of UO₂ is analyzed using molecular dynamics (MD) simulations. All simulations are done using LAMMPS package with embedded-atom method (EAM) potential. A simulation cell of size 10x10x10 unit cells (containing 12000 atoms) is constructed, the Xe and Kr atoms are randomly inserted in octahedral positions (mimicking non-equilibrium conditions) at different concentrations say 0.5% and 1.0%. The system is heated to T = 2500 K and then quenched to 300 K; Further it is equilibrated in isobaric-isothermal (NPT) ensemble for 0.5 ns at a desired temperature. After ensuring equilibration and thermalization, the NPT ensemble is decoupled and connected to microcanonical (NVE) ensemble. The whole simulation is done for 4 ns. The thermal conductivity (TC) is computed via Green-Kubo formalism.

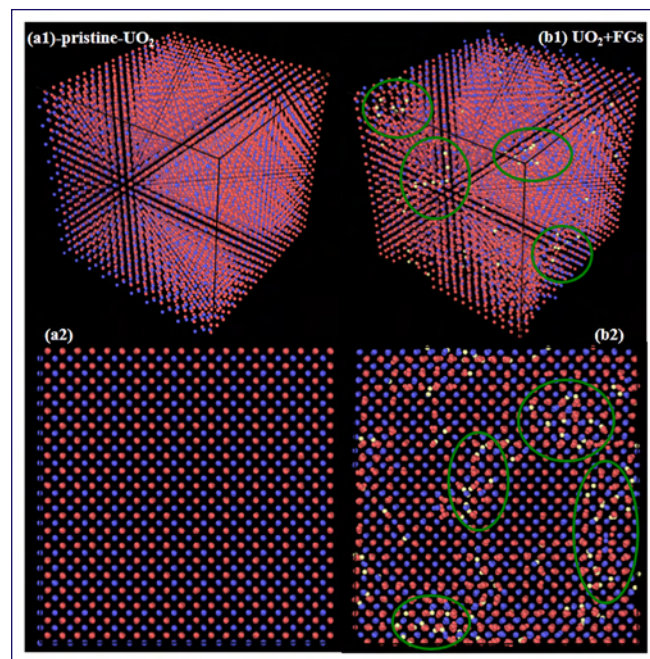


Fig. 1 Optimized geometries of pristine (a1-a2), and fission gas (Xe and Kr) inserted UO₂ (b1-b2). Top and bottom panels are perspective and top view, respectively. Red, blue and white balls represent O, U and fission gas atoms respectively. The gas molecules in UO₂ matrix is highlighted with green circles as guide to eye

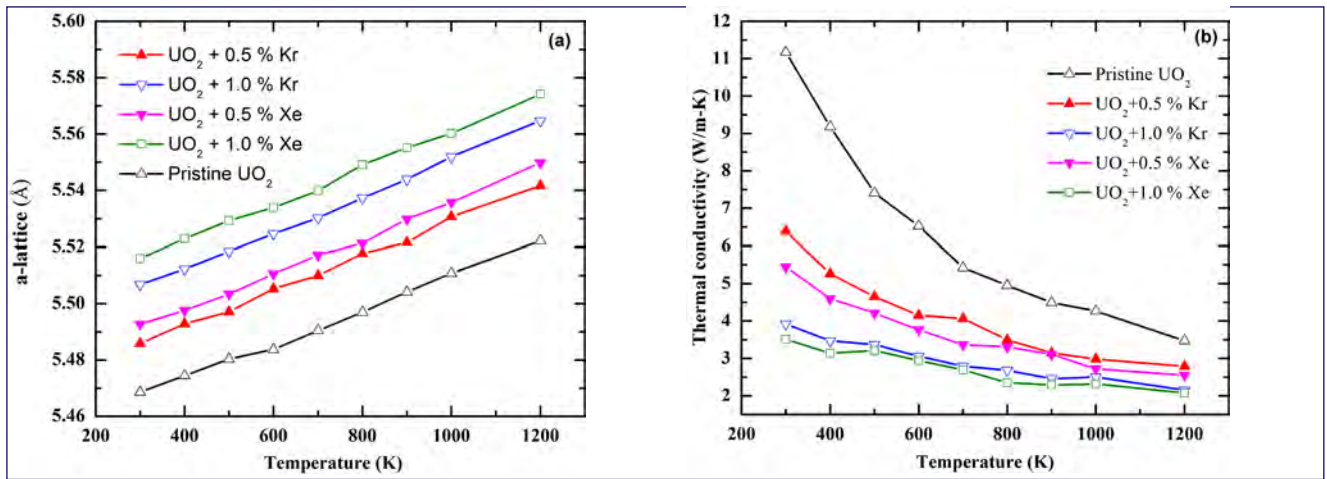


Fig. 2 (a) Thermal expansion and (b) thermal conductivity of pristine and fission gas inserted UO_2

Figure 1 shows the optimized geometries of pristine and FG inserted UO_2 (UO_2 +FGs) systems at 300 K. After equilibration, the fission gas atoms (white balls) occupy random octahedral positions in UO_2 matrix, which induces a local distortion in the lattice. Temperature evolution (300 K - 1200 K) of *a*-lattice parameter and TC of both pristine and UO_2 +FGs are shown in Figure 2. Fission gases exert a residual stress in the lattice, which leads to the expansion of lattice in UO_2 +FGs systems. The higher atomic radius of Xe (216 pm) with respect to Kr (88 pm) causes more residual stress, which results in higher expansion of lattice in the case of UO_2 +Xe.

Thermal conductivity plot shows that there is a substantial reduction in the TC of UO_2 when FGs are inserted (Fig 2 b). The percentage of degradation (w.r.t. pristine UO_2) is shown in Table 1. The TC of UO_2 with 0.5 and 1.0% Xe is 51.52 and 68.59% smaller than that of pristine UO_2 . Similarly for UO_2 +Kr system, the TC values are reduced by 42.79 and 64.90% for 0.5 and 1.0% Kr insertion, respectively. The large degradation in TC of UO_2 +FGs system is attributed to the emergence of phonon-defect scattering in these systems. The phonons get scattered from the FGs and hinder the thermal energy transport. There is a systematic degradation in TC with concentration of FGs; at higher concentration more defect scattering centers are available, and

contribute significantly to thermal resistance. Among Xe and Kr, the scattering strength associated with Xe is higher than that of Kr, hence the TC values of UO_2 +Xe is lower than that of UO_2 +Kr. At low temperatures, a significant difference between the TC values of pristine and UO_2 +FGs is observed, where the phonon-defect scattering is the dominant contribution towards thermal resistivity. At high temperatures, the phonon-phonon scattering dominates over phonon-defect scattering, hence the difference in TC values is not significant as observed at low temperatures.

In summary, effect of fission gases (FGs) on thermal transport in UO_2 is analyzed using classical MD simulations. A substantial reduction in thermal conductivity of UO_2 +FGs system is observed at low temperatures with respect to pristine, and it is attributed to the phonon-defect scattering, which hinder the thermal energy transport. At high temperature, phonon-phonon scattering dominates over the phonon-defect scattering, hence the TC difference between the pristine and UO_2 +FGs is not significant compared to low temperature regimes. The present work enables us to understand the degradation mechanism of fuel thermal conductivity by radiation induced fission gases under operating conditions.

Table 1: Thermal conductivity and lattice parameter of pristine and fission gas inserted UO_2 at 300 K

System	(a-lattice) (Å)	% increase w.r.t pristine	Thermal-conductivity (W/m-K) at 300 K	% degradation w.r.t pristine
Pristine UO_2	5.469	-----	11.173	-----
UO_2 + 0.5 % Xe	5.493	0.44	5.449	51.23
UO_2 + 1.0% Xe	5.516	0.86	3.509	68.59
UO_2 + 0.5 % Kr	5.486	0.31	6.392	42.79
UO_2 + 1.0 % Kr	5.507	0.69	3.922	64.90

III.28 Numerical Methodology for the Estimate of Asymptotic Crack Size and Comparison with A16 Master Curve Prediction

Fast Breeder Reactor (FBR) piping components are subjected to many cyclic loading conditions during various stages of their operation. These variations lead to fatigue loading, and it is one of the potential mechanisms, which can lead to a situation where the surface crack becomes the asymptotic crack. At this condition, the relative crack depth ratio (a/t) becomes unity and it is represented in Figure 1. One of the essential safety criteria to be demonstrated for achieving the required level of structural integrity for FBR piping system is that the postulated part-through-crack size on the pipe surface ($2C_0$) shall not become $2C_S$ during the period between two successive in-service inspection/repair schedules. Presently the ' $2C_S$ ' estimate for the LBB design of the FBR piping system is performed as per the design guideline given in RCC MRx A16 with LBB Master Curve (Figure 2). ' $2C_S$ ' is one of the critical parameters used to demonstrate Leak-Before-Break (LBB) requirement of the piping system. This study aims to broaden current knowledge of the estimate of ' $2C_S$ '.

The X-axis of the LBB master curve (Figure 2) is the relative stress factor (X) and it depends upon the magnitude of the range of membrane and bending stress variation for a cyclic condition as defined in Figure 2. The Y-axis represents the ratio of asymptotic crack length with thickness (C_S/t). i.e. C_S is estimated based on the thickness of the geometry and the applied stress range. The literature mentions that the Master curve is derived based on the fatigue crack growth studies performed on a plate geometry with a small semi-elliptical surface defect using the cyclic stress intensity factor (ΔK) derived from Newman Raju compendium. In this fatigue crack growth (FCG) study, the crack size variation is determined up to ' a/t ' ratio of 0.8 using Paris law and the remaining variation is obtained by linear extrapolation method.

Figure 2 suggest that the extreme conditions for the values of ' C_S ' are, viz., (i) $X=0$ corresponds to the

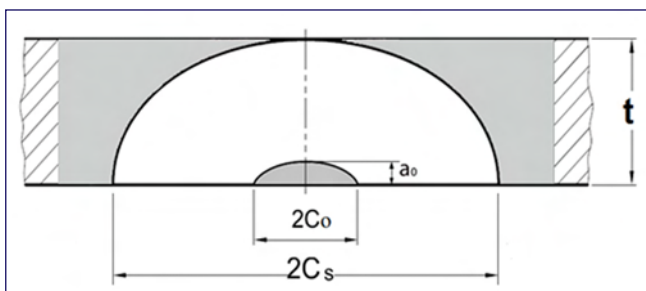


Fig. 1 Definition of $2C_S$

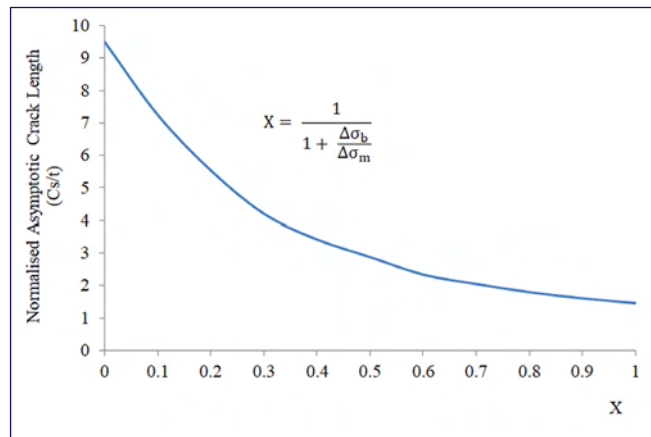


Fig. 2 RCC MRx A16 LBB master curve

case of pure bending loading condition and (ii) $X=1$ corresponds to the pure membrane loading condition. The relative representations of ' C_S ' for these conditions are given in Figure 3. It can be seen from Figure 3a that for a similar condition, the bending dominant loading results in a relatively high value of ' C_S ' than that of the membrane conditions. The predominant loading condition responsible in the design of the FBR piping system is the thermally originated bending stress variation, and the membrane stress contribution is negligible and it is more close to the situation represented in Figure 3b. Thus, an accurate/more realistic estimate of ' C_S ' will have an essential role in achieving economic LBB design criteria.

An alternate method for estimating ' C_S ' for an FBR representative pipe bend is presented here. Necessary pipe bend geometrical details are given in Figure 4,

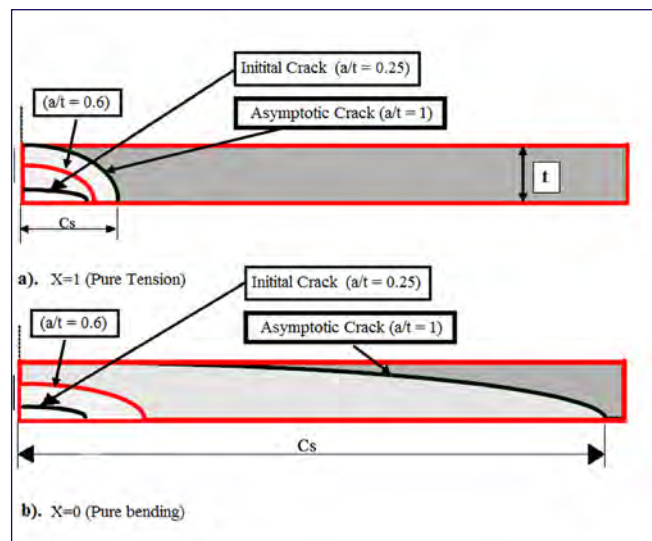


Fig. 3 Crack growth behaviour under different loading conditions (a) pure membrane and (b) pure bending

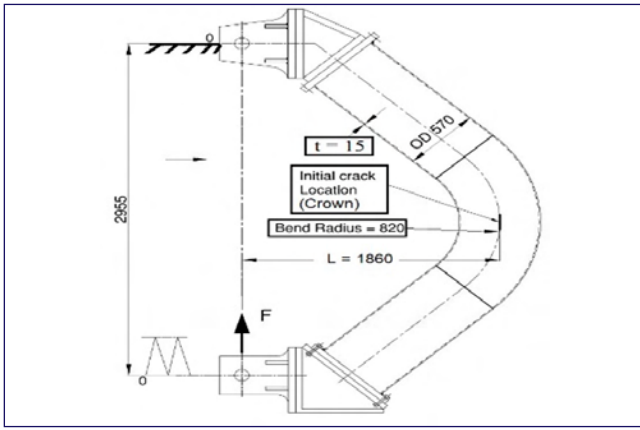


Fig. 4 Pipe bend geometrical details in mm

and it is subjected with a cyclic load variation as shown in Figure 4. Two loading situations that correspond to the cases viz., (i) $X = 0.01$ for bending dominant crack growth behaviour and (ii) $X=0.4$ with both membrane and bending stresses governing crack growth behaviour are considered, and the results are compared with A16 prediction.

Numerical Fatigue Crack Growth Analysis

Numerical FCG analysis has been performed using ZENCRACK software in companion with the general purpose finite element (FE) solvers. Linear elastic fracture mechanics (LEFM) based analysis is performed. An initial semi-elliptical surface crack size of 2.4 mm along the thickness direction (a_0) and 22.6 mm along the longitudinal direction ($2c_0$) is introduced to perform the FCG analysis of the pipe bend. Crack tip singularity is achieved by adopting 20 noded collapsed brick element as a quarter-point wedge element at the crack tip. Accuracy in the finite element method (FEM) simulation is achieved by controlling the local aspect ratio of the crack-block elements at the expense of local mesh relaxation in the surrounding elements.

FCG studies on the pipe bend are performed up to $'a/t' = 0.8$ the loading conditions belong to the cases $X = 0.01$ and $X = 0.4$. The observed maximum crack

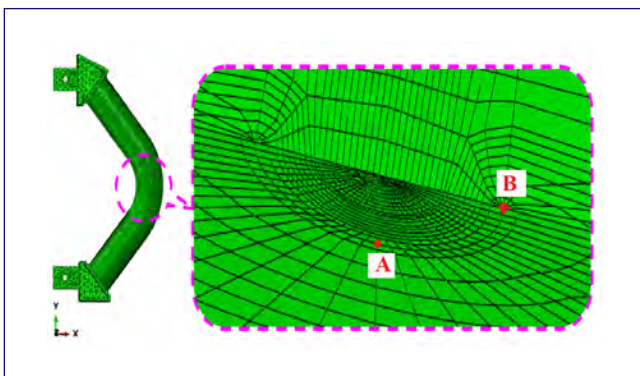


Fig. 5 FE model of the cracked pipe bend

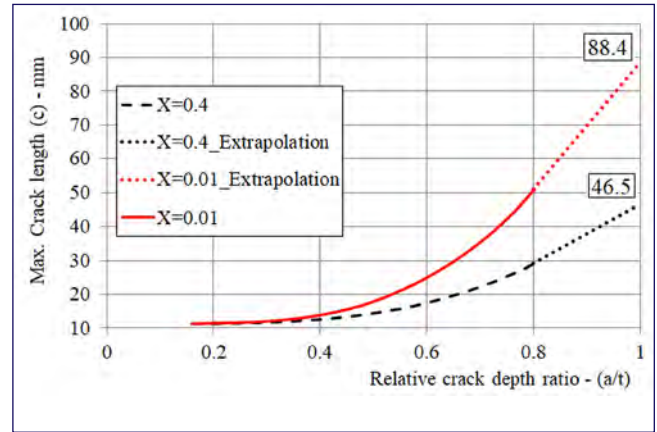


Fig. 6 ' C_s ' estimate based on the FCG analysis

growth behaviour at the deepest location ($'a'$: location A from Figure 5) and along the surface direction ($'c'$: location B from Figure 5) are presented in Figure 6. Internal pressure and bending moments are applied such that the resultant membrane and bending stress combination should match $X = 0.01$ and $X = 0.4$.

The numerically obtained $'a/t'$ vs $'c'$ for both the cases are further linearly extrapolated from the value of a/t' 0.8 to 1.0 to obtain the estimate of ' C_s ' as presented in Figure 6. Accordingly obtained ' C_s ' for the loading case $X = 0.01$ is 88.4 mm and for the case, $X = 0.4$ it is 46.5 mm. Whereas the respective values as per the A16 methodology are 139.0 mm for the case $X = 0.01$ and 51.5 mm for the case, $X = 0.4$. These values are given in Table 1. The relative comparison of the ' C_s ' estimated based on the numerical assessment as well as the current design code approach of A16 methodology suggest that predicted values are 36.4 % lower for the loading case of $X = 0.01$ and the 9.7 % lower value for the loading case of $X = 0.4$ as given in Table 1.

Cases	A16 Method	Numerical	% variation
$X=0.01$	139.0	88.4	-36.4
$X=0.4$	51.5	46.5	-9.7

FBR piping system loading conditions are more close to the situation, similar to $X = 0.01$. Thus, the deployment of numerical method can provide a relatively low and accurate estimate of ' C_s ' in the LBB design of the FBR piping system. A relatively lower value of ' C_s ' directly affects the safety margin available under LBB demonstration criteria. Hence it is recommended to adopt the numerical estimate of ' C_s ' in the LBB design of FBR piping system.

III.29 Suppression of Pressure Induced Phase Transformation In Neutron Irradiated Fe₂B

Borides of metals have wide industrial applications because of their hardness, corrosion resistance and refractory nature. Borides are also of importance to the nuclear industry. Neutrons being electrically neutral and small in size can travel large distances in solids without scattering. Concrete, B₄C and Steels have been commonly used for shielding the neutrons in a reactor. In a pool type fast reactor such as the Prototype Fast Breeder Reactor (PFBR) at Kalpakkam, in-vessel shielding is provided to minimize the radiation at the IHX location so that the dose rate due to secondary sodium activity in the steam generator building is within acceptable limit. The neutron attenuation coefficient determines the thickness and size of the inner vessel or in-vessel shielding. The neutron attenuation measurements at the Kalpakkam Mini reactor (KAMINI) reveal that ferroboron has neutron attenuation coefficients comparable with B₄C. Ferroboron, a mixture of Boron and Iron, has been found to be six times cheaper. It reduces the weight of the core by 15% and is being considered actively as an in-vessel shield material for future FBRs. Ferroboron has been found to have three phases FeB, Fe₂B and Fe₃B. Of the three phases only FeB and Fe₂B phases exist in the equilibrium phase diagram of Fe-B. The high pressure structural stability of FeB and Fe₂B have been studied by our group previously. The orthorhombic structure of FeB remains stable up to 24 GPa, whereas the tetragonal structure of Fe₂B undergoes a phase transition at about 6 GPa. Phase transition is sluggish,

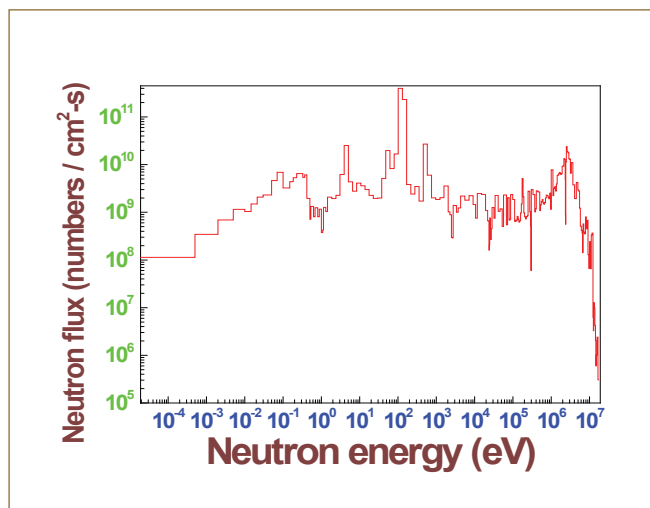


Fig. 1 Neutron flux spectrum at shielding corner location of KAMINI

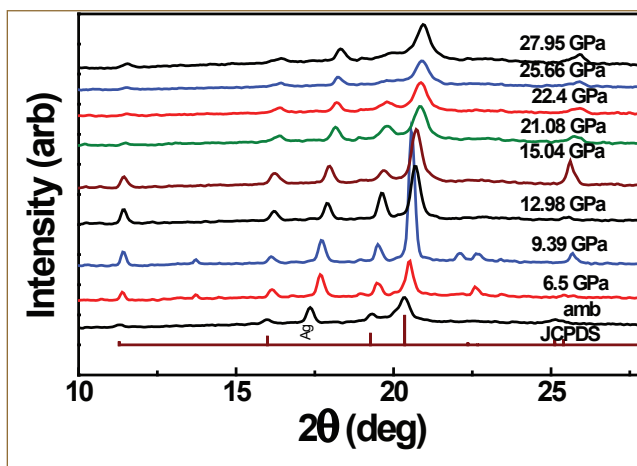


Fig. 2 High pressure XRD patterns for neutron irradiated Fe₂B

the parent phase and the orthorhombic daughter phase coexist up to the highest pressure of 20 GPa. Here we report structural stability of neutron irradiated Fe₂B under pressure.

Experimental and computation

Fe₂B (99% pure) powders were procured from M/s Alfa Aesar. The sample was irradiated for about 25 hours at the shielding corner location of the KAMINI reactor operated at 20 kW power. The neutron spectrum at the irradiation location of KAMINI is given in Figure 1. The total flux is estimated to be 1.23×10¹² neutrons cm⁻²s⁻¹. The High Pressure XRD (HPXRD) on the irradiated sample was carried out by using a Mao-bell type Diamond Anvil Cell (DAC). The DAC consisted of two diamonds with a culet size of 500 μm in opposed anvil

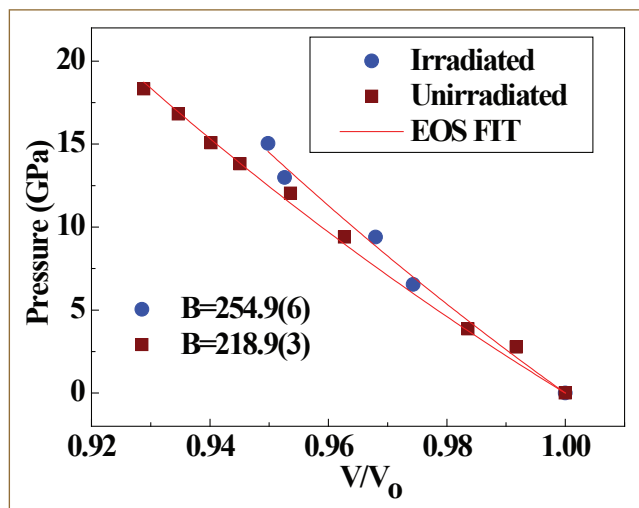


Fig. 3 P-V curve for neutron irradiated and un-irradiated Fe₂B

configuration. A stainless steel gasket was pre indented to 60 μm thickness. In the indented region a 300 μm hole was drilled which acts as a pressure chamber. In this chamber, the sample, pressure transmitting medium and the pressure callibrant were loaded. Methanol-Ethanol-Water (MEW) in the ratio of 16:3:1 was used as pressure transmitting medium and ruby was used as pressure callibrant. The XRD data was collected in angle dispersive mode with a rotating anode X-ray generator (Rigaku-ULTRAX-18) with Mo target ($\lambda = 0.7107 \text{ \AA}$). XRD data was collected by a mar345dtb image plate detector. The collected two dimensional patterns from the image plate were integrated by fit2d program. The defects are estimated by use of SRIM-2013 software as below. The average energies of the Fe and B PKAs (Primary Knock-on Atom) produced due to interactions of neutrons are estimated from the PKA spectra calculated by using the CRaD code in 198 energy group structure. The necessary evaluated nuclear data used for this purpose are extracted from ENDF/B-VII.1. Subsequently, these PKA energies are given as the energies of incident ions to perform simulations on Fe_2B polyatomic target using the SRIM-2013 software. The density of Fe_2B is considered to be 6.0273 g/cm^3 (number density of atoms is $1.09 \times 10^{23} \text{ atoms/cm}^3$). For each PKA, 5000 ions are simulated in the K-P mode with the default surface and lattice binding energies. The number of displacements is calculated from the damage energies obtained from SRIM-2013 simulations by using the NRT formula. The threshold lattice displacement energy for the material is assumed to be 40 eV. The atom-displacement (dpa) cross section of Fe_2B due to an incident neutron of energy E is calculated as follows:

$$\sigma_{D,NRT(\text{Fe}_2\text{B})}(E) = \frac{2}{3} P_{\text{Fe}}(E) v_{\text{Fe}/\text{Fe}_2\text{B}}(E) \sigma_{n,\text{Fe}}(E) + \frac{1}{3} P_{\text{B}}(E) v_{\text{B}/\text{Fe}_2\text{B}}(E) \sigma_{n,\text{B}}(E) \quad (1)$$

Here, the total dpa cross section of Fe_2B is the weighed sum of the dpa cross sections due to Fe and B PKAs, where P_{Fe} and P_{B} denote the probabilities for creation of the respective PKAs in Fe_2B . P_{Fe} and P_{B} are calculated from the respective fractional cross sections (out of the total cross sections in Fe and B) for interactions with neutrons. The weights 2/3 and 1/3 are assigned from the stoichiometries of Fe and B in the compound. The energy-dependent v functions denote the numbers of displacements per PKA; $\sigma_{n,\text{Fe}}$ and $\sigma_{n,\text{B}}$ are respectively the neutron interaction cross sections of Fe and B. The

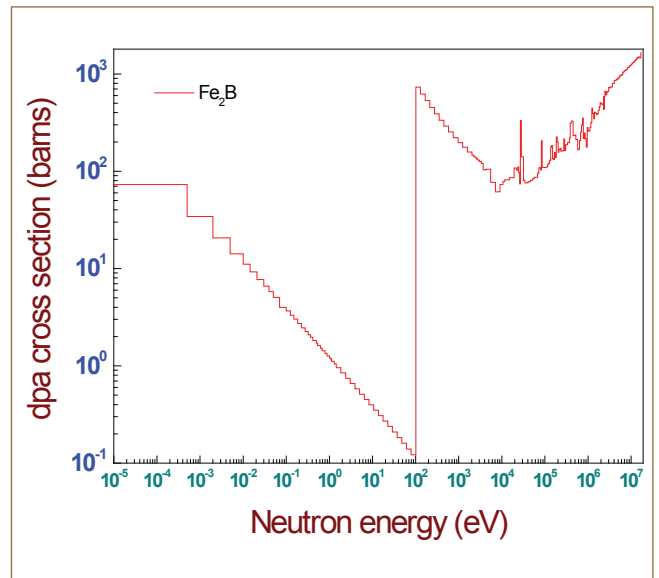


Fig. 4 Total dpa cross sections in Fe_2B

neutron spectrum-averaged values of probabilities for the creation of Fe and B PKAs are found to be 0.198 and 0.802 respectively. The neutron spectrum-averaged PKA energies are found to be about 60.7 keV (for Fe) and 434 keV (for B).

The XRD pattern of the neutron irradiated Fe_2B at various pressures is shown in the Figure 2. We observe that the $2\theta_{\text{hkl}}$ shift to right with increase in pressure. Also noticed is that the width of $2\theta_{\text{hkl}}$ positions increase with pressure. The XRD patterns do not show any obvious differences with pressure expect those mentioned earlier implying that the irradiated sample is stable under pressure. This is in variance with the behaviour of un irradiated Fe_2B .

The pristine Fe_2B shows a phase transition at a pressure of 6 GPa from the tetragonal to orthorhombic structure. Thus irradiation suppresses the structural phase transition under pressure. The bulk modulus was obtained by fitting the P-V data shown in Figure 3. The bulk modulus obtained by 3rd order Birch-Murnaghan EOS with B_0' fixed at 4 is 254(5) GPa which is higher than the pristine sample whose bulk modulus is 218(3) GPa. The increase in bulk modulus may indicate the increase in the hardness up on neutron irradiation. The total dpa cross section of Fe_2B is presented in Figure 4. After folding the dpa cross sections with the neutron spectrum, finally the total number of displacements per unit volume in Fe_2B is obtained as 6.03×10^{18} . Total dpa in Fe_2B for the irradiation fluence is found to be 5.53×10^{-5} . As the phase transition is sluggish in pristine sample and could be assumed to be of displasive transition. Thus it can reasonably be conclude that the presence of defects may lead to suppression of the phase transition.

III.30 Effect of Thermal Ageing on Thermal Diffusivity of Ni-Based Hardfacing Alloy Deposit

Ni-core structural materials in liquid Na cooled fast reactors are susceptible for self welding and galling. Hence they are hard faced with Ni-based alloys that exhibit superior high temperature wear and corrosion resistance and have better stability in terms of physical and chemical properties. Generally, Ni-based hardfacing alloys are deposited on austenitic stainless steel (SS) through welding route, which requires fine control of the process parameters to obtain crack free deposit and also involves post machining steps, resulting in huge material loss. In addition dilution of the deposit adversely affects the desired properties and puts higher threshold for the minimum thickness requirement. To overcome these difficulties, laser rapid manufacturing technique was used for hardfacing SS with Deloro 50®, a Ni-based alloy. Ni-13Cr-3.2Si-3.6Fe-0.5C-2.2B (wt%) was deposited on 304L SS using 2 kW fiber laser. The deposit was then aged in the temperature range of 823-1123 K for durations of up to 100 h. This changes its thermal properties especially Thermal Diffusivity (TD), which was estimated in correlation with phase evolution and microstructure. Type of phases present was identified using X-ray Synchrotron technique and thermal diffusivity was measured using laser flash analyzer. Evolution of microstructure with aging in terms of change in the morphology, type and volume fraction of various phases was monitored through quantitative microstructure analysis. Equilibrium phase stability information as well as coarsening behaviour of precipitates was obtained combining Thermo-Calc® and Dictra® computations. Variation in the hardness of the deposit with heat treatment is given in Figure 1 which shows a reduction in hardness beyond 1123 K, with 5h of heat treatment.

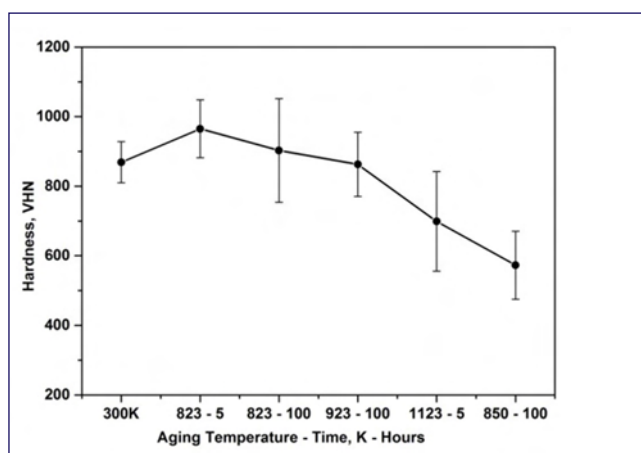


Fig. 1 Variation in hardness of Deloro50® deposit with heat treatment

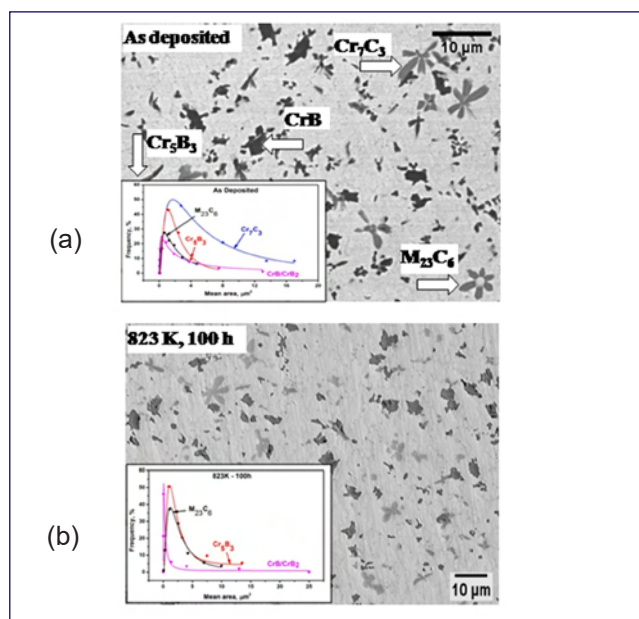


Fig. 2 Optical micrographs showing morphology of various precipitates in (a) as deposited and (b) heat treated Deloro50®; frequency distribution of the phases is given as an inset

Primary phases identified were $M_{23}C_6$ and M_7C_3 type carbides, Cr_5B_3 and CrB/Cr_2B type borides existing in g-Ni matrix. Morphology, distribution and volume fraction of these phases changed with heat treatment as shown in the optical micrographs in Figure 2, and frequency distribution of precipitates given as an inset. Thermal diffusivity of all the samples increased linearly with increase in temperature. When compared to “as deposited” samples, TD was the lowest for 823 K - 5 h sample, followed by 823 K- 100 h aging and the highest for 1123 K-100 h (Figure 3). Further analysis to understand the aging related TD variation is in progress.

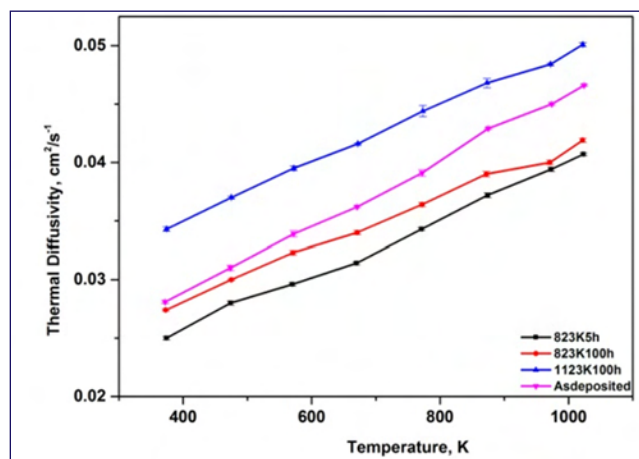


Fig. 3 Variation in thermal diffusivity of Deloro50® deposit with aging

III.31 Heterogeneous Microstructure and Creep Behavior across the P91 Steel Weld Joint

P91 steel has been used in the fossil and nuclear power plants. Fusion welding technique is generally employed to fabricate the power plants components using P91 steel. The weld thermal cycle induces microstructural changes across different regions that experience different peak temperatures. 9Cr ferritic/martensitic steels weld joint (WJ) consists of weld metal (WM), heat affected zone (HAZ) and base metal. The HAZ consists of coarse prior-austenite grain (CGHAZ) region adjacent to weld metal, fine prior-austenite grain (FGHAZ) region and intercritical (ICHAZ) region which is merging with unaffected base metal (BM). Heterogeneous microstructures across the weld joint generate heterogeneous creep deformation behaviour in WJ. The 12 mm thick steel plates having chemical composition (in wt.%): 0.01 C, 8.84 Cr, 0.90 Mo, 0.46 Mn, 0.32 Si, 0.22 V, 0.05 N, 0.08 Nb, 0.10 Ni, 0.01 S, 0.01 P and the balanced Fe were normalized (1313 K for 30 minutes) and tempered (1033 K for 2 hours) (NT), and were subsequently welded by employing activated-tungsten inert gas (A-TIG) technique followed with post weld heat treated (PWHT) at 1033 K for 1 hour.

The creep deformation assessed at WM, CGHAZ, FGHAZ, ICHAZ and BM using impression creep test at 923 K under 300 MPa punching stress is presented in Figure 1 a, wherein ICHAZ exhibits higher deformation and CGHAZ experienced significantly less creep deformation in comparison to other regions. BM and FGHAZ deformations were comparable, whereas ICHAZ region deformed at faster rate than the BM, FGHAZ, CGHAZ and WM. Further, the soft ferrite in the weld metal leads to deformation at higher rate than the BM, FGHAZ and CGHAZ. The creep deformation rate of coarse grain region was the lowest. Distinct

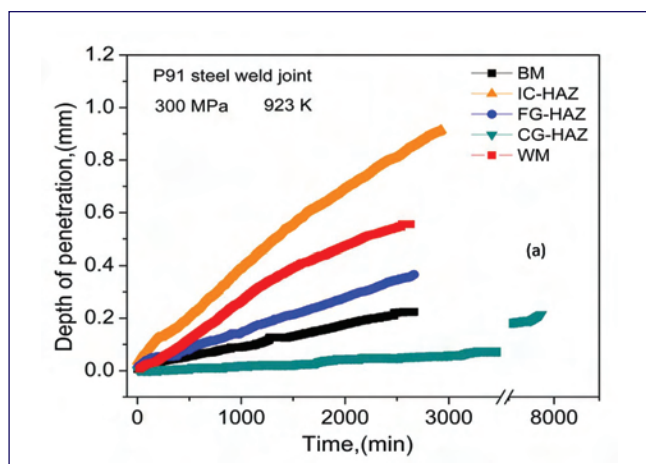


Fig. 1 Depth of penetration with time for weld metal, CGHAZ, FGHAZ, ICHAZ & base metal

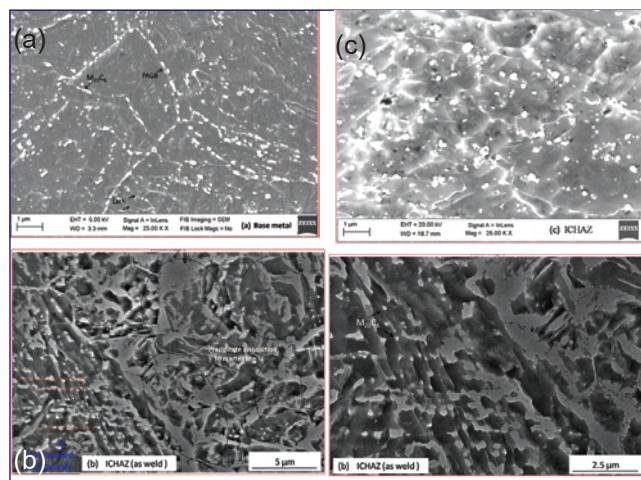


Fig. 2 Microstructure of (a) base metal, (b) ICHAZ in the as-weld condition depicting the partial transformation to austenite and untransformed martensite upon heating during weld thermal cycle, and (c) ICHAZ in the PWHT condition

heterogeneity in deformation behavior between the regions ultimately resulted in the premature failure of the joint by localized deformation and creep cavitation in the ICHAZ due to microstructural heterogeneity within the ICHAZ, and acceleration of deformation constraint/damage contributed by the adjacent stronger regions in the weld joint. The higher equivalent strain assist in cavity nucleation and constraint of plasticity assists cavity growth. Grain boundary sliding to accommodate the constraint relaxation process leads to higher number of cavities in the region having higher number of grain boundaries (ICHAZ), resulting in loss of creep rupture strength of the actual A-TIG joint at 923 K for a life of about 10^4 h by about 30% as compared to the base metal.

The P91 steel in the NT condition exhibited prior austenite grain size (PAG), lath width and $M_{23}C_6$ precipitate of sizes about 20 μm , 700 nm and 100 nm, respectively. MX precipitates were predominantly observed in the intra-lath region, which provides strength to the steel by impeding the movement of dislocation; $M_{23}C_6$ precipitates along the PAG and sub-grain boundaries were observed, which strengthen the boundaries through restricting the migration by pinning (Figure 2). The microstructural features, viz, PAG size, $M_{23}C_6$ precipitates size in different regions across the PWHT joint varied significantly (Figures 3 and 4). Finer grain size, coarser $M_{23}C_6$ precipitates, and more extensive subgrain formation with reduction in dislocation density were observed in the ICHAZ as compared to

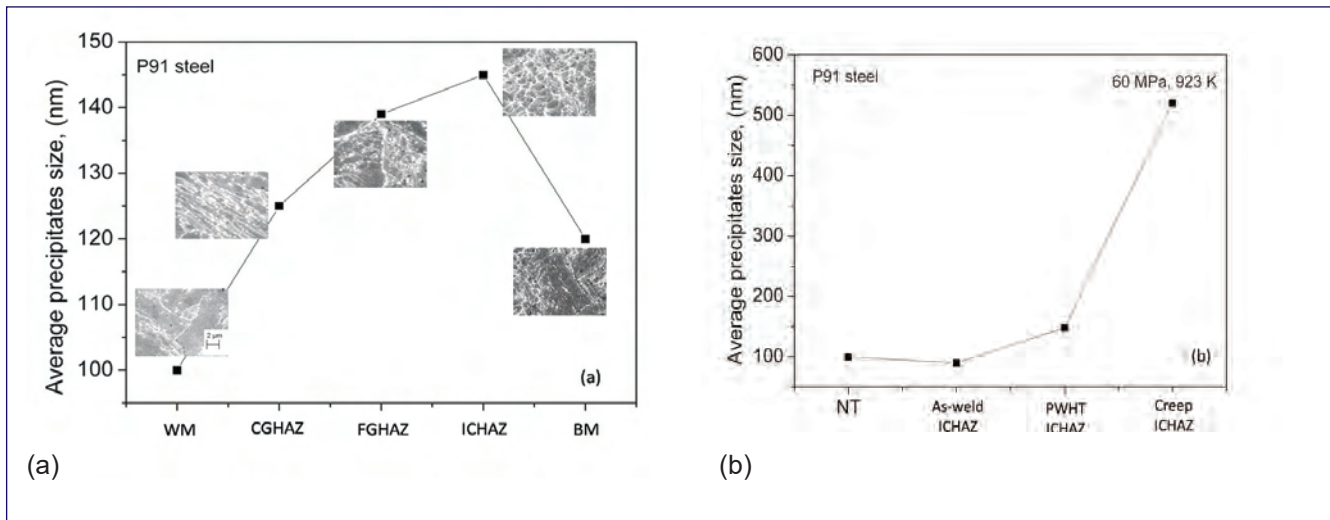


Fig. 3 Variation of $M_{23}C_6$ precipitates size across the (a) PWHT weld joint and (b) ICHAZ at different condition in the P91 steel joint

other regions in the joint. Partial dissolution of $M_{23}C_6$ precipitates during welding was observed in the ICHAZ (Figures 2 and 3). Undissolved precipitates in the ICHAZ during welding were further coarsened during PWHT. Coarsening of $M_{23}C_6$ precipitates after PWHT was higher in the ICHAZ as compared to that of base steel in the pre-weld conditions (Figure 3). In addition to significant coarsening of precipitates during welding, boundaries decorated by the particles were lost due to α to γ transformation and migration under very high temperature in the ICHAZ. Transformation of α to γ upon heating, and γ to α' on cooling and dissolution of $M_{23}C_6$ precipitates were also observed in the ICHAZ (Figure 2), where precipitation of $M_{23}C_6$ precipitates occurred subsequently during PWHT. EBSD inverse pole figure (IPF) Z-map superimposed with low and high angle grain

boundary map revealed the presence of significantly finer grain structure composed of coarser substructure (equiaxed structure from elongated lath structure) in the ICHAZ than in the WM, CGHAZ, FGHAZ and BM (Figure 4). The fractions of CSL boundaries ($\Sigma 3$, $\Sigma 11$ and $\Sigma 25b$) were noticed to be lower in the ICHAZ region than in other regions in the joint. CSL boundaries improve the creep strength by minimizing the boundary sliding in the steel. Heterogeneity in strain distribution is higher in the ICHAZ than the other regions in the joint. In addition to the heterogeneous combination of softer and more strain region, the boundary dislocation density and precipitates are higher in the ICHAZ region. The presence of more precipitates without pinning the boundary is not much useful for long term creep. Also, presence of more dislocations due to lower martensite start temperature contributed by local increase in chromium due to dissolution of precipitates and smaller prior austenite grain size in ICHAZ. The low chromium and carbon content near the undissolved precipitates region results in martensite structure with low dislocation density, which further softened during post weld heat treatment. Under short term creep and at lower test temperature, softer regions might contribute to strengthening by work hardening under applied stress, resulted in base metal failure in the WJ. Increase in temperature and reduction in applied stress restricts the advantage of work hardening of soft regions of the ICHAZ, concurrently harder regions containing dislocation structure tend to recover, which ultimately leads to loss in strength at high temperature (Fracture at ICHAZ of WJ). Elimination or reduction of heterogeneity in microstructural constituents across the weld joint would enhance the creep rupture strength of the weld joint as compared to its base metal.

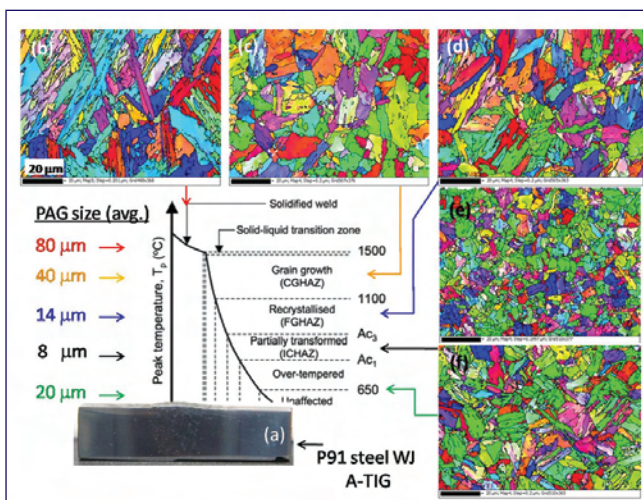


Fig. 4 (a) A-TIG weld joint of P91 steel, EBSD-IPF map across the (b) weld metal, (c) coarse grain, (d) fine grain, (e) inter-critical region, (f) base metal

III.32 Assessment of Mechanical Properties of Creep exposed Modified 9Cr-1Mo steel using Small Punch Technique

The conventional mechanical test methods for determining tensile, creep, fatigue and toughness properties are practically difficult when material availability is limited in situations such as weld joints, coatings, exotic or new alloys, failed or service exposed components and radioactive materials. In such situations, use of alternative test methods using specimen sizes much smaller than the standard test specimens are promising. The small punch (SP) test is one such small specimen test technique to determine the mechanical properties of material such as yield strength (YS), ultimate tensile strength (UTS) and fracture toughness using specimen sizes of typically 8.0 mm diameter and 0.5 mm thickness. In SP test (Figure 1), the specimen clamped between a set of dies, is deformed using a spherical punch to failure and the load-displacement curve (Figure 2) recorded during specimen bulging is analyzed for yield stress, maximum stress and energy to fracture. One of the attractive features of SP test is its capability to detect a transition temperature (T_{SP}) corresponding to a shift from ductile to brittle fracture of ferritic steels with decreasing temperature, similar to DBTT (ductile-to-brittle transition temperature) of conventional Charpy V notch (CVN) impact test. The SP experimental setup and test methodologies together with finite element modeling have been developed at author's laboratory and put to use for various applications. A code of practice for SP test procedures and analysis methodologies (CWA15627) was formulated by European Committee for standardization in 2007 and recently ASTM has published a standard (E3205-20) for SP test, evolved through round robin test exercise, in which IGCAR was also a participant.

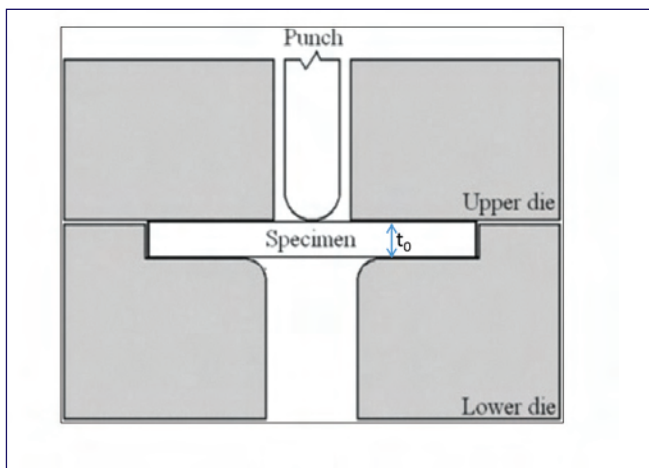


Fig. 1 Schematic of small punch loading configuration

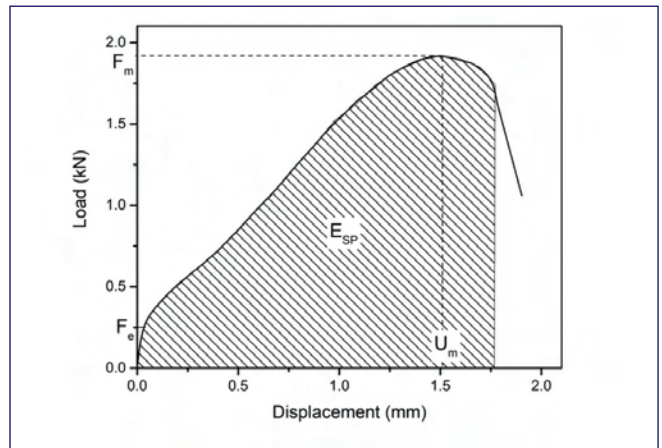


Fig. 2 Typical load-displacement curve of SP test

Small punch test technique has been employed to evaluate the changes in mechanical properties of mod 9Cr-1 Mosteel caused by creep exposures. This steel, a candidate material for fast reactor components and for piping/tubing of fossil fired power plants, under creep exposure above 600°C experience microstructural degradation leading to loss of mechanical strength. Several researchers have employed non-destructive techniques such as replication metallography, measurements of strain, hardness, electrical resistivity and ultrasonic velocity to monitor the creep damage in service exposed components. However, quantification of mechanical properties after creep exposure is very sparse primarily due to the limitation of volume of materials available for tensile or impact tests. Alternatively, small punch test requiring small volumes of material lends itself for such a quantification.

The different creep exposed micro structural conditions

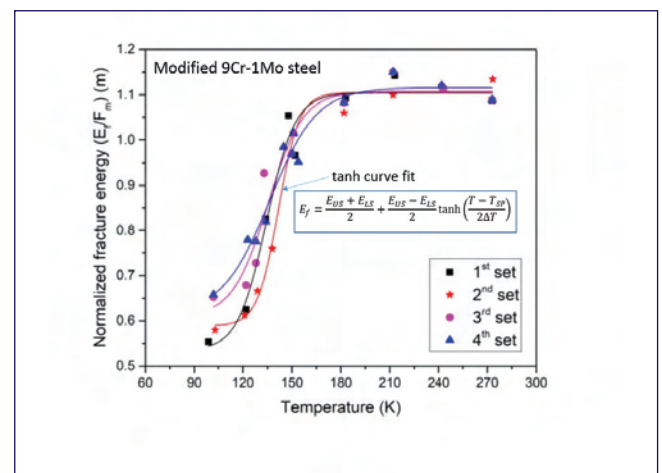


Fig. 3 Fracture energy vs temperature

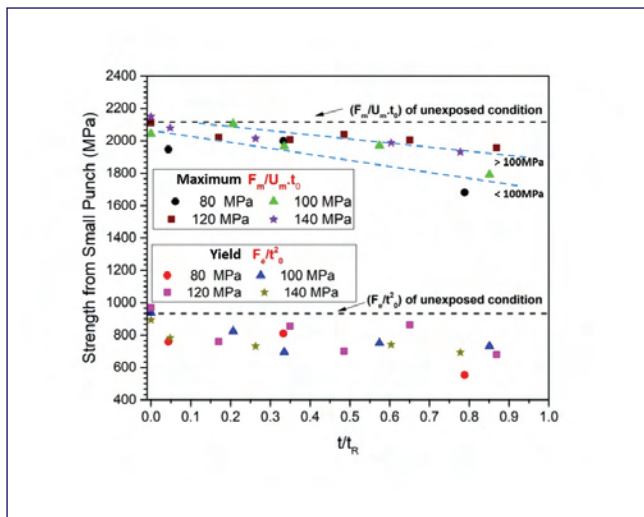


Fig. 4 Plot showing the decrease in strength of SP tests with TSP estimated using tanh fit parameters with increasing t/t_R

were experimentally generated by conventional creep testing of mod 9Cr-1Mo steel at 650°C under stress levels of 80-140 MPa and interrupted at various time fractions of rupture life (t_R). The gage portion of the creep exposed samples corresponded to aging under both temperature and stress. Disc specimens (8.0mm diameter and t_0 :0.5 mm thick) extracted from gage portions of various creep exposed conditions were tested in SP loading configuration using a screw-driven universal test machine (UTM) fitted with an environmental chamber. With 12-16 specimens required to generate the fracture energy-temperature curve (Figure 3) for evaluating T_{SP} , a total of over 300 SP

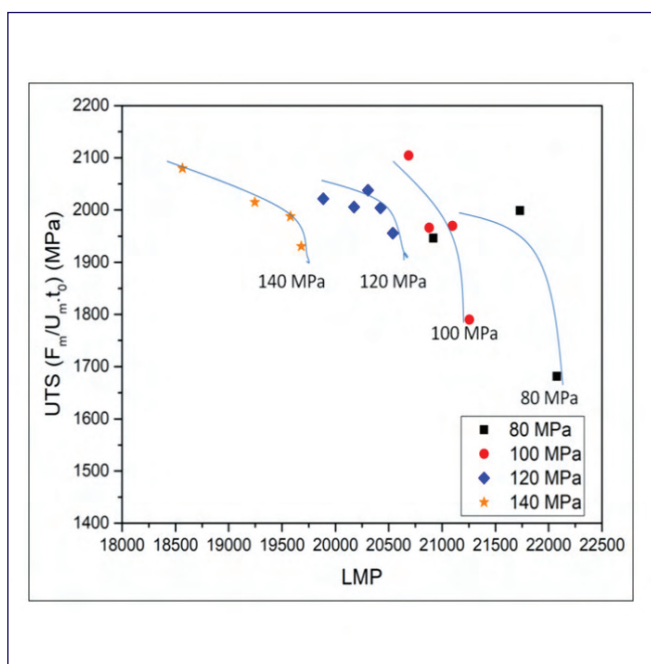


Fig. 5 Maximum strength from SP test as a function of LMP showing larger decrease for lower creep stress

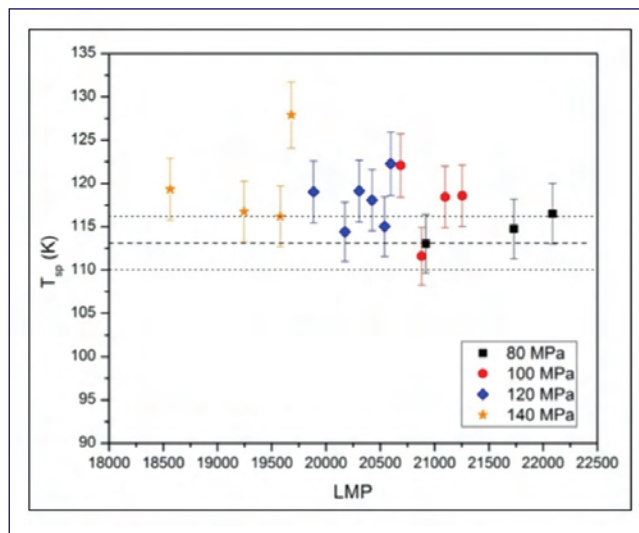


Fig. 6 Transition temperature (T_{SP}) as function of LMP showing negligible changes due to various creep exposures

tests were conducted in the temperature range (-)196°C–0°C for various creep exposed conditions. The strength parameters ($YS \sim A F_e/t_0^2$, $UTS \sim B F_m/t_0 \cdot U_m$, A & B- constants) were determined from load-displacement data and T_{SP} estimated by curve fitting ('tanh' function) of the sigmoidal fracture energy-temperature curve (Figure 3) for various creep exposures.

The plot of YS and UTS for various stressed conditions (Figure 4) as a function of creep life fraction (t/t_R) reveals progressive strength decrease with increasing t/t_R , with extent of strength decrease being higher for low creep stress exposures (80 MPa and 100 MPa) compared to that of high creep stress (120 MPa & 140 MPa). This is also reflected in the plot of UTS (Figure 5) with Larson Miller Parameter ($LMP = T(20 + \log t)$, T is temperature in Kelvin and t is time in hours) signaling a shift in the softening trend beyond creep stress of 100 MPa. The transition temperature of small punch (T_{SP}) plotted against LMP (Figure 6) however showed no appreciable change or shift due to the creep exposures at 80 MPa-140 MPa.

It is concluded that creep exposures in mod 9Cr-1Mo steel at 650°C has a significant effect on yield strength and ultimate tensile strength, while their effect on ductile-brittle transition temperature for creep exposures at 80 MPa-140 MPa for durations of 3h-8500 h is insignificant. These findings can be extended to the study of irradiated 9Cr-1Mo steel for decoupling the effects of creep exposures and neutron damage on strength changes and shifts in DBTT. This study demonstrates that small punch technique is very promising for evaluating the current state of damage in service exposed plant components using small coupons extracted from the component in a minimally invasive manner.

III.33 Air Oxidation of 9Cr-1Mo Steel: Depth Profiling of Oxide Layers using Glow Discharge Optical Emission Spectrometry

Modified 9Cr-1Mo steel is used as a steam generator tube material of fast breeder reactors. Although air oxidation behavior of modified 9Cr-1Mo steel is qualitatively studied, the exact nature of oxide layers formed across the thickness of the film from nanometer to several microns depth is not studied systematically. In this work, the oxide scales formed on modified 9Cr-1Mo steel on air oxidation at 650°C up to 200 hrs duration using Glow Discharge Optical Emission Spectrometer (GDOES) with depth profiling, X-ray Diffraction (XRD), Laser Raman Spectroscopy (LRS) and Scanning Electron Microscopy coupled with Energy Dispersive Spectroscopy (SEM-EDS) were investigated.

The weight gain of modified 9Cr-1Mo as a function of the oxidation durations varying from 25 to 200 hrs was recorded. Initially, the weight gain was low upto 50 hrs, but the weight gain was significant at higher exposure duration. Overall, the weight gain increases continuously up to the total duration of oxidation, 200 hrs. Figure 1 shows the surface morphology of the oxidized samples for 25, 50, 100 and 200 hrs durations, respectively. Very dense oxide globules with different morphologies formed all over the surface of the samples. As the time of oxidation increased the size of the oxide globules increased by coalescing.

The SEM and XRD analysis provides the qualitative information of the oxides formed. In contrast, the GDOES allows a qualitative interpretation of the elemental distribution throughout the oxide scale as a function of depth. In addition to the detection of light elements like O, the information obtained from GDOES is more quantitative than SEM-EDS. Besides, the time

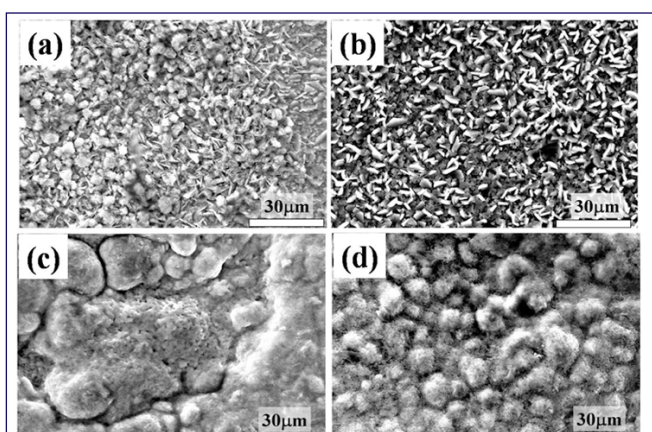


Fig. 1 SEM images of modified 9Cr-1Mo oxidized at 650°C in air for 25 hrs (a), 50 hrs (b), 100 hrs (c) and 200 hrs (d)

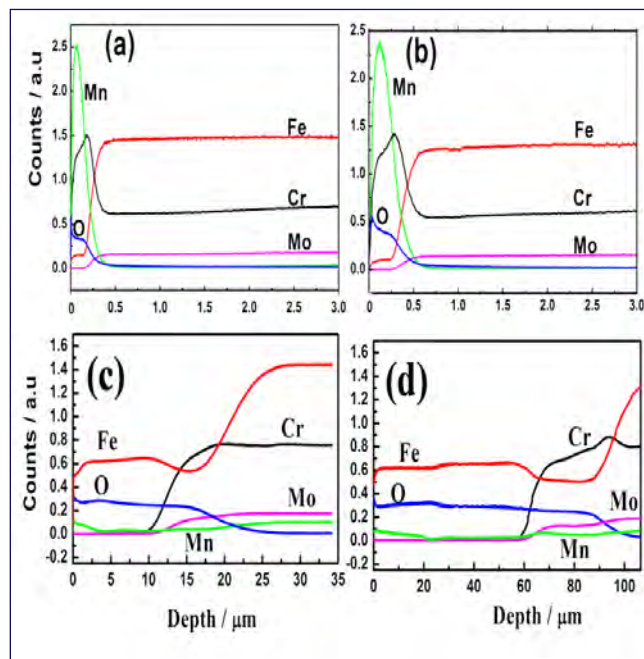


Fig. 2 GDOES depth profiles of air oxidized modified 9Cr-1Mo steel at 650°C; (a) 25 hrs and (b) 50 hrs, (c) 100 hrs and (d) 200 hrs.

required for GDOES analysis is less compared to SEM-EDS technique. The GDOES analysis was carried out throughout the thickness of the oxide scales. The top layer for the 25 and 50 hrs oxidized samples (shown in Figure 2a and 2b) indicated the presence of Cr, Fe, O and Mn without Mo, evidencing the formation of a multi oxide layer during air oxidation at shorter durations. Figure 2 (c)&(d) provides the GDOES depth profiles of the oxidized steel for 100 and 200 hrs. At the top surface of the oxide layer; a plateau observed for Fe, indicating that thick Fe based oxides. Beneath this Fe rich oxide layer, Fe reduces and Cr and Mo intensities enhanced at the oxide/alloy interface indicating the presence of multi component oxides of Fe, Cr and Mo. Using GDOES depth profiles the oxide layers thickness was found to be 230 nm, 370 nm, 21 μm and 96 μm, respectively for 25 to 200 hrs durations. The top layer of oxide scales of 25, and 50 hrs oxidation consists of $MnCr_2O_4$, Cr_2O_3 and Fe, Cr spinel oxides; however, the oxide scales of 100 and 200 hrs samples mainly consist hematite as evidenced by GDOES, XRD and LRS analysis.

GDOES technique, along with DiP (depth profiling) providing a better understanding to the multi-component oxide scale profile was demonstrated.

III.34 Threshold Displacement and Defect Formation Energies of $Y_4Zr_3O_{12}$ and its Implication in Radiation Stability of Zr and Al-containing ODS Alloy

There is an increased demand for highly radiation tolerant and corrosion resistant structural materials for core nuclear reactor applications. Ferritic steels which have high incubation dose for void swelling are considered to be better than austenitic stainless steels in nuclear core structural material applications. But ferritic steels are limited by their inferior high temperature strength. Oxide dispersion strengthened (ODS) ferritic steels, with high density of thermally stable and radiation resistant dispersoids are observed to have high creep resistance along with radiation tolerance in reactor operating temperature and dose range. Typical ODS steels containing Y–Ti–O dispersoids are found to be stable up to 150 dpa at 700 °C. Recently, there has been renewed interest in Al containing Oxide Dispersion Strengthened steels due to their enhanced corrosion resistance in super critical water and lead bismuth eutectic environments. However, upon addition of Al, fine (2-10 nm) titanium rich Y- Ti – O complexes of Ti-ODS, which are mainly $Y_2Ti_2O_7$ or Y_2TiO_5 get replaced by coarse (20 – 100 nm) Y – Al – O complexes and this deteriorates the ultimate tensile strength of the steel. Addition of Zr refines the size of precipitates in Al containing alloys to the desired size range of 2-10 nm. The nanoparticles in Zr and Al containing ODS steels are identified to be rhombohedral δ - $Y_4Zr_3O_{12}$. The radiation tolerance of ODS alloys hinges on the radiation stability of the dispersoids.

The $Y_4Zr_3O_{12}$ belongs to a class known as delta (δ) phase ($A_4B_3O_{12}$, $R\bar{3}$), which is an oxygen deficient fluorite derivative structure ($A_2B_2O_{8-\delta}$, A^{3+} and B^{4+} are rare-earth or transition metal species) like cubic pyrochlore

($A_2B_2O_7, Fd\bar{3}m$), disordered fluorite ($A_2B_2O_7, Fm3m$), and monoclinic pyrochlore ($A_2B_2O_7, P2_1$). These structures are also well known for their exceptional radiation tolerance and phase stability at elevated temperatures. Upon irradiation, most of the pyrochlores transform to a disordered fluorite structure before they are fully amorphized. The critical amorphization doses are less than 1 dpa for titanate pyrochlores. Zirconate pyrochlores are more radiation resistant than titanate pyrochlores. However, there are only a few studies discussing the radiation stability of delta (δ) phase compounds. The threshold displacement energy (TDE), which is the most fundamental quantity governing the creation and evolution of radiation cascade in a material is widely used to estimate the number of Frenkel pairs an energetic primary knock-on atom (PKA) generates in a material. Thus calculating the threshold displacement energies of $Y_4Zr_3O_{12}$ is the primary step in understanding the radiation response of these compounds. This provides new insights into the radiation behavior of Zr and Al containing ODS alloys also.

The phase $Y_4Zr_3O_{12}$ belongs to space group $R\bar{3}$ with inversion triad along [111] direction of the rhombohedron. It has two ordered structural vacancies in 6c positions along its inversion triad. Oxygen occupies two sets of 18f general positions. Both sets of oxygen form two octahedra, one being centered at body centre (denoted as O) and the other (denoted as O') at 3a cation. Consequently, the cation in 3a position is co-ordinated to six oxygen atoms and that in 18f positions are co-ordinated to seven oxygen atoms. Further, *ab-initio* molecular dynamics (AIMD) calculations to determine

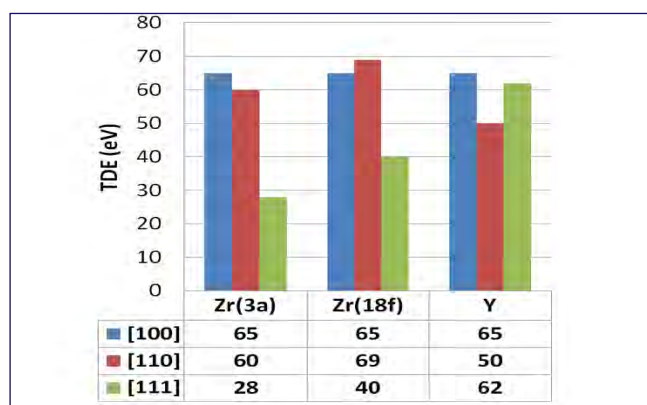


Fig. 1 The threshold displacement energies of cations in $Y_4Zr_3O_{12}$, calculated using AIMD simulations

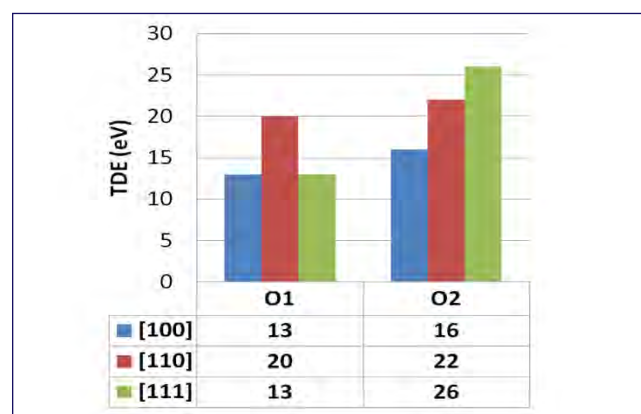


Fig. 2 TDE of two types of oxygen of $Y_4Zr_3O_{12}$

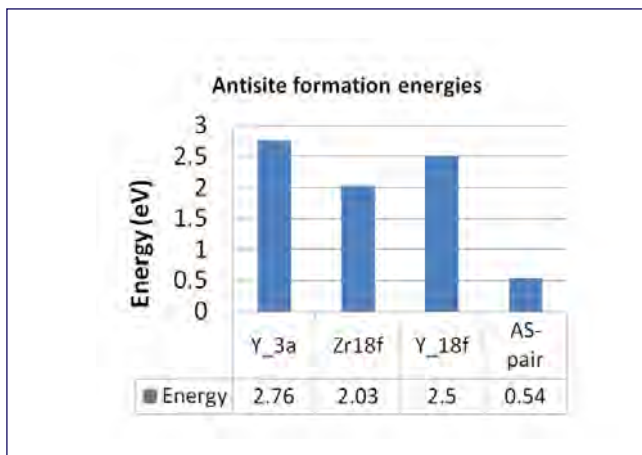


Fig. 3 Calculated antisite formation energies of $Y_4Zr_3O_{12}$

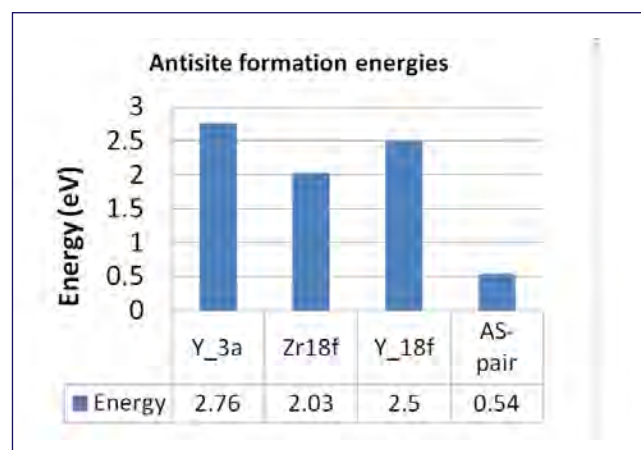


Fig. 4 Frenkel pair formation energies of $Y_4Zr_3O_{12}$ for different Frenkel-pair configurations

the TDE of anions and cations in $Y_4Zr_3O_{12}$ are carried out in an orthogonal supercell containing 456 atoms constructed from a rhombohedral unit cell using the transformation matrix $(-2, 1, 2; 2, 1, 2; 0, -2, 2)$. After equilibrating the supercell at 300 K for 3000 time steps (300 fs), an atom (Zr_{3a} , Y_{18f} , Zr_{18f} or O_{18f}) is chosen as primary knock on atom (PKA) and energy is given to it in three main crystallographic directions. The atom trajectories are traced for at least 2 ps. If the PKA is not returned to its original position after the end of simulations (2 ps) it is assumed to be a displaced atom. The calculated TDEs for cations and anions are summarized in Figures 1 and 2 respectively. The minimum E_d values of $Y_4Zr_3O_{12}$ are found to be 28 eV for Zr_{3a} PKA, 40 eV for Zr_{18f} and 50 eV for Y recoils.

For O and O' minimum values are 13 eV and 16 eV respectively. Zr_{3a} , Zr_{18f} and O have the least E_d values along [111] direction. Yttrium has a minimum E_d along [110] direction and O' has a minimum value along [100] direction. In all directions except the direction in which the inherent structural vacancy is aligned, the cations tend to occupy another cation site. Anions have a tendency to stabilize at a vacant 6c site. The body centre position inside anion octahedron also is a stable site for Zr cation. A material with high displacement energy is expected to have higher radiation tolerance because of smaller number of initial defects upon irradiation. The calculated values of TDEs of anions and cations in $Y_4Zr_3O_{12}$ are similar to previously reported values of $Gd_2Zr_2O_7$, which is the most radiation resistant pyrochlore (Figures 3 & 4).

III.35 Atomistic Simulation on Formation of Stacking Fault Tetrahedra due to Irradiation in FCC Metals

Stacking fault tetrahedra (SFT) are three dimensional defects commonly observed in FCC metals and alloys, when subjected to plastic deformation, irradiation by energetic particles and quenching from high temperature. A typical SFT consists of six stair-rod dislocations with Burgers vectors of $b = \frac{a}{6} [110]$ along the edges of tetrahedron bounded by triangular stacking faults on four equivalent $\{111\}$ planes. These SFT are highly stable and act as an obstacle to dislocation glide causing work hardening during deformation, embrittlement and plastic instabilities during irradiation. Hence, it is crucial to understand the mechanism of formation of SFT during irradiation as they play an important role for failure of materials.

In case of irradiation, defects such as vacancies and interstitials are produced in pairs. The vacancies aggregate via diffusion forming clusters, voids and triangular vacancy platelet. In this report, atomistic MD simulation has been carried out to study the evolution of SFT from both triangular platelet of vacancies and random vacancies with or without involvement of Frank loop in case of low stacking fault energy Ag and an intermediate stacking fault energy Ni metals. The results are visualized by common neighbor analysis (CNA) and analysed by dislocation extraction algorithm (DXA) methods.

To demonstrate the formation of SFT by Silcox-Hirsch mechanism with involvement of Frank loop from triangular

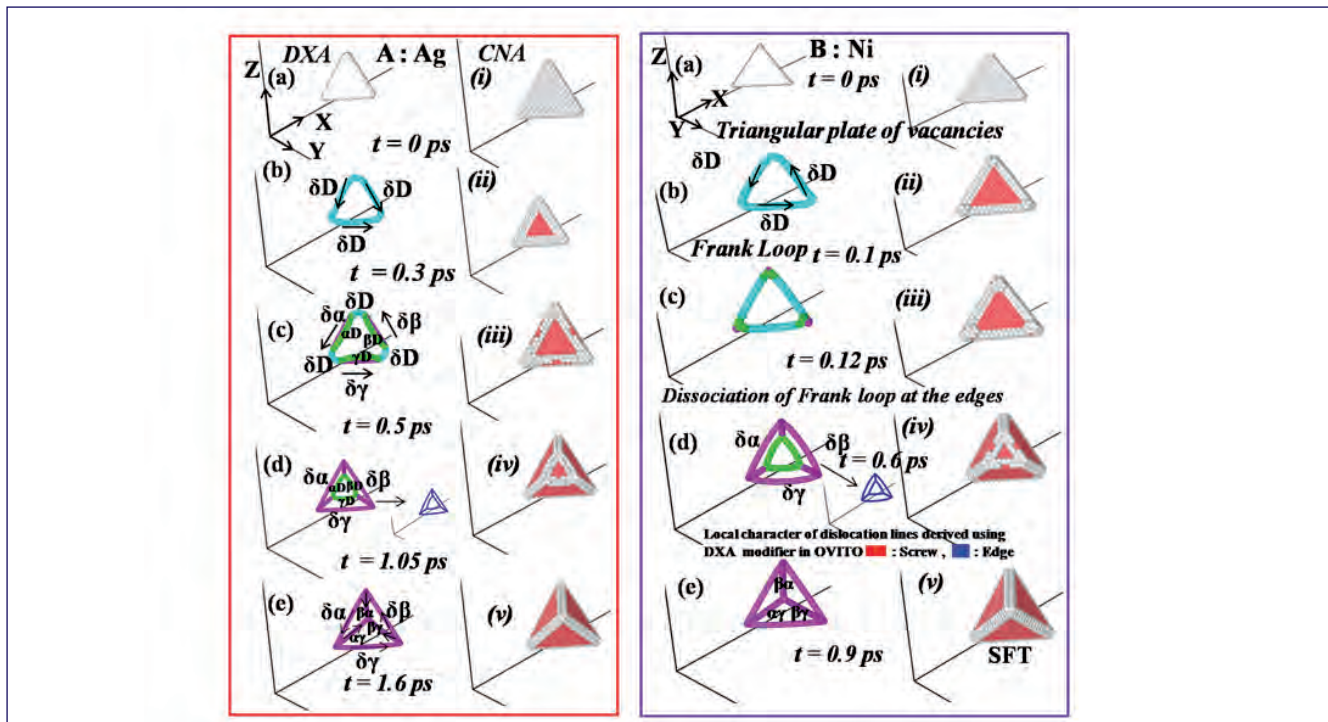


Fig. 1 Atomic snapshots at different times by DXA (a-e) and CNA (i-v) methods to show the step wise evolution of SFT via Silcox-Hirsch mechanism in case of (A) Ag and (B) Ni respectively. Shockley partial dislocation, Stair-rod dislocation and Frank partial dislocation are represented in green, magenta and cyan colours respectively in DXA method. Atoms in red and white colour are hexagonal close packed (HCP) atoms and other atoms, respectively in CNA method

vacancy platelet at low temperatures, Ag and Ni unit cells (20x20x20) containing 32000 atoms are created. A triangular platelet containing 120 vacancies was created by removing 15 atoms on each edge in (111) plane. It is evident from the Figure 1 that the triangular platelet of vacancies collapses to a Frank loop (δD) with Burgers vector $\frac{a}{3}[\bar{1}\bar{1}\bar{1}]$ in both Ag and Ni at 0.3ps and 0.1 ps respectively. The three edges of the loop dissociate into stair-rod and Shockley partial dislocations. The edge part of leading Shockley partials move towards the apex of the tetrahedron to produce four Stacking faults on {111} planes and six stair rods ($\delta\gamma, \delta\beta, \delta\alpha, \alpha\gamma, \beta\gamma$ and $\beta\alpha$) of Burgers vectors $\frac{a}{6}\langle 110 \rangle$ along its edge.

To simulate SFT from random vacancies, the system (Ni) was maintained at a high temperature of 1000K

using NPT ensemble and Nosé-Hoover thermostat. The vacancies represent an individual entity at the beginning of simulation and start to cluster with time as shown in Figure 2. Two defect clusters were produced at 0.005 ns due to vacancy diffusion. One of the defect clusters collapses to Frank loop and the other one forms a truncated SFT at 0.215 ns. The defect cluster collapsing to Frank loop was found to be unstable at such a high temperature and could not form SFT via Silcox-Hirsch mechanism. These simulations can be correlated experimentally to the formation of single vacancies produced under irradiation at different temperature, which then form clusters of any number of vacancy atoms. These clusters evolve to SFT by void collapsing without going through the Frank loop as evident from Figure 2.

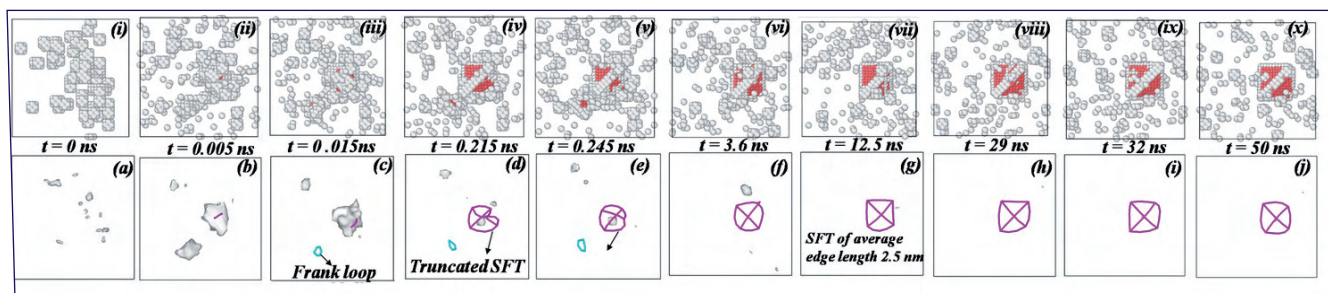
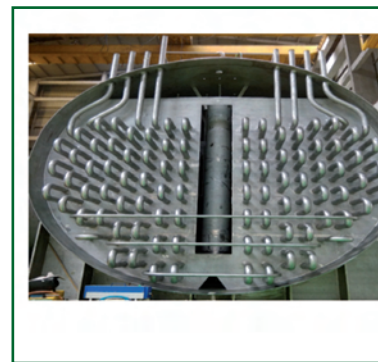
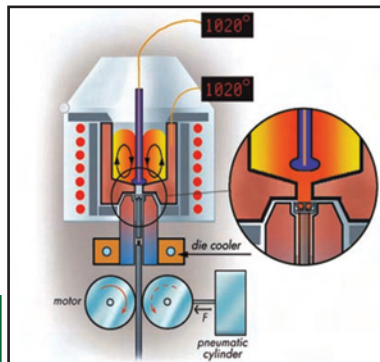
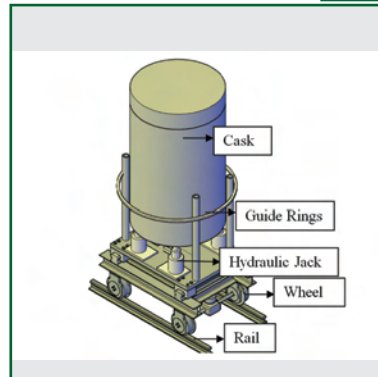


Fig. 2 Atomic snapshots at different time to illustrate the formation of SFT during the evolution of vacancies in case of Ni at temperature of 1000 K. Two sets of images (a-j) and (i-x) represent the atomic snapshots obtained from MD simulations by DXA and CNA methods. Cyan line and magenta line represent Frank partial dislocation and stair-rod dislocation respectively.



CHAPTER IV

Fuel Cycle

IV.01 Fast Reactor Fuel Cycle Facility - Current status

Fast Reactor Fuel Cycle Facility (FRFCF) is being built with the objective of closing the fuel cycle and ensuring sustained fuel supply for Fast Breeder Reactors (FBRs) at Kalpakkam. FRFCF is a multi-unit mega project of DAE, co-located along with PFBR and being built in coordination with BARC, IGCAR & NFC. FRFCF is an integrated facility housing five major plants in the nuclear island for carrying out reprocessing, fuel fabrication, assembly and waste management. Construction was commenced after obtaining all the statutory clearances and regulatory approval.

In the infrastructure area, Construction of Utilities and Service buildings such as Central Surveillance Safety & Health Physics Building, Central Workshop, Diesel Generator Building, Centralized Water Chilling Plant, Air Compressor Building and Fuel Oil Storage building have been completed. Infrastructure buildings such as Administration Building, Training Centre and Central Stores Buildings have also been completed. Gold rated Green Building Certificate from Indian Green Building Council (IGBC) has been received for the Training Centre of FRFCF, the first Green building in DAE.

In the nuclear island, civil construction works of nuclear plant buildings are progressing well. Civil construction of Solid Waste Management Building has been completed whereas civil construction of Core Sub-assembly Plant (CSP) (Figure 1a), Reprocessed Uranium Oxide Plant (RUP), Plant Water Pump House & Delay Tank are in the advanced stages of completion. Civil construction of Waste Management Plant (WMP) (Figure 1b) building Zones-4 & 5 have been structurally completed and the other zones have reached (+) 6.0 m elevation. Core Sub-assembly Plant (CSP), Reprocessed Uranium Oxide Plant (RUP), Fuel Fabrication Plant (FFP), Fuel Reprocessing Plant [FRP] (Figure 1c) have reached (+) 19.0 m, (+) 5.0 m, (+) 4.5 m & (+) 3.5 m elevation respectively. Construction of 60 m tall RCC stack for FFP, RUP & CSP has been completed.

Major pours involving placement of temperature controlled concrete have been undertaken to expeditiously complete civil construction. Cumulative concreting of about 4.93 Lakhs cubic meters has been completed for structural components such as raft, footings, columns and tie beams, with concurrent engineered soil backfilling of about 30.2 lakhs cubic meter. All the 10 numbers of pours of heavy density concreting of around 7280 cu.m for Waste Tank Farm [WTF] Slab of FRP Block-1 have also been completed.



Fig. 1 (a) Core sub-assembly plant, (b) waste management plant, (c) fuel reprocessing plant, (d) 200 ton compactor and (e) ion chromatograph

All the 14 numbers of large sized Over-Dimensional Consignment (ODC) waste tank farm storage tanks with a total of 16 km piping inside have been manufactured, received and are being erected in the FRP. Bulk raw materials such as stainless-steel plates, rounds for fabrication of process vessels and radiation shielding lead components have been received at FRFCF site. Process tanks and Special quality Stainless Steel pipes required for in-cell piping applications are being received at FRFCF Project site progressively.

First group of radiation shielding optical glass slabs required for fabrication of radiation shielding windows has been received at FRFCF site and fabrication of the second group of optical glass slabs is in progress. Several equipment viz. master slave manipulators, lead bricks, annular tanks, differential pressure transmitters etc., are being received at FRFCF site in a phased manner. WMP equipment such as Centrifugal fans, Dilution Hot Cell System, 200 MT capacity Compactor (Figure 1d), Isolation Dampers of Ventilation System & Electrical System Panels have been received at FRFCF site.

All the equipments pertaining to Analytical Certification Laboratory of FFP such as Ion chromatograph (Figure 1e), thermogravimetry, ED-XRF and surface area analyser have been received, installed and commissioned. Procurement of MOX fuel fabrication equipments for first process stream of FFP is completed and Glove box integration of equipment for Analytical Certification Laboratory is in progress.

Installation & commissioning of Fire Detection & Alarm System and Plant Communication System in infrastructure buildings has been completed. Procurement of area gamma & wide gamma monitors, criticality alarm systems, network switches and other I&C components are in progress.

IV.02 Design, Development & Mockup of the Hull Tilting System for Chopped Radial Blanket and Fuel Subassembly Pins of PFBR for Fast Reactor Fuel Cycle Facility

In the reprocessing of the used nuclear fuel, after the dissolution of the fuel meat, the clad tube and the spacer wire are left behind along with the insoluble residue. These constitute the major portion of the solid waste discharged from the reprocessing plant. Due to the residual radioactivity present in the hulls due to both the activation products and the insoluble radioactive residue, these need to be safely transported and disposed of as solid waste. The preliminary step towards this is the separation of the washed hulls from the dissolver solution. These need to be loaded into a container called the hull basket for monitoring the residual activity. The dissolution is usually carried out in a batch mode. After every batch of dissolution, the hulls from the hot cell that houses the chopper are transferred through a connecting chute to a buffer cell. This transfer is accomplished through a special device called the hull tilting system (HTS). One such “first-of- its-kind” system has been designed to handle the hulls discharged after dissolving the fuel blanket (obtained from the Radial (blanket) Sub-Assemblies (RSA) to be handled at the Fuel Reprocessing Plant at the Fast Reactor Fuel Cycle Facility (FRFCF). The important components of the HTS are the cage, locking plate, support hinges, electrical actuator / gear box with motor and its associated instrumentation (Figure 1).

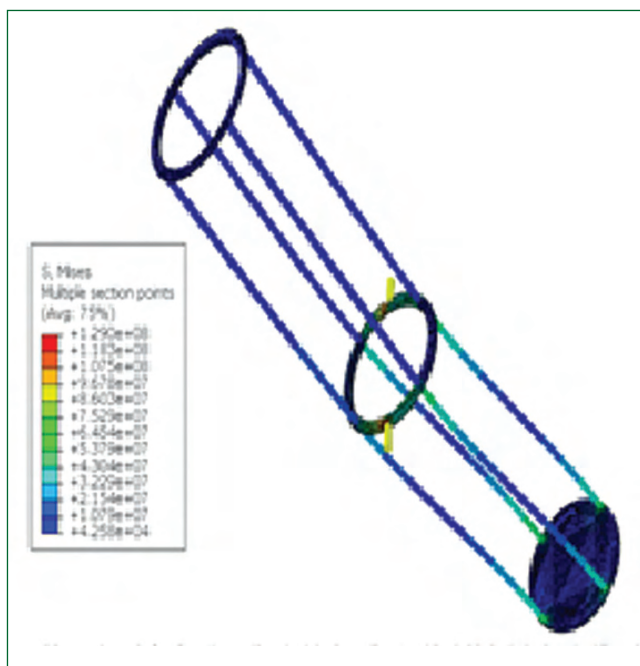


Fig. 1 Stress analysis of cage due to self-weight

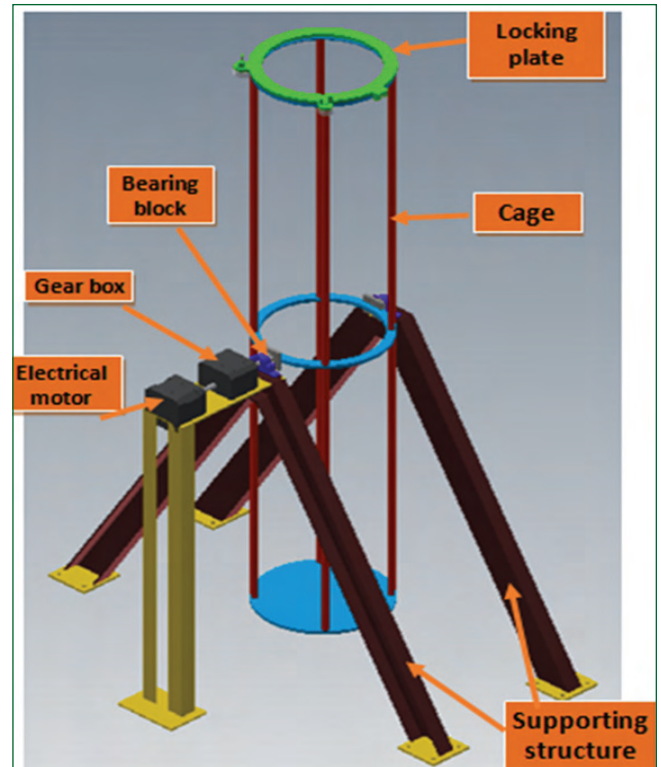


Fig. 2 GA drawing of HTS

A basket carrying the hulls is lifted, positioned and lowered into the cage of HTS vertically (Figure 2). Subsequently the cage is tilted to transfer the hulls into the chute. A special mechanism with a prismatic joint has been provided to tilt the cage. An electrical actuator / gear box with the motor was chosen for the drive for tilting the entire assembly. After inserting the basket into the cage, it would be locked with the upper flange through a remote operation carried out with the help of a master slave manipulator.

The key prerequisites of the above mechanism that had to be designed in-house are the following.

Ø The component had to be designed with close tolerances and yet should enable facile assembly and dismantling.

Ø Special attention needs to be paid to the materials of construction, keeping in view both their strength and resistance to corrosion.

In addition, the HTS had been designed to suit the space available within the hot cells housing it. A detailed review to analyze its integrity and suitability for remote handling has also been carried out.

IV.03 Design and Analysis of Vertical Cask with Electrically Operated Trolley for Transportation of Hexagonal Wrapper of FSA and RSA from FRP/FRFCF to WMP

The used fuel discharged from the nuclear reactor has to be transported safely and in conformity with the regulations pertaining to transport of radioactive material. A special shielded container called the cask is often used for this purpose. These casks are usually held in the horizontal position during both handling and transportation. In the context of PFBR, two different kinds of used fuel subassemblies would be discharged. These are the Fuel Sub-Assemblies (FSA) and the Radial Sub-Assemblies (RSA). To suit the provisions at the site, it has become necessary to transport these SAs through a cask that needs to be held vertically. Hence a vertical cask has been designed for transportation of hexagonal wrapper of the FSA and RSA from the Fuel Reprocessing Plant (FRP) to the Waste Management Plant (WMP), both co-located at the Fast Reactor Fuel Cycle Facility (FRFCF) site. Different key aspects pertaining to its design, viz., classification, structural integrity, leak tightness, facile decontamination of its exterior surface, provision for water draining etc. have been taken into consideration while optimizing the design. Further, the integrity of this cask has to be practically demonstrated through an actual drop test from a specific height as prescribed by the regulators.

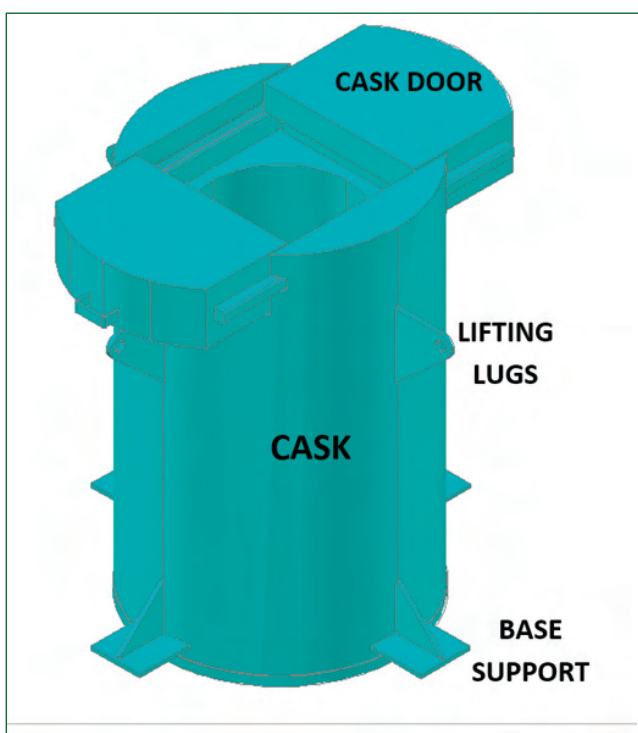


Fig. 1 Conceptual design of the dolly

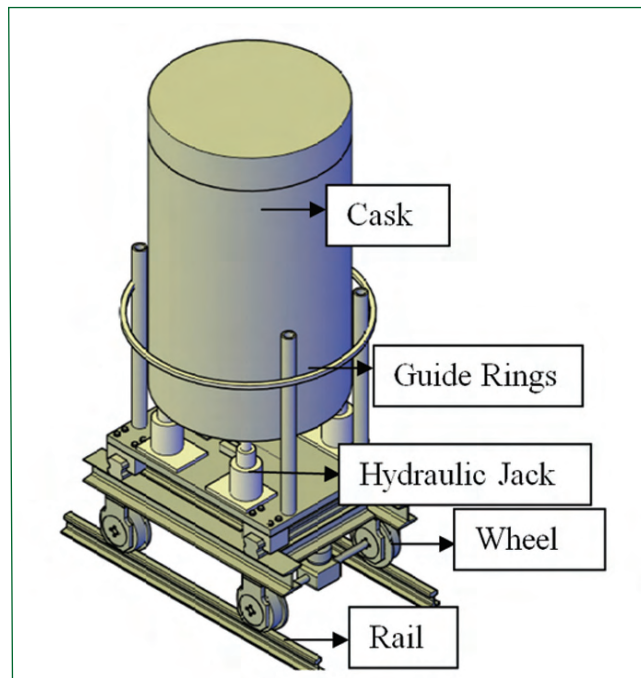


Fig. 2 The cask with the dolly used in the thermal FEA simulation

In addition, an electrically operated trolley weighing about 25 tons has also been designed and its suitability for transportation of the cask has also been analyzed. Many different design estimations and choice of the components had also been made. These include the driving effort & torque, selection of an appropriate gearbox, bearing, motor, wheels, chain and sprocket and pinion. This “vertical cask” is a first of its kind component to be designed and deployed.

Important requirements

- Ø The alignment of this cask with its corresponding transfer port located on the hot-cell is a prerequisite through which the radioactive hulls need to be transferred to the hull basket
- Ø The design of this cask had been completed with appropriate fits and tolerance to enable easy assembling and dismantling of its constituent components
- Ø The materials of construction of all the parts were chosen keeping in view their strength as well as corrosion resistance

The analysis of the cask thus designed has been carried out by using finite element method (FEM).

IV.04 Campaigns for FBTR Spent Fuel Reprocessing at CORAL

CORAL, an acronym for COmpact Reprocessing of Advanced fuels in Lead cells, currently is the only operating facility in the world for reprocessing of fast breeder reactor (FBR) fuels on a regular basis. The fundamental objective of CORAL is to process the irradiated mixed carbide fuel discharged from FBTR with varying specific activities to gain operating experience with plutonium rich carbide fuels. CORAL had thus laid the foundation for the development of future fast reactor fuel reprocessing technology in India. The main objective of this facility is to establish and optimize a PUREX process based aqueous technology, suitably modified to handle Pu-rich FBR spent fuel discharged from FBTR. CORAL facility has been utilized in optimization of various operating process parameters, evaluating equipment design and testing them in pilot plant scale to understand their performance in actual test bed conditions.

CORAL serves as a hotbed for evolving the technology and equipment related to FBR fuel reprocessing. Based on the experience gained, two new plants with higher capacity had been designed, namely Demonstration Fast Reactor fuel reprocessing Plant (DFRP) and Fuel Reprocessing Plant (FRP). DFRP is in an advanced stage of commissioning while FRP is under construction as a part of the Fast Reactor Fuel Cycle Facility (FRFCF).

The major objectives realized from CORAL operations are as follows-

- Successful design, operation and improvisation of remote-handling tools for hot-cell operation
- Indigenous design and development of centrifugal extractors
- Optimized process flow sheet for processing mixed carbide fuel in a single cycle operation

- Indigenous design, development and deployment of centrifugal extractor drive-motors and its scale-up for deployment in DFRP
- Reprocessed Pu was refabricated into fuel and it is generating power in FBTR. Closure of FBR fuel cycle has thus been demonstrated.

With the completion of processing of 14 subassemblies of FBTR fuel, CORAL realized its initial design mandate in February 2017. After extensive deliberations and complying the stipulations of the regulatory authority, CORAL was relicensed by AERB for further operations from 01st September 2018 to 31st August 2023. Currently the plant is in regular operation. Subsequent to the relicensing, 12 campaigns have been successfully completed.

In spite of the lock-down and the subdued operations due to the prevalence of the COVID-19 pandemic, the plant continued to operate successfully. After obtaining requisite permissions, one campaign was also completed during the lockdown period. By adhering to the regulations based on the ALARA principles and by optimizing the dose expenditure, this campaign had the least man-rem expenditure, even though it took four long months to complete the same. Another major achievement was the drastic reduction of man-rem expenditure due to strict operational controls exercised in tune with ALARA measures. For four completed campaigns, the dose expenditure was approximately 80% of sanctioned dose budget by AERB for three campaigns. Waste generation and disposals were as per approved norms and all the discharges/disposal to waste management agency were within the stipulated AERB limits.

IV.05 Design and Development of Special LED Lighting System for Lead Wall Shielded Hot Cells in DFRP

Hot cell is a closed containment to handle radioactive materials. In these cells, materials are handled using remote handling devices like the master slave manipulators (MSM) by viewing through radiation shielding windows. At the Demonstration Fast Reactor fuel Reprocessing Plant (DFRP) there are many such cells. In order to provide adequate lighting within the cells, two lighting windows have been provided at the sides of each viewing window. The entire containment box is shielded by a lead wall. Openings are provided across, into which the lights are mounted. At the rear of these lights, thick lead plugs are mounted to provide shielding. The illumination inside the hot cell should be more than 1000 lux. The high lux requirement coupled with the limited dimensions of the openings pose challenges in designing appropriate lights and fixtures. A special purpose, “first of its kind”, 40 W heat-pipe based Chip On Board (COB) LED lamp with copper fins was found to be the best fit to our requirement (Figure 1). This was custom made with design inputs provided to the manufacturer after surveying a wide variety of commercial products available in the market. This LED light source produces about 85% of input power as heat. To achieve maximum expected lifetime, the temperature of LED must be maintained below 85°C (Figure 2). However, the surface area of the LED chip is quite small and the COB package itself is expected to release only a little heat into the atmosphere. Hence, a heat sink is mandatory for the LED to dissipate the heat generated. A heat pipe based thermal system is attached to the LED. The heat pipe has the thermal conductivity in the range

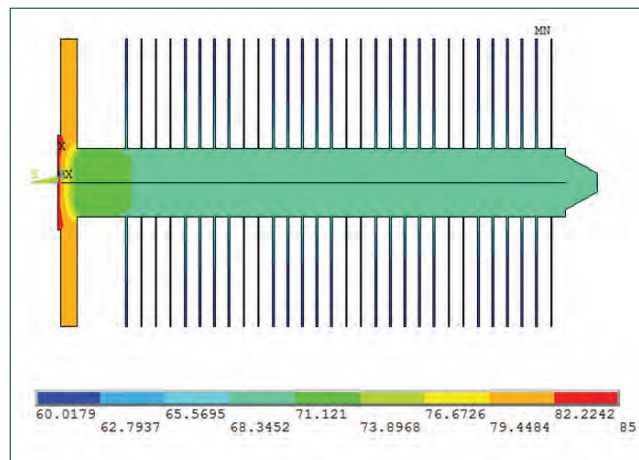


Fig. 2 Simulated cross section temperature distribution (°C)

of 4000 to 100000 W/m², which is very high as compared to the thermal conductivity of copper which is 396 W/m². The high thermal conductivity facilitates greater heat transfer, thereby maintaining the LED at a temperature lesser than 85°C. This system was installed in DFRP and tested. Each LED light is of 40W. The average illumination obtained inside the hot cell containment box is more than 2000 lux (Figure 3).

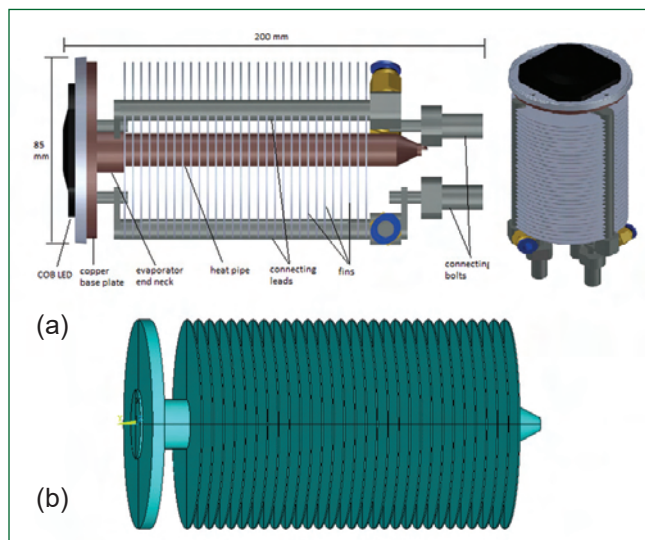


Fig. 1 (a) Conceptual design of LED lamp and (b) model for thermal FEA simulation

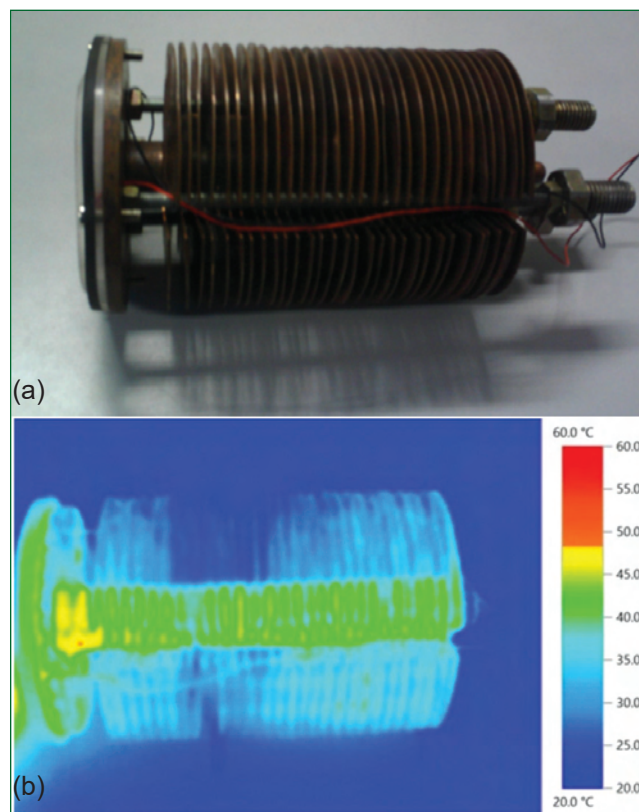


Fig. 3 (a) Developed model of COB LED light and (b) thermal image of glowing lamp

IV.06 Development and Commissioning of Radiation Monitoring Systems for Stack Effluent in DFRP

Continuous monitoring of the air-borne radioactivity of the Stack effluent is a regulatory prerequisite for the reprocessing plants. At the Demonstration Fast reactor fuel Reprocessing Plant (DFRP), in order to ensure that the environmental release is within permissible limits a similar system has been incorporated (Figure 1). This system would monitor the levels of the most critical radio isotopes viz., Krypton-85 and Iodine-131 in the stack effluent. Two identical systems have been provided in which one is operational and the other is standby.

The gross alpha and beta particulates are detected by using a dual phosphor detector which is a sandwich of ZnS(Ag) and a plastic scintillator. The detection is accomplished through monitoring the radioactivity of the particulates collected on a high efficiency particulate activity (HEPA) filter paper. Krypton-85 is detected by allowing the effluent air to pass through a chamber with large volume containing a cylindrical plastic scintillation detector coupled with a suitable PMT. Iodine - 131 is captured on to a charcoal filter backed up with glass fiber placed in a marinelli beaker and the same is measured by NaI(Tl) flat type crystal. The effluent air is continuously sampled at the rate of 50 lpm. The set up has been developed and commissioned at DFRP stack monitoring room (Figure 2).

The suction system helps draw the air through the filter and the air sampler assembly. This system contains an inlet header and outlet header, both connected to the effluent duct. A noise free, dry type, oil-less vacuum pump has been used for this purpose.



Fig. 1 DFRP stack monitoring system

The detector modules have in-built high voltage circuit and pulse shaping circuits. The electronic unit has a counter module with independent counting channels corresponding to each of the detector outputs. The detected count events were registered by the counter module. Display & control module using industrial grade HMI displays the activities as count rates and generates audio-visual alarm if they exceed the pre-set values. The electronic unit was connected to the Main Plant SCADA using modbus RTU protocol over Ethernet. The SCADA enables continuous display in the Control Room with data logging, provisions for raising an alarm and report preparation.

All the measurement channels were tested and calibrated with standard radioactive sources. The continuous communication of all the readings to the SCADA and Control Room are also tested and validated.

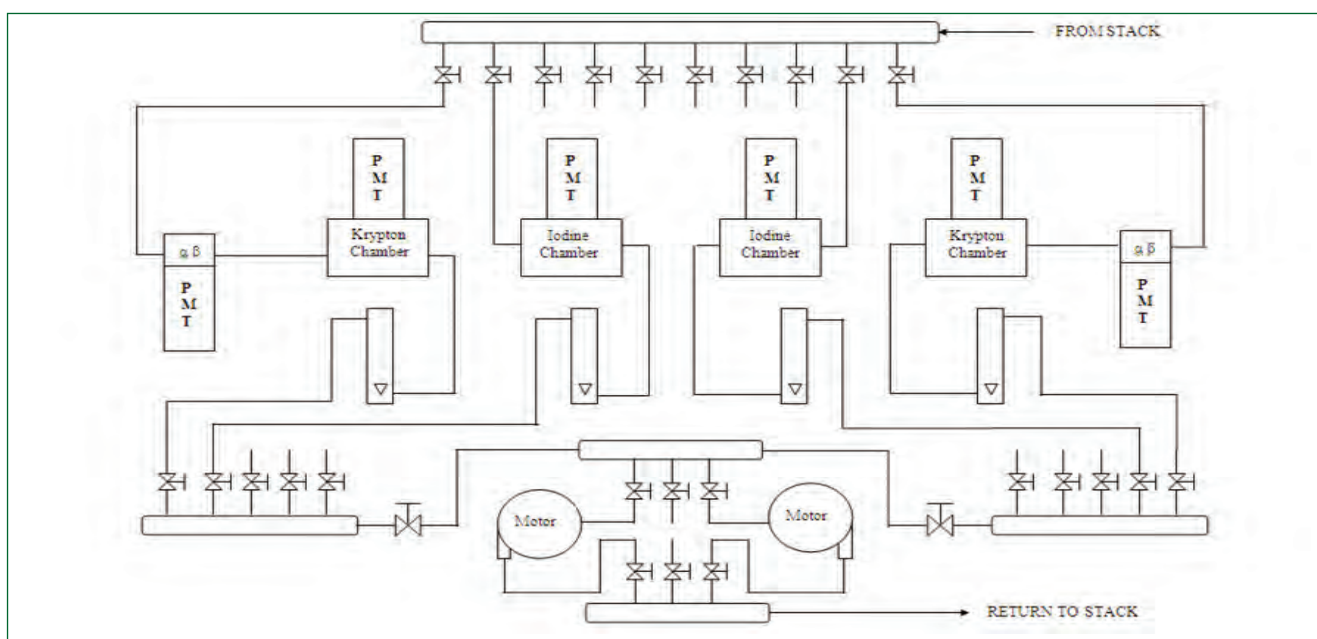


Fig. 2 Schematic of DFRP stack monitoring system

IV.07 Design & Commissioning of Mini Crane and Electrolyser Vessel for DOR Facility Inside Glove Box

A laboratory is being setup for conversion of metal oxides to metal based on high temperature molten salt electrolysis method. In this Direct Oxide Reduction (DOR) method, the metal oxide in the form of pellets are taken as the cathode in an electrolytic cell containing $\text{LiCl-Li}_2\text{O}$ as the electrolyte kept at 650°C . Upon electrolysis using platinum anodes, the oxygen in the metal oxide is stripped off and the metal remains at the cathode. The facility houses five glove boxes interconnected in a train housed with molten salt electrolyser & its accessories. To assist the material handling, a mini crane is designed, fabricated, assembled, tested and installed inside an inert atmosphere glove box.

Glove box crane is designed for a Safe Working Load (SWL) of 50 kg, with duty factor M7 (class II) within permissible limit of deflection for 125% SWL. It is made of stainless steel construction and designed for handling loads in the customized glove box of size: 2150 mm (L) x 1100 mm (W) x 1200 mm (H). Since the crane performs critical jobs in a limited space, the hook reach for Long Travel (LT) is very important. The crane is designed for hoisting with minimum head room and LT movement using motor with manual override facility. All controls of the crane motions are operated from push button pendant station mounted on the suitable bracket outside the glove box. The design drawing is shown in Figure 1.

All the drive systems are compact, electrically operated, low in dead weight and are amenable for easy maintenance / replacement. The crane has provision for speed selection through potentiometer and the speed for long travel is 1.0 m/min and less than 0.5 m/min for hoisting. All the gear, wheels, drive shafts etc. are made out SS 420 materials and hard chrome plated. The various safety features like limit switches and proximity sensors have been provided for LT and hoisting in addition to mechanical stopper. Overload and short-circuit protections for control elements have been provided with the help of MCB's and protection fuses wherever required.

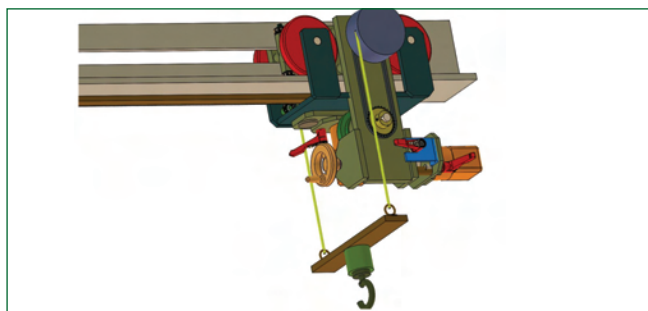


Fig. 1 Mini glove box crane



Fig. 2 Mini crane installed inside glove box

The crane (Figure 2) has been installed inside the glove box and all the necessary testing like load testing, deflection at 100% load, long travel and hoisting speed measurement, LP and UT examination of crane hook has been carried out.

The electrolysis of 2 kg UO_2 will be conducted using sintered pellets of UO_2 . The electrolyser consists of furnace vessel (Size: 350 x 425 mm) made out of 6 mm thick Inconel-600 and main vessel (Size: 320 mm x 540 mm) made out of 6 mm thick SS-316L (Figure 3). The vessels are designed for an operating pressure of 1 bar at elevated temperature of 650°C in highly corrosive environment. It is designed to handle up to 2 kg of heavy metal oxide loaded in the cathode basket and crucible to handle 15 kg salt. The furnace vessel, which acts as an outer containment vessel, is attached to the intermediate flange which is welded to the glove box and sealed by O-ring (material: Viton). The flange of the furnace well is cooled by specially designed detachable cooling water jacket. This arrangement helps in maintaining the temperature of the furnace well flange $<100^\circ\text{C}$.

The main vessel is positioned into the furnace vessel and cooled by fins inside the glove box. This arrangement limits the temperature in the top flange to $<80^\circ\text{C}$ (Figure 4). The anode and cathode electrodes are designed with special feed through to provide the required DC power and also to electrically isolate the cell and also to vent exhaust gas from the electrolyser main vessel.



Fig. 3 Electrolyser vessel



Fig. 4 Vessel welded in GB

IV.08 Installation and Commissioning of Continuous Casting System Inside Glove Box for Fabrication of Metal Fuel Blanket Slug

Continuous casting system is designed to cast blanket metal fuel slugs towards fabrication of sodium bonded metal fuel pin for test irradiation in fast breeder test reactor. Continuous casting technique is proven for mass production and higher yield with minimum heel to cast long and slender slugs. The system has induction heating system for melting the charge under controlled atmosphere housed inside the water cooled double walled process chamber, graphite mould for solidification of fuel slugs to near-net shape with required dimension tolerances under controlled cooling rate and drawing roller assembly to retrieve solidified slugs at desired pulsed velocity. The low frequency electromagnetic stirring power is achieved by the use of pulse width modulation technology for better homogeneity of charge. The schematic of continuous casting system is shown in the Figure 1. Continuous casting system is housed inside the inert atmosphere glove box to handle pyrophoric and reactive uranium and zirconium metal charge and cast slugs. For housing the continuous casting system inside the glove box, a rigid supporting structure was fabricated for mounting process chamber, die cooling block housing and rod drawing unit. It facilitates ease of operation during unloading and loading the starter bar & graphite crucible, viewing the charge inside the chamber during melting, replacement of induction heater and maintenance of drawing unit, load sensor, other process service lines like water & gas

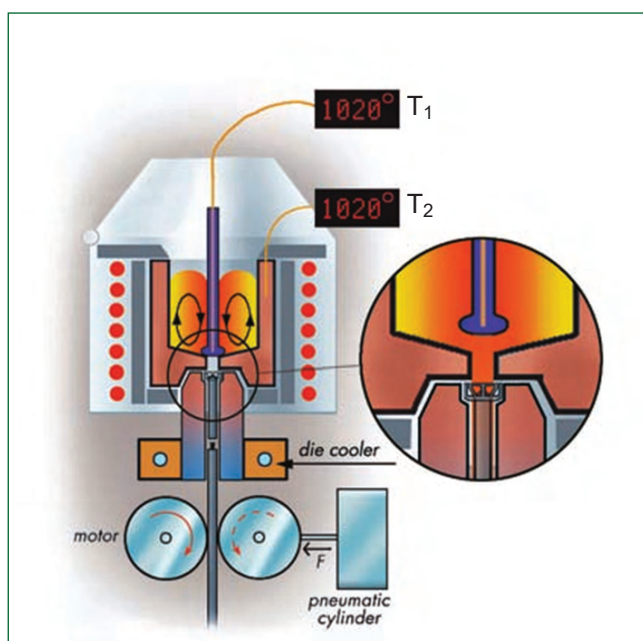


Fig. 1 Schematic of continuous casting system

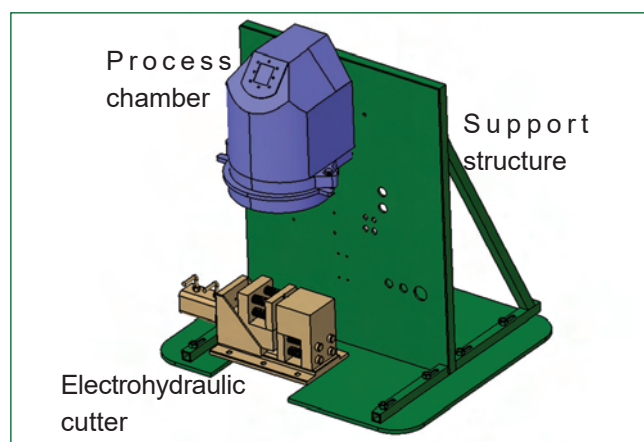


Fig. 2 Vertical support structure SOLIDWORKS model

lines and signal & power cable feed through (Figure 1). Process chamber, die cooling block housing and drawing units assemblies were mounted to maintain geometrical tolerance on the support frame. Induction heater, water & gas tube lines were routed through leak tight feed-through's from outside the glove box for operating the system using control panel. Process chamber with support structure modelled in "SOLIDWORKS" is shown in Figure 2. Leak testing of process chamber, cooling lines for die block and induction heater and gas lines was carried out before trial casting runs.

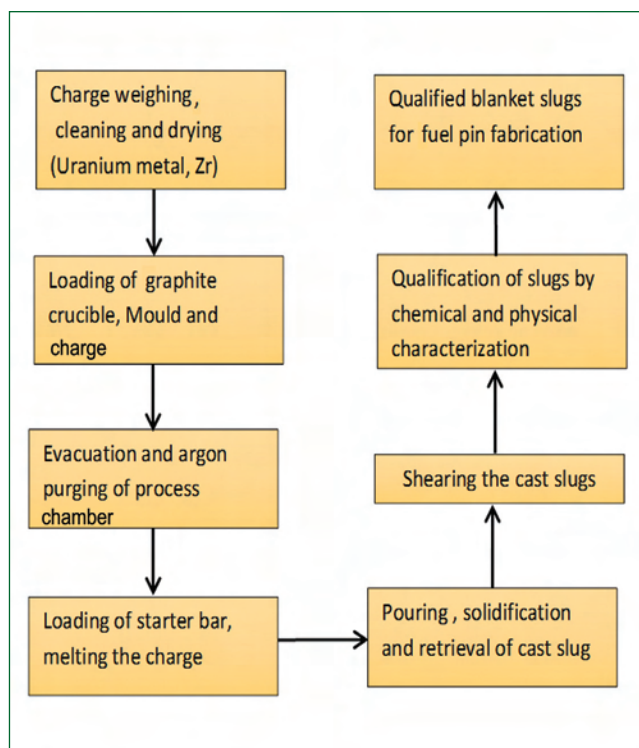


Fig. 3 Flow chart for the fabrication of blanket metal fuel slug



Fig. 4 Continuous casting system housed inside the glove box

The 15 ton hydraulic cutter has capacity up to 10 mm dia., single acting spring assisted cutting blade and compact in construction. The flow chart for the fabrication of blanket metal fuel slug is given in Figure 3.

Glove box was leak tested to minimize the air ingress. Thermal analysis was carried out to calculate the temperature and solidification profiles which helped in optimising the parameters like casting speed, pouring temperature and air gap between mould and cast rod. During the solidification, surface defects such as oscillation marks were formed which were overcome by modified design of the roller. The photograph of the glove box with continuous casting system is shown in Figure 4.

Initially trial runs were carried out to check the integrity and performance of heater, cooling and drawing units using copper metal as charge of weight 250 g to cast copper rod of diameter 5 mm and length 1.2m. The casting parameters like melt peak temperature, induction heating system frequency, die block water flow rate and casting cycle speed were studied by casting the binary alloy slug of Cu-20%Ni. The graphite crucible with mould, charge and cast binary alloy slug of Cu-20%Ni are shown in Figures 5 & 6.

SEM micrograph and spectrum of nickel and copper in



Fig. 5 Graphite crucible and charge



Fig. 6 Cast slugs

Table 1: EDXRF Elemental Analysis Results		
Sample position	Copper (%)	Nickel (%)
Top	78.90	21.1
Middle	80.43	19.57
Bottom	79.21	20.79

the cast slug are shown in Figures 7 & 8, respectively. The elemental analysis of Cu – 20 wt.% Ni slugs samples from top, middle and bottom portion were analysed using EDXRF. The results given in Table 1 shows the copper and nickel are uniformly distributed in the matrix.

Physical and chemical characterizations of cast slugs were completed for measuring the theoretical density and homogenous distribution of alloy.

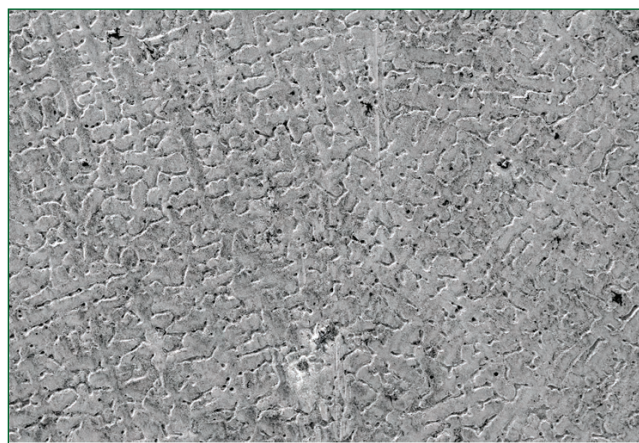


Fig. 7 Micrograph of Cu - 20% Ni cast slugs

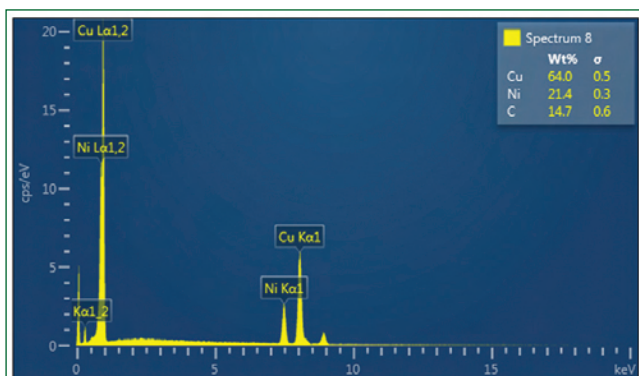


Fig. 8 Elemental chemical analysis spectrum of Cu - 20% Ni cast slugs

IV.09 Glove Box Adaptable Hydrogen Gas Determination for MOX Fuel

Fuel Fabrication Plant (FFP) of Fast Reactor Fuel Cycle Facility (FRFCF) is designed for production of Mixed Oxide (MOX) fuel pins to meet the annual reload requirement of PFBR. FFP houses Analytical and Certification Laboratory (ACL) to cater to the analytical requirements for physical/chemical quality control (PQCL/CQCL) and characterization of nuclear fuel samples. At different stages of fabrication, MOX samples are subjected to chemical characterization in ACL to meet specifications for heavy metal content (U,Pu), Isotopic content, ^{241}Am , metallic impurities, non-metallic impurities, oxygen to metal ratio, total gas content etc. Hydrogen gas is one of the important non-metallic critical impurity for fast reactor fuel. In Fast Reactors, hydrogen gas diffuses out from the fuel through cladding material at operating condition. Also in presence of Cl^- and F^- , it reacts to form HCl and HF which cause corrosion in the cladding material. The allowed concentration of hydrogen in fast reactors fuel is $< 3\text{ppm}$ and it needs to be measured using a suitable system. Hydrogen determinator is able to measure the hydrogen concentration from 0.1 to 5000 ppm.

In the determinator, the sample is heated in a resistance heating furnace upto 2000°C for extraction of hydrogen gas. Ultra high pure nitrogen gas is used as carrier gas. The impurities present in carrier gas is purified using ascarite and anhydrone. Thermal conductivity detector (TCD) based on Wheatstone Bridge is used for detection of hydrogen gas. The system is calibrated with various standards of hydrogen concentration before doing analysis of samples. The gas flow diagram and typical spectrum of the determinator is shown in Figure 1.

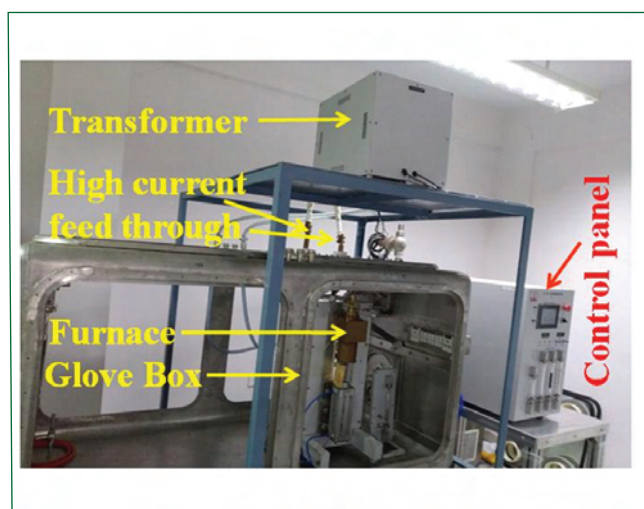


Fig. 2 Photograph of hydrogen determinator

In radiochemistry laboratory of ACL, the radioactive materials are handled inside glove boxes and fume hoods. The resistance heating furnace is kept inside of the glove box while the control unit, detector, transformer for heating furnace, water chiller etc. are installed outside the glove box. The leak tight feed through for applications pertaining to gases/water pipes & high current cables are provided on the glove box panel. Photograph of the determinator is shown in Figure 2. In order to keep maintainable components outside of glove box, special leak tight feed throughs for electrical controls and gas application have been established. The hydrogen determinator is modified and adapted to glove box and commissioned successfully at FRFCF site.

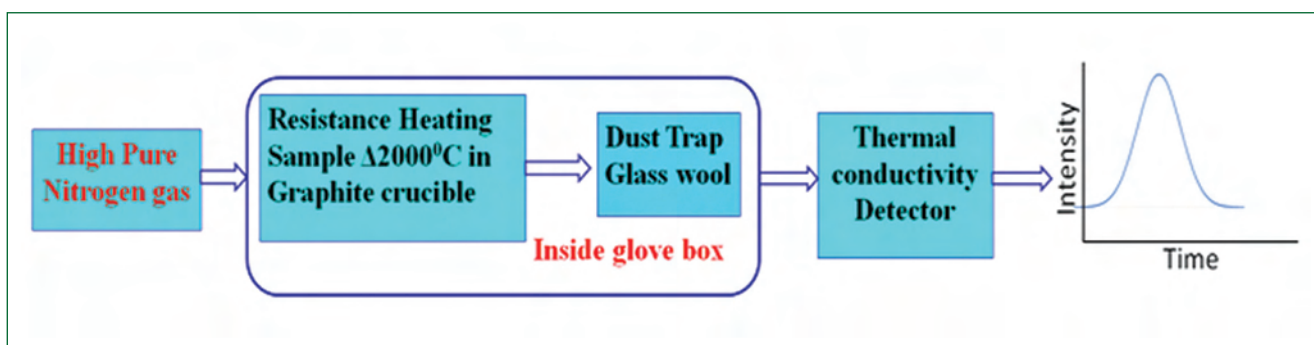


Fig. 1 Gas flow diagram and typical spectrum of hydrogen determinator

IV.10 Commissioning of Isopiestic Experimental Set-up for Vapour Pressure Measurements

Isopiestic experimental facility for vapour pressure measurement was set up in MC&MCFG. Many different techniques are available for the measurements of vapour pressures and are classified into static, dynamic, effusion and equilibration methods. Static method mainly uses different gauges, like bourdon gauges, sickle gauges, spiral gauges, etc. Examples of dynamic methods are boiling point technique, transpiration techniques, etc. Mass loss techniques, momentum sensor techniques and Knudsen cell mass spectrometry are classified as effusion methods. Equilibration with a gas mixture, isopiestic method comes under the purview of equilibration methods. Isopiestic can be further classified as isothermal isopiestic and non-isothermal isopiestic method. The present experimental setup is based on the non-isothermal isopiestic method.

Photograph of the experimental facility is shown in Figure 1. The experimental set up consists of a quartz tube (1), with a vaporisable species (2) at the bottom end, compatible crucible (3) containing weighed sample (4) is placed one over the other as shown in the Figure 2a. A thermowell (5), with thermocouple (6) is shown adjacent to the sample containing tube. The quartz tube containing the sample is vacuum-sealed on the top (7). The experimental facility consists of a temperature gradient furnace (Figure 1) and a thermocouple movement mechanism.

The temperature gradient is achieved by placing two furnaces one above the other and maintaining different set temperatures in each furnace (Figure 2b). The top (T) and bottom (B) furnace are controlled by separate controllers (C). Movement mechanism (M) and stepper motor drive (D), control the movement of the



Fig. 1 Photograph of the experimental facility

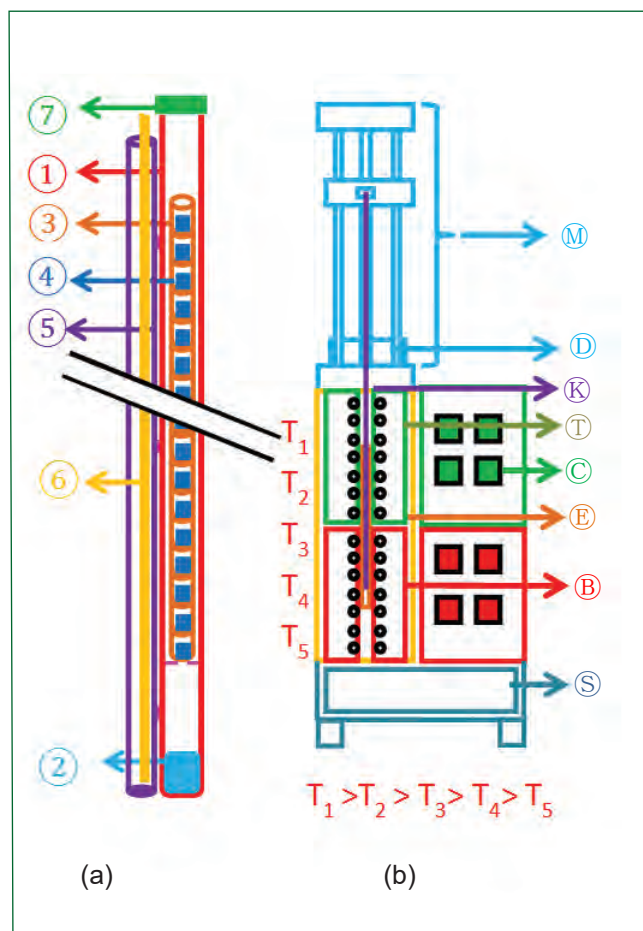


Fig. 2 Schematic of the (a) experimental set up and (b) isopiestic furnace

thermocouple (K), along the side of the experimental setup (E). The entire setup stands on a support stand (S). After the equilibration, the experimental set up is quenched and taken inside the glove box to take the weight of samples in the crucible.

Activity determined through this technique is given by ,

$$a = \frac{p_R^o}{p_S^o},$$

where p_R^o is the saturated vapour pressure at the reservoir temperature and p_S^o is the saturated vapour pressure at the sample temperature. The activity determined can be used to determine the partial thermodynamics quantities.

The technique is simple as it contains only a temperature gradient furnace and a mechanism to measure temperature of each sample. This technique is used to measure vapour pressures in the range 10^{-1} to 10^{-10} atm.

IV.11 Conceptual Design and Development of a Robot for loading the Fuel Pin into a Magazine

The first step in the reprocessing of the used fuel discharged from the Prototype Fast Breeder Reactor (PFBR) is the dismantling of the Fuel Sub-Assemblies (FSA) to retrieve the fuel pins. Subsequently these would be stacked in the Fuel Pin Can (FPC) and in turn, would be transferred to the dissolver cell after loading them in to a magazine. A multi-pin chopper capable of cutting 10 fuel pins at a time had already been designed and the demonstration of its prototype completed. The fuel pin magazine facilitates the progressive feeding of fuel pins into the chopper. In order to automate the retrieval of fuel pins from the FPC stationed in the dismantling cell, transfer and load them into the fuel pin magazine located at dissolver cell, a special and unique FSA Fuel Pin Loading Robo (FPLR) has been conceptually developed, the integrated view of which is shown in the Figure 1. This essentially consists of the following sub-systems; Fuel Pin Can (FPC), Inter Cell Transfer System (ICTS), Pick and Place Mechanism (PPM) and Fuel Pin Loading System (FPLS).

Fuel Pin Can (FPC) – This would hold 80 pins arranged in a matrix of 8 rows and 10 columns and has been designed to be critically safe. Each vertically placed slot has been designed to accommodate 8 fuel pins placed horizontally one over the other in their designated slots provided with a wider mouth to facilitate easy insertion and pick up. A schematic of the FPC is shown in the Figure 3a.

Inter Cell Transfer System (ICTS) – This has been designed to enable the transport of FPC from the dismantling cell to the buffer cell, FPLS from the buffer cell to the dissolver cell and vice versa, through a Double Door Transfer Port (DDTP) that ensures leak tightness as well. It facilitates motions in two axial directions. The schematic view of the ICTS has also been depicted in the Figure 3b.

Pick and Place Mechanism (PPM) – This system is capable of picking 8 vertically stacked fuel pins at a time together and transfers them from FPC to the FPLS. This is so designed as to have motion in three orthogonal axes, corresponding to the gripping mechanism (actuated by a rotary drive), z-vertical and y-transverse. A schematic representation of this system has also been provided in the Figure 2.

Fuel Pin Loading System (FPLS) – This system would

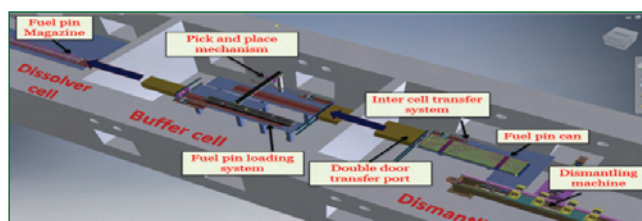


Fig. 1 Integrated view of FSA FPLR

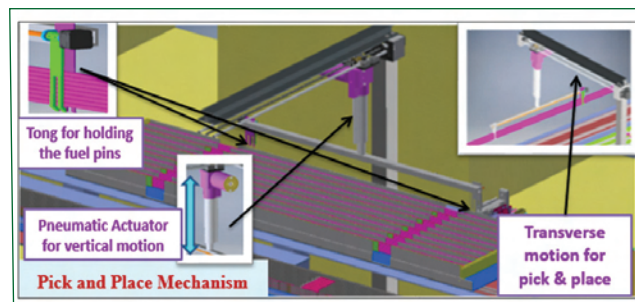


Fig. 2 Pick and place mechanism

hold 80 pins in a matrix of 10 rows and 8 columns with a pitch of 20 mm, the latter to match with the magazine that inserts the fuel pin into the chopper. A schematic view of FPLS is shown in Figure 3c. It is so designed that, in a single stroke, it will push the bottom most 10 fuel pins from the FPLS into the fuel pin magazine. During the loading of fuel pins into the magazine, the FPLS would be held inside the DDTP to minimize any possible α contamination from dissolver cell.

The following challenge was faced in the design of the system. Extreme care needs to be exercised in handling the fuel pins as they are very slender. The transfer of fuel pins from the dismantling cell (not designed to handle gas release) to the buffer cell (could handle gas release occasionally) and then to dissolver cell (designed to handle gaseous discharges) demands hermetic sealing within the confines of the specified leak tightness during transfer. These systems warrant incorporation of components that are compact, robust and modular in construction and are amenable for remote operation and maintenance.

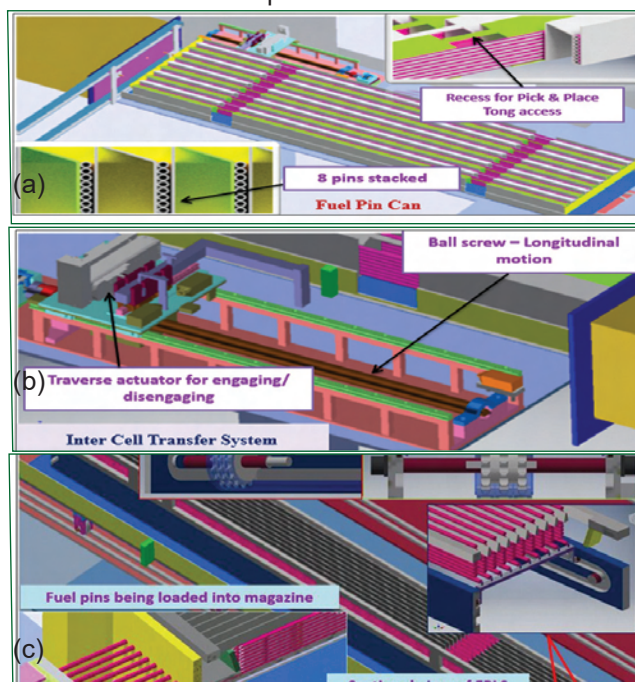


Fig. 3 Conceptual design of (a) fuel pin can (b) inter cell transfer system and (c) fuel pin loading system

IV.12 Setting up of a Sol-Gel Facility in Walk-in Fume Hood for the Production of Ceramic Microspheres Through Internal Gelation Process

A sol-gel facility was commissioned inside a walk-in fumehood at Fuel Chemistry Division of MC&MFCG. The main objective for setting up this facility is to deploy the internal gelation process to produce urania microspheres. This also serves as a platform to optimize the process parameters in the production as well as a fore runner to the uranium based mixed oxide microspheres containing plutonium and minor actinides through internal gelation process inside the glove box or hot cell. A walk-in fumehood of dimensions 2 x 0.9 x 1.8 m (L x B x H) is used for the commissioning of the sol-gel facility. The components of the internal gelation setup are (i) 1.6 m tall modular glass column for gelation, (ii) silicone oil reservoir with resistive heater and temperature controller, (iii) stainless-steel support structure with polytetrafluoroethylene holder, (iv) feed tank with chilled water recirculation setup, (v) electromagnetic vibrator with frequency and amplitude controller, (v) booster pump with flow controller, (vi) stainless-steel cooling tank for broth preparation and storage, (vii) oil separator / mesh container and (viii) wash tank with air agitator. All these components were housed inside the fumehood and the corresponding controller, chiller and gas cylinder were placed adjacent to the fumehood. The photograph



Fig. 1 Internal gelation facility commissioned inside the fume hood

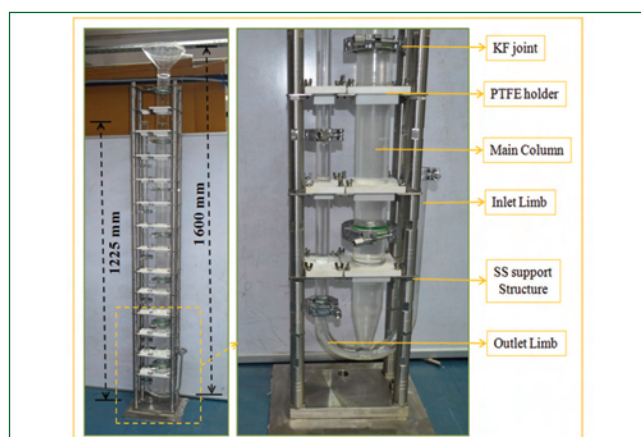


Fig. 2 Modular glass column for internal gelation

of the facility commissioned inside the fumehood is shown in the Figure 1.

The gelation column consists of a main column and two side limbs as shown in the Figure 2. The main column (L = 1600 mm; Φ = 50 mm) is a modular column which can be separated into four parts that are fitted to one another by standard KF joint, viton O-ring and an aluminum chain clamp. The top of the main column has a funnel with small outlet through which overflowing oil is returned to the oil tank. One of the side limbs (Φ = 25 mm; L = 350 mm) is used as inlet for pumping hot oil into the glass column. The other limb (Φ = 25 mm; L = 1225 mm) is used as outlet for the hot silicone oil. There is a flexible silicone tube connected to the outlet limb, which terminates just above the oil separator. A double walled stainless-steel tank of 40 L capacity was fabricated in-house. The silicone oil [viscosity coefficient of 100 cSt at 298 K] is maintained at 368 K using a resistive heater with temperature controller and is pumped into the gelation column using a centrifugal pump (EVOPLUS, small DAB pump, Italy). From the outlet limb and the funnel

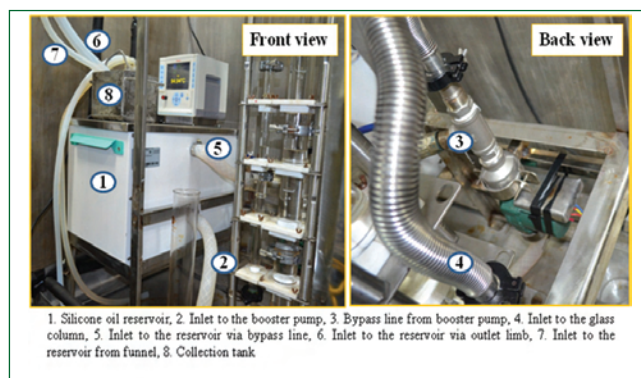


Fig. 3 Silicone oil recirculation through gelation column

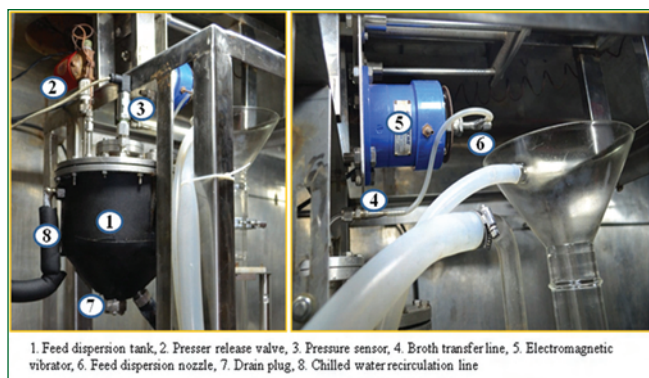


Fig. 4 Feed dispersion system

outlet, the oil is received back to the tank. By this oil is circulated through the gelation column in a closed loop (Figure 3). A double walled stainless-steel tank of 1.5 L capacity jacketed with heat insulator is used as feed tank. The top flange of the feed tank has provisions for (i) fill the feed solution through an air-tight veeco coupling with O-ring, (ii) gas inlet for pressurization, (iii) pressure gauge, (iv) outlet for broth solution, (v) gas release vent. Through the double walled chamber, refrigerated liquid (a mixture of distilled water and ethylene glycol) is circulated from the chiller to maintain the feed solution at desired temperature. The bottom of the tank is conical and is fitted with a drain plug for cleaning the tank. The photograph of the feed dispersion system is shown in Figure 4.

The feed solution is pressurized into a dispersion head (known as dispersion nozzle) attached to an electromagnetic vibrator. The nozzle is made of $\frac{1}{4}$ " PTFE rod through which a stainless-steel capillary of desired dimension is inserted. A constant overhead pressure was maintained in the tank. To separate the gelated microspheres from hot silicone oil, following components were designed and fabricated. (i) a cylindrical stainless steel mesh container ($\Phi = 120$ mm; $L = 150$ mm) to collect the microspheres, (ii) a cubical stainless steel funnel (200 mm x 200 mm x 200 mm) to collect and drain the hot silicone oil into the reservoir. After draining the silicone oil, the cylindrical mesh container with microspheres was transferred to the washing vessel. The washing vessel consists of a stainless-steel tank (200 mm x 200 mm x 250 mm) with an outlet at the bottom, fitted with a suitable ball valve for draining off the wash effluents. The hot silicone oil (368 K) and was circulated through the gelation column. The flow was controlled through the controller of the booster pump. Depending on the pumping speed, the rate of oil flow varies and accordingly the height of the silicone oil in the central column increases. The flow rate of the silicone oil with respect to the pumping power (in %) is

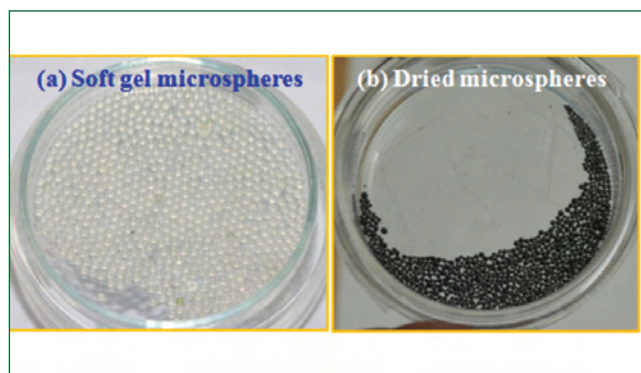


Fig. 5 Photograph of the titanium dioxide microspheres

investigated. Below 40%, pumping is insufficient and the silicone oil does not flow out of the glass column, while 50% causes the silicone oil to overflow from the funnel of the central column. The maximum flow rate achieved was 9 LPM which is more than sufficient to transport the microsphere through the silicone oil stream without settling at the bottom of the glass column. The functionality of this facility was demonstrated by preparing TiO_2 microspheres.

Desired quantities of metal solution (such as titanium oxychloride for the preparation of titanium dioxide microspheres) and HMTA-urea solutions (gelating agent) were cooled in broth cooling station for 30 minutes. The broth solution was prepared by mixing the solutions at 273 K. Droplets were prepared by forcing the feed solution through a capillary ($\Phi = 1$ mm) by pressure siphoning. The dispersion nozzle was vibrated at 1000 Hz with the electromagnetic vibrator. The broth solution was prepared by mixing the solutions at 273 K.

Droplets were prepared by forcing the feed solution through a capillary ($\Phi = 1$ mm) by pressure siphoning. The dispersion nozzle was vibrated at 1000 Hz with the electromagnetic vibrator. The imposed vibration helps in controlling the breaking up of the fluid stream into droplets of uniform size. The droplets on falling into the gelation medium gelled in a few seconds. These soft gel microspheres were separated from oil and collected in a mesh container. These gel spheres were subsequently transferred into the wash tank by transferring the mesh container. The gel spheres were washed 5 times with sufficient quantity of carbon tetrachloride to remove the oil adhered on the surface of the gel particles. The oil free gel particles were then washed with 8 % ammonium hydroxide solution to remove the residual chemicals. Finally, to remove the excess water from the gel spheres, isopropanol was used. The microspheres were then dried in air for 24 h and calcined at 923 K. The photographs of the dried and calcined microspheres are given in the Figure 5.

IV.13 Design & Structural Analysis of Sub-Assembly & Pin Magazine Handling System with Shielding for Core Sub-Assembly Plant

Core Sub-Assembly Plant (CSP) is an integrated facility of Fast Reactor Fuel Cycle Facility (FRFCF) for manufacturing Sub-assemblies (SA) for PFBR and future FBRs. Fuel and blanket pins in the Pin Magazine (PM) will be supplied from Fuel Fabrication Plant (FFP) and Reprocessed Uranium Plant (RUP) to CSP for manufacturing the SAs. Pin magazines delivered to CSP will be stored in a thick concrete wall vault to limit radiation exposure and subsequently, they will be transferred to different work stations on mezzanine area of CSP for fabrication. Fabricated SAs will be transferred back to the storage vault. The handling system with shielding arrangement is designed for transferring the SAs & PMs between workstations, storage vault and mezzanine area of CSP.

The handling system is conceived and designed for CSP, consists of shielding enclosure also called Shielding Bell, attached with the electric overhead crane through wire rope to specialized attachment or supporting structure as shown in Figure 1. In order to make shielding enclosure interchangeable for SA and PM, special provisions of guide sleeves attachments are provided. Electric chain pulley hoist is mounted on the special attachment for lifting and lowering the SA and PM. The shielding bell and the chain hoist are designed and arranged to move together as well as independently, according to process requirement.

The shielding bell is a composite cylindrical structure made up of high density polyethylene (HDPE density 0.9 g/cc) layer sandwiched between two layers of mild steel (density 7.8 g/cc) and comprises auxiliary members to facilitate the assembly and smooth handling of operations. The bore of the shield structure has a diameter of 280 mm while the inner MS layer, HDPE layer and outer MS

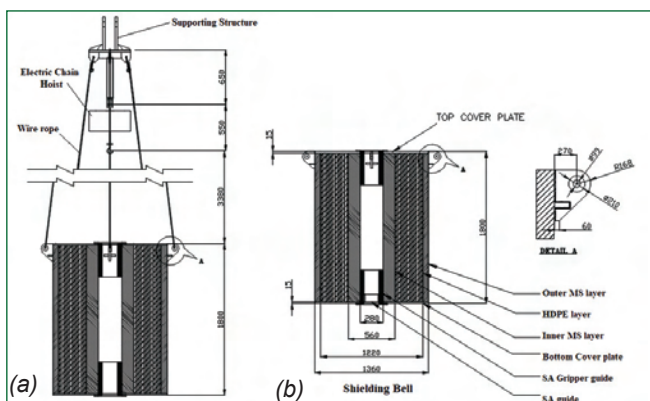


Fig. 1 Conceptual design of PM and SA handling system (a) elements of system (b) shielding bell

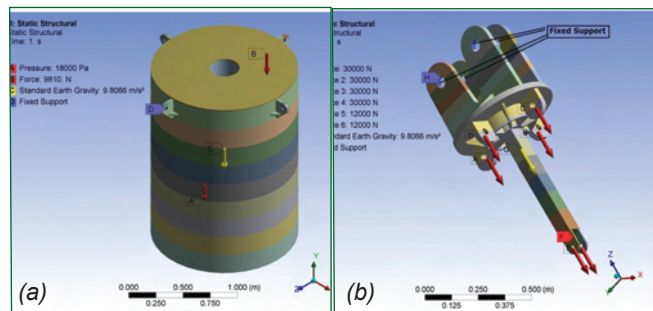


Fig. 2 Loading and boundary condition in (a) shielding bell and (b) structural support

layer have a thickness of 140 mm, 330 mm, and 70 mm respectively. The length of the shield structure is kept 1800 mm for providing shielding to radiation emitting portion of SA and PM (Figure 1). The dimensions of the structural members like pad eye of the system are calculated by analytical method in compliance with ASME BTH-1:2005.

The structural analysis of the system was performed by iterative method using Finite Element (FE) Analysis software in order to optimize the design of the structural support and shielding bell. The boundary conditions and loads applied on the members shown in Figure 2 are similar to that of actual working conditions. The analysis is performed for transient loading condition (level A service limit) and stresses generated in structural support and shielding bell are shown in Figure 3. The design of system is in compliance with ASME Section III, Division-1, Subsection NF and induced deflection and stress values are compared with the ASME Section III Mandatory appendix 1141-1.

The induced deflection and stress values for working loading condition in supporting structure and shielding bell was found to be acceptable from the FE analysis. Design of material handling system that is safe under transient loading condition for SA and PM of CSP has been completed.

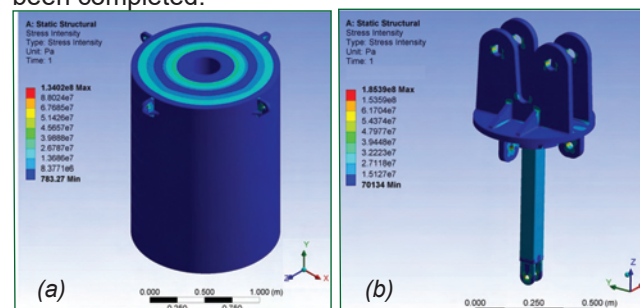


Fig. 3 Stresses in the (a) shielding bell and (b) supporting structure

IV.14 Conceptual Design & Structural Analysis of Three Sub-Assembly Transfer Cask (TSTC) Dolly for Handling PFBR Sub-Assemblies

The used fuel subassemblies discharged from the Prototype Fast Breeder Reactor (PFBR), have to be transported to the Fuel Reprocessing Plant (FRP) of FRFCF for further processing. In order to accomplish this, a shielded cask needs to be designed. This fuel transfer cask would be received in the fuel handling area at FRP with the help of a low bed trailer, and would be unloaded by using a “failure proof” crane and kept on a mobile structural unit called dolly. The basic utility of this dolly is to support and align the cask with the cell shielding unit located alongside the fuel transfer port of the hot cell. In order to ensure the perfect alignment of the cask with the fuel transfer port, the dolly has to be equipped with movements along longitudinal, transverse and vertical axes (Figure 1).

A Three Sub-Assembly Transfer Cask (TSTC) has been designed to transport three Fuel Sub-Assemblies or Radial Sub-Assemblies (FSA or RSA) at a time together. This cask would weigh about 80 tons. The fuel transfer port is located at an elevation of + 1180 mm which poses challenges in design of the cask dolly which need to incorporate provisions for both vertical and lateral movement and alignment with very close tolerances.

The TSTC is a cylindrical cask with diameter of about 1.5 m and a length of about 5.8 m. A pit needs to be provided at the fuel handling area to accommodate a cask of these dimensions along with its dolly and rail track system. However, there is a restriction of 0.5 m in the depth of this pit. All these demanded a robust design to ensure perfect fitting of the dolly in to the available space with minimum head room and being able to handle the intended load. With all these due considerations, a TSTC dolly and rail track system was conceptualized as depicted in the figure.

The critical load on the dolly was arrived at. Calculations were performed as per IS:3177 to arrive at the load on

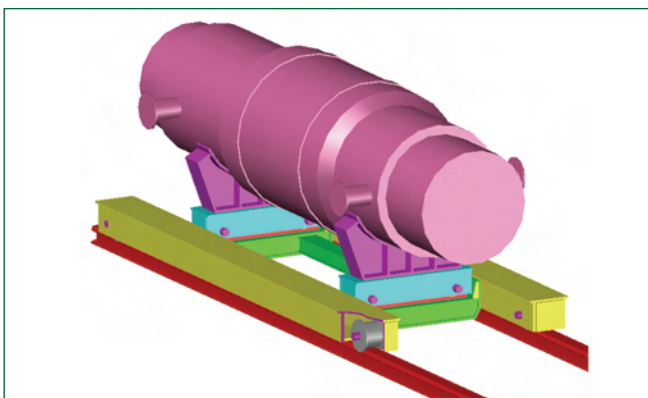


Fig. 1 3-D Conceptual view of TSTC with dolly

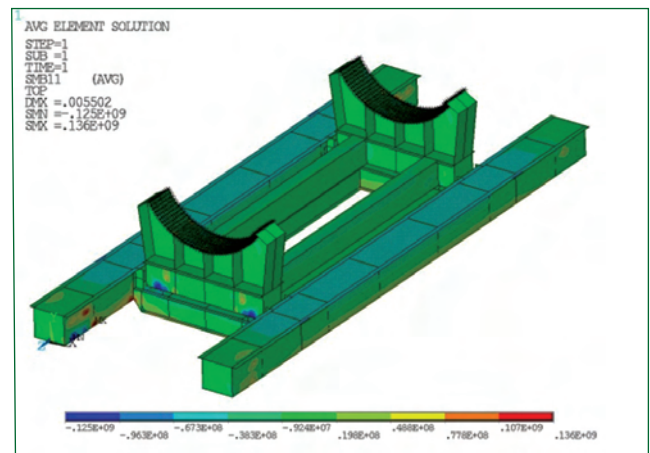


Fig. 2 Maximum primary membrane + bending stress plot

the rail, wheel, cross travel (CT) and long travel (LT). The design optimization of the basic structural members was done by the analytical method. Since this a class-2 component as per the safety classification of systems in FRP, the design and analysis were done in compliance with ASME Section-III, Subsection NF by considering plate and shell type support.

Finite Element (FE) analysis of the TSTC cask dolly was accomplished using a standard FE software package. The dolly was modeled using shell elements with four nodes. The mass element was used for lumping the mass of the cask on dolly. In order to carry out the impact analysis, it was assumed that a 100 Ton mass lumped on the wear plate on the saddle support. Node coupling are constraints were appropriately used to simulate the condition that LT and CT are welded together. The wheel connections to the corresponding structural members were modeled by using Multi Point Constraint (MPC) element and appropriate boundary conditions were imposed.

The structural analysis of the dolly was performed by carrying out many iterations in FE analysis in order to optimize the sizes of the structural members for LT, CT, saddle support and structural connections by introducing stiffener and gussets to control the induced stresses. The maximum deflection observed was 5.5 mm. The maximum induced primary membrane stress was found to be 108 MPa and primary membrane and bending stress together was 136 MPa. This is within the limits permissible as per the design code. Thus, the structural integrity has been ensured. The stress distribution plots for primary membrane plus bending stress is shown in the Figure 2. Thus, a compact, robust and low head TSTC dolly with its associated rail track system was conceptualized and designed as per IS 3177 to qualify its structural integrity.

IV.15 Study Of Continuous Cerium (III) Oxalate Precipitation in A Scraped Surface Precipitator

Plutonium (IV) oxalate precipitation is the most widely employed method for deriving plutonium oxide from the spent plutonium solutions obtained from used fuel reprocessing. At present, this process, often referred to as the reversion, is being carried out in batch / semi batch mode. As compared to the batch process, the continuous reversion process would be more appropriate for use in plants with larger capacity. Further it has the potential of reducing the radiological burden to the operator due to lesser human interventions during processing. In order to develop such a continuous precipitator, a bench scale scraped surface crystallizer (SSC) as shown in Figure 1 that could handle 2 L of process solution has been commissioned and cerium oxalate precipitation studies had been successfully carried out.

The performance of this crystallizer is influenced by many operating parameters like for instance, the intensity of mixing and residence time. Initially, the batch precipitation studies were carried out with solutions of cerium nitrate and oxalic acid. Aqueous solutions of cerium nitrate containing 0.5, 1, 2, and 3M nitric acid were used. The cerium oxalate precipitates prepared from neat cerium nitrate and those comprising 0.5 and 1 M nitric acid were lumpy. However free flowing oxalate powders were obtained when solutions containing nitric acid in excess of 2M were used. In view of the higher solubility of precipitates obtained from solutions containing more than 3M nitric acid the maximum acid concentration was restricted to 2 M.

The dependence of product quality on the residence time were examined for typical durations varying from 10 to 30 minutes at a constant speed of rotation. The suspension was filtered from the outlet upon reaching



Fig. 1 Scraped surface crystallizer system

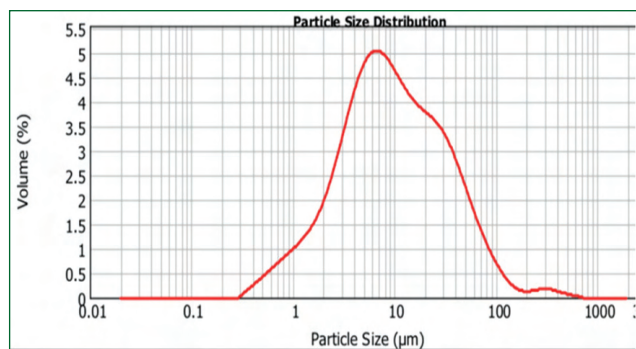


Fig. 2 Size distribution of cerium oxalate particles

the steady state, residue washed, and dried at 100^oC to obtain the cerium oxalate powder. The final product was characterized for the size distribution of particles and specific surface area (SSA). The effect of the speed of mixing at a constant residence time was also studied. With a threefold increase in speed, the mean particle size decreased by about 30% while surface area nearly increased by 1.5 times.

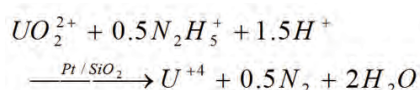
A precipitator model was used for predicting the mean particle size from the SSC. The kinetic parameters pertaining to the precipitation reaction of cerium oxalate reported in the literature were used in the simulation. The values predicted have been shown in the Table 1. Since the values obtained from the model were significantly found to be overestimates, $D[4,3]$ was evaluated using the well-known relationship from Mixed Suspension Mixed Product Removal (MSMPR) model ($D[4,3] = 4G.t$, where t is the residence time) and the calculated mean diameters were comparable to that predicted by our model prediction. The growth rates were back calculated using MSMPR model utilizing the experimental data and they were in the range of 0.23 to 0.52 $\mu\text{m} / \text{minute}$. The results suggest that the model over estimated due to the use of a rather higher value for G , while in actuality the G values were considerably lower and the particles were non-uniform.

Table 1: Properties of the cerium oxalate powder

Properties	Residence time (min)		
	10	20	30
SSA_{EXP} (m^2/g)	1.34	1.26	1.09
$D[4,3]_{EXP}$ (μm)	20.8	24.1	27.4
$D[4,3]_{Model}$ (μm)	104.0	208.0	312.0
$D[4,3]_{MSMPR}$ (μm)	105.6	211.2	316.8

IV.16 Process Optimization for the Catalytic Reduction of Uranyl Nitrate with Hydrazine Over Silica Supported Pt Catalyst by Response Surface Methodology

In the PUREX process, U(IV) is generally produced by the electrochemical reduction of U(VI) using Pt or Ti electrodes with hydrazine nitrate as a stabilizing / holding agent. This method suffers from poor kinetics, lower efficiency (50-60%) and necessitates frequent maintenance of the electrodes. We had developed an alternative chemical method based on the catalytic reduction of U(VI) using hydrazine itself as the reducing agent, with Pt supported over silica as the catalyst. Different process parameters including the mixing speed, catalyst loading, concentrations of nitric acid, hydrazine and uranium as well as the temperature of the reaction were optimized by using the response surface methodology. A suitable quadratic equation was derived to predict the experimental results. The catalytic reduction was performed in a batch SS reactor of about half a liter capacity. The reduction reaction could be represented by the following equation.



In order to understand the interaction between different process variables, the statistical tool “central composite design (CCD)” was used. The parameters, viz., temperature and the concentrations of uranium, nitric acid and hydrazine were screened in as key variables and were further optimized using CCD. These four variables were varied in five independent levels as depicted in the Table 1. In all, as many as 31 experiments were conducted with different combination of variables.

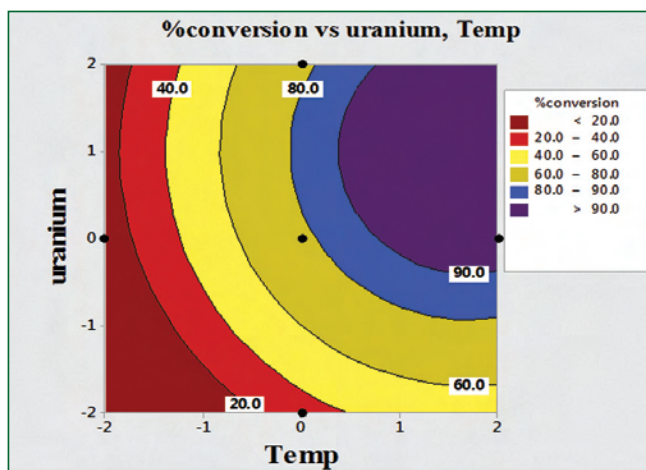


Fig. 1 Contour plot for U(VI) reduction as a function of Temp. and [U(VI)]

Variables	Levels				
	-2	-1	0	+1	+2
HNO ₃ (M)	0.6	0.8	1.0	1.2	1.4
N ₂ H ₄ (M)	0.8	1.0	1.2	1.4	1.6
Temp (K)	313	323	333	343	353
U(VI)(M)	0.08	0.17	0.25	0.33	0.42

The experimental results were analyzed using MINITAB-19 software and the following expression was obtained by using a quadratic regression.

$$\% \text{ conversion} = 76.7 + 21.9 T + 11.5 U(VI) - 6.1 HNO_3 + 2.3 N_2H_4 - 6.4 T \times T - 5.7 U(VI) \times U(VI) - 4.3 HNO_3 \times HNO_3 - 2.7 N_2H_4 \times N_2H_4 + 1.9 U(VI) \times N_2H_4 + 3.6 HNO_3 \times N_2H_4$$

Analysis of variance (ANOVA) of the experimental results showed that this expression had a probability factor (P) less than 0.05, suggesting an acceptability of the proposed model at 95% confidence interval. The validity of the model expression was further verified by conducting five more experiments at different experimental conditions. The results obtained in these experiments agreed within 6 % of the values predicted by the model.

The contour plot shown in Figure 1 indicates above 90% conversion when the [U(VI)] is varied in the range 0 to 2 level (0.25 to 0.42 M) and temperature 0.5 to 2 level (338 to 353K). Under these conditions HNO₃ and N₂H₄ are at middle level i.e. 1.0 M and 1.2 M respectively. From the response optimizer, better than 90% conversion is obtained at 350 K and U(VI), N₂H₄ & HNO₃ concentrations 0.42 M, 0.8 M and 0.8 M respectively in 60 minutes as the optimized condition.

Thus the catalytic reduction of U(VI) could be described by the response surface methodology with 90% reliability and could be gainfully used for the scale up.

Exp	%of U(VI) conversion		% Error
	Exp.	Pred.	
1	92	96.8	5.2
2	87	88	1.1
3	68.8	69.4	<1
4	64.8	67.9	4.8
5	76.7	72.3	5.7

IV.17 Characterization of Insoluble Residue Found in Centrifugal Extractor's Bowl

High burnup (155 GWd/T) and short cooled (< 2 years) used fuel discharged from FBTR is being reprocessed in the CORAL facility for the past two decades. Plutonium oxide obtained after reprocessing has also been re-fabricated into fuel and charged back into the reactor for operations. Thus, the fuel cycle pertaining to the second stage of Indian Nuclear Power program has been successfully closed. The continuous operation of equipment like, extractors and airlifts, could lead to the deposition of an insoluble residue in bowls of the centrifugal extractors (CE) as well as at the motive air entry points of the airlift systems. This would hamper the normal operations of the plant. Hence, it is necessary to characterize these solids to choose the appropriate solvent for their removal. Experiments have been performed on the dissolution of the insoluble residue collected from the CE bowl. Different solvents viz., concentrated nitric acid, sodium carbonate and a mixture of nitric acid and hydrogen peroxide with different compositions have been used. Results presented in the Table 1 indicate that sodium carbonate (10%) was found to be a promising solvent as it dissolves the insolubles to the extent of 90-95 %. Solubility of this residue in an aqueous solution of sodium carbonate indicates that the insoluble residue contains a plutonium phosphate complex.

In a typical experiment, a portion of the residue retrieved from the CE bowl was washed with alcohol to remove the organic residue and then with acidified water and dried. The product was treated with sodium carbonate solution and a known quantity of the latter was heated with fuming perchloric acid to near dryness. The

Table 2 Determination of phosphate content and calculation of plutonium nitrate phosphate complex

No	Volume of aliquot (ml)	W t . o f phosphate obtained (mg)	Wt. of Pu obtained (mg)	Mole ratio, $[P O_4^{3-}] / [Pu]$
1	0.05	1.89	2.37	2.00
2	0.10	1.94	2.45	1.99
3	0.15	1.93	2.48	1.95
4	0.20	1.94	2.41	2.02

product was dissolved in distilled water and analyzed by spectrophotometry after converting it into ammonium phosphomolybdate blue complex. In order to examine the presence of residual Pu and phosphate the residue was used without fuming with perchloric acid.

The UV-Visible absorbance spectrum did not evidence the presence of phosphate in the samples that were not treated with perchloric acid. In the samples treated with fuming perchloric acid, the phosphomolybdate test revealed the presence of organic phosphates. The results shown in Table 2 further confirm the presence of plutonium nitrate DBP complex ($Pu(NO_3)_4 \cdot 2DBP$) in the residue which is more than 90% soluble in 10 % sodium carbonate. Hence, it is recommended to use 10 % sodium carbonate for the de-choking of airlift in plant which was choked due to collection of insoluble residues at motive air entry point. De-choking of airlift was successfully accomplished with 10 % sodium carbonate. Similarly, ultra sound aided sodium carbonate cleaning has also been recommended for cleaning the CE bowl.

Table 1: Dissolution of insoluble residue with different dissolvent

No.	Nature of solvents	Solubility	Remarks
1	HNO ₃ , 8 M	Insoluble	No phosphate is found in supernatant after per-chloric acid treatment
2	HNO ₃ + H ₂ O ₂	Insoluble	
3	Na ₂ CO ₃ (5%)	Partially soluble	Phosphate is found in supernatant after per-chloric acid treatment
4	Na ₂ CO ₃ (10 %)	Soluble ≈90-95%	
5	Na ₂ CO ₃ (10 %)	Soluble ≈90-95%	No phosphate is found in supernatant without per-chloric acid treatment

IV.18 Investigation of Phase Equilibria in LiCl-KCl-SmCl₃ Ternary System

Eutectic LiCl-KCl melt is used as the liquid electrolyte medium in the pyrochemical reprocessing of spent metallic fuel, known as electrorefining process. Spent metallic fuel is anodically dissolved in the LiCl-KCl melt and fuel elements (Uranium and Plutonium) are selectively electrodeposited at the cathodes leaving the fission product in the melt. Samarium is one the rare earth fission products. In order to understand the interaction of SmCl₃ with LiCl-KCl melt, ternary SmCl₃-LiCl-KCl phase diagram was investigated by differential thermal analysis (DTA) and X-ray diffraction (XRD) methods.

Samples were prepared by mixing high pure LiCl, KCl and SmCl₃ at 10 mol% interval in the LiCl-KCl rich regions inside an argon atmosphere glove box. Sufficient amount of the sample mixtures were loaded inside decarburised iron crucibles and sealed by TIG welding housed in an inert atmosphere glove box. Further, the samples were pre-equilibrated and leak-checked. They were studied by DTA from 25°C to 700°C at controlled heating rates of 2, 3 and 5°C min⁻¹ and 3°C min⁻¹ cooling rate. Figure 1 shows the representative DTA traces of seven samples. Various thermal events, like ternary eutectic (T), compound formation (F), phase transformation (P), secondary crystallization (S) and liquidus (L) temperatures were deciphered from the heating DTA traces.

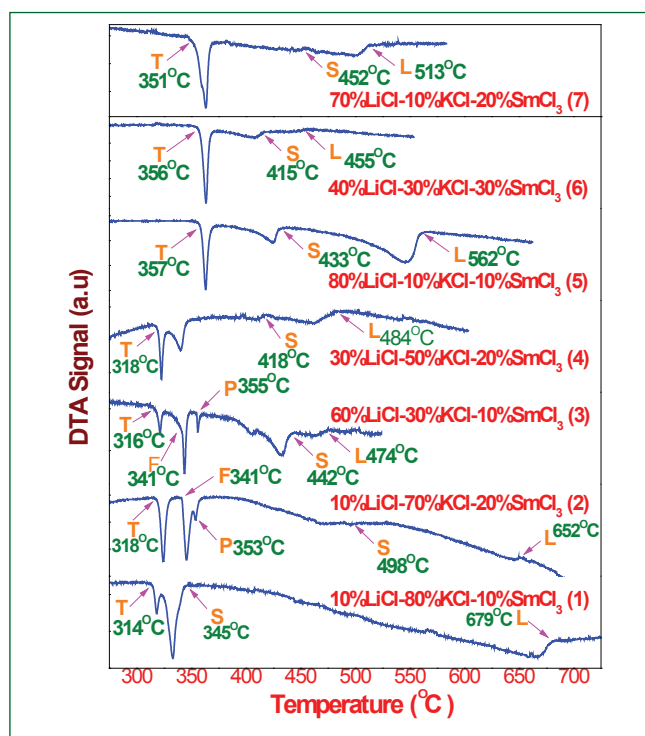


Fig. 1 DTA traces of LiCl-KCl-SmCl₃ samples

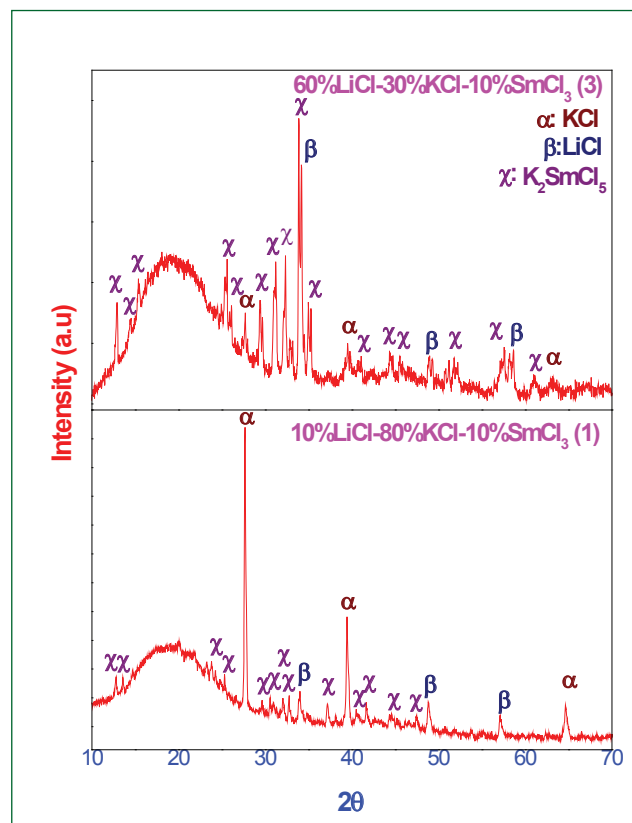


Fig. 2 XRD pattern of sample equilibrated at 280°C. Co-existing phases identified: LiCl, KCl and K₂SmCl₅

The ternary eutectic temperature was observed at 316°C for the samples (nos.1 to 4 in Figure 1) whose compositions were lying in the LiCl-KCl-K₂SmCl₅ pseudo-ternary section. K₃SmCl₆ formation and its phase transformation temperatures (monoclinic to cubic) were observed at 341°C and 354°C respectively. The ternary eutectic temperature was observed at 356°C for the samples (nos. 5 to 7 in Figure 1) whose compositions are lying in the LiCl-K₂SmCl₅-SmCl₃ pseudo-ternary section. Further, secondary crystallization and liquidus temperatures were also determined from the DTA traces.

In order to identify the co-existing phases in the solid state, several samples were prepared and equilibrated at 280°C for 400 h. The equilibrated samples were loaded in specially designed XRD sample holder and sealed by polymeric tape inside glove box to prevent moisture absorption. It was taken out of the glove box and analyzed by XRD using CuK_α radiation. The co-existing phases were characterized from the XRD pattern. The XRD results showed the presence of LiCl, KCl and K₂SmCl₅ (Figure 2) for the samples whose compositions are bound by LiCl-KCl-K₂SmCl₅.

IV.19 Ionic Liquid as the Novel and Unique Solvent for the Separation of Actinides and Fission Products

Ionic liquids (ILs) are finding considerable applications in the area of spent nuclear fuel reprocessing. ILs are organic salts that exist in the molten state at temperatures lower than 373 K. Due to their fascinating properties such as negligible vapor pressure, high solvating capability, high ionicity, high extractability and high radiation stability, they are regarded as the potential substitute to the traditional molecular solvent system. Ionic liquids overcome many of the challenging tasks, those usually encountered in the case of conventional molecular diluent(s) (e.g., *n*-Dodecane (*n*-DD)), during the reprocessing of the spent nuclear fuel through solvent extraction route. Some of the novel accomplishments acquired in MC&MFCG laboratory using ionic liquid as the solvent for the separation of actinides and fission products are highlighted in the report.

Avoiding third phase formation using Ionic Liquid medium

Third phase formation is an undesirable event in a solvent extraction procedure and it is of serious concern when fissile metal ions are concentrated in third phase. It has been established in our laboratory that ionic liquids can completely avoid the unwanted third phase formation even at very high metal/acid loading in the organic phase due to their high polar and solvating nature. The illustration is displayed in Figure 1. For instance, no third phase was encountered during the extraction of high concentration of Ln(III) (stoichiometric level) and nitric acid in a solution of ionic liquid diluents containing the molecular extractants such as carbamoylmethylphosphine oxide (CMPO) and *N,N,N',N'*-tetra(2-ethylhexyl) diglycolamide. The ionic liquid used for the studies

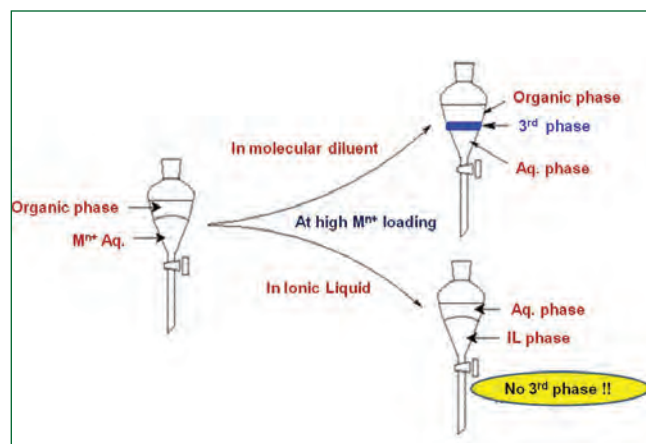


Fig. 1 Illustration of absence of third phase formation in Ionic liquid solvent

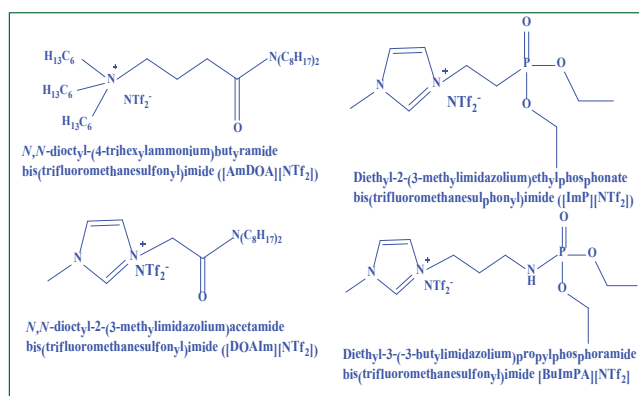


Fig. 2 Structure of some TSILs developed

were imidazolium and ammonium based (1-butyl-3-methylimidazolium bis(trifluoromethanesulfonyl)imide ([C₄mim][NTf₂]); Methyltrioctylammonium nitrate ([N₁₈₈₈][NO₃])). The extraction of nitric acid or the metal ion into the ionic liquid phase leads to the formation of polar acid (or metal)-solvate species that are essentially stabilized by the polar nature of ionic liquid, which in turn, results in the dispersion of polar aggregates and avoiding the third phase formation. This is in contrast to the molecular solvent *n*-dodecane, wherein the third phase appears at early stage of acid or metal loading that hampers the smooth hydrometallurgical process. Unlike the IL phase, the polar aggregates formed at high metal/acid loading in the organic phase are not stabilized enough due to the nonpolar surrounding and essentially undergo demixing leading to third phase.

Selective separation of plutonium(IV) over uranium(VI) and americium(III) using Task Specific Ionic Liquids (TSILs)

During spent fuel reprocessing, there exists a difficulty in separation of the tetravalent plutonium(IV) from the hexavalent uranium(VI) as they coordinate to the equal extent with the neutral molecular extractant in conventional diluent medium. Our findings using ionic liquid as the solvent revealed that it is quite convenient to separate Pu(IV) from U(VI) and other actinides and fission products with remarkably high separation factors, by functionalizing a suitable ligating moiety on to the cation or anion of otherwise a traditional ionic liquid (known as task specific ionic liquid (TSIL)). Owing to the presence of functional group, the resultant ionic liquid is expected to exhibit the properties of both ionic liquid and organic functionality. Figure 2 represents couple of novel TSILs bearing phosphonate, amide

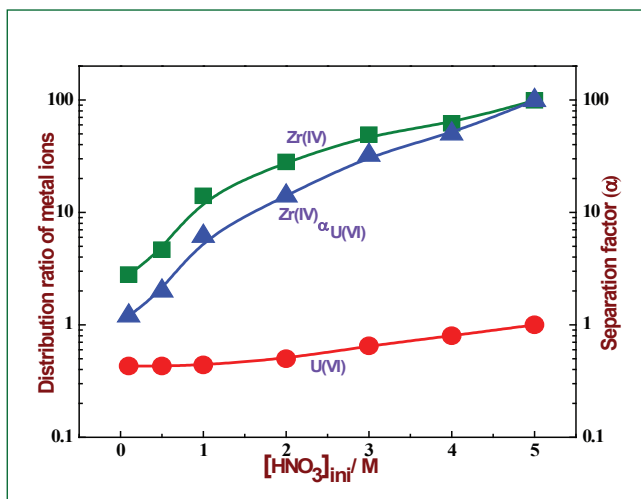


Fig. 3 Extraction and separation factors of Zr(IV) over U(VI) in ionic liquid medium

and phosphoramidate functional groups developed in our laboratory, which offer remarkable separation factors for Pu(IV) from U(VI), Am(III) and fission products while extracting from nitric acid as well as the high level liquid waste (HLLW) solution. The separation factor of Pu(IV) from other metal ions was found to be in the range of $\sim 10^2$ - 10^5 . Most importantly, these TSILs are recyclable and reusable. The selectivity of these TSILs for Pu(IV) and incredible rejection of U(VI) and other metal ions present in the nitric acid medium definitely offers the merit in employing ionic liquid solvent for the single step separation of Pu(IV) rather than following the traditional co-extraction stripping cycle those encountered in the case of molecular diluent (*n*-DD).

Selective Separation of Zirconium(IV) from Uranium(VI) in Ionic Liquid medium

With respect to the reprocessing of spent metallic fuel, the presence of zirconium in the spent metallic fuel (as ~ 6 to 10% of zirconium is present in the metal fuel: U-Zr and U-Pu-Zr alloy) poses several challenges during the dissolution and subsequent aqueous reprocessing of the spent nuclear fuel to recover the fissile materials. Therefore, it is essential to remove zirconium from the dissolver solution before subjecting it to solvent extraction. In this context, a strongly hydrophobic ammonium based ionic liquid based solvent system was employed for the selective separation of zirconium from uranium present in the nitric acid. The ionic liquid used was methyltributylammonium bis(trifluoromethylsulfonyl) imide ($[N_{1444}][NTf_2]$) containing a benzodioxamide (BenzoDoda) ligand. The results showed the high possibility of removing zirconium from the bulk quantity of uranium present in the dissolver solution with high magnitude of separation factor (Figure 3).

Mutual Separation of lanthanides(III) and actinides(III) in Ionic Liquid medium

The most challenging task at the back end of the nuclear fuel cycle is the lanthanide–actinide separation using molecular diluents in the extracting phase. This is obviously due to the similarity in the physical and chemical properties of lanthanides and actinides present in high-level liquid waste. However, the minor differences in their chemical reactivity towards certain complexing reagents are being exploited during the process of lanthanides/actinides separation. In this context, the mutual separation of lanthanides/actinides in ionic liquid medium was explored, using Eu(III) and Am(III) as the representative of lanthanide(III) and actinide(III), respectively. The ionic liquid diluent, 1-octyl-3-methylimidazolium bis(trifluoromethanesulfonyl) imide ($[C_8mim][NTf_2]$) was conjuncted with the acidic extractants such as bis(2-ethylhexyl)phosphoric acid (D2EHPA) and bis(2-ethylhexyl)diglycolamic acid (HDEHDGA) for the separation study. Separation of Eu(III) from Am(III) using ionic liquid medium is illustrated in Figure 4. Our studies confirmed that these extractants in conjunction with $[C_8mim][NTf_2]$ provide excellent extraction and separation of Eu(III) from Am(III) present in the aqueous phase of widely differing compositions of feed acidity and the aqueous complexing agent (diethylenetriaminepentaacetic acid (DTPA)).

Overall, the potential of IL as a novel and unique solvent is meticulously explored in all possible dimensions in our laboratory in the context of spent nuclear fuel reprocessing.

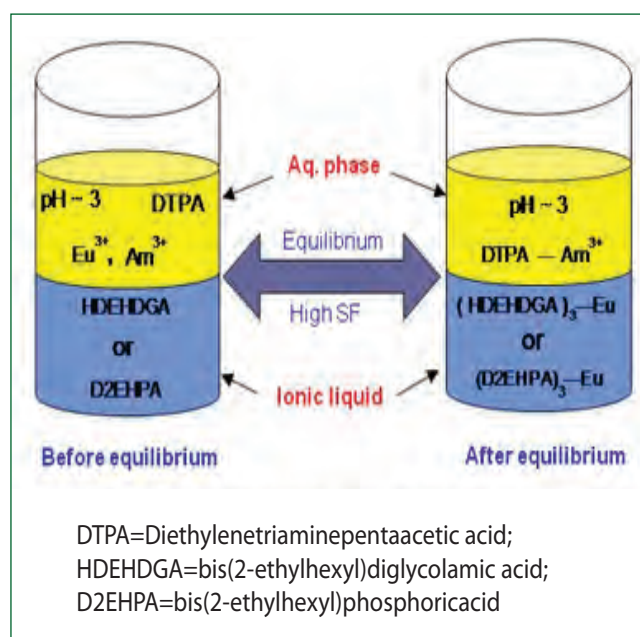


Fig. 4 Illustration of Eu(III)/Am(III) separation in ionic liquid medium

IV.20 Recovery of Zr from Raffinate Solutions using Tri-n-butyl Phosphate and Tri-iso-amyl Phosphate Solvents

In the recent past, a method based on PUREX process as an alternate to the pyro-processing of metallic fuels has been examined in our laboratory. In this method U-Zr and U-Pu-Zr metallic fuels were dissolved in nitric acid medium followed by separation of U and Pu from Zr using tri-n-butyl phosphate (TBP) and tri-iso-amyl phosphate (TiAP) based solvents. A solution of Zr in nitric acid medium (Raffinate) is generated from the above extraction experiments. Recovery of Zr from raffinate is important with respect to waste management. Solvent extraction studies in the cross-current mode were carried out to recover Zr from raffinate solutions. The extraction of Zr by 1.1 and 1.47M Trialkyl Phosphates (TalP, TBP and TiAP) in *n*-dodecane from Zr feed solutions in cross-current mode was evaluated. The concentrations of Zr in the feed solution are around 5 g/L, in 4 and 6M HNO₃. The cross-current experiments were carried out until the quantitative extraction and stripping was achieved. The extraction of Zr(IV) by TBP and TiAP was found to be higher from 6M compared to that of 4M nitric acid (Figures 1 and 2). The extraction of Zr by 1.47M TalP is higher than that of 1.1M TalP. However, the extraction of Zr by TBP based systems is higher than that of TiAP. The extraction (%) of Zr and the number of stages required for the extraction of Zr by TBP and TiAP based solvents are presented in the Table 1. Subsequently, stripping of Zr from loaded organic phase was carried out using 0.01M HNO₃ in cross-current mode. Quantitative stripping of Zr (>99%) was observed in 3 stages. It is concluded from these studies that the extraction of Zr is higher in the case of 1.47 M TalP/*n*-DD and was found

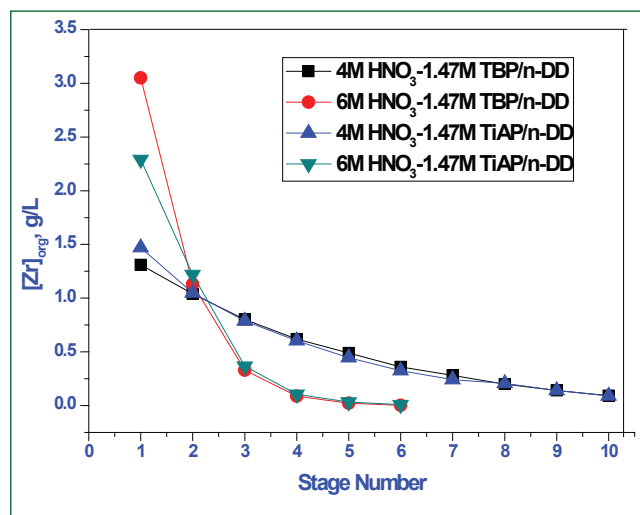


Fig. 2 Organic stage profiles for Zr during the extraction from 4 and 6M HNO₃ by 1.47M TalP/*n*-DD at 303K

to be >99% within 5 stages for both TBP and TiAP from 6M HNO₃; whereas in the case of 1.1M TalP/*n*-DD-4M HNO₃ system, the quantitative extraction (>99%) of Zr was achieved in 7 and 8 stages, respectively, for TBP and TiAP systems. However, quantitative extraction of Zr could not be achieved even up to 10 stages, in the case of extraction by 1.1M or 1.47M TalP/*n*-DD systems from 4M HNO₃. Based on the results of cross-current experiments, mixer-settler runs were carried out with 1.47M TBP/*n*-DD using Zr feed solution (~ 5 gpl in 6M HNO₃). Quantitative extraction (6 stages) and stripping of Zr (3 stages) was achieved in mixer-settler experiments. These studies may pave way for the development of flowsheets for the recovery of Zr from raffinate solutions.

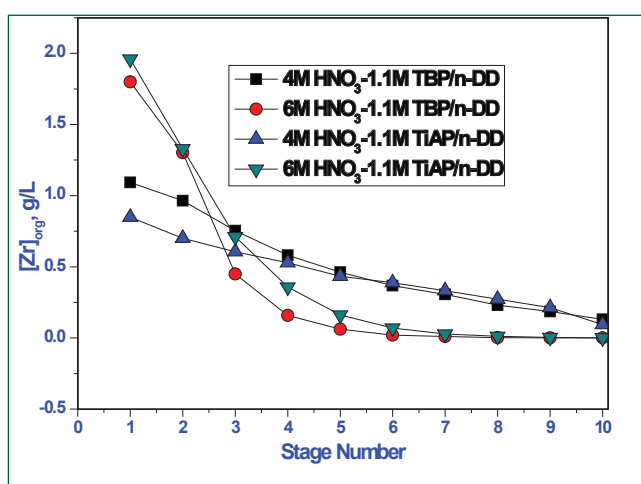


Fig. 1 Organic stage profiles for Zr during the extraction from 4 and 6M HNO₃ by 1.1M TalP/*n*-DD at 303K

Table 1: Extraction (%) of Zr and the number of stages required for the extraction of Zr by TBP and TiAP

System	Zr extraction (%)		Number of stages required to achieve % of Zr extraction	
	TBP	TiAP	TBP	TiAP
4 M HNO ₃ -1.1 M TalP/ <i>n</i> -DD	91.8	82.3	10	10
6 M HNO ₃ -1.1 M TalP/ <i>n</i> -DD	>99	>99	7	8
4 M HNO ₃ -1.47 M TalP/ <i>n</i> -DD	96.7	95.1	10	10
6 M HNO ₃ -1.47 M TalP/ <i>n</i> -DD	>99	>99	5	5

IV.21 Studies on Some of the Auxiliary Processes of Pyrochemical Reprocessing

Pyrochemical reprocessing based on the molten salt electrorefining is best suited for reprocessing metal based irradiated fuels because of its various advantages over the conventional aqueous reprocessing. The process flow sheet with important process steps is shown in the Figure 1. The process is carried out under inert atmosphere. Electrorefining is a key process step of the flow sheet, where actinides from the irradiated fuel are separated from the fission products. LiCl-KCl eutectic along with 4 to 6 wt.% actinide chlorides is used as an electrolyte and the electrorefining is carried out at about 773 K. There are possibilities of conversion of actinide chlorides to their oxides/oxychlorides by reacting with the residual impurities of oxygen and moisture and also with the accidental leakage of atmospheric air into the process lines. The product also gets contaminated and efficiency of the process reduces with time due to the accumulation of the fission product chlorides. This necessitates the development of auxiliary process steps. As a part of it, (i) studies on the conversion of oxides to their chlorides with the aid of AlCl_3 and (ii) the studies on the conversion of chlorides to oxides/oxychlorides by sparging with different gases and reacting with Li_2O have been taken up and the details of the experiments are given below.

Studies on the conversion of samarium oxide to samarium chloride in LiCl-KCl with AlCl_3

Electrorefining is carried out at 773 K where LiCl-KCl eutectic along with 4 to 6 wt.% actinide chlorides is used as an electrolyte. The actinide chlorides get

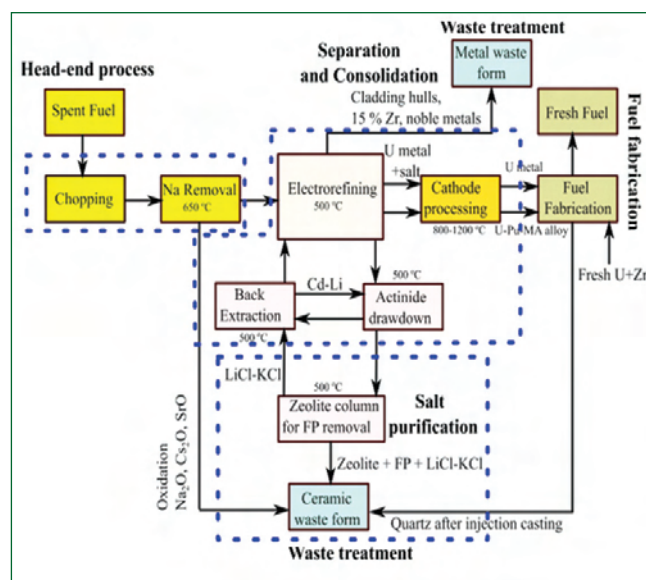


Fig. 1 Process flow sheet - pyrochemical reprocessing

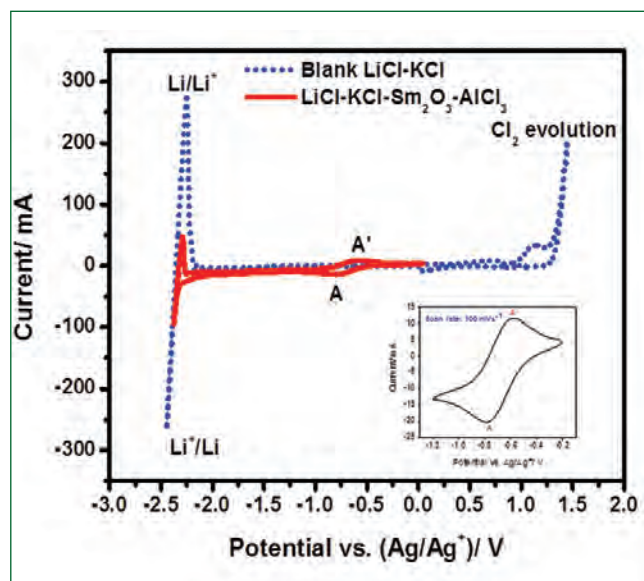


Fig. 2 Cyclic voltammograms of blank LiCl-KCl and equilibrated LiCl-KCl- Sm_2O_3 - AlCl_3 melt at 773 K

converted to their oxides/oxychlorides by reacting with the residual impurities of oxygen and moisture and also with the accidental leakage of atmospheric air into the process lines. The loss of actinide chlorides will lead to a decrease in process efficiency as well as decrease in quality of the final product. Therefore the conversion of oxides and oxychlorides of actinides back to their tri-chlorides is important. AlCl_3 is used as one of the chlorinating agent to convert the oxides and oxychlorides of actinides to their chlorides. As lanthanides have similar chemical properties like actinides, lanthanide oxides may react with the chlorinating agent and form their chlorides and may influence the chlorination of actinide oxides. Therefore, detailed study of the chlorination process of lanthanide oxides is important to control the conversion process of actinide oxides. Samarium is being one of the constituent of the lanthanide fission products, the conversion reactions of Sm_2O_3 to SmCl_3 with AlCl_3 have been taken up.

Sm_2O_3 (3.3 wt%) was equilibrated with AlCl_3 in 100 g LiCl-KCl for 16 hours at 773 K inside high pure argon atmosphere glove box (O_2 and moisture < 10 ppm). AlCl_3 being volatile at the experimental temperatures, more than the stoichiometric amount was taken. After equilibration, the products were analysed by cyclic voltammetry and UV-VIS spectroscopy. Figure 2 shows the cyclic voltammograms (CV) of blank LiCl-KCl and equilibrated LiCl-KCl- Sm_2O_3 - AlCl_3 melt at 773 K on W electrode. Ag/1wt.%AgCl in LiCl-KCl melt in quartz membrane was used as the reference electrode. The

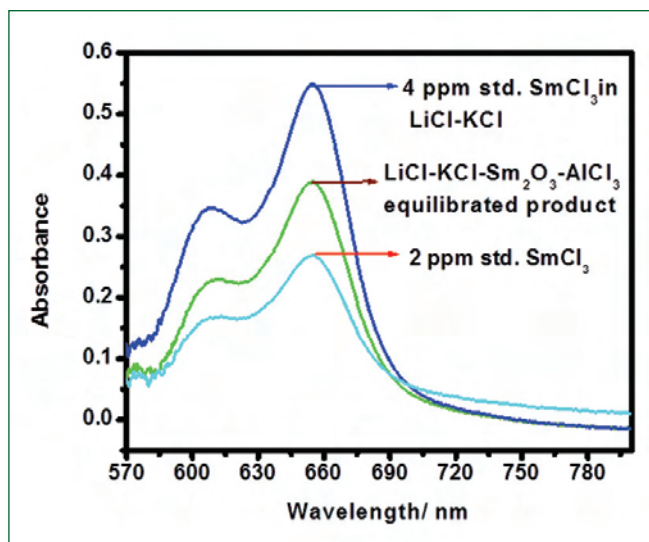


Fig. 3 UV-VIS spectroscopy of standard references and LiCl-KCl-Sm₂O₃-AlCl₃ equilibrated

CV of blank LiCl-KCl shows Li deposition at -2.35 V and chlorine evolution at +1.25 V. The CV of LiCl-KCl-Sm₂O₃-AlCl₃ equilibrated melt shows a pair of redox peaks (A/A') other than the Li/Li⁺ redox couple. The reduction peak at -0.73 V is due to Sm³⁺, which infers the conversion of Sm₂O₃ to SmCl₃ in the melt as Sm₂O₃ is insoluble in the LiCl-KCl melt.

The LiCl-KCl-Sm₂O₃-AlCl₃ equilibrated samples were also analysed by UV-VIS spectroscopy (Figure 3). The samples were dissolved in water and residue was filtered out. The dissolved samples were dried and made up with HNO₃. The dissolved portion of the samples showed absorbance at 608 and 654 nm which are similar to the standard SmCl₃ solutions. The standard samples were prepared by dissolving SmCl₃ in HNO₃ and analysed by UV-VIS spectroscopy to find the reference absorbance peaks. The UV-VIS analysis confirms the presence of Sm³⁺ ions in the equilibrated LiCl-KCl-Sm₂O₃-AlCl₃ melt.

Analysis of the product by cyclic voltammetry and UV-VIS spectroscopy confirms that AlCl₃ converts Sm₂O₃ to SmCl₃ in LiCl-KCl electrolyte at 773 K and will be influencing the chlorination process of actinide oxides when actinides and rare earth oxides present together. Studies on the separation of the by product Al₂O₃ are being worked out.

Studies on the conversion behavior of rare earth chlorides (CeCl₃ and NdCl₃) to oxychlorides/oxides by sparging with different gases and reacting with Li₂O

As already mentioned, electrorefining is carried out at 773 K where LiCl-KCl eutectic along with 4 to 6 wt.% actinide chlorides is used as an electrolyte. This is a batch process and with each batch of electrorefining of

irradiated fuels, the alkali, alkaline earth and rare earth fission products get converted to their chlorides as their chlorides are more stable than actinide chlorides and accumulate in the electrolyte. The accumulation of fission product chlorides deteriorates the product and process efficiency. This necessitates the purification of the electrolyte from the fission product chlorides. One of the methods proposed is to convert the chlorides to their oxychlorides/oxides and precipitate. As a part of it, studies on the conversion behaviour of rare earth chlorides CeCl₃ and NdCl₃ to oxychlorides/oxides in LiCl-KCl melt at 773 K by sparging with wet argon, dry and wet oxygen and reacting with Li₂O have been taken up. About 6.6 wt.% of CeCl₃ and NdCl₃ were taken individually for each run and loaded into 20 g of LiCl-KCl eutectic melt. The LiCl-KCl salts were vacuum dried and chlorinated under chlorine gas at about 773 K prior to use in the experiments. The sparging with gases have been carried out at a flow rate of 25 ml/min for about one hour. The reactions with Li₂O have been carried out by taking stoichiometric amount of Li₂O and the reaction time was about one hour.

The cyclic voltammograms of LiCl-KCl-CeCl₃ taken after the reactions are shown in Figure 4. Cyclic voltammograms confirm that the significant conversion of rare earth chlorides to oxychlorides/oxides takes place when Li₂O is used as reactant. Whereas the gaseous sparging of rare earth chlorides in LiCl-KCl melt results in partial conversion. The partial conversion is probably due to the slow kinetics of gas-liquid(molten salt) reactions.

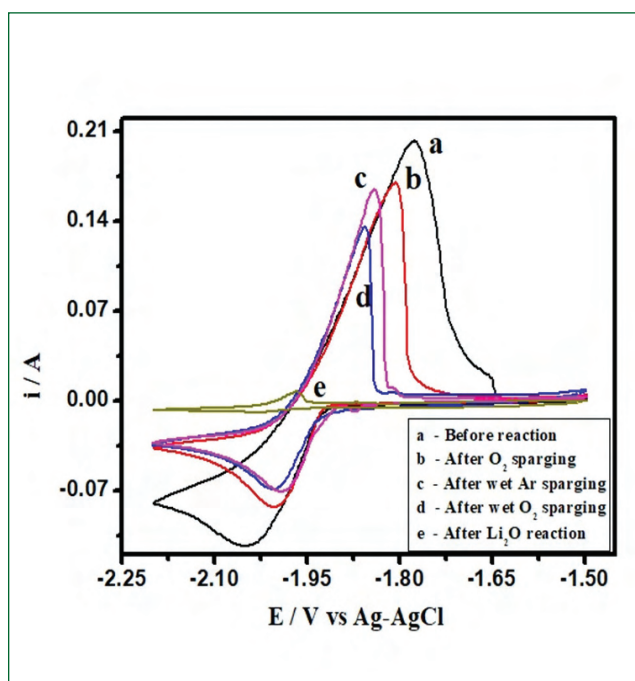


Fig. 4 Cyclic voltammograms of LiCl-KCl-CeCl₃ taken after the reactions

IV.22 Achieving Leak Tightness in 500 m³ Argon Containment Box of Pyro Process R&D Facility

Pyroprocess R&D Facility (PPRDF) is being set up for scaled up studies on alloys of natural uranium at 10 kg per batch scale so that the experience will be generated for designing a Pyroprocess plant. This facility has an argon atmosphere Containment Box (CB) of 500 m³ volume. The CB houses several process equipments such as a High Temperature Electro Refiner (HTER) and an Automated Vacuum Distillation & Melting system (AVDMS) along with in-cell crane and power manipulator for enabling remote operation. The CB has a number of openings with installed viewing glass panels, electrical and instrument lines feed through, antechambers, etc. Leak into the CB through these openings or weld joints would be detrimental for the purity of inert gas and hence, of the final product. Leakage rate test of CB is therefore required to ensure the purity of argon inside the CB and also to limit release of radioactive material from it under design basis accident conditions. The purpose of this test was to estimate the overall leakage rate of the PPRDF CB at both positive (+100 mmWC) and negative (-100 mmWC) pressure for comparison with the maximum allowable leakage rate (0.1 Box vol% / h).

PPRDF CB is a large rectangular box of inside dimensions 18.5 m x 3.5 m x 6 m. It is a large leak tight box made of stainless-steel plates with side wall thickness of 6 mm and floor thickness of 10 mm and the box is reinforced with carbon steel structural members. Acrylic viewing windows and lighting windows are provided at side walls and roof respectively. There are 39 numbers of viewing windows on side walls. All windows are having double O-ring flanges with provision for inter seal pressurization. There are several circular feed-through flanges along the length of CB for giving electrical and instrument connections. CB is provided with 3 transfer ports. Transfer port doors are having motorized sealing mechanism. CB is also provided with a hood of 1.3 m (B) x 4.3 (L) x 2.5(H) at top for accommodating a 2 Ton hoist. It is also having penetrations for argon, salt, gas sampling, chilled water and vacuum lines. Figure 1 shows the photograph of CB.

The test was conducted as per the detailed test procedure in compliance with ISO-10648 (Part-2). The test was divided into three stages. In the first stage, gross leak of CB was checked, in the second stage, leakage rate was determined using pressure drop method at 100mmWC and in the third stage, leakage rate was determined using pressure rise method at -100mmWC. Each stage was an iterative process involving, leakage rate determination, leak point identification and repair.

The main challenges faced during the leak determination were due to large number of weld joints, openings and penetrations such as electrical feed-through, gloves, lighting & viewing windows, transfer ports, motor shafts, gas and salt lines. Due to large size of CB, multiple temperature sensors were installed inside the CB to measure average gas temperature inside CB. To minimize the influence of change in atmospheric temperature and pressure on leak rate determination, the leak tests were mostly conducted only for 1 hour after 4pm during which the atmospheric pressure is steady. To find leak location in CB, various techniques, starting from sound, human touch, acoustic method, soap bubble method, thermal imaging, to argon sniffing were used. Innovative methods like checking of inter-seal pressurization line of each viewing & lighting windows of CB using balloon was very helpful in bringing down the leak rate in CB. To determine leak location in CB using argon sniffing method the concentration of argon inside 500 m³ CB was raised to 10 vol% by purging of argon into it. Argon sniffer was then used to locate the leak points in CB. This method was found to be more sensitive than other methods and very helpful in determination of leak points in CB.

The leakage rate of PPRDF CB was determined to be around 0.12 vol% of box per hour at both +100 & -100 mmWC. Figures 2 and 3 shows the CB leak rate determined after each iteration at +100 & -100 mmWC of CB pressure respectively. Efforts are in progress to achieve the targeted leak tightness.



Fig. 1 PPRDF 500m³ CB

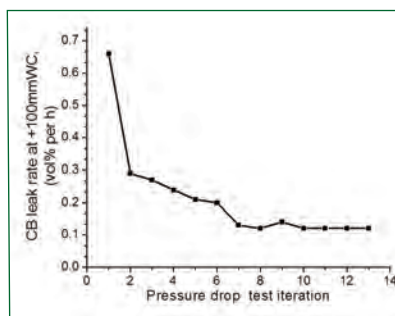


Fig. 2 CB leak rate at +100mmWC

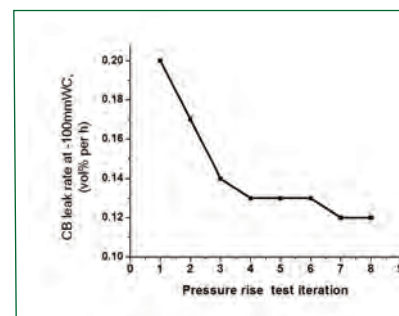


Fig. 3 CB leak rate at -100mmWC

IV.23 Application of Lithium-Tagged Zeolite for Spent Salt Treatment in Back-End of Pyroprocessing

In pyroprocessing flow sheet, once LiCl-KCl eutectic melt gets loaded with fission products, it requires a stage of purification since their presence affects the co-deposition behaviour of uranium and plutonium at liquid cadmium. This is due to the deposition potential of actinides and typical lanthanides in liquid cadmium being very close since thermodynamically, the respective chlorides differ in stability by less than 10 kJ/g-equiv of Cl, and at the same time, the respective activities in the melt are also similar. In such a case, it is necessary to have a stage of purification cycle so that the recycled melt can be used again in subsequent electrorefining campaign. The spent salt treatment therefore, should have two purposes; one to effectively remove the fission products and the other to ensure that a large fraction of the melt is recycled. The traditional approach is to use zeolites for trapping the fission products in its pores and cage structure by ion-exchange and occlusion mechanisms. In the former mechanism, ion-exchangable sodium in the aluminosilicate matrix is replaced by univalent, di-valent and trivalent fission products when the spent salt is equilibrated with zeolite 4A at 500 °C. Sodium from the zeolite phase diffuses into the melt phase and forms NaCl. Presence of NaCl does not affect the electrorefining process but increases the melting point of the melt. The molar eutectic ratio of Li/K also is affected and thus, it is important to address the issues related to contamination of sodium in the melt. In pyroprocessing stream, there are two ways by which sodium can contaminate the melt; one in the head-end step wherein bonded sodium gets dissolved in the melt during dissolution of the fuel, and the other in the back-end step during the spent salt treatment. In

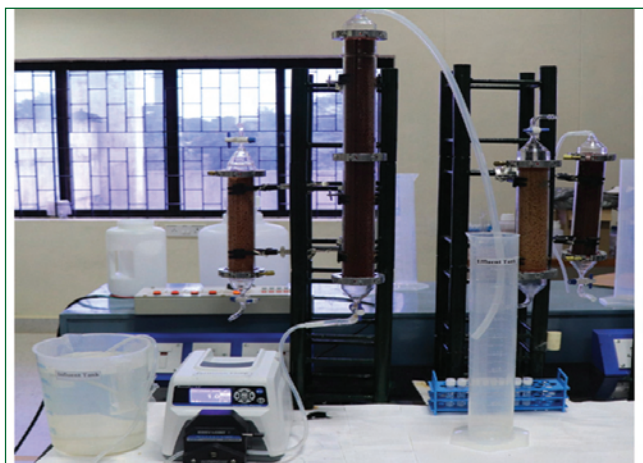


Fig. 1 Ion-exchange column set-up for preparation of Li-zeolites

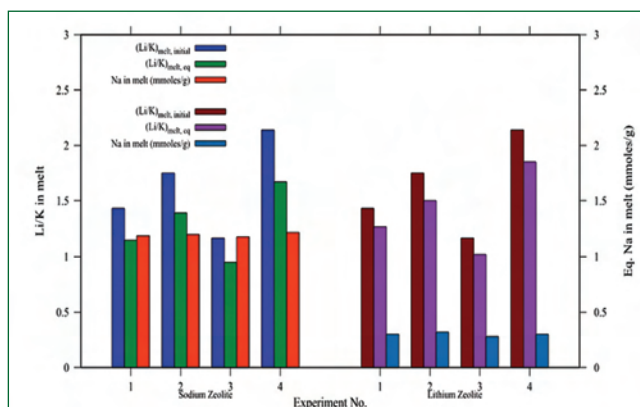


Fig. 2 Comparison of molar Li/K ratio and Na contamination in melt after equilibration of melt with Na- and Li-zeolites at 500 °C

such a scenario, it is necessary to modify the zeolite 4A so that sodium contamination can be partially, if not completely, reduced. In MC&MFCG, an attempt was made to convert the commercial sodium zeolite 4A to lithium-tagged zeolite using ion-exchange column. The commercial form of sodium zeolites is represented as $\text{Na}_{12}(\text{AlO}_2)_{12}(\text{SiO}_2)_{12}$, and it is converted to lithium-tagged zeolite represented by $\text{Li}_x\text{Na}_{12-x}(\text{AlO}_2)_{12}(\text{SiO}_2)_{12}$ where x may vary from 8-10 that is, the average loading of lithium may vary from 66 to 83% of total ion-exchangable sodium initially available. Complete conversion to lithium form is practically difficult to achieve as sodium occupies two different sizes of cavities in the zeolite structure and the size of the smaller cavity is around 2.2 Angstroms in which ion-exchange of sodium is hindered. The conversion to lithium-tagged zeolite was initially demonstrated with 600 g batch and then in 1 kg batch of thermally and vacuum dried Zeolite 4A in which aqueous LiCl solution was passed through the column at a specified flow rate (Figure 1). Based on chemical analysis of residual sodium in the effluent, and that in the zeolite matrix, an average of 80% loading of lithium was achieved on a consistent basis. The zeolite was then vacuum dried at 140 °C before it was used in high temperature experiments. In order to compare the effect of ion-exchange of Na with Li on molar Li/K ratio, LiCl-KCl mixtures with various initial Li/K molar ratios were equilibrated at 500 °C with sodium zeolites and independently with lithium zeolites. Results on both forms of zeolite are compared in Figure 2. As seen clearly from the histogram, for the same Li/K molar ratio, the corresponding sodium contamination is 1.2 and 0.3 mmoles/g of zeolite for sodium and lithium zeolites, respectively. In the latter case, the final molar Li/K ratio

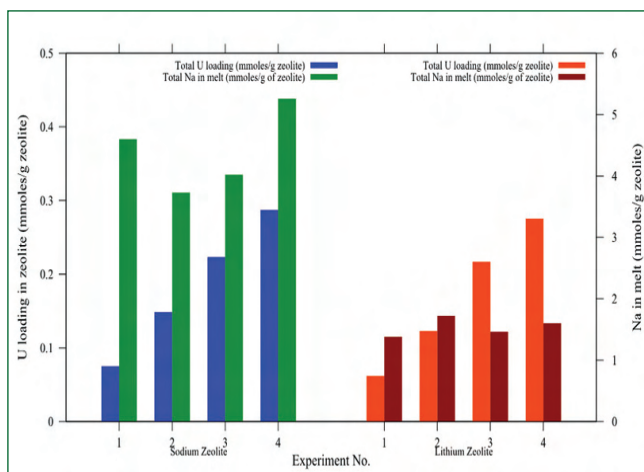


Fig. 3 Comparison of uranium loading and Na contamination in melt when LiCl-KCl-UCl₃ is equilibrated with Na- and Li-zeolite at 500 °C

is also close to that of initial Li/K ratio as against in the former case. Thus, it is clear that lithium form of zeolite 4A is more effective in so far as the relative change in molar Li/K and average sodium contamination in the melt is concerned. Lithium-tagged zeolite was also equilibrated with various compositions of LiCl-KCl-UCl₃ melt at 500 °C to compare the average sodium contamination with that in sodium zeolites when equilibrated with the same

respective melt. Results are shown as a histogram in Figure 3. From the figure, it is clear that uranium loading is more or less similar in both the forms of zeolite whereas average sodium contamination is 5 and 1.5 mmoles/g of zeolite for sodium and lithium-tagged zeolites, respectively. For large scale experiments with spent salt, the contamination of sodium in melt if sodium form of zeolite 4A is used is significant. The similarity of loading behaviour of trivalent actinides suggests that the loading behaviour of trivalent lanthanides should be similar in both the forms of zeolite.

In terms of adsorption isotherms of typical fission products such as Rb, Cs, Ba, Sr and lanthanides, both sodium and lithium zeolites are similar, and therefore, based on the lower contamination of sodium in the latter case, they can be recommended to be used in spent salt treatment. Since the charge to radius ratio of sodium and lithium is different, the occlusion behaviour of LiCl and KCl may not vary significantly although it may be difficult to ascertain experimentally the occlusion fraction. On an average, total Li+K loading in either form of zeolite is seen to be 5.5 mmoles/g of zeolite. Additional experiments to further investigate the co-loading of alkaline earths and lanthanides in lithium zeolites is currently underway.

IV.24 Modified Diglycolamide Solvent Systems for the Treatment of High-Level Waste Solutions from Metallic Fuel Reprocessing Streams

It has been roughly estimated that the aqueous reprocessing of one tonne of spent nuclear fuel generates approximately 3000-4000 liters of high-level waste (HLW) solution. The selective partitioning of highly radiotoxic trivalent actinides [Am(III) and Cm(III)] (commonly known as the minor actinides) from HLW solutions is considered as one of the most essential steps before final disposal of these waste solutions in geological repositories. Solvent extraction methods have been widely proposed for the above partitioning step and usually they involve multiple separation stages due to the co-extraction of trivalent lanthanides and other fission products. Zirconium is one of the important fission products which usually interfere during minor actinide partitioning. The amount of Zr(IV) in the HLW solutions originated from the reprocessing of U-Pu-Zr metallic fuels would be several times higher than the zirconium content in conventional HLW solutions originated from oxide or carbide fuels. The complex aqueous chemistry of Zr(IV) aids in the selective extraction

of zirconium in the solvent systems used for minor actinide partitioning, thereby lowering the extraction of minor actinides. Moreover, the extracted zirconium easily gets precipitated as curd in the organic-aqueous interphase of the solvent extraction systems, creating additional problems in the extraction process.

Diglycolamide (DGA) based ligands such as *N,N,N',N'*-tetraoctyldiglycolamide (TODGA) are widely studied for minor actinide partitioning by different groups all over the world. However, our studies showed that most of the diglycolamide solvents were not suitable for the extraction of even moderate amounts of zirconium from nitric acid solutions. The extraction of increasing concentrations of Zr(IV) from 4 M nitric acid medium in different DGA solvents is shown in Figure 1. Among the different solvents studied, a solvent system comprising of 0.1 M TODGA/n-dodecane along with 0.25 M HDEHP (di-ethylhexyl phosphoric acid; a phase modifier) was found to have good extraction capacity for Zr(IV). This solvent

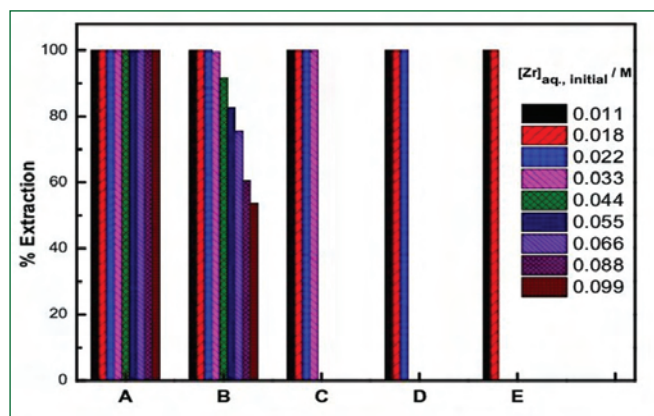


Fig. 1 Extraction of Zr(IV) from 4 M nitric acid in different extractant systems below the crud formation limits. Organic phase A: 0.1 M TODGA + 0.25 M HDEHP B: 0.1 M TODGA + 1 M DHOA C: 0.1 M TODGA + 0.5 M DHOA D: 0.1 M TDdDGA E: 0.1 M D³DODGA. Diluent: *n*-dodecane

was found to extract up to 9 g/L of Zr(IV) without any crud formation, while other solvent systems in the study such as *N,N,N',N'*-tetradecyldiglycolamide (TDdDGA) and *N,N*-didodecyl-*N',N'*-dioctyldiglycolamide (D³DODGA) showed crud formation when Zr(IV) concentration was 3-5 g/L. Dynamic Light scattering studies showed that the aggregation of TODGA in *n*-dodecane diluent during the extraction of Zr(IV) was effectively minimized in the presence of HDEHP, as compared to other phase modifiers such as DHOA (di-hexyl octanamide). Figure 2 shows the comparison of zirconium extraction and average aggregate sizes measured for TODGA-DHOA and TODGA-HDEHP solvents under similar conditions. It was found that HDEHP was just a 'reactive' phase modifier by participating in the extraction of Zr(IV), along with minimizing the aggregation of TODGA. Therefore, the TODGA-HDEHP solvent was studied for the extraction of different metal ions from simulated HLW solutions from metallic fuel reprocessing streams, containing Zr(IV) varying from 0.6 g/L to 8 g/L.

The TODGA-HDEHP solvent, however, showed crud formation after equilibration with simulated HLW solutions containing Zr(IV) 4 g/L or above. In order to eliminate the crud formation under these conditions, it was necessary to reduce the extraction of zirconium in this solvent by suitable masking agents. The masking of Zr(IV) extraction by the use of complexing agent CyDTA (trans-1,2-diaminocyclohexane-*N,N,N',N'*-tetraacetic acid) was studied by adding various amounts of CyDTA (0.05 M to 0.3 M) in aqueous solutions containing different concentrations of Zr(IV) in 4 M nitric acid and then estimating the amount of free zirconium (Figure 3). The results showed that the addition of 0.1 M CyDTA to different solutions effectively masked nearly 0.1 M (10 g/L) of Zr(IV) in each case. The masking efficiency of CyDTA was found to be lowered when used with simulated HLW

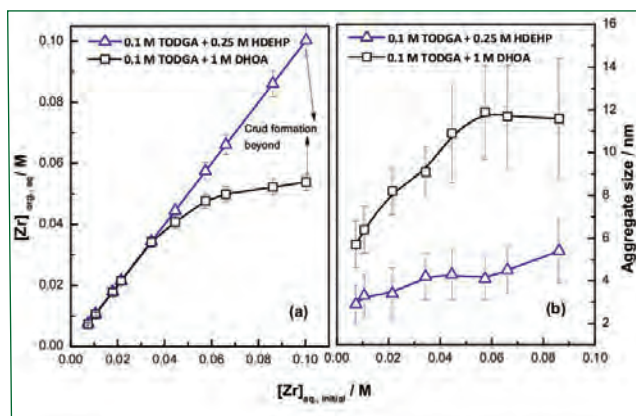


Fig. 2 Extraction of Zr(IV)(Grid a) and the variation in the average aggregate size (Grid b) observed in the organic phases containing 0.1 M TODGA/*n*-dodecane having different phase modifiers studied at different initial aqueous concentrations of Zr(IV). Aqueous phase: 4 M nitric acid containing Zr(IV) concentration varied from 0.01 M (1 g/L) to 0.09 M (10 g/L)

solutions. Nearly 60% of the zirconium content in the waste solution remained in the aqueous feed after extraction by TODGA-HDEHP solvent, when 0.1 M CyDTA was added to the simulated HLW solutions as masking agent. Also, the crud formation was avoided and the extraction of trivalent metal ions was improved under these conditions, enabling a better separation of target metal ions (trivalent actinides and lanthanides).

In summary, a solvent system consisting of 0.1 M TODGA along with 0.25 M HDEHP in *n*-dodecane is ideally suitable for the treatment of HLW solutions from metallic fuel reprocessing streams, where the zirconium content is expected to be rather high (6-8 g/L). Batch studies with simulated HLW solution containing up to 8 g/L of zirconium showed quantitative separation of targeted trivalent metal ions in this solvent and no crud formation or phase disengagement problems were observed in the solvent when 0.1 M CyDTA was used as the masking agent in the aqueous feed.

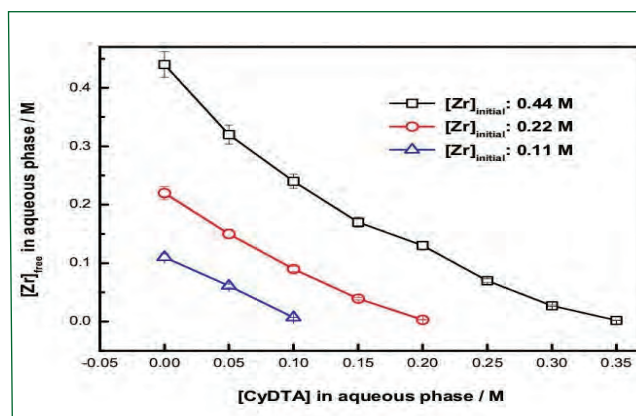


Fig. 3 Decrease in the amount of free (uncomplexed) zirconium after addition of CyDTA to 4 M nitric acid solutions containing different initial amounts of zirconium

IV.25 Study on Attenuation Relationship in Controlled Blasting for Bedrock Excavation of Near Surface Storage & Disposal Facility

Foundations of nuclear power plant structures, dams and other heavily loaded structures are often supported on competent rock strata which are moderate to slightly weathered rock. Excavation in rock strata is often carried out by mechanical chiselling, hydraulic splitting, expansive grouts and blasting. However, the choice of bed rock excavation depends on the quantum of rock to be excavated, strength and type of the rock and safety of adjacent structures. Controlled blasting is an advanced rock excavation technique which is employed for hard rock (like chanochite type) excavation, where in safety of the adjacent existing structures is not affected. Excavation using controlled blasting involves use of explosives and non electric detonators. These release shock waves which exert pressure on the rock, resulting in fragmentation of rock mass. Controlled blasting is designed with suitable burden, spacing and depth of blast holes, stemming, and delayed detonation to ensure the required fragmentation. Performance of controlled blasting is usually evaluated using a parameter called Peak Particle Velocity (PPV) and this value is limited to 2 mm/s as prescribed by Directorate General of Mines Safety (DGMS) to minimize the damage to existing nearby structures. With a known PPV value, the charge per delay can be estimated by conducting a site specific trial blast study. The PPV is usually expressed in terms of scaling distance and site specific constants as

$$V = K \times SD^{-B} \quad \text{----- (1)}$$

where K, B; are site constants; V is the PPV in mm/s and SD is the scaling distance in mm.

Scaling distance (SD) is defined as the ratio of distance at which PPV measured from source to the charge to the quantity of explosive, used per delay in blasting. Different relations are available in literature (Table 1) for calculating possible blast wave PPV.

In this study, site specific constants were evaluated from a trial blast for Near Surface Storage and Disposal Facility (NSSDF) of FRFCF and the actual controlled blasts were monitored to update the site specific constants. As a first step, trial blast was carried out to establish range of blast charge and delay to be followed for the main rock excavation. The attenuation relation obtained from trial blast study for DGMS relation is as follows,

$$V_{\max} = 178.6 (D/\sqrt{Q})^{-1.19} \quad R^2 = 0.79 \quad \text{---- (2)}$$

$$V_{\max} = 250.24 (D/\sqrt{Q})^{-1.19} \quad R^2 = 0.79 \quad \text{--- (3)}$$

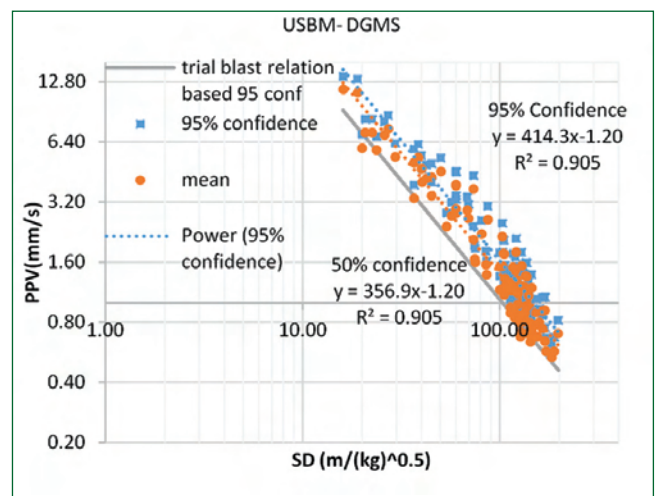


Fig. 1 Plot for attenuation relation by DGMS

Velocity in mm/s and 50% and 95% confidence level are represented in Equation (2) & (3) respectively.

The actual blasts were monitored at different locations and PPV was observed for different specific charge. The observed PPV value was compared with the PPV value predicted from the site specific attenuation relation Equation (3) established from the trial blasts. The comparison indicates that, the PPV values observed are around 40% higher than those predicted from eq (3). Best fit for data with attenuation relation by DGMS has been plotted (Figure1). The site specific constants were predicted using other empirical relations available in literature and indicated in Table 2. Charge required for limiting PPV is assessed with all relations for varying distances.

Table 1: Predictor relations for attenuation	
Proposers of attenuation relations	Equations
United States Bureau of Mines (USBM); DGMS (by Duvall and Fogelson)	$v = K \left(\frac{R}{\sqrt{Q}} \right)^{-B}$
Ambraseys- Hendron (AH)	$v = K \left(\frac{R}{\sqrt[3]{Q}} \right)^{-B}$
Langerfors- Kihlstrom	$v = K \left(\frac{R^{1/3}}{\sqrt{Q}} \right)^{-B}$
Indian Standard (IS) predictor	$v = K \left(\frac{R^{2/3}}{Q} \right)^{-B}$

Site specific relation established from trial blast studies using DGMS correlations are not conservative for distance beyond 200 m and provides higher specific charge per delay in comparison with other relations. Ambraseys- Hendron (AH) relation shows a better correlation and the predicted PPV values are comparable with the actual field values. The site specific relation established using AH formulation provides least specific charge per delay and hence recommended for carrying out controlled blasting in the sites having similar geology with charnockite rock type as that of NSSDF site, Kalpakkam.

Predictor Relation	K	B	R ²	K95%	B95%
USBM (adopted by DGMS)	356.9	1.2	0.90	414.37	1.2
Ambraseys- Hedron (AH)	716.8	1.23	0.92	832.15	1.23
Langerfors- Kihlstom	5.47	2.3	0.6	6.35	2.3
Trial Blast	178.7	1.19	0.8	250.38	1.19

IV.26 Effective Civil Construction of Waste Tank Farm Roof Slab and SS Lined Pedestals

Waste Tank Farm (WTF) is being constructed to receive and store high level liquid waste in Fuel Reprocessing Plant (FRP) in Fast Reactor Fuel Cycle Facility (FRFCF). 14 no.s of Over Dimension Consignment (ODC) tanks are to be erected on SS lined pedestals in WTF at EL(-) 10.5 m. Provision for ventilation ducts and sampling tubes are made in the concrete structure while ensuring adequate shielding through compensatory shielding blocks (CSB) and heavy density concrete (HDC). In WTF, highly congested reinforcement, openings for ducts and its associated erection of CSB and erection of SS plates for pedestals in confined space were challenging tasks. The challenges were addressed with a systematic approach involving field mock up studies, development of high performance HDC, stringent quality control & safety, development of methodology for erection of CSB & heavy SS plates in confined space and design of a flowable concrete mix for pedestal construction.

With an objective of constructing defect-free concrete meeting shielding, durability and process requirements, field mock-up studies were done at site. After successful completion of field mock-ups and statutory approvals, construction of WTF roof slab of 108 m x 54 m size using 7280 cu.m heavy density concrete H 30 was initiated. A special HDC mix was designed to meet the strength, durability and pumpability requirements using hematite iron ore as coarse & fine aggregate and fly ash as mineral admixture to achieve the desired pumpability of 30 cu.m/h, wet density of 3600 kg/cu.m and slump of 130-180 mm. The entire roof slab was taken up in

10 pours with suitable construction joints and a single largest portion of 880 cu.m of concrete was completed in 30 hrs. Photograph of the heavy density concrete works at WTF is shown in Figure 1 and an ariel view of slab is shown in Figure 2. Upon completion of 10 numbers of HDC pours with required strength, post concrete inspections were taken up in parallel with CSB erection at EL (-) 1.3 m in the confined area i.e bottom of WTF slab using specially designed lifting frames meeting safety requirements.

The slab needs to accommodate ventilation ducts, its associated compensatory shielding, numerous process monitoring & sampling pipe sleeves with associated shielding blocks, embedded LLW pipelines, hatch openings and embedded SS plates. The critical aspects

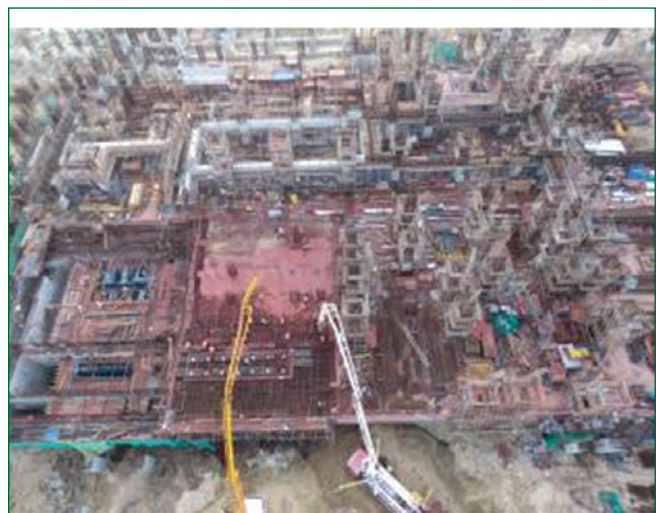


Fig. 1 Heavy density concrete pour at WTF slab



Fig. 2 Areal view of WTF Slab

in the construction of waste tank roof slab was the erection of 16 no.s ventilation ducts with max. size 2000 mm x 750 mm and associated CSB of 31MT in weight. Fabrication of CS plates were taken up at site fabrication yard as per the approved drawings and were lowered to EL (-) 10.5m using tower crane. Special lifting frames were designed and fabricated to erect the CSB. After lowering, the plates were moved to the erection location and subsequently lifted using a chain pulley block of 10 MT capacity. Individual plates were lifted and stacked one over another and welded & inserted through hanger rods. Fit up of plate assembly was then carried out using welding with already embedded plates available at the bottom of slab. Liquid Penetrant examination was carried out for the welds as per the quality assurance procedure. The erected plates were cleaned and painted to avoid corrosion as shown in Figure 3.

The WTF slab has to support 14 Nos of ODC tanks and 28 supporting pedestal structure that is to be casted with 50 mm SS plate (each plate weighing 2MT). The pedestal is to be concreted with N 45 grade concrete and 50 mm thick SS plate needs to be embedded into the pedestal. A special concrete mix was successfully designed to ensure free flow in the highly congested and confined space of pedestal



Fig. 3 Erected CSB at EL (-) 1.3m of WTF Slab

Table 1: Details of mix proportion	
Cement	380 kg
Fly ash	140 kg
Coarse aggregate	773 kg
Fine aggregate (Crushed stone sand)	897 kg
Admixture	2.08 kg
W/C ratio	0.345

and details of this mix proportion is given in Table 1. The various physical properties of the concrete cubes developed from the mix at the end of 28 days is given in Table 2. Based on the mock-up study at site, the size of the pedestal was increased to 1050 mm for free flow of concrete within gap of 100 mm between SS plate and pedestal edge. The plates were transported through chain pulley block and erected over the specified locations for concreting of pedestal and specified tolerance of 1 mm between the pedestals was successfully achieved. The ODC tanks are to be rested on SS lined pedestals of size 5000 mm x 950 mm x 250 mm. The completed pedestal inside WTF tank is shown in Figure 4.

Using this integrated approach involving design, execution, quality and safety. The WTF roof slab was constructed and handed over for erection of ODC tanks in time.

Table 2: Physical properties of N45 concrete	
Cube Compressive strength	60.25 MPa
Cylinder compressive strength	52.23 MPa
Split tensile strength	6.05 MPa
Flexural strength	7.53 MPa
Water permeability	10.5 mm



Fig. 4 The completed SS pedestal inside WTF

IV.27 QA & NDE Practices During Fabrication of Waste Tank Farm (WTF) Tanks for FRFCF

Waste Tank Farm tanks with storage capacity of 212 m³ weighing around 78 MT (Figure 1) are being used in reprocessing plants to store high level radioactive liquid waste of category 5 (activity > 104 µci /ml).

Atypical WTF tank possesses 4600 mm OD and 12000 mm length. These tanks are having lot of internals such as cooling coil arrangements with ballast tanks (Figure 2). Cooling coils are provided to remove decay heat generated due to radioactive decay of fission products.

Since the tanks are not accessible for maintenance once they are put into service due to the presence of high radioactivity, meticulous QA practices shall be put in place during fabrication. Since WTF tank is having lot of internals such as cooling coil, ballast tanks, deep feed nozzles and baffle plates, integrating fabrication sequence and quality assurance plan is inevitable before proceeding with the production activities. Sequence of operations for welding of internals & assembling requires meticulous planning to ensure accessibility for NDE/inspection.

AISI 304L grade austenitic stainless materials in the form of plates, pipes, round bars are selected as workhorse material for WTF tanks. All raw materials are qualified with restricted chemistry, inclusion control and C test for detecting susceptibility to intergranular corrosion in nitric acid environment in addition to stipulated ASTM specification. All raw materials are qualified by both normal & angle beam ultrasonic inspection to ensure freedom from lamination and inclusions.

Totally 8 nos. of cooling coils have been fabricated using AISI 304L material of size DN 80 Sch 40 pipes. These coils were arranged with the pitch of 229 mm through 5 numbers of baffle plates. In order to keep number of cooling coil pipe butt welds as minimal as possible, forged 180° return bends of AISI 304L pre-qualified to the service requirements of tanks (Figure 3) has been used in-lieu of Miter joints for facilitating directional change of cooling coils. All butt welds of cooling coil

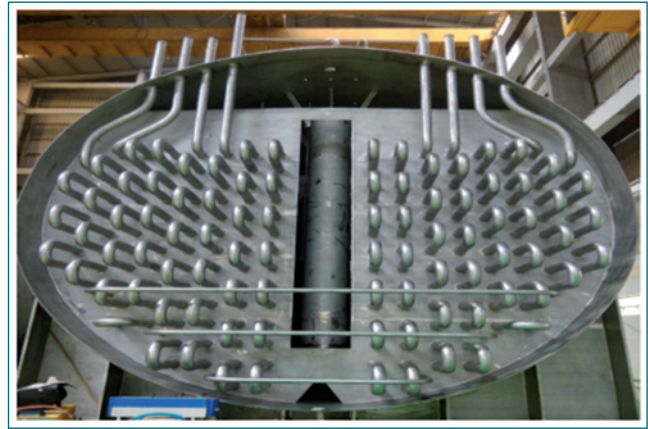


Fig. 2 Cooling coil arrangement in the tank

are volumetrically qualified by radiography using X-rays with double wall.

The NDE of some complex joints such as cooling circuit end connection joints and nozzle to shell (Hill side) joints are not possible by the conventional methods and procedures available due to space constraints and curvature effect. Lot of mockup trials has been performed on set-in nozzle (Hill side) joints (Figure 4) to establish ultrasonic testing procedure aims at 100 % inspectability and differentiating from the spurious false signals.

Numerical controlled automated dished end forming by spinning method is employed to form dished ends. To have a check on effectiveness of post forming heat treatment of formed dished ends, production test coupons made up of same material, thickness & configuration with same fiber elongation has been kept along with product during heat treatment. IGC Practice C testing was performed on PTC for qualification of heat treatment process.

Field deployable effective QA & NDE practices were evolved, validated and implemented during fabrication of WTF tanks aiming at fabricability & 100 % inspectability of all components.



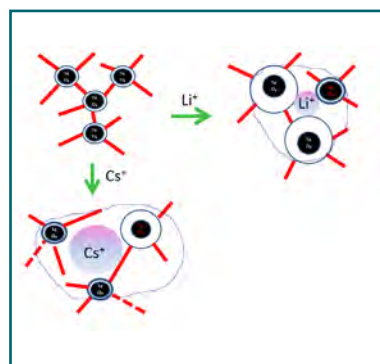
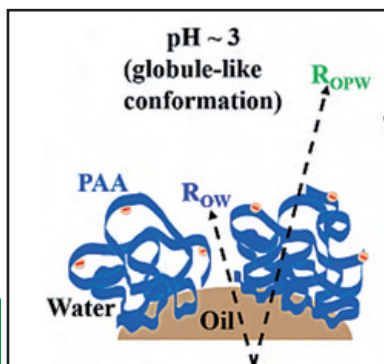
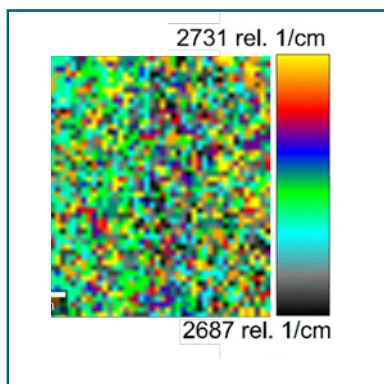
Fig. 1 HLW tank assembly



Fig. 3 Forged 180° return



Fig. 4 Mock-up UT of hill side nozzles



Basic Research

CHAPTER V

V.01 Synthesis of Phase Pure AgInO₂ for Gas Sensing Applications

AgInO₂, an n-type transparent oxide has been reported to form under high temperatures and pressures with residual silver impurity. In this context, we reported the formation of phase pure AgInO₂ by hydrothermal method using nitrates of silver and indium as starting precursors for the first time by conceiving the factorial design approach to identify optimum conditions for the synthesis of phase pure product.

The XRD of the product prepared with the hydrothermal conditions of 180 °C, 4 M KOH and 24 h of dwell time matches with the rhombohedral R3 \bar{m} (166) system of AgInO₂ (Figure 1). The increase in relative intensity of (006) to (012) facets (i.e., I(006)/I(012) = 0.40) to 3.26 indicates texturing. The Rietveld refined unit cell parameters of AgInO₂ are found to be $a = 3.27668(10)$ Å and $c = 18.8838(7)$ Å with the unit cell volume of $175.585(14)$ Å³. The quantitative estimation shows no secondary phases were present.

The factorial analysis is performed by considering 2 level - 3 factorial design and splitting the experimental runs into two blocks. Treating the fractional intensities of the most intense peaks of AgInO₂, Ag and In₂O₃, calculated from the XRD patterns of the samples as response, two design matrices of two levels were constructed. In the first block of experiments, the dwell time shows least significance. Even though a raise in temperature from 150 °C to 180 °C appears to be a favourable factor, its interaction with the concentration of KOH produced an opposite effect. Calculated effects for the second block of experiments indicate that an increase in temperature from 180 °C to 210 °C produced a composite mixture instead of a pure phase. The high negative value of the temperature effect (~ -17) dominates over the positive contribution from the interaction terms. Overall, the conditions for the formation of a pure phase derived from responses show that a

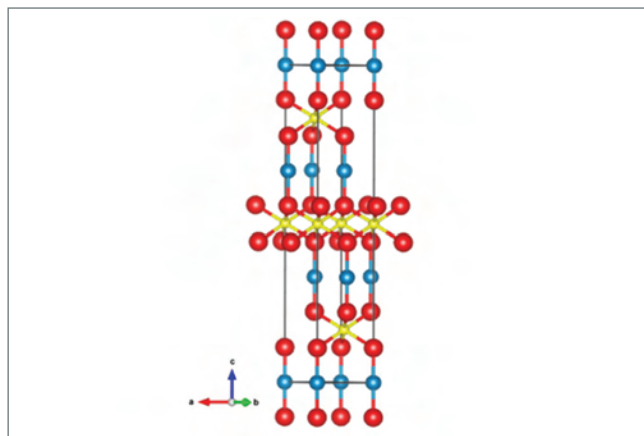


Fig. 1 Crystal structure of AgInO₂ (blue, yellow & red balls indicate Ag, In & O respectively)

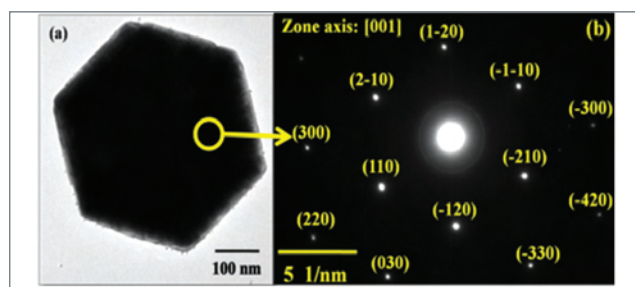


Fig. 2 (a) High magnification TEM image of phase pure AgInO₂; (b) SAED pattern along the [001] zone axis

temperature of 180 °C and 4 M KOH as the optimum parameters with no dependence on dwell time in the range from 24 to 60 h.

FE-SEM disclosed the hexagonal-shaped plate like morphology with an average width of ~ 300 nm and thickness of ~ 70 nm. EDX analysis confirmed the atomic ratio of Ag:In to be 0.98 with no evidence of potassium. The TEM of AgInO₂ grain shows a hexagonal plate-like shape (Figure 2a) and its SAED pattern (Figure 2b) revealing the dominance of (001) facet complementing the XRD results. The percentage fraction of the surface area of the dominantly exposed (001) facets to the total is unusually higher (52 %) than the theoretical estimate of 2 % for isotropic specimen.

XPS survey spectrum of AgInO₂ nanoplates indicated the presence of only Ag, In, C and O. The high resolution scans indicate the presence of Ag and In in +1 and +3 oxidation states respectively along with three oxygen signatures correspond to that of lattice O²⁻, adsorbed O_x⁻ and hydroxyl groups. AgInO₂ exhibited a specific surface area of about 48.5 m² g⁻¹ and the phase is thermally stable up to 595 °C in air. Its optical band gap is 2.20 eV and the activation energy for electrical conduction is found to be 0.24 eV/f.u.

The stabilization of Ag(OH)₂⁻ in strong basic medium, mutual solubility of Ag(OH)₂⁻ and In(OH)₃ in KNO₃ solution and processing temperatures varied from 150 °C (4.8 atm) to 210 °C (18 atm) under hydrothermal conditions are the order of visualization to optimize preparative conditions like temperature, pH and dwell time to realize phase pure AgInO₂. The compound was tested for sensing hydrogen from 1 to 10000 ppm of H₂ in air and it exhibits high degree of selectivity (over NH₃, NO_x, LPG and HCHO) and repeatability.

In conclusion, the importance of factorial design approach towards preparation of phase pure AgInO₂ composed of hexagonal nanoplates is demonstrated and its application for synthesis of other high pressure delafossites/compounds is stressed.

V.02 Large-scale Induction Melting of Iron Phosphate Glass (IPG) in Alumina Coated Inconel Alloy Vessel

IPG is a potential matrix for the immobilization of high level radioactive waste (HLW) of fast reactor origin. For vitrification of HLW in IPG (Iron Phosphate Glass), the glass constituents (Fe_2O_3 and P_2O_5) and the HLW must be melted at temperatures above 1223 K and quenched. In the present study IPG melting at 1 kg scale in an alumina coated Inconel meter vessel by induction heating was demonstrated.

Inconel 600 was the material of choice for the melter vessel. From the previous studies, it was observed that Inconel 600 has poor compatibility with IPG melt at high temperatures. In the present investigation, direct contact of IPG melt with the Inconel melter vessel was avoided by coating the inner melter surface with alumina by plasma spray coating technique. The alumina coating was about 200-250 micron thick. IPG melting was carried out by using RF induction generator set-up in-house. There were two induction coils, one for heating the main melter vessel and the second one to heat the drain pipe. Both the coils were operable independently. First the main heater vessel coil was activated and pristine IPG precursor (1 kg) placed in the melter vessel was melted at 1273 K and then the drain pipe coil was

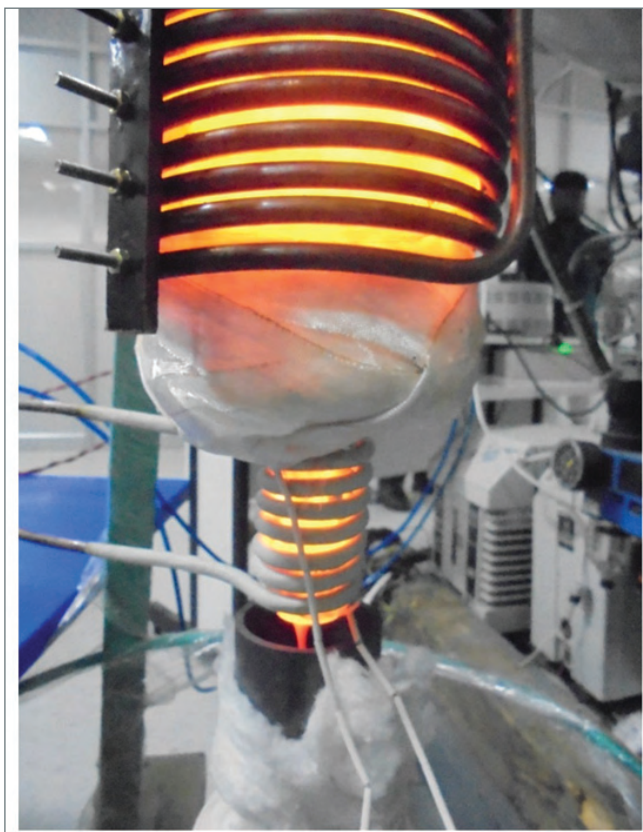


Fig. 1 Induction melting of IPG at 1273 K



Fig. 2 Iron phosphate glass monolith (964 g)

activated to melt the IPG glass seal in the drain pipe, resulting in quenching of IPG melt by bottom draining (Figure 1). The glass melt drained into a graphite crucible and formed a monolith (Figure 2) on cooling. Amorphous nature of the quenched glass melt was confirmed by XRD characterization (Figure 3). The melting experiment was repeated thrice and the integrity of the alumina coating was found to be good.

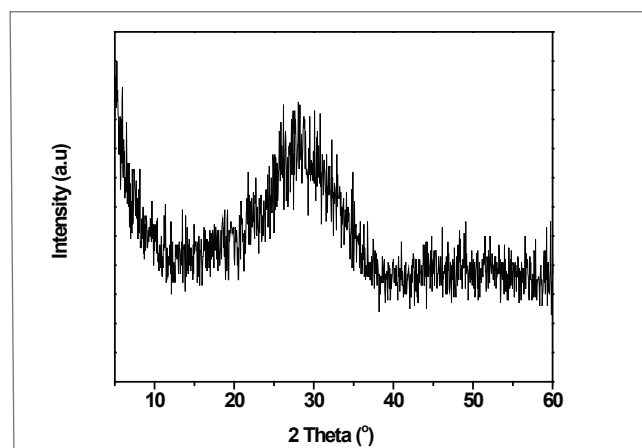


Fig. 3 XRD pattern of IPG monolith

V.03 A Very Low Temperature Crystallization of Amorphous-Ge Thin Film on Glass With High Carrier Mobility

Polycrystalline (*poly*)-Ge thin film on low-cost non-crystalline insulating substrates (glass, polyimide, etc.) are envisaged for applications like high-performance flexible electronics, advanced flat panel displays, high-speed TFTs, and high efficiency solar photovoltaics. Because of the low-temperature requirements, metal-induced crystallization (MIC) processes, wherein a metal in contact with the semiconductor (SC) lowers the crystallization temperature (T_{cryst}) of the SC, have emerged as a key synthesis process. In particular, a controlled MIC process known as metal-induced layer exchange (MILE) crystallization developed to obtain *poly*-Si on glass is extended to *poly*-Ge.

With Au as the metal, amorphous (*a*)-Ge thin film has been crystallized into *poly*-Ge on glass at $\sim 170^\circ\text{C}$, well below its reported bulk $T_{cryst} \sim 500^\circ\text{C}$, using Au-induced layer exchange (AUILE) crystallization process. In this process, while Au catalyzes the lowering of T_{cryst} , the

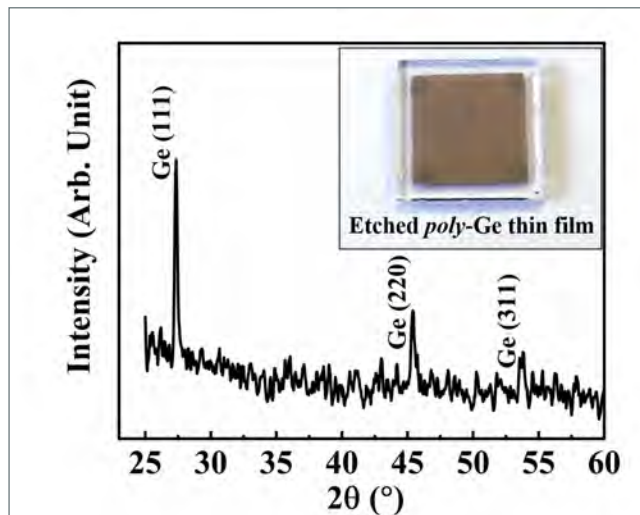


Fig. 2 GIXRD of the Au etched *poly*-Ge thin film on glass

layer exchange phenomenon enables the realization of Au free *poly*-Ge thin film directly on glass. To achieve the same, a thin film stack having *a*-Ge(50 nm)/*a*-GeO_x(2

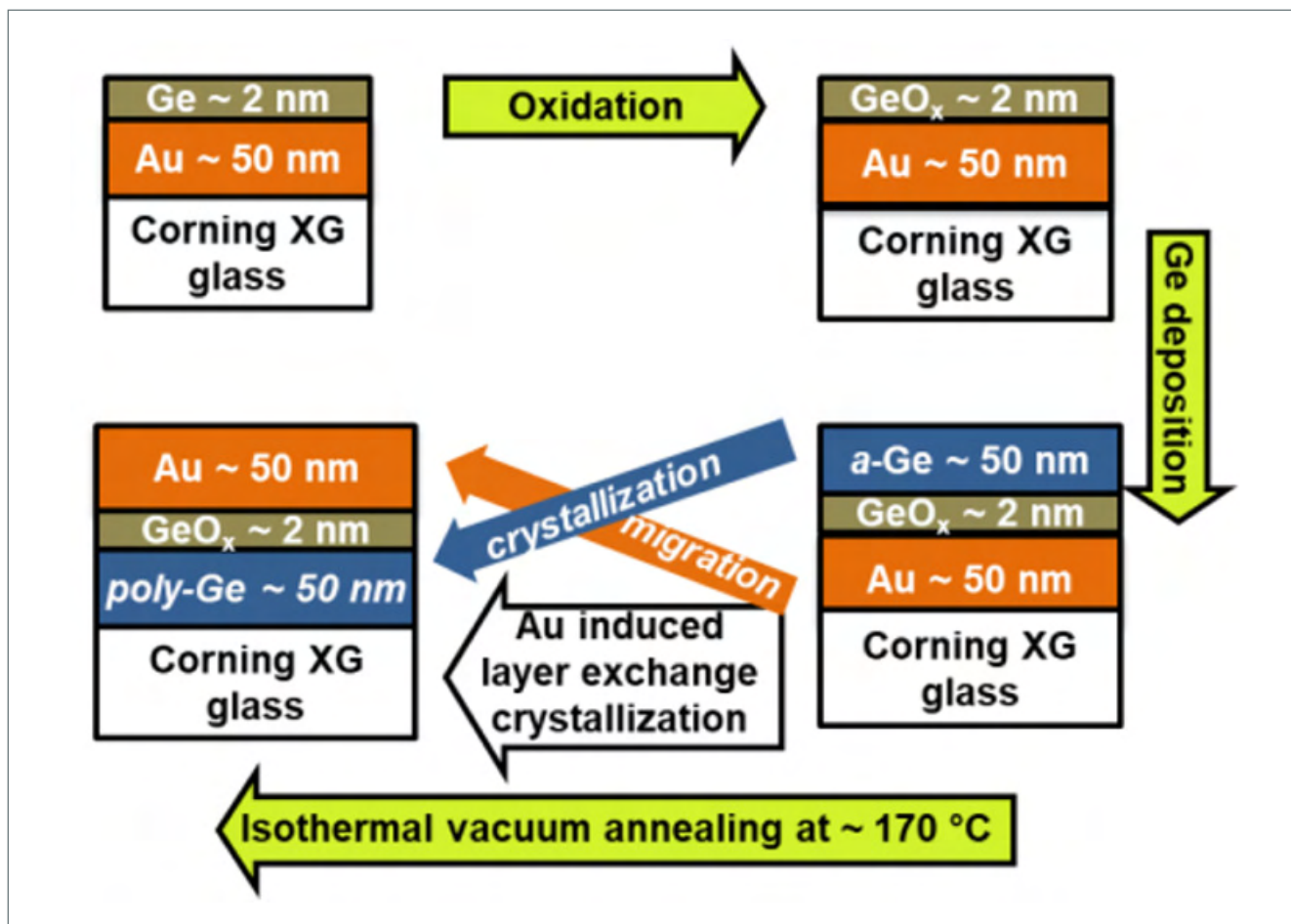


Fig. 1 Schematic of AUILE crystallization process

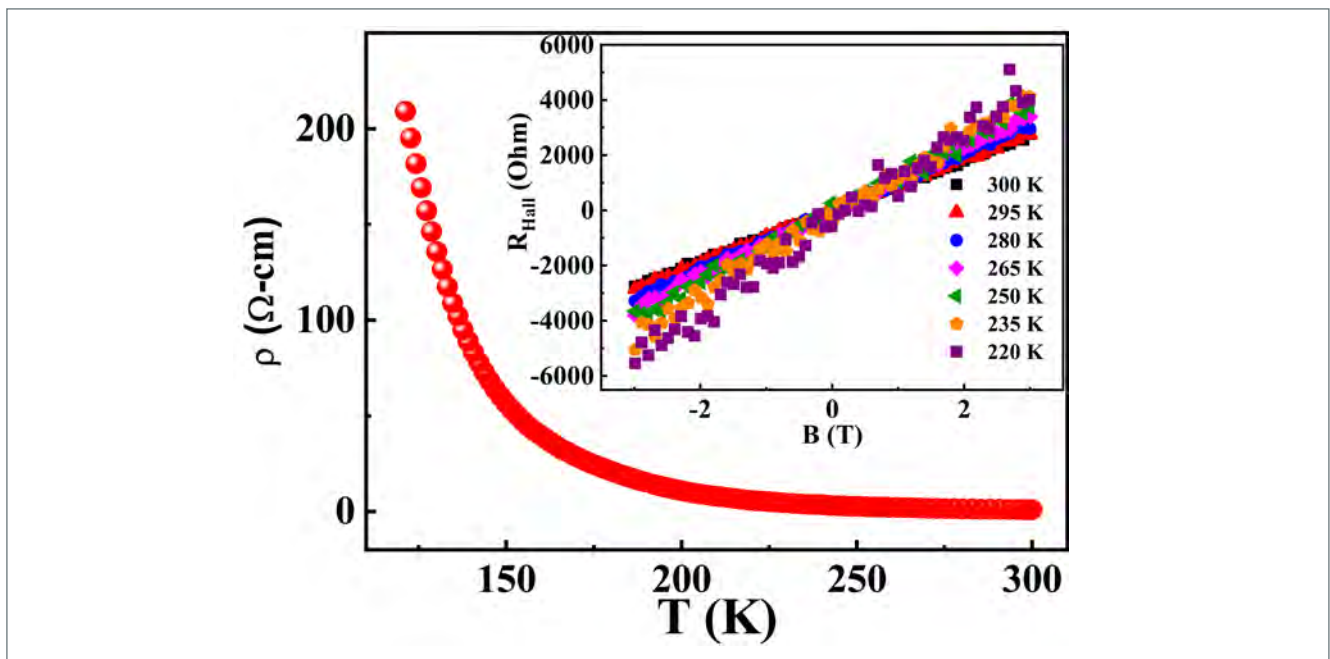


Fig. 3 P-type semiconducting behavior

nm)/Au(50 nm) structure was deposited on an XG glass substrate. The *a*-Ge and Au layers were deposited using electron beam evaporation and DC sputtering, respectively. The *a*-GeO_x layer was formed by deposition of ~ 2 nm *a*-Ge thin film followed by exposure to ambient air for a few hours. This layer controls the kinetics of the crystallization, the layer exchange process, and the grain size of the resulting *poly*-Ge thin film. A schematic illustration of the Au-induced layer exchange (AUILE) crystallization process is shown in Figure 1. The isothermal annealing to induce AUILE was performed at 170 °C in a high vacuum (~ 10⁻⁸ mbar) for up to 16 h. The reason for the low-temperature crystallization is of thermodynamic origin (minimization of Gibb's free energy), involving a crucial balance in the energies of the surface and interfaces. The Au grain boundaries (GB) were found to play a vital role, as without the GB wetting (of Au) by Ge atoms, the crystallization process was either retarded or entirely suppressed. The concurrent layer exchange (of the Au and Ge layer) during crystallization results from the strain induced by the growing *poly*-Ge phase inside the Au layer.

Finally, the Au thin film now at the top position after the AUILE process is etched off using a dilute KI/I₂ solution to leave only a *poly*-Ge thin film on the glass. The GIXRD pattern from the etched *poly*-Ge thin film is shown in Figure 2, along with the film's image. The *poly*-Ge exhibits semiconducting behavior as demonstrated by the resistivity (ρ) vs. temperature plot in Figure 3. The positive Hall coefficient (determined from

the slope of Hall resistance vs. magnetic field “B”) shows that the film is *p*-type. The origin of this *p*-type behavior was investigated by analyzing the activation energy using Arrhenius formalism. The analysis shows that holes were generated due to point defects induced acceptor levels. The temperature dependence of hole mobility is shown in Figure 4. Although the mobility was limited by grain boundary scattering, the mobility of 50 cm² V⁻¹ s⁻¹ at 300 K is the highest to be reported for a *poly*-Ge thin film formed at such low temperature. This result is promising as the observed mobility can be further enhanced by optimizing the AUILE process to achieve *poly*-Ge thin films with larger grains.

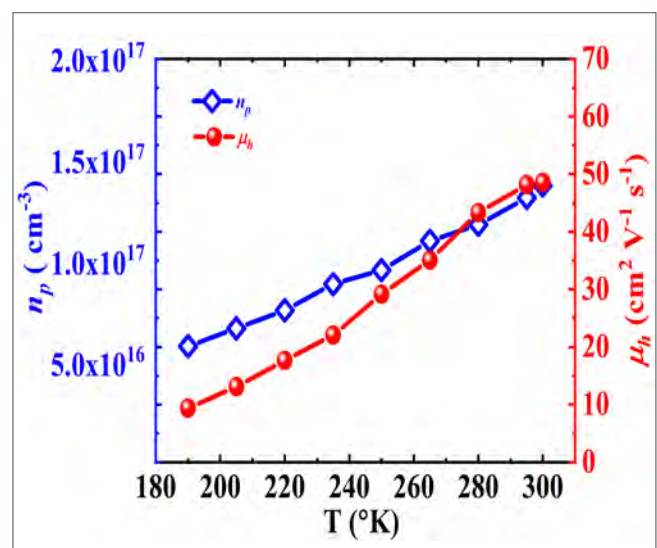


Fig. 4 Temperature dependence of hole mobility and hole concentration

V.04 Structural Insights at Different Length Scales in Alkali-Modified Tellurite Glasses to Tailor Optical Properties

Investigating the length-scales of order in glasses is important to understand glass properties and the underlying glass structure. A variety of structural parameters, such as, connectivity, nature of bonding, spatial dimensionality, chemical species and their concentration in the network, govern glass structure, and the way each of them influence the structural signatures is difficult to decipher. One way to overcome this difficulty is to synthesize glasses with controlled structural modifications and study them. With this aim to study the relationship between glass structure and modification, we have investigated tellurium oxide/tellurite (TeO_2) glasses doped with alkali-cations at a specific molar concentration. TeO_2 -based glasses have recently become much popular owing to their promising properties such as wide infrared transmittance and high non-linear optical constants. Addition of alkali oxides ($M_2\text{O}$) in tellurite glass is well-known to modify its network and alter properties by conversion of its basic structural units of TeO_4 to TeO_3 and increasing the conversion upon further addition of $M_2\text{O}$. We carried out Raman and Brillouin scattering investigations on $0.12M_2\text{O}:0.88\text{TeO}_2$ ($M = \text{Li, Na, K, Rb}$ and Cs) glasses with an aim to study the effect of the specific alkali cation (M) at fixed composition, on the resulting network structure that determines their interesting optical properties.

The glasses were synthesized from the commercially available TeO_2 and $M_2\text{CO}_3$ by rapid splat quenching of the melts. The Raman spectra were excited using the 514.5 nm line of an Ar^+ laser and the spectra were recorded using a micro-Raman spectrometer. The spectra were corrected for the thermal population factor and the reduced spectra were fitted with Gaussian line shapes to extract the peak parameters. Low-frequency

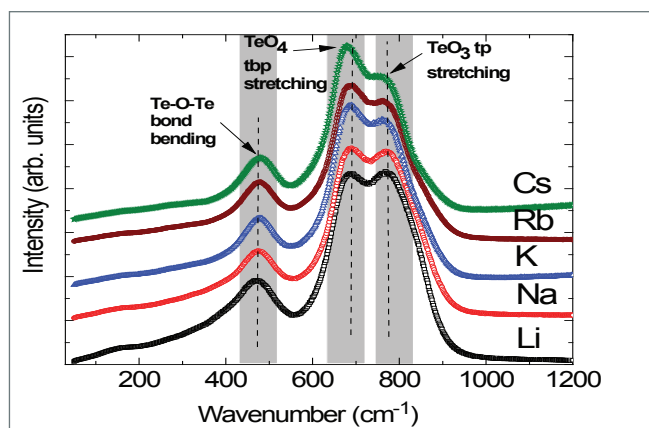


Fig. 1 Raman spectra of $0.12M_2\text{O}:0.88\text{TeO}_2$ glasses

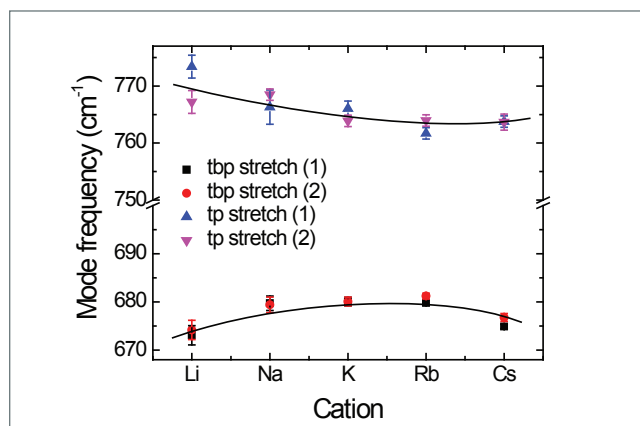


Fig. 2 Cation dependence of mode frequencies of TeO_4 *tbp* stretching and TeO_3 *tp* stretching modes

Raman spectra were excited with a diode-pumped solid state laser ($\lambda = 532$ nm) and were recorded using a high-resolution double monochromator. The spectra were reduced for the excess vibrational density of states using the correction for Boson peak. The line shape of the Boson peak was fitted using a log-normal function to estimate the peak position. Brillouin scattering experiments were performed with a (3+3)-pass tandem Fabry-Perot interferometer using the 532 nm line from a single-mode diode-pumped solid state laser. The Brillouin spectra were analyzed for mode frequencies through Lorentzian curve fitting.

From high frequency Raman spectra (Figure 1), providing information at length scales of ~ 2 Å, we observed that the Te-O-Te bending and TeO_4 stretching modes stiffen, while the TeO_3 stretching vibrations soften with decreasing polarizing power from Li^+ to Cs^+ (Figure 2). This further showed that as the degree of covalency decreased with M , the distortion of TeO_4 units reduced which lead to lesser conversion of TeO_4 to TeO_3 units

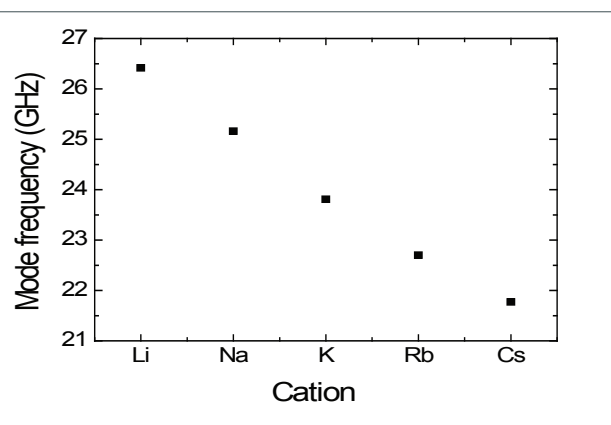


Fig. 3 Brillouin shift of the longitudinal acoustic (LA) mode

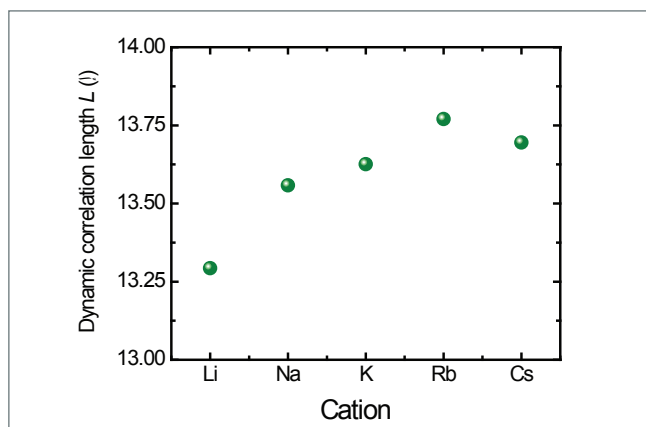


Fig. 4 Cation dependence of the dynamic correlation length (L)

(observed from the relative intensity ratio of TeO_4 and TeO_3 vibrations). It was also shown that the effect of bigger, massive cations M is to create more number of terminal TeO_4 units, along with reduction in the number of units with bridging oxygen bonds and hence reduction in the non-linear susceptibilities, as reported in literature. It was also concluded using Raman spectroscopy that the bond length disorder decreased with increasing size of M . Acoustic modes, arising from long wavelength vibrations of the structures at length scales of ~ 100 nm, exhibited a reduction in elastic rigidity in the glasses with increasing mass of M from Li to Cs (Figure 3). This indicates that the bigger size and mass of M disrupts the network chains and weakens the structure at larger length scales. This also concurred with the fact that formation of more NBOs occurs with M varying from Li to Cs as seen using Raman spectroscopy. Finally, from low-frequency Raman spectroscopy, which throws light on the structure at length scales of ~ 2 nm, we observed the dynamic correlation length (L) depicting the medium range order, increases with increasing M size (Figure 4). This is attributed to the fact that as the size of the cation increases from Li^+ to Cs^+ , it helps distribute the same electric charge on larger number of anionic structural groups of the network, and thus, increase the correlation length while simultaneously decreasing the network strength.

Figure 5 depicts a schematic diagram of the alkali-modified tellurite glass generated from the insights obtained from a multi length-scales structural study. When the Te atoms (in the unmodified glass, see Figure 5) are replaced with smaller cations such as, Li, the sudden volume contraction changes the intra-molecular bond strength of the network moieties (TeO_4 and TeO_3) as seen from the variations of the Raman mode frequencies (Figure 2). The TeO_4 vibrations stiffen (depicted pictorially by the shrinking of the TeO_4 units when $M = \text{Cs}$), while the TeO_3 vibrations soften (depicted by expansion of the TeO_3 units), as M changes from Li^+

Table 1: Band gap values and refractive index values using the ASF method. The refractive index values obtained using Lorentz-Lorenz method is also provided for comparison

M	Band gap (eV) (indirect)	Refractive index, n (Absorption spectrum fit method)	Refractive index, n Lorentz-Lorenz method
Li	2.14	2.68	2.33
Na	2.25	2.63	2.22
K	2.20	2.65	2.17
Rb	2.30	2.62	2.0
Cs	2.54	2.53	

to Cs^+ . However, a reduction in disorder as observed from the narrowing Raman mode-widths (not shown here) with increasing size of M indicates a less strained structure. Along with this, it is observed that the fraction of terminal TeO_4 (with NBO) units increases with larger size and mass of M , such as $M = \text{Cs}$. This is represented by the red-lined interconnections/ networking replaced by the dashed dot linkages from TeO_4 units in Figure 5. This, in fact, causes the non-linear susceptibilities and elastic modulus to reduce by introducing greater number of network breakages. Also the refractive index reduces while the band gap increases monotonically (Table 1) as the polarizing power of cation decreases with increasing M size. However, the medium-range correlations slightly increase as the network strain reduces and the cation void structure encompasses the same electric charge of the alkali cation on larger number of tellurite structural units of the network. This is represented by the regions enclosed by blue dotted lines. Thus, a multi-length scales structural study provides an insight into the overall glass structure and such studies will help in tailoring potential properties, such as refractive index, non-linear susceptibility and elastic rigidity.

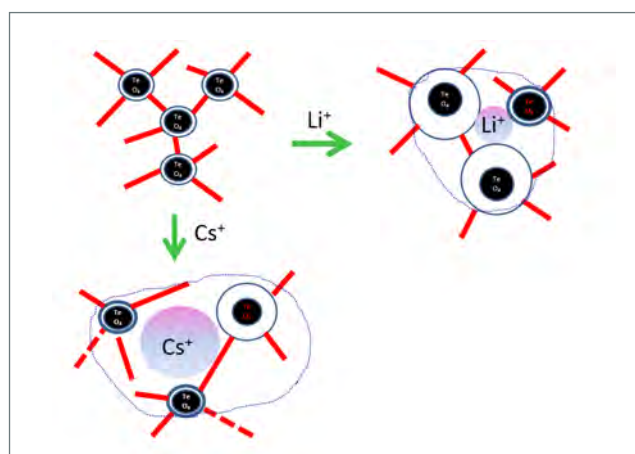


Fig. 5 Schematic of the structural modification at various length scales caused by the alkali cation M in $0.12M_2O:0.88\text{TeO}_2$ glasses

V.05 Ultra Thin Ni Films for Synthesis of Graphene on Diamond Thin Films and Enhanced Electron Field Emission Properties

Graphene is one of the interesting 2D materials. By doping impurities like boron or nitrogen, band gap of graphene can be opened up a little bit, which has numerous applications. Graphene is normally grown by CVD on metal foils and it is transferred to the required substrate for device fabrication, which may affect its intrinsic properties. Here, graphene is grown on H-doped micro-crystalline diamond film (MCD) and B-doped MCD grown by depositing ultrathin nickel films and rapid thermal annealing (RTA) at 950°C for a minute in Ar atmosphere. Nickel behaves as a catalyst on crystalline diamond to get graphene layer precipitated to the surface. Ultra thin Nickel films are deposited at room temperature using a low power e-gun in a recently installed molecular beam epitaxy (MBE) system under ultra-high vacuum. Laterally conformal coating is obtained only after a thickness of 19 nm in H-doped MCD and 3 nm in B-doped MCD. Figure 1 shows micro-Raman spectra obtained from the samples. In pristine MCD, Raman peaks of diamond F_{2g} symmetry peak, defect peak D, sp^2 peak G are seen. In RTA annealed samples with Ni/MCD, there is dominant evolution of 2D and G peaks corresponding to graphene. From the fitting of 2D peaks with six components and Raman intensity ratio of $I_{2D}/I_G < 1$, graphene is found to be of trilayer thickness in both samples.

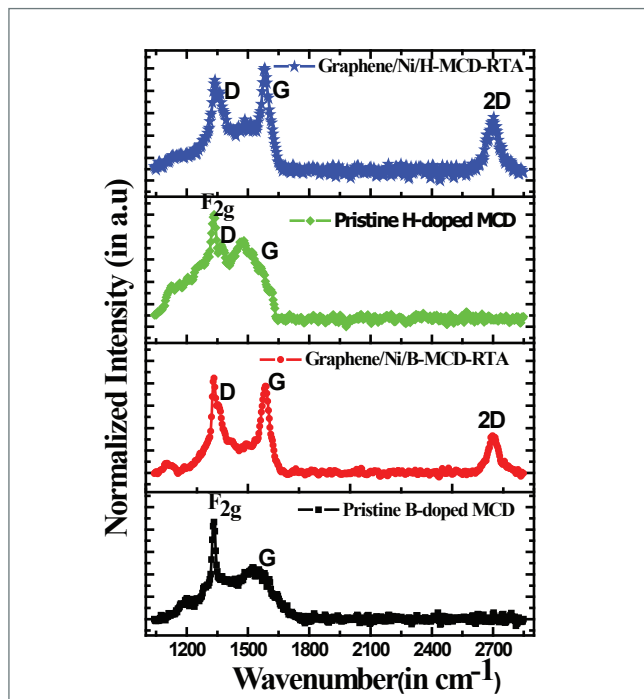


Fig. 1 Raman spectroscopy spectra from pristine MCD and graphene/Ni/MCD samples

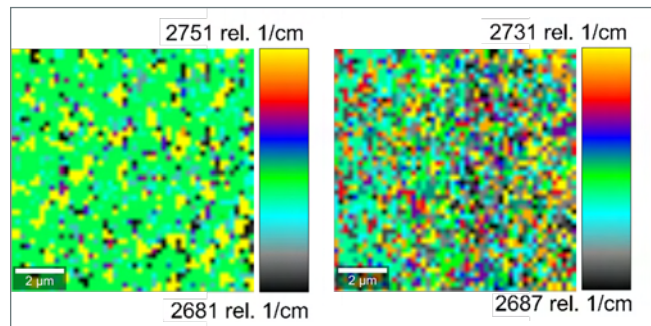


Fig. 2 Raman maps of 2D peak position

Micro-Raman maps of 2D peak position of graphene in RTA annealed Ni deposited H-doped MCD (left) and B-doped MCD (right) are shown in Figure 2. The maps show domain and domain boundaries of graphene. In the Raman maps of both the samples, 2D peak position of graphene is higher at the domain boundaries than that at the domains. This redshift in 2D peak implies the presence of uniaxial strain which can arise from the incorporation of defects and dopants into domain boundaries. In H-doped MCD, H-atoms will be intercalated between graphene layers and graphene/MCD interface, with higher H-concentration at the boundaries. In the case of B-doped MCD, boron is likely to get doped into graphene with a higher concentration at the boundaries, which in turn can open up the band gap.

Electron Field Emission (EFE) measurements are carried out in these samples. Figure 3 shows the variation of tunneling current density (J) versus the applied voltage. H-doped MCD shows lower turn on field of 70 V/ μ m compared to B-doped MCD (140 V/ μ m) due to its lower work function. With the growth of graphene on Ni/MCD, the turn on field is reduced further to 43 V/ μ m in H-doped and 88 V/ μ m in B-doped graphene on MCD samples. It is evident that graphene enhances the EFE properties of diamond.

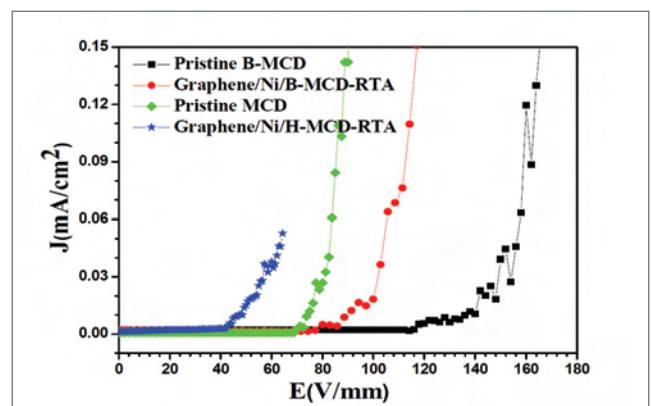


Fig. 3 Electron field emission measurements

V.06 Tuning Photoluminescence Emission of Nanocrystalline Diamond Films by N Doping

Over the past several decades, diamonds have attracted much attention of researchers due to their exceptional and superlative physical, chemical and mechanical properties. It is well known that diamonds are being utilized extensively in mechanical industry for a long time. In the recent past, diamond based electronics and single photon emitters in quantum communications have become active fields of research after the successful demonstration of electronic grade synthetic diamonds by chemical vapor deposition (CVD). The superior electronic properties combined with high tolerance to radiation and harsh chemical environments makes diamonds attractive candidates in several high performance device applications, especially in electronic devices which can operate at high temperature, high frequency & high power, high energy ionizing radiation and particle detectors. Though single crystals are ideal for such applications, the low cost CVD grown polycrystalline (PX) diamonds are still useful in measuring high energy beam currents at very high doses in particle accelerators where conventional detectors do not work. Further, the PX diamonds are also used as fluorescence screen in monitoring beam position in particle accelerators in which the optical emission characteristics of diamond is crucial. This work highlights the photoluminescence studies of nanocrystalline diamond (NCD) films grown by hot filament CVD at different nitrogen concentrations. Although N is the most preferred impurity for n-type doping, N does not provide excess carrier at room temperature due to its deep energy levels in diamond. However, these energy levels can emit luminescence

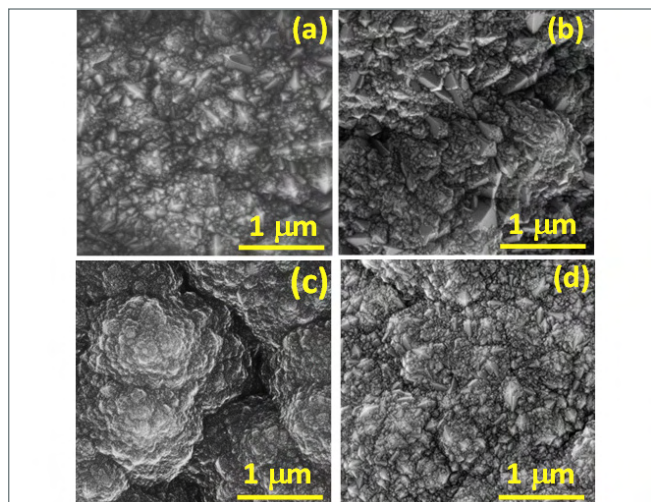


Fig. 1 SEM micrographs of NCD films grown under different N/C ratios in the feedstock at (a) 0, (b) 0.13, (c) 0.35, and (d) 0.75

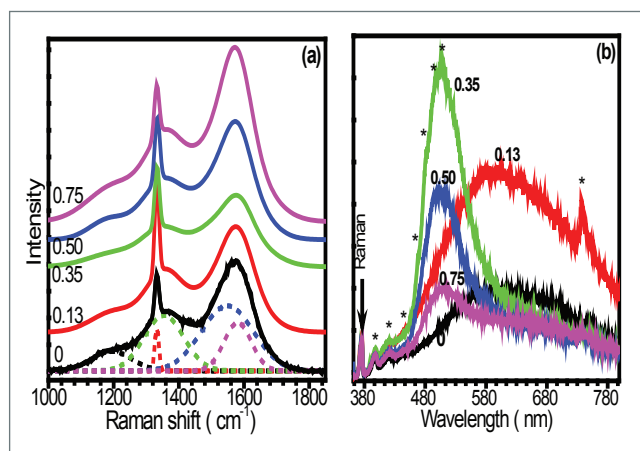


Fig. 2 (a) Raman spectra and (b) photoluminescence spectra of N doped diamond films recorded under the excitation of 355 nm laser. The numbers in the graphs indicate the nominal N/C ratios in the feedstock

under suitable excitation either by light or high energy irradiation. Further, the intensity of the luminescence can be tuned by varying the concentration of N in the diamond lattice by controlling the flow ratio of CH_4 , H_2 and NH_3 in the feedstock.

Figure 1 shows the SEM micrographs of NCD films grown under nominal N/C ratio in the range of 0 - 0.75 in the feedstock. The observed microstructure of these films is found to be nano-crystalline with crystallite sizes of $\sim 10 - 16$ nm, as evidenced by X-ray diffraction. The thickness of the films varies from 1.1 to 2.7 μm depending upon the feedstock ratio. Figure 2a depicts the UV-Raman spectra of the NCD films. A careful analysis of the spectra indicates a compressive strain in diamond films that increases monotonically as a function of N/C ratio up to 0.50. Furthermore, a unique Raman mode at 1195 cm^{-1} is observed (not shown in Figure) corresponding to the C=N-H vibrations indicating a significant N concentration in the NCD films when excited with 532 nm laser.

Figure 2b displays the room temperature PL spectra of the diamond films grown at different N/C ratio in feedstock by an excitation wavelength of 355 nm. PL studies reveal the presence of several N-related colour centres with multiple emission lines in the range of 380 – 700 nm. An optimally N doped diamond film grown at N/C ratio of 0.35 in feedstock shows a significant enhancement in room temperature PL emission at ~ 505 nm which is attributed to H3 and other aggregates of N related colour centers. Such diamonds with enhanced PL emission have potential applications in luminescence based radiation detectors which can work under extreme environments.

V.07 Mask-less Single Step Nanofabrication by Focused Ion Beam – Scanning Electron Microscope Dual-Beam Technique

The combination of focused ion beam (FIB) and scanning electron microscope (SEM) system, with its dual beam facility and beam cross-over, has emerged as a powerful tool for the present day nanofabrication. Further combined with a gas injection system (GIS), the FIB-SEM dual-beam combination has become even more versatile. Due to the modern technological developments, today's dual beam equipment are capable of producing very sharp beams sizing less than 3 nm (ion beam about 2.5 nm and electron beam < 1nm). Therefore, the dual beam system with such capabilities are very well suited and applied for nanolithography works. Addition of a high speed and high resolution pattern generator to stir both the beams (from nano to micro meter scales) makes the system an excellent nanolithography tool as well. Ion beam induced sputtering or beam induced deposition (with GIS) can be performed at nanoscale to create various shapes (simple to complex nanopatterning) with high precision.

Beam induced deposition is possible for a wide variety of materials (from insulators to conductors). Both electron and ion beam could be used for this purpose. However, the deposited material quality depends on the beam properties. The unique advantage of a dual-beam system (with GIS and pattern generator) is that it is a single-step direct write process. It does not require a mask layer deposition, exposure and developing as used in typical mask-based lithography techniques (e.g. electron beam lithography). The mask-based techniques are tedious and need ultra- clean and smooth surfaces for patterning. In this report, we show a few examples of one-step, mask-less nanopatterning from our work carried out with such a dual beam FIB-SEM system (Model: Auriga, Make: Carl Zeiss, Germany). Figure 1 shows examples for nanofabrication with beam induced deposition and milling. Figure 1a is a nano-world map fabricated on the surface of a Si wafer in one-step deposition of Pt

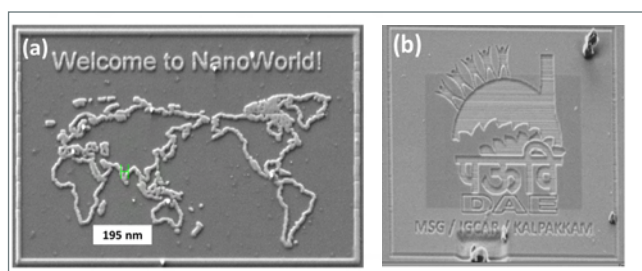


Fig. 1 (a) World map fabricated on Si wafer by ion beam induced deposition, width of India is ~195 nm; (b) DAE emblem carved on Si wafer by ion milling

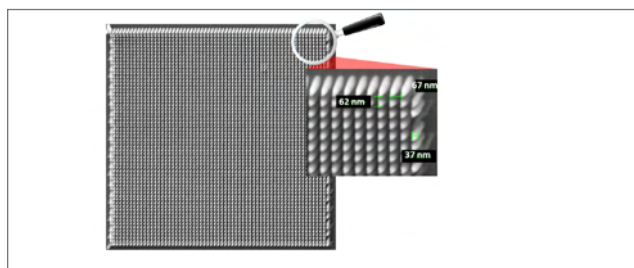


Fig. 2 Closely-packed Pt nanorods on Si wafer fabricated by electron beam induced deposition

(via decomposition of a metal organic precursor by ion beam). Figure 1b shows a DAE emblem carved on a Si wafer by ion beam milling. Note that in both examples the surface of the substrate is not very smooth, but the nanofabrication is not affected by that. Figure 2 shows an example of the placement accuracy of electron beam induced deposition. About 37 nm thick Pt nanodots were grown on Si wafer with a small spacing of about 60 nm. Figures 3a and 3b shows an application of the dual beam assisted patterning. Pt nanodots patterned on Si wafer could be used as a template for the growth of GaN nanorods. Pt dots provide seed locations for the nanorod growth. Similarly, in Figures 3a and 3b another example for template-assisted growth is shown. Nano-etch-pit pattern on Si wafer covering an area of 0.5 mm X 0.5 mm is used as a template for the growth of GaO_xN_y nanoparticles.

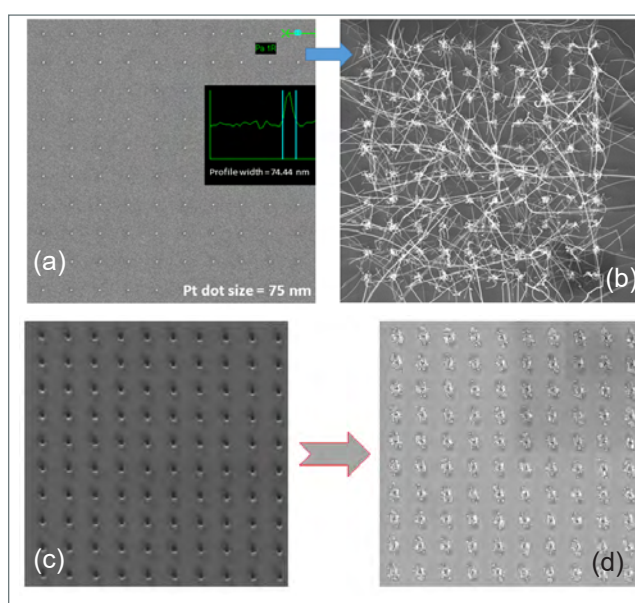


Fig. 3 Template- assisted growth of GaN nanorods on Si wafer. (a) Si wafer with Pt nanodots (seeds) as a template; (b) GaN nanorods originated from the seed positions (c) etch-pits made by Ga ion beam milling; (d) GaO_xN_y nanoparticles grown on the template

V.08 Atomic Scale Study of Defects in Co_2FeAl : A Promising Spintronic Material

Full Heusler compounds of type X_2YZ are predicted to exhibit half metallicity leading to 100% spin polarization of charge carriers which makes them suitable for spintronic devices like spin filter, spin injection and spin transfer torque devices. Co based Heusler compounds including Co_2FeAl are strikingly important with respect to a good ferromagnetic (FM) property having T_c up to 1000 K. In general, most ordered Co_2FeAl should acquire L_{21} structure, in which $8c(1/4, 1/4, 1/4)$, $4b(1/2, 1/2, 1/2)$ & $4a(0, 0, 0)$ are occupied by Co, Fe & Al respectively (Figure 1). But occurrence of different type of antisite defects such as Fe(Al), Fe(Co) and Fe/Al/Co lead to different type of disordering in the system such as B2, DO_3 and A2 respectively resulting in change of local structure which in turn affects FM and magneto-transport properties drastically. This work is aimed to investigate the role of Al related defects in altering structural and magnetic properties extensively in arc melted Co_2FeAl (A) subjected to different non-equilibrium treatments using ^{57}Fe based Mössbauer (MS) study at Fe sites in terms of hyperfine parameters such as isomer shift (δ), quadrupole splitting (D), hyperfine fields (B_{hf}). Lattice parameter of Co_2FeAl founds to be $5.7322(4)$ Å using Rietveld refinement with predominance B2 type of disordering whereas in $\text{Co}_2\text{FeAl}_{0.95}$, A2 structure is dominant. The value of saturation magnetization (M_s) is found to be around $5.3 \mu_B/\text{f.u.}$ in the case of Co_2FeAl and is higher than that of the value of M_s ($4.7 \mu_B/\text{f.u.}$) as observed in the case of $\text{Co}_2\text{FeAl}_{0.95}$. Both of these values of M_s

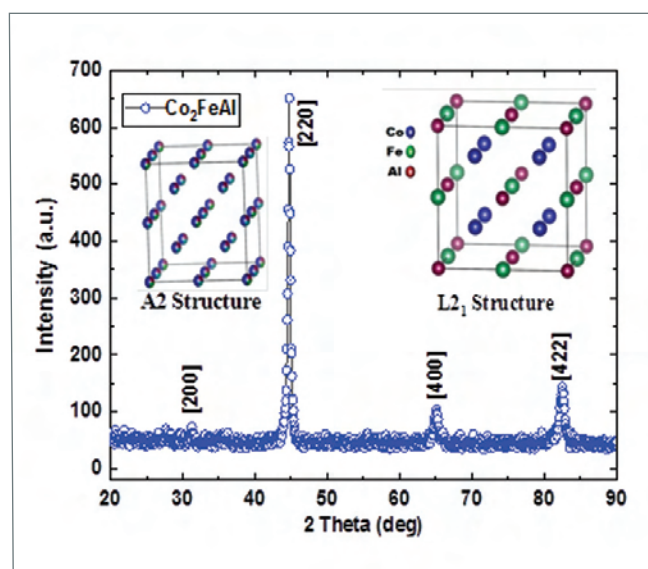


Fig. 1 XRD pattern of Co_2FeAl alongwith L_{21} & A2 shown as inset

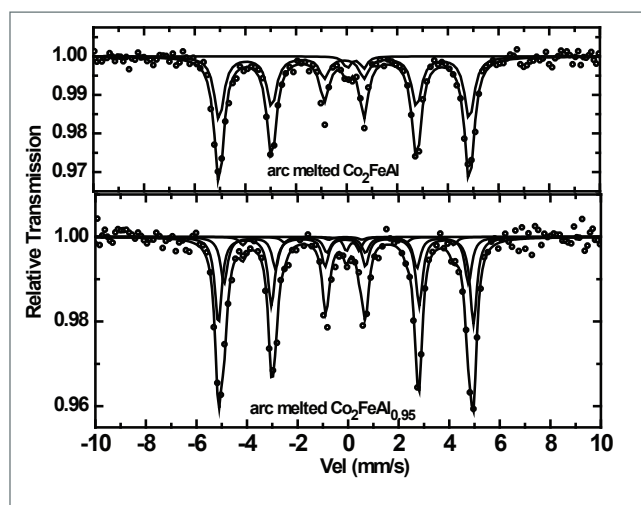


Fig. 2 Mössbauer spectra for Co_2FeAl & $\text{Co}_2\text{FeAl}_{0.95}$

are found to be different from the value of $5 \mu_B/\text{f.u.}$ as expected based on Slater-Pauling rule indicating the role of defects towards modification of magnetic properties. Mossbauer spectrum as obtained in the as arc melted Co_2FeAl could be de-convoluted dominantly in to three six line patterns with hyperfine magnetic field B_{hf} varying 29-31 Tesla and a doublet. But for $\text{Co}_2\text{FeAl}_{0.95}$ an additional fraction experiencing a hyperfine field close to 25 Tesla occurs which is understood to be associated with slightly differing defects configuration caused due to quenched in Al vacancies. Importantly the values of isomer shift and quadrupole splitting corresponding to these sites occupied by Fe atoms are much larger than that of all the other fractions implying that this fraction is associated with lattice defects having valence state quite different from that of other fractions. Detailed analysis of MS spectra reveals that almost close to 35% of the fraction of Fe atoms are found to be associated with A2 type of disordering in as melted Co_2FeAl which gets reduced to about 20% following annealing treatment at 873 K for a long time. In the case of A2 type of disordering Fe-Co exchange interactions get reduced due to Fe-(Fe)_{Co}, Fe-(Al)_{Co}, where (Fe)_{Co}, and (Al)_{Co} refer to anti site defects with Fe, Al occupying Co sites. This study thus demonstrates the important role of defects especially that of Al vacancies in altering the FM properties of Co_2FeAl bearing significant influence on the spin polarization properties of this system. Low value of spin polarization (35%) as reported in the literature against the half metallicity (100%) as predicted theoretically in Co_2FeAl is attributed to Al vacancies based on the understanding of the results of the present study.

V.09 Low Temperature Magneto-Caloric Studies on Rare-Earth Selenide Systems

The magneto caloric effect (MCE) is a phenomenon in which a change in adiabatic field leads to a change in the temperature of a magnetic system. For example, in the case of simple ferromagnetic materials, the material heats up when an external magnetic field is applied adiabatically, and cools down when the external field is turned off. Magnetic refrigeration (MR) technology based on the magneto caloric effect is in many ways advantageous compared to conventional gas compression based refrigeration technologies. Potential applications of magneto caloric effect based magnetic refrigeration include air conditions/air coolers, food freezers, liquefaction industries, space applications and ultra-low temperature applications. For technologically relevant MR applications, it is important to explore new magnetic materials with requisite MCE properties.

In general, magnetic materials containing magnetic rare-earth (RE) ions with large effective Bohr magneton number (μ_{eff}) as constituents show large isothermal magnetic entropy changes (ΔS_M), near the magnetic transitions. Rare earth based chalcogenide EuSe has been reported to have significant and isotropic magnetocaloric properties, in the low temperature regime. EuSe (cubic crystal structure, space group: Fm3m) has complex low temperature magnetic structures. It undergoes a paramagnetic (PM) to a NNSS type ($\uparrow\uparrow\downarrow\downarrow$) antiferromagnetic (AFM) transition at $T_N \sim 4.6$ K in zero external field and the spin/magnetic structure transformation from the NNSS AFM to a more complex NNS+NSNS type ($\uparrow\uparrow\downarrow + \uparrow\uparrow\downarrow\downarrow$) ferrimagnetic

structure at $T \sim 2.5$ K. In the AFM state (for $T < T_N \sim 4.6$ K), the application of magnetic field causes a field induced transition from the AFM to ferromagnetic (FM) structure. Both the paramagnetic (PM) to a NNSS type ($\uparrow\uparrow\downarrow\downarrow$) antiferromagnetic transition at $T_N \sim 4.6$ K and the field induced magnetic transition from the AFM to ferromagnetic (FM) structure for $T < T_N \sim 4.6$ K are first order in nature.

In most of the first order magnetic transformations, several of the magnetocaloric parameters such as the maximum value of isothermal magnetic entropy ($|\Delta S_M^{\text{max}}|$) change and also the nature/broadness of the $\Delta S(T)$ curves values are affected by the magnetic irreversibility and metastable phases, when these parameters are evaluated from magnetization data. In this study, we aimed to examine whether the magnetocaloric properties of EuSe are affected by the thermomagnetic history by performing the magnetization measurements in two different protocols and evaluating the magnetocaloric properties in each case.

Figure 1(a) shows a schematic representation of the two magnetization measurement protocols used in the study (Zero field cooled (ZFC) and remanence warmed (RW) mode) and Figure 1b presents the isothermal magnetic entropy change evaluated from the magnetization data for the two methods. The results indicate that there is only negligible effect of thermo-magnetic history/hysteresis on magnetic and magneto-caloric properties of the EuSe system.

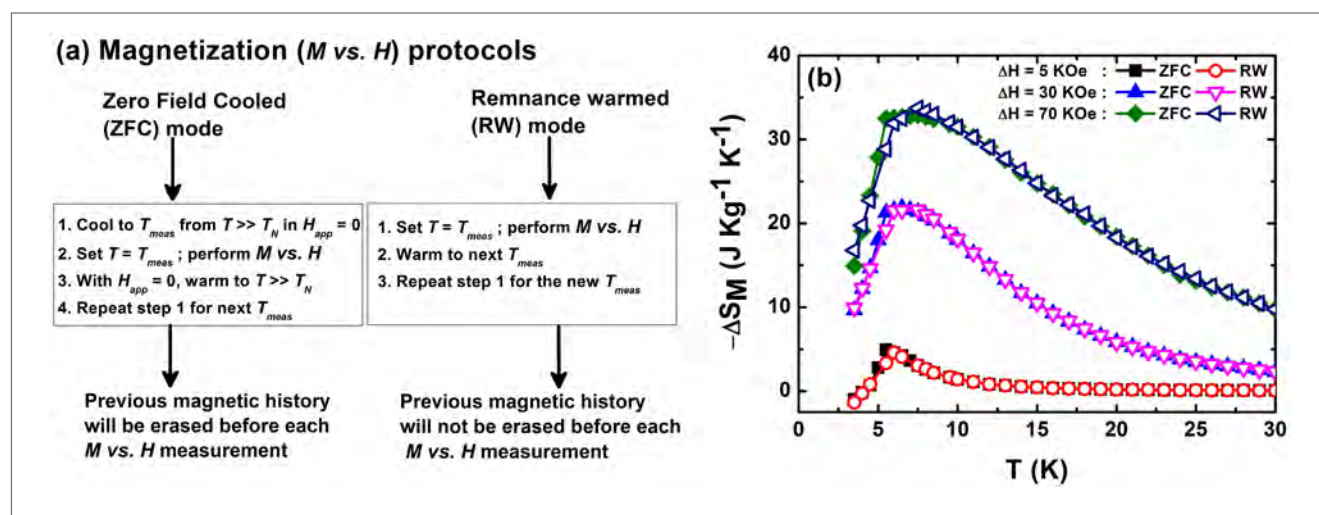


Fig. 1 (a) The schematic representation of the zero field cooled (ZFC) and Remnance Warmed (RW) mode magnetization measurements protocols and (b) isothermal magnetic entropy change evaluated from the magnetization data for the two modes

V.10 Enhancement of Hyperthermia Efficiency in Magnetic Nano-Emulsions at Acidic Ph: Role of Conformational Changes of the Stabilizing Moieties

Magnetic fluid hyperthermia (MFH) is being developed as an alternate cancer therapy, where the primary challenges are the restrictions imposed on the magnetic nanoparticle dosage and radio frequency alternating magnetic field (RFAMF) parameters considering biological safety. However, enhanced efficiency of chemo and radiotherapy techniques in the synergistic presence of mild MFH opens up the possibility of multi-modal MFH therapy. Magnetically polarizable oil-in-water nanoemulsions (size ~ 100 - 200 nm) are potential candidates for multi-modal MFH due to the availability of larger volume that is conducive for loading with anti-tumour drug and photo-active agents, thereby imparting multi-functionality. Such magnetic nano-entities are surface functionalized for enhancing colloidal stability and circulation time within the bodily fluids. However, acidic micro-environment in the vicinity of the cancerous cells invariably influences the surfactant behavior, leading to variations in global heating efficiency. To elucidate the effect of medium pH on RFAMF induced heating efficiency, in the present study, MFH studies are reported, as a function of pH, for a poly-electrolyte stabilized magnetic nanoemulsion. Experiments were performed on poly-acrylic acid (PAA) stabilized oil (octane)-in-water magnetic nanoemulsions loaded with oleic acid coated Fe_3O_4 MNPs (size ~ 10 nm and saturation magnetization ~ 70 emu/g) in the oil phase. The solution pH was varied from ~ 3 - 9 and the RFAMF

induced heating efficiency was estimated at a fixed frequency of ~ 126 kHz and under varying amplitudes (~ 25.7 - 33.1 kA/m). The heating efficiency was quantified in terms of specific absorption rate (SAR), which is defined as the power generated per unit mass of the magnetic content and the highest SAR values (at 33.1 kA/m) were $\sim 64.3 \pm 1.6$ and $\sim 42.7 \pm 1.7$ W/gFe at pH values of ~ 3 and ~ 9 , respectively. Figure 1 shows the variation of SAR, as a function of medium pH for varying RFAMF amplitudes, where it can be seen that SAR increased by $\sim 50\%$ when medium pH was decreased from ~ 9 to ~ 3 . As the MNP loading remained constant for all the cases, the SAR enhancement at acidic pH was attributed to the pH-dependent conformational changes of the PAA molecules adsorbed at the oil water interface.

With increase in solution pH, the PAA molecules adsorbed at the oil-water interface underwent progressive ionization resulting in globule to coil conformational changes. The fraction of charged monomers increased with pH (Zeta potential ~ -6 and ~ -63 mV at pH ~ 3 and ~ 9 , respectively), resulting in an increased inter-monomer screened Coulombic repulsion that prevented globule formation at higher pH and augmented the monomer-water interaction leading to a hydrated coil-like conformation at higher pH. These pH-dependent conformational changes caused two distinct effects, viz. an increase in the hydrodynamic diameter of the nanoemulsion droplets and associated changes in the local density of the PAA molecules near the oil-water interface. Dynamic light scattering studies indicated $\sim 24\%$ increase in hydrodynamic size at higher pH (hydrodynamic diameter ~ 223 and ~ 277 nm at pH ~ 3 and ~ 9 , respectively). However, Neel-Brown relaxation based theoretical analyses indicated insignificant contributions towards global SAR from the variations in hydrodynamic diameter of the droplets. Hence, the observed increase in SAR at lower pH was attributed to the conformational changes of the adsorbed PAA molecules that significantly influenced the interfacial heat transfer.

The heat transfer from octane to water is mediated through two parallel pathways, viz. octane-to-water (OW) direct heat transfer for the uncovered regions of the emulsion droplets and octane-PAA-water (OPW) heat transfer for the covered droplet surfaces. Among these two, OPW is the rate controlling path due to

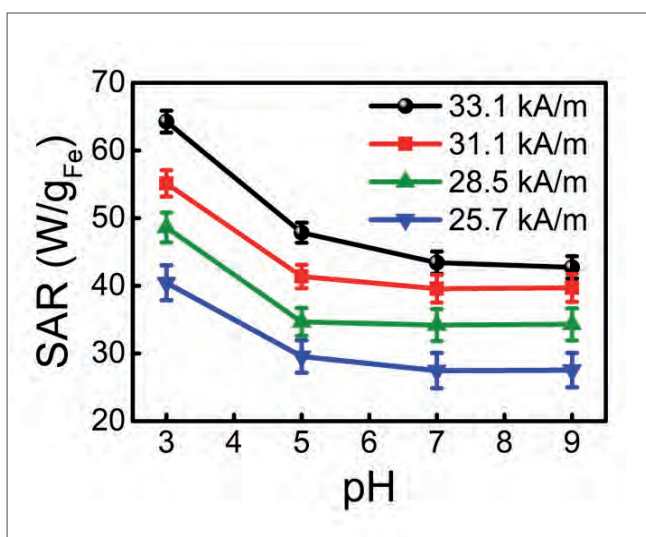


Fig. 1 Variation of SAR (heating efficiency) as a function of medium pH at varying field amplitudes

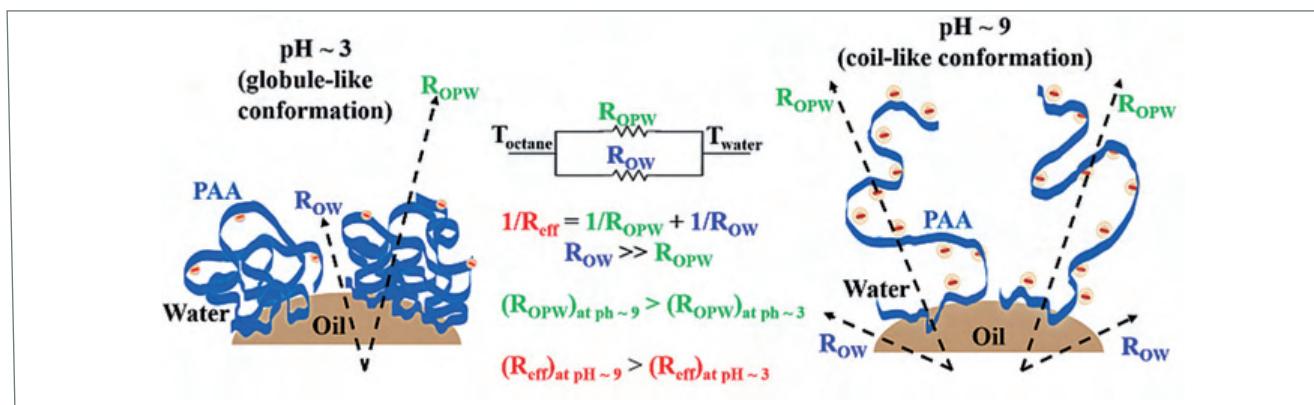


Fig. 2 Schematic showing the effects of pH-dependent conformational changes on heat transfer across oil-water interface (R = thermal resistance)

its significantly higher thermal conductivity. Coil-like conformation at higher pH decreased the local density of PAA in the vicinity of the interface, thereby reducing the overlap between the vibrational density of states, which caused a lowering of heat transfer efficiency across the oil-water interface, leading to a lower SAR

at higher pH, as confirmed from experimental findings. The phenomenon is schematically shown in Figure 2. The experimental findings, demonstrating enhanced MFH efficiency at acidic pH, is beneficial for designing efficient pH-responsive nano-carriers for multi-modal hyperthermia.

V.11 Dispersion Module using Time-Varying Source Terms In Online Decision Support System ONERS

Radiological dispersion module in Online Nuclear Emergency Response System (ONERS) which is operational at Kalpakkam, DAE site is originally designed with calculations using uniform source term (UST) approach, where the release rate of noble gases and particulates is taken uniform throughout the release period. However, the actual source term in an accidental scenario may vary with time. The time varying release behaviour in association with the prevailing weather condition during the release period may affect the sector of maximum radiological impact.

To address this non-uniform nature of source term, a new module called Time-Dependent Source Term (TDS) is developed using PHP in ONERS. The TDS provides full flexibility for real-time online radiological consequence assessments using time-varying accident source terms from the emergency control room. As part of the TDS the FLEXPART dispersion model of ONERS is modified to use the hourly release data of 25 radiologically significant radionuclides for any type of accident. Inputs on release start time, duration, ground/stack release, accident case or direct data are taken from the TDS interface and model is executed online.

This computes the radiological dose through various pathways and updates spatial database of dispersion and doses. The time-varying accident source terms for various postulated reactor accidents are incorporated in TDS as reference database. In addition, operators can directly specify the release rate data by uploading the files to the system.

The ONERS-TDS module is tested for the case of Off-Site Emergency Exercise conducted at Kalpakkam, DAE Site on 27 September. The hourly release data for 25 radionuclides provided by NPCIL for postulated LOCA-ECCS and containment EP Failure for MAPS-PHWR reactor was used. The release is assumed to start at 10.30 IST and continue for 66 h on 27 September. Projected cumulative inhalation dose for uniform and time-varying releases is presented in Figure 1. The plume was carried to NE, N, NW sectors by the monsoon and sea breeze circulation. The maximum dose is projected in the northeast and north sectors in the case of TDS and in the northwest in the case of uniform release (Figure 1a). The differential dose distribution pattern in the two cases is due to the maximum release occurring under different wind flow directions.

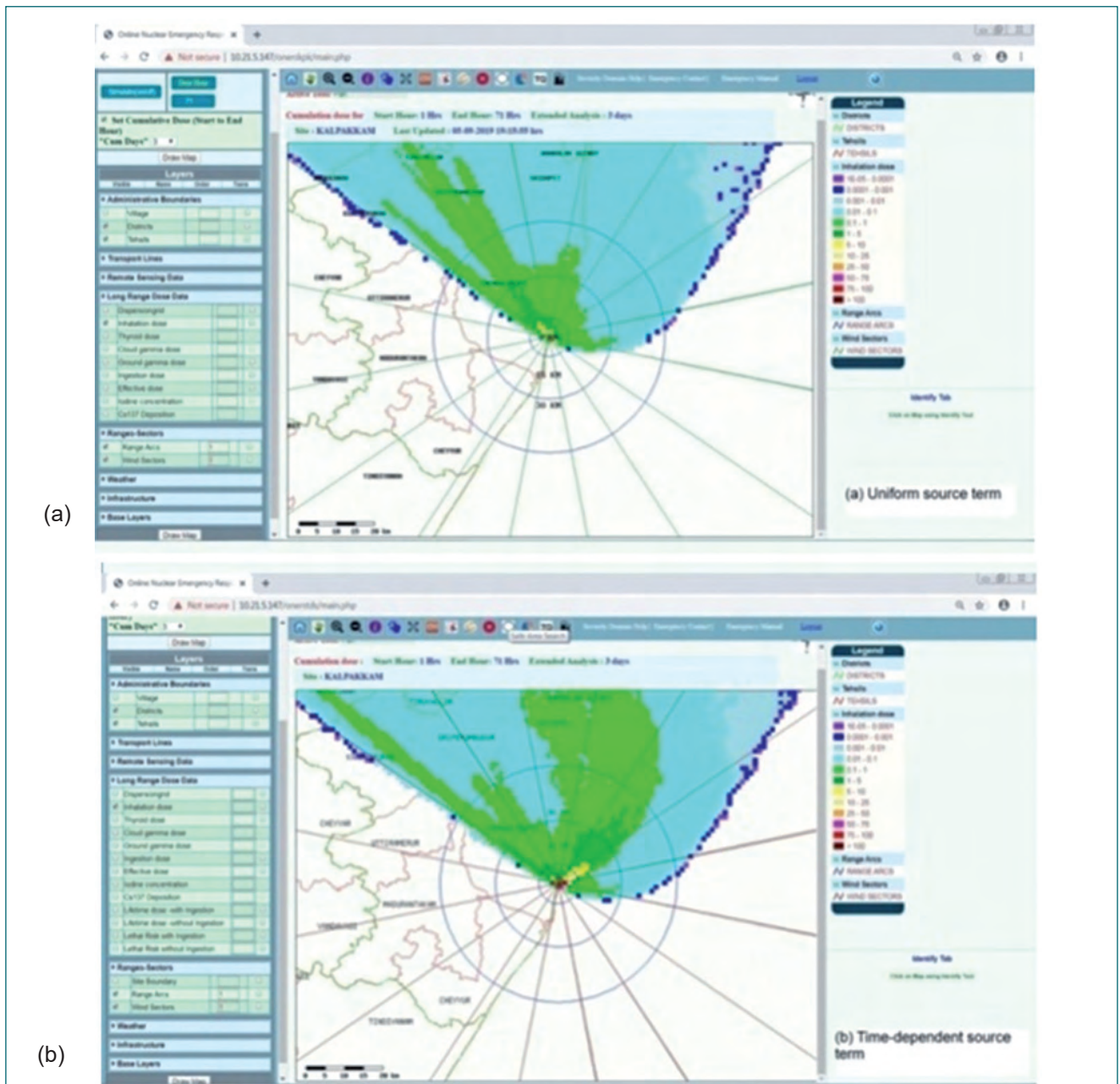


Fig. 1 Total cumulative inhalation dose for the release period (a) uniform source term (b) time-dependent source term

The differences are more clearly seen from the dose in NE, NW and N sectors ((Figure 2). Calculations indicate that though the area of impact is similar in both uniform and time-varying release scenarios, the time-varying release provides more accurate assessment in terms of identification of most affected sector under complex meteorological conditions. However, both approaches would nearly converge when the maximum release occurs under the most frequent wind flow condition. The approaches are complementary to each other for response actions given the requirements of rapid assessments with gross source terms in the initial phases and more refined assessments with detailed source terms in the later phases of emergencies.

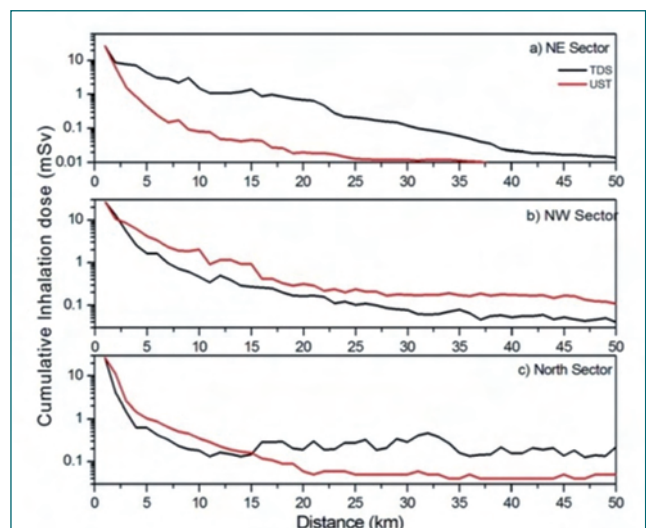


Fig. 2 Variation of cumulative inhalation dose in (a) NE sector (b) NW sector and (c) north sector

V.12 EPR, TL and OSL based Retrospective Dosimetry

As a nodal centre for handling radiological emergencies, HSEG, IGCAR has the mandate of providing dosimetry services to all radiation workers during normal and emergency conditions. Retrospective dosimetry facility is established for carrying out dosimetry during emergencies using a X-band Electron Paramagnetic Resonance (EPR) spectrometer (Figure 1). The EPR spectrometer was calibrated and used for the reconstruction of dose from irradiated finger nails as part of retrospective dosimetry. A methodology for dose reconstruction from RFID chips present in identity cards of IGCAR employees has been established using stimulated luminescence techniques.

Calibration of EPR spectrometer

Before searching for EPR signal in unknown samples, the modulation amplitude and the reference phase are adjusted. The modulation amplitude should match the linewidth of the EPR signal else the signal gets distorted. The intensity of the EPR signal is proportional to the cosine of phase difference between reference signal and modulated EPR signal and hence needs to be optimised for better signal intensity.

Dose assessment from finger nails using EPR

Radiation induced free radicals produced on irradiated finger nails can be quantified using EPR spectrometer and can be used for the screening of population for medical triage during radiological/nuclear emergencies. EPR measurements were carried out on finger nail pairing collected from adult volunteers after optimising the standard parameters like frequency power, modulation amplitude etc. The EPR spectrum of the unirradiated and irradiated finger nails recorded at different time interval is shown in Figure 2.

For the assessment of dose, a dose response curve was established from the EPR measurements of finger

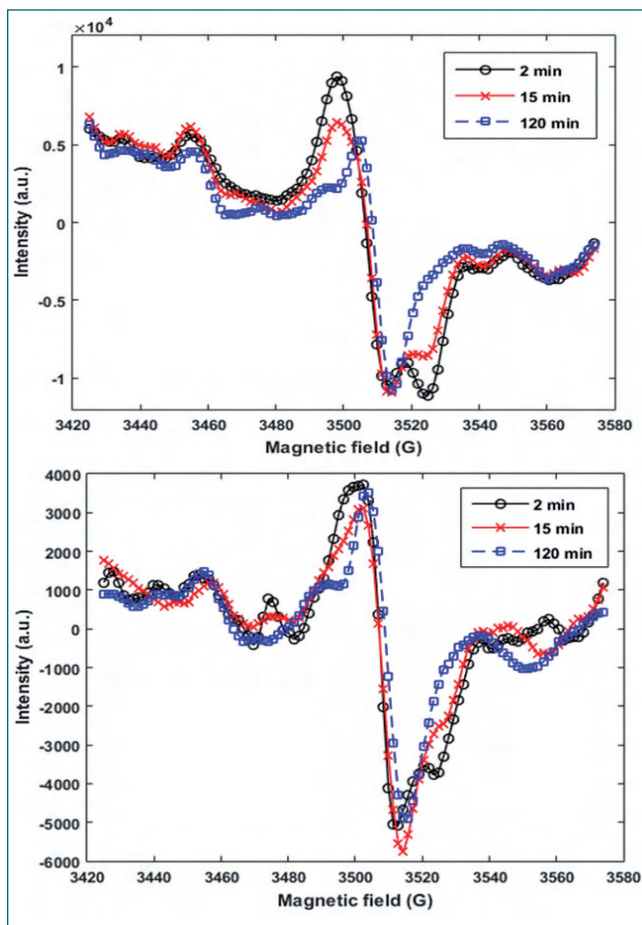


Fig. 2 EPR spectrum of unirradiated and irradiated finger nails

nails irradiated to different doses. It was observed that the response is linear upto 30 Gy (Figure 3). Additive dose technique was employed for the reconstruction of

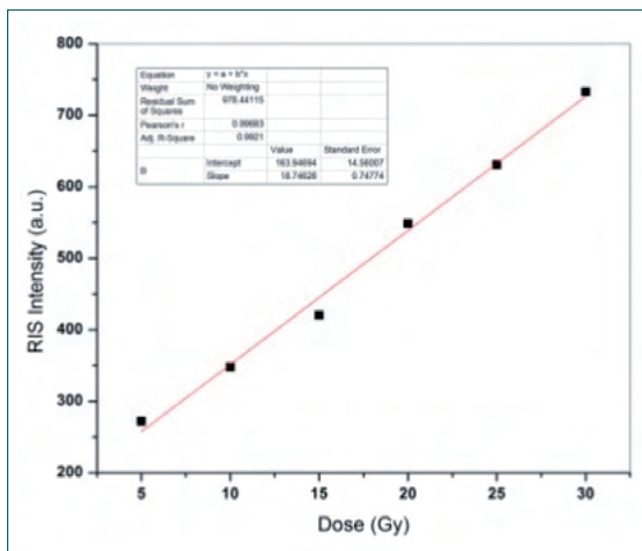


Fig. 3 Dose response of finger nails



Fig. 1 Photograph of EPR spectrometer

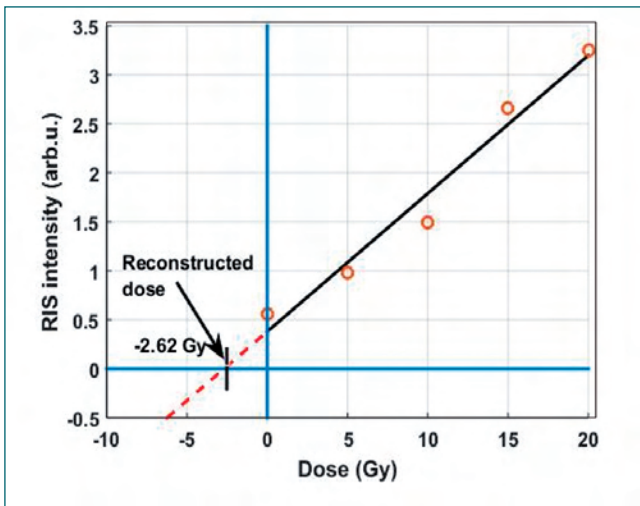


Fig. 4 Additive dose technique for dose reconstruction

dose from irradiated finger nails and a dose of 5 Gy is reconstructed as 5.17 Gy (Figure 4).

Dose assessment from RFID chips using Optically Stimulated Luminescence (OSL) technique

RFID based identity cards issued to employees and research scholars of IGCAR were irradiated to gamma radiation and OSL measurements were carried out on the extracted silica chips using RISO TL/OSL reader. The location of the silica chips were identified using radiographic and thermographic imaging (Figures 5a and 5b). The OSL light output (Figure 4 c) in the first one second is used for determination of dose due to external radiation. The response of the RFID chips was found to be linear from 200 mGy to 15 Gy. Single Aliquot Regenerative (SAR) technique (Figure 6a) was used for the reconstruction of dose from irradiated chips. The methodology was validated by reconstruction of doses

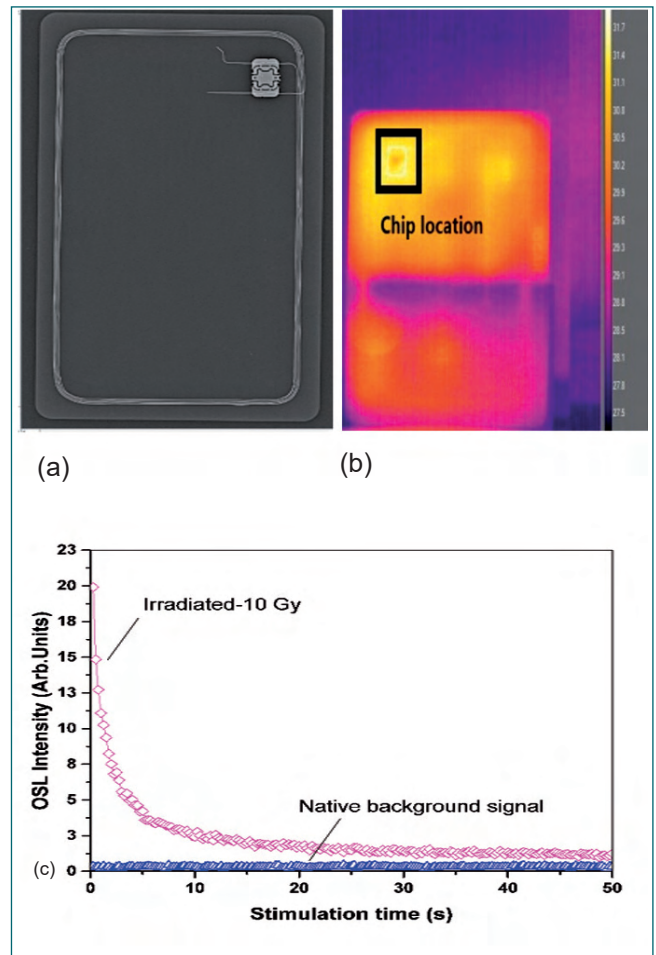


Fig. 5 (a) Radiographic and (b) thermographic image of identity cards showing the location of RFID chips and (c) OSL decay curve of RFID chips

from other chip cards like bank cards, SIM cards and employee ID cards of BARC facilities at Kalpakkam (Figure 6b).

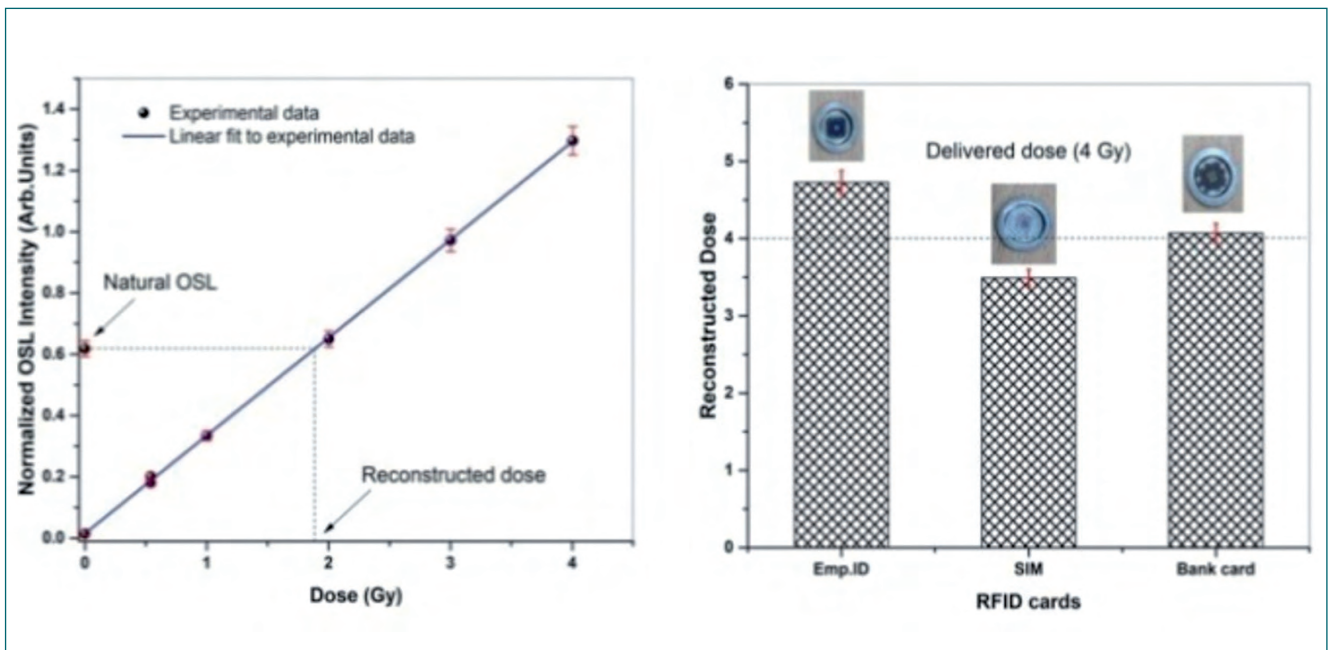


Fig. 6 (a) SAR technique for dose reconstruction (b) validation of dose reconstruction

V.13 The Nature of Phosphoryl Binding in Uranyl Nitrate Complexes

Understanding the chemical bonding in actinide metal complexes, where a carbonyl- or a phosphoryl-based ligand is used, will provide fundamental insights towards the design of various mono- and polyfunctional ligands for its selective extraction. With this goal in mind, the difference in the coordination behavior of various carbonyl- and phosphoryl-based ligands with uranyl nitrate was investigated by applying quantum chemical calculations.

The geometries of corresponding metal complexes were optimized at Density Functional Theory (DFT) level and are characterized as energy minima by evaluating real harmonic vibrational frequencies. The calculations indicated that the electronic charges on both C=O and P=O groups are more polarized towards the electronegative oxygen atoms in the free ligands and a positive net electronic charge is estimated for both the groups. The computationally estimated binding energies show a preference for the phosphoryl based ligands with the largest value estimated for uranyl nitrate complex with tri-*n*-butyl phosphate (TBP). To unravel the contributing factors of the large complexation energy of phosphoryl-based ligands, an Energy Decomposition Analysis (EDA) was performed. The EDA analysis indicated that the large stabilizing orbital interactions compensate the destabilizing steric and strain interaction

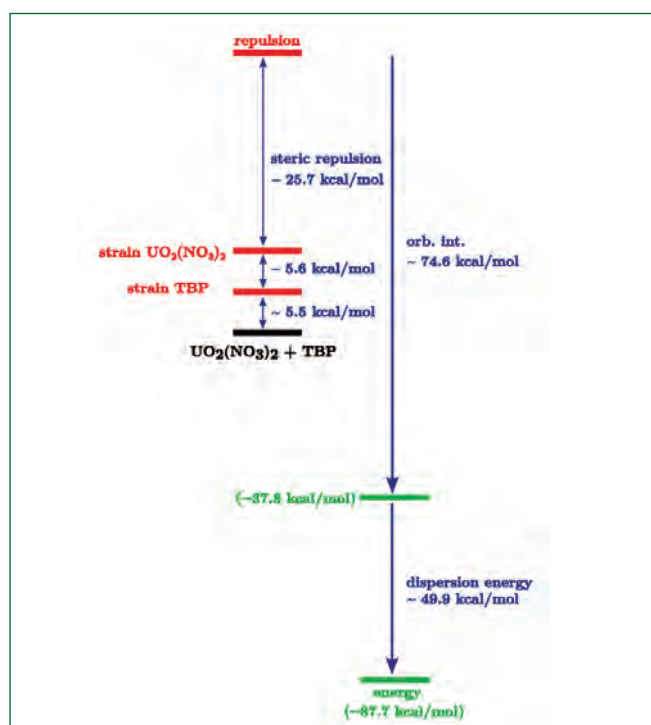


Fig. 1 Energy Decomposition Analysis performed on $\text{UO}_2(\text{NO}_3)_2 \cdot 2\text{TBP}$ complex (scale is arbitrary)

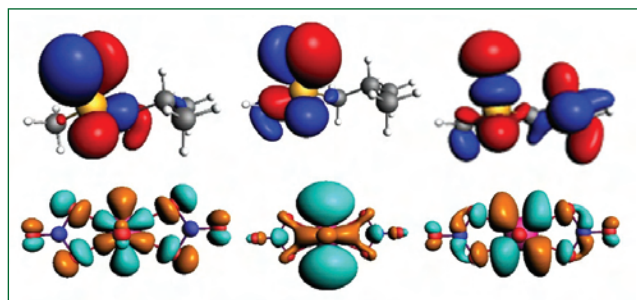


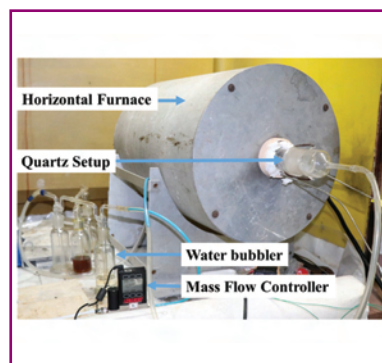
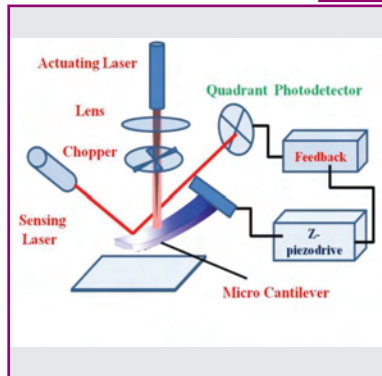
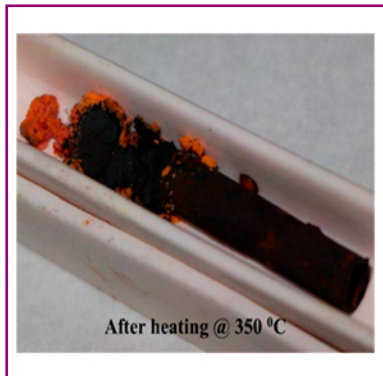
Fig. 2 The shapes of important donor orbitals (π_x , π_y , and σ_{P-O}) of the ligands (top row) and acceptor orbitals (f_{σ^*} , dS_{σ^*} , and d_{π^*}) of $\text{UO}_2(\text{NO}_3)_2$ (bottom row)

energies between the metal-ligand units. It is further shown that the absolute values of the stabilizing interactions are more in the case of phosphoryl ligands, and the largest is observed for TBP (Figure 1). The EDA analysis also highlighted the importance of dispersion interactions as it is providing additional stabilization in uranyl nitrate complexes (Table 1).

The observed moderate weakening of C=O and P=O bonds upon complex formation indicates a possible charge transfer from the respective molecular orbitals of the ligands to the vacant acceptor orbitals of metal nitrate. This conclusion is further supported by the electron charge and molecular orbital analysis. Molecular orbital analysis indicated a considerable amount of charge transfer from π_x and π_y donor orbitals of ligands to the vacant f_{σ^*} and ds_{σ^*} acceptor orbitals of the uranyl nitrate unit (Figure 2). The f_{σ^*} orbital has a significant contribution from the $5f_z^3$ orbital of uranium while the ds_{σ^*} orbital is an admixture of uranium $6d_z^2$ and $7s$ orbitals. It is observed that the amount of charge transfers increases as we move from a carbonyl to a phosphoryl ligand, and a maximum value is estimated for the complex $\text{UO}_2(\text{NO}_3)_2 \cdot 2\text{TBP}$. TBP occupies a unique position where both orbital interaction and dispersion energy contributions are relatively large (-74.6 and -49.9 kcal/mol respectively).

Table 1: Summary of the energy decomposition analysis on uranyl nitrate complexes (positive value: destabilizing; negative value: stabilizing) with various ligands. Energy values are in kcal/mol

Ligand	Strain (ligand)	Strain $[\text{UO}_2(\text{NO}_3)_2]$	Steric repulsion	Orb. int.	Dispersion energy
MIBK	+3.7	+2.9	+8.5	-51.1	-17.7
MIB-PO	+3.0	+5.4	+10.9	-70.2	-23.3
DBC	+4.1	+3.1	+15.0	-53.9	-26.6
DBP	+4.8	+4.4	+18.2	-66.7	-36.1



Directed Basic Research

CHAPTER VI

VI.01 Development of Alloy 617 ODS for High Temperature Applications

Nickel based super Alloy 617 is one of the prime candidate materials for advanced ultra-super critical power plants and high temperature reactors owing to its excellent oxidation resistance, superior mechanical properties at high temperatures. In order to further increase the creep strength of the alloy upto 1000°C, 0.6 wt. % of nanocrystalline Y_2O_3 is dispersed to produce oxide dispersion strengthened Alloy 617 (Alloy 617 ODS). High energy ball milled Alloy 617 ODS powder was consolidated by Spark Plasma Sintering (SPS) technique followed by annealing at 1050°C to produce a dense compact.

The stress-strain behavior of Alloy 617 ODS was investigated by indentation technique using a spherical indenter of radius 7.6 μm . Stress strain curve of alloy sample is shown in Figure 1. The forged Alloy 617 softens back to its original strength when annealed at 1050°C after initial strengthening at 650°C owing to dissolution of the γ' precipitates and coarsening of carbides. However, the alloy 617 ODS retains its strength up to 1050°C and there is nearly 50% increase in yield strength over the Alloy 617 under similar conditions. The enhanced high temperature (1050°C) strength is attributed formation of complex dispersoids after reacting with the matrix. Figure 2a shows $M_{23}C_6$, Al_2O_3 together with fine dispersoids. STEM High Angle Annular Dark Field (HAADF) and Energy Dispersive Spectroscopy (EDS) maps shown in Figures 2b to 2c reveal dark faceted particles that are rich in Al and O. These are Y-Al-O complex oxide (garnet) dispersoids. On the other hand, the relatively brighter particles are precipitates rich in Ni, Y, Al and O. Their chemistry and structure are rather complex and further analysis is currently in progress. Figure 2d shows an atomic resolution

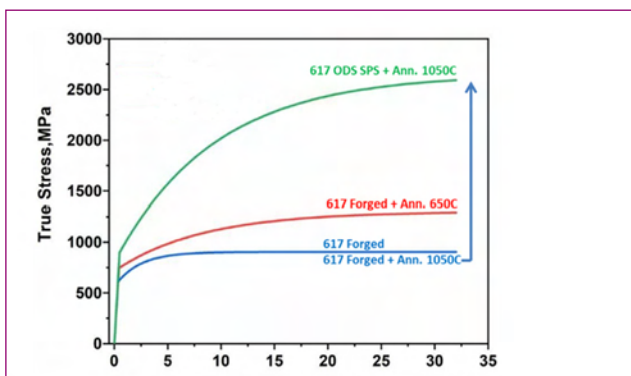


Fig. 1 Stress-strain behaviour of Alloy 617 and 617 ODS extracted from nanomechanical studies

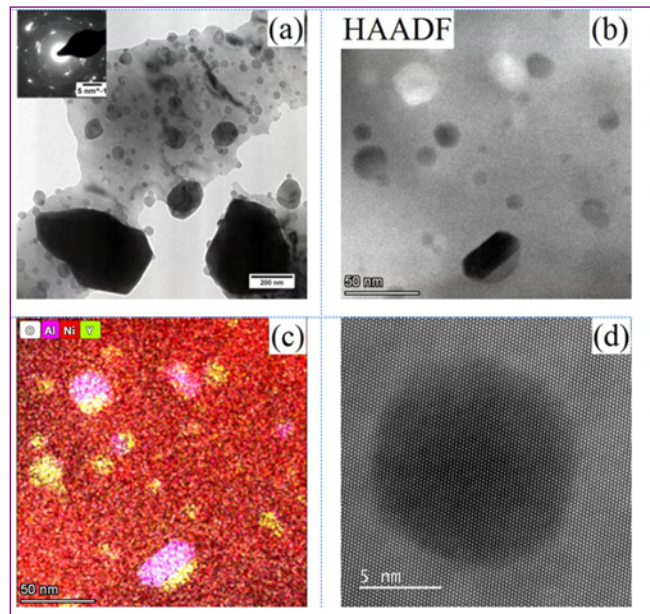


Fig. 2 1050°C annealed alloy 617 ODS samples (a) TEM BF, (b) STEM HAADF, (c) EDS map and (d) high resolution aberration corrected STEM HAADF of Y-Al-O complex oxide

aberration corrected STEM HAADF image of a highly coherent Y-Al-O complex oxide with a size ~ 10 nm. Figure 3 shows the atomic column chemistry (EDS) of homogeneously distributed major substitutional alloying elements such as Ni, Cr and Co. It is observed that the dispersoids are fine and stable up to 1050°C without any appreciable coarsening. Thus the improvement of yield strength in the Alloy 617 ODS is mainly attributed to Y-Al-O based dispersoid strengthening.

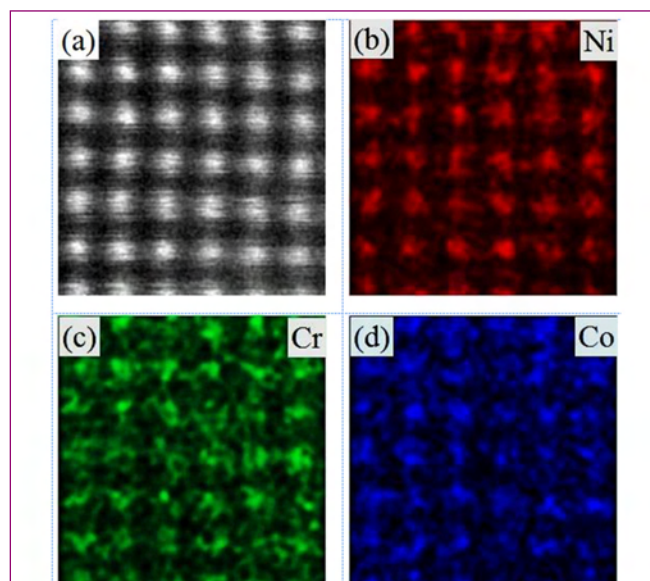


Fig. 3 Atomic column chemistry (EDS) of the alloy matrix (a) HAADF image, (b) Ni, (c) Cr and (d) Co

VI.02 Development and Demonstration of Manufacturing Process for Mass Production of Long Seamless Tubes of Ni-Based Super Alloy 617M

IGCAR is consortium partner in Indian Advance Ultra Super Critical (AUSC) mission, which envisages to design, build and operate a coal fired 800 MWe AUSC power plant (AUSCPP) operating at 710/720°C steam temperature and 310 bar steam pressure with 46% thermal efficiency and 18-20% less CO₂ emission. Alloy 617M (UNS N06617), a solid solution strengthened, Ni-Cr-Co-Mo alloy with exceptional combination of high temperature strength and oxidation resistance, is the primary material for seamless boiler tubes for the 800 MWe Indian AUSCPP. In Alloy 617M, Mo and Co provide solid solution strengthening, M₂₃C₆ carbides provide precipitation hardening, while, Ni and Al form the gamma prime (γ') intermetallic over a range of temperatures providing additional strengthening.

Typically long seamless tubes of minimum 7 m individual length are envisaged to reduce inevitable large nos. of weld in the boiler. Indigenous capability to manufacture such long boiler tubes of Alloy 617M fulfilling all qualifying requirements under Indian Boiler Regulations (IBR) is key to successful implementation of the Indian AUSC Mission. These tubes would also have potential application in Gen IV Super Critical Water Reactor (SCWR) too as secondary heat exchanger tubes. Towards this goal, IGCAR in collaboration with NFC and MIDHANI, had successfully completed the challenging indigenous manufacturing of IBR qualified long seamless tubes of Alloy 617M up to 9.5 m individual length meeting all the critical requirements of chemistry, mechanical properties, NDT & dimensional tolerances. The seamless tube manufacturing process encompassing alloy melting and refining, hot forging, hot deep hole expansion, hot tube extrusion, multistage cold pilgering and high temperature controlled heat treatments have been established, commercially demonstrated and documented for 52 mm OD x 12 mm WT X 9500 mm



Fig. 2 Orientation micrograph of final tubes

long seamless tubes with chemical composition as given in Table 1. These tubes are qualified as per IBR for usage in high temperature and pressure application in AUSC boiler.

Pictures of the Alloy 617M billets and tubes during various stages of manufacturing are shown in Figure 1. The extruded and solution annealed blanks were multiple pass pilgered to reach final tube dimensions due to high strain hardening of Alloy 617M. The final tubes were characterized for integrity using visual inspection, ultrasonic testing with stringent defect standard of 5% WT notch depth, hydrostatic pressure testing, microstructure and mechanical properties. The microstructure of the final tubes (Figure 2) shows fully recrystallized equiaxed grains free from grain boundary precipitation as desired. Fine Cr Rich carbide precipitations are observed inside grain matrix. The yield strength, ultimate strength and ductility as shown in Figure 3 also satisfactorily meet all the relevant specifications.

Table 1: Chemical composition of tubes

Elt.	C	Mn	Si	Mo	Cr	Cu	Al
Wt %	0.0638	<0.01	<0.1	8.45	22.2	<0.01	1.18
Elt.	Fe	Co	Ti	B	N	S	Ni
Wt %	0.09	11.8	0.46	0.0025	0.0105	0.0051	Bal

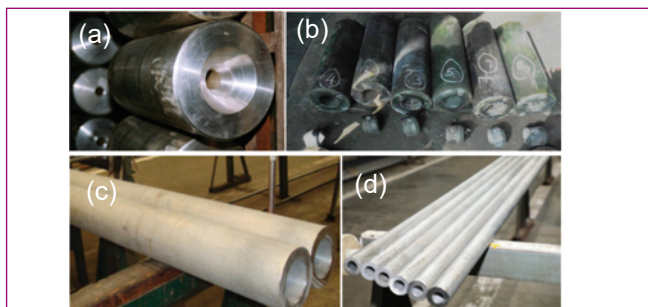


Fig. 1 Indigenous alloy 617M billets and tubes (a) forged & machined billets (b) deep hole expanded billets (c) final pilgered and (d) annealed tubes

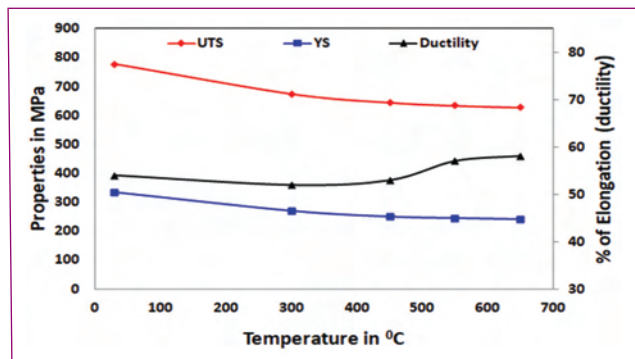


Fig. 3 Mechanical properties of final tubes

VI.03 Development of Oil-Absorbent Iron Oxide/MnO_x Magnetic Nanoparticles and its Applications in Oil Recovery

Oil-pollutants are a major concern because of their adverse effects on marine and aquatic ecosystems, environment, and economy. The conventional ways of oil remediation on water such as in-situ burning, skimming and sorbents have many limitations in terms of their efficacy and cost factors. Nanotechnology offers promising routes for oil remediation with better removal capacity than conventional remediation techniques. Nanomaterials based sorbents for oil–water separation has gained significant interest. Among them, magnetic nanomaterials offer the unique advantage for in-situ remediation of contaminated water using an external magnetic field where the oil loaded magnetic materials are separated from the solution using gradient separation without secondary pollution.

Towards oil removal applications, core-shell $\gamma\text{-Fe}_2\text{O}_3/\text{MnO}_x$ magnetic nanoparticles with core diameter of $\sim 31 \pm 3$ nm and saturation magnetization ranging from 55 to 70 emu/g, using an inexpensive, facile and environmentally friendly approach was developed Figure 1. The synthesis was done through acid catalyzed reduction of KMnO_4 and carboxymethyl cellulose (CMC) capped iron oxide in water. XPS results showed that MnO_x coated iron oxide contains iron in Fe^{3+} state, Mn in +3 and +4 states. The surface of the nanoparticle contained hydroxyl groups and oxidized fragments of CMC polymer. Mn% is varied from 9 to 13% with increase in the $\text{KMnO}_4:\text{Fe}_3\text{O}_4$ ratio from 0.2 to 0.5 where as the ratio of oxidation state of $\text{Mn}^{3+}:\text{Mn}^{4+}$ and surface hydroxyl groups showed decreased tendency from 7:3 to 6:4 and 14 to 11% with increase in the $\text{KMnO}_4:\text{Fe}_3\text{O}_4$

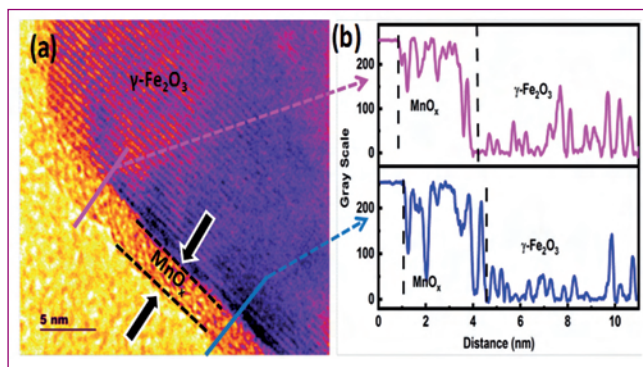


Fig. 1 (a) Pseudo-colored image processing of HRTEM image of the sample showing the core $\gamma\text{-Fe}_2\text{O}_3$ with a lattice fringe spacing of 0.243 nm, corresponding to the (311) plane and an amorphous shell of MnO_x with a thickness ~ 2.9 nm shell (b) intensity variation in gray scale across the length (red and blue lines) of core-shell regions of Figure 1a

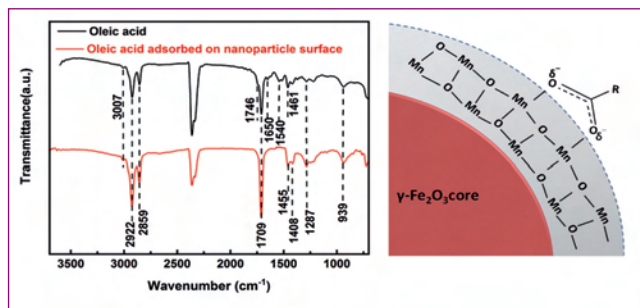


Fig. 2 (a) FT-IR ATR of pure oleic acid and oleic acid adsorbed on core shell $\gamma\text{-Fe}_2\text{O}_3/\text{MnO}_x$ indicating a peaks in the symmetric and asymmetric shift of COO due to the formation of carboxylate on the surface of magnetic nanoparticle shown in the schematic (b) where R corresponds to hydrocarbon unit

ratio, respectively. The magnetic nanoparticles with amorphous MnO_x nanoshell showed superior stability for a range of pH. Oil removal experiments were carried out using contaminated gear oil, aged transformer oil, vegetable oil and oleic acid. The adsorption of oleic acid on nanoparticle surface resulted in a shift of COO symmetric and asymmetric stretch to lower wave numbers at 1455 and 1408 cm^{-1} , respectively, because of the formation of carboxylate on surface Figure 2. The reusability recycling experiments of the prepared particles showed $>93\%$ oil removal efficiency after six cycles. Figure 3 the adsorption or the affinity of the COOH units of the oils was found to be due to Mn^{3+} cations and the amorphous nature of MnO_x nanometer shell. The presence of Mn^{3+} enables the formation of OH groups on the surface, which exchanges with the COOH of the oil. It was also found that the C-C/H units from the decomposed fragments of cellulose also participate in binding with the non-polar groups that favors the oil adsorption.

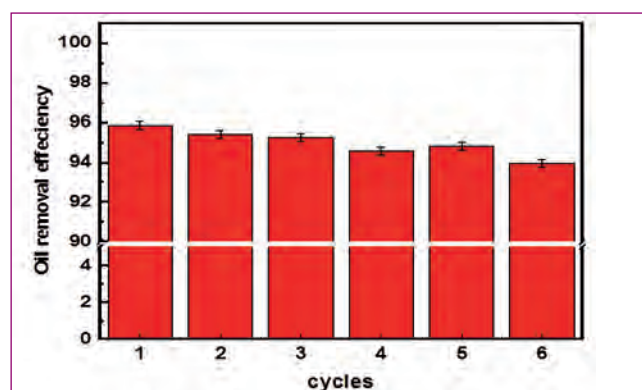


Fig. 3 Regeneration studies using 3.4 wt% of core shell $\gamma\text{-Fe}_2\text{O}_3/\text{MnO}_x$ magnetic nanoparticles showing $>93\%$ gear oil removal efficiency after six cycles

VI.04 Thermal Oxidation of Commercially Pure Titanium for Enhanced Resistance to Corrosion and Biofilm Formation

Commercially Pure Grade 2 Titanium (CP-Ti) due to its excellent properties of strength, corrosion resistance and lesser density is a favourite material for medical, aerospace, power plants, marine, chemical processing and desalination industries. Corrosion resistance and antibacterial properties are the prime factor that determines its service life in the chloride containing natural aqueous environments. There are no systematic studies to understand the role of surface morphology, crystallinity and thickness of nanoscale TiO₂ films grown by thermal oxidation on the corrosion and antibacterial properties of CP-Ti. We show here a facile and novel approach for enhancing the corrosion and antibacterial properties of CP-Ti through nanoscale TiO₂ film engineering by using thermal air oxidation.

An anomalous enhancement of corrosion resistance and antibacterial property of the CP-Ti surface was observed in the presence of a uniform defect-free rutile phase TiO₂ film of ~ 15 nm thickness, grown by thermal oxidation at 400 °C for 1 h. The corrosion resistance of CP-Ti with TiO₂ film grown over, by thermal air oxidation at ≤ 400 °C for 1 h, is increased with the films thickness in Cl⁻ medium, but corrosion resistance was lower CP-Ti with the films grown at ≥ 500 °C. The thickness of the TiO₂ films formed over CP-Ti due to the air oxidation at different temperatures for 1 h and their corresponding polarization resistance in the Cl⁻ medium is provided in the Table 1. The oxide films grown ≤ 400 °C were relatively smooth and defect-

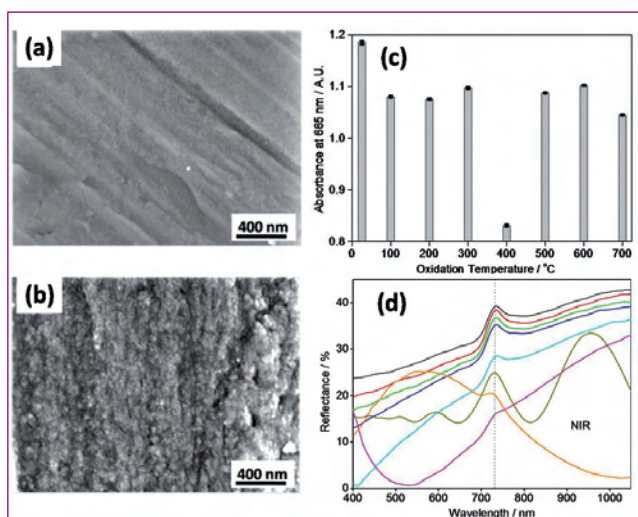


Fig. 1 Surface morphology of the oxide layers formed over CP-Ti air oxidized for 1 h at (a) 400 and (b) 700 °C. (c) Comparison of the absorbance values of the methyl blue solution at 665 nm wavelength light for the oxidized CP-Ti specimens after 4 h exposure to visible light. (d) Comparison of the reflectance from the oxide layers formed over the CP-Ti specimens air oxidized for 1 h at 25-700 °C

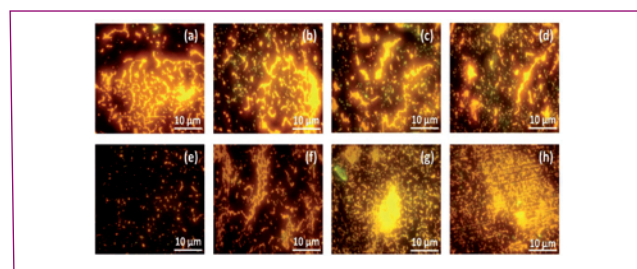


Fig. 2 Epifluorescence micrographs of the biofilms of *Pseudomonas sp.* attached on the CP-Ti specimens thermally oxidized for 1 h at (a) room temperature (25-30), (b) 100, (c) 200, (d) 300 (e) 400, (f) 500 (g) 600 and (h) 700 °C exposed to visible light for 4 h

free while those grown at ≥ 500 °C showed an increased nanoscale surface roughness as shown in Figures 1a and 1b. The increased surface area due to the nanoscale surface roughness reduced polarization resistance and enhanced bacterial attachment. The photocatalytic activity of TiO₂ films formed on the CP-Ti surface by thermal oxidation was assessed by evaluating the degradation of methylene blue (MB) solution under visible light exposure. The absorbance values of MB solution after 4 h exposure with different Ti specimens are shown in Figure 1c. The photocatalytic activity of the TiO₂ films, under visible light was nearly independent of the TiO₂ phase and thickness. The ~ 15 nm thick rutile phase TiO₂ film showed a significant photocatalytic activity and thus the antibacterial property due to thin film interference where the blue light (~ 410 nm) is preferentially absorbed (Figure 1d) due to matching of energy with the band gap (~ 3.0 eV) of the rutile phase that enhanced the electron-hole pair generation and their recombination time. Epifluorescence micrographs of *Pseudomonas sp.* biofilms attached on different CP-Ti specimens under illumination are shown in Figure 2. CP-Ti thermally oxidized at 400 °C showed the least density of bacterial cells, indicating the dominant role of photocatalytic activity of the oxide layer in reducing the bacterial cell attachment.

Table 1: Different oxidation temperatures with thickness formed and related polarization resistance

Oxidation temperature / °C	TiO ₂ thickness / nm	Polarization resistance / MΩ.cm ²
25 (RT)	3±0.2	1.0±0.2
100	5±0.3	9.0±1.0
200	6±0.4	39±4
300	11±1	56±4
400	16±1	90±13
500	32±2	65±4
600	85±5	52±5
700	540±30	54±3

VI.05 Studies on the Oxidation behavior of Sodium-bonded U-Zr with Clad (T91) in the Context of Aqueous Reprocessing of Metallic Fuel

Reprocessing of metallic fuel is a major challenge in the fast reactor fuel cycle. Metallic fuel is preferably reprocessed by pyro-metallurgical reprocessing route. However, alternate processes such as aqueous reprocessing are being explored for the reprocessing of metallic fuel by suitably converting the alloy to metal nitrate solution. Aqueous reprocessing technology is proven and well established and being in use for the reprocessing of spent fuel once the fuel is converted to nitrate solution. Conversion of alloy to nitrate solution needs dissolution of alloy in concentrated HNO_3 . However, based on the information reported in the literature that direct dissolution of U-Zr fuels in nitric acid medium results in violent exothermic reaction due to the presence of δ - phase of UZr_2 . Therefore, direct dissolution of the alloy in nitric acid medium must be avoided.

Further, the metallic alloy fuels (U-Zr and U-Pu-Zr) were bonded with sodium to improve the thermal conductivity. Chopping of metallic fuel pins followed by dissolution in nitric acid medium could not be carried out as sodium reacts violently with aqueous medium. To avoid these issues, studies were undertaken to oxidize the alloy under controlled oxygen partial pressure to convert the metallic alloy to oxide form. The dissolution of oxides is relatively free from evolution of hydrogen and associated eventualities.

The oxidation of alloy fuel was conducted under controlled oxidation ambient. The oxidation set-up for U-Zr and Na-bonded U-Zr with T91 clad samples is shown in Figure 1. The oxidation chamber is a cylindrical

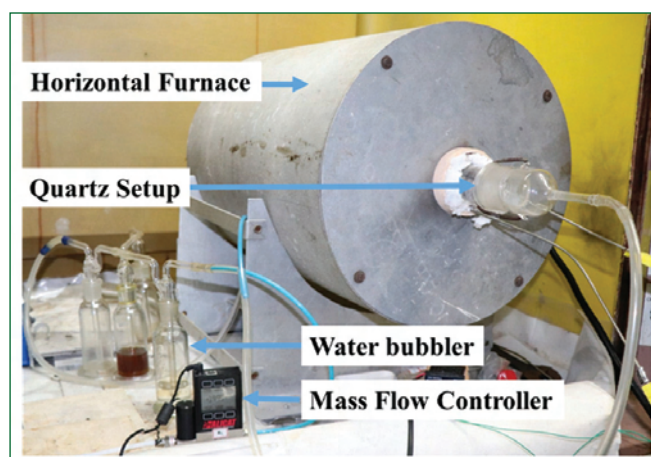


Fig. 1 Experimental setup for oxidation study

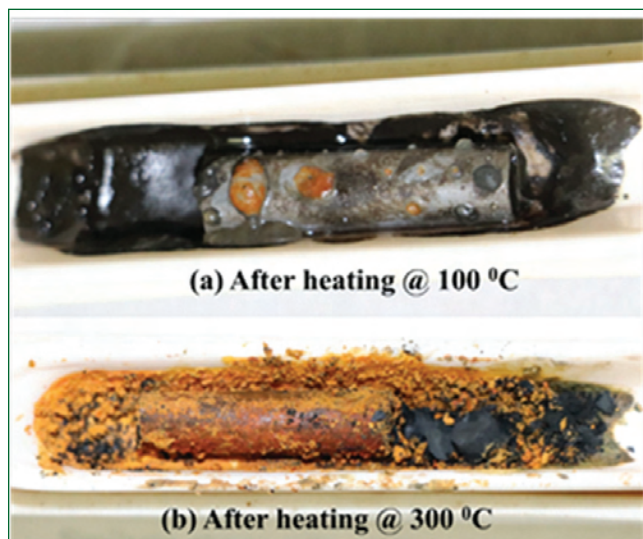


Fig. 2 Formation of oxidation products of Na-UZr+Clad (T91) after heating at (a) 100°C & (b) 300°C for 65 h & 60 h respectively

quartz tube with both ends closed by quartz ground joints. It has provisions to accommodate a K-type thermocouple close to the sample kept in a quartz/alumina boat in constant temperature zone of the furnace. Provisions are made to purge the sample chamber with commercial argon (5-10 ppm of oxygen). The sample oxygen partial pressure was maintained by passing 20 sccm (standard cubic centimeter per minute) of argon gas (contains 5-10 ppm of oxygen) bubbled through water (at 250°C). U-Zr samples were wetted with sodium at 550°C for ~10 days; the percentage of sodium wetting to U-Zr samples was around 1 to 1.5% (this was done to simulate the Na-bonded U-Zr slug). The samples were heat-treated at various temperatures starting from 100-300°C range. The samples were first heat-treated at 100°C for 65 h then taken out of the furnace and physically examined, and subsequently characterized by XRD. The physico-chemical changes observed on the Na-bonded U-Zr samples on heat-treatment at 100°C is shown in Figure 2a. The sample on further heat-treatment at 300°C for 60 h under moist argon ambience shows the formation of yellow orange patches on the powders (Figure 2(b)). The samples on further heat-treatment at 350°C for 60 h shows intense yellow –orange coloured patched with black flaky mass as shown in Figure 3. The powders were examined by XRD and the results were shown in Figure 4. The XRD pattern of the samples heat-treated

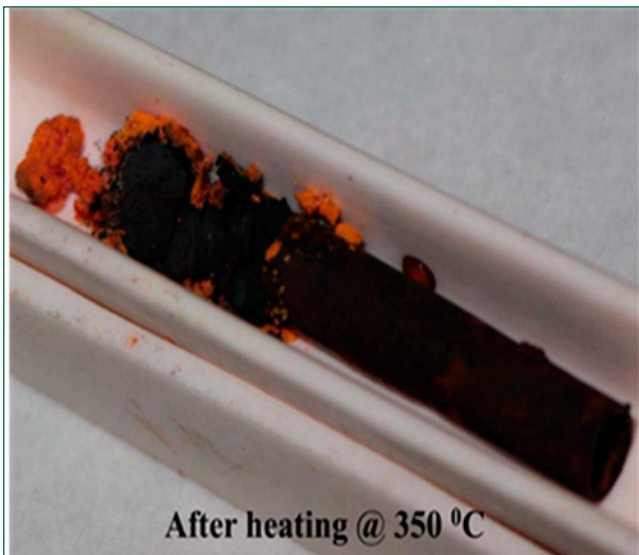


Fig. 3 Formation of oxidation products of Na-UZr+Clad (T91) after heating at 350°C 60 h

at 350°C shows the formation of U_3O_8 , $U_{0.86}Zr_{0.14}O_2$ and $Na_2U_2O_7$ in the oxidized powder. The effect of heat-treatment on T91 clad at 100°C pertaining to its dissolution behaviour was not prominent/noticeable in comparison to dissolution behaviour of U, Zr and Na elements present in the sample. Furthermore, no crystallographic phase corresponding to oxidized products of T91 clad material was found in the XRD pattern. However, the T91 clad get affected on heating at higher temperatures. The objective of oxidizing the Na-bonded U-Zr with T91 clad was to explore the possibility of avoiding the sodium distillation step before dissolution of the sodium bonded fuel; because on oxidation, Na and the fuel elements will be converted to corresponding oxides that are easy to handle for the dissolution of

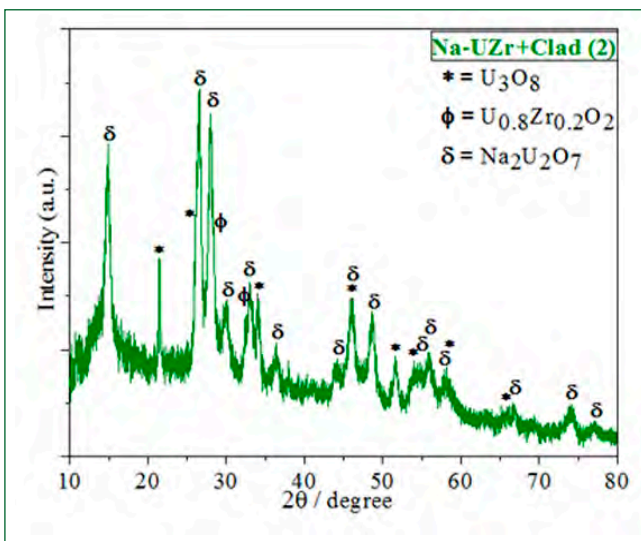


Fig. 4 XRD pattern of the products of Na-UZr+Clad (T91) oxidation at 350°C

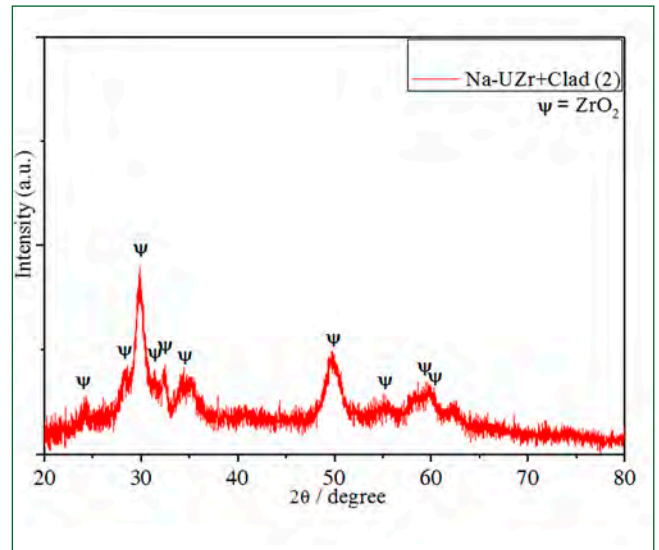


Fig. 5 XRD patterns of post-dissolution residues of Na-UZr+Clad (T91)

the fuel in nitric acid for reprocessing. The effect of temperature on oxidation of the T91 clad was noticeable when it was heat-treated at and above 300°C. Since T91 clad is 9-Cr-1-Mo steel, on dissolution in nitric acid, the concentration of Cr and Mo would increase in the dissolver solution, consequently, higher concentrations of Cr and Mo may pose problem during vitrification of the nuclear waste. The dissolution studies of the oxidized products were carried out in 12 M HNO_3 -0.2 M HF. Percentage weight loss on dissolution of the T91 clad heat-treated at 300°C was observed to increase with increase in HF concentration (wt. loss was ~ 37.6 % in 12M HNO_3 -0.2M HF). The dissolution of elements increases with HF concentration in nitric acid medium and was observed to be highest for Fe and lowest for Ni (i.e. $Fe \gg Cr > Mo > Mn > V > Si > Ni$). The order of leaching of elements is in agreement with the composition of elements in T91 clad. Quantitative dissolution (>99%) of U with partial dissolution of Zr (10-30%) was achieved in HNO_3 and HNO_3 -HF medium. Simultaneously, the sodium wetted U-Zr samples with clad were oxidised initially in argon followed by moist argon (3 % moisture). Kinetics of oxidation of U-Zr alloy was found to be very slow when U-Zr samples were oxidised along with clad; this is due to the limited exposure of fuel materials to oxygen, because T91 clad was acting as a barrier and preventing the intimate contact of wet Ar with U-Zr present inside clad. Preliminary results indicate that 1600-1800 h is required for complete oxidation at 100°C. The dissolution of U and Zr was found to be around >95% and ~ 20%, respectively. The residue of the dissolved product was examined by XRD (Figure 5). The XRD shows the residue to be ZrO_2 .

VI.06 Characterization of Low Cycle Fatigue Behaviour of Simulated Microstructures and Actual Weld Joint of P91 Steel

Modified 9Cr-1Mo ferritic/martensitic (P91) steel has been chosen as the structural material for the steam generator (SG) components of the prototype fast breeder reactor (PFBR) owing to its optimum combination of mechanical properties and better resistance to environmental induced degradation. The microstructure of the base metal part in welded components of the steel gets markedly modified due to the thermal cycles imposed during welding, with the highest temperature attained by the heat affected zone (HAZ) that lies closest to the weld fusion zone. This results in a complex variation of the microstructure and mechanical properties within a narrow band of the HAZ. Frequent start-ups and shut-downs lead to damage from low cycle fatigue (LCF) in the SG components. Thus, damage due to LCF in high temperature structural components is an important design consideration. Systematic investigations were carried out on the LCF behaviour of different microstructural regions of P91 weld joint towards understanding the initiation and progression of damage leading to the final failure of the microstructurally heterogeneous weldment at elevated temperatures.

Three principal microstructures of the HAZ, viz., inter-critical heat-affected zone (ICHAZ), fine grained heat-affected zone (FGHAZ) and coarse grained heat-affected zone (CGHAZ) were simulated through isothermal furnace heat treatments at 1138 K, 1208 K and 1473 K, respectively. All simulated microstructures predominantly developed tempered martensite after oil quenching followed by tempering (1033 K / 3 h). Grain and precipitate sizes and microhardness for each simulated constituent was determined and compared with those of the actual weld joint to ensure accuracy of the simulation through heat treatments. LCF tests were carried out on each constituent microstructures and the actual weld joint at strain amplitudes in the range, ± 0.25 to $\pm 1.0\%$ using triangular waveforms at a nominal strain rate of $3 \times 10^{-3} \text{ s}^{-1}$ and a temperature of 823 K. The chemical compositions of

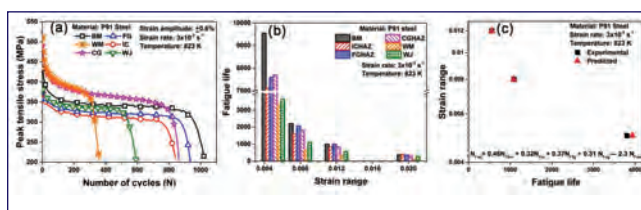


Fig. 1 (a) Cyclic stress response curves shown by different regions, (b) fatigue life-strain range bar charts for different microstructures and (c) comparison of experimental and predicted fatigue lives of actual weld joint of P91 steel at 823 K

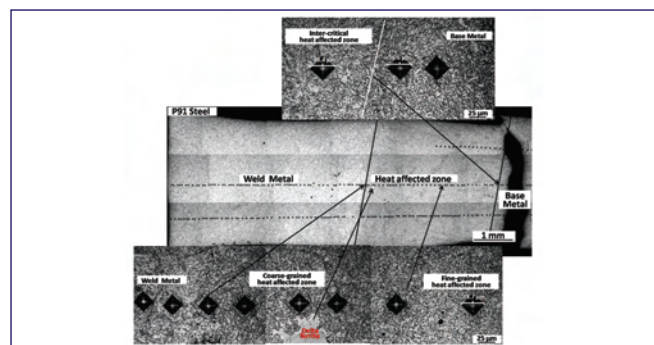


Fig. 2 Micrographs showing the failure location in actual weld joint under LCF cycling at 823K

the base metal and weld filler wire are presented in Table 1. Irrespective of the difference in the microstructures, the steel showed typical cyclic softening at all strain amplitudes as shown in the representative (Figure 1a) Among all microstructural constituents of the joint, the weld metal exhibits the lowest fatigue life, followed by the ICHAZ and CGHAZ (Figure 1b). A common empirical relationship to estimate the fatigue life of the weld joint using weightage factors along with the fatigue lives of all major microstructural constituents was established Figure 1(c). The actual weld joint specimen failed at the interface between the ICHAZ and the base metal Figure 2. Factors such as the grain size, strength of various phases, precipitate size (de-cohesion around coarsened carbides in the ICHAZ), differences in the volume of microstructural regions in the actual weld joint, differences in plastic strain accommodation/accumulating capacity of individual microstructures and their evolution during fatigue deformation are found to affect the crack propagation behavior and the resultant fatigue life (Figure 3).

Element (wt.%)	C	Cr	Mo	V	Nb	Ni	Mn	N	Fe
Base metal	0.11	9.3	0.99	0.25	0.1	0.14	0.46	0.068	Bal.
Filler wire	0.082	9.0	1.0	0.24	0.055	0.70	0.55	0.055	Bal.

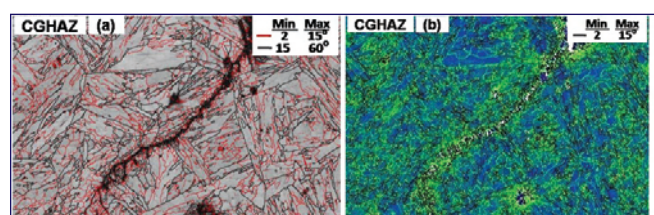


Fig. 3 Crack propagation through low angle grain boundaries (LAGBs): (a) grain boundary map and (b) kernel average misorientation (KAM) map with grain boundary misorientation distribution

VI.07 Creep Deformation and Damage Evolution in 316LN SS with Varying Nitrogen Content in the Framework of Continuum Damage Model

316LN stainless steel with 0.06 to 0.08 wt.% Nitrogen is being used as a structural material for primary components of sodium cooled fast breeder reactors. As a part of the development of high strength austenitic stainless steel suitable for longer design life, the influence of nitrogen in the range of 0.07-0.22 wt.% on high temperature mechanical properties (tensile, creep and fatigue) of 316LN stainless steel are being investigated extensively. Design against the creep deformation and damage is one of the primary considerations in the high temperature design of components. It is thus important to evaluate the evolution of deformation and damage rates and also the predominance of one over the other as a function of nitrogen content. In view of the above, the influence of three nitrogen contents (0.07, 0.14 and 0.22 wt.% N) on the creep deformation and damage behaviour of 316LN SS is proposed for investigation in the frame work of the Kachanov-Rabotnov (K-R) model, at a temperature of 923 K. The coupled equations representing the evolution of strain rate ($\dot{\epsilon}$) and damage rate ($\dot{\omega}$) are given in the K-R model as

$$\dot{\epsilon} = \frac{\dot{\epsilon}_0}{(1-\omega)^m} \quad \text{and} \quad \dot{\omega} = \frac{\dot{\omega}_0}{(1-\omega)^q}$$

where $\dot{\epsilon}_0$ and $\dot{\omega}_0$ are the characteristic strain rate and characteristic damage rate, respectively and m and q are constants. The unknown constants in the K-R model were optimised using interior point algorithm. For a given stress, low least-square error values signify the minimum difference between the predicted and experimental creep strain values.

At all test conditions, the values of constants were obtained from the best-fit creep strain-time data. The fitted data is shown in Figure 1 for 0.07% N as an example. Apart from the fitting, the iso-damage contours are generated on the simulated creep curves obtained for different stress levels of 316LN SS having different nitrogen contents. The final results indicated that the evolution kinetics of coupled strain and damage is unique for a given applied stress level for all the nitrogen contents. Irrespective of nitrogen content, the

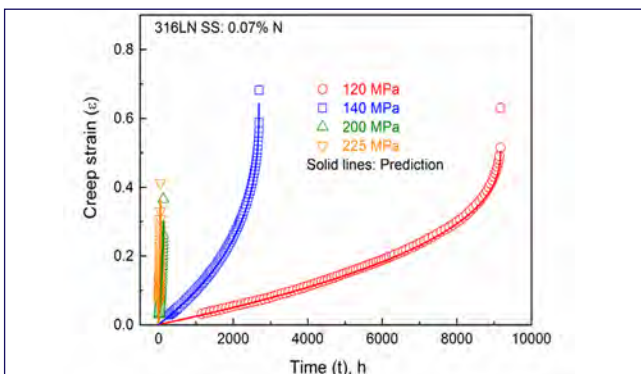


Fig. 1 Description K-R model for the steady state and tertiary creep behaviour of 316LN SS

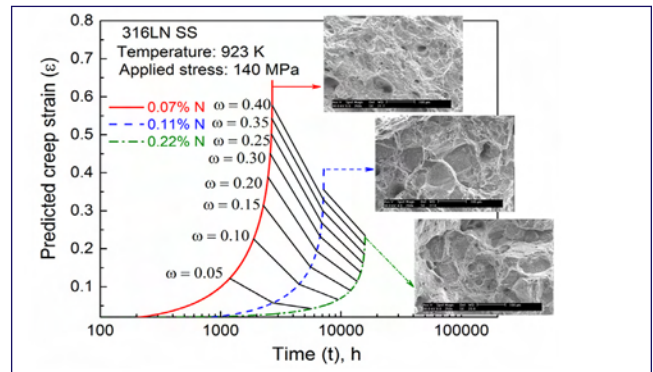


Fig. 2 Iso-damage contours superimposed on the predicted creep strain (ϵ) - time (t) curves for different nitrogen contents of 316LN SS at 923 K

time to reach a particular value of damage increases with a decrease in applied stress values. However, the strain to reach a particular value of does not show a similar trend. The observed strain to reach the particular damage value is highest for the lower nitrogen contents at all the stress levels compared to those values observed at high nitrogen content as shown by Figure 2.

Moreover, the observed ratio between strain rate and damage rate is the highest for 316LN SS with 0.07% content and the lowest for the steel having 0.22% N, irrespective of the same applied stress level or ratio (applied stress/yield stress) level Figure 3. The estimated lower ratio (strain rate/damage rate) values reflected in the lower creep rupture ductility associated with the reduction in dimple fraction for 0.22% N compared to other nitrogen contents. The above results clearly indicated that the increase in the tendency to intergranular fracture was expected for 316LN SS having high nitrogen content. The model and experimental outcomes therefore indicate that the nitrogen content (X) should be restricted i.e., in the range $0.07 > X < 0.14\%$ for obtaining optimum creep deformation and damage resistance in the steel. In addition, accurate prediction of creep ductility and rupture lifetime using the model demonstrated the applicability of the model for 316LN SS.

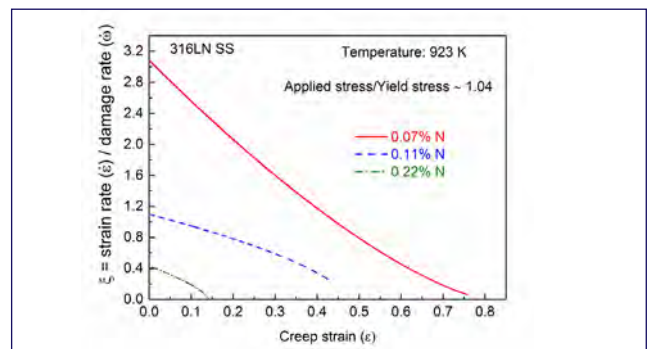


Fig. 3 Variations in the ratio between strain rate and damage rate i.e. ξ with creep strain at 923 K for different nitrogen contents of the steel

VI.08 Effect of Temperature on Fatigue Crack Growth (FCG) Threshold (ΔK_{th}) of 316LN Stainless

Extensive literature survey and in-house experience indicate that the austenitic stainless steel of type 316LN stainless steel has potential application for the high temperature components of sodium cooled Fast Breeder Reactors (FBR) and for various other industries at different temperatures and environmental conditions. The operating temperature range of sodium cooled FBR is 623-823 K. Many of these components are subjected to static, cyclic thermo-mechanical and flow induced vibrational loads that cause different types of damage like creep, low cycle fatigue, creep-low cycle fatigue interaction and high cycle fatigue. Several research reports are available on the evaluation of tensile, creep and fatigue properties of this material. For the damage tolerant design of components made of this steel, inter alia its FCG properties at different temperatures are required. This study attempts to determine the effect of test temperature on the FCG behaviour of 316L (N) stainless steel in both Paris and threshold regimes since these are important as suggested in the ASME and RCC-MR codes.

An attempt to describe the temperature effects considering the temperature dependence of elastic modulus and yield strength was not satisfactory. Anomalous FCG behaviour of 316LN stainless steel in Paris (Figure 1) & ΔK_{th} -threshold (Figure 2) regimes is attributed to the occurrence of dynamic strain ageing (DSA). DSA is a function of temperature & crack tip strain rate. The plot of crack tip strain rate vs temperature Figure 3 exhibits two slopes behaviour which is an indication of the occurrence of two stage DSA. The one

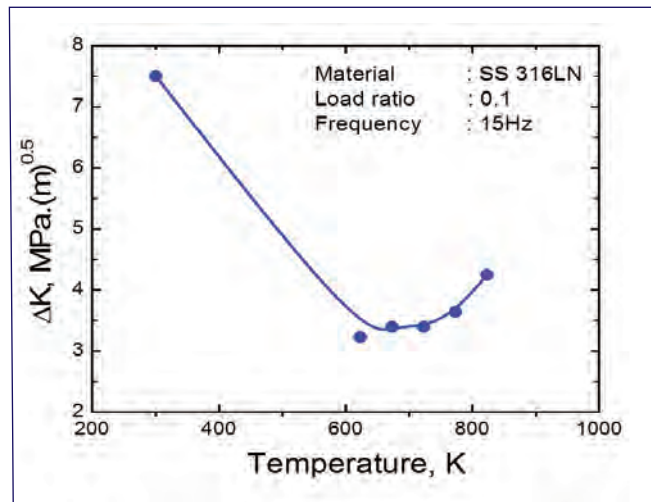


Fig. 2 Effect of temperature on threshold (ΔK_{th})

which is operative in the temperature range 623-723 K gives an activation energy of 90 ± 2 kJ/mole, which corresponds to that for carbon diffusion in austenitic steels (47-90 kJ/mol). The higher slope corresponding to the temperature range 723-823 K gives an activation energy value of 160 ± 5 -kJ/mole, which corresponds to that for nitrogen diffusion in stainless steels. Therefore interstitial diffusion is responsible for the occurrence of two stage DSA in the entire test temperature range.

Table 1 : Chemical composition of SS316L(N)									
C	N	Mn	Cr	Mo	Ni	Si	S	P	Fe
0.027	0.08	1.70	17.53	2.49	12.20	0.22	0.0055	0.013	Bal.

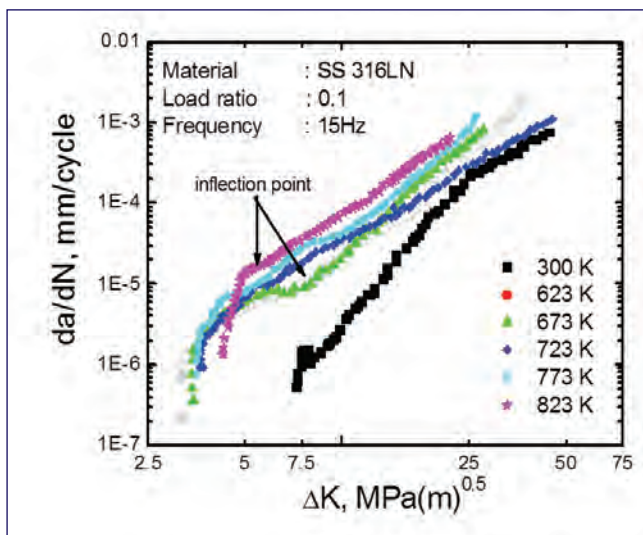


Fig. 1 Effect of test temperature on FCG behaviour of SS316L(N) near threshold and Paris regimes

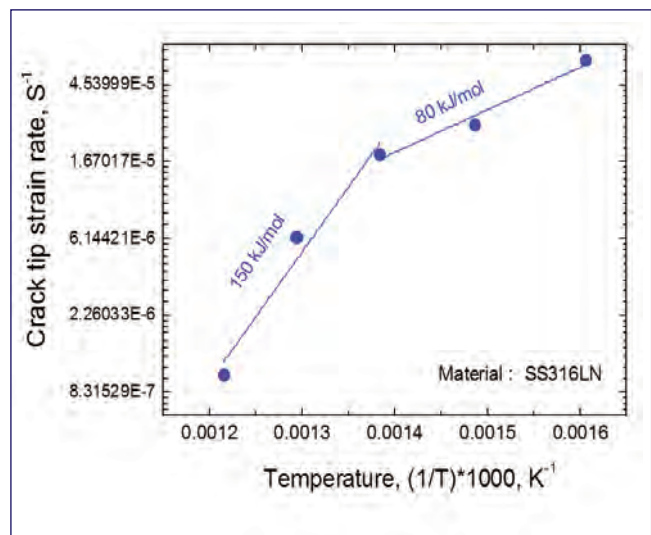


Fig. 3 Arrhenius type relation between crack tip strain rate and temperature for activation energy determination

VI.09 Effect of Nitrogen on Grain Boundary Character Distribution in AISI Type 316L Stainless Steel

AISI 316L (N) stainless steel (SS) is a structural material used in Fast Breeder Reactor (FBR) and it will be used in FBRs with its higher nitrogen variant in future. Grain boundaries play an important role in improving mechanical properties and corrosion resistance of FCC materials. Grain boundary character distribution (GBCD) and grain boundary network (GBN) greatly influence material properties. GBCD are described by low Σ ($\Sigma \leq 29$) CSL (coincidence site lattice) and random boundaries. Based on connectivity of grain boundary junctions, material can have three different kind of triple junctions such as 0 low Σ CSLB, 1 low Σ CSLB, 2 low Σ CSLB and 3 low Σ CSLB. It has been suggested that the material having higher fraction of low energy $\Sigma 3$ CSL boundary junction would have better resistance to corrosion. Therefore, a systematic study has been initiated in the present investigation, following thermo-mechanical processing route to improve GBCD in nitrogen free (316L) and high nitrogen 316L (N) SSs. Annealed AISI 316L and 316L(N)SS stainless steels were subjected to 5 - 75 % rolling deformation followed by annealing at 1050 °C/1h. Subsequently, annealed specimens were subjected to sensitization heat treatment at 675°C for 1h and these specimens were designated as AR_675 and GBE_675. The corrosion behavior of all specimens were tested using double loop electro chemical Potentiokinetic reactivation (DLEPR) technique in aerated 0.5M Sulphuric acid and 0.01 M Potassium Thiocyanate using three electrode arrangement with a saturated Calomel Electrode (SCE) as reference electrode, Platinum mesh as counter electrode and the specimen as working electrode. DLEPR tests were performed using scan rate of 1.667 mV/s. Degree of sensitization [DOS = $(I_r/I_a) \times 100$] was evaluated using reactivation current (I_r) and activation

current (I_a) and compared to understand the resistance against sensitization of the investigated steels.

Material used in the present work was 12 mm thick commercial grade 316L stainless steel having chemical composition (in wt.%): 17.84 Cr, 12.43 Ni, 1.41Mn, 0.01 C, 0.41 Si, 0.036 P, 0.006 S and the balanced Fe, 316L(N)SS with chemical composition (in wt.%): 17.61 Cr, 10.46 Ni, 1.98 Mn, 0.024 C, 0.48 Si, 0.036 P, 0.01 S, 0.144 N, and the balanced Fe. The influence of percentage deformation on CSL boundaries fraction and grain size after annealing at 1050 °C for 1 h is shown in Figure 1a. From the figure, it is apparent that CSL boundary fraction in 316L SS remains similar (~ 50 %) between 5 and 10 % deformation and then it decreases monotonically to 12 % with increasing deformation to 75 %. On the other hand, it increases from 66 % to 85 % in 316L (N) SS with increased deformation from 5 to 10 %, subsequently it decreases monotonically to 20 % after 75 % deformation. It is observed that all S boundary fraction $\Sigma 29$ is highest in 10 % deformed 316L (N) SS specimen compared to other conditions. The increasing ratio of $\Sigma 9$ and $\Sigma 27$ boundaries to $\Sigma 3$ boundaries is an indication of multiple twinning. Twinning frequently occurred in the wake of GBs migrating during recrystallization or reorientation of boundaries in low stacking-fault-energy fcc metals. The effect of CSL, grain boundary junctions and multiple twinning occurs in GBE 316 and 316LN SS specimens are closely related to corrosion resistance of the respective steel. As the CSL number fraction increases from 68.6 to 85.4 %, the DOS value Figure 2b drops significantly suggesting improvement in sensitization resistance in GBE high nitrogen AISI 316LN SS. It is also seen that random boundaries are more fragmented in AISI 316L(N)SS than in AISI 316L SS

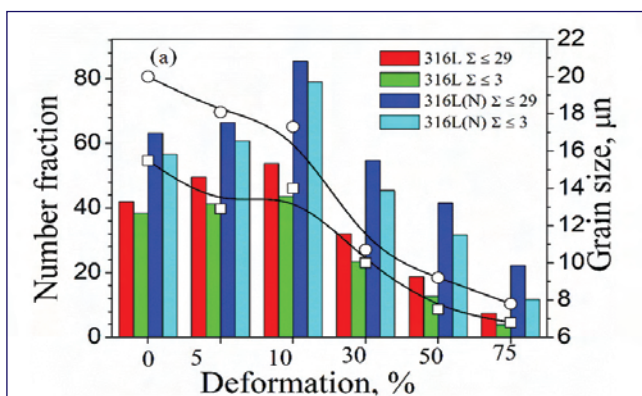


Fig. 1 The influence of percentage deformation on CSL boundaries fraction and grain size after annealing at 1050 °C for 1 h

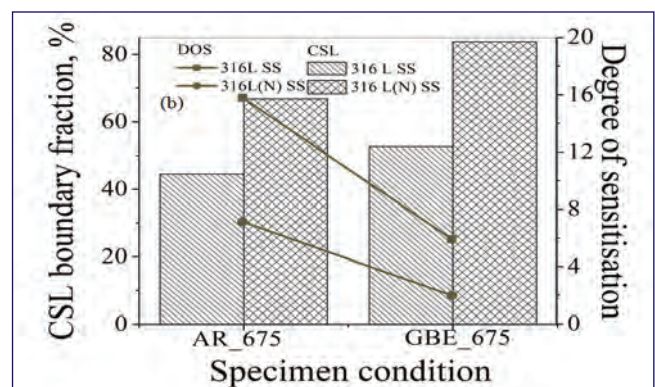


Fig. 2 CSL boundary fraction versus DOS value and improvement in sensitization resistance

VI.10 Effect of Nitrogen on the Intergranular Stress Corrosion Cracking Resistance of 316LN Stainless Steel

Austenitic stainless steels (SSs) undergo sensitization during thermal exposure (slow heating or cooling) within the temperature range of 450 to 850°C. Sensitization occurs mainly due to the precipitation of chromium carbide ($Cr_{23}C_6$), leading to depletion of chromium to less than 12% in the regions adjacent to the grain boundaries resulting in the susceptibility of SSs to intergranular corrosion (IGC) and/or intergranular stress corrosion cracking (IGSCC) in corrosive environments. Here the effect of nitrogen on the intergranular stress corrosion cracking (SCC) resistance of sensitized Type 316LN stainless steel containing different amounts of nitrogen is reported.

The prime objective of this work was to study the influence of nitrogen on tensile and IGSCC behavior of sensitized Type 316LN SS. DL-EPR (Double-Loop Electrochemical Potentiokinetic Reactivation) tests were performed to quantify DOS (Degree of Sensitisation) and was correlated with stress corrosion cracking (SCC) resistance. Electron backscatter diffraction (EBSD)-based coincidence site lattice (CSL) characterization has been used to estimate and correlate with DOS. Scanning electron microscope (SEM) characterization and X-ray diffraction (XRD) of fractured surface were performed to understand the underlying mechanism.

SCC studies were performed at 70% of yield strength. SEM observation of complete “ditch” structure in all of the SSs indicates that they were sensitized Figure 1. A ditch structure results due to continuous grain boundary precipitation of $Cr_{23}C_6$ and/or Cr_2N and associated Cr depletion. Double-loop electrochemical potentiokinetic reactivation technique was used to quantify degree of sensitization (DOS) that was correlated with SCC resistance Table 1. Band contrast images obtained from

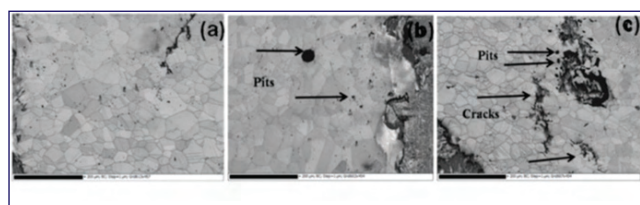


Fig. 2 Band contrast images for three varying nitrogen-containing steel (a) 0.07 wt%, (b) 0.14 wt% and (c) 0.22 wt% Type 316LN SSs showing pits as precursor to SCC

EBSD clearly show formation of numerous pits on the surface of all three nitrogen containing steels. Many pits in the vicinity of a larger pit get linked together and form cracks, namely pit-assisted cracking/corrosion Figure 2. A linear inverse relationship exists between DOS and CSL with a standard deviation of 0.99, which is very close to unity Figure 3a. It clearly implicates that with the increase in nitrogen content from 0.14 wt% to 0.22 wt%, CSL content decreases. This confirms that an optimization of the nitrogen content up to 0.14 wt% is crucial in case of sensitized 316LN SS, beyond which it shall be deleterious (Figure 3b). SCC time to failure increased from 220 h to 285 h with increasing nitrogen content from 0.07 wt% to 0.14 wt%, but decreased drastically to approximately 120 h at 0.22 wt% nitrogen (i.e., beyond N solubility limit) Figure 3c, due to excessive

Nitrogen content, wt. %	O C P , (VSCE)	C C P , (VSCE)	C C P - O C P , mV	D O S , %	t _f , h
0.07	-0.370	-0.347	32	10.16	223
0.14	-0.414	-0.347	73	6.44	283
0.22	-0.408	-0.350	50	44.28	124

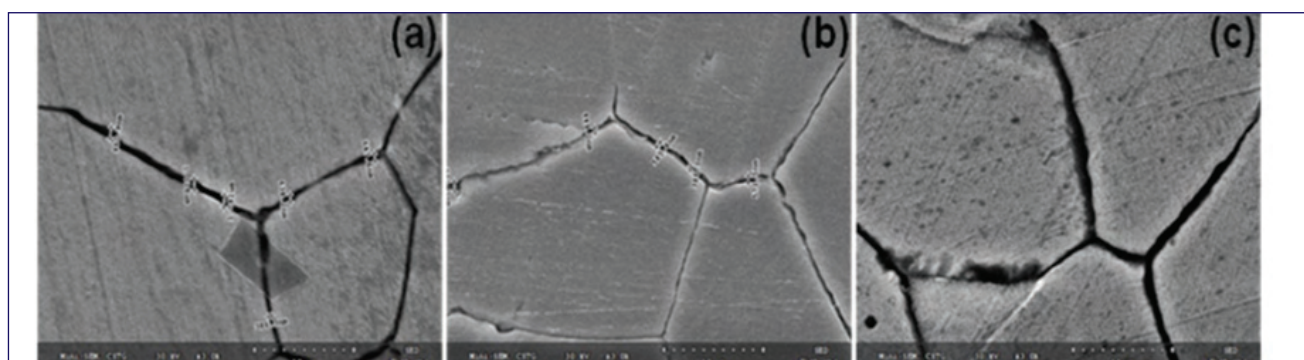


Fig. 1 Width of chromium depletion measured using SEM for sensitized Type 316LN SS with different nitrogen contents: (a) 0.07 wt% (b) 0.14 wt% and (c) 0.22 wt% after DLEPR tests

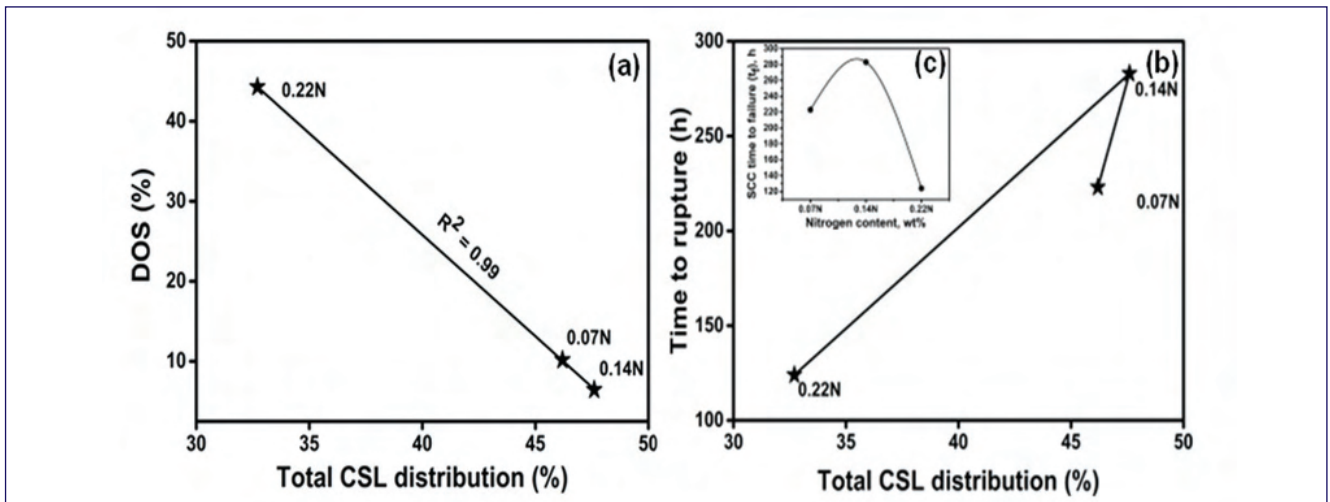


Fig. 3 Relationship between DOS and total CSL distribution (a) and Influence of CSL on SCC resistance (b) of three different sensitised nitrogen-containing Type 316LN SSs. Inset (c) shows SCC resistance with varying nitrogen content

precipitation of Cr_{23}C_6 and Cr_2N and drastic reduction in the coincidence site lattice (CSL) boundary distribution from 48% to approximately 32% Figure 3b. It is possible to correlate DOS, which is a quantitative measure of the sensitization and SCC time to failure (t_f) for determining SCC susceptibility for sensitized nitrogen containing SSs. As indicated in Table 1, the DOS changed from 10.17% to 44.28% and correspondingly t_f from 223 h to

124 h for 0.07 wt% and 0.22 wt% nitrogen-containing SSs. Through DOS, t_f , and total CSL, it was derived that 0.14 wt% nitrogen was optimum for corrosion resistance and beyond 0.14 wt%, further increasing the nitrogen content would be deleterious. Therefore, DOS value is an indicator of SCC susceptibility. Hence, SCC resistance could be estimated for sensitized austenitic SSs if the DOS value is known.

VI.11 Performance Evolution of Gamma Computed Tomography System as per ASTM Standards

Most of the nuclear industry uses first generation gamma ray transmission cum emission CT system for identification of special nuclear material and transuranic material inside radioactive waste material. Waste assay computed tomography system and CT reconstruction techniques have been indigenously developed for characterization of nuclear waste. The system is also being used for non-destructive evaluation of material to generate the 3D internal image of a scanned object through transmission imaging. It is necessary to quantify the performance of the system to authenticate the results. The quality of CT Image depends on data acquisition and reconstruction of the image. The performance of the Gamma CT system has been evaluated as per ASTM standards.

The Gamma CT System is First generation CT system which consists of a gamma source with shielding, shielded HPGc detector and object translational and

rotation unit (Figure 1). The HPGc detector with 100 % relative efficiency is cylindrically shielded with 5 cm thick lead. The front face of the detector is provided



Fig. 1 Waste assay CT system

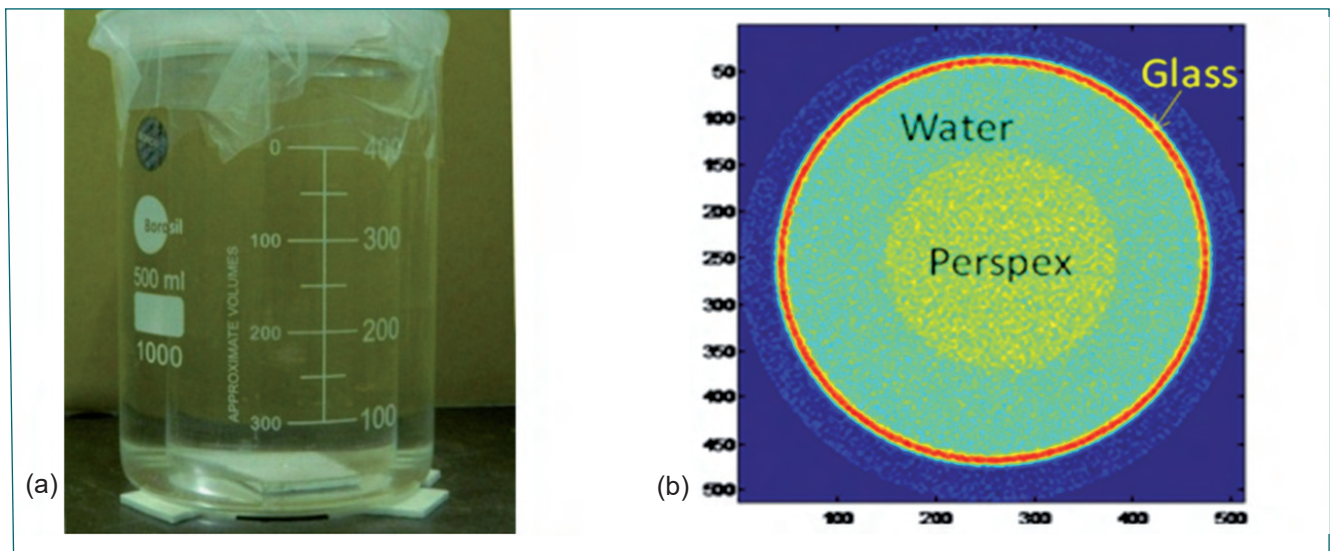


Fig. 2 (a) Photograph and (b) CT image of phantom

with a variable size interleaved tungsten collimator. A ^{75}Se (10 Ci) gamma transmission source is provided with 10 cm thick tungsten shielding.

Test phantom made-up of cylindrical Perspex material (dia: 44 mm and ht.: 100 mm) was placed in a glass beaker (dia: 80 mm, ht.: 110 mm) and filled with water (Figure 2a). Gamma ray source and HPGe detector were collimated with a diameter of 3 mm and 4 mm respectively. The effective beam width is 2.5 mm.

CT scanning is carried out by collecting 212 rays per projection with an interval of 0.5 mm. Totally 180 projections were made. Transmission sinogram of 264 keV of ^{75}Se is reconstructed using Filter Back Projection and the reconstructed image of the phantom is shown in Figure 2b.

According to ASTM standard 1695-95(2013), spatial resolution is calculated using Modulation Transfer Function (MTF). For the reconstructed image, estimated

MTF values are plotted against the frequency (Figure 3a). As per ASTM standard, the frequency at 10% of the MTF is accepted and found to be 0.4633 mm^{-1} . The minimum resolution of the system is $1/0.4633 = 2.158 \text{ mm}$.

Contrast Discrimination Function (CDF) curve expresses the ability to discriminate a contrasting feature of size D (in mm) or D^* (in pixel) from the base at a certain noise level. As per ASTM standard, CDF is calculated and plotted with respect to tile size (Figure 3b). Contrast ($\Delta\mu$) of the reconstructed image is calculated to be 20.3. Any tile size having the CDF value below 20.3% can be viewed with good contrast. Hence, any object size greater than 0.5 mm can be detected with good contrast. Resolution and contrast of the system have been evaluated as per the ASTM standards. The resolution of the system is found to be 3.5 mm at 10% contrast. This study reveals that system can resolve any object size greater than 0.5 mm.

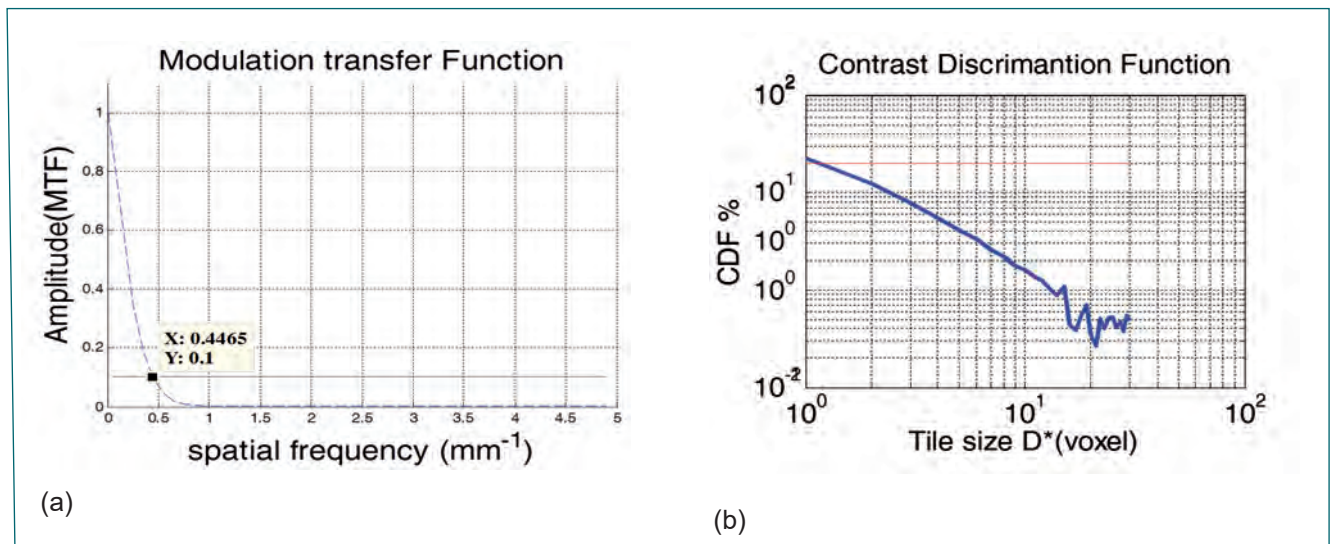


Fig. 3 (a) MTF and (b) CDF curve

VI.12 Multi-NDE Techniques for Detection of Inclined Flaws in Small Diameter Ferromagnetic Steel

Small diameter tubes are widely used as heat exchangers, boilers and condensers in petrochemical, nuclear, oil and gas industries. Various types of flaws such as pits, wall loss, corrosion, cracks, etc. are generally formed in these tubes due to the environmental and working conditions. As real-world flaws (flaws like slivers) rarely have symmetry, the influence of inclination of flaws assumes importance for their quantitative sizing. As single NDE technique is not sufficient to detect all the flaws of different inclinations present in small diameter tubes, use of multi-NDE techniques approach is attractive. Multi-NDE techniques viz., magnetic flux leakage (MFL), remote field eddy current (RFEC) and ultrasonic internal rotary inspection system (IRIS) techniques have been explored for reliable detection and sizing of inclined flaws in a seamless low carbon steel tube of 19.05 mm outer diameter and 2.77 mm wall thickness.

Experimental studies were carried out using a multi-NDE instrument (Figure 1) that consisted of four different NDE modules, namely MFL, RFEC, IRIS and eddy current (EC) techniques. At a time, one technique could be used by connecting the probe to the particular module of the instrument. Ten artificial notches (13.87 mm length, 1.00 mm width and 1.39 mm depth) of different inclinations from 0° to 90° in steps of 10° with respect to the tube axis were fabricated by electro-discharge machining (EDM) on the outer diameter (OD) of the carbon steel tube as shown in Figure 2. Numbers N0-N90 indicate the notches with inclination angles from 0° to 90° , respectively in steps of 10° .

Figures 3a to 3c show the response of MFL, RFEC and IRIS testing of the ten artificial inclined notches in the carbon steel tube. As can be seen from Figure 3a MFL technique detected the notches with inclinations from 40° to 90° . The signal-to-noise ratio (SNR) of the 40° inclined notch was found to be 8 dB. The notches with inclinations from 0° to 30° were not detected as

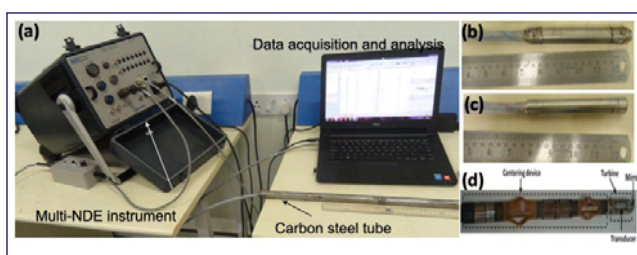


Fig. 1 (a) Experimental set-up, (b) MFL, (c) RFEC and (d) IRIS probes

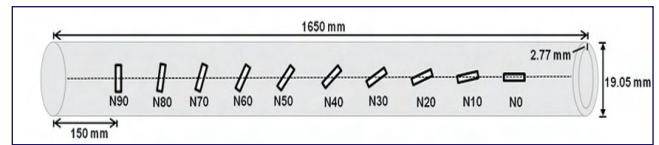


Fig. 2 Schematic drawing of inclined notches (13.87 mm length, 1.00 mm width, 1.39 mm depth) with different inclinations in the carbon steel tube

there was no detectable leakage field due to the axial magnetization being parallel to the length of the notch. As against this, the RFEC technique detected all the notches with good SNR (Figure 3b). Therefore, the detectability of inclined notches is better in RFEC in comparison with MFL technique. This is attributed to the higher through transmitted magnetic flux into the notch area as compared to MFL technique which is generally less sensitive to OD notches due to less detectable leakage magnetic flux from the OD notches. As can be seen from Figure 3c, the IRIS technique clearly detected all the notches. The region corresponding to notches N40-N0 are not visible in Figure 3c although they were also detected with similar sensitivity. As compared to MFL and RFEC techniques, IRIS could provide additional information about the geometry and size of the flaws (within $\pm 8\%$ error) from B-scan and D-scan images, however, it is about 5 times slow. IRIS technique could also be used as a complementary technique to verify the results of the MFL and RFEC techniques. This study reveals that the multi-NDE techniques could be advantageously used for more reliable detection and enhanced information about the structural integrity of the tubes.

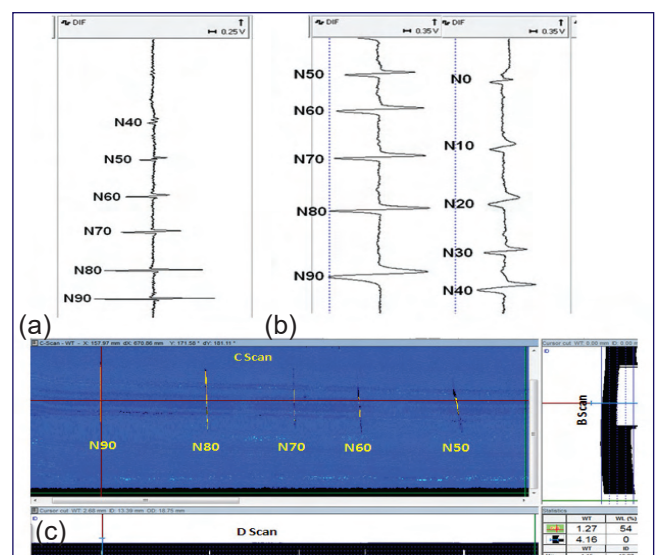


Fig. 3 Response of (a) MFL, (b) RFEC and (c) IRIS testing for inclined notches in the tube

VI.13 Simulation of Gas Entrainment Phenomena Inside FFLM due to Interaction of Free Liquid Jet with Liquid-Gas Interface

The Failed Fuel Location Module (FFLM) is used to monitor the coolant sodium samples exiting from the subassemblies for the presence of delayed neutrons. The presence of delayed neutrons in the sample, above a threshold value indicates the failure of the fuel pins in that particular subassembly. Three FFLMs, each having 66 sampling tubes are housed in the control plug to sample coolant exiting from of Fuel Subassemblies (FSA). Sodium exiting from FSA passes through the sampling tube to the selector plug which selectively permits sodium from the desired FSA. A DC conduction pump (DCCP) connected to the other end of the selector plug draws sodium from the sampling line and delivers it to a sodium capacity positioned at the top level of control plug. Sodium returns back to the hot pool as free liquid jet from the capacity through a flow meter. This liquid jet with a free jet length of 850 mm during fuel handling condition interacts with free sodium surface which causes entrainment of argon gas bubbles in the liquid pool inside FFLM. There is a concern that these gas bubbles may enter into the selector valve through the annular passages provided in the valve housing. Finally, these gas bubbles may be dragged into DCCP suction line which may create operational difficulties for the pump. Argon gas also can get trapped inside selector valve housing during initial sodium filling. These bubbles will also get released and get dragged into the DCCP suction line during initial running of the pump. Therefore, an experimental study using water was carried out to visually observe the formation of gas bubbles and their movement inside FFLM.

The experimental test section is positioned inside a transparent Perspex tank to carry out the visual observation studies. An external centrifugal pump was used in this experiment. A return line with the geometrical features same as in prototype is modeled. The end portion of this return line is also made of transparent Perspex tube. A scale is attached to the outer Perspex tank to measure liquid column height. The pump was placed above the model so that if any gas bubble entrained into DCCP suction line has the similar escape path as in prototype. Initially the model was filled

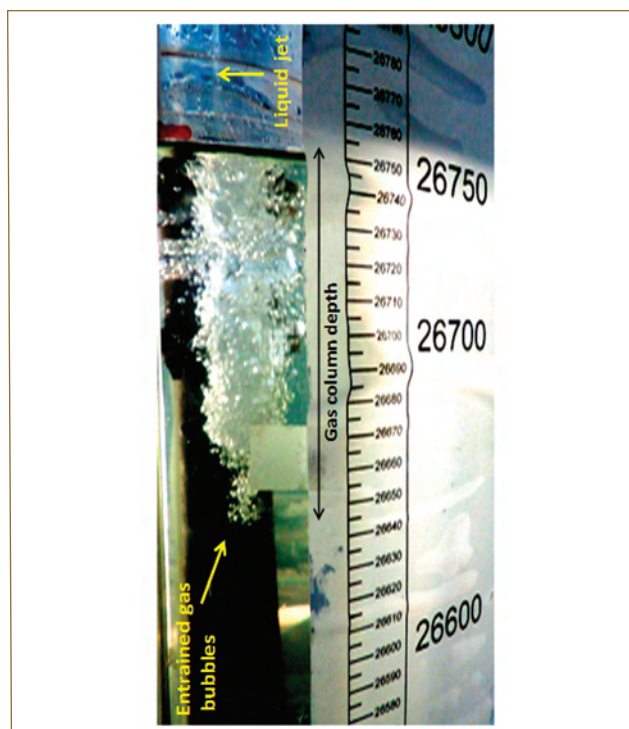


Fig. 1 Photograph showing typical gas bubble formation and subsurface gas column depth

with water up to the nominal level. The nominal flow rate through DCCP duct is set as per velocity similitude which is $3.6 \text{ m}^3/\text{h}$. A rotameter installed at the pump discharge is used to set and monitor the volumetric flow rate of water. Penetration depth of gas bubble and free jet length were measured using a linear optical scale. Measurements were repeated at different water levels. Visual observation revealed that significant amount of gas is trapped inside the selector plug during filling process. These gas bubbles were seen continuously coming out through DCCP suction line during initial operation of the pump (≈ 5 to 10 min.). Intermittent releases of these gas bubbles in smaller quantity through DCCP suction line were seen for a period up to 2 hours. The liquid jet after exiting from the return line interacts with the free surface and forms subsurface gas bubbles. Penetration of these gas bubbles inside the liquid depends on free jet length, jet exit velocity and other hydraulic properties of liquid and gas such as density, surface tension and viscosity. It was visually observed that these subsurface gas bubbles are not getting carried into the DCCP suction line even the free jet length is

more than 1000 mm. The formation of gas bubbles and the subsurface gas column height is shown in Figure 1. In PFBR FFLM, the sampled sodium is sent to sodium capacity by DCCP for detection of fission fragments with the help of delayed neutron detector (DND). Complete filling of sodium capacity and continuity in flow is necessary for proper functioning and getting reliable output from DND. Visual observations confirmed that the sodium capacity is completely filled at the tested flow rate range of 0.15 m³/h to 0.5 m³/h, which covers the nominal flow rate of 0.36 m³/h (100 cc/s). The flow through the sodium capacity tank and the return line is found to be continuous. It is also confirmed from this study that there is no gas entrainment through the exit during liquid flow condition.

The effect of jet exit velocity and the free jet length on the subsurface gas bubble column depth were studied. The jet exit velocity is calculated by dividing the flow rate with nozzle exit area. The jet length and the bubble column depth were measured using the scale fitted with the model. However, the average bubble column depth was approximately determined by analyzing the videographs taken for each case. Maximum uncertainty of ±15 mm is associated with this measurement. The free fall length of the jet was varied by lowering the liquid level in the tank which was done by draining water from the tank. The variation of average gas bubble column depth w.r.t jet length for the nominal flow rate condition (Q = 100 cc/s) is shown in Figure 2. It was observed that, as the jet length increases, more subsurface gas bubbles were formed but the penetration depth of gas bubble column was reduced. This is due to the fact that, at the exit from the nozzle, the liquid jet is of cylindrical

shape but as it falls freely, the jet velocity is increased during free fall. This increased jet velocity along with the action of surface tension makes the jet unstable (Plateau-Rayleigh instability of free jet) and formation of liquid droplets and spreading of jet takes place. When this jet interacts with the free surface, more subsurface bubbles are formed covering more area compared to undisturbed jet. These subsurface bubbles initially move downward due to inertia they gained during formation but started rising up because of buoyancy force. This upward movement of bubble cluster provides a cushioning effect which in turn reduces the bubble column height. The dependency of gas bubble column depth on jet exit velocity was also studied. The jet length was kept as 850 mm corresponding to the fuel handling condition. The variation is plotted in Figure 3. It can be seen from this figure that as the jet exit velocity increases, the depth of the gas bubble column also increases. This is because, the velocity of the jet before impact with free surface increases with increase in exit velocity of the jet. Therefore, the subsurface bubbles are formed with more inertial force, which in turn increases the depth of bubble column.

The experimental measurement cannot be directly transposed to reactor condition because the governing forces influencing the size of subsurface bubbles and its penetration depth can not be accurately simulated using water. However, since, this experiment was carried out in a geometrically similar full scale model with velocity similitude and the hydraulic properties of water and sodium are almost similar, the expected value of gas bubble column in sodium will not differ much from the measured values.

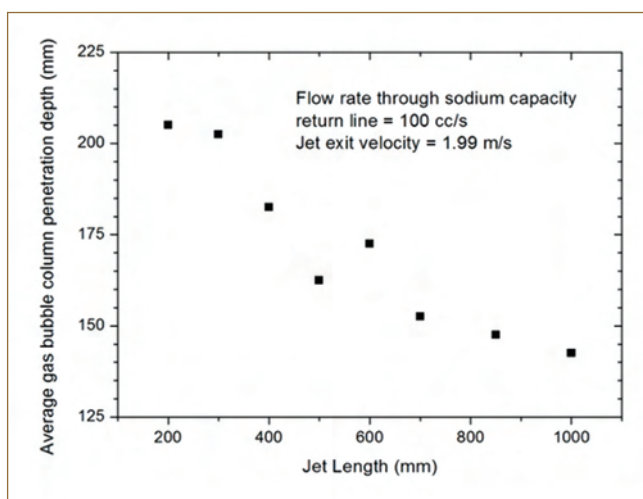


Fig. 2 Dependency of gas bubble column height with free jet length

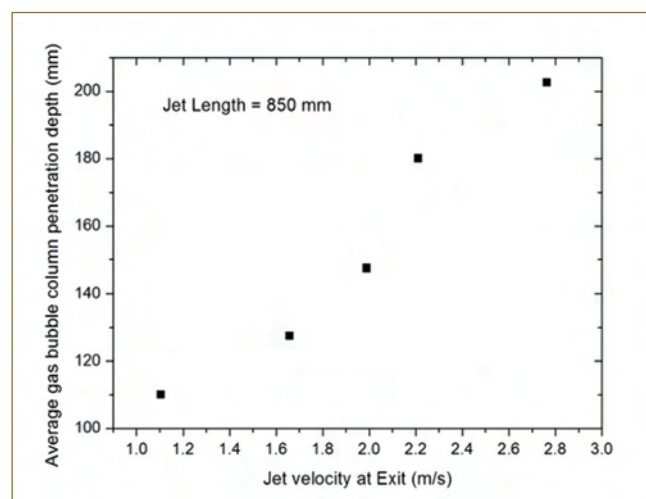


Fig. 3 Variation of gas bubble column height w.r.t Jet exit velocity

VI.14 Microcantilevers for Humidity and Temperature Sensing Applications

Microcantilever (MC) sensors have emerged as a promising technology in the recent past for various sensing applications which include ultrasensitive mass measurements, environmental monitoring, biomolecular sensing and detection of chemical analytes such as explosives. In the present work, uncoated SiO₂ microcantilevers were explored for measuring the Relative Humidity (RH) changes during human breath cycles and Au coated Si MCs for sensitive temperature measurements.

SiO₂ Microcantilevers for human breath monitoring applications

SiO₂ MCs can be effectively used for ultrasensitive and ultrafast RH sensing without any functionalization (i.e. uncoated) because of the presence of the hydroxyl groups on their surface which facilitates water molecule adsorption through hydrogen bonding. When water molecules are adsorbed on MC surface, the effective mass of MC increases and the added mass can be precisely estimated by measuring the resonance frequency shift. In the present work, SiO₂ MCs were explored for monitoring the fast RH changes during human breath cycles. SiO₂ MCs (210 μm × 40 μm × 980 nm) with controlled micropatterns (4 μm × 4 μm × 15 nm) on their surface were fabricated using direct laser writer and wet chemical etching methods by

two-layer lithography process. FESEM image of a typical SiO₂ MC is shown in Figure 1a. It may be noted that the presence of micropatterns on the MC surface may improve the sensitivity of these devices without deteriorating the response and recovery times, which is crucial for breath monitoring applications. Breath monitoring experiments were performed by exposing the MCs to the inhale and exhale breath cycles of a healthy adult male subject and by continuously measuring the shift in the peak amplitude at resonance of these devices using a nano vibration analyzer (Figure 1b). The MCs were placed inside an airtight chamber and were excited using a piezo-actuator. Figure 1c shows a typical sensor response when exposed to normal breathing cycles. From this figure it is evident that the peak amplitude at resonance decreases/increases during exhale/inhale cycle indicating resonance frequency shift in these MCs due to mass loading/unloading. Response and recovery times from this graph are estimated and found to be ~ 1 s which is significantly faster than the commercial capacitive RH sensors (> 30 s).

Ultrasensitive temperature sensing using Au/Si bimaterial microcantilevers

Bimaterial MCs (BMCs), MCs coated with thin metal films (Au or Al) on their surface, are studied in recent times for ultrasensitive temperature measurements owing to

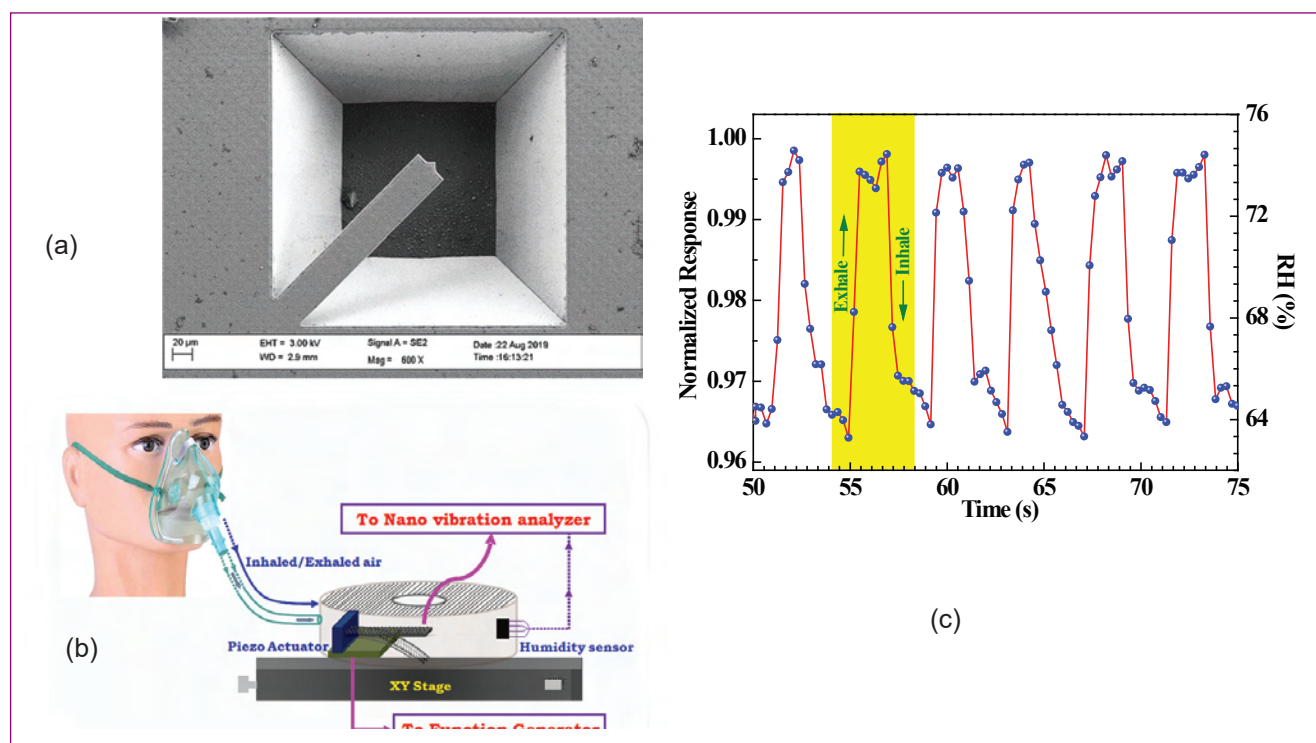


Fig. 1 (a) FESEM image of SiO₂ microcantilever with controlled micropatterns on its surface (b) experimental setup used for human breath monitoring using NVA and (c) SiO₂ microcantilever response during exhale and inhale breath cycles,

their unprecedented sensitivity (of sub-mK) and fast response time (in ms). In the present work, the deflection/temperature sensitivity of BMCs ($450 \times 49 \times 2.5 \mu\text{m}^3$ with 50 nm Au coating) was investigated using an AFM head (Figure 2a), while exposing them to a laser source at their free end. Laser parameters such as wavelength (UV- near IR region), power (0 to 10 mW) and modulating frequency (DC to 2 kHz) were optimized to enhance the sensitivity. Figure 2 b shows a typical photothermal deflection response in Au/Si BMC for a single ON-OFF cycle of UV laser ($\lambda \sim 405 \text{ nm}$, 2 mW) exposure on its Au surface. When the laser is switched ON, MC responds by bending from its equilibrium position to a steady state with a peak deflection and response time of 280 nm and 2.3 ms, respectively. Figure 2c shows the effect of laser wavelength on the deflection sensitivity of these devices (blue dots correspond to experimental data). Peak deflection magnitude was found to decrease with increasing wavelength and is explained on the basis of wavelength dependent absorptivity of the exposed BMC surface and the corresponding temperature rise at the free end of MC. Experimental results were analyzed using two different models based on a) heat transported to heat sink near the MC fixed end: continuous red line considers heat conduction through BMC alone and b) heat loss that includes both conduction through BMC and convection

losses to surrounding air – represented by continuous green line. It is evident that the latter one explains the experimental results better. Corresponding temperature rise at the MC free end was also independently validated through micro-Raman thermometry. Moreover, the MC response as a function of incident laser modulating frequency was also studied. It was found that MC deflection sensitivity remained stable up to a certain cutoff frequency $\sim 320 \text{ Hz}$ (equivalent to $\sim 3.1 \text{ ms}$) and rolls off thereafter. This dynamic response is explained in terms of duration of ON time vs BMC time constant that is basically governed by the rate of diffusion of heat and convection loss mechanisms across the length of the BMC. These experiments revealed that a maximum deflection sensitivity of $\sim 0.13 \text{ pm/nW}$ can be achieved by tuning the laser parameters in Au coated Si MCs. The resultant estimated rise in temperature, due to absorption of incident photons is found to be $\sim 28.5 \text{ K}$ which translates to an equivalent temperature sensitivity of $\sim 109 \mu\text{K/pm}$ with a time response of 2.3 ms. These results are of value for the development of thermal sensors and photothermal deflection spectroscopy applications using BMCs, in the UV-visible region. Applications include understanding the thermodynamic behavior of biological materials, identifying the molecular signatures of chemicals and quantification of explosives such as TNT, RDX.

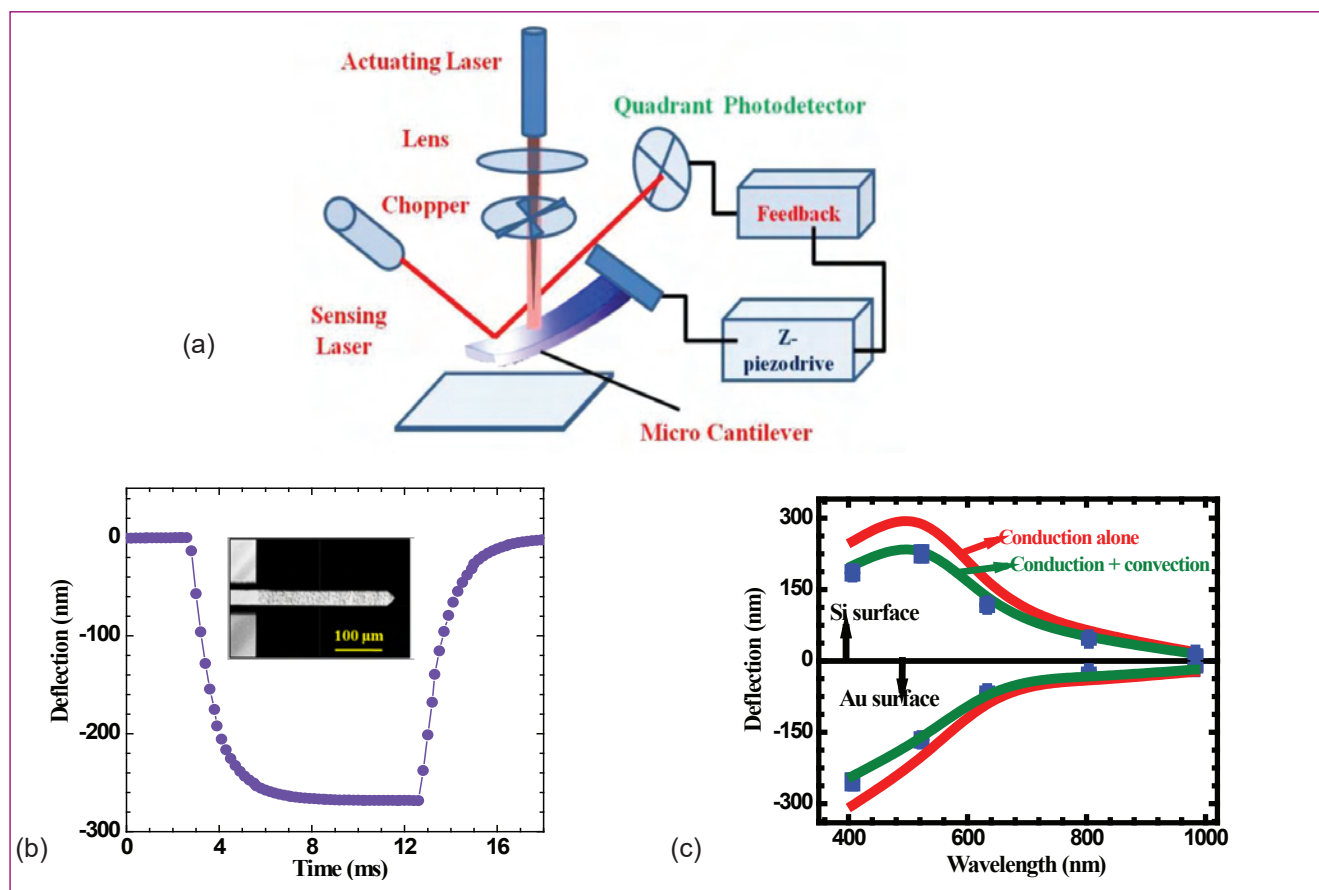


Fig. 2 (a) Experimental setup used for measuring the deflection in BMCs (b) typical deflection response of a BMC when exposed to a UV laser source and (c) effect of laser wavelength on the deflection magnitude of BMCs

VI.15 Indigenous Instrumentation Development for Automated Ion Implantation and Ion Beam Analysis Experiments with Nanometric Resolution

In modern electronic technology, especially in the areas of ultra-large scale integrations, Metal Oxide Semiconductor Field Effect Transistors, there is a constant requirement for handling nanometer sized devices, variety of materials, growth and characterization of ultrathin films ($< 100\text{\AA}$) and film structures. In this context, there have been constant efforts to analyze thin films with sub nm resolution. Achieving such high depth resolution with conventional ion scattering experiments is not possible due to limitations in energy resolution of semiconductor detectors.

High resolution Rutherford backscattering spectroscopy (Hi-RBS) is a proven technique based on medium energy ion scattering (MEIS), for analysis of thin films with a sub nanometer (0.1–0.2 nm) depth resolution. At Materials Science Group, a state of the art Hi-RBS and a molecular beam epitaxial thin film growth system for preparation of ultra-thin films have been installed and commissioned at 30° ultra-high-vacuum beam line of a 1.7 MV tandem accelerator. This augmentation not only complements the ongoing ion beam implantation and ion beam analysis (IBA) activities but also forms an advanced material growth and characterization facility. A block diagram representation of the Hi-RBS system is shown in Figure 1, while Figure 2 shows a photograph of the main scattering chamber of the Hi-RBS with various components. The main components of the Hi-RBS system include a main scattering chamber equipped with a high precision sample manipulator, a Toroidal Electrostatic Analyzer (TEA) or torus for angle resolved detection of backscattered ions, an ion fraction measurement system and a sample loading chamber. The main electronics and instrumentation of the system consists of a) entrance and exit slits, b) the TEA, c) High voltage power supplies ($\pm 25\text{ kV}$, 4.8 mA) for biasing

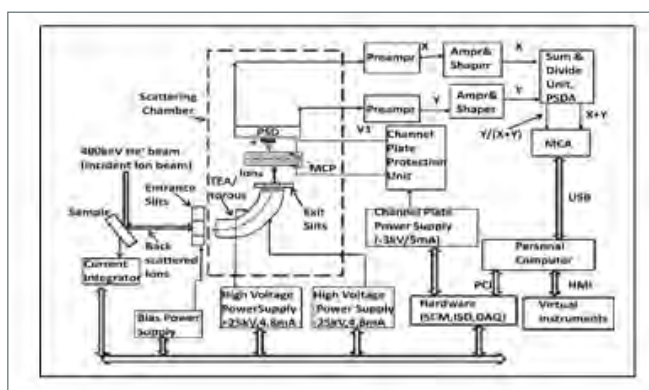


Fig. 1 Block diagram of automated Hi-RBS measurement system

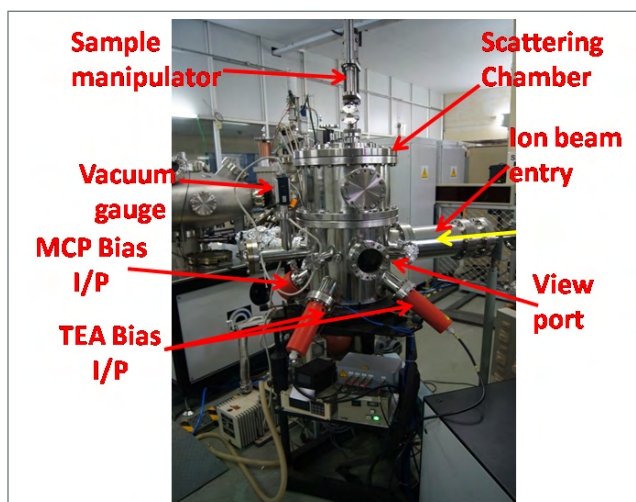


Fig. 2 Photograph of main scattering chamber of Hi-RBS measurement system

TEA electrodes, d) microchannel plate assembly, e) channel plate power supply (0 to -3 kV) and protection unit, f) position sensitive detector (PSD), g) charge sensitive pre-amplifiers, h) amplifiers /shapers, i) sum/divide unit and position sensitive detection analyzer and k) multi-channel analyzer. Manual control and monitoring of ion implantation and analysis experiments involving complex tasks like precise sample positioning, fluence control, various backscattering spectra acquisition without much beam induced effects are not only challenging processes but also tedious and time-consuming. Hence, we have developed and established a personal computer (PC) based indigenous instrumentation for automation of multiple sample ion implantation, standard Rutherford Backscattering spectrometry (RBS), and Hi-RBS experiments. The system uses various signal conditioning circuitry, isolation amplifiers, and transistor drivers along with cost-effective and off-the-shelf commercial components like a general purpose, multifunction data acquisition card. A five axis goniometer is used for handling the automated positioning of multiple samples according to the commands from the PC over RS232 interface. Key tasks carried out in the automation of the system include control and measurement of ion beam fluence, selection of back scattered particles through screening of their energies by controlling a set of $\pm 25\text{ kV}$ and -3 kV high voltage power supplies, controlled collection of backscattered yield using single and multi-channel analyzers, controlling the region-of-interest windows in the energy spectra and the cumulative counts in them. Controlling the position of samples and

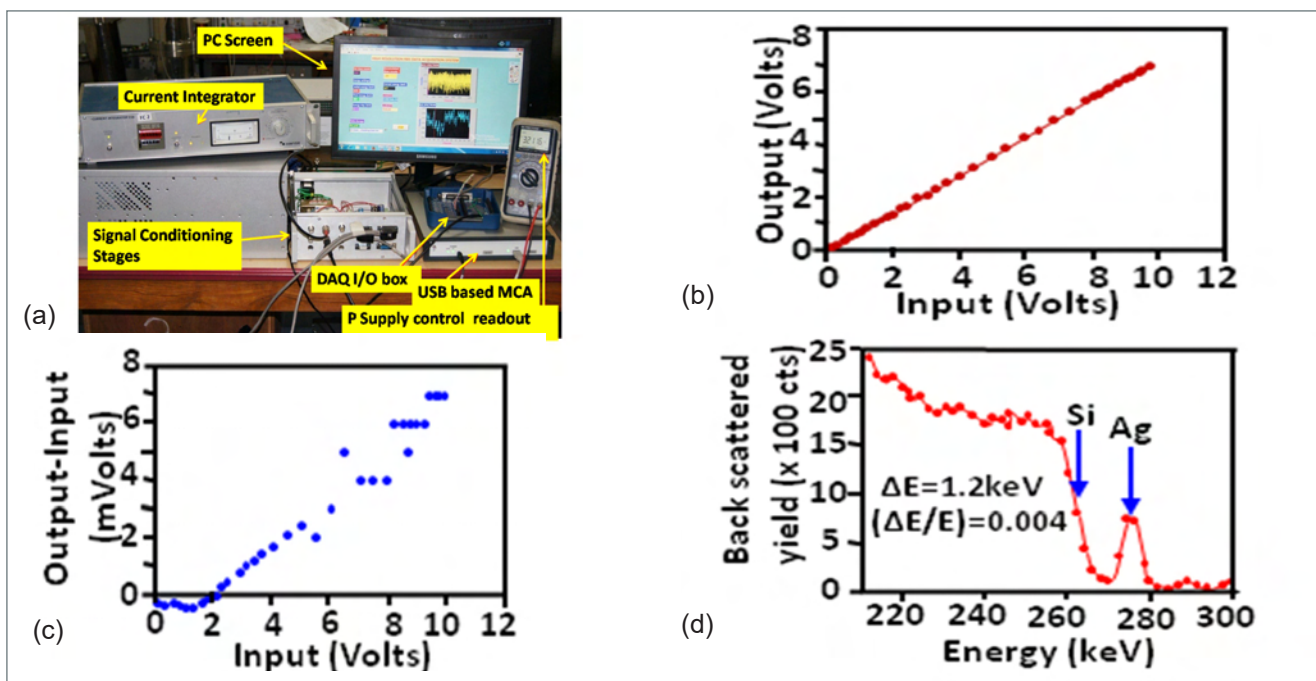


Fig. 3 (a) Lab testing of the set up (b) linearity tests of signal conditioning and isolation amplifier stages (c) difference between the output and input as a function of input (d) Hi-RBS from a 3 nm thick Ag film taken with 300 kV H^+ ion beam

facilitating experiments on multiple samples, online display of energy spectra and their storage, and vacuum interlocking are also automatically done. Developed using windows based LabVIEW, the versatile and user-friendly virtual instrument based automation software provides a slew of advantages like easy portability to different computer platforms, short development time, easy reconfiguration to meet changes in experimental demands or hardware, amenability to add other ion beam analysis experiments, increased experimental throughput and least human intervention. Several tests were carried out for checking the performance of various hardware and software modules. Tests on V_{con} , the control inputs to the ± 25 kV and -3 kV high voltage power supplies, showed very good characteristics of the control signals with $<0.1\%$ accuracy, $<0.05\%$ linearity, very low drift of 50 ppm, 0.01% precision, and <1 mV rms output noise. The results of linearity tests of the signal conditioning circuit and the isolation amplifier are shown in figure 3. Testing the dose counter over a time period varying from 10's of seconds (corresponding to fluence conditions of $\sim 10^{10}$ ions/cm²) to many hours ($\sim 10^{17}$ ions/cm²) revealed an excellent matching within 0.1% between the fluence computed from the accumulated charge counts and the actual fluence. The vacuum interlocking scheme was tested by feeding 1–9 V DC externally, setting a vacuum threshold covering a range of 10^{-5} mbar to 10^{-9} mbar, and testing the status of high voltage enable signals and the output voltages of the ± 25 kV and -3 kV high voltage power supplies. Various other functions like the multi-channel analyser control, computing the region-of-interest counts, on-line display

of energy spectra, region-of-interest counts versus TEA bias voltage and their auto storage were independently tested. Integrated tests carried out to verify the automatic conduct of ion implantation, standard RBS and Hi-RBS experiments established the satisfactory lab performance of the automated setup. The system was successfully integrated in the 30° beam line and implantation beam line of the 1.7 MV Tandatron accelerator. The field performance of the system was observed with many trial experiments with H^+ and He^+ ion beams in the energy range of 1–2 MeV. A set of Si samples was irradiated with different ion beams and different fluences. A close agreement of $<3\%$ between the fluence obtained from the standard RBS analysis and the fluence recorded by the automated system was observed. Hi-RBS was carried on a 3 nm thick Ag film grown on Si substrate using 0.3 MeV H^+ ion beam. The recorded HiRBS spectrum in the energy range of 200–300 keV shows well separated Si edge and Ag peaks. From the experimental data, the energy resolution and relative energy resolution ($\Delta E/E$) of 1.2 keV and $\sim 0.4\%$ respectively were obtained. The automation has drastically reduced both experimental time (from many hours to tens of minutes) and the efforts required for completion of a single experiment. Almost all the functions that were previously done manually are being now done automatically with very good precision and reliability at the click of virtual buttons. Thus the automation has had a huge impact on our work load, improved efficiency and provided a better performance in experiments involving both single sample and sample batches. It can be extended to integrate other IBA experiments.

VI.16 An in-house Developed Auto Titrator Unit using Pulsating Sensors for Analytical Applications

An automatic titrator unit is successfully developed to cater to the needs of laboratories where a large number of samples are analyzed through titration. Figure 1 shows the photograph of the PC based titration set up. The unit is completely in-house developed and consists of a low volume dispensing syringe pump, an actuator assembly, stirrer and associated electronic measurement system. The operation of the system is carried out through an HMI software for data acquisition, configuration of parameters and control of titrations using a personal computer. The titrator can dispense the titrant in steps as low as one μL in a highly reproducible manner. pH, conductometric and thermometric titrations can be carried out using this compact unit. One of the unique features of this titration set up is that, the signal generated from the probe is directly in digital domain in the form of rectangular pulses of 5V amplitude. Counting these pulses for a fixed duration gives the frequency. Giving birth to the signal directly in digital domain avoids pre-amplification, signal conditioning and analog to digital conversion that are normally encountered in commercial instruments. During titration, information on the parameter being monitored inside the reaction vessel is extracted by using a pre-established mathematical relationship between frequency and pH/conductivity/temperature and the same is plotted as a function of volume dispensed from the titrator. It takes a couple of minutes for each analysis and the entire

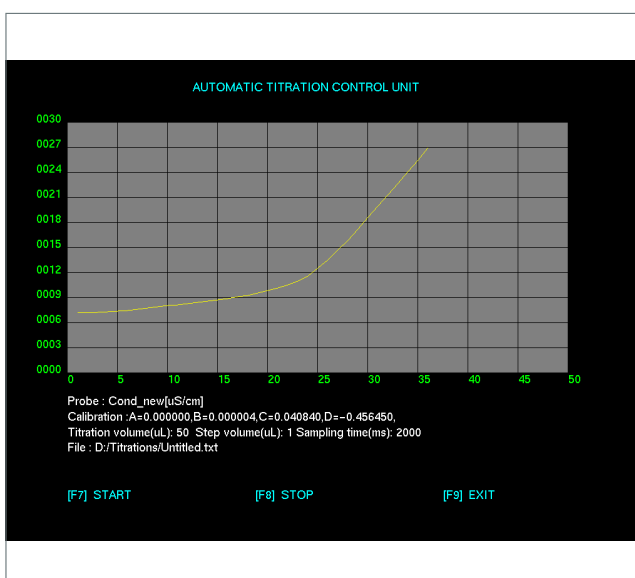


Fig. 2 0.1N NaHCO_3 titrated against 0.1N HCl in 1 μL steps

titration is carried out under the control of software. Figure 2 shows a typical titration plot generated using the autotitrator unit. By deploying this unit, errors associated with manual addition of titrant and user fatigue will be completely eliminated. Finally, the unit will find application in the quality control laboratory of MAPS for the assay of boron in heavy water and in laboratories dealing with the chemical characterization of aerosols generated by sodium fire.

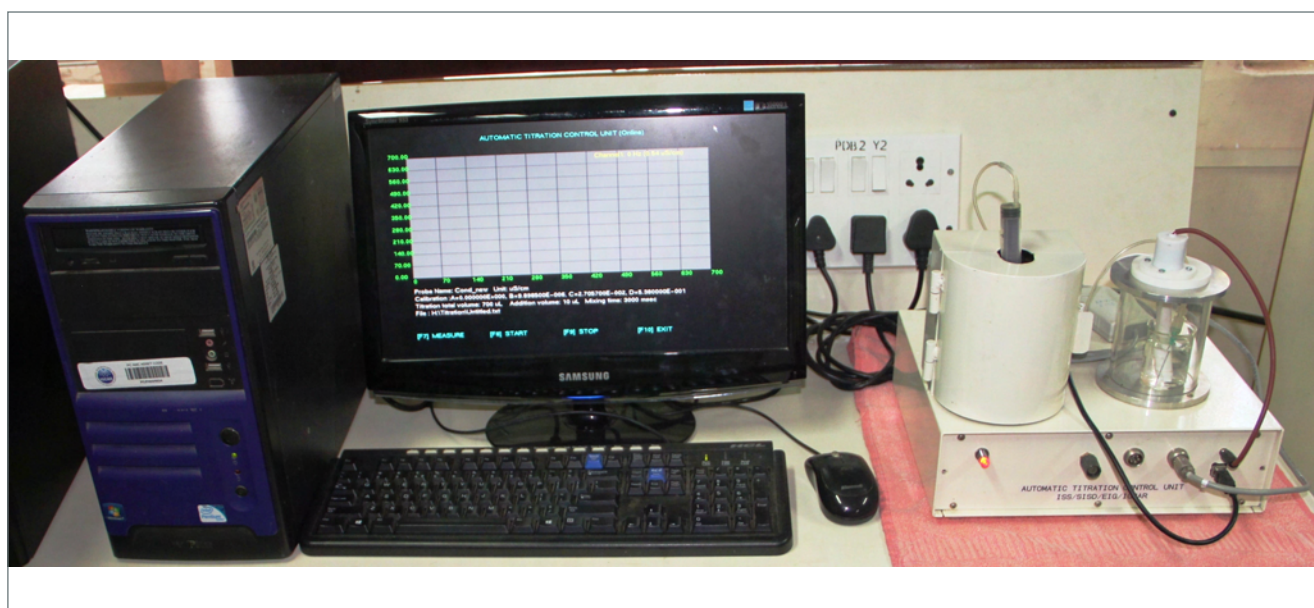


Fig. 1 Photograph of the automatic titrator set up

VI.17 Thermophysical and Thermochemical Properties of U-23wt.%Pu-6wt.%Zr Alloy Fuel: Computational and High Temperature Mass Spectrometric Studies

Vaporisation studies were carried out over the liquid region of U-23wt.%Pu-6wt.%Zr ($U_{0.65}Pu_{0.21}Zr_{0.14}$) alloy, (proposed fuel for future fast reactor) in the temperature range 1487-1641 K using Knudsen Effusion Mass Spectrometer (KEMS) housed inside an argon atmosphere glove box (negative pressure). KEMS (Figure 1), developed in-house is equipped with quadrupole triple filter analyser and Secondary Electron Multiplier (SEM) operating in pulse ion counting mode (M/s Hiden Analytical, UK). The molecular beam emanating out of the Knudsen cell orifice was ionised by electrons with an energy of 28.8 eV and at an emission current of 200 μ A. Pu(g) was found to be the species observed in vapour phase over this alloy. Measurements on temperature dependence of partial pressures of Pu(g) yielded the pressure-temperature (p-T) relation: $\log(p_{Pu(g)}/Pa) = (-20336 \pm 208)/T + (10.08 \pm 0.13)$. The combined second law plot of $\log(p_{Pu}/Pa)$ vs $1/T$ (K^{-1}) of Pu(g) over U-23wt%Pu-6wt%Zr alloy is shown in Figure 2. Subsequently, the apparent enthalpy of vaporisation of Pu(g) at 1564 K was deduced by second law method. Vaporisation studies on this alloy have been carried out for the first time. Also, fractions of various phases present

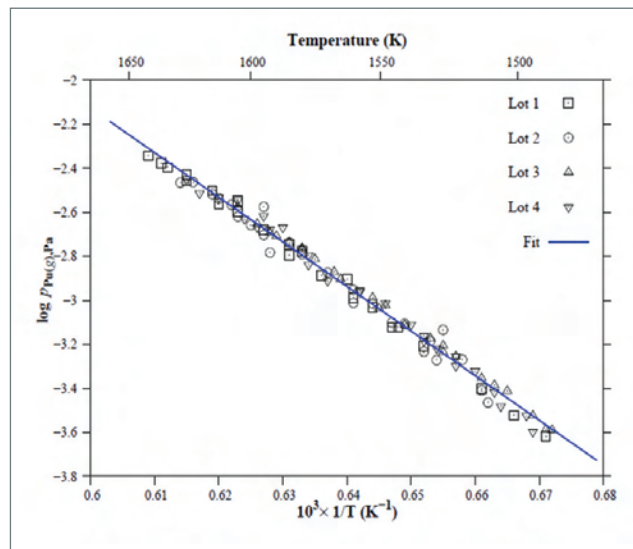


Fig. 2 Combined second law plot of $\log(p_{Pu}/Pa)$ vs $1/T$ (K^{-1}) of Pu(g) over U-23wt%Pu-6wt%Zr alloy

in U-19Pu-6Zr and U-23Pu-6Zr fuel compositions were calculated and a comparison was made between the phase fractions and overall thermal conductivity.

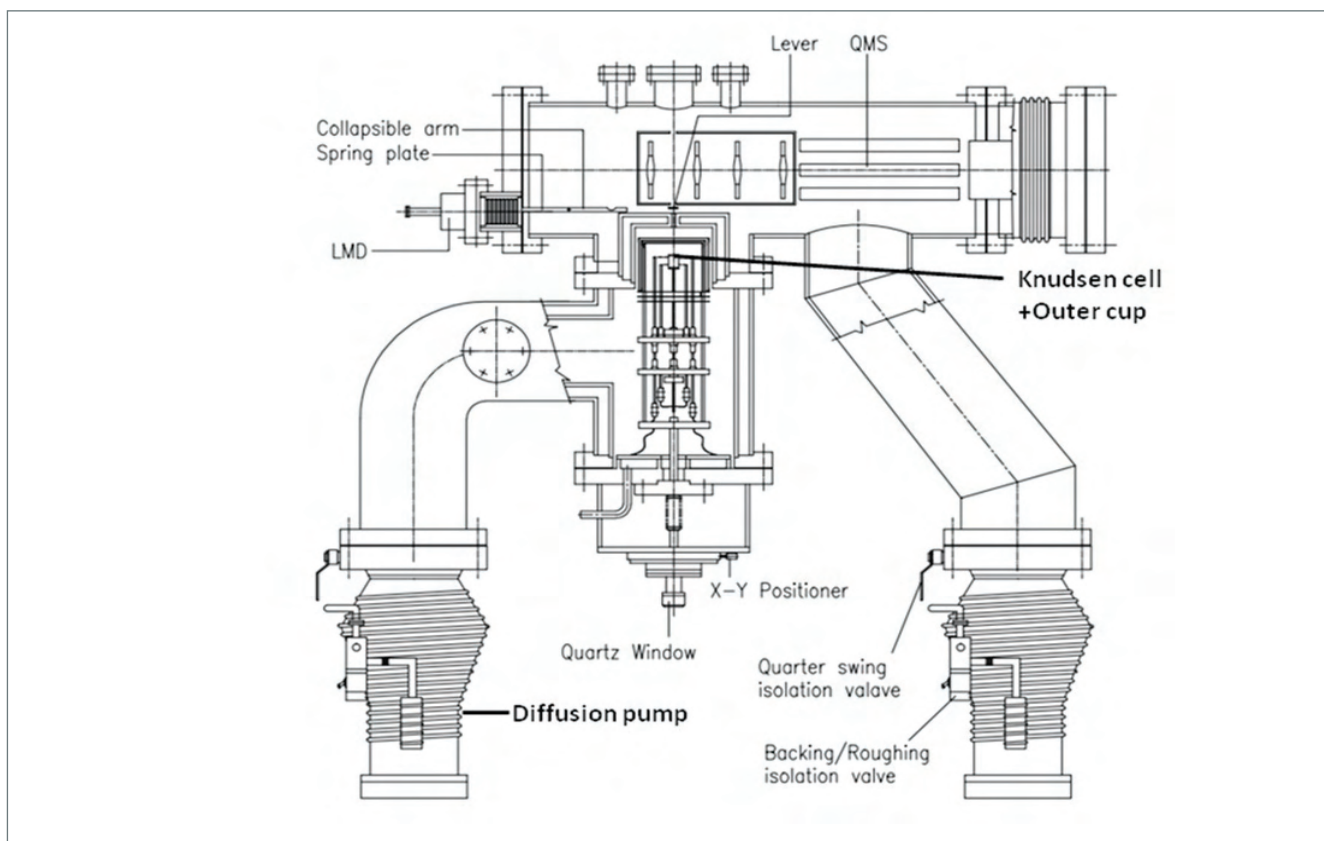


Fig. 1 Schematic of High Temperature Mass Spectrometer housed inside the glove box

Table 1: Comparison of activity of Pu(Pu,liq.) over U-23Pu-6Zr & U-19Pu-6Zr alloys calculated using data of pure liquid Pu with those obtained from database of Kurata & Leibowitz et al.

T (K)	U-23Pu-6Zr $a_{(Pu)}$	$a_{(Pu, liq)}$ in U-23Pu-6Zr calculated from partial pressures of Pu(g) by KEMS(present study) and literature data of pure Pu								
	From Leibowitz	Calculated from Kurata	Maeda et al.	Alcock et al.	Phipps et al.	Mulford	Kent	Ackermann & Rauh	Bradbury & Ohse	Kim & Hofman
1500	0.204	0.121	0.017	0.090	0.017	0.016	0.018	0.022	0.015	0.033
1550	0.204	0.122	0.020	0.108	0.019	0.019	0.021	0.026	0.017	0.039
1600	0.204	0.123	0.023	0.129	0.022	0.022	0.024	0.030	0.020	0.045
1650	0.204	0.124	0.026	0.151	0.025	0.025	0.028	0.034	0.023	0.051
T (K)	U-19Pu-6Zr $a_{(Pu)}$	$a_{(Pu, liq)}$ in U-19Pu-6Zr calculated from partial pressures of Pu(g) by KEMS and literature data of pure Pu								
	From Leibowitz	Calculated from Kurata	Maeda et al.	Alcock et al.	Phipps et al.	Mulford	Kent	Ackermann & Rauh	Bradbury & Ohse	Kim & Hofman
1500	0.156	0.099	0.004	0.019	0.003	0.003	0.004	0.005	0.003	0.007
1550	0.156	0.097	0.004	0.024	0.004	0.004	0.005	0.006	0.004	0.009
1600	0.157	0.097	0.006	0.031	0.005	0.005	0.006	0.007	0.005	0.011
1650	0.157	0.098	0.007	0.040	0.006	0.006	0.007	0.009	0.006	0.013

The activities of plutonium, $a_{(Pu,liq.)}$, over U-19Pu-6Zr and U-23Pu-6Zr alloys were computed in the temperature range 1450-1800 K using CALPHAD method. The required input data for this was obtained using the Reaction module of FactSage 6.4 package, and the Gibbs energy functions of U-Pu-Zr system obtained from CALPHAD modelling by Kurata. The data obtained for selected temperatures are given in Table 1. We also computed activity coefficient of plutonium (γ_{Pu}) using the following expression (eqn-1) given by Leibowitz et al.

$$RT \ln(\gamma_{Pu}) = \frac{-3800 X_U^2 X_{Zr}}{(1-X_{Pu})} \quad \text{----1}$$

Where X-represents the atom fraction of the corresponding element. From γ_{Pu} , activity of Pu over U-23Pu-6Zr was computed and these data are also given in Table 1. As can be seen from the table, the a_{Pu} & γ_{Pu} computed from Leibowitz data are higher than the

experimental data by a factor of 2 at mean experimental temperature of the present investigation (1564 K).

The activity data of Pu over the U-19Pu-6Zr & U-23Pu-6Zr alloys were derived from KEMS by using p_{Pu} reported over the pure plutonium and these data are also given in Table 1. These values indicate a negative deviation from ideality. As can be seen from Table 1, $a_{(Pu,liq.)}$ computed using CALPHAD method for 19Pu and 23Pu alloys are in reasonable agreement with KEMS data deduced using the data of Alcock et al. but not so in other cases. Activity data calculated using Leibowitz et al. for both the alloy compositions show relatively less negative deviation compared to the data obtained through CALPHAD and KEMS experiments. The a_{Pu} over the two alloy compositions, computed, using the $p(Pu)$ obtained by KEMS and $p(Pu)$ data over pure plutonium available in the literature, showed a good internal consistency for each of the alloy compositions.

VI.18 A Feasibility Study to Measure Magnetocardiogram in Unshielded Environment

Measurement of cardiac magnetic fields offers unique diagnostic information which is complementary to that obtained using conventional electrocardiography (ECG). Deployment of Magnetocardiogram (MCG) in demanding applications in clinically relevant problems is well recognized by cardiologists. Superconducting quantum interference devices (SQUIDs) operating at a working temperature of 4.2 K inside a magnetically shielded room (MSR) are used to record MCG with a clinically acceptable signal-to-noise ratio. However, development of a cost effective MCG system is essential for its wide-spread adoption. Reports on such ventures are popular for their suggestions on dispensing with the need for an expensive MSR to reduce magnetic noise present in the environment.

A feasibility study was conducted at the bio magnetic measurement facility at IGCAR to explore the possibility of recording MCG in an open environment. This pilot study was aimed to address all possible pre-requisites for setting up an unshielded MCG system which included a site survey, recording and processing of signals, qualitative and quantitative comparison and evaluation of signals measured against those measured inside MSR. The fact that cardiac signals are relatively high in magnitude with well recognizable features and their time occurrence could be inferred from a simultaneously recorded ECG were conducive for this attempt for unshielded MCG.

A location within the premises of the laboratory area was identified to have a relatively low average electromagnetic noise (~ 60 nT) using a three-axis flux gate sensor. A flat-bottomed liquid helium cryostat containing four SQUID sensors was used for the measurements. The measurements were performed on eight healthy subjects and each subject was positioned under the tail of the cryostat in supine posture for sequential scanning to be performed over the thorax on thirty-six designated measurement locations. A single channel ECG configured in lead 1 position was simultaneously recorded along with MCG. Superconducting gradiometers consisting of two loops wound in opposition are used to selectively couple cardiac signals to SQUID sensor while cancelling distant noise. Electromagnetic noise due to power line frequencies was of the order of $1 \text{ nT}_{\text{rms}}/\sqrt{\text{Hz}}$ and it dominated the noise spectrum in the chosen site, whereas the white noise measured was $1 \text{ pT}_{\text{rms}}/\sqrt{\text{Hz}}$. Conventionally, MCG systems consisting of higher order

gradiometers with more than two loops are preferred to attenuate background noise in unshielded environments. However, such gradiometric configurations are known to be efficient in noise reduction at the cost of attenuating the MCG signals especially from deep signal sources. A notable difference between earlier reports and the current work was the use of first order gradiometers coupled to SQUIDs. In addition, the present study a signal de-noising method namely, ensemble empirical mode decomposition (EEMD) technique was used to manage excess extraneous noise in the unshielded site.

Figure 1 shows the as recorded MCG which is totally noisy. On the other hand, the ECG shows readable cardiac cycles. The time instants of the R wave peaks of ECG were used as cues to epoch the noisy MCG time series and they were averaged to generate a single trace representative of the whole time series as shown in the figure. The same procedure was followed to record thirty-six traces from each scanning position. The signal averaged MCG traces still contained other high frequency wiggles which were then de-noised by thresholding the noisy components present in the intrinsic mode functions obtained from EEMD decomposition. Discernible cardiac features such as the P, QRS and T waves are seen in EEMD de-noised MCG trace (Figure 1). MCG measured on the same location for the same subject inside MSR is also shown for comparison. Magnetic field maps generated from the signal averaged unshielded MCG traces of all the measurement locations of a subject and their shielded counterparts are also shown to highlight the consistency of the cardiac source information obtained in both cases. Computation of field map angle and current dipole angle are indicated. These results imply that the information obtained in shielded and unshielded cases are same and there was no compromise in the information content. However, this demonstration also hints that averaging of many beats alone could make MCG conspicuous and the scheme is inadequate for investigations in which beat-by-beat dynamics in electrophysiology is expected to occur such as in conduction anomalies. It is well known that the averaging process could destroy the beat-to-beat information. Ample scope exists to improve signal extraction using hardware and software methods and these results encourage the possible use of MCG in practical work environments in a hospital set-up or in sites where the background noise is relatively low.

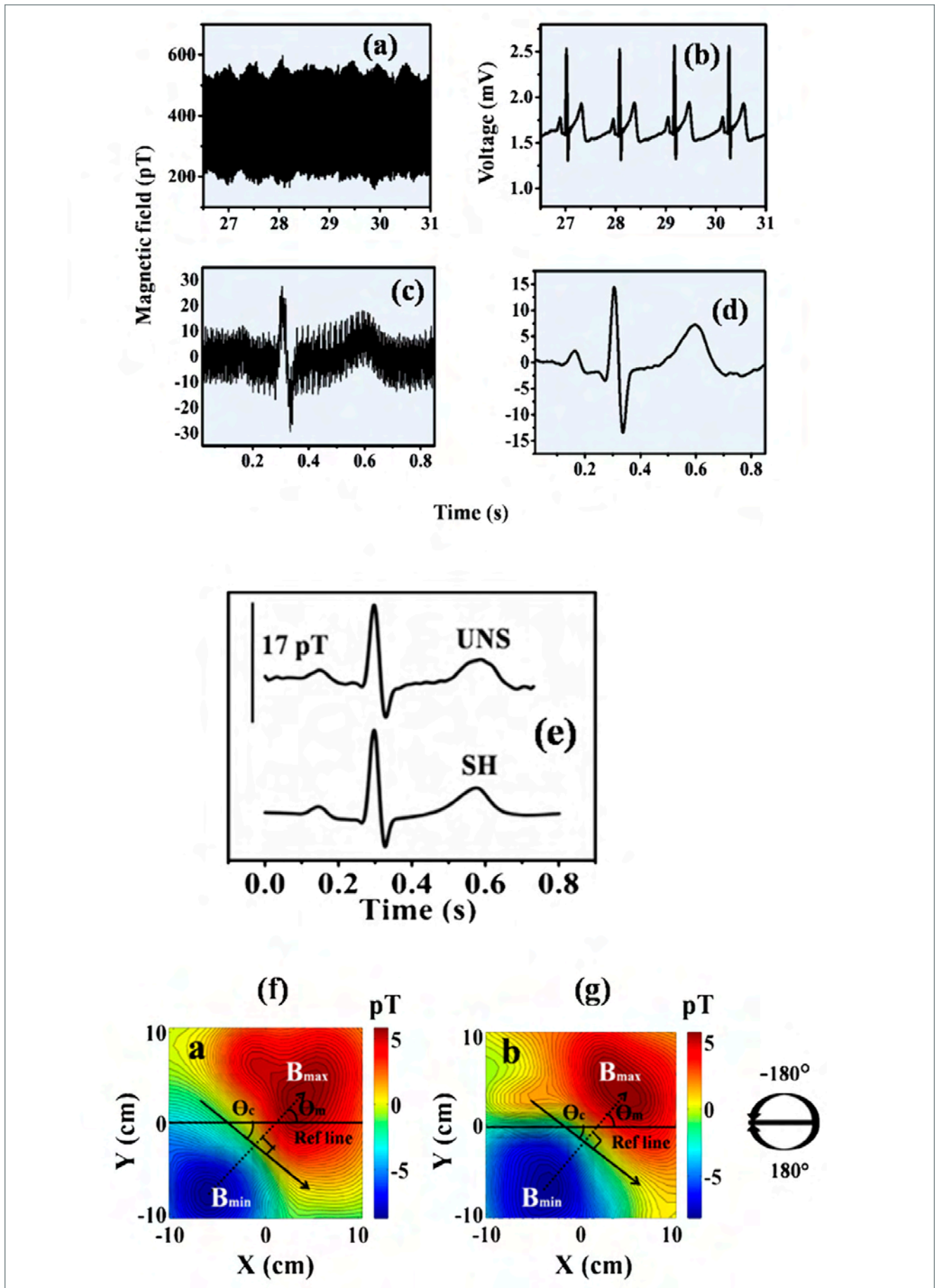
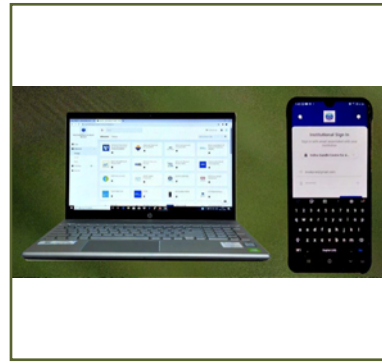


Fig. 1 (a) Raw MCG in an unshielded site; (b) simultaneously recorded ECG time series; (c) signal averaged MCG time series in (a) by inferring R peak instants in (b); (d) EEMD de-noised MCG trace; (e) comparison of the processed MCG trace in shielded (SH) and unshielded (UNS) locations; (f) and (g) magnetic field maps generated from averaged MCG traces from all thirty-six locations exhibiting computation of quantitative parameters such as field map angle and dipole angle respectively



Infrastructure, Resource Management & Biodiversity

CHAPTER VII

VII.1 Manufacture of Large Size Test Vessels for Sodium Technology Complex

Sodium Technology Complex (STC) is an upcoming advance test facility at IGCAR for testing and qualification of large size (full scale) fast breeder reactor components such as reactor shutdown systems and fuel handling machines before installation and commissioning in the fast breeder nuclear reactors. Two large size Sodium Test Vessels (STVs) which are major components of the advanced test facility have been manufactured conforming to ASME Section VIII, Division-1 code. STV-1 has an ID of 1.5m and overall height of 14 m. STV-2 has an ID of 1 m & height of 14 m. The primary material of construction for STV-1 & 2 is austenitic stainless steel of grade 316 LN plate having thickness 12mm and 8mm respectively (Figures 1 and 2).

STVs are vertical cylindrical vessels with a tori-spherical dished end at the bottom end and flange assembly at the top. Nozzles are provided on various parts of each STV to facilitate the flow path and process requirements. Reinforcement pads are also provided to higher size nozzles to bring down the local stress level. The manufacturing of STVs was a challenging task due to the need of precision machining of ring flanges having O-ring grooves for leak-proof sealing, cover flanges with stringent dimensional & geometrical tolerances besides more extended welding requirements [61 m of 2-2T radiography quality butt welds & 263 m of fillet welds]. Welding procedure qualification was established for the automated TIG welding process using column and boom type welding machine and same machine was utilized for production to minimize the fabrication time for longitudinal & circumferential seam welding of cylindrical shells.



Fig. 1 Sodium Test Vessel -1



Fig. 2 Sodium Test Vessel -2

In this endeavour, a unique automated gas purging system was developed and used, which resulted in the reduction of defects and welding costs as well.

These test vessels require high levels of quality in all stages of material selection, manufacturing, inspection & testing. The quality requirements also include achieving stringent geometrical tolerances. Due to poor thermal conductivity and higher coefficient of linear expansion of the base materials, weld distortion is inevitable. Hence, planning, sequencing and execution of fabrication activities, including cutting, forming, welding and use of appropriate fixtures to minimize weld distortion and to achieve specified geometrical tolerances were challenging tasks.

To ensure very high quality of the test vessels, a quality assurance plan was prepared and followed. Inspection of all the vessels were carried out jointly by CWD and a third party agency QAD, IGCAR at all stages of manufacture including welding procedure qualification, performance qualification, material inspection, stage & final inspections.

Integrity testing was carried out using compressed air medium at 3.25 bar (g) and 2.5 bar(g) pneumatic pressure for STV-1 & STV-2 respectively. Both the vessels are subjected to helium leak testing under vacuum and allowable global leak rate is less than 1×10^{-9} Pa m³ /s. Both the test vessels passed the qualification test and subsequently surface treatments such as pickling and passivation were carried out. The manufactured and leak tested vessels were filled with 0.1 bar nitrogen gas, and dispatched to Sodium Technology Complex.

VII.2 Transfer and Transportation of Sodium from Heavy Water Plant, Baroda

Heavy Water Plant (HWP), Baroda has installed, commissioned and operated a 2 kA electrolytic sodium cell to manufacture sodium. Sodium manufactured was stored in carbon steel storage tanks after initial purification. It was decided mutually by HWB and IGCAR to transfer 3 tonnes of sodium metal to IGCAR for R&D activities. Clearance was obtained for safe transfer and transportation of sodium to IGCAR from Sodium Safety Panel of IGCAR. A transportation tank of suitable size was identified for transporting the sodium from Baroda. This is a horizontal cylindrical stainless steel tank with tori-spherical dished ends and saddle support. The tank is provided with surface heaters, thermocouples, leak detectors and insulation with cladding and electrical panel as well as instrumentation chassis. The tank is also provided with level probes for indicating middle and high levels corresponding to sodium hold up of 1.75 m³ and 3.5 m³ respectively. Sodium hold up of tank is 3.5 m³ at 150°C. A suitable departmental truck necessary for transporting the sodium tank was arranged. A carbon steel support structure was designed, manufactured and tack welded to the truck body for mounting the sodium transportation tank. Over this support structure, the tank was rigidly bolted to ensure safe transportation of the sodium tank. In addition to base support, the tank was also rigidly supported on the truck body by using ropes between the hooks in tank and truck body. The empty tank was transported to HWP, Baroda by road.

The transfer operation of sodium metal from storage tank to transportation tank was carried out in a closed shed area at HWP, Baroda. Sodium storage tank and sodium transportation tank were positioned on floor level inside the shed for carrying out the sodium transfer operation.



Fig. 1 Transportation tank with frozen sodium on receipt



Fig. 2 Unloading of transportation tank

The sodium transfer line connecting the storage tank and transportation tank was erected with a bellows sealed, micro filter in between. Surface heaters, thermocouples and thermal insulation were provided to transfer pipe line to enable preheating to 150°C. The temperature of storage tank and transportation tank was maintained at 120°C and 150°C respectively. Sodium in the storage tank was transferred to the transportation tank.

Once the sodium transportation tank was filled with sodium, same truck was sent to HWP Baroda for transporting the sodium tank back to Kalpakkam. At HWP, Baroda, the sodium transfer tank with frozen sodium was positioned on truck body and bolted. The tank was rigidly supported on the truck body by using ropes. Argon pressure of 0.5 kg/cm² (g) was maintained in the tank and the cover gas header was isolated. The tank was covered with two layers of tarpaulin sheets. Figure 1 shows the tank with sodium after removing tarpaulin sheets. Sufficient DCP fire extinguishers were kept on the truck for use in emergency. During transportation, based on statutory rules for transportation of sodium metal on road in India, requirements like predominant display of name plate with chemical name and classification, training of truck drivers with respect to chemical/fire safety, availability of transport emergency cards, were ensured. The cover gas pressure was periodically monitored during transportation and found to be maintained at 0.5 kg/cm² {g}. The tank with sodium was unloaded at Engineering Hall-III, IGCAR. Figure 2 shows unloading of sodium transportation tank from the truck at Engineering Hall-III.

VII.03 Design and Development of Advanced Base Station Module with Fault Tolerant Architecture

Wireless Sensor Network consists of multiple sensor nodes, router nodes and a central data receiver. Sensor nodes are installed for acquiring data from sensors. Router nodes relay/ forward the acquired data towards the central data receiver, called the Base Station (BS). It is a single interface point to the plant data network. In nuclear applications where high data availability is essential, the failure of BS will have severe impact on the plant operations. To achieve high availability, it is decided to introduce fault tolerance to the BS. It has been designed following dual redundant architecture by introducing two numbers of BS cards. The Redundancy Management and Control Device (RMCD) will manage them to work in sync with each other. Prototype Advanced BS is shown in Figure 1.

BS cards have been programmed to receive data from RF transceiver and forward it to the server program running in the PC via ethernet. BS cards relay health status of its RF transceiver, ethernet connectivity etc. to RMCD and controls the RF operation of transceiver based on the signals from RMCD.

For experimental purpose, WSN nodes in Large Scale Test Bed setup(LSTB), located in WSN Lab, IGCAR, have been configured to transmit data every one second once. Application software has been developed to receive data from the BS. As part of testing, one BS card has been failed intentionally; it was observed that RMCD took 150 microseconds approximately to indicate the failure of BS card to another working card. In this configuration, RF transceiver in the standby card needs

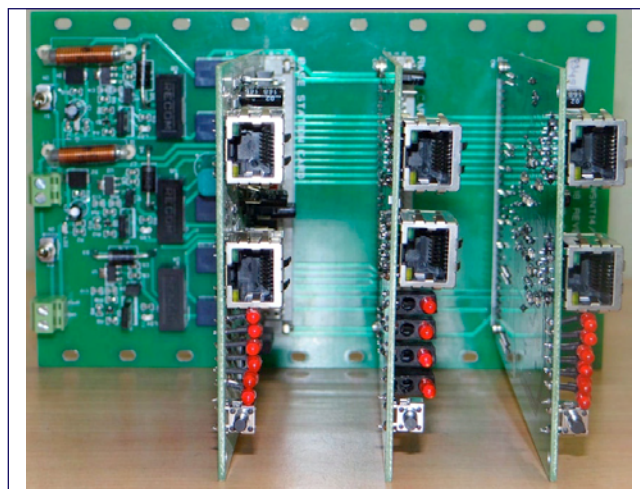


Fig. 1 Advanced base station setup

to be energized before entering to listen mode. Activation time for RF transceiver found to be sufficiently large to result in packet loss.

Hence to reduce the activation time, the RMCD has been programmed to control the BS cards in hot-standby mode. Upon failure of one BS card, it indicates to another card; which then broadcasts a message in the network thereby reducing the loss of packets during the transition(Figure 2).

Experiments are being conducted to study the performance by analyzing the network parameters such as packet drop, throughput and packet switchover time in application layer under various network conditions with varying number of nodes. The results will be useful in network architecture design for indoor WSN with node density of 100 – 200 nodes.

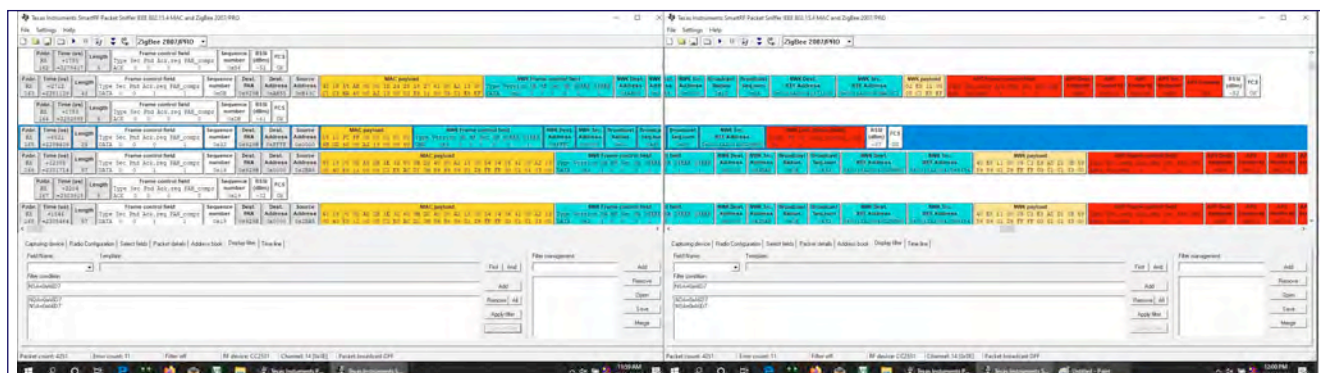


Fig. 2 Sniffed data packets

VII.04 Development and Implementation of Indigenous Video Conferencing (VC) Solution - IGCAR Vi-Meet

Across the world, COVID-19 pandemic related lockdowns and travel restrictions provided an impetus to depend more on online solutions to conduct meetings, share documents, carry out collaborative works, etc. In this context, considering the confidentiality and sensitivity of the data handled by IGCAR and other units of DAE, Computer Division decided to develop in-house solutions to support unhindered functioning of various departmental activities. IGCAR Vi-Meet is one such solution developed to conduct online meetings securely.

IGCAR Vi-Meet is a clientless VC system developed using open-source tools and packages with on-premises infrastructure. It is independent of any third-party server/licensing. It consists of a server-class machine with a hardened Linux operating system. It listens on TCP port 443 (HTTPS) and can communicate with authenticated users through UDP port 10000, and the entire traffic is fully encrypted. The VC system is constituted by the following modules – Scheduler, Authenticator, Signalling server, Selective Forwarding Unit (SFU) or Video relay and Turn server. The entire system and its modules have been hardened, and security audited to confirm that they are free from vulnerabilities. A network firewall also protects it.

Scheduler: The scheduler module is developed using Python, Shell script and MySQL DB. It is used to schedule the meetings, generate meeting IDs, hosting IDs and random passwords, and control the validity of the meetings as per the schedules.

Authenticator: The authenticator module consists of a web portal developed using PHP and javascript. It acts as the front-end where the users will provide the meeting ID, password and user details for authentication. After successful authentication, users are redirected to the virtual meeting room. The module also monitors the connection between the user and the server, and kills the session when the connection is lost.



Fig. 1 A presentation with presenter’s video as PIP



Fig. 2 A press meet through IGCAR Vi-Meet

Signalling server: This module is constituted by an open-source XMPP server and conference focus server. It is responsible for starting a virtual meeting and connecting the participants to it. It has been configured in such a way that the virtual meeting can be started only by a moderator after authenticating using the hosting ID and password.

Video relay: The SFU or Video relay module is an open-source service that routes media traffic between the meeting participants. It uses UDP port 10000 for communication.

Turn server: When a participant is located behind a firewall, UDP port 10000 will not be accessible. In such cases, to enable the communication between the participant and the Video relay, an open-source Turn server has been configured. It listens on TCP port 443 (HTTPS) for the media traffic and forwards it to the Video relay.

The client-server communication in IGCAR Vi-Meet is based on WebRTC protocol. Since it is well implemented in latest Chromium-based browsers such as Google Chrome, latest Microsoft Edge, etc., they can act as the client to the IGCAR Vi-Meet VC system, even if the participant is connecting from a smartphone. Wherever necessary, an open-source mobile app is also provided to join the meetings.

IGCAR Vi-Meet VC system also supports features like desktop or presentation sharing with presenter’s video as PIP, displaying meeting banners and server-side recording facility (Figure 1). IGCAR Vi-Meet is widely being used by IGCAR and other DAE units to host peer review committee meetings (e.g. SO-C to SO-D), project review meetings (e.g. PFBR review), pre-dispatch inspections, PhD Viva Voce exams, training programs, webinars, press meets, DPS vendor meets, etc. (Figure 2). Till Dec 2020, nearly 1000 meetings have been conducted through it.

VII.05 Installation, Configuration and Deployment of Audio Video Streaming Facility

Traditionally people used to gather in a seminar hall / auditorium to attend invited talks or lectures. To facilitate users to attend various programs from desktop itself, it was planned to establish a professional audio-video streaming facility at Computer Division (CD) of IGCAR. To achieve this, software based streaming servers have been procured, installed, configured, tested and deployed in the campus backbone network of IGCAR. The architecture and configuration details of streaming facility setup are described in the following sections

Various components of streaming facility

The setup comprises of three numbers of rack mountable high-end servers running on Intel X64 platform, Hardware based audio video encoder and a Gigabit network switch. Block diagram of the setup is given in Figure 1.

The streaming engine software installed on Linux OS (Operating System) provides a web-based management graphical user interface for carrying out configuration steps. The software has been configured to receive input audio and video from encoder and deliver the digital streamed content to end user over local area network. It supports RTMP (Real-Time Messaging Protocol) Unicast / Multicast, RTSP (Real-Time Streaming Protocol) Unicast / Multicast delivery technologies. Three servers, each running its copy of streaming software, is configured in cluster mode with load balancing and high availability modes to provide uninterrupted content streaming. The software provides preview window feature to watch

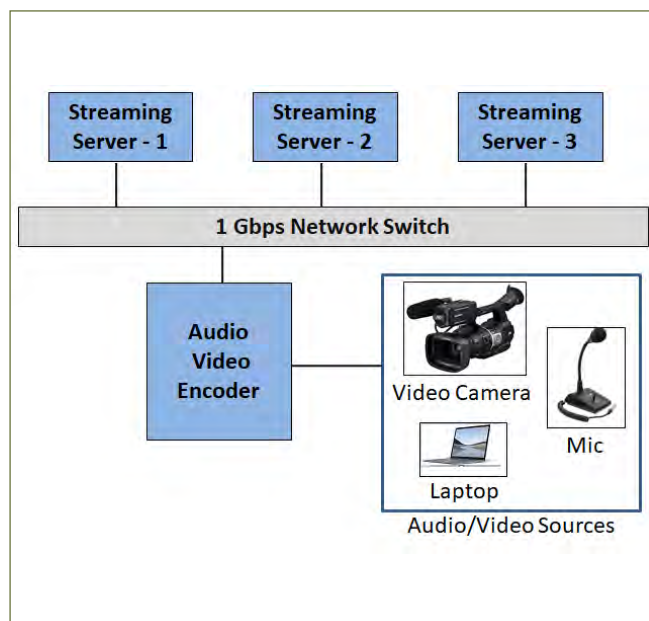


Fig. 1 : Block diagram of the streaming facility

the streaming content from the server itself to get a feel of how it is streamed to end user.

The hardware-based audio video encoder is capable of handling multiple audio and video inputs through HDMI, RCA and XLR interfaces and encodes & multiplexes these inputs. The multiplexed AV output is given to streaming server with custom screen layout. The system supports a maximum resolution of 1080p with frame rate of 60 fps (frames per second).

The Gigabit network switch provides high bandwidth traffic highway between streaming engine and encoder & streaming clients.

A streaming client application can range from media player to mobile device. Any user can view the streamed content by simply copying the URL into streaming client.

Some salient features of the streaming facility setup

- Supports live streaming to multiple concurrent users around 5000
- Supports simultaneous streaming of various programs / events
- Text embedding / Watermark feature on streaming channel
- Built-in recording facility
- Capable of streaming Live events, Webinars, VC meetings and On-demand streaming from AV (Audio-Video) media files
- Any user connected over intranet (Internet if required) can view the streaming content in near real time (with about 30 seconds delay)
- Built-in authentication feature to authenticate encoders before accepting input
- Supports analog and digital inputs from AV devices like Video camera, Mic, Laptop, VC Codec etc
- Easy to live stream any event happening across the campus by shifting the audio video encoder alone to the event location and connect the encoder to the nearest campus network switch

Conclusion

The established professional audio video streaming facility at CD, IGCAR is being used to live stream the HBNI webinars, Official functions, Training school classes etc. In the current global pandemic situation, the setup is very helpful to stream the programs / events to user desktops.

VII.06 Indigenous Access Control Systems for Security Buildings of DAE Kalpakkam Complex

Access Control System (ACS) is an essential electronic security gadget which provides access to authorised personnel and restricts unauthorised entry to any nuclear facility. Also the features of ACS of a nuclear facility must be dynamic, upgraded periodically and customized to keep pace with ever changing security scenario. The customized requirements of ACS of nuclear facilities are not met by commercial off-the shelf systems, thus the need for development of complete in-house access control system. The system consists of access controllers (each controller can control 4 doors / dual turnstile) and server application for communicating with controllers. These indigenously developed Access Control systems are deployed at several areas including Main gate Security Complex(MGSC), IGCAR cum BARCF Security Building (IBSB) and Kokilamedu Security Buildings (KSB) (Figure 1).

A total of 35 controllers along with full height turnstiles are installed at MGSC, IBSB and KSB, to provide authorised access to all employees of MAPS, IGCAR, BARCF and contractor employees. All employees and contract personnel passing through these turnstiles shall be authenticated with their RFID card credentials with the database stored in access control system before granting access.

The indigenously developed access control system does a two stage verification of the RFID card. In the first stage, the card is verified for the secret key (issued



Fig. 1 Access controllers installed at IBSB

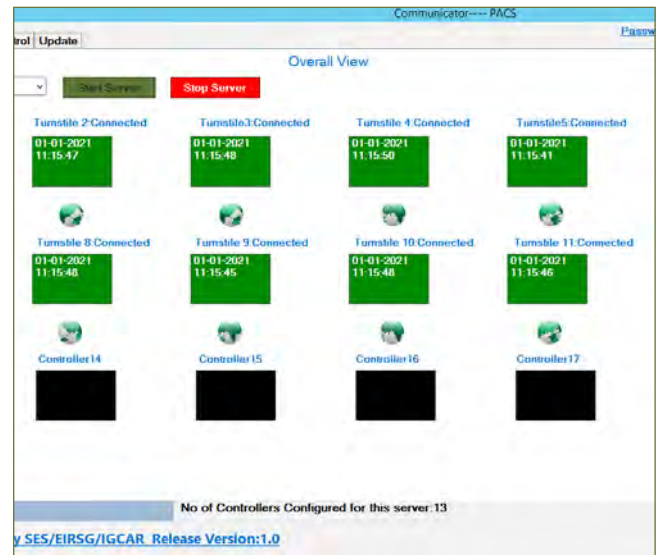


Fig. 2 Server application of access control system

by DAE) and also separate secret key for contractor personnel. In the case of mismatch of the secret key, the access denied. If the secret key matches, the verification proceeds to the second stage. In the second stage, the card's credentials are verified, and provides access by activating the turnstile solenoid. The system is designed such that, for each successful card verification, only one personnel is allowed to pass through the turnstiles.

Every access made through the turnstiles is recorded by the access controller with time stamp and sent to a server (Figure 2) over the Ethernet and stored in a database. Every day, the transactions made at IGCAR gate entrance are parsed by the Biometric Attendance Recording System (BARS) and used for recording the IN timings of IGCAR employees. On average 5000 transactions are made every working day through the turnstiles at IGCAR gate. A circular buffer technique is implemented in the local memory of access controller boards to store 10,000 transactions per controller. A real time operating system and intelligent task switching implemented on the access controller makes sure that the system is always responsive even in peak times and also ensures that all transactions are passed on to server.

The cost of implementation of indigenous access control system is estimated to be at most 1/6th of the cost of implementation of commercial access control systems without customised features like AntiPassBack (APB), Dual key authentication, Tailgating etc..

VII.07 Retrofitting and Refurbishment of LV System (Phase-1) to Improve Safety & Reliability

Many of the Office/Lab/stores buildings in IGCAR were built more than four decades ago, during early stages of the campus development. Certainly the LV electrical systems of these buildings are, of technology available on those days. The old technologies pose challenges for maintaining reliable and safe electrical system, because of updated safety regulations, limited scope for enhanced safety, obsolescence of worn out components, necessity of frequent inspection/ replacement of components and more equipment failures due to ageing. The numbers of electrical complaints received from such buildings are abnormally high compared to the newer buildings. ESD took the initiative by systematically studying the LV distribution system of the campus and formulated corrective measures to be implemented, towards achieving safer and reliable electrical system. It has been planned to implement the corrective measures in a phased manner to all the buildings. To understand the practical difficulties in implementing the corrective measures and to gain actual field scenario, Design block building, a two storey office building has been chosen for refurbishment. The following activities have been carried out without any major disturbance to the users. Efforts have been put during planning and execution stages to achieve best results.

Electrical Power distribution panel replacement

Electrical distribution panel of the building was old, Industrial type without complete internal segregation. It has out dated & worn out components, which made the panel no longer serviceable. The old panel has been replaced with new FORM-4B metal clad (internal segregation) type cubicle panel with recent technology. Retrofitted LV distribution panel is shown in Figure 1. The panel construction ensures safety to the operating personnel against accidentally accessing live parts.



Fig. 1 Retrofitted LV panel for design block building



Fig. 2 Earth leakage current monitoring relay

Core Balanced Current Transformer (CBCT) based earth leakage current monitoring and protection scheme ensures local isolation of electrical fault and better planning of preventive maintenance.

Aluminium wire replacement

Internal wiring of the building was done with aluminium conductor with VIR insulation. Over the period of time the wires become rigid and frequent insulation failure has occurred due to thermal cycling and ageing.

Aluminium wirings are no longer an efficient and safe option for internal wiring.

The Aluminium wirings of the buildings are replaced with copper conductor wiring. Utmost care has been taken to remove the old Aluminium wiring completely, from the embedded conduits, so that the existing routes can be reused for new copper wiring and disturbance to civil structure will be very minimal.

Implementing CBCT based protection scheme

Core Balanced Current Transformer based protection scheme was implemented at power distribution panel level, to ensure personnel and equipment safety against dangerous earth leakage current. For improving overall system reliability & minimal disturbance to other buildings, earth leakage current detection and corresponding faulty feeder disconnection is done at downstream (building) level.

Micro processor based relay is provided for continuously monitoring and displaying the Earth leakage current occurring downstream of the panel. Panel mounted earth leakage relay is shown in Figure 2. This will give the maintenance personnel the real time status of system insulation, incipient faults and facilitate them for planning preventive maintenance of the system.

Converting Fuse DB to PPI MCB DB

Fuse distribution boards, which were employed for lighting, fan and single phase power distribution of the buildings, lacks protection against earth leakage current

due to direct or indirect contact. Moreover, Fuse DBs were integrated as a part of industrial panel that made it hard for frequent maintenance.

The fuse DBs were replaced with Per Phase Isolation type MCB DB, for selective isolation of the earth leakage fault at downstream level. This limits the disturbance. MCB DBs are physically separated from power distribution panel for ease of maintenance. Retrofitted PPI MCB DBs are shown in Figure 3.

Conventional light fixtures to DC light fixtures

Fluorescent light fixtures of the buildings are replaced with energy efficient, longer life DC LED light fixtures. Energy efficient DC ceiling fans are also incorporated. With DC lighting and Fans in place, the system is expected to serve longer without any major maintenance.

Trunking system for single phase power outlets

Completely worn out single phase power sockets and switches of the buildings are no longer serving its purpose and many extension boxes were used for meeting minimum functionality. This made the power



Fig. 3 Retrofitted PPI MCB DB

distribution inside the office rooms unsafe and clumsy. UPVC trunking system installed for single phase power distribution inside the room, which is modular, flexible, corrosion free, aesthetically good, easy for installation and do not require modification in civil structures.

After gaining the experience from the first building, tender floated and work initiated for two more buildings.

VII.08 Unified Portal for Efficient Utilization, Management and Monitoring of High Performance Computing resources

High Performance Computing (HPC) facility of HIGCAR consists of supercomputing clusters, high-end servers, graphics intensive workstations, license

servers, firewall servers, large size printers and plotters. A comprehensive web portal is developed for efficient usage and management of HPC facility with different levels of

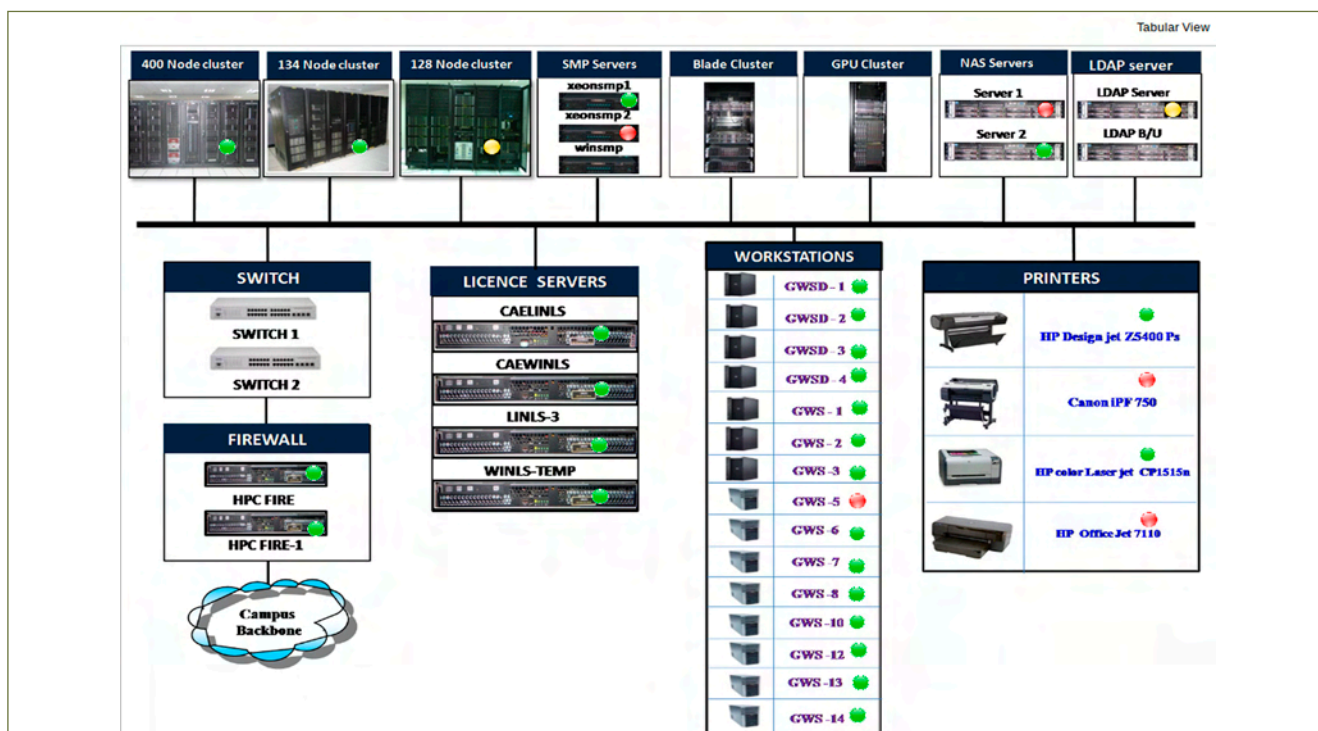


Fig. 1 A page showing status of HPC systems



Fig. 2 A page showing RTC shift roster

usage privileges for administrators, operators and users. The portal collects and displays real time information on the utilization of systems and software applications from various HPC resources like clusters, servers and workstations. These information are useful for users as well as operators in status finding and selecting resources. The portal also facilitates in improved managerial decision making by providing historical accounting information about the HPC resources over a period of time.

Apart from the needs of system administrators of the HPC facility, the portal is developed for satisfying various requirements of users, round-the-clock shift operators and shift-in-charge. Each set of users have different levels of privileges and can view data or perform actions according to their privilege level. Authentication to the portal is integrated with centralized authentication mechanism.

A consolidated view about the status of all HPC systems is provided in real time that helps in easy understanding of what resources are available. The statuses are categorized (with colour codes) like “system is down”, “system is up”, “system is up in degraded mode” (Figure 1).

Users of HPC facility can submit user account requests, print requisition forms and feedback forms through the portal. Users can upload files for printing, and once the print request is approved, shift operators can download the file from portal. Hardware and software details of all HPC systems and detailed invocation procedure for all software applications is included in the portal. The portal is used for managing round-the-clock shift operation of Computer Division. Shift roster can be viewed from the portal by concerned authorities (Figure 2) and shift-in-charge can update the roster according to employee leaves and shift changes.

Information about HPC clusters such as load level, submitted jobs & status, running processes, status of compute nodes, logged in users, log messages, status of parallel file system and storage utilization are collected in real time and stored and displayed in the portal. Historical data regarding utilization of clusters and job submissions by different users/groups are stored and presented as graphs and tables (Figure 3). Data regarding usage and availability of application software licenses are collected from license servers and displayed in the portal. Manuals and reports on HPC facility can be uploaded, viewed and edited in the portal. Manuals can be in the form of a file or a note which can be edited from the portal itself.

The portal is developed using PHP, MYSQL, Javascript and AJAX. Model View Controller (MVC) pattern is followed for server side development. Scripts developed in Perl are running periodically in HPC clusters and license servers for collecting data on various system parameters and sending it to portal. A process listening on the web server of the portal is receiving incoming data and logging the data into a database.

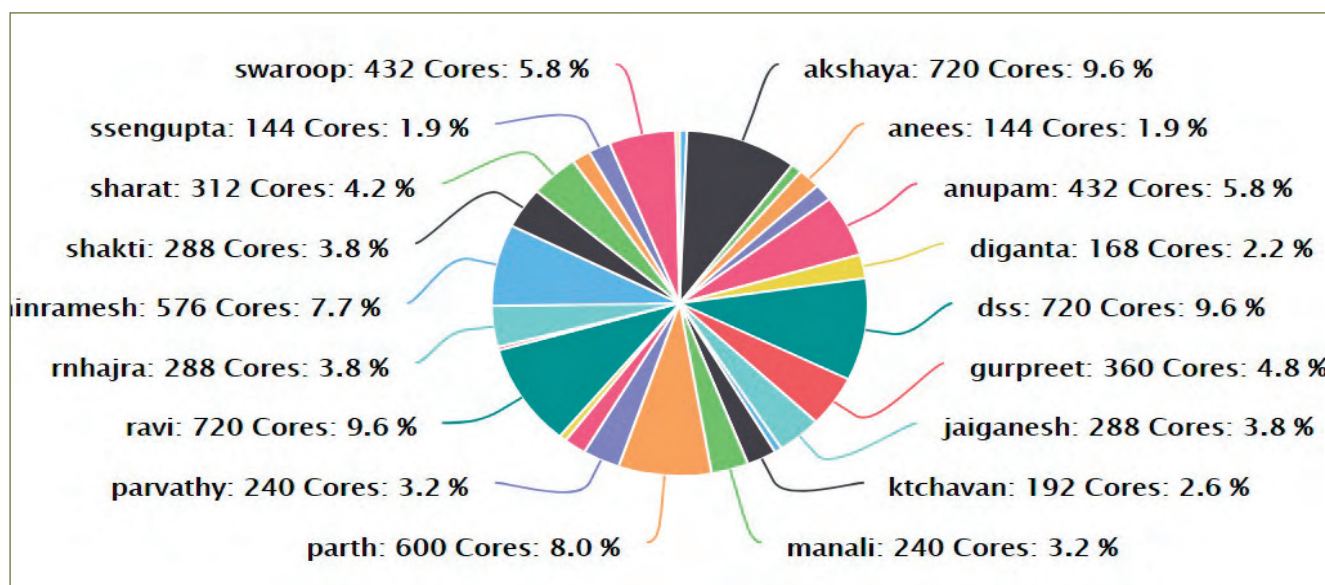


Fig. 3 Chart showing cluster utilization

VII.09 In-house Development of Customized Application Framework for E-Services (CAFE)

An organization essentially consists of many resources of which important ones are popularly known as Men, Money and Machines which indicate human resources, financial resources and material resources. Technology plays a vital role in effective management of these resources in the organization. In IGCAR, an enterprise resource planning software package, known as Automated Workflow Management System (ATOMS), is being used since 2010 for automating and integrating the organizational processes in these areas. During one decade of operation of ATOMS, the technology has changed many folds especially the one used at the client side. The new client side technologies, developed during the last ten years, provide better outlook and ease of operations to the end users. In order to provide new features in the existing and forthcoming online services, it was inevitable to switchover to a newer platform. The challenge was to develop a new platform in-house by integrating several open source technologies which can be adapted to migrate the existing online services by incorporating new features and also adding enhanced application security. Towards this, several open source technologies were studied, evaluated and selected for building a new framework. As a result, a new “Customized Application Framework for E-services (CAFE)” has been developed in-house. The CAFE framework has been developed using open source components which have been customized and integrated to work in sync within the system. This framework will be used for migrating e-services available under ATOMS.

The framework components can be divided into three categories, i.e. front-end, middleware and backend technologies. The front-end technologies include open source components which are visible to the end users and provide functionalities of ease-of-use, look & feel etc. It deals with the presentation of information to the users. The open source front-end technologies HTML5, JQuery, Ajax, Font awesome, Sweet alert and Bootstrap have been used for developing CAFE. These open source projects have been amalgamated to provide

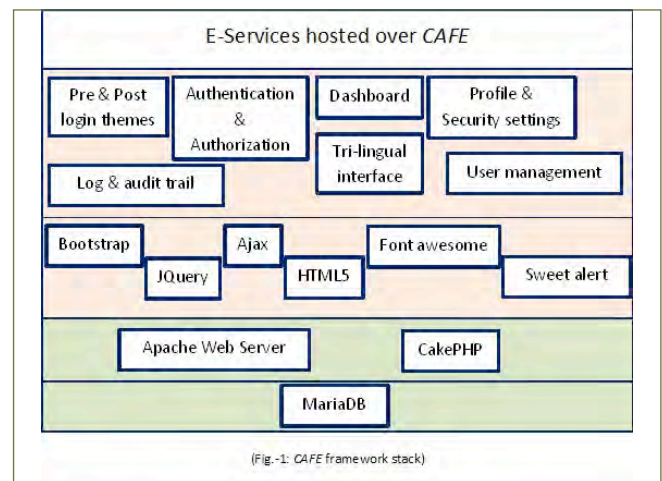


Fig. 1 CAFE framework stack

elegant, user friendly and seamless web components to the end users. The middleware technologies of the CAFE framework consist of components which host the services and also implement security protocols. Middleware of this framework includes Apache webserver and CakePHP implementation for providing model-view-controller (MVC) architecture to the framework. The back-end technologies of the framework include the software components which deal with storage, retrieval and management of data dealt by the application. For development of this framework, free and open source database “MariaDB” has been used at the back-end. The integrated view of the framework components has been shown in Figure 1.

The above mentioned open source technologies have been customized to add common functionalities viz., Pre and post login themes, authentication and authorization, integrated dashboard, Tri-lingual interface, user profile and security settings, user management and Logging & audit trail as part of the CAFE framework. The framework has robust security mechanism to deal with cross-site request forgery (CSRF), SQL injection, authorization, sessions and cross site scripting (XSS).CAFE framework has been successfully tested by developing few applications in it by incorporating roles, workflows and digital signature. The development of ATOMS 2.0 has been taken up using the CAFE framework.

VII.10 Development of Secure Webmail Service

Prior to the COVID-19 induced lockdowns, access to the IGCAR email facility was restricted to IGCAR Intranet except for a few higher officials who could access the facility from official laptops which are configured to connect to the Intranet through VPN. But, during the work-from-home period, a need has arisen for the senior officials of IGCAR to communicate with each other to carry out their duties effectively.

Considering this requirement and the sensitivity of the data handled by IGCAR and DAE in view, Computer Division has decided to provide a secure access of IGCAR email facility over the Internet. Hence a web interface, webmail, has been developed using open-source software to access IGCAR mails from a web-browser.

Security: A dedicated email server is configured with IMAP protocol to support the webmail. Both the webmail server and the email server are isolated from rest of IGCAR Intranet using DMZ (demilitarized zone). HTTPS protocol is configured and used with the industry-standard cryptographic algorithms to protect the data between the users and webmail over the Internet. Further to thwart any brute-force login attacks, a CAPTCHA (Completely Automated Public Turing test to tell Computers and Humans Apart) module was developed and integrated to the login page.

Authentication: Besides the standard password based user-authentication, an OTP (One-Time-Password) based two-factor authentication (2FA) module was designed and implemented. Used in combination with a password, 2FA greatly enhances the security of user authentication.



Fig. 1 IGCAR webmail login page with CAPTCHA

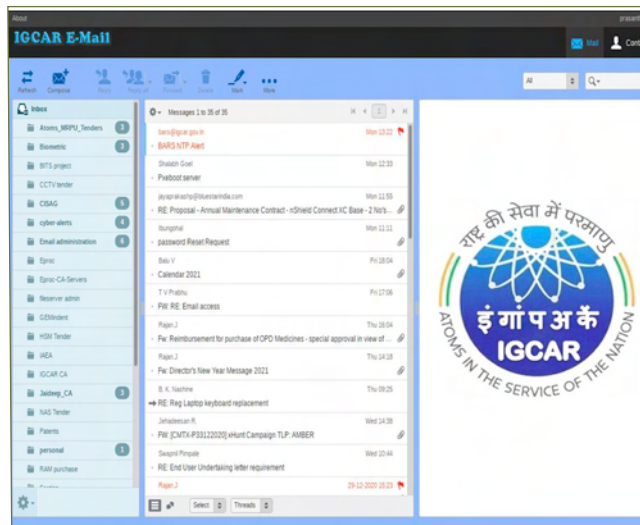


Fig. 2 IGCAR webmail

During the login phase, this 2FA module first authenticates the user using standard password and then sends an OTP on their pre-registered mobile number and personal-email-ID. Sending OTP over both mobile and email ensures reliable delivery. Also, a two-way HTTPS based authentication module was developed and deployed to support DSC (Digital Signature Certificate) based authentication as the 2nd-factor.

Authorization: An authorization module is developed to register the users. A web-interface has been developed and deployed for the same. Details such as personal mobile number, email ID and Date-of-Retirement (DOR) are collected through the portal and registered in webmail. Once registered, an alert is sent to the user over his mobile and email ID along with user guide as attachment. DOR is used to automatically disable the user's account after this date.

Features: To enhance user experience, features such as password management, user signature, import contacts, and automatic contact collection are provided. To prevent sender address spoofing, SMTP envelope sender address field has been made immutable for the users. Platform: IGCAR webmail was developed using open-source tools and packages on a server-class machine with a Linux operating system. Module development was carried out in PHP, Shell script and MySQL DB. All the software components such as operating system, web service, database etc are hardened and audited.

IGCAR Webmail is being used widely by the officials of IGCAR, GSO, BHAVINI, BARC Facilities and MRPU.

VII.11 Design & Simulation Centre with High-end Graphics Workstations

In order to address the ever growing visual computing requirements for carrying out advanced computer aided design, analysis and simulation studies, a new Design and Simulation Centre facility has been setup at Computer Centre of IGCAR. The facility consists of 32 numbers of high-end workstations with twelve-core Intel Xeon dual processors, NVIDIA Quadro (16GB) graphics cards, 128 GB DDR4 RAM and a local storage capacity of 6 TB. Compute and graphics intensive application software like ANSYS, ABAQUS, COMSOL, SYSWELD and CFD-ACE are loaded and configured in these workstations.

Several administrative and resource level configurations are implemented for better and optimized utilization of the workstation facility. Centralized user authentication, network attached additional storage, folder redirection and automated backup of user data are the major features implemented in the facility for achieving better resource utilization.

All these workstations are configured to form a common domain. Active Directory Domain Service (AD-DS) is configured and implemented for achieving centralized user authentication and policy management. By implementing this, users get the flexibility of using the same account on any of the workstations. In order to ensure high availability, primary and secondary Active Directory servers are configured.

The users of the facility are categorized into two groups namely common users and power users. Power users are created based on authorized requests from the respective group and are prioritized for certain workstations. Both common as well as power users get equal privileges for accessing application software and other major resources.

A centralized Network Attached Storage (NAS) system which is configured with RAID is connected through LAN such that the data is safe and available across any of the workstation where a user logs in. Each domain user is provided with additional storage space from this centralized storage. Folder redirection is enabled for the common users with the help of the centralized storage. This enables profile related folders such as 'My documents', 'Downloads', 'Desktop', 'Favorites', 'Pictures' etc. in getting redirected to the NAS storage by default. The files in these folders are available across all

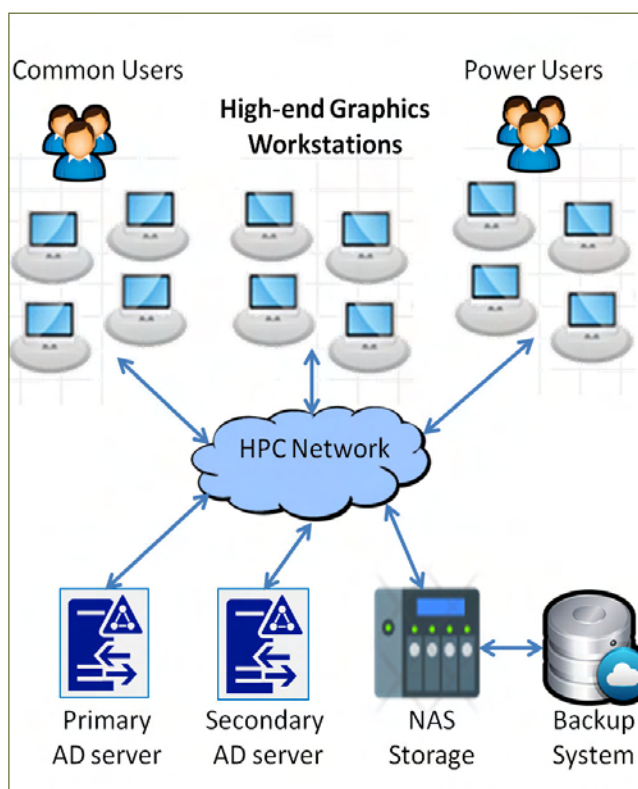


Fig. 1 Overall view of design & simulation centre

workstations wherever the user logs in. By default, 500 GB storage space from the NAS storage is assigned for every user and that can be increased when requirement arises. A Backup system is configured to automatically create periodic backups of user data from the centralized NAS storage.

A separate scratch storage space is also provided to the users from the local hard disk drives to store temporary data while jobs are getting run. This scratch space is getting cleared periodically without any backup. If the users want to get the relevant data available in all workstations, they are allowed to manually copy those data from the scratch space to the redirected folder.

A dedicated physical access control system is implemented for this facility. This restricts the physical access of the facility only to the workstation users with the help of the employee ID cards. The facility is run in 24x7 basis with the help of round-the-clock shift members of Computer Division. High availability of the facility is ensured with the support of UPS. The overall configuration of the facility is depicted in Figure 1.

VII.12 Enhancement and Customization of Online APAR for Deployment at other DAE Units

Online APAR Software has been developed in-house in Computer Division of IGCAR to make the entire APAR creation & submission process online with the implementation of digital signature. It is a full-fledged end to end APAR system all process of creation of APAR by the administration, online filling & submission by the employee, work assessment by the reporting officer, review of work by the reviewing officer, acceptance by the accepting officer, communication of APAR by communicating officer and final acceptance/non-acceptance by the employee. The workflow of online APAR is shown in Figure 1. The APAR server distribution network is shown in Figure 2. The portal was developed with open source packages and in-house developed rapid application development platform. The portal was successfully developed and deployed to IGCAR in the year 2018. The online APAR portal is enhanced with following sub modules.

APAR Communication

The module facilitates the designated communicating officer to view the awarded grading by the accepting officer and fill the remarks. After successful validation the generated APAR communication part is signed digitally and forwarded to the respective employee for further processing.

Employee Acceptance & Non Acceptance

The module facilitates the employee to view the awarded final grading along with the remarks submitted by the communication officer. After marking the acceptance/non-acceptance the details are saved in database and also embedded in APAR communication template. The final APAR communication with Acceptance/Non-Acceptance form is signed digitally by the employee and sent to respective communicating officer.

Employee APAR Creation & Management by Administration

The module facilitates the Administrator to create Employee APAR for a specific period by filling up the

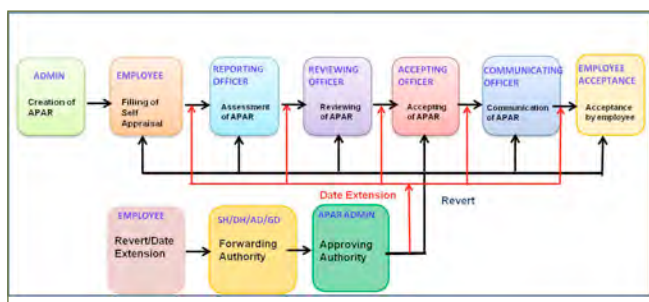


Fig. 1 APAR workflow

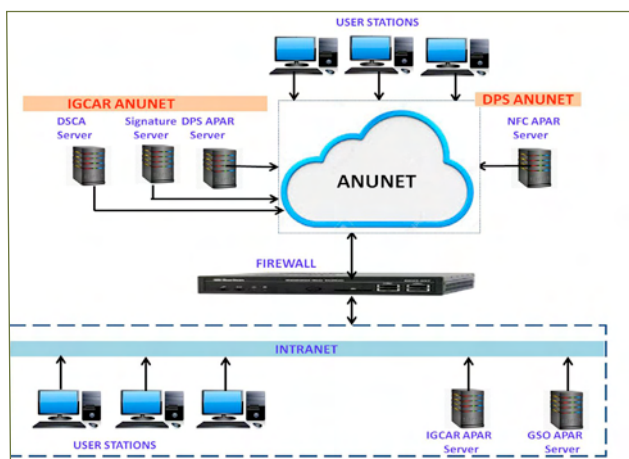


Fig. 2 APAR server distribution network

personal, leave and authority (reporting, reviewing, accepting officer) details. The details entered by the administration department are validated against the predefined character limits and types based on the employee designation and category (Admin/ Scientific/ Technical). After successful verification, APAR template for the given period is created to enable the employee to fill & submit the APAR online. The module also provides a facility to view the detailed APAR submission analytics for the administration to keep track of the APARs pending at each stage.

Date Extension

The APAR software does not allow the employee to process the APAR after deadline set for each stage (Self Appraisal/Reporting/Reviewing/Accepting) of APAR workflow. The time extension module facilitates the officer to submit a date extension request online through the designated forwarding authority to the APAR administrator. Once the APAR administrator approves the request the software enables the employee to process the APAR until the new deadline.

APAR Unlock/Reversion

The module provides a facility to the accepting authority to revert the submitted APAR for any corrections. The request is forwarded through concern approving authority indicating the stage to be reverted to the APAR administrator. After the administrator's approval the APAR is reverted to the specified stage for further modification and resubmission.

Digital signature based online APAR software has been enhanced, customized and successfully deployed in IGCAR & other DAE units - NFC,DPS & GSO. The software is effectively utilized by these units to make the entire process paperless with digital signature.

VII.13 Improving Availability of Central Water Chilling Plant by Predictive Maintenance Strategy

Air-Conditioning and Ventilation System Division of Engineering Services Group is responsible for providing uninterrupted and reliable air-conditioning and ventilation services to various radioactive laboratories, computer center, office buildings etc. of IGCAR throughout the year. Central Water Chilling Plant [CWCP], consisting of 6 large centrifugal chillers and associated utilities like centrifugal pumps, cooling towers are working continuously to meet this requirement along with air handling units [AHU] at users' premises.

Reliable operation of all these rotating equipment is necessary to sustain the uninterrupted air-conditioning services to the center. In order to achieve this goal, predictive maintenance strategy is adopted for the equipment. Predictive maintenance is a proactive maintenance strategy that monitors equipment condition on regular intervals and predicts its failure in advance so that maintenance work can be performed before that happens. This approach promises cost saving by reducing the frequency of maintenance & breakdowns and eliminating unnecessary preventive maintenance. Thus, it is regarded as condition-based maintenance carried out as suggested by estimations of the degradation state of an item. The main objective of predictive maintenance is to allow convenient scheduling of corrective maintenance, and to prevent unexpected equipment failures. The following predictive maintenance tools are used for rotating equipment of CWCP:

1. Vibration monitoring & analysis
2. Noise monitoring
3. Thermography analysis
4. Oil analysis

Table 1: Vibration levels of AHU before correction

RMS vibration in mm/s	AHU Motor		AHU Fan	
	DE	NDE	DE	NDE
Vertical	14.8	14.7	6.8	12.2
Horizontal	20.1	20.3	15.8	5.6
Axial	10.0	7.7	7.8	4.3

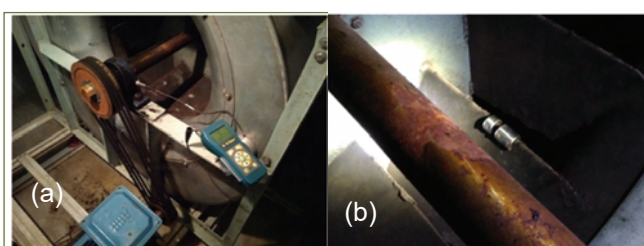


Fig. 1 In-situ dynamic balancing of AHU fan

Table 2: Vibration levels of AHU after correction

RMS vibration in mm/s	AHU Motor		AHU Fan	
	DE	NDE	DE	NDE
Vertical	5.2	6.7	3.9	6.3
Horizontal	6.1	6.4	5.6	4.3
Axial	5.6	5.4	5.5	3.4

5. Laser shaft alignment
6. Dynamic balancing.

Utilizing the above 6 predictive maintenance techniques in combination, the equipment of CWCP is monitored on regular basis. Availability of CWCP equipment has been increased considerably by adopting predictive maintenance strategy.

A systematic approach is adopted in monitoring the healthiness of 234 Nos. of air-conditioning equipment periodically i.e. monthly or bi-monthly based on their criticality, vibration severity, noise level, thermograph of all equipment and lubricant condition (for chillers only) are monitored and the equipment are categorized into satisfactory, un-satisfactory (still acceptable) and unacceptable category. A detailed analysis is carried out for unhealthy equipment to identify their defects and necessary corrections are carried out without affecting the operation schedule and system reliability.

Wear particle concentration and oil parameters are monitored periodically to diagnose any abnormal wear of chiller internal components.

Infrared thermography imaging technique is utilized to identify potential problems in electrical panels due to loose connections, damaged insulation etc.

Following predominant defects are observed across the equipment:

1. Imbalance
2. Misalignment
3. Lack of structural rigidity

Table 3: Vibration levels of cooling tower fan No. 10 before correction

RMS vibration in mm/s	Motor	
	DE	NDE
Vertical	9.2	11.5
Horizontal	5.1	4.1
Axial	13.5	10.4

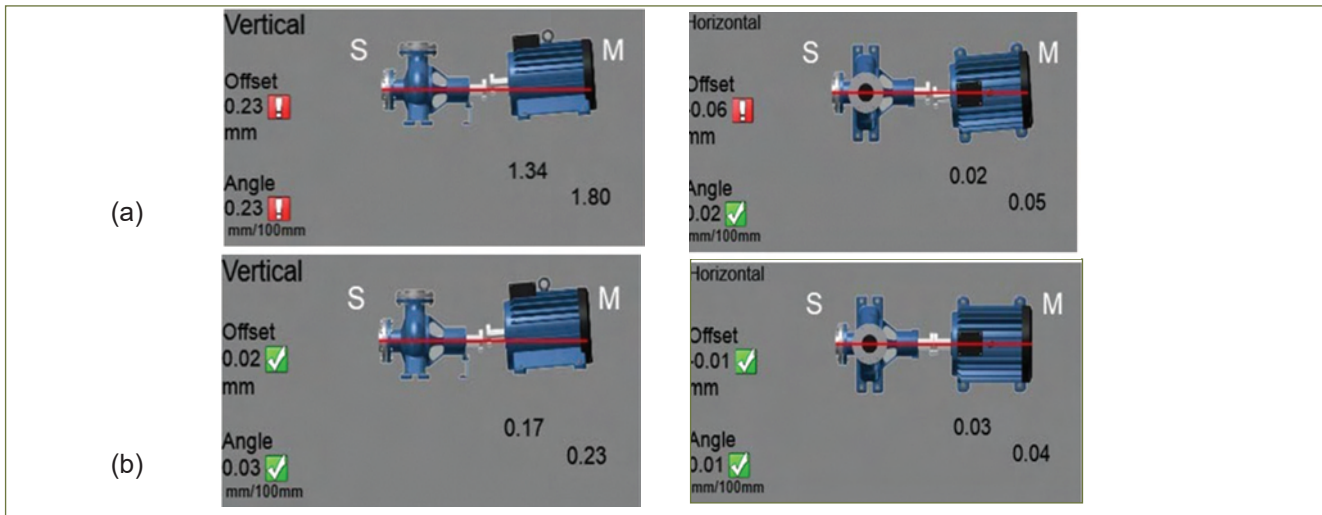


Fig. 2 Misalignment (a) before and (b) after correction

- Other defects such as bearing defects, pulley belt damage, electrical looseness, poor oil condition etc.

Correction

Necessary corrections such as in-situ dynamic balancing, laser alignment, bearing lubrication or replacement, improving structural rigidity etc. are carried out on the equipment in order to restore their normal operating condition.

Some of the major corrections on critical equipment are discussed below:

AHU 2 of High Density Computing Facility

2 AHUs are operating for air-conditioning of High Density Computing Facility [HDCF] at computer center, IGCAR. Failure of these AHUs may lead to undesirable reduction in capability of computing facility. The vibration levels as recorded on AHU 2 before correction are furnished in Table 1.

As per IS 10816 the acceptable vibration level for this equipment is 7.1 mm/sec. On detailed analysis of vibration spectrum and phase it is observed that multiple defects exist with un-balance of the fan as dominant defect. Minor defects such as pulley misalignment, replacement of belts were carried out before balancing the AHU fan. In-situ dynamic balancing of the AHU fan was carried out and 30 gms. of mass was added to the fan as shown in the Figure 1.

The vibration levels of the AHU after corrections are indicated in Table 2. Vibration levels of the AHU are brought down to acceptable condition by in-situ dynamic balancing of the fan.

Cooling Tower Fan No.10 at CWCP

16 cooling tower fans are operating at Central Water Chilling Plant to reject the condensation heat to atmosphere. Failure of the cooling tower may lead to tripping of chillers hence affect the overall plant capacity. Vibration level observed in cooling tower from No. 10 is shown in Table 3.

As discussed earlier the acceptable level is 7.1 mm/sec and the vibration level of equipment is un-acceptable condition. Detailed analysis of vibration Fast Fourier Transform (FFT) spectrum indicates misalignment between the fan & motor coupling. Laser based optical alignment was carried out on the equipment using laser alignment tool. Figures 2a and 2b shows the screen-shots of instrument display panel indicates misalignment before and after the correction.

The observed vibration levels after correction of misalignment is shown in Table 4. The vibration levels has improved and the equipment is operating in acceptable condition

A comparison of equipment healthiness for 2019 and 2020 is shown in the Table 5.

Due to implementation of predictive maintenance strategy availability of more number of equipment could be ensured in the last year.

Table 4: Vibration levels of cooling tower fan No. 10 after correction		
RMS vibration in mm/s	Motor	
	DE	NDE
Vertical	5.4	5.9
Horizontal	5.1	5.3
Axial	6.5	6.9

Table 5: A comparison of equipment healthiness for 2019 and 2020		
Equipment healthiness condition	Nos. of equipment	
	2019	2020
Satisfactory(Acceptable)		
Un-satisfactory	172 Nos.	195 Nos.
(Still Acceptable)	23 Nos.	20 Nos.
Un-acceptable	39 Nos.	19 Nos.
Total	234 Nos.	234 Nos.

VII.14 Buildings for State of Art Doppler Weather Radar and Wind Profiler Weather Surveillance Systems

It is planned to install weather surveillance system at IGCAR, Kalpakkam for enhancing the existing meteorological observation. Two systems have been planned, one is Doppler Weather Radar and the other is Wind Profiler in a complex near Edaiyur creek. Both the systems are being developed and installed in collaboration with ISTRAC–ISRO Bangalore. IGCAR is supporting the design and execution of the buildings and technical support for installation and operation will be provided by ISTRAC.

Site Location

The location of these buildings has been selected meticulously near coast where no building development has taken place and there is least possibility of development in the future. The Doppler Weather Radar is located on a greater height without any possibility of obstruction from nearby buildings and to avoid interferences and beam blockage. Both the buildings are located in a complex near Edaiyur creek separated by a distance of 40 m (Figure 1). A separate DG room is located in the complex to cater both the buildings.

Doppler Weather Radar

Doppler Weather Radar (DWR) is an active remote sensing instrument forecasting storms, cyclones and other severe weather conditions. DWR provides unique capability to capture the movement of weather systems upto 500 km for monitoring and early warning.

The building is planned in octagonal shape for both aesthetic and functional reasons (Figure 2). The total area of building is 510 sq.m. The building is designed structurally for holding a point load of about 5 tonne in the radar area with an antenna rotational speed of 6 rpm inside radome at 21.9m level. The building rises as a

tower like structure with parking and lobby area at ground floor and later floor are with staircase and lift to reach higher levels.

At +9600 Lvl. there is materials storage area and space for HVAC system. The AHU ducts are raised through shaft to the next floor. The electrical duct is provided along the staircase wall to carry the electrical services above and access is provided in staircase mid-landing. At +13200 lvl the main floor with control room, electrical panel room with UPS has been provided. False flooring is provided to take all the service lines (Figure 3). There is a chute connected from terrace floor to the control room for communication. The control room is provided with maximum glazed area to observe the exterior environment. Special earthing has been provided for building safety. The building comes under high rise category, fire shaft and fire water tank of 10000 litre capacity are provided. The radome is located such that there is complete clearance at 0 degree elevation. It is a foam sandwich spherical radome with 6.7m diameter. The antenna is 4.2m diameter prime focus parabolic dish. It has dual polarimetry capability.AC cooling requirement inside radome and control room is 20-22 °C.

Wind Profiler

Wind Profilers are clear air Doppler phased array radars. Detects Reflection from Turbulence and eddies. It is an important research tool in the investigation of prevailing winds, waves (including gravity waves), turbulence and atmospheric stability inputs in atmospheric dispersion studies. The operating frequency is 205 MHz, aperture size is 13 m dia. and observation range is 12 km maximum height and minimum height coverage is of 100 m.

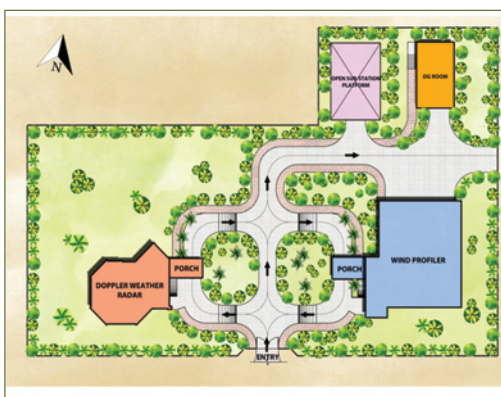


Fig. 1 Site layout showing location of weather surveillance buildings



Fig. 2 Floor plan of doppler weather at +13600 lvl



Fig. 3 Section through the building

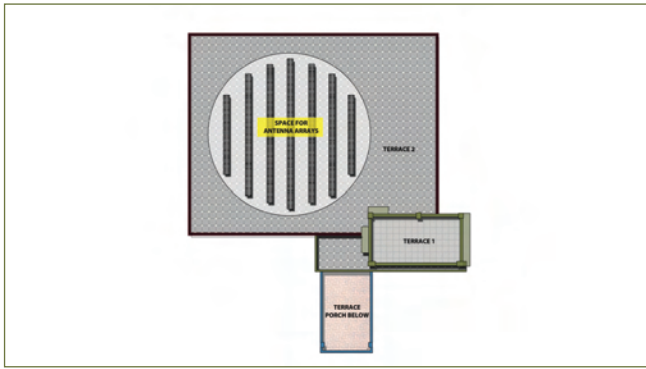


Fig. 4 Terrace floor plan of wind profiler



Fig. 5 Section of wind profiler

The wind profiler is housed in G+1 Structure with an area of 630 sq.m. The total height of the building is 10 m (Figure 4). The amenities like storage room, electrical panel room, shift in-charge room with pantry area are at ground floor. The instrumentation and TR module room are located at first floor is supported with UPS and battery system and temperature control will be done by floor mounted AC. A temperature of 23 ± 2 °C with RH $\pm 5\%$ temperature and 24x 7 operations is considered.

Control room of size 4 m x 4 m and electrical panel room are planned at this floor. A refuge platform is provided to cater to any emergency situation. Special earthing is done for the building. The faraday cage is provided during construction and is earthed to protect the person in control room from EMI radiation.

The antenna arrays are installed on the roof top mounted on individual concrete pedestal and guarded by a M.S Fence. The TR module will be suspended from first floor the ceiling. The antenna installation is in an area encircling a radius of 6.75 m (Figure 5).

Structural Design Features

The structural system of Doppler Weather Radar building is essentially a RC framed structure of height 19.2 m and central four circular columns raised above roof level to support the Doppler Weather radar weighing 5 tonnes. Tie beams are provided along the height of the building for every 3.3 m and RC walls are provided in the building between the columns up to 13.2 m level to avoid detrimental soft storey effect induced by bare frame without brick in-fills under lateral loads such as earthquake. False flooring at 13.2 m level with 600 mm sunken has been checked for integrity. The beams supporting the pedestals where Doppler Weather Radar is supported are designed to restrict maximum tilt of the radar to 0.5 degrees under wind speed of 200 km/hr. This building is analyzed and designed for static, seismic and wind load cases.

These weather monitoring equipment’s will help us in weather monitoring ,early detection of disaster and allow us for better emergency preparedness to face the natural disaster like storm and cyclone. It will facilitate research activities in the field of metrology.

VII.15 Microanalytical Methods Aiding the Study of Old Concrete Structures

The case study pertains to a building built in the 1970s and has always been the most utilized office space in the campus. Being one of the first buildings in the campus several novel architectural features like slender columns, waffle slab, a hanging staircase, long wide windows with deep sunshades were conceived to give a perfect ambience for a well ventilated design office. The structure has seen a life span of 48 years with proper maintenance. It has been observed recently that, few of the columns have started cracking. The distress in columns started with vertical cracking in the cover concrete, followed by

spallation. There was visible distress in masonry and window panes associated with the columns. This study aims at estimating the extent and type of degradation of the building chemically and micro-analytically and interpreting the results.

Upon conducting a structural analysis it was found that external columns were sway columns with high slenderness ratio, according to ACI318 . Axial loads in the columns were exceeding the Euler critical load applying the stiffness variation in columns due to age related cracking, creep, and column non-linearity. Hence peripheral columns were failing



Fig. 1 (a)Colorimetric method to check free and bound chloride (b)carbonation test

due to instability and buckling resulting in vertical cracking. Further chemical analysis of concrete was done to assess chloride penetration and carbonation. The chloride content in concrete was determined from broken core samples of the concrete member, in accordance with IS: 14959 (part 2) . As per IS 456, the maximum total Acid Soluble Chloride content for reinforced concrete or plain concrete containing embedded metal is 0.6 kg/m^3 . pH was determined using Hanna make HI991300 model portable pH meter.

A colorimetric method based on Mario Collepari , by spraying Fluoresceine and a Silver Nitrate solution was used to determine the presence of free and bound chloride(Figure1a) and its penetration into the concrete structure as it has been generally assumed that free chloride ions can promote the corrosion process of steel reinforcement.

The carbonation test was carried out as per RILEM CPC-18. The reduction of the pH value could be made visible by applying a 1% phenolphthalein solution to a freshly fractured surface of concrete. The non-carbonated areas turn red or purple while carbonated areas remain colourless (Figure1b) The phenolphthalein solution was sprayed on the freshly cored concrete surface and the colour change was observed Chemical analysis showed high chloride content (1.4 kg/m^3) in external concrete and 0.9 kg/m^3 at internal columns. Similarly, carbonation depth as high as 40 mm was observed in external columns where as 10 mm in internal columns. XRD of fresh concrete usually shows, the crystalline peaks of hydration products, Calcium hydroxide, gypsum, ettringite, continuous bumps of calcium silicate hydrate gels, calcium carbonate etc. and quartz phase from aggregate and cement. In the sample, calcium hydroxide or Portlandite phase at 2θ of 18° & 34° were missing, which were replaced by peaks at $23-25^\circ, 26-27^\circ, 39-40^\circ, 78^\circ$, as calcite/vaterite and aragonite, the polymorphs of calcium carbonate(Figure 2). Calcite which is in abundance in the 40mm layer of the concrete is the most stable polymorph.

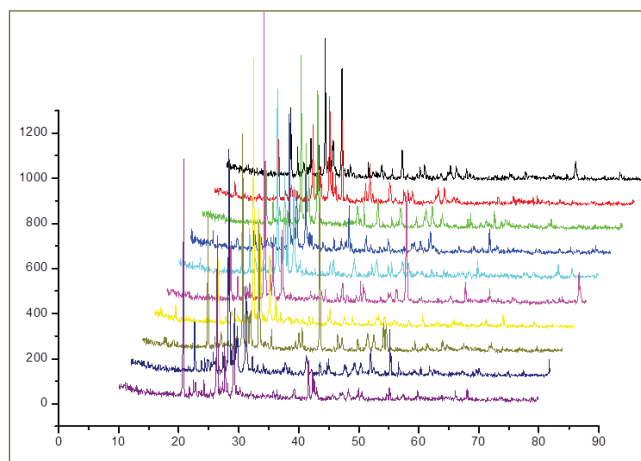


Fig. 2 XRD of concrete

Vaterite, is in concrete due to the high ambient temperature at site and aragonite, due to the presence of chloride. Other crystalline products identified were bassanite ($\text{CaSO}_4 \cdot 5 \text{H}_2\text{O}$) (at $20.72^\circ, 23.23^\circ, 29.7^\circ, 42.45^\circ$), and langbeinite (potassium magnesium sulphate etc.)(at $21.92^\circ, 25.39^\circ, 26.93^\circ, 31.2^\circ, 39.55^\circ, 41.69^\circ, 43.1^\circ$). These are products formed due to the instability of gypsum and ettringite in carbonated environment along with high temperatures. Quartz phase from $20.85^\circ, 26.65^\circ, 36.54^\circ, 39.46^\circ, 50.14^\circ, 60^\circ$ and 68° were evident in some samples of external/internal columns, but not in all which shows ageing. Calcium monosulphates (10.2°) and Friedel salt (11.05°) also appeared in some inner layers of samples. The peaks at $13-14^\circ$ indicate free chloride.

Chemical analysis showed high chloride content (1.4 kg/m^3) in external concrete and 0.9 kg/m^3 at internal columns. Thus the source of chloride is assessed to be internal, that would have admixed during hydration (say CaCl_2). Concrete core from an inner column showed evidence of bound chloride from chemical analysis and in XRD, which explained the absence of corrosion in the internal elements, even though total chloride content was exceeding the threshold value (of 0.6 kg/m^3).

The grade of OPC cements used in the 1970's contained high C_3A content of 10, which explained the formation of Calcium chloroaluminate (Friedel salt). But XRD of spalled concrete from external columns were not showing Friedel salt peaks. The outer columns were heavily carbonated, and at high carbonation levels the Friedel salt is unstable hence breaks into free chloride which corrodes the rebars. Depth of Carbonation was high at lower levels of external columns and no carbonation was evident at the inner columns. The reason for higher carbonation at the lower levels of column is the structural cracking and the conjugal higher permeability. It can be inferred that, structural instability in the columns lead to the cracks, which further increased the carbonation, chloride diffusion, leading to corrosion of rebars, expansion and spallation.

VII.16 Quality Assurance and Non-destructive Examination for FBRs and Fuel Recycle Projects

Quality assurance activities ensures the quality requirements specified in technical specifications right from raw material inspection at procurement stage to final integrity tests of fabricated components. Non-destructive examination includes RT, UT, HLT and measurements of geometric features using optical alignment techniques. The QA & NDE works executed in 2020 are shown in the Pie chart (Figure 1).

QA & inspection activities were executed during fabrication of the following components: of Nickel detectors of PFBR (12 numbers Figure 2), ALIP ducts (4 numbers) transfer arm guide & rails (2 numbers), guard pipe spool (4 sets) for IHX & DHX nozzles large diameter wear rings (4 numbers), hexagonal lower guide rail assembly (2 numbers), VT, surface & core hardness (15 numbers) of LRP bearing balls (Figure 3) made of ASTM A 295, 1 number of DSRDM & CSRDM, 160 m length of cold drawn seamless nickel tubes and fluorescent penetrant examination on 15 numbers of EB₄C pellet specimens, sodium sampler and vacuum pot for STC, Special glove box (Figure 4), sodium expansion tank and electrolyser for Direct Oxide Electro Reduction (DOER) projects.

For PRP, 14 numbers of SG nozzles were tested for their chemical composition using XRF, 14 nos. of tanks for Waste Tank Farm (WTF) and 38 numbers of cylindrical tanks & 8 numbers of annular tanks for FRFCF. Established UT technique for corner joints (Figure 5) and used special fixtures and copper chills with water cooling arrangement (Figure 6) to maintain annular gap in annular tanks by controlling weld distortion.

Radiography examination using X Ray were carried out for a) explosive weld joints developed for FBR steam

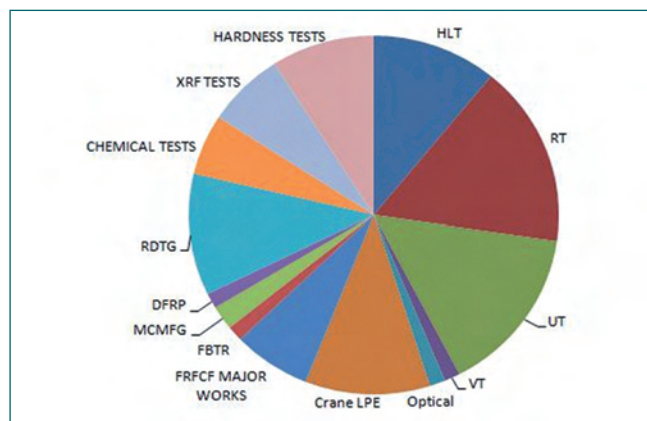


Fig. 1 The QA & NDE works executed

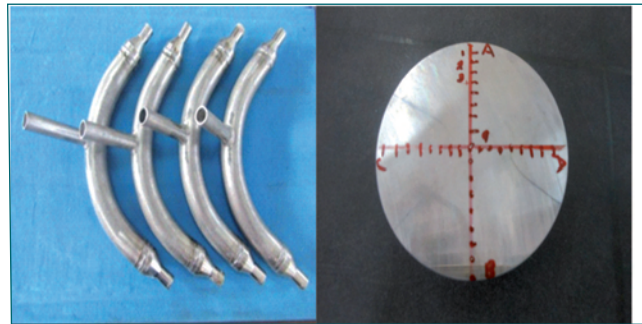


Fig. 2 Nickel detectors

Fig. 3 LRB bearing balls



Fig. 4 Special stainless steel glove box

generator tube plugging, b) yttria pellets for stack level measurement, digital radiographic inspection of sodium pressure measurement devices (SPMD) for sodium void measurements. For FBTR, detection of sodium level in indirect temperature monitoring devices.

Ultrasonic examination on 4 numbers of foot to hexcan welds of PFBR fuel subassemblies (FSA) were conducted using phased array ultrasonic examination (PAUT) method at IFS building.

Evaluated stellite hard faced sleeves of control rod & sheath assembly for FBTR using Immersion ultrasonic testing. Helium leak tests under vacuum were conducted on nickel diffuser assemblies of PFBR and D9 end plug welds for the weld qualification. Measured horizontality



Fig. 5 UT of corner Joints



Fig. 6 Fixtures & copper chills

of LRP bottom raceway of PFBR using optical alignment telescopes.

During Covid-19 pandemic, inspections were carried out on video conferencing mode and also by personal visits.

Cell shielding unit and lead cask (Figure 7) compensatory shielding unit, economizer for cold trap (Figure 8), sodium to air heat exchanger, fire alarm system and high temperature sintering furnaces were inspected.



Fig. 7 Lead cask

Fig. 8 Economizer for cold trap

VII.17 Remotely Operable Dry Chemical Powder Dispenser for Sodium Fire Extinguishment

In case of sodium leak, the leaked sodium may catch fire in pool, spray or combined mode and lead to production of smoke, flame and heat. The smoke released during sodium combustion contains oxides of sodium which are toxic and corrosive in nature. Hence, quick mitigation of sodium fire is a necessity. Manual extinguishment of sodium fire using dry chemical powder (DCP) is difficult due to the presence of dense smoke of sodium combustion aerosol and the sodium fire extinguishant has to be operated from a long distance to avoid aerosol inhalation. Hence, a remotely operable DCP dispenser system has been developed (Figure 1).

The system comprises of a mobile chassis, DCP dispensing module, data monitoring and control module. The chassis comprises of 4 wheels, DC motors, DC batteries, sensors, camera and control unit. Nitrogen gas is used for dispensing of DCP instead of compressed CO₂ to prevent secondary fire due to decomposition of CO₂. The nitrogen cylinder provided with double stage pressure regulator is maintained at 10 bar pressure. Commercially available DCP fire extinguishant unit (9 kg capacity) is suitably modified with solenoid valve control. The DCP dispenser unit consists of a conventional DCP extinguishant without cartridge. The lid is suitably modified with a nitrogen gas inlet and DCP outlet. DCP delivery pipe with crank rocker mechanism is provided for horizontal arm movement. An expander cone is provided at the end of delivery pipe for smooth delivery of DCP over burning sodium. A joystick was used for

its navigation near the fire. A push button based drive was used for solenoid valve ON/OFF control. Obstacle sensor, temperature sensor and Pi optical camera are mounted on the mobile chassis. A Raspberry Pi processor based data logging and monitoring system is built. Communication for sensor data logging and video surveillance between PC and remotely operated sodium fire extinguishment system is done by VNC (Virtual Network Computing).

The performance of the system was evaluated by testing in MINA facility. This facility consists of a leak tight stainless steel lined steel chamber with 143 m³ volume. The steel door of MINA facility was closed and then sodium pool fire was generated in a hot plate by heating sodium (100 g) upto 340 °C. The DCP dispenser system was operated remotely and dispensed DCP smoothly and uniformly over the burning sodium from a distance of 0.5 m from the sodium fire. The wired programmed motion control module worked effectively for positioning the mobile chassis near the sodium fire (pool) and the arm of the dispenser smoothly dispensed DCP effectively over the sodium fire. The image captured during the extinguishment of sodium fire using the indigenously developed remotely operable DCP dispenser system is shown in Figure 2. After extinguishing the sodium fire, the dispenser was retrieved back without any damages. Integration of intelligent onboard sensors in the mobile chassis is in progress.



Fig. 1 Remotely operable DCP dispenser



Fig. 2 Sodium fire extinguishment captured by camera in the mobile chassis

VII.18 Industrial and Fire Safety Activities

Industrial and Fire Safety Section assists IGCAR management for fulfilling its obligations, statutory & concerning prevention of personal injuries by maintaining safe work environment. Industrial & Fire safety inspections and physical hazard surveillance are being carried out on regular basis. The quality & usage of personal protective equipment provided to all workers conforming to relevant Indian Standards.

To ensure worker's safety and health at work, all the workers has been trained as per AERB recommendation. In 2020, as per AERB guidelines, 60 departmental employees, 111 trainees (CAT I & CAT 2) and 414 contract workers are trained in industrial and fire safety. Height pass system for work at heights more than 2.5 m above ground or below floor level has been established and 232 workers had undergone height pass test (Figure 1).

Safety surveillance was made in all construction sites on regular basis and the safety related deficiencies observed at the construction site are communicated to the respective engineer-in-charge in the form of Safety Related Deficiency Report (SRDR) for taking prompt action against it and ensuring the safety in the work environment. In 2020, a total number of 44 SRDRs were issued. As a part of hierarchy in control of hazard, safety work permit system is implemented for critical activities in construction site and issued after physical verifying at the site. Totally 141 safety work permits of different nature were issued.

Physical hazard (Noise & Illumination level) surveillance and industrial hygiene surveillance were carried out in various facilities of IGCAR. One industrial and fire safety training program was conducted for departmental employees (Figure 2).

All material handling equipments (MHE) are being examined by competent person once in a year for its

structural integrity and functionality as per Rule 35 of AEFR, 1996. 25 numbers of MHE's were tested in this period. In-service inspections (Non-destructive examination and hydrostatic pressure test) of 11 numbers of pressure vessels were carried out.

In IGCAR, about 3050 numbers of portable first aid fire extinguishers of various types and capacities are installed in all facilities. They are maintained once in three months to check their healthiness and also to meet regulatory requirements as per IS:2190 requirement. Fire drills are carried out regularly to assess the responses and any lapses found therein. In 2020, total number of 10 drills was conducted.

As per the Factories Act-1948 and Atomic Energy (Factories) Rules-1996, root cause analysis and corrective actions are taken to prevent recurrence of accidents. All reportable accidents are reported to AERB. Accidents statistics for the year 2020 is given below.

Periodic medical examinations for radiation workers are conducted in coordination with Occupational Health Centre, IGCAR as per AERB guidelines. Thermal Health Screening of employees is conducted in connection with COVID 19 pandemic along with the Medical Officer, IGCAR. As a part of COVID-19 management, vitals of mild and positive cases are being monitored in COVID Care Centre in Anupuram and Facility Quarantine Centre in both Anupuram and Kalpakkam Townships.

During Covid-19 Pandemic, hand sanitizers are prepared in-house and distributed to all the facilities/laboratories in IGCAR. Periodic sanitation of buildings, CISF main gates, buses and all department & hired light vehicles are executed.

Year 2020	Reportable	Non reportable	Near miss	Fatal	Fire accidents
No. of accidents	2	1	1	0	1



Fig. 1 Training for height pass test



Fig. 2 Training for fire fighting

VII.19 Role of Media in Positive Publicity of Nuclear Energy

Media publicity is a tool to ensure the visibility of Department of Atomic Energy Activities and its services to the public. During 2019-20, few press meets were organised to highlight various programs of the department and 19 press releases were made. Few of the events covered by various Media in 2020 are listed below.

Media coverage of Check dam across Palar

Press tour and press release was organized for the inauguration of Check dam across Palar river. Wide publicity was given for this event and various media houses were invited to the site of check dam to emphasize upon the fact that our department is actively involved in CSR activities for the surrounding villages. Overwhelming media responses were received on this. Figure 1 shows the completed construction of dam visited by the journalists.

Swatchtha Pakhwada

Press tour is conducted every year to spread awareness on cleanliness practised in DAE as part of the 'Swachhta Pakhwada'. Media team was taken around DAE townships to see the different initiatives of DAE for a cleaner township. We have received wide covering on these events from various media houses.

Inauguration of Incubation Centre

Press invites and press release was organised for the inaugural function of IC-IGCAR at Anupuram. Due to Pandemic, remote online video conferencing press meet was organized for the first time in the inaugural function of Incubation Centre (Figure 2). About 16 Media persons attended the meet in person and 10 attended via video conferencing. Wide publicity was given through news coverage in electronic and print media.

Media publicity of off-site & Site emergency drill conducted for neighbourhood villages

Press release of off-site emergency drill, conducted in the neighbourhood of Kalpakkam by evacuating the surrounding villages in coordination with state machinery was widely publicised through wide press coverage. The surprise site emergency conducted at Kalpakkam plant



Fig. 1 Visit of media team to check dam site



Fig. 2 Press meet during inauguration of Incubation Centre

site during Pandemic was also given wide coverage. This news has been given as press release to all media houses to emphasize how our department systematically holds such exercises for emergency preparedness (Figure 3).

Preparedness of MAPS unit 2 for Nivar Cyclone

Madras Atomic Power station (MAPS) had issued press release mentioning that unit no.2 was operating at its full capacity of 220MW. All the plant systems were operating normal and were expected to successfully withstand the impact of Cyclone Nivar, when it crosses the coast. The release mentioned about the cyclone protection machinery of MAPS being activated and all the preparedness measures including placing sandbags on the coastal side, clearing of storm drains, and inspection of plant buildings and structures being completed. This news on preparedness to face the cyclone was a shot in the arm for the safety & reliability of Nuclear power plants.

The most important use of any medium is that it's an opportunity for our organisation to highlight our activities and to garner the public acceptance of Nuclear energy in general. This helps in instilling confidence in the minds of the public about positive application of Nuclear energy and its benefits to the society.

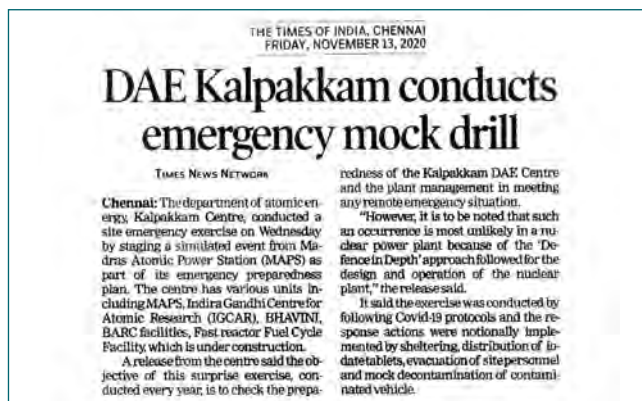


Fig. 3 Media coverage during on site emergency exercise

VII.20 Digitally Transformed Research Library

Scientific Information Resource Division (SIRD) is providing information resources to the scientific, academic and administrative fraternities of DAE campus at Kalpakkam, including IGCAR, BARC(F), MAPS and HBNI. It has an extensive collection of resources, including 62,000 books, 48,000 back volumes, 550 e-journals, 15,000 standards and two lakh technical reports.

SIRD has facilitated the Remote Access to IGCAR Subscribed E-resources (RAISE) facility through a mobile app, which can be accessed via individual desktops or smartphones of the registered users on a 24/7 basis anywhere off the campus (Figure 1). RAISE allows an authorized user to discover the journals in the field of interest, to organize the articles of choice in the user's mobile or laptop and to download & read the articles offline anytime. The user can also share the link to another registered user. Book marking, read aloud the highlighted text of the articles, voice to text search, auto sync across the gadgets, etc. are some of the additional features of RAISE. Usage statistics is available with admin users of RAISE. It is presently made available to Research Scholars.

During the pandemic period, SIRD has put maximum efforts to run the library smoothly. Circulation activities were carried out without a break. Library premises were sanitized and counter operations were continued as per Covid-19 protocols. Continuous plagiarism checks to keep research outputs high was effectively accomplished by SIRD. With physical access to the campus restricted due to the pandemic, SIRD proactively provided remote access to its e-resources, including the Royal Society of Chemistry, Proquest, Institute of Physics, Springer nature and Scifinder.

The library portal was revamped to act as the gateway to the resources and services available at the library. The new WebOPAC includes single window access to all the holdings, online reservations/renewal/purchase suggestions, auto linking of cover image and table of content pages from Google books or Amazon. Other features of the portal include discovery tools, e-Resource

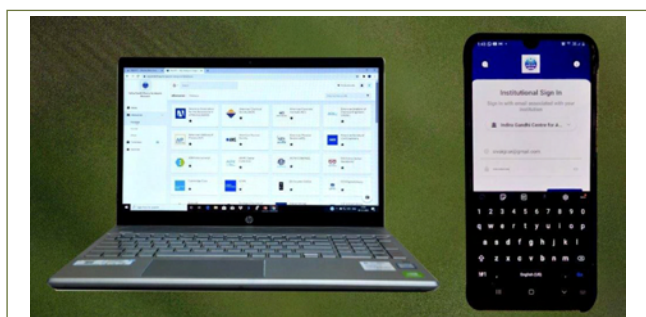


Fig. 1 Access to RAISE on mobile and web platforms



Fig. 2 Library gateway portal (Vaigai)

retrieval gateways, scholarly assistance tools like Grammarly, citation databases, plagiarism tools, etc. Online Services include work flow management of copiers maintenance with user approvals and invoice generation, online requisition to auditorium facility, similarity checking, reprography, publication, photography, etc. Additionally, auditorium events and up-to-date booking status are made available in the portal. The e-books are organized based on subjects/publishers and linked in the Web OPAC (Figure 2).

Centralized institutional repository including the publications by IGCAR collated by SIRD, news clips on DAE from newspapers, theses submitted by Research Scholars, in-house publications like Annual Report, Newsletters and IGC Reports are being continuously augmented.

Research contributions of IGCAR were analyzed using citation databases like Scopus, Web of Science and Google Scholar and H-Indices were generated for organization and groups for publishing in annual report and PRIS. Subscriptions and renewals of resources were continued including print/e-journals, e-books, e-standards, abstracting databases and various research assistance tools.

To promote the public and academic libraries in the neighborhood, SIRD in association with the Madras Library Association - Kalpakkam Chapter organized a free workshop on "RFID Technology for Library" on the February 19, 2020 at Kalpakkam. Sixty delegates attended the workshop and benefitted by the experts talks from SIRD in the field of RFID technology, KOHA based Library Management System and Digital Library. SIRD commemorated the National Librarians Day (12th of August) by showcasing posters detailing the extensive resources and services offered by SIRD.

SIRD has recorded in the form of short films on events which included whole body count, Hindi scientific seminar, demo of hot cell operation, thermal scanning and monitoring, incubation centre inauguration and press meet to name a few.

VII.21 Implementation of Budget Automation System (DAEBAS) for DAE Units

The budget proposals for Revised Estimate (RE) for current financial year and Budget Estimates (BE) for next financial year are called for from respective DAE units by Budget Planning Office, DAE. Earlier, the data was collected and compiled manually in excel spread sheets at DAE level for submitting to Secretary DAE / Chairman AEC, Member (Finance) AEC and to Ministry of Finance for obtaining approval of the Parliament. The entire work of collection, compilation, checking & validation and preparation of various formats for submission to authorities for approval were done manually.

DAE Budget Automation System:

The manual process of data collection was tedious and prone to error. Though the budget was called for in a prescribed format, at times, the format submitted by the DAE Units was different from that sought by DAE. In order to overcome these issues, the DAE Budget Automation System (DAEBAS) has been developed and implemented over Anunet. (Figure 1)

Need for DAE Budget Automation System

The new system automates the entire budget cycle, viz. (Figure 2)

- (1) Online submission of Budget proposals by Units and report generation,
- (2) Budget processing at DAE
- (3) Generation of various MIS reports for submission to authorities for review and finalization of budget
- (4) Submission of proposals in the format of Statement of Expenditure budget (SBEs) to Ministry of Finance for approval
- (5) Intimation of ceilings/approvals to all Units for submission of revised break up for approved RE / BE

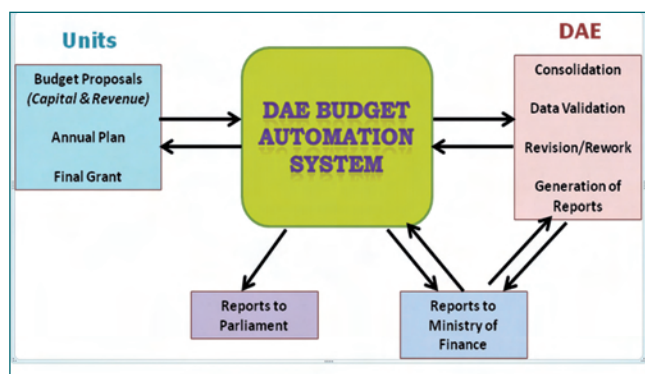


Fig. 1 DAE budget automation system

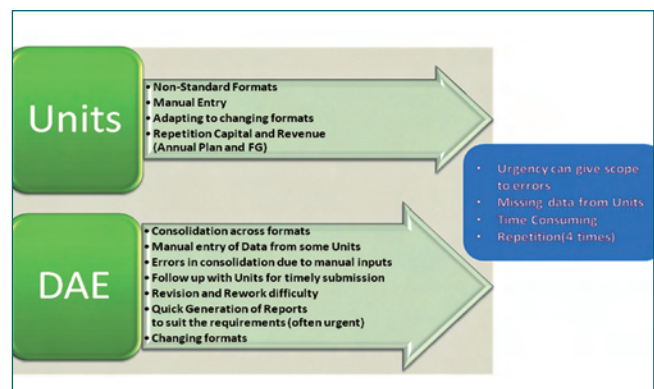


Fig. 2 Need for DAE budget automation system

- (6) Generation of reports for excess/savings against different sub head levels for approval of Secretary DAE / Member (Finance) AEC / Ministry of Finance
- (7) Generation of reports for Re-appropriations (re allocation of savings / surrenders to different Units / Head of Accounts under Capital / Revenue section)
- (8) Generation of reports for “Surrenders” (list of items under which unspent funds surrendered to Ministry of Finance)
- (9) Preparation of Demands for grants along with annexure in the prescribed format for printing and submission to the Parliament for approval
- (10) Generation of various reports as part of Management Information System.

Flow sheet of Finalization of Budget

- (i) Request by DAE to its Units to submit their budget requirement in the month of July every year
- (ii) Compilation and consolidation of data at DAE
- (iii) DAE budget section to convey the respective units to submit revised Budget proposal, in case of any change
- (iv) DAE would submit budget proposal to Ministry of Finance for its approval
- (v) The amount sanctioned by the Finance Ministry would be intimated to the Units for submitting the breakup for the approved budget.
- (vi) Budget Monitoring would be done at DAE.

Features of DAEBAS:

System Security:

- DAE Budget Automation System is deployed through ANUNET

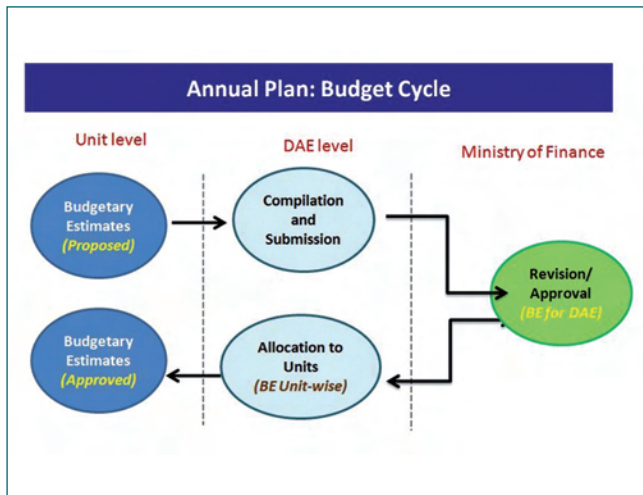


Fig. 3 Budget cycle

- ▶ Within IGCAR, access is restricted based on the IP address
- ▶ Anti-virus software is installed in server to prevent detect and remove malware

Authentication:

- ▶ Access is only for authorized users with valid credentials
- ▶ Only a DAE Administrator can create an User id and set password

System Data Backup:

- ▶ Automatic backup of complete Database daily .
- ▶ Database backup files are in another system in a different location for redundancy.

Benefits of the DAE Budget Automation System:

- ▶ Online data collection eliminates the need for repeated data entry
- ▶ Role based system - Each user has an access relevant to their role (facilitated by taking to a screen giving appropriate access)
- ▶ Adopting of Master Database reduces errors
- ▶ Automatic validation of proposed budget (RE / BE) – Comparison made with the Sanctioned cost of the Capital Project.
- ▶ Generation of statutory formats / reports
 - by units for submission to DAE
 - & in turn by DAE to Audit, Ministry of Finance and Parliament
- ▶ Automation of consolidation / compilation process

- ▶ MIS reports to monitor periodical progress review
- ▶ Monitoring of data-entry activity of units and provision for final submission by Units (automatic closure of entry provision after the cut-off date)
- ▶ Rework / resubmission feature by enabling “edit option”
- ▶ Provision for minor alterations in the program for “quick generation of consolidated reports”
- ▶ User friendly screens – menu based operation
- ▶ Provision made for accurate calculation of Pay, DA, TA & HRA with automatic calculation of Annual Increment etc.

The budget cycle work flow for the annual plan is shown in the Figure 3.

Screens from the DAEBAS system:

Establishment Budget Entry:

Establishment module is very useful in calculating the Salary component of the unit precisely, as it enables to calculate the increment component for any pay level for all the four categories (Scientific, Technical, Admin, Auxiliary) of employees separately.

Also it is useful in calculating DA, HRA, TA, PRIS, update allowance, etc., more accurately.

Revenue Budget Entry:

This module is useful in submitting Revenue budget (RE and BE) requirement for the unit. The provision is given to enter the reason for variation in case of any.

Additional Requirements in the DAEBAS:

A provision to generate various MIS reports (~30 nos.) has been provided to the DAE budget section to monitor the periodical progress and for various review meetings.

These reports were very useful for giving inputs for the meeting with various senior authorities at DAE for efficient budget monitoring.

The automation of Budget process at DAE by implementation of DAEBAS has resulted in the elimination of data re-entry at DAE, improved accuracy of information, aided quick decision making, avoided manual checking & validation of voluminous data submitted by various Units and has enabled adherence to timelines fixed by Ministry of Finance, etc.

VII.22 Procedure for Formulation of New Capital Projects at IGCAR

At IGCAR, various R&D facilities, laboratories and allied infrastructure are set up using the funds obtained through capital projects. The Salary and Operation & Maintenance (O&M) of the facilities are funded through Revenue Budget. The Department obtains the funds from Ministry of Finance, GoI and allocates to various units for executing the projects-creation of assets and for O&M. At present there are 18 projects, continuing from earlier plan period (12th Plan) and 18 new apex projects formulated under the Vision Schemes of DAE. The procedure involved in formulation of new capital projects at IGCAR has been enumerated in this article.

Formulation of Capital Projects:

During the final year of any of the ongoing plan/ vision period, directives would be issued by DAE to all Units to formulate & submit new/fresh project proposals with the recommendation of Unit Council & Vision Subcommittee concerned. Earlier, this exercise was carried by Planning Commission as “five-year Plan”. Later NITI Aayog (National Institution for Transforming India) was established and the 5-year plans have been replaced by rolling-plans in which new projects can be formulated anytime, based on the need. In line with this, DAE has identified/framed 11 Vision Schemes under which the new projects has to be formulated. There are 10 sub-committees formed to review the new project proposals and recommend them to the apex Project Appraisal Committee (PAC), DAE. The Vision sub-committees are mandated to appraise the projects and submit periodical report to PAC.

As per NITI Aayog directive, all the new projects of DAE are to be approved in-principle by Atomic Energy Commission (AEC). New programmes envisaged to be taken up shall have Short-term (3years), Medium term (5years) and long term (15 years) deliverables. At present, the projects for realising short-term (3 years) objectives are taken up for approval by DAE. Most of the projects of IGCAR would be covered under the Vision Scheme No.3 – Fast Reactor and Back-End Fuel Cycle for the Second Stage of Nuclear Power Programme.

Within IGCAR, new projects are called for from various Groups. New requirements / gap-areas are identified with their corresponding time schedule and cost details are firmed up.

After the initial approval at the group level, preliminary discussions with Group Directors and senior officials would be held by the IGCSG, under the chairmanship of Director, IGCAR. During review, objectives of the

project, executing agency, expected deliverables/ output, estimated cost of the projects would be discussed in detail and suggestions for improvements, if necessary, would be made. Greenfield projects and projects for setting-up of large facilities/ plants may also include funds for salary proposed for additional manpower sought.

After initial reviews, the projects are submitted for in-principle approval by AEC. Subsequently, the Detailed Project Report (DPR) in the prescribed format is prepared for each project with completion date / tenure as $T_0 + X$ months, where T_0 represents the date of sanction of the project and X represents the number of months.

The Apex projects so proposed may have one or more sub projects. A senior level official is identified as Project Coordinator for each apex project and sub projects, and would be responsible for achieving the specified objectives within the time and cost limits. The yearly phasing of expenditure would also be provided in the DPR.

The project requirements are critically reviewed at each level with a view to optimise the resources Viz. Plant / Machinery / Human Resource / Funds. The projects with overlapping nature or similar objectives are combined for effective implementation.

All the project proposals need to obtain Vision Subcommittee recommendation and are further scrutinized by the PAC under the chairmanship of Director, BARC and ad-hoc specialist committees constituted by PAC, as per the need. The approved proposals along with the recommendation from the PAC are submitted to DAE for obtaining financial sanction. Secretary, DAE only has the powers to accord financial sanction to any new project. Invariably, all the proposals shall be submitted with the approval of Internal Finance & Unit Head. The various sequential stages for project formulation & approval is shown in Figure 1.

Classification of Expenditure

As per the Government of India accounting requirement, the estimated cost of the project requires to be accounted/ divided into Machinery & Equipment (M&E), Supplies & Materials (S&M), Major Works (MW- Civil, Electrical, AC&V works & Mechanical works, Cost of land), Salaries, Domestic Travel (DTE), Foreign Travel (FTE), Office expenses (OE), motor vehicles (MV), consultancy / collaborations (PS), Contingency expenditure etc.

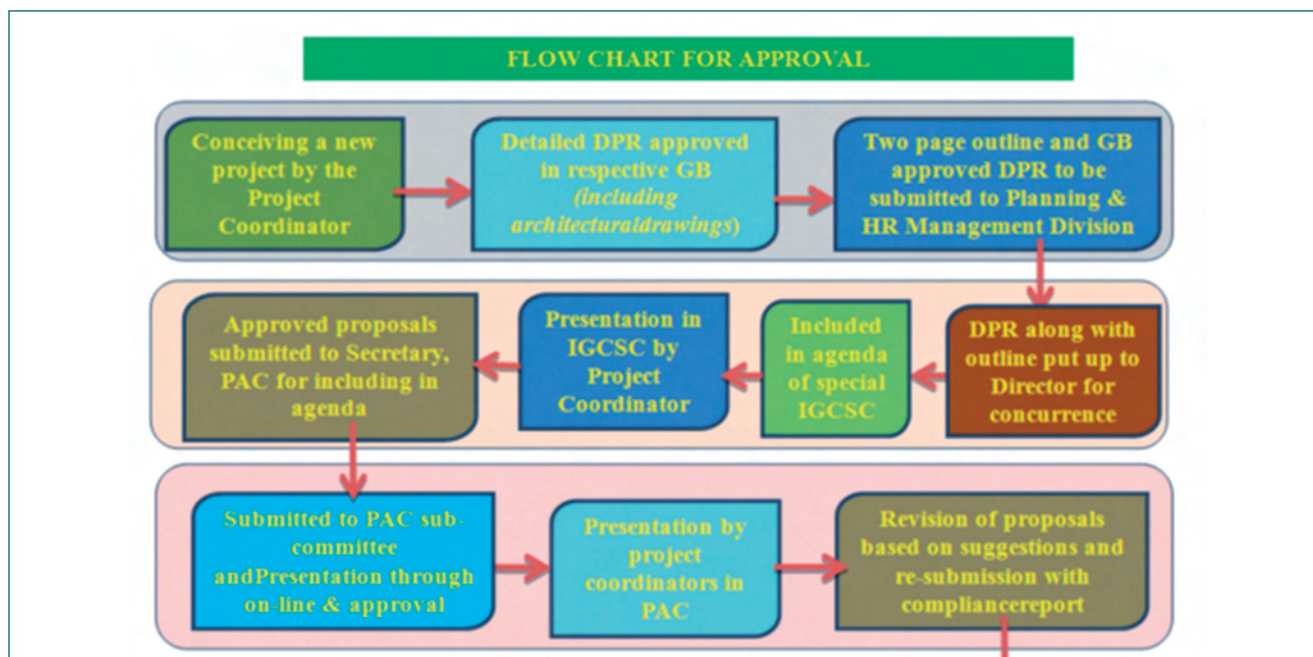


Fig. 1 Flow sheet for project approval

Financial Sanction & Project Implementation

After scrutiny at DAE, financial sanction for the project is accorded by the competent authority based on the estimated cost of the project. Once the financial sanction is obtained for a project, the apex project coordinator and the respective DAE unit would be responsible for project implementation. No expenditure shall be incurred unless the financial sanction is accorded by the Department.

The project is implemented through procurements and execution of works contracts. Also the professional services / consultancy contracts are awarded.

Internally, the project would be reviewed by respective Group Boards / IGCSC with emphasis on timely implementation.. Periodical review would be undertaken by Vision sub-committee and PAC.

Budget allocation

Upon financial sanction, the funds for implementation of projects will be allocated through annual budgets being presented by the Finance Minister in the Parliament for the ensuing Financial Year (April – March). The funds allocated by Government to the Department are then allocated to various Units & Projects by DAE. The initial fund allocation is called Budget Estimate (BE) and is allocated before commencement of a financial year. During the currency of the financial year, based on the periodical reviews, a revised budget is proposed / approved, called Revised Estimates (RE). The funds so allocated at BE stage may be increased or decreased based on the project progress by the respective unit head at RE stage.

Also additional funds can be obtained or surrendered at Final Grant (FG) stage, normally by end of 3rd quarter (December).

Project Completion

The execution of projects within the scheduled date of completion and sanctioned cost is of essence. In case of deviations in respect of project parameters like cost, time or scope / objective, a proposal for revision needs to be submitted, which shall be approved by all the authorities discussed earlier for approving a new project. Upon completion of the project, a report in the prescribed format shall be submitted by the project coordinator to PAC with the approval of Internal Finance and the Unit Head. The completion report will be discussed at PAC meeting and its observations will be recorded.

Role of Planning & Human Resource Management Division (PHRMD)

PHRMD is acting as a nodal agency in IGCAR with respect to formulation of capital projects and plays an active role in every stage since project conceptualisation until project completion and thereafter replying to Audit queries relating to the Projects. PHRMD is coordinating with the Project authorities within IGCAR, the Vision Sub-committees, apex PAC and DAE (R&D Section) for obtaining the financial sanction. Towards annual budget allocation and utilisation, PHRMD coordinates with IGCAR Accounts, Stores, MRPU / MRAU and DAE (Budget Section). Regular budget monitoring and assessment is done at PHRMD towards submission of BE / RE / FG and annual plans. PHRMD is also involved in preparation & submission of suitable replies to Audit Queries (IIW/ C&AG Audits) and the Parliament questions relating to Capital Projects.

The various R&D programmes of IGCAR and related infrastructure development activities are carried out, under various capital projects at IGCAR

VII.23 Biodiversity Documentation at the DAE Complex

Scientific Information Resource Division (SIRD) of IGCAR has documented the avian fauna of the DAE campus in Kalpakkam and in association with Salim Ali Centre for Ornithology and Natural History (SACON), has identified the bird species and classified them.



Fig. 1 Peafowl

This year, the peafowl (Figure 1) numbers have increased on the campus.



Fig. 2 Rosy starling

Rosy starling (Figure 2), a migrant species, visited in thousands and was spotted on every tree on campus.



Fig. 3 Blyth reeds warbler

Blyth's reed warbler (Figure 3) was another species recorded for the first time. It is significant to note that Blyth's reed warbler is listed under special migrants by SACON and Department of Environment, Tamilnadu in state of India's birds' book.

In 2020, SIRD started documentation of butterflies in the campus.

Butterflies are great bio-indicators of an ecosystem as they are susceptible to environmental conditions such as temperature, sunlight, humidity, and rainfall patterns. Their presence, patterns, and migration assist in mapping the climatic health of a region, and they are perhaps the most studied insect group across the world.



Fig. 4 Butterfly poster

September 2020 was declared as the butterfly month by the Tamilnadu government. SIRD has brought out a poster (Figure 4) on Butterfly documentation activity in the DAE complex of Kalpakkam.

Documentation of Butterflies is challenging due to the

random and fast movement of butterflies without specific patterns. SIRD has so far documented 66 species.

Butterfly abundance and diversity patterns are directly related to the availability of vegetation forms. DAE campus at Kalpakkam has more than 40 different species of butterflies in a single area, which is indicative of a Butterfly Hotspot.



Fig. 5 *Small Cupid*

The butterflies found in the DAE complex may be attributed to the dense vegetation found within the complex. Wild cattle and pigs available on the campus indicate the availability of minerals necessary during the butterflies' reproduction phase. Among the butterflies recorded, the smallest is Small Cupid (Figure 5) at 20mm, and the largest is Blue Mormon (Figure 6) at 12-20cm in length.



Fig. 6 *Blue Mormon*

Butterflies are classified into three super families called the True butterflies, Moths, and Skippers. SIRD has recorded 56 True butterflies, 5 Moths, and 5 Skippers.



Fig. 7 *Plain Tiger*

The prestigious Wynter-Blyth butterfly Association (WBA), from Nilgiris Tamilnadu, has chosen one of the photographs on butterflies, under the action category, from SIRD IGCAR, for its 2021 calendar through an open competition shown in the Figure 7.

Few other butterflies captured through lens of the IGCAR photographer includes peacock pansy (Figure 8) and common silverline.

The Peacock Pansy derives its common name from

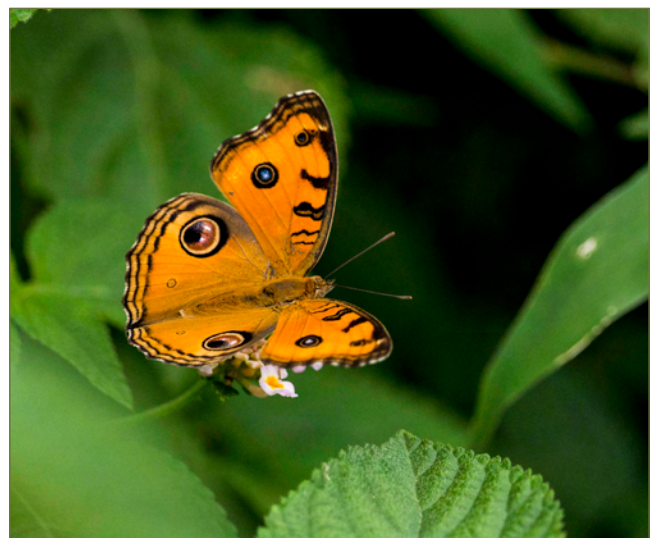


Fig. 8 *Peacock Pansy*

the prominent spots on its wings. Peacock Pansy butterfly (Figure 8) has a bright orange upper side with conspicuous eyespots on the hindwings. Its mostly available in the grassy area like in front of SDL lab, Helipod area, WIP Marsh, etc.

The Common Silverline (Figure 9) is a small-sized,



Fig. 9 *Common Silverline*

colorful butterfly with orange and white bands lined with black. It has a prominent two hairy tails on the hindwing. A rare visitor of DAE kalpakkam complex spotted near SDL lab at IGCAR.

SIRD, IGCAR will continue the biodiversity documentation.

VII.24 FISH - Translocations for Retrospective Biodosimetry

Chromosomal translocations (TLs), the hallmark aberrations for retrospective biodosimetry, are detected using Fluorescence in situ hybridization (FISH) technique. Unlike dicentric chromosomes, translocations survive through mitosis and get passed on to the daughter cells successfully and this persistence makes them suitable for retrospective dose determination. International Atomic Energy Agency (IAEA) recommends that any laboratory intending to carry out biological dosimetry should establish its own Dose response Curve (DRC) to avoid inter-laboratory variation and associated uncertainty in dose estimation. Studies have been carried out in IGCAR to establish a FISH-TL DRC towards attaining retrospective biodosimetry capability. Besides, chromosome specific translocation frequencies were also determined to understand the relationship between chromosome size and number of aberrations formed upon radiation exposure.

Blood sample collected from a healthy individual was exposed to ^{137}Cs gamma radiation (0.1, 0.25, 0.5, 0.75, 1, 2, 3, 4 and 5 Gy) at 0.1 Gy/min dose rate. Then, samples were cultured, harvested and stained with FISH DNA probes (XCP Mix Metasystem cocktail of chromosome #1, #2 and #4 painted in red, green and yellow) following standard procedure as per IAEA guidelines (2011). Metaphase spreads were captured in Metafer microscope and scored for aberrations using the PAINT nomenclature.

The distribution pattern of translocations was analysed by standard u -test and found to follow Poisson distribution with u value ranging from -0.06 to -1.45 indicating uniform radiation exposure of samples. The FISH-translocation DRC was constructed for γ -rays considering all the dose points and was fitted by iteratively re-weighted least squares method using "Poly Fit" software (Figure 1). The curve obtained followed a

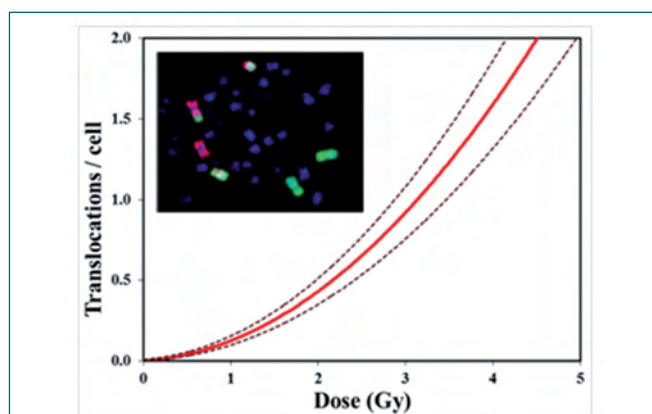


Fig. 1 FISH dose response curve for gamma radiation

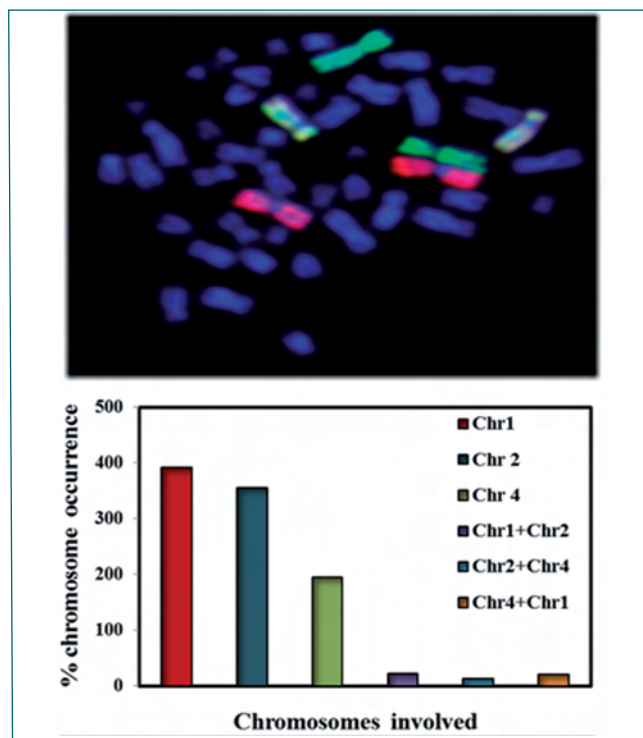


Fig. 2 Chromosome specific translocation frequency

linear-quadratic trend with α (linear) and β (quadratic) co-efficients as 0.0301 ± 0.005 and 0.0916 ± 0.0073 respectively. The goodness of fit was tested by Chi-square method and the value obtained was 9.44 against 14.067 for degrees of freedom 7 at $p < 0.05$. Blind test method was used to validate the dose response curve.

The chromosome specific translocation frequency data has been obtained at each dose points of dose response curve. It was observed that the involvement of chromosome 1 and chromosome 2 in radiation induced translocation formation is equal but significantly higher than that of chromosome 4 (Figure 2). This could be due to their relatively larger size since chromosomes with higher genome content may lead to higher probability of radiation hit thus resulting in more chromosomal aberrations. But the combinative involvement of chromosome 1&2, 1&4 and 2&4 show some deviation with respect to their genome size and frequency of translocations. These preferential translocations occurring between neighboring chromosomes might cause this deviation in the expected aberration frequency with respect to their genome content and size.

Dose response curve for chromosomal translocation induced by ^{137}Cs gamma rays at low dose rate has been established for population in southern part of India.

VII.25 Relative Biological Effectiveness for Alpha Particles

Accidental exposure of alpha particles in nuclear occupational workers would have detrimental health effects. In-depth understanding of biological effects of alpha particles and its comparison with sparsely ionizing radiations (X-rays or γ -rays) is an essential aspect to determine risk and subsequent health consequences. International Commission on Radiation Protection (ICRP) has assigned a value of 20 for Relative biological effectiveness (RBE) for alpha particles emitted from uranium, radon and americium relative to reference X-rays and gamma radiations to compare biological effects of ionizing radiations.

Although the value of RBE is 20, still uncertainty exists on actual RBE and it varies with respect to endpoint investigated, cell type chosen, reference radiation type, dose rate etc. To carry out experiments for studying alpha particle effects and owing to short path length and significant loss in energy of alpha particles in the atmosphere, it requires a specially designed system for alpha irradiation. BARC BIOALPHA, an alpha particle irradiator (Figure 1) with Am-241 source has been installed for carrying out radiobiological experiments. Dosimetry of alpha irradiator was performed using CR-39 detectors. As an initiative study to determine RBE, cytogenetic damage induced by Am-241 alpha radiation using Cytokinesis Blocked Micro-Nucleus (CBMN) assay was carried out and compared with Cs-137 gamma radiation as a reference radiation.

Irradiation of CR-39 discs (40 mm dia x 500 μ m thick) in BARC-BIOALPHA irradiator for different time durations (30 sec to 20 min) was done followed by chemical etching with 6N KOH (at 60°C for 5h) for tracks development. Scoring of tracks was done using Zeiss Imager M2. Results showed that the mean number of tracks increased with duration of irradiation. Energy of alpha particles reaching the target was calculated to be

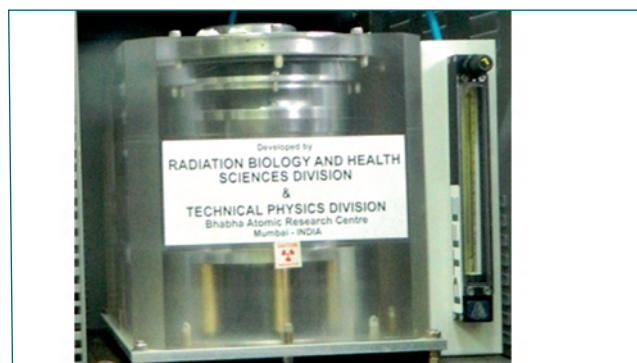


Fig. 1 BARC BIOALPHA irradiator

4.3 MeV (SRIM CODE). An average of 90 alpha tracks/cm²/sec was scored and the corresponding dose rate was calculated to be 54 mGy/h.

To determine the RBE value for α -particles by micronucleus (MN) induction in lymphocytes, peripheral blood samples were exposed to various doses of Am-241 alpha particles (0.01Gy to 0.1Gy) and Cs-137 gamma rays (as reference radiation, 0.1-2.0 Gy) and subjected to Cytokinesis Block Micro Nucleus (CBMN) assay. MN scoring in binucleated cells was done using Metafer microscope and dose responses were plotted using CABAS 2.0 & Polyfit softwares. RBE was calculated as a ratio between the linear coefficients of the dose response curves of alpha and gamma rays.

Baseline MN frequency obtained was 0.018 MN/cell which is in agreement with literature reports. Nuclear Division Index for both radiations were calculated to be 1.8 ± 0.08 indicating that cell proliferation was not affected by radiation doses. As expected a dose dependent increase in MN frequencies was observed for both ¹³⁷Cs gamma and ²⁴¹Am alpha radiations (Figure 2). The dose response pattern obtained was linear for ²⁴¹Am alpha radiation and linear-quadratic for ¹³⁷Cs gamma rays (Figure 3). The calculated RBE value for ²⁴¹Am alpha radiation is 6.2.

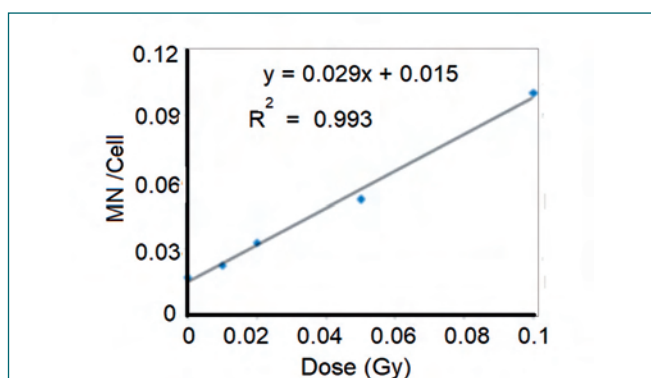


Fig. 2 Dose response for alpha radiation

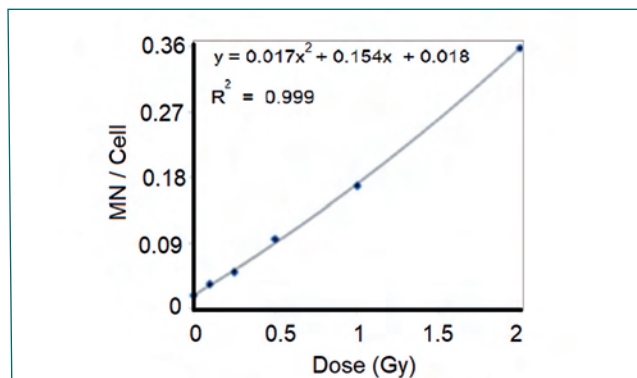


Fig. 3 Dose response for gamma radiation

VII.26 Marine Ecological Studies in and around Kalpakkam Coast and Southwestern Bay of Bengal

Marine ecological studies have become the limelight at the global as well as at the Indian scale. Indian coastal zone, particularly the peninsular region is highly diversified and Kalpakkam coastal waters. Coastal water quality along with biodiversity study of Kalpakkam coast is of great importance due to the existing and upcoming nuclear facilities as seawater is being used by power plants for a long time. Among different biodiversity components of this coastal water, the diversity of phytoplankton, zooplankton, macrobenthos, fish, and shellfish are given below.

- Phytoplankton - ~ 450 Species
- Zooplankton - ~ 230 Species
- Benthos - ~ 170 Species
- Fish and Shellfish - ~ 300 Species

Results on phytoplankton and zooplankton revealed that the post-Northeast (NE) monsoon and pre NE monsoon period were favorable for phytoplankton growth and proliferation followed by zooplankton (Figures 1a & 1b). It is hard to identify the phytoplankton species in a natural way; hence the species undergoes the process of acid cleaning for accurate identification (Figures 2a, 2b and 2c). Kalpakkam coastal water is highly nutrient-rich, which encounters frequent phytoplankton blooms i.e. outbursts of a single species or multiple species (Figure 2d and 2e).

The Kalpakkam coastal water is enriched with Zooplankton (Figures 2f&2g) and macrobenthos (Figures 2h & 2i) which are vital components for the water and sediment nutrient cycling in the marine milieu. Phyto and zooplankton

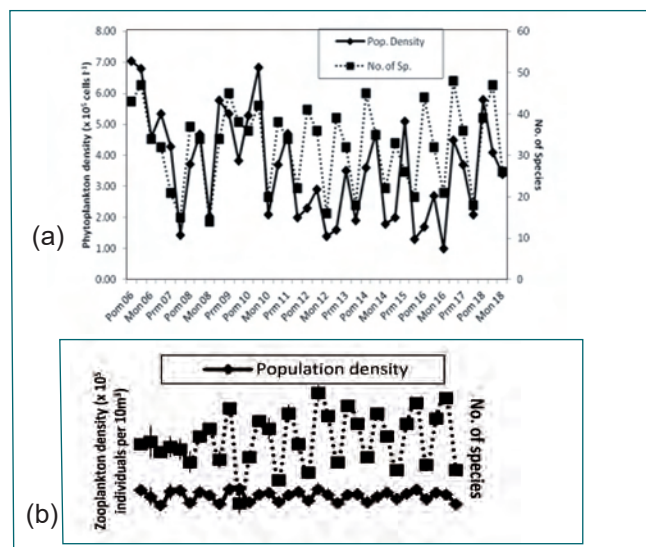


Fig. 1 Population density & diversity of (a) phytoplankton and (b) zooplankton

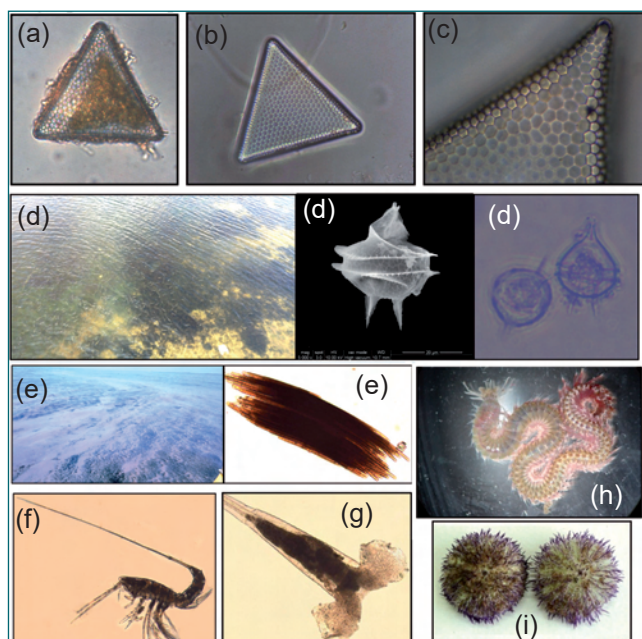


Fig. 2 Phytoplankton species (a) natural, (b&c) acid cleaned (*Triceratium favus*), (d) *Dinoflagellate Peridinium steinii* Bloom in Sadras backwater mouth (First record of *P. steinii* bloom from the World Ocean), (e) *Trichodesmium erythraeum* bloom, (f&g) Zooplankton (*Macrosetella gracilis* & (*Creceis acicula*) and (h&i) Macrobenthos (claw worm and purple sea urchin)

act as hosts to specific epibionts (Figures 3 a&b) (Growth of organisms on the body surface of phyto and zooplankton creating associations like, symbiotic, parasitic, commensalism etc.). Discovery of new variety of Fish and sand crab species (Figures 4a&b) proves high fertility of Kalpakkam coastal water.

Water and sediment quality studies are being carried out covering around 100 km² at twelve different locations.

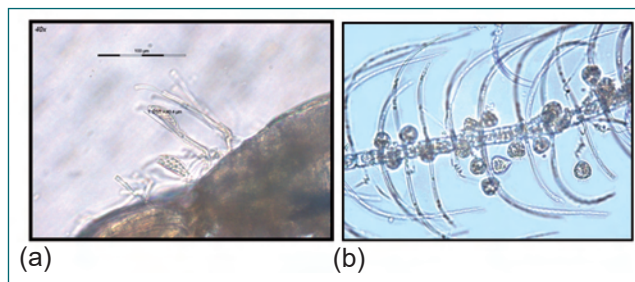


Fig. 3 Epibionts (a) Growth of *Pseudohimantidium pacificum* Hustedt & Krasske colonies on the exoskeleton of the copepod *Corycaeus Dana* and (b) Photographs of ciliate epibiont *Vorticella oceanica* showing attachment throughout the chain of diatom *Chaetoceros coarctatus* cells (First record in Indian Ocean)

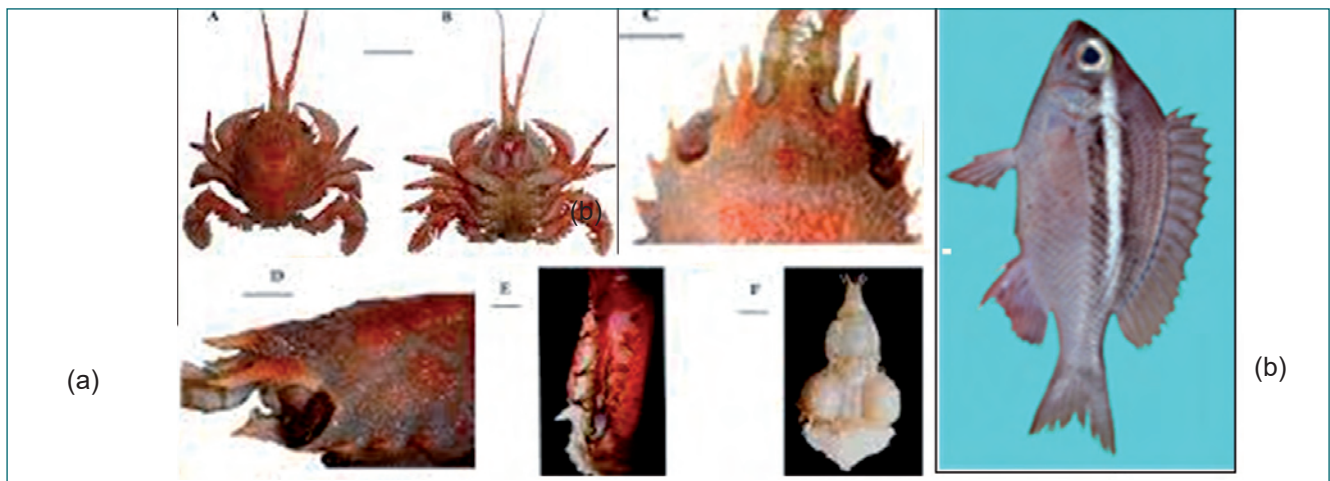


Fig. 4 (a) *Jonas kalpakkamensis* and (b) *Scolopsis igcarensis* (New species to the World)

Most of the water quality parameters revealed significant spatial and seasonal variability. The concentrations of nitrate, phosphate and silicate nutrients are higher in the bottom waters than the surface. Overall water quality was affected mainly by the NE-monsoon due to freshwater runoff from the backwater and rivers. Chlorophyll-a concentration was higher during summer in surface water and lower in bottom waters; the other seasons were contrasting from this pattern.

Heavy metal concentrations were measured in sediment (Figure 5) and edible fishes (Figure 6) from the Kalpakkam coast. Annual average of metals in sediment showed the following order: Al > Fe > Mn > Cr > Ni > Zn > Co > Cu > Pb > Cd. Seasonally, Al, Fe, Cu and Cd concentrations were relatively high during the post-monsoon period as compared to other seasons. Metals such as Mn, Ni, Zn and Pb were relatively high during monsoon season, indicating their external input.

Silt and clay fractions of the samples showed a positive correlation with the accumulation pattern of most of the metals. The geoaccumulation index, which denotes the

accumulation with respect to unpolluted reference values from earth cores, was negative for most of the metals with some unnatural accumulation of Cd in few cases. Pollution load index values were below 1 for most of the samples indicating low metal pollution at this location.

Metals in muscle tissue showed great variability among the fish species. Fe and Zn are the major contributing elements to the total metal content (70% of total metal) of 72 species of fishes. These two metals are the essential elements involved in many biological functions of the fishes as well as humans. Toxic elements such as Cd and Pb were found to be the least accumulating metals in fish. The study concludes that the ingestion of metals through the consumption of the studied fishes does not present any health risk to the average consumer.

The above observations indicated that Kalpakkam coast is relatively unpolluted and pristine, which boasts high biological diversity and needs continuous monitoring for future impact assessments.

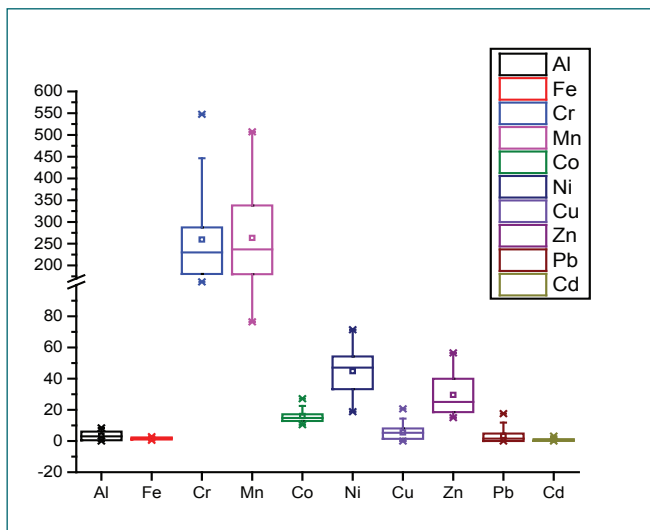


Fig. 5 Annual average of metals in the marine sediment at Kalpakkam coast

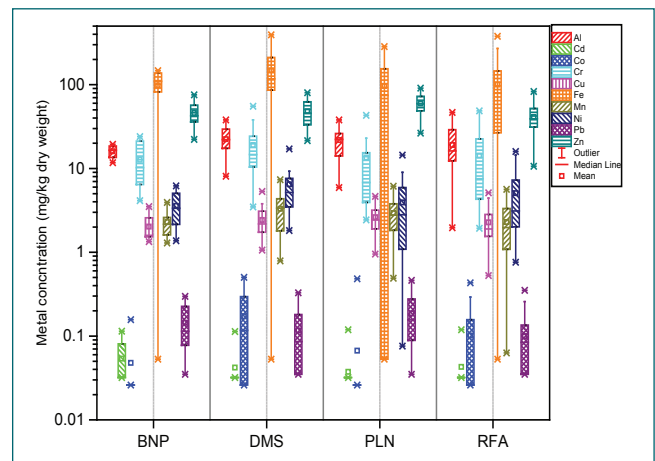


Fig. 6 Overview of metal concentrations in muscle tissue of marine fishes based on their habitat preference [BNP-Benthopelagic, DMS-Demersal, PLN-Pelagic-neritic, RFA-Reef associated]

CHAPTER VIII

Awards/Publications/
Events/Organisation

Awards & Honours

Dr. Arun Kumar Bhaduri, Distinguished Scientist & Director, IGCAR and **Dr. M. Vasudevan**, MMG are named in the World's top 2% Scientists Data Published by Stanford University, USA, 2020 in the Year 2019 Category

Dr. John Philip, MMG has been named in the World's top 2% Scientists Data Published by Stanford University, USA, 2020 in two categories - the Career Long and Year 2019.

Dr. John Philip, MMG has been elected as a Fellow of National Academy of Sciences.

Dr. M. Vasudevan, MMG has been selected as Editor, Transactions of the Indian Institute of Metals.

Dr. M. Vasudevan, MDTD has been selected as the Editorial Board member, International Journal of Pressure Vessels and Piping

Dr. Arup Das Gupta, MMG has been appointed as Managing Editor, Transactions of Indian Institute of Metals, Kolkata.

Shri. Surojit Ranoo received the Dr. K. V. Rao Scientific Society Annual Research Award (Runner up 1 for 2020) for the paper titled "Enhancement of heating efficiency in magnetic hyperthermia based cancer therapy upon in-situ orientation of magnetic nanofluids"

Dr. Hara Prasanna Tripathy, MMG, has been awarded the Young Scientist award for the year 2019 by Indian Thermal analysis Society (ITAS), Mumbai

Dr. Raj Narayan Hajra, MMG has been awarded the ITAS-SETARAM Calorimetry award for the year 2019 by Indian Thermal analysis Society (ITAS), Mumbai

Dr. Chanchal Ghosh, MMG has been awarded 'EMSI-Excellence in Microscopy' by Electron Microscopy Society of India, Bhopal

Ms. S. Sujee, SQRMG has been awarded Consolation Prize for Online Book Review Competition Conducted by Town Official Language Implementation Committee, Chennai

The Scientific Information Resource Division, SQRMG has been awarded the Library Commitment to Uncovering Real Impact Award for 2020 by Emerald Publishers, UK

Best Paper Awards

C. Anushree and John Philip

Synthesis of Water Based Fe₃O₄ Nanoparticles by Oxidation - Precipitation and its Application in Removal of Methylene Blue Dye

National Symposium on Recent Advances in Chemistry, (NSRAC 2020), February 18-19, 2020, Pondicherry University, Puducherry

R. Basu, and S. Dhara

Observation of cumulative spin-excitation in VO₂ using polarized TERS study

International Conference on Perspective of Vibration Spectroscopy.(ICOPVS-2020, Feb. 24-29) JNCASR, Bangalore

V. Sivasankar, E. Soundararajan and S. Rajeswari

Migration of Integrated Library Management System to KOHA : A Case Study of Scientific Information Resource Division

4th International Conference of Asian Libraries (ICAL-2020), February 26-28, 2020 Indian Institute of Management, Lucknow (IIML)

V. Sivasankar, E. Soundararajan and S. Rajeswari

Challenges and Impacts of RFID Technology in a Research Library

Springer International Conference on Communication Systems and Networks (ComNet 2019), December 12-13, 2019 Mar Baselios College of Engineering & Technology, Kerala

Best Poster Awards

International Conference on Nano Science and Technology (ICONSAT-2020), March 5-7, 2020 Biswa Bangla Convention Centre, New Town, Kolkata

S. Balasubramanian, K. Prabakar and S.R. Polaki

Surface enhanced microcantilever for ultrasensitive humidity sensing

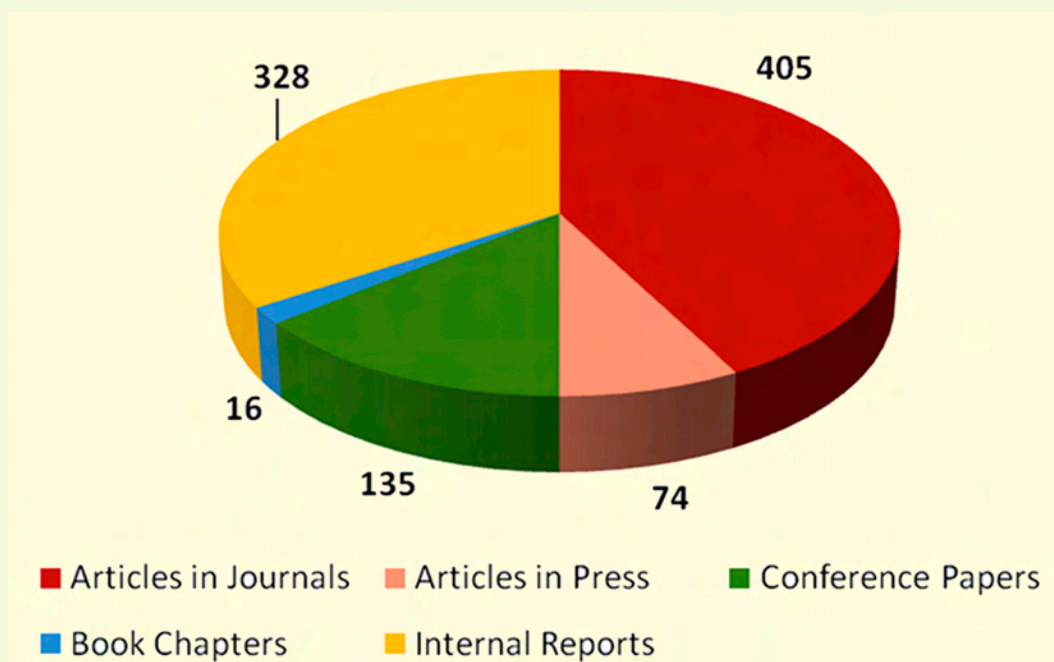
C. Abinash Bhuyan, Kishore K. Madapu, and S. Dhara

Large-Area Synthesis and Transfer of Monolayer MoS₂ onto Flexible Substrate

Dillip Kumar Mohapatra and John Philip

Effect of Magnetic Field Ramp Rate on Microstructure Formation in Magnetic Nanoemulsion

IGCAR Publications during the Year 2020



H-Index of IGCAR

Scopus : 104 | Web of Science : 98 | Google Scholar : 118

Events

Seminars, Workshops and Meetings

1. "ISNT Level II Certification Programme in Visual Testing", January 06-10, 2020
2. World Hindi Day Celebration - All India Hindi Scientific Seminar (AIHSS-2020) for Southern Regions, "Oorja Ke Kshetra Me Bharatiya Vigyan Evam Takniki Pragati", January 9-10, 2020,
3. "Theme Meeting on Advances in I&C Technologies, Computational Intelligence and Security Systems", January 29, 2020
4. "Swachhta Pakhwada" , February 16-28, 2020
5. Workshop on "Planning, Preparedness and Response to Radiation Emergencies for Medical and Security Officers", February 17-20, 2020
6. Workshop on "RFID Technology for Libraries", February 19, 2020
7. "Wealth from Garbage" by Shri M. S. Premnath, Superintending Engineer (Retired), Chennai Corporation, February 28, 2020.
8. "Plastic E-Waste Management" by Shri S. N Nandhagopal, Consultant and Expert Pyrolysis, February 28, 2020.

Webinars

1. BITS Pilani Student Orientation Lecture on "Non-destructive evaluation and its role" by Dr. B. Venkatraman, Director, SQRMG and ESG, May 28, 2020
2. "Graduation Function of the 14th Batch of Trainee Scientific Officers of BARC Training School at IGCAR", July 27, 2020
3. Celebration of Hindi Fortnight, September 14-30, 2020
4. Training Programme on Pension & Retirement Benefits, Life Management Post Retirement by ATI", September 15, 2020
5. National Conference on " Corrosion Management in Nuclear Industry (CMNI, 2020)", September 21-22, 2020
6. Awareness Programme on "Vigilance Awareness Week", October 19, 2020
7. 12th Dr. Placid Rodriguez Memorial Lecture (PRML) by Dr. Surya R. Kalidindi, Georgia Institute of Technology, Atlanta on "Accelerated Materials Innovation Using Knowledge Systems and High Throughput Experiments", October 29, 2020
8. 28th Prof. Brahm Prakash Memorial Lecture 2020 by Dr. U. Kamachi Mudali, Former Chairman and Chief Executive, Heavy Water Board, DAE, on "Urban Mining of E-waste: Challenges and Technologies to Reduce, Reuse and Recycle of Materials", November 28, 2020
9. Two days Course on "Advanced Manufacturing (CAM) for research scholars and industry professionals", December 10-11, 2020
10. Training Programme "Pre-examination training classes for the post of APO by Variant Faculties", December 12, 2020
11. Springer Materials Data Base user awareness lecture by Evelyn Ramforth, Senior Product Manager, Springer Nature, December 15, 2020
12. National Webinar on "Biofilms, Biofouling & Microbial Corrosion" by MMG in association with IIM, Kalpakkam Chapter, December 19, 2020

ISNT Level II Certification Programme in Visual Testing

January 06-10, 2020



Participants of the ISNT Level II Certification Programme in Visual Testing

Indira Gandhi Centre for Atomic Research in collaboration with Indian Society for Non-destructive Testing (ISNT), Kalpakkam Chapter, conducted ISNT Level II Certification Programme in Visual Testing in accordance with IS 13805 requirements during January 06-10, 2020 at Quality Assurance Division (QAD) of Safety, Quality & Resource Management Group (SQ&RMG) IGCAR. Twenty six participants from various organizations such as NPCIL-QA Directorate, QUEST Inspection Services, NAPS, BARCF and different groups of IGCAR had attended the Programme.

Shri S. Athmalingam, Associate Director, HSEG & Head, QAD, inaugurated the course on January 06, 2020. Seasoned visual testing experts Prof. O. Prabhakar, IIT Madras, Shri Mani Mohan, Former Head-NDT Labs, BHEL, Shri R. Subbaratnam, Ex IGCAR and officials from QAD delivered lectures on various topics related to Visual Testing. Practical Session was conducted by the experts from QAD, IGCAR. As part of the certification programme, both theory & practical examinations were conducted on January 10, 2020 and Dr. B. Venkatraman, Director, SQ&RMG, appointed by NCB, ISNT HQ, officiated as the external examiner.

All India Hindi Scientific Seminar (AIHSS-2020)

January 09-10, 2020



Inauguration of All India Hindi Scientific Seminar (AIHSS-2020) (L to R): Shri J. Srinivas, Dr. Awadesh Mani, Dr. Arun Kumar Bhaduri, Distinguished Scientist & Director, IGCAR & GSO, Shri Neeraj Sinha, Advisor (S&T), Niti Aayog, Dr. Kallol Roy, CMD, BHAVINI, Dr. B. K. Nashine AD, SFG/RDTG and Shri O. T. G. Nair, Director (P&A)

The Official Language Implementation Committee (OLIC) of Indira Gandhi Centre for Atomic Research (IGCAR) and General Services Organization (GSO), Kalpakkam in collaboration with NITI Aayog, New Delhi and BRNS, Mumbai jointly organized a two day All India Hindi Scientific Seminar (AIHSS-2020) titled "Oorja Ke Kshetra Me Bharatiya Vigyan Evam Takniki Pragati" (Indian Scientific and Technological Progress in the field of Energy), during January 9-10, 2020. The Seminar was organized as part of promoting official language Hindi in Scientific and Technical writing. The event was inaugurated by Shri Neeraj Sinha, Advisor (S&T), NITI Aayog, New Delhi in the august presence of Dr. Arun Kumar Bhaduri, Distinguished Scientist & Director, IGCAR & GSO and Dr. Kallol Roy, CMD, BHAVINI. Besides the dignitaries, senior members of the OLIC, Shri O. T. G. Nair, Director (P&A), Dr. B. K. Nashine, Dr. Awadesh Mani from IGCAR, were also present.

The Seminar comprised of five oral sessions and a poster session. Highlights of various scientific works performed in the areas pertaining to conventional & non-conventional sources of energy and associated technological advancements were discussed in the seminar. Around 150 delegates from BARC, HWB (Mumbai), NPCIL, NTPC (New Delhi), RMP & AMD (Bengaluru), NFC & ECIL (Hyderabad), RRCAT (Indore), NISER & IOP (Bhubneswar), VNIT (Nagpur), CBRI (Roorkee), VECC (Kolkata), besides BHAVINI, MAPS, BARCF, IGCAR & GSO from Kalpakkam, participated in the seminar. In addition to 12 invited lectures by eminent scientists and experts, nearly 50 papers were presented in poster and oral sessions. The cultural team of BARC, Mumbai presented two scientific skits depicting the importance of peaceful uses of atomic energy, in the evening of 09.01.2020. Best paper and poster presentations were awarded cash incentives. While the inaugural and main technical sessions were held in the Sarabhai Auditorium in IGCAR, the final and valedictory sessions were conducted at GSO, Kalpakkam.

Swachhta Pakhwada - 2020

February 16-28, 2020



Visit by the members of Swachhta Cell



Certificate of appreciation was awarded by Shri M. S. Premnath, Superintending Engineer (Retired), Chennai Corporation for the best three clean locations during the closing ceremony of Swachhta Pakhwada.

Shri M. S. Premnath, Superintending Engineer(Retd.), Chennai Corporation & Shri S. N. Nandhagopal, Consultant & Expert (Pyrolysis of Plastic e-Waste Management) during the closing ceremony

Indira Gandhi Centre for Atomic Research observed “Swachhta Pakhwada” during February 16-28, 2020. During this period E-waste management and cleaning of surroundings within the plant site and cleaning of office premises were carried out. In order to provide a boost to the swachhta activities, members of IGCAR Swachhta Cell visited various Divisions/Groups and selected three best kept locations in the Centre. Certificate of appreciation was awarded for the best three clean locations during the closing ceremony of Swachhta Pakhwada. Guest lectures by Shri M. S. Premnath, Superintending Engineer (Retired), Chennai Corporation on “Wealth from Garbage” and Shri S. N Nandhagopal, Consultant and Expert Pyrolysis on “Plastic E-Waste Management” were organized on the closing day. Essay, slogan and poster competitions on the topic “Cleanliness towards Nation’s Development” were conducted and prizes were distributed to the winners during the closing ceremony.



Swachhta Pakhwada - event held during the cleanliness drive in township

Radiation Emergency Management Workshop

February 17-20, 2020



Workshop on “Planning, preparedness and response to radiation emergencies for medical and security officers”

A workshop on “Planning, preparedness and response to radiation emergencies for medical and security officers” was organized for the first time, at Health, Safety and Environment Group, SQRMG, IGCAR during February 17-20, 2020. The Workshop was inaugurated by Capt. Loganathan, Indian Navy, Kalpakkam. A total of 44 Officers including medical officers from southern naval units, DAE hospital, Kalpakkam and security officers from army and CISF at Kalpakkam participated in the four day workshop. Lectures on topics like planning, preparedness for effective response Role of Crisis Management Group, DAE and Role of Emergency Response Centre during nuclear and radiological emergencies, decontamination procedures, Medical management of radiation injuries etc., were delivered by faculty members from IGCAR, BARC and DAE Hospital. Technical visits were arranged for the participants to various radioactive facilities at Kalpakkam. Major General P. K Hasija, MG, MED, Dakshin Bharat Area, Chennai, was the chief guest in the valedictory function and participation certificates were distributed by him. In the valedictory address, he stressed upon the need for sharing the medical management experience to deal with nuclear and radiation emergencies. Dr. Prodig Bhattacharjee, MS, DAE Hospital, Kalpakkam participated as the guest of honour in the function.



Participants of the workshop during lecture



Major General P. K Hasija distributing certificates to participants

One Day Workshop on RFID Technology for Libraries

February 19, 2020



Dr. B. Venkatraman, Distinguished Scientist and Director, SQ&RMG & ESG and senior colleagues during the inaugural session

A one day Workshop on Radio Frequency Identification Technology (RFID) for Libraries was organized by IGCAR in association with Madras Library Association -Kalpakkam Chapter (MALA-KC) on 19-02-2020 at Sarabhai Auditorium, IGCAR, Kalpakkam. The objective of the workshop was to familiarize RFID technology and gadgets to Public Librarians in the neighbouring districts of Kalpakkam. Around 60 delegates including Librarians from academic and public domain, information technology professionals and Research Scholars attended the Workshop.

The Workshop was inaugurated by Dr. B. Venkatraman, Distinguished Scientist and Director, SQ&RMG & ESG, Smt. S. Prabavathi, Treasurer, MALA-KC welcomed the gathering. Dr. T. S. Lakshmi Narasimhan, Associate Director, Resource Management Group/SQRMG delivered the special address. Smt. S. Rajeswari, Head, Scientific Information Resources Division (SIRD) and President MALA-KC delivered the key note address on “Role of libraries in promoting digital services”. Dr. B. Venkatraman, Director SQRMG and ESG released the new SIRD intranet portal (<http://vaigai>) and delivered the presidential address emphasizing the need for integrating digital technology in every aspect of library services. Shri E. Soundararajan, Secretary, MALA-KC, proposed the formal vote of thanks.

The Workshop included lectures by colleagues from SIRD in the field of RFID technology, KOHA based Library Management System and SIRD Digital Library Services. A hands-on session on RFID technology was arranged. This workshop facilitated good interaction amongst the Librarians, students and professionals in the area of RFID technology and Integrated Library Management System.



Participants of the workshop

Technical Meeting on “Current Practices & Quality Assurance in Welding”

February 19-21, 2020



Shri. G. Nageswara Rao, Chairman AERB inaugurated the technical meeting and delivered the inaugural address. Dr. A.K. Bhaduri, Director IGCAR, presided over the inaugural function as the Chief Guest. Dr. Kallol Roy, CMD BHAVINI was the Guest of Honour at this technical meeting

A Technical Meeting on “Current Practices & Quality Assurance in Welding” was organized by SRI-AERB at the Seminar Hall, SRI Guest House, Anupuram during February 19-21, 2020. The aim of this technical meeting was to provide a platform for experts from AERB and various DAE units such as BARC, IGCAR, NPCIL and BHAVINI to share the current state of the art in the area of welding and NDE technology, especially those that are applied in nuclear industry and to disseminate updated information on the present state of the art of welding quality assurance.

Around 70 engineers from the utilities, regulators and research organizations from various DAE units participated in the technical meeting. Sixteen invited talks were delivered by speakers from various DAE units, AERB and IITs in six sessions, over a period of two days.

The deliberations in the technical meeting have provided better understanding of the welding process and qualification criteria and also provided several insights for defect minimization and improvement of weld reliability, which will further help in improving safety of critical components of NPP.



A view of Delegates during technical meeting session

Orientation Program for Engineers and Supervisors involved in Construction

February 21, 2020

A one day Orientation Program was organized on February 21, 2020 at Fast Reactor Fuel Cycle Facility (FRFCF) for engineers, supervisors, technicians, draftsmen and skilled assistants engaged in construction site works in various disciplines viz. Civil, Mechanical, Electrical, Instrumentation and Safety. Dr. B. P. C. Rao, Project Director, FRFCF inaugurated the event and explained the significance of this multi-unit mega project in realizing the goals of the department. He also highlighted the importance of integrity, quality and safety aspects in the work carried out.



USNRC Delegates visit to IGCAR

February 21, 2020

A delegation from USNRC led by Ms. Annie Caputo, Commissioner, visited various facilities and held discussions with senior colleagues at IGCAR on 21 February, 2020. They visited FBTR, Shake Table facility and Online Nuclear Emergency Response System



4th Discussion Meeting
with Collaborative Institutes/Labs on Indian AUSC Projects, Kalpakkam
 March 02-03, 2020



The meeting was chaired by Shri S. C. Chetal, Ex-Director, IGCAR and AUSC Mission Director accompanied by Dr. Arun Kumar Bhaduri, Distinguished Scientist & Director, IGCAR and Dr. Shaju K. Albert, Director, MMG and MSG, IGCAR

IGCAR has been a consortium partner in the multi-agency R&D project "Development of Advanced Ultra-Super Critical (AUSC) technology for thermal power plants on a Mission Mode" approved by the Cabinet Committee on Economic Affairs (CCEA). The other two partners in the consortium are BHEL and NTPC. The multi-agency R&D mission project is being executed by the AUSC Mission Directorate under the Department of Heavy Industries (DHI), Government of India. In this project, there has been high emphasis on the use of indigenously developed materials and technologies for the Indian AUSC Power Plant.

Roles assigned to IGCAR in the Indian AUSC Consortium are advanced design analysis, materials development, manufacturing technology, testing and evaluation. Generation of material property data is an important part of the R&D phase of the AUSC project, and thus specific projects of relevance to the AUSC Mission have been identified by IGCAR and awarded collaborative projects under the national AUSC Mission to various Academic Institutes/ National Labs for the evaluation of important material properties. The collaborative projects would also establish a National network of high temperature material testing infrastructure for carrying out future material testing and evaluation works related to the AUSC technology and other high temperature applications.

The collaborative projects are being reviewed every six months through presentations by the respective project investigators. The latest project review meeting, which is fourth in the series, was held during March 2-3, 2020 at IGCAR. About 35 faculties/scientists from various Academic Institutes (IIT Bombay, IIT Kharagpur, IIT Bhubaneswar, IIT Roorkee, IISc Bangalore, VNIT Nagpur, NIT Warangal, Jadavpur University Kolkata and CSIR-NML Jamshedpur) had presented the status of projects. About 35 scientific officers from IGCAR and 2 officers from BHEL Corporate R&D, Hyderabad had also participated in the review meeting. The Two-day review meeting was chaired by Shri S. C. Chetal, Ex-Director IGCAR and AUSC Mission Director accompanied by Dr. Arun Kumar Bhaduri, Distinguished Scientist & Director, IGCAR and Dr. Shaju K. Albert, Director, MMG and MSG, IGCAR.

Signing of MoU between IGCAR and UGC-DAE CSR, Kalpakkam Node & Inauguration of 200 kV accelerator

March 11, 2020



Dr. A. K. Sinha, Director, UGC-DAE CSR, Indore and Dr. Arun Kumar Bhaduri, Distinguished Scientist & Director, IGCAR, exchanging MoU between IGCAR and UGC-DAE CSR

On March 11, 2020, signing of MoU between IGCAR and UGC-DAE CSR, Kalpakkam Node and inauguration of the 200kV accelerator was held at UGC-DAE CSR, Kalpakkam Node.

A memorandum of understanding (MoU) between IGCAR and UGC-DAE CSR, Kalpakkam Node was signed by the Director, IGCAR, Dr. A. K. Bhaduri and the Director, UGC-DAE CSR, Dr. A. K. Sinha on March 11, 2020. On this day, inauguration of the 200kV accelerator at UGC-DAE CSR, Kalpakkam Node was also done.

The accelerator, installed in the UGC building in September of 2018, had recently received the AERB clearance and hence is fully operational now. The accelerator is a low energy ion implanter system, which will help in studying radiation effects and damages, ion implantation, doping of material, etc, and is also a user facility like all other facilities of the Node.



Dr. A. K. Sinha, Director, UGC-DAE CSR, Indore inaugurating 200 KV accelerator at UGC building



Audience during the meeting session

About BITS Summer Practice School at IGCAR

May 22 - June 26, 2020



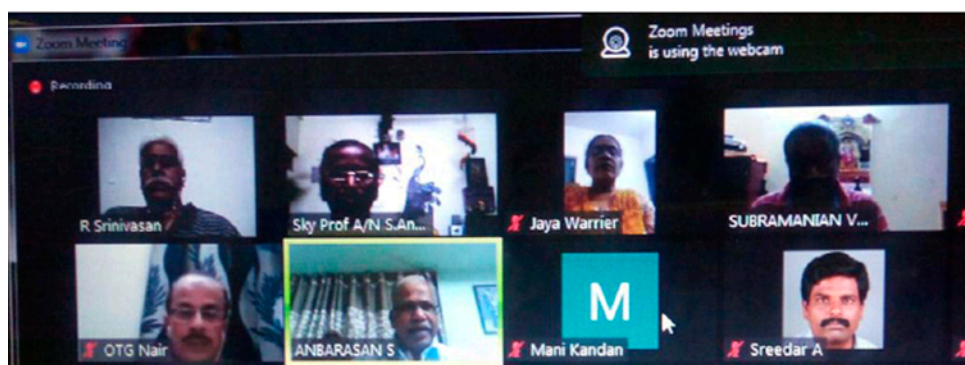
Dr. Arun Kumar Bhaduri, Distinguished Scientist & Director, IGCAR and GSO inaugurated the practice school programme via online and interacted with the students

Forty Nine students from BITS Pilani, Hyderabad and Goa Campuses pursuing degrees in various disciplines like Mechanical, Chemical, Civil, Electrical & Electronics, Electronics & Instrumentation, Electronics & Communication, Computer Science and B.Sc., / M.Sc., Physics underwent summer practice school during May 22 to June 26, 2020 through virtual mode using video conference facilities. Dr. Sanket Goel and Dr. Sandip Deshmukh from Hyderabad campus were the program coordinators from BITS. Dr. Arun Kumar Bhaduri, Distinguished Scientist and Director, IGCAR & GSO inaugurated the practice school programme via online and interacted with the students on May 22, 2020. Dr. B. Venkatraman, Director, SQRMG and ESG delivered an orientation lecture to all the students on "Non-destructive evaluation and its role" including details about the R&D at IGCAR on May 28, 2020. The students carried out challenging projects through interaction with enthusiastic faculty at IGCAR and their expert guidance. Bi-weekly review system with one to one interaction between student and faculty along with coordinators from BITS and IGCAR ensured proper imparting of knowledge to the students without compromising the quality in this new methodology of interactions this year. The final project work presentations, group discussions and viva-voce were all conducted successfully in the remote mode. The programme successfully concluded on June 26, 2020 and the certificates have been dispatched by post to the students.

6th International Day of Yoga

June 21, 2020

The sixth International Day of Yoga was observed on June 21, 2020 at IGCAR, Kalpakkam through an online programme. A demonstration of yoga practices in the morning followed by a special lecture of Sr. Prof. K. R. Munirathinam, Sky Yoga, Chennai was arranged. Many employees of IGCAR and other DAE Units at Kalpakkam participated in the programme and were benefitted by it.



The participations interacted online

Training School Placement committee for OCES-2019

July 28, 2020



Training School Placement committee for OCES-2019 under the Chairmanship of Dr.B.Venkatraman, Director,SQ&RMG and ESG interacting through video conferencing mode

The placement committee for OCES-2019 under the Chairmanship of Dr.B.Venkatraman, Director,SQ&RMG and ESG met on 28th July 2020 with members from IGCAR and representatives from other Units interacting through video conferencing mode. Amongst the 21 TSOs, 8 were placed at IGCAR, 3 at AERB, 2 at BARC, 3 at BHAVINI and one each at HWB, NFC and NPCIL.

Prof. D. R. G. Achar Memorial Lecture Award 2020 by The Indian Institute of Welding, Chennai branch

August 25, 2020

The Indian Institute of Welding, Chennai Branch had instituted a memorial lecture award in the name of Late Prof. (Dr.) D.R.G. Achar, a faculty member of the Department of Metallurgical and Materials Engineering, IIT Madras and an active member of Chennai Branch. It is awarded to honour a branch member who has made outstanding contributions in the field of Welding Science & Technology and recognition of their distinguished services to the Welding Fraternity. The Managing Committee of IIW India, Chennai Branch, conferred the Prof. D. R. G. Memorial Lecture Award 2020 on Dr. Arun Kumar Bhaduri, Director, Indira Gandhi Centre for Atomic Research (IGCAR) during a web based event on 25th August 2020 during which he delivered an award lecture on the topic "Welding of Materials used in Advanced Nuclear & Thermal Power Plants". The event was organised on hybrid webinar mode from IGCAR Kalpakkam with wide participation from outside



Dr. Arun Kumar Bhaduri, Distinguished Scientist & Director, IGCAR delivering the award lecture on hybrid webinar mode from Blue room, IGCAR Kalpakkam.



Prof. DRG Achar Memorial Award 2020 received by Dr. Arun Kumar Bhaduri, Distinguished Scientist & Director, IGCAR from Dr. Shaju K Albert, Director, Metallurgy & Materials Group and Materials Science Group, IGCAR alongside members of IIW-India, Chennai

Tree Plantation of 5000 saplings at DAE Campus, Kalpakkam

October 02, 2020

A program on development of green-cover has been initiated in collaboration with Tamil Nadu Forest Department by planting 5000 saplings of rich species specification pertaining to local land. The shallow jungle area is cleared and tree plantation initiated.



Dr. Arun Kumar Bhaduri, Distinguished Scientist & Director, IGCAR planting saplings in IGCAR



Dr. B. Venkatraman, Director, SQRMG planting saplings in IGCAR

Incubation Centre Inauguration at Kalpakkam

October 30, 2020

Aligning with the Government's mission of Atma Nirbhar Bharat and the DAE's initiative of setting up of incubation centers to facilitate in-house technology promotion and transfer, it is matter of great happiness that Incubation Centre - IGCAR has been remotely inaugurated by Chairman, AEC and Secretary DAE on October 30, 2020.

The 111th birth anniversary of Dr. Homi Jehangir Bhabha. On this occasion, four MoUs for collaboration and transfer of technologies have been signed.



Dr. Arun Kumar Bhaduri, Distinguished Scientist & Director, IGCAR during inauguration



Dr. B. Venkatraman, Director, SQRMG addressing during inauguration

IGC COUNCIL



Chairman

Dr. Arun Kumar Bhaduri

Distinguished Scientist & Director, IGCAR

Dr. Arun Kumar Bhaduri, a graduate and Ph.D. in Metallurgical Engineering from Indian Institute of Technology, Kharagpur, joined Department of Atomic Energy in 1983. He is with Metallurgy and Materials Group at Indra Gandhi Centre for Atomic Research, Kalpakkam since 1984, where he is presently Distinguished Scientist and Director since July 2016. He is also a Senior Professor, Homi Bhabha National Institute (University). He received Research Fellowship from Alexander von Humboldt Foundation, Germany in 1994 for a 2-year post-doctoral research at University of Stuttgart, Germany. He pilots the design and technology development of sodium-cooled fast reactors and its associated fuel cycle for the second stage of India's nuclear power programme, and anchors the development of materials and their fabrication technologies for Indian programmes on sodium-cooled fast reactors, fusion reactors and advanced ultra supercritical thermal power. He specialises in the field of materials joining, and has to his credit more than 270 journal publications, 410 conference presentations and 2 international patents. He is Fellow of Indian National Academy of Engineering, Indian Institute of Metals and Indian Institute of Welding. Some of his notable recognitions include: Doctor of Science (2017), Jadavpur University, Kolkata; Distinguished Alumnus Award (2017), IIT Kharagpur; Jaeger Lecture Award (2017), International Institute of Welding; GD Birla Gold Medal (2017), Indian Institute of Metals; Carl von Bach Commemorative Medal (2016), MPA University of Stuttgart, Germany; VASVIK Award (2005), Vividhlaxi Audyogik Samshodhan Vikas Kendra, Mumbai; DAE Group Achievement Awards 12 times during the period from 2006 to 2016, including four times as Group Leader; National Metallurgists' Day Metallurgist of the Year Award (2003), Ministry of Steel; DAE Homi Bhabha Science & Technology Award (2002). He has been an elected member of the Board of Directors of the International Institute of Welding (2016–2019), and President of The Indian Institute of Welding (2017–2019).

Members



Dr. A. K. Mohanty, a well-known nuclear physicist, completed his Bachelor's degree in 1979 from MPC College, Baripada and Master's degree in Physics in 1981 from Ravenshaw College, Cuttack which was at that time under Utkal University, Bhubaneswar. Dr. Mohanty graduated from the 26th batch of the BARC Training School and joined Nuclear Physics Division of Bhabha Atomic Research Centre in 1983 and got his PhD degree from Bombay University later on. He has taken over as Director, BARC on 12th March 2019. Before his appointment as Director BARC, Dr. Mohanty has held the position of Director of Saha Institute of Nuclear Physics, Kolkata from June 2015.

During the past 37 years, Dr. Mohanty has worked in several areas of nuclear physics covering collision energy from sub-Coulomb barrier to relativistic regime. It includes experiment using Pelletron accelerator at TIFR, PHENIX and CMS experiments at Brookhaven National Laboratory (BNL), USA and CERN, Geneva respectively. Dr. Mohanty has

held several honorary positions. To name a few, he served as Secretary and Member Secretary of BRNS Basic Science Committee from 2004-2010, General Secretary of India Physics Association (IPA) 2012-2016 and later on President of IPA 2018-2020, India-CMS Spokesperson 2013-2015 and Dean, Academic, Physical & Mathematical Sciences, BARC, Homi Bhabha National Institute. Dr. Mohanty has been recipient of several awards and recognitions during his illustrious career. Some of Dr. Mohanty's awards and recognitions are: Gold medal in Graduation, 1979, Young Scientist Award of Indian Physical Society (IPS, Kolkata, 1988), Young Physicist Award by Indian National Science Academy (INSA, New Delhi 1991) and DAE Homi Bhabha Science & Technology Award (2001) by Department of Atomic Energy, Mumbai. He was also conferred the CERN Scientific Associate position at CERN, Geneva from 2002-2004 and thereafter again from 2010-2011. Dr. Mohanty has been Director on the Board of NPCIL w.e.f. 1st April 2019.



Dr. B. Venkatraman, is from the 27th batch of Bhabha Atomic Research Centre Training School. With a research career spanning 36 years, he has specialised in application of ionizing and non ionizing radiations for non-destructive evaluation of materials and processes. During the last ten years, he has focused on enhancing, existing and establishing newer facilities as part of broad based radiation and environmental research programs at IGCAR.

He is a Member of AERB, SARCAR Committee and Convenor of BIS CHD 30 Sub Committee on Radiation Protection. He was a visiting scientist at Fraunhofer Institute of NDT Saarbrucken, Germany 2006-2007, has served as an expert for IAEA in Digital Radiology. He has more than 200 publications, is the recipient of Homi Bhabha Science and Technology Award 2007, INS Gold Medal 2005, seven Group Achievement Awards of DAE, D & H Schereon Award of IIW 1993, ISNT-NDT Man of the Year Award (R & D) 2001, IIW sharp tools award 2011, ISNT international recognition award 2013, and has won more than 10 best paper awards. He has been invited to deliver keynote, plenary and invited talks in international and national conferences. He is the Honorary Fellow of Indian Society of NDT and Fellow of Chennai Academy of Sciences. He is the President of Indian Society for NDT (ISNT) and President, Indian Association for Radiation Protection (IARP). He has guided about 6 students for their Ph D and is presently guiding 6 students. He is presently Distinguished Scientist and Director, Safety, Quality and Resource Management Group and Director, Engineering Services Group at IGCAR



Dr. Shaju K. Albert, Director of Metallurgy & Materials Group and Material Science Group graduated in Metallurgy from The Indian Institute of Science in 1984 and subsequently joined Dept. of Atomic Energy. After one year of training in Nuclear Engineering at BARC, he joined Indira Gandhi Centre for Atomic Research (IGCAR) in 1985. Since then he has been working in the area of welding and joining. He obtained his Ph.D. in 1997 from The Indian Institute of Technology, Bombay. He is a Fellow of the Indian Institute of Metals. He is recipient of STA and JSPS fellowships of Government of Japan and worked as Research Fellow under these fellowships in National Institute of Materials Science, Tsukuba, Japan. He has published extensively in the area of material joining and hardfacing, and is recipient of Gold Medal of Indian Nuclear Society, Science Technology Excellence Award of Dept. of Atomic Energy and many best paper awards of the Indian Institute of Welding. In 2015, IIW-INDIA honored him with Sir L.P. Mishra Memorial Award Lecture in the National Welding Seminar held at Jamshedpur. He is currently Chairman of the MTD-11, Welding General and Application Sectional Committee of Bureau of Indian Standards (BIS) and till recently Vice President of the Indian Institute of Welding. He is a member of Safety Review Committee of Operation Plants (SARCOP) of Atomic Energy Regulatory Board.



Dr. Kallol Roy, an Outstanding Scientist, is B.Tech in Electrical Engineering from NIT-Calicut; M.Tech in Electronics Design from CEDT-Indian Institute of Science; Ph.D. in Fault Diagnostics–Systems & Controls from IIT, Bombay and Post Doctorate in Computer Process Control from University of Alberta, Canada. He is from the 28th Batch of BARC Training School. Dr. Kallol Roy's field of specialisation includes Total Maintenance Management of Reactors, Upgrading and Retrofit of C&I and Computer Based Systems, EMI / EMC Studies and Modelling in Plants, Fault Diagnostics of Systems and Equipment Reactor Safety, Surveillance & Tech-Specs, Analysis (CRP with IAEA) using Bayesian Estimation techniques and Safety and Security aspects of Computer based Systems. He was also a Professor of HBNI. Dr. Kallol Roy took charge as Chairman & Managing Director, BHAVINI on 31st March 2016.



Dr. B. Purna Chandra Rao, an Outstanding Scientist, is from the 29th batch of BARC Training School, and joined the Department in 1985. As Project Director, Fast Reactor Fuel Cycle Facility (FRFCF), IGCAR, he is spearheading the construction, commissioning and management activities of FRFCF towards closing the fuel cycle of FBRs. Dr. Rao has developed and effectively implemented innovative approaches for construction of fuel reprocessing, fuel fabrication and waste management plants of FRFCF through systematic review & monitoring strategies with milestone-targets, responsibilities and timelines clearly set for Civil, Mechanical, Electrical, E&I, Quality Assurance, Safety, Service activities. Dr. B.P.C. Rao has ensured fabrication & procurement of process equipment, storage tanks, material handling equipment, IGC qualified SS plates, rounds & fittings, steel pipes, radiation monitoring instruments, analytical certification lab equipment etc. He has developed methodologies for civil construction such as Mega pours, Hematite ore-based heavy density concreting, equipment erection & installation, and comprehensive QA methodologies for forged fittings, master-slave manipulators, and glove boxes of FRFCF. Dr. Rao has guided & motivated engineers and efficiently managed construction & procurement activities by paying proactive attention to critical-path aspects. He has steered condition assessment of concrete structures of radiological and reprocessing plants and life management activities. Dr. Rao developed advanced NDE techniques & probes for inspection of fast reactor components and extended expertise to several organisations to solve challenging problems related to inspection, welding, corrosion, condition monitoring, structural integrity assessment and failure analysis. Dr. BPC Rao has nearly 200 research publications to his credit. In recognition of his research contributions, he has been conferred Homi Bhabha Science & Technology award of DAE, National NDT award & International recognition award of ISNT and Indian Nuclear Society Gold Medal and several DAE group achievement awards. As a Senior Professor of HBNI, Dr. BPC Rao has guided several PhD, M.S and M.Tech students.



M/s. Sushma Taishte joined as Joint Secretary in the Department of Atomic Energy, Government of India on 08-04-2020. She is a post graduate in Medical Microbiology from Haffkine Institute, Parel, Mumbai. She is the In-charge of Research and Development wing of the DAE handling Bhabha Atomic Research Centre (BARC), VECC, Kolkata, RRCAT, Indore, IGCAR, Kalpakkam and all aided institutions (eleven) in the Department. International Projects such as, ITER, LiGO, also fall under R & D Division. She has served in various capacities in Ministry of Defence, Ministry of Health & Family Welfare, National Health Systems Resource Centre, Ministry of Petroleum and Natural Gas and Department of Justice, Ministry of Law & Justice, Government of India during 1991 - 2020.



Shri O.T. G. Nair joined IGCAR as Director (P & A) in June, 2018. He joined the Department of Atomic Energy in 1984. During the 35 years of his service in the Department, Shri Nair has worked in different capacities like Assistant Personnel Officer, Section Officer, Administrative Officer, Under Secretary, Deputy Secretary, Chief Administrative Officer and Director (P&A) and handled many portfolios in DAE Secretariat, BARC and IGCAR. He has received DAE Special Contributions Award - 2010

Organisation and Activities of Various Groups

Electronics and Instrumentation Group



Ms. T. Jayanthi
Director, EIG



Dr. D. Thirugnanamurthy
AD, E&CG



Shri A. Venkatesan
AD, RC&IG



Shri R. Jehadeesan
Head, CD



Shri N. Sridhar
Head, ED



Shri M. Sakthivel
Head, I&CD



Shri R. P. Behera
Head, RTSD



Shri G. Prabhakara Rao
Head, SISD

Electronics and Instrumentation Group is focused on design and development of indigenous technology in the areas of Electronic Instrumentation & Control systems for fast breeder reactors and reprocessing plants that include Development of Distributed Digital Control System, Safety Critical and Safety Related Systems, Safe & Secure PLC, Virtual Control Panel based Control Room, Full-scope Operator Training Simulator, 3D modeling, animation & visualization of FBR subsystems and VR walkthrough of structures, Cyber Security Management for IT and I&C systems. Design and Development of advanced equipment and technology such as, indigenous Wireless Sensor Networks for nuclear facilities, strategic and societal applications, Time Domain Electromagnetic for Deep Seated Atomic Minerals Exploration, Plutonium Condition Air Monitoring System for reprocessing plants, Test Instrument for Steam Generator Tube Inspection, Radar Level Probe for Liquid Sodium Level Measurement, radiation resistance MEMS based sensor for nuclear applications and innovative sensors and instruments for nuclear facilities have been completed. Considerable expertise exists in designing, building and maintaining state-of-the-art high-performance supercomputing facility that continues to meet large scale compute- and data-intensive requirements in multi-disciplinary domains. Implementation of IT-enabled Nuclear Knowledge Management system for Fast Reactors and associated domains, computational intelligence systems, cryptography, cyber security solutions, knowledge management and development and deployment of modern security systems for access control and physical protection of nuclear complexes are initiated.

Engineering Services Group



Dr. B. Venkatraman
Director, ESG



Shri B. Harikrishnan
AD, CEG



Shri T. Johnny
AD, TSG & Head, CWD



Shri H. R. Sridhara
Head, ASED



Shri N. Suresh
Head, CED



Shri Sudipta Chattopadhyaya
Head, CM&MWD



Shri Biswanath Sen
Head, AC&VSD



Shri K. P. Kesavan Nair
Head, ESD

The Engineering Services Group is responsible for the development of infrastructure in line with the mandate & the vision program of the centre. It provides quality services and activities pertaining to Civil, Electrical, Mechanical engineering including Voice Communication Systems, Air-conditioning and Ventilation Systems. In the mechanical engineering domain, one key element is the manufacturing of critical components towards the development of fast reactor & reprocessing technologies. The group also coordinates with BSNL for providing data communication and for mobile communication. The group has a mandate to establish additional infrastructure requirements so as to meet Design, R&D and operational objectives of IGCAR which includes the backend fuel cycle. The group consists of expert teams with capability to design, engineer and execute systems under their jurisdiction. Aesthetically designed buildings & structures, providing reliable power supply, potable water, quality-air and other services including services from Central Workshop are being extended to other units of DAE located at Kalpakkam. The group is also involved in the horticulture development, which enhances the green cover and maintenance of roads and drainage system. The nature of work involves interaction with several State and Central Government Organisations. The group is responsible for providing reliable air-conditioning and ventilation services to various R&D facilities of the Centre. The group ensures that all infrastructural developments are carried out in harmony with environment.

Fast Reactor Fuel Cycle Facility



Dr. B. Puma Chandra Rao
Project Director



Shri. V. Manoharan
Chief PE



Shri L. Davy Herbert
Additional CE



Shri. C. Chandran
Additional CE



Shri K. Gopal
HEAD, BP&FED



Dr. D. Ponraju
Head, I&FS

Fast Reactor Fuel Cycle Facility (FRFCF) Group is entrusted with planning, design, construction and commissioning of plants for closing the fuel cycle of PFBR. FRFCF is a multi- unit project of DAE involving IGCAR, BARC, NRB and NFC. FRFCF Group has completed detailed engineering design of the facility and obtained necessary regulatory clearances and financial sanction. The Group has made significant progress in construction of 5 radiological plants in the nuclear island viz. Fuel Reprocessing Plant (FRP), Fuel Fabrication Plant (FFP), Reprocessed Uranium oxide Plant (RUP), Core Subassembly Plant (CSP) and Waste Management Plant (WMP) with all the plants' civil construction reaching the ground level from -23 m level. The Group completed construction of all infrastructure buildings such as Administrative Building, Training Centre, Centralized Surveillance, Safety & Health Physics Building and Utility & Service buildings such as DG building, Central Chilling Plant, Air Compressor building etc. The Training Centre of FRFCF is the first Green building of DAE with Gold rated certification by Indian Green Building Council (IGBC). After completion of design & development of process equipment, advanced actions have been initiated to ensure procurement of large quantity of long delivery items like SS plates, IGC qualified SS process pipes, Over Dimension Consignment storage tanks and radiation shielding glasses. Concurrently, process equipment for the 5 plants are being manufactured and received at FRFCF project site in a phased manner for commissioning of the plants. Successful commissioning of FRFCF is an essential step for embarking on construction of Second Stage nuclear power plants based on Plutonium fuel that would pave the way for achieving energy security for the nation.

Materials Chemistry & Metal Fuel Cycle Group



Dr. N. Sivaraman
Director, MC&MFCG



Dr Kitheri Joseph
AD, MFRG



Dr. V. Jayaraman
AD, F&MCG



Shri T. V. Prabhu
Head, CF&ED



Dr S. Ghosh
Head, MFPD



Shri B. Muralidharan
Head, PPED



Dr. R. Kumar
Head, AC&SD



Dr. A. Suresh
Head, FCD



Dr. Rajesh Ganesan
Head, MCD

The Materials Chemistry and Metal Fuel Cycle Group (MC&MFCG) is involved in research and development studies relating to metal fuel program, establishing pyrochemical reprocessing of metal fuel, development of aqueous reprocessing methods, including reprocessing of metal fuels, sodium chemistry and development of novel chemical sensors for detection of hydrogen, ammonia, NO_x etc. Some important current activities include installation of injection casting system for casting U-Zr slugs, pyroprocessing of irradiated U-Zr in hotcells in lab scale batch, preparation of 1 ton of eutectic salt mixture containing LiCl-KCl for electrorefining uranium metal, direct oxide reduction of uranium oxides to uranium metal, optimization of parameters towards oxidation of metal fuel prior to its dissolution in nitric acid medium followed with extraction of heavy metals using TBP/n-DD, thermochemical properties of fuel materials as well as pyrochemical salt samples, phase diagram studies on fuel materials, development of non-destructive methods for assay of plutonium, Studies on development of synthetic inorganic matrices for immobilization of waste from fast reactor fuel reprocessing, synthesis of phase pure AgInO₂ towards hydrogen sensing, production of ⁸⁹Sr for societal applications, etc.

MC&MFCG also provides expert Analytical support and Radioanalytical services to various programmes in the Centre and for other DAE units. Some important activities include, development of analytical methods for assay of metal fuel and samples originating from pyrochemical process, measuring isotopic composition of boron and heavy metal ions and assay of primary sodium samples for actinides and fission products. Besides the above, some basic R&D studies are undertaken to study intermolecular interactions using matrix isolation spectroscopy, development of metal organic frameworks for sorption of lanthanides and actinides, supercritical extraction and recovery of metal ions; development of extraction chromatographic methods for recovery of actinides from lean streams, recovery of zirconium from aqueous waste and computational study on the structural aspects of extractants and actinide complexes.

Materials Science Group



Dr. Shaju K. Albert
Director, MSG



Dr. M. Kamruddin
AD, A&NG



Dr. N. V. Chandra Shekar
Head, CMPD



Dr. Sandip Kumar Dhara
Head, SND



Dr. R. Govindaraj
Head, MPD

The Materials Science Group (MSG) comprising of Accelerator and Nanoscience Group (A&NG) and Condensed Matter Physics Division (CMPD) has the mandate of pursuing basic research on topical problems in Materials Science relevant to fast reactors. The Accelerator and Nanoscience Group (A&NG) consists of Materials Physics Division (MPD) and Surface and Nanoscience Division (SND). MPD focuses on the studies on defects, defect-impurity interactions in reactor structural materials and are supplemented by computations. Ion beam radiation damage studies are carried out using a 1.7 MV tandem accelerator and a 400 keV in-house built linear accelerator either in single or dual ion beam modes of irradiations for the studies of defects and radiation response in materials of relevance for fusion and fission reactors at MSG. Defects, in particular open volume defects such as vacancies and their clusters are studied using positron annihilation spectroscopy. Positron beam based Doppler broadening studies have been mainly used for depth resolved defects studies in irradiated materials. Ion beam based characterization techniques such as high resolution RBS, channeling are being used extensively in addition to ion beam induced luminescence studies. Irradiation creep studies are being planned with proton beam of energy (2-3 MeV) and high beam current. Various experimental results related to defects are analyzed using detailed computations with a variety of simulation and ab-initio codes. High speed cluster computers at IGCAR are being extensively utilized for computation of materials properties. Besides there is also an intense effort towards quantum metrology based research studies using entangled photons.

Surface and Nanoscience Division focuses on the study of monolithic and multilayered thin films and nanostructures using a variety of techniques such as secondary ion mass spectrometry, nanomechanical testing, Focused Ion Beam (FIB) based nanostructuring and nanopatterning, Scanning Probe Microscopy based characterization of various electrical and mechanical properties at nanoscale, nanospectroscopy with tip enhanced Raman spectroscopy (TERS) and Nanoscopy with near-field scanning optical microscopy (NSOM) imaging at sub-diffraction limit using polarized light. The division also specializes in high temperature tribological studies for structural materials as well as novel nano- and micro-crystalline diamond thin film. Furthermore, development of novel nanomaterials of 0D transition metal oxide (TMO), 1D noble metal, and nitrides, 2D TMOs, and transition metal dichalcogenides (TMDs) for advanced sensor applications is being carried out. Research activities relating to sensors based on micromachined cantilevers are also being pursued.

Condensed Matter Physics Division (CMPD) pursues several theme based research programs: investigation of structure and physical properties of materials under extreme conditions such as high pressures, low temperatures, high temperatures and high magnetic fields. Further, over the years various facilities for the synthesis of novel, superhard materials have been established including Laser Heated Diamond Anvil Cell (LHDAC) facility. The systems under investigation encompass nuclear materials, superconductors, strongly correlated systems, magnetocaloric materials, topological insulators, multiferroics, frustrated systems, f-electron based intermetallics and oxides, glasses and super hard transition metal borides. Research is also pursued to investigate emergent phenomena and proximity effects in heterostructures. The Division also concentrates on the development of technologically important single crystals for detector applications. Dynamic light scattering and confocal microscopy are utilized for studies on soft condensed matter. Optical trapping and manipulation of mesoscopic particles using holographic optical tweezers (HOTs) to study inter-particle interactions in colloidal suspensions/ biological systems are being pursued SQUID based systems for Magneto-Cardiography (MCG) and Magneto-Encephalography (MEG) have been successfully designed, assembled, standardized and used for clinical studies. Further, SQUID based measuring systems such as high field SQUID magnetometer, SQUID VSM, SQUID based set-up for Non- Destructive Evaluation (NDE) have been developed.

Metallurgy and Materials Group



Dr. Shaju K. Albert
Director, MMG



Dr. S. Raju
AD, MCG



Dr. R. Divakar
AD, MEG



Dr. John Philip
Head, CSTD



Dr. P. Parameswaran
Head, PMD



Dr. Anish Kumar
Head, NDED



Dr. M. Vasudevan
Head, MDTD

The Metallurgy and Materials Group (MMG) of IGCAR has been actively driving the development of advanced nuclear structural materials, processes and technologies for Sodium Cooled Fast Reactors (SFR) and associated

closed fuel cycle technologies through a directed metallurgy and materials research and development programme. MMG has made major strides towards the successful development of structural materials aimed at withstanding demanding operating and environmental conditions which include austenitic and ferritic steels, ODS alloys with improved swelling resistance for reactor core applications, 316L(N) austenitic stainless steel for reactor components and modified 9Cr-1Mo steel with controlled B for steam generator applications. MMG is also involved in the development of an array of novel application specific functional materials such as ferroseals for sodium pumps, magnetic fluids for hyperthermia applications, super hydrophobic materials with superior corrosion protection and antifouling characteristics, corrosion resistant materials and coatings for aqueous and pyrochemical reprocessing applications, tungsten carbide for enhanced in-core shielding of life-determining core permanent structures and iron based soft magnetic alloy for control rod applications. Extensive post-irradiation examination facilities have been effectively utilized for obtaining extremely valuable data on in-pile performance of indigenous fuels, structural and shielding materials to aid materials optimisation for future FBRs and life-extension of FBTR. Further, the group has contributed towards developing a spectrum of Non-Destructive Evaluation (NDE) techniques for inspection, qualification and surveillance of large-sized and intricate reactor components both during their fabrication and while they are in service. The NDE expertise is offered not only for FBRs but also for PHWRs, aerospace, defense and other industries. The group has also made contributions towards assessment of weldability of alloys and development of advanced welding techniques for joining special materials, with tight control over process parameters and component integrity. The extensive facilities for evaluation of mechanical properties of FBR materials include small specimen testing techniques and evaluation of mechanical properties in severe environments such as dynamic sodium and steam under multi-axial loading. On the theoretical front, modeling protocols for predicting high temperature phase stability, thermophysical properties, deformation behavior and mechanical properties of materials under various loading conditions etc. are being pursued. MMG houses state-of-the-art materials characterization facilities that have been employed for catering to materials development issues of fission and fusion nuclear reactors. In 2020, a state-of-the-art ultra high resolution analytical transmission electron microscope, corrected for probe spherical aberration and fitted with a Wien filter type monochromator, with a point resolution of 53 pm in STEM mode and energy resolutions of 990 and 160 meV without and monochromator, respectively has been installed and commissioned. MMG houses advanced facilities for corrosion studies and corrosion monitoring and is involved in corrosion control and prevention activities include estimation of corrosion behavior of structural materials and concrete structures of reactor systems and reprocessing plants. Recently a state-of-the-art chemical vapor deposition facility for coating pyrolytic graphite on high density graphite crucibles used in pyro processing applications have been commissioned. Besides a unique atmospheric plasma spray (APS) and high velocity oxy fuel (HVOF) system is used for high temperature ceramic coatings for pyrochemical reprocessing applications. Presently, MMG is also closely working with M/s BHEL and M/s NTPC for Government of India's Mission Project on Development of Advanced Ultra Super Critical Power Plant (AUSCPP) to develop materials, fabrication and inspection technologies and to generate material data base required for design and construction of the first AUSCPP in the country. Due to its focussed and balanced developmental efforts, the Group is able to sustain vibrant HBNI academic programmes at the Centre for students and research fellows pursuing M.Tech. and doctoral degrees respectively. The Metallurgy and Materials Group thus maintains a seamless synergy between academic, research and technological developmental activities.

Reactor Design & Technology Group



Shri S. Raghupathy
Director, RDTG



Ms. R. Vijayashree
AD, NSDG



Dr. B. K. Nashine
AD, SFG



Dr. S. Murugan
AD, CD&HG



Shri Jose Varghese
Head, CH&MD



Shri Sriramachandra Aithal
Head, RC&AD



Dr. K. Devan
Head, RND



Dr. A. John Arul
Head, RS&DD



Shri U. Parthasarathy
Head, SHTD



Dr. B. Babu
Head, DD&RSD



Shri V. A. Suresh Kumar
Head, RIOD



Shri V. Vinod
Head, ETHD



Shri Joseph Winston
Head, RH&IED



Dr. B. K. Sreedhar
Head, SE&HD



Shri S. Jalaldeen
Head, SMD



Shri S. Tanmay Vasal
Head, PPCD



Shri K. Natesan
Head, THD

Reactor Design & Technology Group (RDTG) is responsible for the design, structural & thermal hydraulics analysis, core safety & plant dynamics analysis, structural mechanics including seismic testing, manufacturing technology development, engineering development, testing and qualification of Fast Breeder Reactor (FBR) components/systems. In addition, the responsibility of RDTG includes: Development of In service inspection devices & remote handling equipment for FBRs & FBR fuel reprocessing plants, Development of sensors & devices for sodium applications, Planning of irradiation experiments for testing of various fuel, structural and shielding materials

in FBTR, Design, development & fabrication of various irradiation devices for experiments in FBTR, Out-of-pile testing, precision machining and welding of miniature components and planning & execution of Shielding / Foil Activation experiments in KAMINI reactor. RDTG has expertise in design & engineering development of various systems/components of FBRs covering the Nuclear Steam Supply Systems (NSSS) and Balance of Plant (BoP) systems viz. Reactor Physics & Core Engineering, Reactor Assembly, Absorber Rod and Component Handling Mechanisms operating in sodium, Primary & Secondary Sodium Heat Transport Systems, Decay Heat Removal systems, Tertiary Steam Water Systems, Various Plant Auxiliary Systems, Electrical Power Systems, Plant Layout, Sodium Pumps, Electromagnetic Pumps, Cold Trap and Ultrasonic devices for use in sodium. RDTG has indigenously developed the design of Prototype Fast Breeder Reactor (PFBR) of 500 MWe capacity based on its design & analysis expertise, R&D program, technology development exercise and with the support from and in association with various other groups of IGCAR. The group is extending its technical support and design expertise to the PFBR project which is under commissioning by BHAVINI and is responsible for getting design safety clearances for PFBR from the Atomic Energy Regulatory Board (AERB). It also provides analytical support to other groups in the Centre. RDTG constantly provides the design and analytical expertise for the continuous enhancement of fuel & core performance of the Fast Breeder Test Reactor (FBTR) and operation at higher powers and higher operating temperatures focusing on the core engineering design, plant dynamics and core safety analysis. RDTG also plays a major role in the development of future Metallic fuel and has designed the metal fuel pins of different designs and fuel compositions for irradiation testing.

Design validation of critical components of FBRs are achieved through testing in sodium and in water using scaled down/full scale models. RDTG has acquired expertise in the development of sensors and devices for sodium applications, such as electromagnetic flow meters, level probes and leak detectors. Expertise has also been developed in handling of sodium and in the design, construction, commissioning & operation of various high temperature sodium test loops/facilities. The major sodium test facilities of RDTG include 5.5 MWt Steam Generator Test Facility (SGTF) for testing model steam generators of FBRs, SADHANA loop for experimentally demonstrating natural convection based safety grade decay heat removal system, Large Component Test Rig (LCTR) for testing critical full scale components, In Sodium Test facility (INSOT) for creep and fatigue testing of advanced materials, Sodium Water Reaction Test (SOWART) facility to study self wastage & impingement wastage of Steam Generator tubes and a state-of-art Sodium Facility for Component Testing (SFCT) for testing small and medium sized components and sensors. To meet the requirements of future FBRs, a new facility called Sodium Technology Complex is under execution.

Recent achievements of RDTG: Compression & flexure testing of enriched B4C pellets for FBTR poison rods, Hydraulic validation of Poison subassembly for FBTR, Decay heat measurements of structural material in KAMINI, Technical support towards rectification of LRP bearing, Evaluation of rotor dynamic coefficients of sodium pumps through CFD analysis, Simulation of pressure transient under turbine trip event, Performance and endurance testing of 50 m³/h Annular linear induction pump, Design and manufacture of additional nickel detectors for steam generator tube leak detection system of PFBR, Experimental verification of methodology in simulating neutron count rates with 0.1 cps/nv HTFC during initial fuel loading of PFBR, Seismic PSA study for PFBR, Study on the effect of orientation of PFBR fuel subassembly on response of gamma detector in FIZID system, Estimation of guard pipe compartment bellows, Vibration analysis of IHX downcomer, Stability analysis of secondary sodium pump, Vibration limits for ALIP in secondary sodium fill & drain circuit, Design and thermal hydraulic analysis of secondary sodium based decay heat removal system for FBR 1&2, Improved severe accident analysis in SFRs using slug-ejection model, Integrated steady and transient pool hydraulic analysis of primary sodium circuit, Numerical methodology for estimation of asymptotic crack size and comparison with A16 master curve prediction, Numerical analysis of hydrostatic bearing of large sodium pump using ARMD software, Numerical analysis of dynamic seals used in CSRDM, Testing of large sized bellows in sodium environment, Parametric studies to assess the bonding quality of sodium compatible ultrasonic transducers, Sensitivity evaluation of 100 NB permanent magnet flowmeters in sodium, Development and manufacture of 200 NB sidewall permanent magnet flow meter, Development of non-return valves for sodium service, Improvements in regeneration of sodium cold trap by altering geometry of wire mesh top plate, Simulation of gas entrainment phenomena inside FFLM, Finalisation of calibration scheme for eddy current flow meter of primary sodium pump, Performance evaluation of wire type leak detector layout for dished end test section in LEENA facility, Design & development of Reactor core viewing system (RCVS), Design, analysis and development of pressure decay method leak measurement system using mems based pressure sensor and Transfer & safe transportation of 3T of indigenously manufactured sodium from Baroda to Kalpakkam.

Besides providing technical support to PFBR, RDTG is currently engaged, in the development of future FBRs incorporating enhanced safety and improved economy. It has finalised the conceptual design of the future FBR and is currently undertaking the development of key systems and components and detailed engineering. Further, RDTG has evolved the preliminary conceptual design of a metal fuelled 100 MWt test reactor, planned to be

launched after FBTR. These apart, it has a modern design office with many advanced modeling and analysis softwares, experimental facility for testing major Reactor Assembly systems, Structural Mechanics Laboratory (SML) having state-of-the-art facilities for carrying out tests at component level to verify structural integrity at high temperature and a 100 t shake table with six degrees-of-freedom for seismic tests. The shake table is extensively used for the design validation of reactor systems and components of Nuclear Power Plants of NPCIL and other research projects undertaken by BARC.

RDTG also plays a major role in developing highly competent human resources by undertaking academic courses for the various science and engineering disciplines through the BARC Training Schools located at Mumbai, at IGCAR, Kalpakkam and at NFC, Hyderabad and provide guidance to many employees / students / JRF & SRF in their Post graduate, Ph.D and Research Programs.

Reactor Facilities Group



Shri K. V. Suresh Kumar
Director, RFG



Shri A. Babu
AD, OMG



Shri M. S. Chandrasekar
Head, THRDD



Shri K. Dinesh
Head, TSD



Shri G. Shanmugam
Head, RMD



Shri N. Manimaran
Head, ROD

The Reactor Facilities Group (RFG) is responsible for safe operation of Fast Breeder Test Reactor (FBTR), KAMINI Reactor and Interim Fuel Storage Building (IFSB). FBTR is presently rated for operating at a power level of 32 MWt. Towards raising FBTR power level to its design power level of 40 MWt using Mark-I subassemblies and introducing poison subassemblies, a preliminary safety report is prepared and submitted to Regulatory body and it is under review. Progressive modifications are being carried out in FBTR to increase its availability and for gaining newer experience in operation. All post Fukushima & Seismic retrofitting were completed and FBTR is relicensed to operate upto June 2023. Utilizing the reactor for irradiation of advanced fuels and materials for fast reactors and conducting safety related experiments form a major part of RFG's activities. KAMINI Reactor is extensively used for neutron radiography activation studies and testing of neutron detectors. RFG is also responsible for fabrication and safe storage of fuel, blanket and control subassemblies for PFBR and required number of these subassemblies for the first core is fabricated and stored in IFSB. The Training section of the group is responsible for training the O&M staff of PFBR and future FBRs besides training of newly recruited category I & II trainees of IGCAR. The group also takes part in the operational safety review of PFBR project.

Reprocessing Group



Dr. K. Ananthasivan
Director, RpG



Shri K. Rajan
Head, DFRPD



Shri. M. Dhananjeyakumar
Head, RpMD (EEI&C)



Shri. M. Geo Mathews
Head, RpMD (M)



Dr. R. V. Subba Rao
Head, PRCD



Shri Shekhar Kumar
Head, RPOD



Dr. K.A. Venkatesan
Head, RR&DD

The Reprocessing Group at IGCAR has the primary mandate to establish advanced technology for the reprocessing of advanced fast reactor fuels. The major activities in progress in the Group include, design, construction, commissioning and operation of the fast reactor fuel reprocessing plants, development of novel processes and equipment and carrying out the R&D associated with the same. This group comprises the CORAL (Compact facility for Reprocessing Advanced fuels in Lead cells) facility, the Demonstration fast reactor Fuel Reprocessing Plant (DFRP), and a research facility for carrying out advanced research on fast reactor fuel reprocessing. The CORAL facility was commissioned in 2003, continues to operate successfully, processing the mixed carbide spent fuel from FBTR. The facility continues to serve as a test bed and has provided valuable feedback for the design and construction of future reprocessing plants. CORAL has completed its original mandate of reprocessing of FBTR fuel sub assemblies and closing the fast reactor fuel cycle and has been further relicensed for a period of five years by the regulatory body, after upgradation of the safety systems. The DFRP is in an advanced stage of commissioning and the Acid-TBP runs and cold runs with uranium would be taken up shortly. Yet another commercial scale plant suitable for processing the fuel discharged from PFBR is being constructed at the Fast Reactor Fuel Cycle Facility. The responsibility of design, construction and commissioning rests with RpG. In addition the group also lends its expertise in procurement of long delivery items such as the optical glass slabs for radiation shielding windows, various types of master slave manipulators, lead bricks etc. Concurrently focused R&D is being pursued to develop equipment, alternate processes and aqueous processing of metallic fuel.

Safety, Quality & Resource Management Group



Dr. B. Venkatraman
Director, SQRMG



Shri S. Athmalingam
AD, HSEG & Head, QAD



Dr. T. S. Lakshmi Narasimhan
CEO, AIC



Dr. D. Ponraju
Head, SED



Dr. M. T. JOSE
HEAD, HISD



Dr. R. Venkatesan
HEAD, RESD



Ms. S. Rajeswari
Head, SIRD



Dr. Vidya Sundararajan
Head, P&HRMD

The mandate of Safety, Quality & Resource Management Group (SQRMG) is to manage Health Physics, Radiation Safety and Quality Assurance services, studies on Environment Impact Assessment, Severe Accident & Sodium Fire and management of resources like Financial (Budget), Human, Scientific Information services and conduct Academic Programmes of BARC Training School at IGCAR. Health, Safety & Environment Group (HSEG) comprises of Radiological & Environmental Safety Division (RESD), Health & Industrial Safety Division (HISD), Safety Engineering Division (SED) and Quality Assurance Division (QAD). RESD is responsible for providing radiation safety services such as TLD personal monitoring, Bio assay, Bio dosimeter and Whole body counting services to all the occupational workers of the Centre. It also focuses on R&D activities in the areas of atmospheric dispersion and modeling, sodium aerosol science and technology, luminescence dosimetry, radiation safety through modeling & simulation and societal applications of ionizing and non ionizing radiations. HISD provides radiological protection and surveillance of all active plants and also services to meet the mandatory requirements of AERB (such as industrial and occupational health safety) to related projects of IGCAR. SED is carrying out studies on Severe Accident and Sodium Fire Safety. The major experimental facilities are THEME and SOFI for simulation of Molten Fuel Coolant Interaction, PATH facility for post accident heat removal studies, MINA and SOCA facilities for sodium fire studies and SFEF for large scale sodium fire and severe accident studies. QAD is primarily responsible for catering to the quality assurance, inspection, Non-Destructive Testing

(NDT) and quality audit activities during fabrication, construction & erection of System, Structure & Equipments for various Groups of our Centre in order to establish and implement an effective quality management system. QAD also extends its expertise to other DAE units and other strategic sectors. HSEG organizes public awareness programmes on radiation safety and nuclear energy in addition to training and awareness programmes on industrial, radiation and fire safety to occupational workers. The Covid-19 related R&D is another most significant achievement during this period. Technical Co-ordination & Quality Management Section (TC&QMS) is primarily responsible for quality control of several critical equipments for IGCAR manufactured in the western region of the country and provides technical co-ordination services for the centre with BARC as well as the DAE, Mumbai. TC&QMS also participates in R&D activities which are being carried out at BARC towards meeting the mandate of IGCAR, FRFCF/NRB and PFBR.

The significant activities of PHRMD are planning and human resource management, conducting the academic programmes of BARC Training school at IGCAR and stipendiary trainees, formulating and monitoring capital projects towards budget planning and management, facilitating induction of Research Scholars, Research Associates and Visiting Scientists, coordinating the visits of important dignitaries and delegations to the Centre, formulating and facilitating collaborations and MoU including patents and piloting the activities relating to technology transfer.

Scientific Information Resource Division (SIRD) is the second-largest research library in DAE, with about 62,000 books, 48,000 back volumes, 600 journals, 15,000 standards, and two lakh technical reports. SIRD caters to the needs of more than 5000 Scientists, Engineers, Research Scholars, and students of various DAE Units at Kalpakkam. SIRD maintains the centralized institutional repository, the preprint server, and the RFID-based Library Resources databases. Dissemination of resources is through WebOpac, and remote access is through a mobile app. SIRD provides various services like photography, videography, reprography, content creation, auditorium, desktop design, and publication assistance. SIRD has played a vital role in documenting the biodiversity.

An Incubation Centre has been set up at IGCAR to promote and incubate the spin-off technologies from IGCAR. A team has been formed to meet the objectives, set up the necessary infrastructure and to interface with various Groups at IGCAR.

Madras Regional Purchase Unit



Shri G. Padmakumar
RD, MRPU

Madras Regional Purchase Unit (MRPU) is one of the Regional Units of the Directorate of Purchase & Stores, Mumbai. The Material Management activities for IGCAR, GSO, BARCF, AERB southern regional units & HWP, Tuticorin are carried out by MRPU, Chennai. Procurement of goods, supplies and payment to suppliers are handled at Chennai and inventory and accounting are carried out by Central Stores at Kalpakkam and Tuticorin. The procurement activities for the major projects like FRFCF, INRPK, AUSC are being carried out by MRPU. Procurement is carried out through e-tendering system and through the Government e-market place (GeM). MRPU also enters into rate contracts for various medicine and drug purchase for the hospitals at Kalpakkam and other DAE units across the country. During the year 2019, MRPU processed about 2600 indents, released about 2100 purchase orders worth 355 crores. There are about 130 personnel from DPS employed in Purchase, Stores, Administration and Accounts. Another 15 from IGCAR, BARCF and HWPT provide technical and auxiliary support.

Administration & Accounts



Shri O.T. G. Nair
Director (P&A)



Shri M. S. Saravanan
IFA



Shri V. Sivakumar
IFA[FRFCF]



Shri K. Sai Kannan
DCA



Smt S. Jayakumari
AO (E)



Shri Paresh Nath Mahadani
AO (R&V)



Shri R. Srinivasan
AO (L&G)

INDIRA GANDHI CENTRE FOR ATOMIC RESEARCH

Dr. Arun Kumar Bhaduri
Director, IGCAR

IGC Council

IGC Scientific Committee
[IGSC]

Programme Review & Monitoring
Committee [PRMC]

Dr. B. Venkatraman
Director
Engineering Services Group
and Safety, Quality &
Resource Management Group

Shri S. Raghupathy
Director
Reactor Design & Technology Group

Shri K. V. Suresh Kumar
Director
Reactor Facilities Group

Smt. T. Jayanthi
Director
Electronics & Instrumentation Group

Dr. K. Ananthasivan
Director
Reprocessing Group

Dr. N. Sivaraman
Director
Materials Chemistry & Metal Fuel Cycle Group

Dr. Shaju K. Albert
Director
Metallurgy & Materials Group
and Materials Science Group

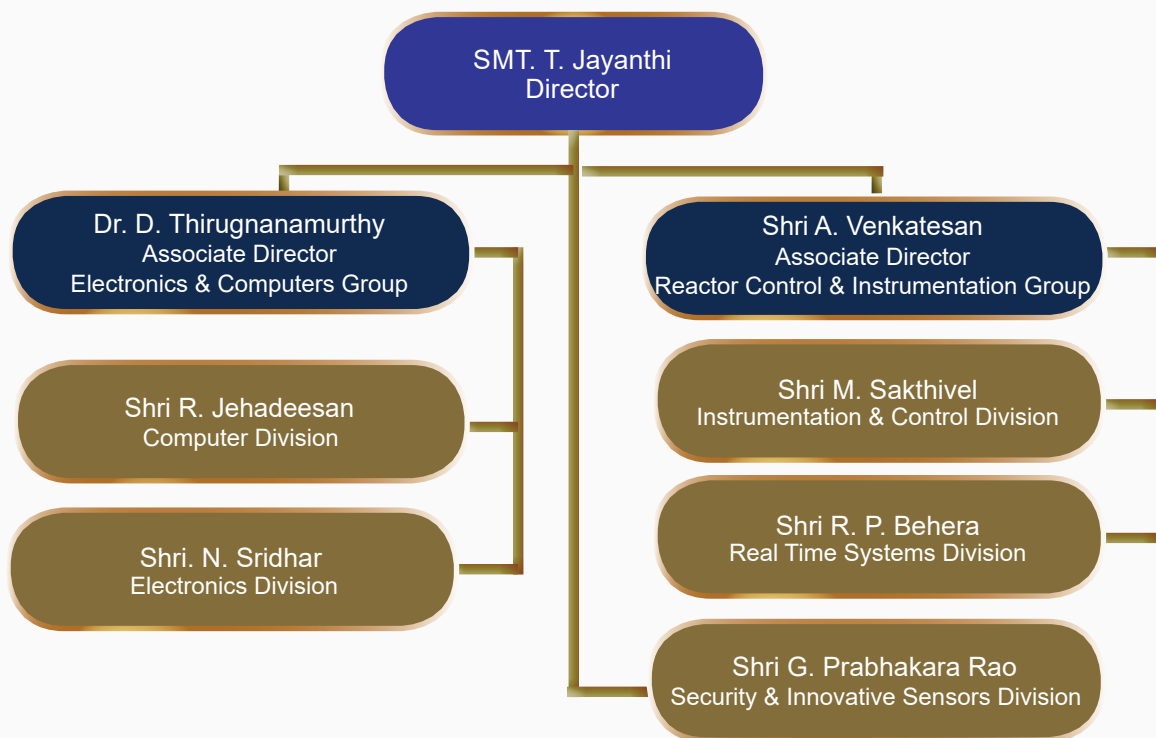
Dr. B. Purna Chandra Rao
Director
Fast Reactor Fuel Cycle Facility

Shri O.T. G. Nair
Director (P&A), Administration

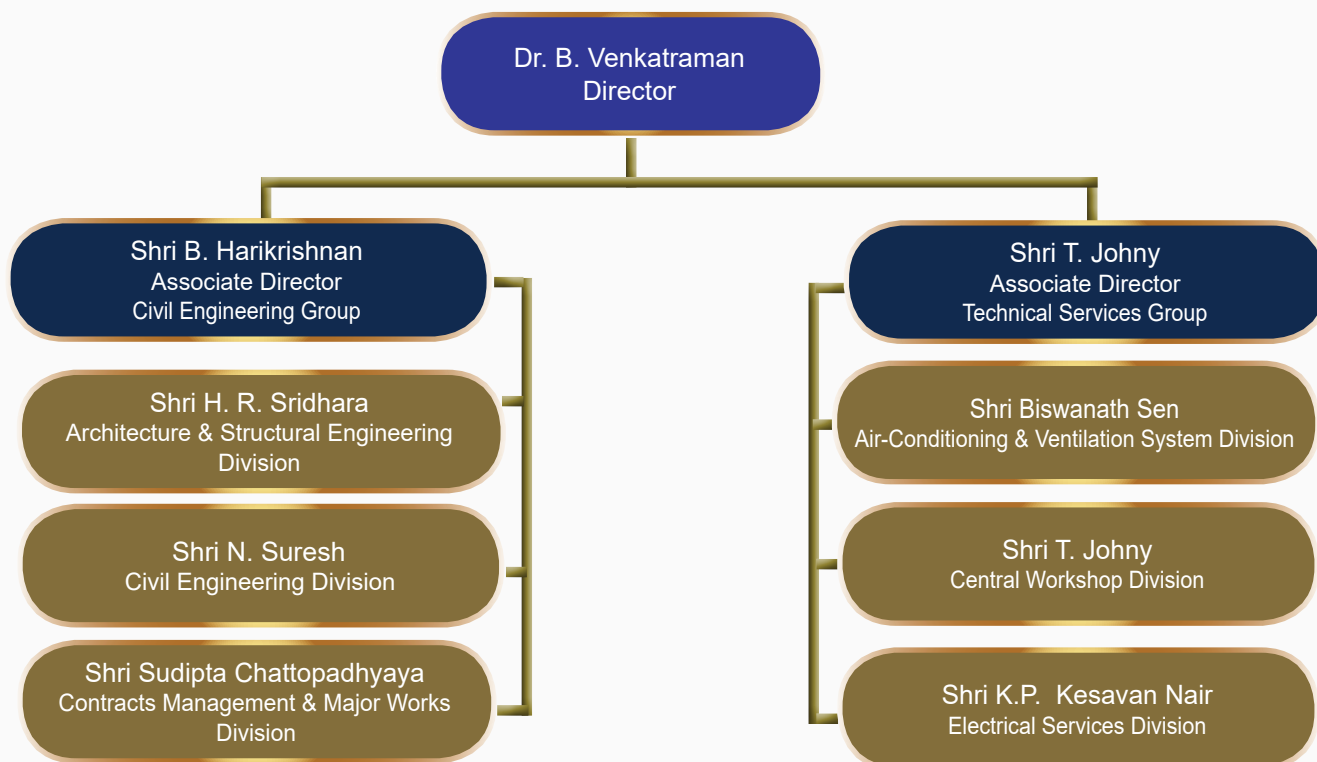
Shri M. S. Saravanan
IFA, IGCAR

Shri V. Sivakumar
IFA [FRFCF]

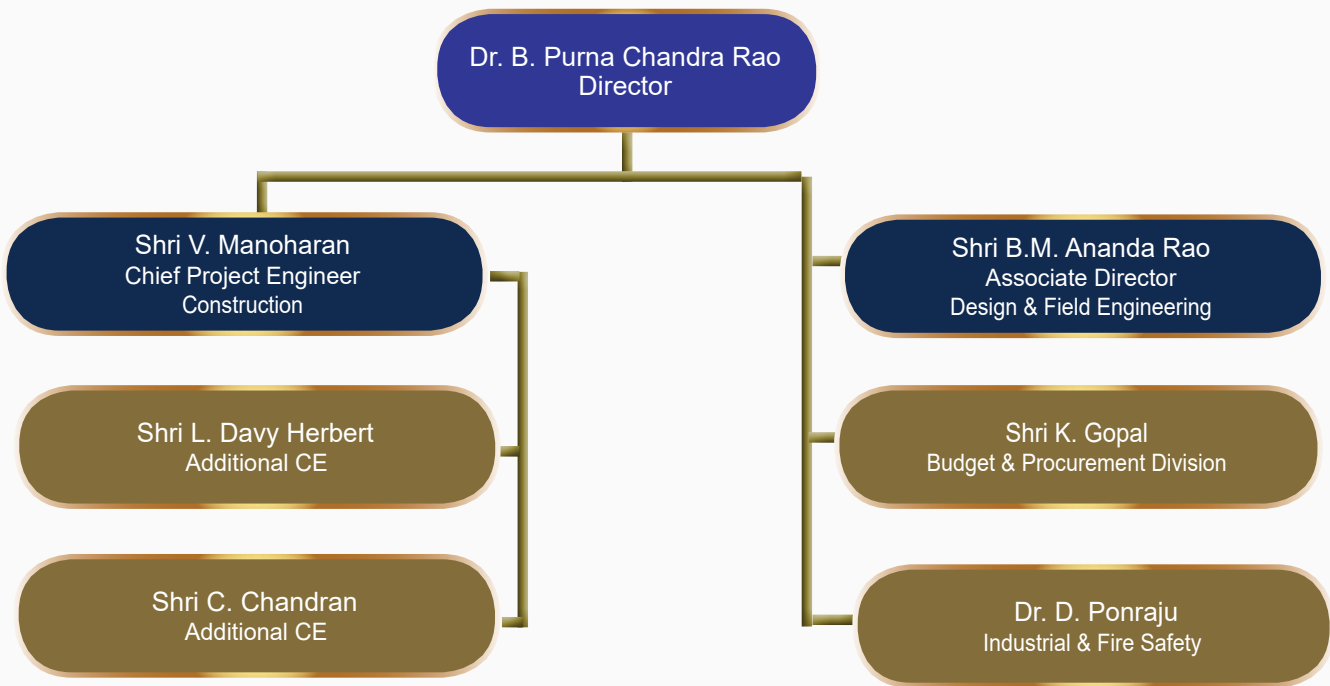
Electronics & Instrumentation Group



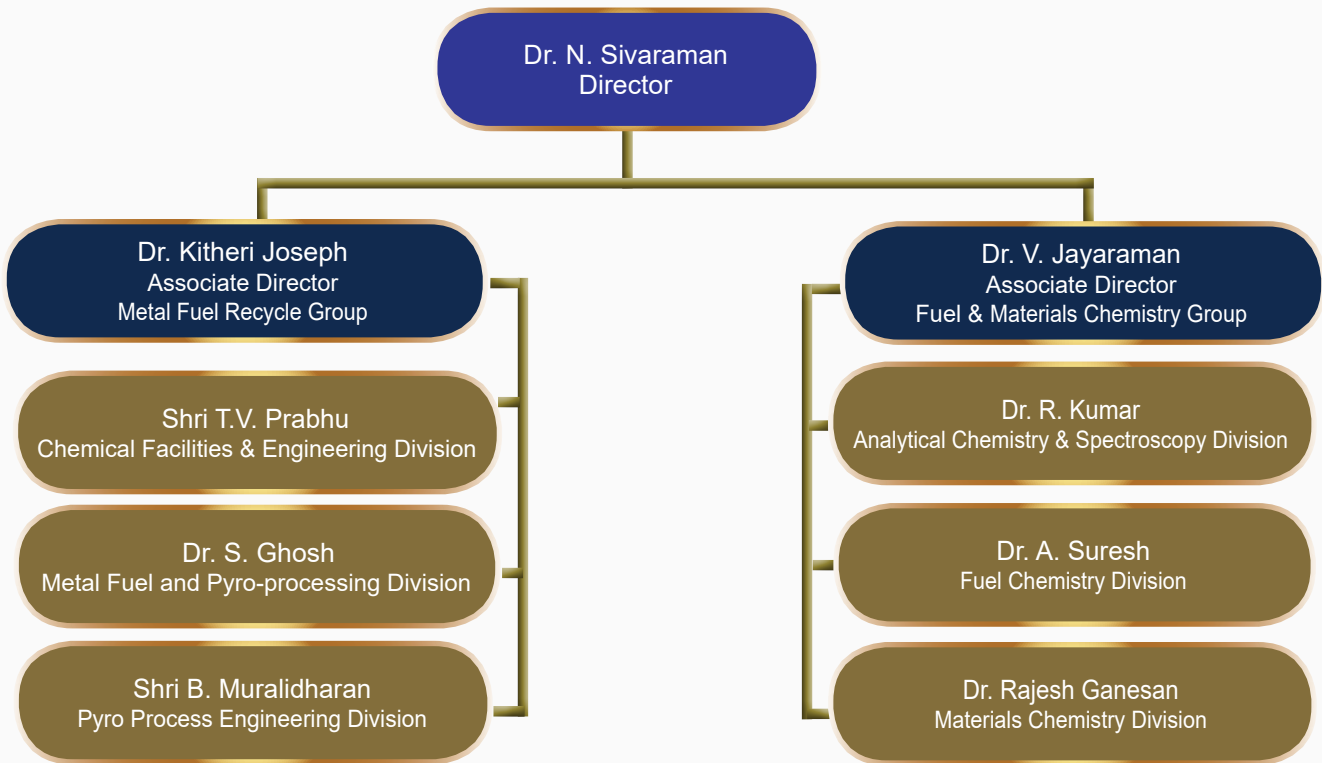
Engineering Services Group



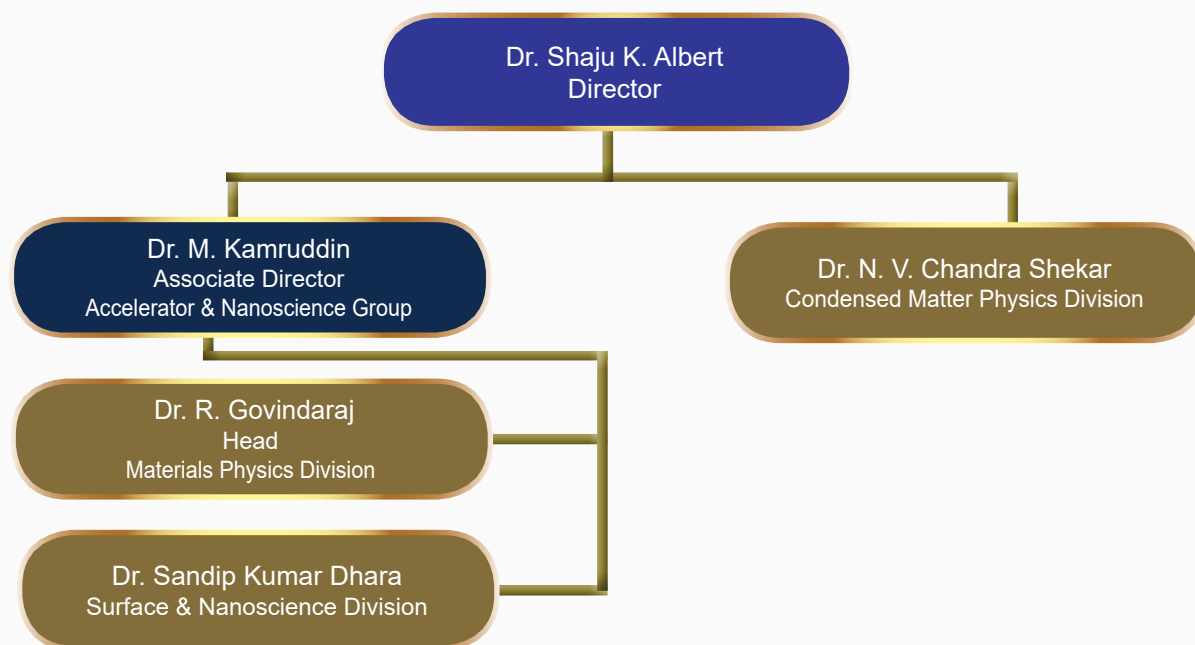
Fast Reactor Fuel Cycle Facility



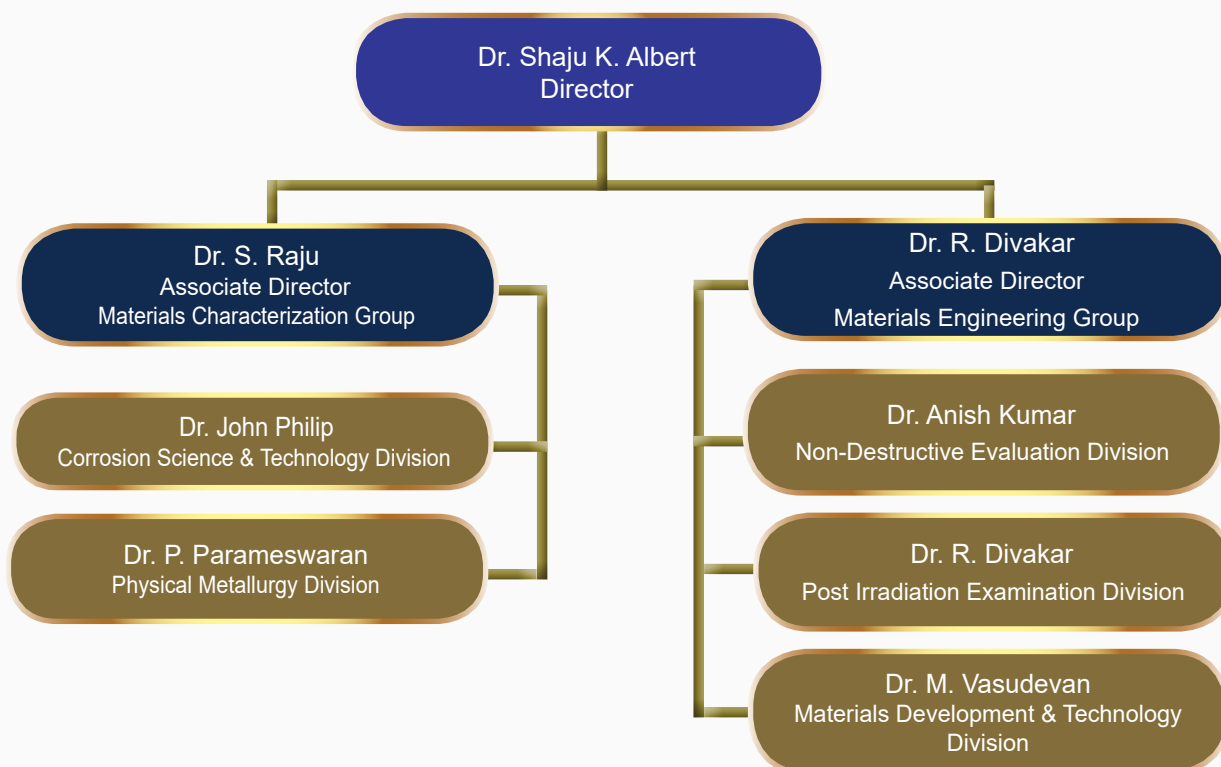
Materials Chemistry & Metal Fuel Cycle Group



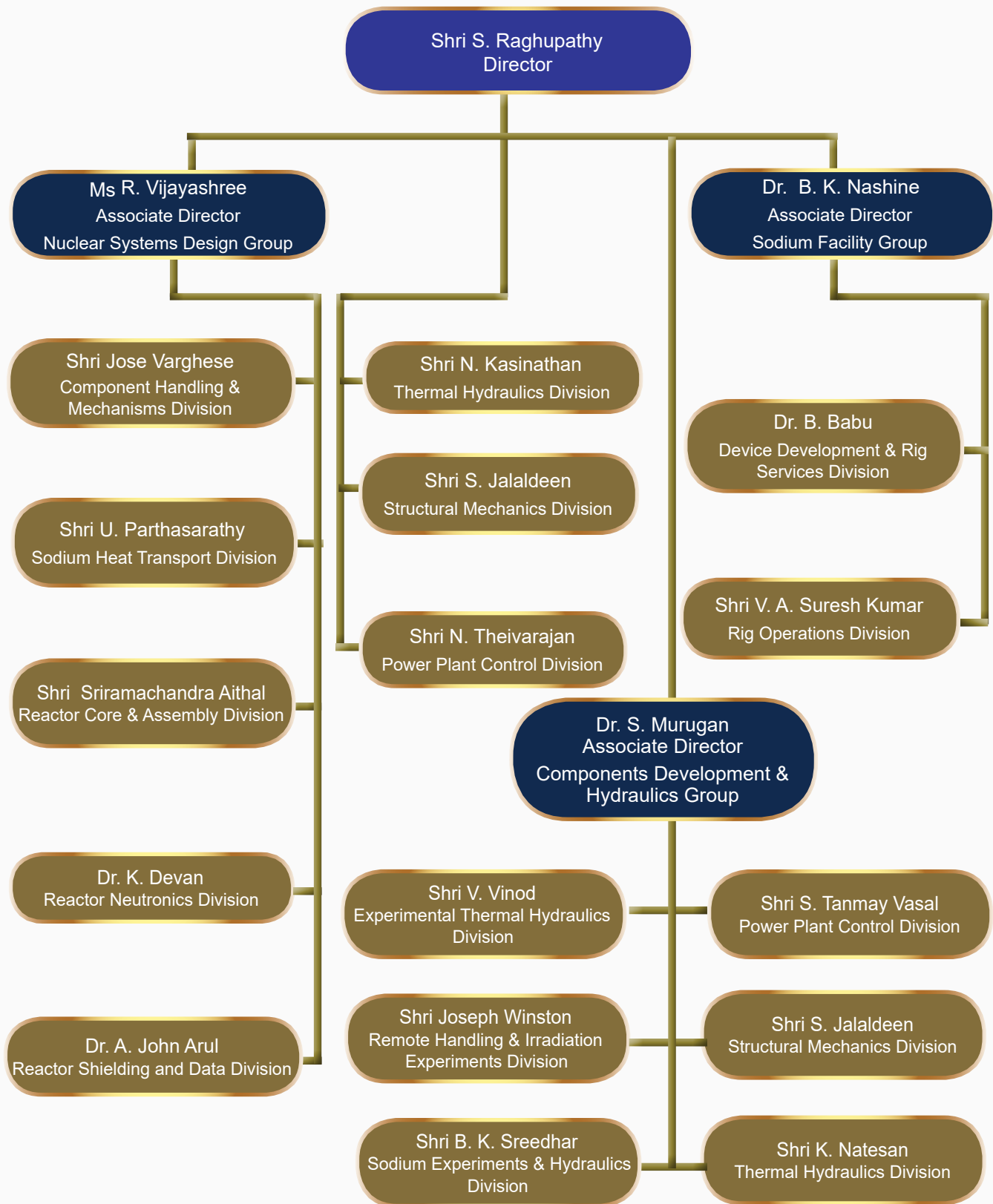
Materials Science Group



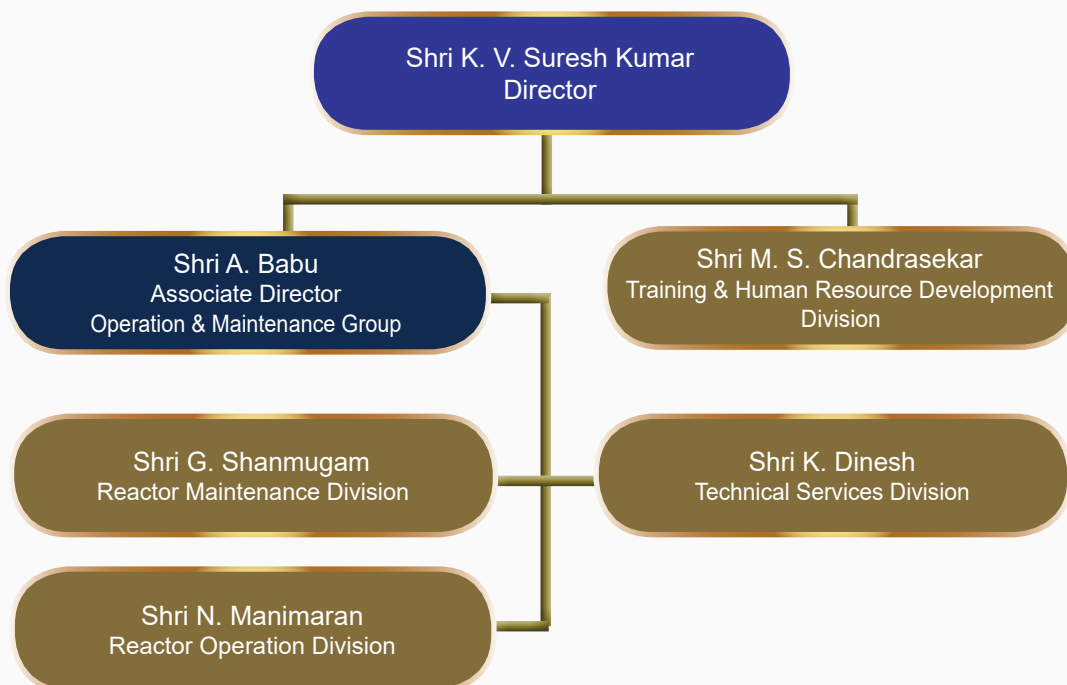
Metallurgy & Materials Group



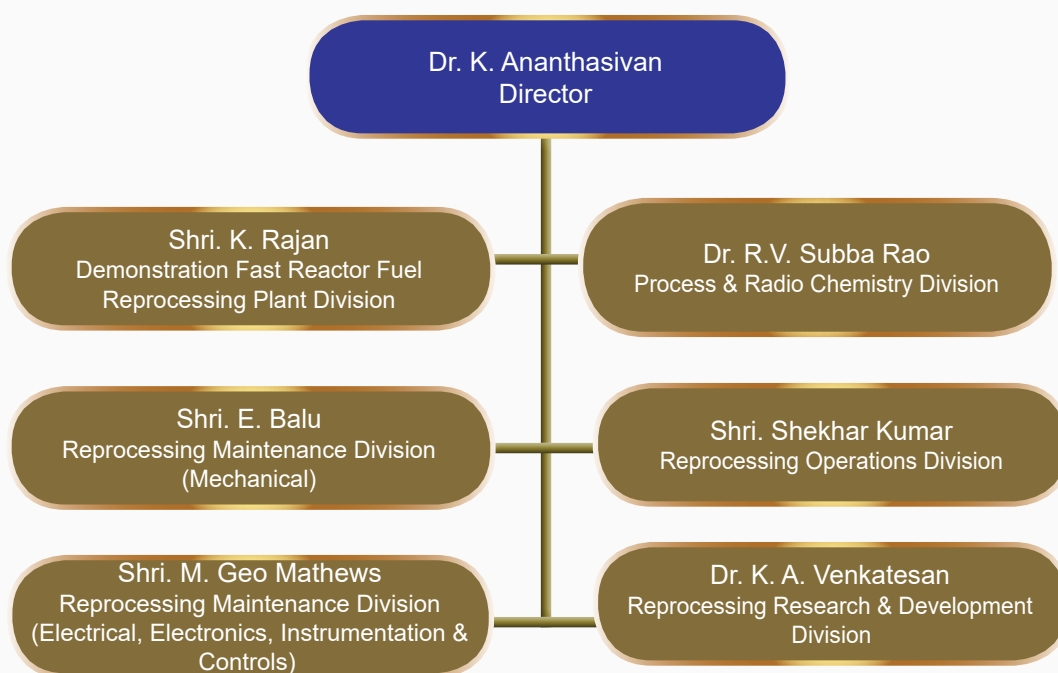
Reactor Design & Technology Group



Reactor Facilities Group



Reprocessing Group



Safety, Quality & Resource Management Group

Dr. B. Venkatraman
Director

Shri S. Athmalingam
Associate Director
Health, Safety & Environment Group

Dr. T. S. Lakshmi Narasimhan
CEO
Incubation Centre

Shri S. Athmalingam
Quality Assurance Division

Dr. Vidya Sundararajan
Planning & Human Resource Management
Division

Dr. D. Ponraju
Health & Industrial Safety Division &
Safety Engineering Division

Smt. S. Rajeswari
Scientific Information Resource Division

Dr. R. Venkatesan
Radiological & Environmental Safety Division

Dr. N. Subramanian
Manager, Incubation Centre

Administration

Shri O.T. G. Nair
Director (P&A)

Shri R. Srinivasan
Administration (Legal & General)

Shri Paresh Nath Mahadani
Administration (Recruitment & Vigilance)

Smt. S. Jayakumari
Administration (Establishment)

Accounts

Shri M.S. Saravanan
IFA

Shri V. Sivakumar
IFA [FRFCF]

Shri K. Sai Kannan
DCA

LIST OF IMPORTANT ABBREVIATIONS

AC&VSD	Air Conditioning and Ventilation System Division	MFPG	Metal Fuel and Pyroprocessing Division
AERB	Atomic Energy Regulatory Board	MMG	Metallurgy and Materials Group
A&SED	Architecture & Structural Engineering Division	MPD	Materials Physics Division
ANG	Accelerator & Nanoscience Group	MRPU	Madras Regional Purchase Unit
BARC	Bhabha Atomic Research Centre	MSG	Materials Science Group
BARCF	Bhabha Atomic Research Centre Facilities	NDED	Non-Destructive Evaluation Division
BHAVINI	Bharatiya Nabhikiya Vidyut Nigam Limited	NFC	Nuclear Fuel Complex
BP&FED	Budget, Procurement & Field Engineering Division	NICB	Nuclear Island Connected Building
CD	Computer Division	NPCIL	Nuclear Power Corporation of India Ltd.
CED	Civil Engineering Division	NSDG	Nuclear Systems Design Group
CEG	Civil Engineering Group	OMG	Operation & Maintenance Group
CF&ED	Chemical Facilities & Engineering Division	PFBR	Prototype Fast Breeder Reactor
CH&MD	Components Handling & Mechanism Division	P&HRMD	Planning & Human Resource Management Division
CMPD	Condensed Matter Physics Division	PHWR	Pressurized Heavy Water Reactor
C&MWD	Contracts & Major Works Division	PIED	Post Irradiation Examination Division
CORAL	Compact facility for Reprocessing Advanced fuels in Lead cell	PMD	Physical Metallurgy Division
CSTD	Corrosion Science & Technology Division	PPCD	Power Plant Control Division
CWD	Central Workshop Division	PPED	Pyro Process Engineering Division
DDRSD	Device Development and Rig Services Division	QAD	Quality Assurance Division
DFE	Design & Field Engineering	RCAD	Reactor Core & Assembly Division
DFRFRPD	Demonstration Fast Reactor Fuel Reprocessing Plant Division	RD&TG	Reactor Design & Technology Group
DFRP	Demonstration Fuel Reprocessing Plant	R&ESD	Radiological & Environmental Safety Division
ED	Electronics Division	RESG	Radiological & Environmental Safety Group
EIG	Electronics and Instrumentation Group	RH&IED	Remote Handling & Irradiation experiments Division
ESD	Electrical Services Division	RMD	Reactor Maintenance Division
ESG	Engineering Services Group	RND	Reactor Neutronics Division
ETHD	Experimental Thermal Hydraulics Division	ROD	Reactor Operation Division
FBR	Fast Breeder Reactor	RFG	Reactor Facilities Group
FBTR	Fast Breeder Test Reactor	RpMD	Reprocessing Maintenance Division
FChD	Fuel Chemistry Division	RpG	Reprocessing Group
FRFCF	Fast Reactor Fuel Cycle Facility	RpOD	Reprocessing Operation Division
HISD	Health & Industrial Safety Division	RRDD	Reprocessing Research and Development Division
HSEG	Health, Safety & Environment Group	RSDD	Reactor Shielding and Data Division
GSO	General Services Organisation	RTSD	Real Time Systems Division
IAEA	International Atomic Energy Agency	RC&IG	Reactor Control & Instrumentation Group
IIT	Indian Institute of Technology	SED	Safety Engineering Division
IMSc	Institute of Mathematical Sciences	SE&HD	Sodium Experiments & Hydraulics Division
I&CD	Instrumentation & Control Division	SFG	Sodium Facility Group
MAPS	Madras Atomic Power Station	SHTD	Sodium Heat Transport Division
MCG	Materials Characterization Group	SIRD	Scientific Information Resource Division
MC&MFCG	Materials Chemistry & Metal Fuel Cycle Group	SISD	Security and Innovative Sensors Division
MCD	Materials Chemistry Division	SMD	Structural Mechanics Division
MDTD	Materials Development & Technology Division	SND	Surface and Nanoscience Division
MEG	Materials Engineering Group	SQRMG	Safety, Quality & Resource Management Group
F&MCG	Fuel & Materials Chemistry Group	THD	Thermal Hydraulics Division
MFFD	Metal Fuel Fabrication Division	THRDD	Training & Human Resource Development Division
		TSD	Technical Services Division
		TSG	Technical Services Group

Annual Report Editorial Team



Ms. S. Rajeswari
Chairman



Dr. V. S. Srinivasan
Secretary



Dr. John Philip



Dr. T. R. Ravindran



Dr. C.V.S. Brahmananda Rao



Shri A. Suriyanarayanan



Shri Biswanath Sen



Shri M. S. Bhagat



Shri G. Venkat Kishore



Dr. Girija Suresh



Shri M. Rajendra Kumar



Shri S. Kishore



Dr. N. Desigan

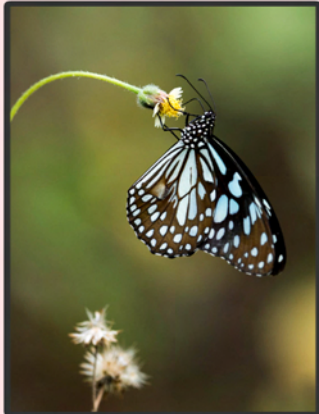


Shri Gaddam Pentaiah



Shri K. Varathan

Birds and Butterflies at DAE Kalpakkam Complex



GOLDEN JUBILEE (1971-2021)

Published by
**Scientific Information Resource Division, SQ&RMG,
Indira Gandhi Centre for Atomic Research, Kalpakkam-603102**